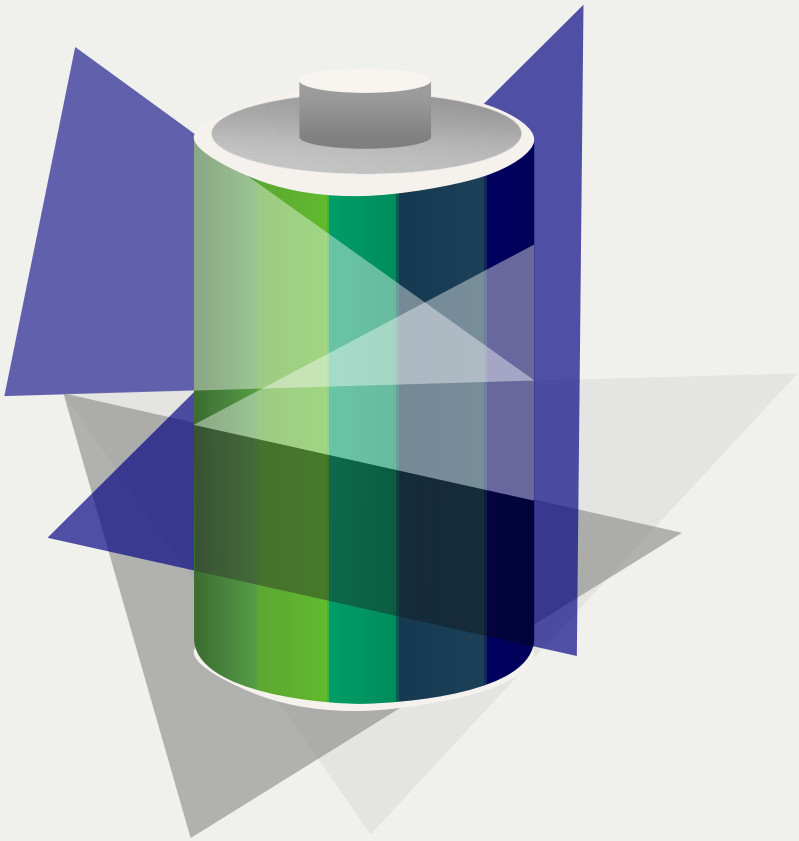
applied
functional
polymers

UNIVERSITÄT
BAYREUTH

Dissertation

Jannik Petry, 2026



The Role of Polymer Architecture in Balancing Ion Transport and Mechanical Stability in Solid Polymer Electrolytes

Dissertation

Zur Erlangung des akademischen Grades eines Doktors der Naturwissenschaften (Dr. rer. nat.)
im Rahmen des Promotionsprogramms Polymer Science der Bayreuther Graduiertenschule für
Mathematik und Naturwissenschaften (BayNAT) der Universität Bayreuth

vorgelegt von

Jannik Petry
geboren in Wiesbaden

Bayreuth, 2026

Die vorliegende Arbeit wurde in der Zeit von März 2020 bis Februar 2026 in Bayreuth in der Arbeitsgruppe für Angewandte Funktionspolymere (AFUPO) unter Betreuung von Herrn Professor Dr. Mukundan Thelakkat angefertigt.

Vollständiger Abdruck der von der Bayreuther Graduiertenschule für Mathematik und Naturwissenschaften (BayNAT) der Universität Bayreuth genehmigten Dissertation zur Erlangung des akademischen Grades eines Doktors der Naturwissenschaften (Dr. rer. nat.).

Form der Dissertation:	Kumulative Dissertation
Dissertation eingereicht am:	02.06.2026
Zulassung durch das Leitungsgremium:	25.06.2026
Wissenschaftliches Kolloquium:	21.10.2026
Amtierender Direktor:	Prof. Dr. Jürgen Senker

Prüfungsausschuss:

Prof. Dr. Mukundan Thelakkat	(Gutachter)
Prof. Dr. André Gröschel	(Gutachter)
Prof. Dr. Georg Papastavrou	(Vorsitz)
Prof. Dr. Josef Breu	

Für Ursula und Ernst

Abstract

Solid polymer electrolytes (SPEs) are considered a promising electrolyte candidate to substitute the flammable liquid systems in next-generation batteries. The key advantages of SPEs are the improved intrinsic safety and compatibility with conversion-type high-energy electrode concepts. Despite these advantages, practical progress is limited by inherent challenges related to the dependence of ion transport on the polymer segmental mobility in general, demanding low glass transition temperatures (T_g) polymer systems to achieve high ionic conductivity. This consequently hampers the mechanical properties of SPEs. Additionally, for the benchmark host material poly(ethylene oxide) (PEO), the strong nature of ether-lithium coordination restrains the cation mobility and results in predominant anion conduction and ion gradients under operation. Carbonyl-based coordination motifs, like esters or carbonates, provide weaker polymer-Li^+ ion interactions and a broad structural variance. Many of these main chain polymers, including PEO and carbonyl-based poly(ε-caprolactone) (PCL), exhibit semi-crystalline properties, leading to reduced amorphous fractions, constrained polymer flexibility at moderate temperatures, and therefore, low ionic conductivity below their melting points.

This dissertation addresses these challenges starting at the monomer level and investigating structural influences on the electrochemical properties on the battery cell level. This strategy aims at establishing structure–property–performance relationships for SPEs. The process begins with rational monomer and polymer design, followed by tailored polymer synthesis to access defined macromolecular architectures. Thermal and structural characterization quantify material properties like the glass transition temperature (T_g), melting behavior, and polymer crystallinity. The correlation between these parameters and the resulting ion transport characteristics is investigated in electrochemical experiments. Subsequently, the translation to cycling behavior and electrode compatibility is evaluated in battery cells.

In the first part of this thesis, ester-containing polymer host materials are explored in a variety of polymer architectures. The macromolecular architecture is used as a central design lever to influence polymer crystallization, glass transition temperatures, and ion-coordination. Grafted, branched, or hyperbranched architectures are of particular interest due to their frustrated polymer packing and suppression of polymer crystallinity. In the first chapter of this thesis, ester-containing polymer analogs in linear and hyperbranched polymer architecture are synthesized and compared in terms of their thermal properties and ionic conductivity. The second chapter focuses on the architectural integration of ester motifs in main chain polyesters, side chain polyesters, and side chain oligoesters. The influence of architectural variation on the thermal properties and ion coordination is investigated in electrolyte systems at a wide range of salt concentrations. Both studies demonstrate the interdependence of polymer architecture, thermal properties, ion-coordination, and resulting electrochemical properties.

The pursuit of higher ionic conductivities is often achieved by lowering the glass transition temperature and suppressing polymer crystallinity. Conversely, the materials can become softer or even liquid-like, introducing challenges for dimensional stability, electrode-electrolyte interface stabilization, cell operation, and ultimately battery lifetime. Therefore, the second part of this thesis expands the scope of polymer design from focusing on the simultaneous improvement of the ionic conductivity and mechanical reinforcement strategies to soft polymer electrolytes. Two studies apply different approaches to soft polymer electrolytes to evaluate the

impact on the mechanical properties and the retention of high ionic conductivity. In the third chapter of this thesis, a comparison of mechanical reinforcement strategies was carried out with a soft PEO-based bottlebrush polymer electrolyte as a model system. The soft polymer is reinforced in different ways: 1) by blending with a high T_g polymer, 2) by filling with nanoparticles, and 3) by block copolymerization with a high T_g polymer segment. These strategies are evaluated and compared in terms of their impact on the thermal and mechanical properties, electrolyte morphology, as well as electrochemical and cycling characteristics.

In the fourth chapter, the key insights of the above studies, including the need for a very soft polymer, the advantage of weakly Li^+-coordinating ester groups, and the necessity of mechanical stabilization, are combined and used to design and synthesize a tailored SPE system. For this, a very low T_g polysiloxane with diester substituents as Li^+-coordination motifs is synthesized. Crosslinking is introduced as a new strategy to provide mechanical stability to this very soft system. The polymer is amorphous in nature, which enabled efficient ion transport, but the electrolyte lacked mechanical integrity due to its soft nature. To introduce mechanical integrity, the polymer is integrated in a semi-interpenetrating network structure using synthesized crosslinking agents, which also have ester functionalities. The combination of the soft and reinforcing constituents retained high ionic conductivity and enabled stable cycling at moderate temperatures.

In summary, this dissertation highlights how the ion transport in solid polymer electrolytes is governed by the interplay between polymer chemistry and macromolecular architecture. The key levers to improve the ionic conductivity are to increase the polymer flexibility by lowering the glass transition temperature and suppressing polymer crystallinity, in combination with reducing the polymer lithium interaction through suitable coordination motifs such as ester groups. At the same time, architecture-dependent factors like packing frustration or coordination-site accessibility need to be considered to enable efficient charge transport. Additionally, the mechanical integrity of soft, low T_g SPE systems needs to be ensured by reinforcement strategies. These must be carefully selected to preserve the ionic conductivity of SPEs. The investigation of this thesis, beginning on the monomer level through polymer design and detailed electrochemical characterization using electrochemical impedance spectroscopy, establishes a framework and practical guiding principles for next-generation solid polymer electrolyte designs.

In the appendix, unpublished data and results from an exploratory study are presented. In addition to the core studies on solid polymer electrolytes, this study focused on the covalent fixing of sulfur in polymer-sulfur composite cathode materials for lithium-sulfur batteries.

Zusammenfassung

Polymer-Feststoffelektrolyte (engl. solid polymer electrolytes, SPEs) gelten als vielversprechende Elektrolyttechnologie, um die brennbaren flüssigen Systeme in Batterien der nächsten Generation zu ersetzen. Die wesentlichen Vorteile von SPEs sind die verbesserte intrinsische Sicherheit und Kompatibilität mit energiedichten, umwandlungsbasierten Elektrodenkonzepten. Trotz dieser Vorteile ist der praktische Fortschritt durch inhärente Herausforderungen begrenzt. Diese sind unter anderem durch die Abhängigkeit der Ionenleitfähigkeit von der Polymerbeweglichkeit bedingt und erfordern Polymersysteme mit niedrigen Glasübergangstemperaturen (T_g), um hohe ionische Leitfähigkeiten zu erreichen. Dies beeinträchtigt folglich die mechanischen Eigenschaften von SPEs. Zusätzlich führt im Referenzsystem Poly(ethylenoxid) (PEO) die starke Ether-Lithium-Koordination zu eingeschränkter Kationen- und einer dominanten Anionenleitfähigkeit, was zu ausgeprägten Gradienten der Ionenkonzentration führen kann. Carbonyl-basierte Koordinationsmotive, wie Ester oder Carbonate, weisen schwächere Polymer-Lithium-Wechselwirkungen und eine große strukturelle Variabilität auf. Viele lineare Polymere, einschließlich PEO und des Carbonyl-basierten Poly(ε-caprolacton) (PCL) weisen semi-kristalline Eigenschaften auf. Dies führt bei niedrigen Temperaturen zu weniger amorphen Bereichen, eingeschränkter Polymerbeweglichkeit, und dadurch zu geringer ionischer Leitfähigkeit unterhalb ihrer Schmelzpunkte.

Diese Dissertation setzt bei diesen Herausforderungen auf der Monomer-Ebene an und untersucht strukturelle Einflüsse auf die elektrochemischen Eigenschaften bis hin zur Batteriezelle. Ziel dieser Strategie ist es, Struktur-Eigenschafts-Performance-Beziehungen für Polymer-Feststoffelektrolyte abzuleiten. Der Prozess basiert auf einem rationalen Design von Monomeren und Polymeren und ist gefolgt von gezielter Polymersynthese zu unterschiedlichen makromolekularen Architekturen. Thermische und strukturelle Charakterisierungsmethoden quantifizieren Materialeigenschaften wie die Glasübergangstemperatur, Schmelzverhalten und Polymerkristallinität. Die Korrelation zwischen diesen Parametern und den daraus resultierenden Ionentransporteigenschaften wird in elektrochemischen Experimenten untersucht. Anschließend werden die Auswirkungen auf das Zyklisierungsverhalten und die Elektrodenkompatibilität in Batteriezellen bewertet.

Im ersten Teil dieser Arbeit werden Ester-basierte Polymere in verschiedenen Polymerarchitekturen untersucht. Die makromolekulare Architektur dient dabei als zentrales Designelement, um Polymerkristallisation, Glasübergangtemperatur und die Ionenkoordination zu beeinflussen. Gepfropfte, verzweigte, oder hyper-verzweigte Architekturen sind dabei von besonderem Interesse, da sie die Packung von Polymerketten und deren Kristallinität stören können. Im ersten Kapitel dieser Arbeit werden Ester-basierte Polymeranaloga in linearer und verzweigter Architektur synthetisiert und hinsichtlich ihrer thermischen Eigenschaften und ionischen Leitfähigkeit verglichen. Das zweite Kapitel konzentriert sich auf unterschiedliche Einbindung von Ester-Koordinationsmotiven in Hauptkettenpolyestern, Seitenkettenpolyestern und kurzen Oligoester-Seitenketten. Der Einfluss der Positionierung der Estergruppen auf die thermischen und koordinativen Eigenschaften wird in Elektrolytsystemen mit unterschiedlichen Salzkonzentrationen untersucht. Diese beiden Studien zeigen die Wechselwirkungen zwischen Polymerarchitektur, thermischen Eigenschaften, Ionenkoordination und den resultierenden elektrochemischen Eigenschaften auf.

Das Erzielen höherer ionischer Leitfähigkeiten wird häufig durch das Absenken der Glasübergangstemperatur und der Unterdrückung der Polymerkristallinität erreicht. Im Gegenzug werden die Materialien jedoch weicher oder weisen sehr niedrige Viskositäten auf. Dies führt zu Herausforderungen in der Formstabilität, der Stabilisierung der Elektroden-Elektrolyt-Grenzfläche, dem Zellbetrieb und der Batterielebensdauer. Daher erweitert der zweite Teil dieser Arbeit den Fokus des Polymerdesigns auf die gleichzeitige Erhöhung der ionischen Leitfähigkeit als auch auf die mechanische Unterstützung von weichen Polymer-Feststoffelektrolyten. In zwei Studien werden unterschiedliche Ansätze verfolgt, um den Einfluss der mechanischen Eigenschaften und die Beibehaltung der ionischen Leitfähigkeit zu untersuchen. Im dritten Kapitel dieser Arbeit werden drei Verstärkungsstrategien in einem Modellsystem aus einem weichen PEO-basierten Flaschenbürstenpolymer verglichen. Dabei wird das weiche Polymer mit einem anderen Polymer mit einem hohen T_g gemischt, mit Nanopartikeln gefüllt, oder mit einem hoch-T_g Polymersegment copolymerisiert. Die Strategien werden hinsichtlich ihres Einflusses auf die thermischen und mechanischen Eigenschaften, die Elektrolytmorphologie und die resultierenden elektrochemischen Eigenschaften evaluiert. Im vierten Kapitel werden die zentralen Erkenntnisse der vorherigen Untersuchungen zusammengeführt. Die Notwendigkeit weicher Polymere, die Vorteile schwacher Ionenkoordination und der Bedarf von mechanischer Stabilisierung werden in einem neuen Polymer-Feststoffelektrolyt berücksichtigt. Dafür wird ein Polysiloxan mit sehr niedrigem T_g und Diester-Substituenten als Lithium-Koordinationsmotive hergestellt. Der Polymerelektrolyt ist amorph und ermöglicht so einen effizienten Ionentransport, weist jedoch keine mechanische Integrität auf. Für die mechanische Unterstützung werden zusätzliche Polymernetzwerke integriert. Dafür wird der Polymer-Feststoffelektrolyt in eine semi-interpenetrierenden Netzwerkstruktur integriert, welches mit Hilfe eines Ester-beinhaltenden Netzwerkbildners etabliert wird. Die Kombination aus weichen und mechanisch unterstützenden Bestandteilen erhält die ionische Leitfähigkeit und ermöglicht zugleich eine stabile Batteriezyklisierung bei moderaten Temperaturen.

Zusammenfassend zeigt diese Dissertation, dass der Ionentransport in Polymer-Feststoffelektrolyten durch das Zusammenspiel von Polymerchemie und makromolekularer Architektur beeinflusst wird. Die zentralen Einflüsse, um die Leitfähigkeit zu erhöhen, sind die Erhöhung der Polymerflexibilität, die Verringerung der Glasübergangstemperatur und die Unterdrückung der Polymerkristallinität in Kombination mit verringerter Polymer-Lithium-Wechselwirkungsstärke durch geeignete Koordinationsmotive. Gleichzeitig müssen auch die Packungsfrustration und die Zugänglichkeit der Koordinationsstellen für einen effizienten Ionentransport berücksichtigt werden. Darüber hinaus ist die mechanische Integrität von weichen Polymersystemen durch geeignete Verstärkungsansätze sicherzustellen, welche die ionische Leitfähigkeit erhalten. Die Untersuchungen dieser Arbeit von der Monomer-Ebene bis hin zur Batteriezelle unter Betrachtung elektrochemischer Eigenschaften etabliert einen Rahmen und praktische Leitlinien für das Design von Polymer-Feststoffelektrolyten.

Im Anhang dieser Arbeit sind weitere nicht veröffentlichte Ergebnisse einer explorativen Studie dargelegt. Diese Studie weicht thematisch von den Kernstudien ab und befasst sich mit der kovalenten Fixierung von Schwefel in Polymer-Schwefel-Composit Kathodenmaterialien für die Anwendung in Lithium-Schwefel Batterien.

Table of Contents

1 Introduction 1

2 Synopsis 71

3 Individual Contributions to Joint Publications 91

I Easily Accessible Linear and Hyperbranched Polyesters as Solid Polymer Electrolytes 97

II Synthesis and Comparison of Main Chain, Side Chain, and Grafted Polyester-based Architectures as Solid Polymer Electrolytes 119

III Comparative Study of the Mechanical Reinforcement by Blending, Filling, and Block Copolymerization in Bottlebrush Polymer Electrolytes 145

IV Semi-Interpenetrating Network Electrolytes Utilizing Ester-Functionalized Low T_g Polysiloxanes in Lithium-Metal Batteries 181

4 List of Publications 221

5 Appendix 223

Danksagung 241

Eidesstattliche Versicherungen und Erklärung 245

1 Introduction

Energy, in all of its forms, is the fundamental driver, from the smallest realms to the scale of the universe and everything in between. The sun provides the Earth with approximately 1350 W m^{-2} a^{-1} and is our primary source of external energy. For millennia, the sun's energy sustained Earth's climate and induced habitable conditions, enabling the photosynthetic production of oxygen and supplying moderate surface temperatures, which resulted in biological growth. However, recent changes in the Earth's atmosphere, primarily due to anthropogenic greenhouse gas emissions, result in a measurable energy imbalance.[1,2] Approximately 1 W m^{-2} a^{-1} is currently being retained within the climate system, leading to a gradual warming of the planet.[3]

While fluctuations occurred regularly over the lifetime of Earth, the current rate and extent of climate change are unprecedented.[1] Carbon dioxide (CO_2) is one of the key greenhouse gases and plays a central role in to global warming. Since the Industrial Revolution, CO_2 concentrations have risen from below 300 ppm to over 400 ppm, the highest since 16 million years.[4] This is largely due to the combustion of fossil fuels for energy production, heating, transportation, and industrial processes. Over 20 years, the total energy supply has risen by 45 % to 622 EJ in 2022.[5] Further increases utilizing today's energy mix would result in disastrous effects and emphasize that a reformation of the energy supply is critical.[5–7] Currently, the main contributions to primary energy are fossil-based. Combined oil, coal, and natural gas constitute 83 % of the energy mix, posing a serious challenge to efforts aimed at reducing greenhouse gas emissions.[6,8] A fundamental shift toward renewable and low-carbon technologies is therefore imperative to prevent further disruption of Earth's energy balance. Sustainable energy sources are already being used; however, the installed production capacity falls short of the projected demand required to keep global warming below 2°C, as agreed by the majority of nations.[9]

The combined renewable global energy potential exceeds the total energy demand many times over. While the exact amount of accessible non-fossil energy (i.e., amount of harvestable energy) is difficult to quantify, realistic estimations under consideration of technological, environmental, and social constraints indicate a sufficient energy supply.[10–12] The main impediment to a paradigm shift is the fluctuating nature of renewable energy availability and the lack of adequate storage mechanisms at different time scales, from minutes to seasonal variation. Possible solutions include mechanical energy storage, power-to-X approaches, or electrochemical energy storage.[13,14]

In recent years, battery research and development have made significant progress and promise huge potential due to scalability, efficiency, and versatility. Batteries can be deployed across a wide range of applications, from small-scale portable devices to large-scale grid installations. Most notably, they represent a viable pathway for the decarbonization of the transport sector, which remains heavily dependent on fossil fuels and has seen the slowest transition toward sustainable energy sources. While the CO_2 emission in the EU for electricity production decreased by 54 % from 1990 to 2023, the emission by the transport sector grew by 23 % in the same time interval.[15] The electrification of the transport sector through battery-powered vehicles offers a direct and immediate strategy to reduce CO_2 emissions. Moreover, grid-connected battery systems are increasingly employed to buffer energy availability fluctuations and enhance grid stability on timescales of hours. As battery technologies continue to advance in terms of energy density, cost, and material sustainability, they are expected to increasingly contribute to a resilient and low-carbon energy future.

1.1 Electrochemical Energy Storage in Lithium-Ion Batteries

1.1.1 Setup of a Battery

Batteries can efficiently store electrical energy in reversible electrochemical redox reactions. The associated energetic difference between the redox states provides the means to utilize the reaction for electrochemical energy storage. Fundamentally, a battery comprises three key components: anode, electrolyte, and cathode (**Figure 1.1**). The anode and cathode are half-cells, i.e., electrodes of different electrochemical potentials. The electrolyte separates the two electrodes and facilitates ionic transfer (salt bridge) but is electrically non-conducting to prevent leakage currents between the electrodes. Operational batteries can consist of complementary materials like current collectors, separators, and additives to improve the battery's performance and safety. During the use of a battery, the high potentials between the anode and cathode can result in the formation of degradation products at the anode (solid electrolyte interface, SEI) and cathode (cathode electrolyte interface, CEI).

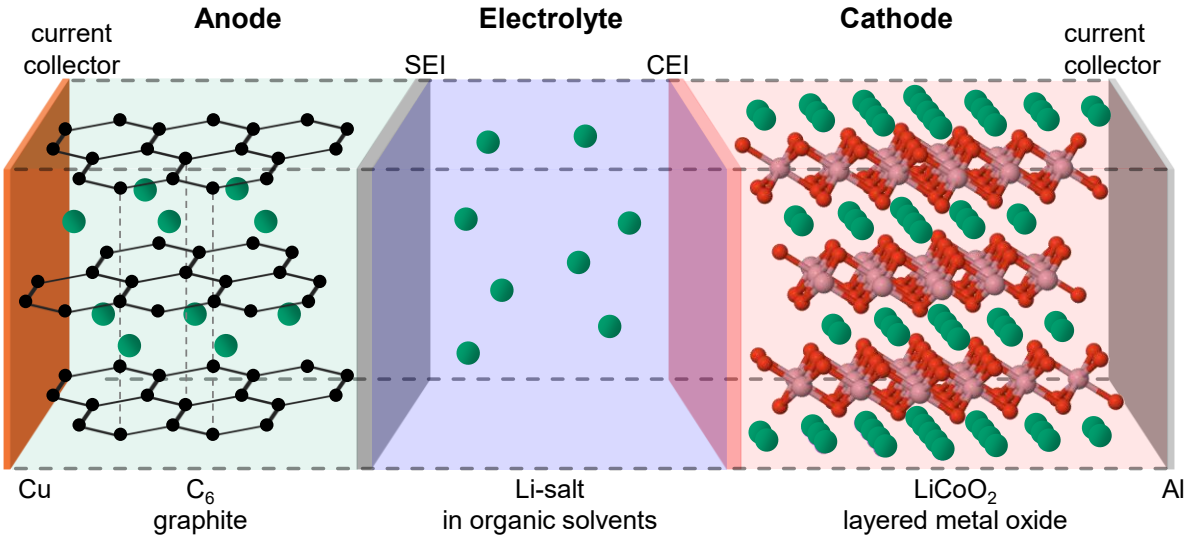


Figure 1.1. Schematic illustration of a typical lithium-ion battery setup consisting of intercalating electrodes, as well as a liquid organic electrolyte (separator membrane not shown here). Lithium ions are depicted as green spheres. LCO structure adapted from reference.[16]

The introduction of the first lithium-ion batteries in the 1980s started a new era of electrochemical energy storage, honored by the Nobel Prize in Chemistry in 2019.[17,18] **Figure 1.1** illustrates the archetypal battery setup proposed and developed by the Nobel laureates Stanley Whittingham, John B. Goodenough, and Akira Yoshino. The electrolyte consists of a lithium salt dissolved in an organic, highly polar solvent that is supported by a porous polymer separator. Petroleum coke or graphite are commonly employed as the anode material that can store lithium ions in its layered structure up to a Li/C ratio of 1/6 as lithiated graphite (LiC_6). The first-generation Li-ion batteries used lithium cobalt oxide ($LiCoO_2$, LCO) as cathode material. The half-cell reaction for the combination of graphite and LCO during the discharge process for the anode and cathode are given by Eq. 1.1 and 1.2, respectively. The total redox reaction summarizes the electrochemical discharge reaction of the battery (Eq. 1.3).

anode:	LiC_6	$\rightarrow$	$C_6 + Li^+ + e^-$	(1.1)
cathode:	$CoO_2 + Li^+ + e^-$	$\rightarrow$	$LiCoO_2$	(1.2)
total:	$LiC_6 + CoO_2$	$\rightarrow$	$C_6 + LiCoO_2$	(1.3)

1.1.2 Thermodynamics of Electrochemical Energy Storage

Reversible electrochemical redox reactions facilitate electrochemical energy storage. An electrochemical cell can either be a galvanic or an electrolysis cell. In galvanic cells (i.e., batteries during discharge), electrochemical reactions at the involved half-cells occur spontaneously once the individual half-cells are connected externally, leading to a power output from the galvanic cell by converting chemical energy into electrical energy. Vice versa, electrochemical cells operate as electrolysis cells (i.e., batteries during charge) when power is used to convert electrical energy to chemical energy. In an electrochemical cell, each half-cell represents a specific redox reaction at its electrode|electrolyte interface. The isolated determination of the absolute potential of individual redox processes is not feasible. However, the redox couple can be measured in relation to a reference electrode. The standard hydrogen electrode (SHE) is the most common reference system with a defined potential of 0.00 V. When the evaluation of the redox potential is conducted under standard conditions (1 bar, 25 °C, and an effective concentration of 1 M), the determined potential is the standard potential ($E^{\ominus}$). The standard potential is related to the standard Gibbs free energy ($\Delta G^{\ominus}$) by Eq. 1.4. Similar considerations hold true for non-standard conditions as well (Eq. 1.5).[19,20]

$$\Delta G^{\ominus} = -n \cdot F \cdot E^{\ominus} \tag{1.4}$$

$$\Delta G = -n \cdot F \cdot E \tag{1.5}$$

The redox reaction of a half-cell reaction represents an equilibrium reaction at the electrode between oxidized (Ox) and reduced (Red) species (Eq. 1.6). The reaction quotient ($Q_r = a_{Red}/a_{Ox}$) depends on the chemical potential of the redox reaction and is used to describe the state of the equilibrium. The redox reaction proceeds until an equilibrium between oxidized and reduced species is reached. This state is called the Nernst equilibrium and is achieved once the exchange current density is identical for oxidation and reduction.[19,20]

$$Ox + e^{-} \rightleftharpoons Red \tag{1.6}$$

Under standard conditions and chemical equilibrium, the reaction quotient equals the equilibrium constant ($Q_\mathrm{r} = K_\mathrm{c}$). Therefore, in the Nernst equilibrium under standard conditions, the standard Gibbs free energy ($\Delta G^{\ominus}$) of the system is related to the chemical equilibrium of oxidized and reduced species by Eq. 1.7. For non-standard conditions, deviations from the Nernst equilibrium are induced. The actual Gibbs free energy is then represented by Eq. 1.8, which depends on external parameters like the temperature or partial pressure.[19,20]

$$\Delta G^{\ominus} = -R \cdot T \cdot \ln(K_c) \tag{1.7}$$

$$\Delta G = \Delta G^{\ominus} + R \cdot T \cdot \ln(Q_\mathrm{r}) \tag{1.8}$$

The relation of the Gibbs free energy to both the electrode potential (Eq. 1.4) and the state of chemical equilibrium (Eq. 1.8) leads to the Nernst equation for the electrode potential (Eq. 1.9). The Nernst equation correlates to Gibbs free energy and describes the half-cell potential ($E_{\text{half-cell}}$) depending on, e.g., concentration, temperature, or pressure at a given electrode.

$$E_{\text{half-cell}} = E^{\ominus} - \frac{R \cdot T}{n \cdot F} \cdot \ln(Q_r) \tag{1.9}$$

1.1.2.1 Electrode Exchange Current Density

A half-cell reaction is an equilibrium reaction between oxidized and reduced species as described above. The redox reaction involves both anodic and cathodic processes at the electrode. In the chemical equilibrium (i.e., at the equilibrium potential, E_q) the current density for both processes is identical, resulting in a net-currentless state. The total current density is given by the combination of anodic and cathodic current contributions. Once a non-equilibrium potential (i.e., overpotential, $\eta = E - E_{eq}$) is applied, the system is pushed out of the equilibrium, resulting in predominantly anodic or cathodic currents depending on the applied potential (**Figure 1.2**a). The Butler-Volmer-Equation (Eq. 1.10) relates the electrode current density of a unimolecular redox process to the electrode overpotential (η).[20] The current density is further influenced by the efficiency of the charge transfer reaction, expressed by the charge transfer coefficients of the anodic and cathodic processes ($\alpha_{a/c}$). The coefficients indicate the fraction of current density facilitated by the overall overpotential, which also includes, e.g., redox activation energies or mass transport limitations.

$$j = j_0 \left\{ exp\left[\frac{\alpha_a \cdot n \cdot F}{R \cdot T} \cdot \eta\right] - exp\left[\frac{\alpha_c \cdot n \cdot F}{R \cdot T} \cdot \eta\right] \right\} \tag{1.10}$$

with j_0 exchange current density; $\alpha_{a/c}$ transfer coefficient; η overpotential.

The Butler-Volmer equation is only valid for small overpotentials, usually for η smaller than the thermal voltage ($V_T \equiv RT/F \equiv kT/e \approx 25$ mV at 25 °C). For overpotentials above the V_T the equation simplifies to the Tafel equation (Eq. 1.11). This is reasoned by the negligible contribution of either anodic or cathodic reactions at sufficiently high overpotentials. At high positive overpotentials (anodic potentials), the current density is dominated by the first term of the Butler-Volmer equation. For cathodic potentials, the second term approximates the total current density. The Tafel plot (**Figure 1.2**b) can be used to extrapolate the exchange current density as the intercept of the Tafel slopes for the equilibrium state (η = 0 V).

$$j_0 \left\{ exp\left[\frac{\alpha_a \cdot n \cdot F}{R \cdot T} \cdot \eta\right] \right\} \overset{anodic}{\longleftarrow} j \overset{cathodic}{\longrightarrow} j_0 \left\{ -exp\left[\frac{\alpha_c \cdot n \cdot F}{R \cdot T} \cdot \eta\right] \right\} \tag{1.11}$$

Due to diffusional limitations and polarization contributions, the current density is usually restricted to a critical current density (cf. Chapter 1.3.2.4).

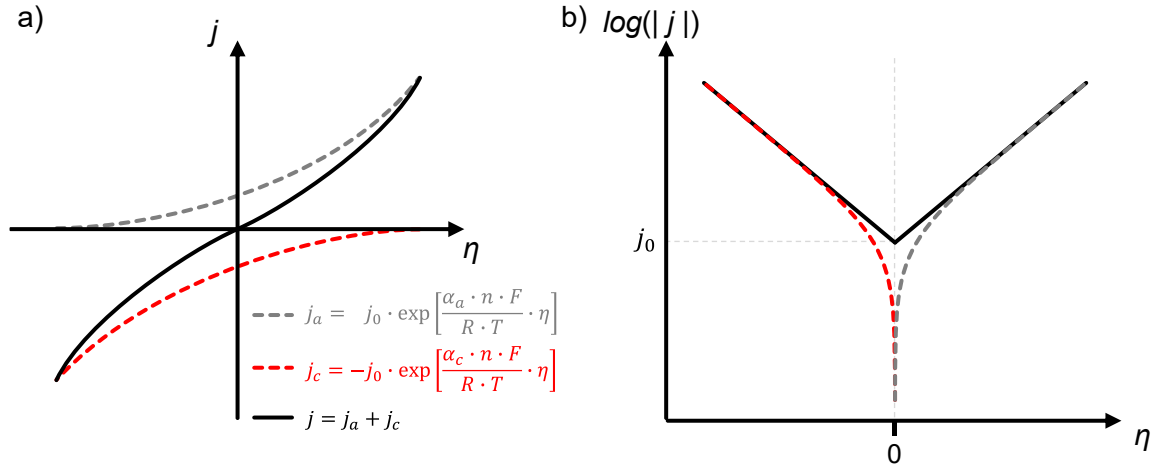


Figure 1.2. (a) Illustration of the (dashed, gray) anodic and (dashed, red) cathodic contributions to the (black) effective current density as the sum of both contributions for small overpotentials.(b) Tafel plot for overpotentials exceeding the thermal voltage. The slope of the linear regime can be used to extrapolate the exchange current density. Illustrations adapted from reference.[20,21]

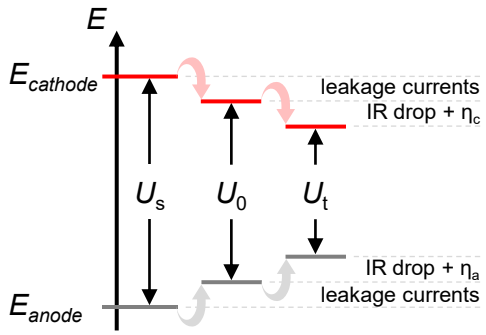
1.1.2.2 Electrochemical Potential of Electrochemical Cells

In electrochemical cells, two half-cells are combined to form a galvanic or electrolytic cell. The cell potential (E_{cell}) is given by the potential difference of both half-cells under currentless conditions. Historically, the potential difference is referred to as electromotive force (emf); more recently, the term source potential (U_s) is used (Eq. 1.12).[22] For the electrochemical cell depicted in **Figure 1.1** and the corresponding total redox reaction (Eq. 1.3), the source potential is given by Eq. 1.13. The source potential is the maximum potential difference for a given electrochemical cell in an ideal cell under currentless conditions.[20]

$$U_s = \Delta E_{\text{cell}} = E_{cathode} - E_{anode} \tag{1.12}$$

$$U_s = E_{Co^{3+}/Co^{4+}} - E_{LiC_6/C_6} = +0.70\,V - (-3.03\,V) = 3.73\,V \tag{1.13}$$

In real electrochemical cells, the electrolyte exhibits a finite resistance, resulting in parallel currents like leakage currents (IR_l) through the electrolyte, which causes a voltage drop across the cell. The corresponding observable cell voltage is the open-circuit potential (U_0, Eq. 1.14). During cell operations and faradaic reaction, currents flowing through the electrolyte lead to further voltage drop due to the electrolyte resistance (IR_e). Additionally, electrochemical processes at the electrodes typically require higher energies due to, e.g., diffusional or kinetic limitations leading to electrode polarization. The associated overpotential is denoted by the symbol η. Thereby, the open circuit potential is further reduced to the terminal potential (U_t, Eq. 1.15) (**Figure 1.3**).



$$U_s = E_{cathode} - E_{anode} \tag{1.12}$$

$$U_0 = U_s - I \cdot R_l \tag{1.14}$$

$$U_t = U_0 - |\eta_c| - \eta_a - I \cdot R_e \tag{1.15}$$

Figure 1.3. Illustration of different voltages associated with an electrochemical cell. Leakage currents and faradaic currents result in a reduction of the source potential.

Both the voltage drop due to the electrolyte resistance and the required overpotential typically scale with the current density, resulting in further development of the voltage hysteresis between the battery charge ($U_{t,ch}(I)$) and discharge ($U_{t,dch}(I)$) potentials (**Figure 1.4**a). From the required overpotentials and voltage drops, it is apparent that for each cycle, some percentage of energy is irrevocably lost. The reduction of electrode overpotentials and electrolytes with low resistance can contribute to increasing the energy efficiency of an electrochemical cell. Furthermore, the proceeding redox reaction during charge and discharge leads to a steady change in the reaction quotient. For a battery, the progress of discharge is commonly reported as the depth of discharge (DoD, in %). The corresponding isolated contribution of the DoD on the terminal potential is represented by Eq. 1.16.

$$E = E^{\ominus}_{Co^{3+}/Co^{4+}} - E^{\ominus}_{LiC_6/C_6} - \frac{R \cdot T}{z \cdot F} ln\left(\frac{[C_6] \cdot [LiCoO_2]}{[LiC_6] \cdot [CoO_2]}\right) \tag{1.16}$$

In the charged state, the lithium ions are located in the interlayers of the graphite anode. During discharge, lithium is continuously deintercalated from the graphite anode and

transported through the electrolyte to be intercalated at the LCO cathode. Thereby, the discharge redox reaction (Eq. 1.16) proceeds to the product side and the reaction quotient increases during the transition to the discharged state. This leads to a decrease in cell potential during the discharge process expressed by Eq. 1.16 (**Figure 1.4**b). For both charging and discharging, cut-off potentials are defined to mark the fully charged or discharged state in order to prevent the electrochemical decomposition of internal components. The dependence of cell potential on current density, temperature, or voltage drops caused by internal processes complicates the exact state of the cell and its cell potential.

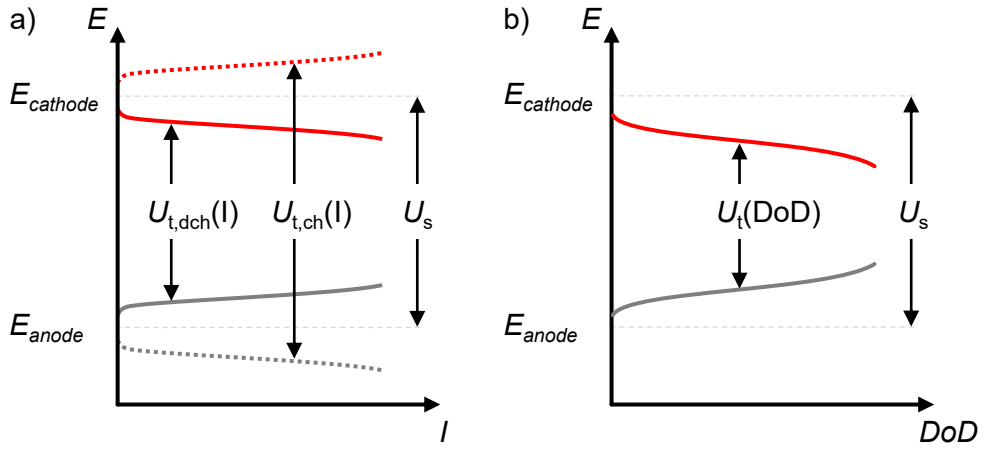


Figure 1.4. (a) Current-dependent overpotentials ($U_t(I)$) for the (solid lines) discharge and (dashed lines) charge in relation to the source voltage (U_s) of an electrochemical cell. (b) Dependence of the cell potential on the depth of discharge (DoD). In (a+b) electrode polarization and internal voltage drops induce the initial deviations from the source potential. Illustration adapted from reference.[21]

1.2 Lithium-based Battery Technologies

In 2019 the Nobel Prize in Chemistry was awarded to the three pioneers of lithium-ion battery technology. Lithium was already known for its high reactivity, high energy density, and lightweight properties, finding application in primary battery cells since the 1960s.[23,24] In the 1970s Stanley Whittingham used alternative cathode systems in combination with lithium-metal anodes to create the first rechargeable lithium-ion battery. He used layered titanium disulfide cathodes in which lithium could be reversibly de-/intercalated during charge and discharge.[25] However, a rather low operating voltage of around 2.2 V of the $LiTiS_2$ cathode in combination with lithium-metal anodes put John B. Goodenough on track to develop higher-voltage cathode systems. He introduced lithium cobalt oxide ($LiCoO_2$) as the breakthrough material for cathode systems.[26] The material exhibits the same fundamental operating principle of intercalation but at a higher operating voltage of around 4 V, doubling the energy density. Both battery systems proposed by Whittingham and Goodenough relied on lithium-metal anodes. Those would develop dendritic whiskers upon cycling, which penetrate the electrolyte and result in internal shorting of the battery. The formation of electrode-connecting dendrites is commonly followed by hazardous side reactions, ultimately leading to thermal runaway reactions and safety issues. Akira Yoshino introduced graphite as an anode active material.[27] As such, the carbonaceous material does not provide any lithium to the battery. However, similar to the cathode side, lithium ions can be stored by intercalation between individual graphite layers. This approach mitigated the formation of metallic lithium and the risk of dendrite formation. The joint advancements in lithium-ion battery technology led to the commercialization of today's lithium-ion batteries from 1991 onwards by Sony and Ashahi Kasei (**Figure 1.5**).

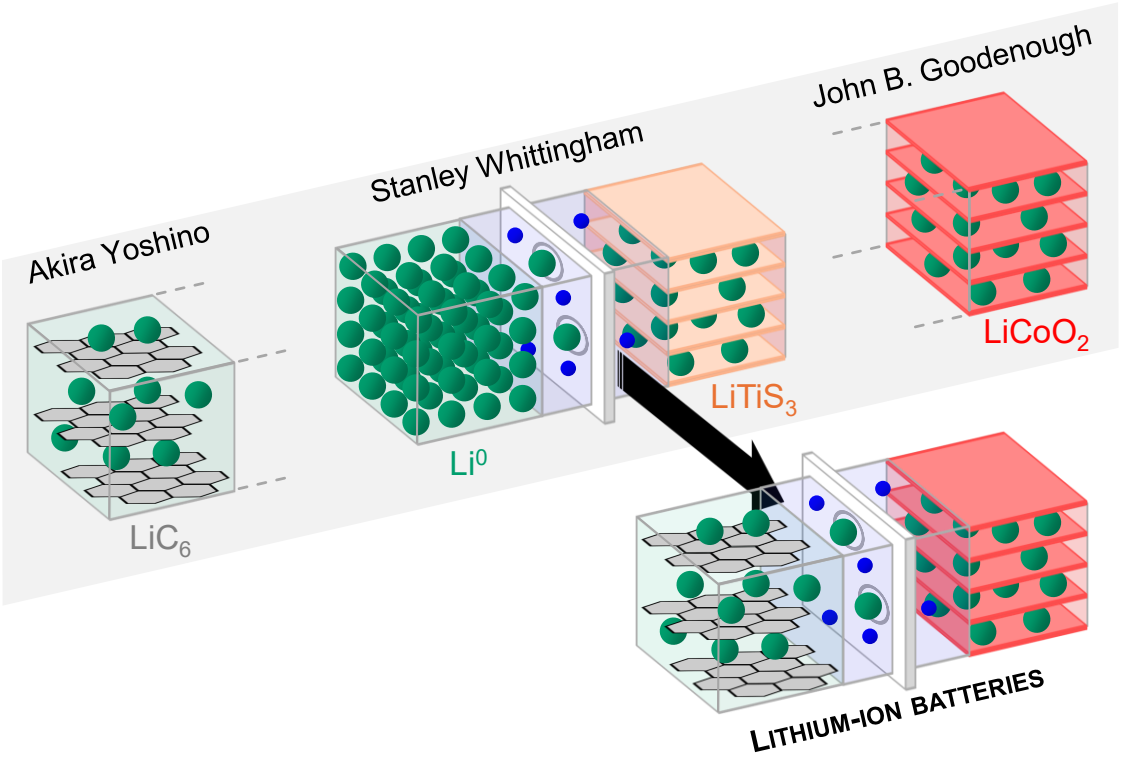


Figure 1.5. Illustration of the different contributions by Whittingham, Goodenough, and Yoshino to the development of the first safe and rechargeable lithium-ion battery by Sony and Ashahi Kasei. Adapted and modified from reference.[17]

Since their commercialization, academic and industrial research have focused on further improvement of lithium-ion battery technology. The adequate presentation of all the research paths would go far beyond the scope of this work. However, selected promising approaches are summarized in **Figure 1.6** and briefly portrayed in the following section and summarized in the appendix (**Table A5.1** and **Table A5.2**). Different technological developments are selected for each of the three fundamental components of a battery (anode, electrolyte, cathode). Some of these are still under investigation and far from commercialization, whereas others are already applied in commercial batteries.

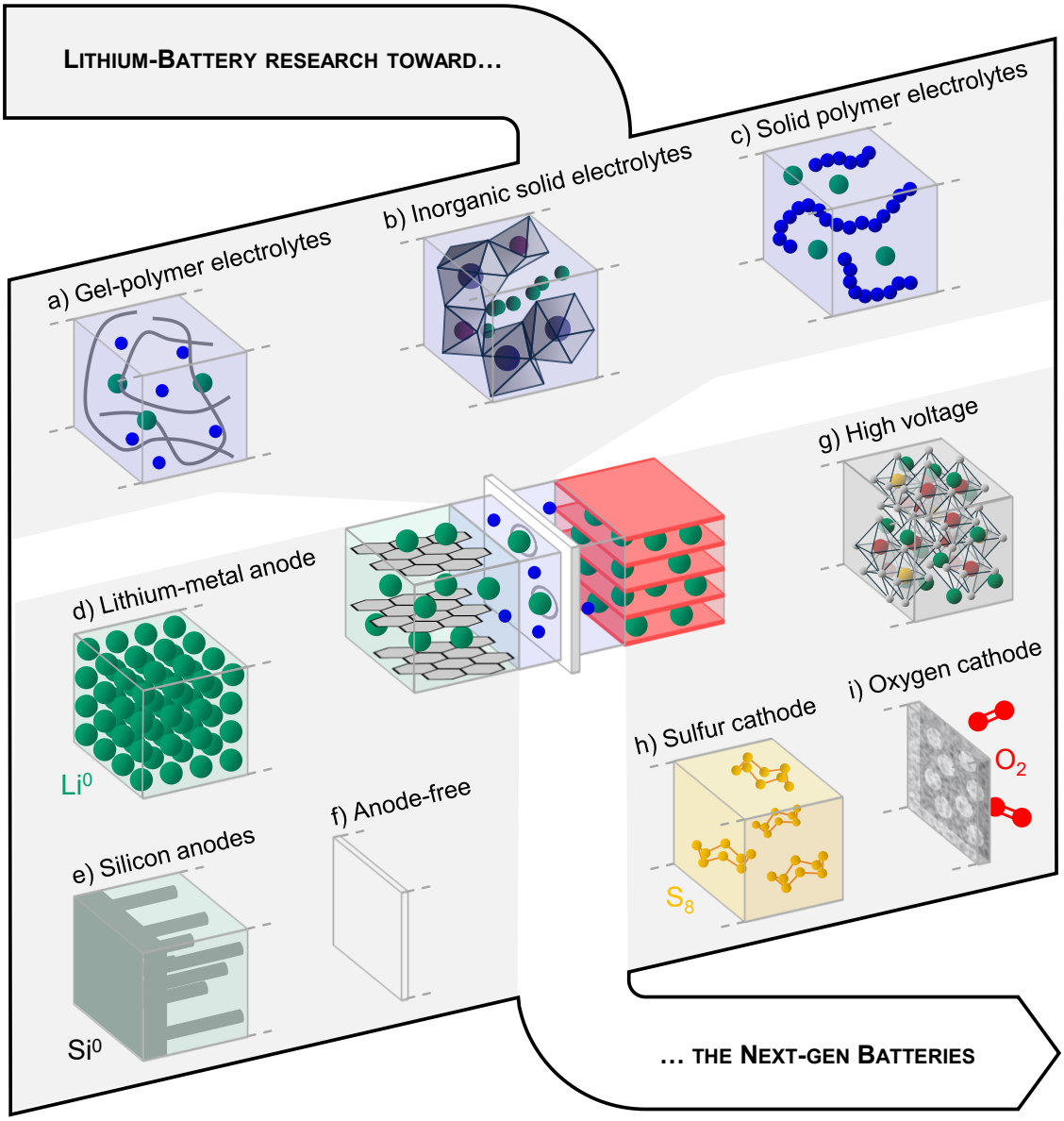


Figure 1.6. Schematic illustration of selected lithium-based battery technologies. (a-c) Electrolyte alternatives to liquid-electrolyte-soaked porous membranes as found in LIBs. (d-f) High-energy anode chemistries for conversion-type storage mechanisms. Research on the cathode side leads to more efficient and stable intercalation-type cathode systems with increased operating potential. (h,i) However, similar to the anode side, conversion-type cathode chemistries using abundant materials (e.g. elemental sulfur or atmospheric oxygen) are under investigation for their high theoretical energy density. Individual illustrations adapted and modified from reference.[17,28,29]

1.2.1 Anode Research

Graphite was introduced as a reliable, safe, and cost-efficient cathode material in the first generation of lithium-ion batteries. The storage mechanism revolves around the reversible intercalation of lithium ions into the layered structure of graphite. Typically, the maximum stoichiometric loading of one lithium ion per six carbon atoms (LiC_6) leads to a specific capacity of 372 mAh h^{-1}. Compared to metallic lithium anodes, the risk of dendrite formation is significantly reduced.[27,30,31] In turn, this increases battery safety concerning internal shorting and thermal runaway reactions. The primary goal of anode research is to increase the achievable energy density of the battery while retaining or improving the positive characteristics of graphite anode systems, like safety, reversibility, and affordability. Increasing the specific capacity and energy density primarily involves a shift of the storage mechanism from intercalation to conversion chemistries (**Figure 1.7**). This approach is also applicable to the cathode side, which will be discussed later. In intercalation-type systems, lithium ions are incorporated into the crystal structure of the host material without significantly altering the material's structure. Contrarily, in conversion-type systems, lithium ions react with the active material to form a new phase. This process can be metallurgical (i.e., metallic plating or alloying) or based on chemical conversion reactions.

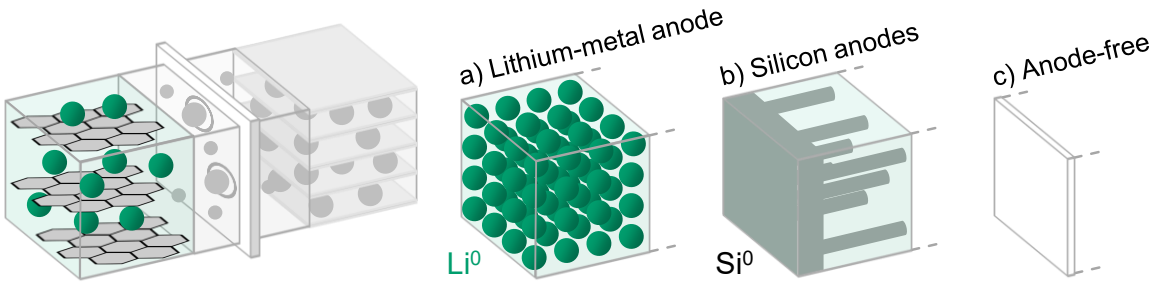


Figure 1.7. Illustration of different anode technologies in lithium-based batteries.

Despite presenting significant challenges due to the inherent risk of dendrite formation, lithium metal anodes continue to be regarded as a potential anode material for future lithium-metal batteries (**Figure 1.7**a). This is largely due to their considerably higher specific capacity of 3861 mAh g^{-1} and the lowest possible redox potential (-3.04 V vs SHE) for lithium. The primary method for facilitating lithium-metal anodes involves using mechanically stable electrolytes, which can reduce the formation of dendrites due to their mechanical robustness. While theoretical considerations suggest that very high moduli of around 7 GPa are required, more recent studies have indicated that softer materials with suitable ductility can also effectively reduce the formation of lithium dendrites.[32–34] Another challenge is that the electrode potential is highly polarizable during charge and discharge. This can restrict the accurate determination of the state of charge (SoC) and lead to reduced capacity utilization of active materials. Additionally, this can raise safety concerns if the operating voltages of electrolytes and cathode materials are violated.

Another class of anode materials is based on silicon. Si-based anodes offer very low operating voltages (0.3-0.5 V vs. Li/Li^+) and can accommodate various alloy stoichiometries up to $Li_{22}Si_5$ with the highest specific capacity of 4200 mAh g^{-1}. Due to the promising storage properties, various approaches to overcome associated challenges and utilize Si-based or Si-assisted anode systems have been developed. One of the main challenges of silicon anodes is the extreme volume change upon de-/lithiation of up to 400 %.[35] This can result in gradual fragmentation and destruction of

the anode structure and delamination from the anode current collector. Therefore, many approaches aim at buffering the volume change. **Figure 1.7**b shows nano-structured silicon anodes, which confine the volume expansion to small feature sizes. Thereby, the lithiation only leads to limited volume variations within the nanostructured pores. Alternatively, encapsulation or incorporation of nano-sized silicon particles into porous matrices like carbon-based materials can help to buffer the volume variations due to the small silicon particle sizes.[36–38]

Pushing the approach of reducing the amount of required materials (e.g., host, alloying material, binders) on the anode side resulted in the concept of omitting the anode active material entirely (**Figure 1.7**c). In this anode-free setup, no designated host/conversion material is incorporated during battery assembly. The concept utilizes the lithium ions present in the cathode material, which are plated directly on the anode current collector during the charging process.[39] During discharge, the entire plated lithium is transferred to the cathode side. However, the plating process directly on the current collector can be irregular, resulting in similar problems as for lithium-metal anodes. To improve the plating characteristics, thin alloying layers of indium are commonly applied to assist in homogeneous lithium plating.[40,41]

1.2.2 Cathode Research

The first cathode systems were based on lithium titanium disulfide ($LiTiS_2$). The materials' fundamental operating principle of ion-intercalation remains the dominating operating mode of modern Li-based batteries. However, the material had a low operating voltage of 2.2 V (vs. Li/Li^+) and a specific capacity of 213 mAh g^{-1}.[18,42] To increase the operating voltage, layered transition-metal oxides based on $LiCoO_2$ were investigated. The material exhibits an operating voltage of around 3.8 V (vs. Li/Li^+) and a theoretical specific capacity of 274 mAh g^{-1}. However, due to the instability of the crystalline phase upon the removal of more than 0.5 equivalents of lithium, this capacity is reduced to an operational capacity of around 137 mAh g^{-1}. Similar to anode research, investigations concerning cathode active materials (CAMs) focus on increasing the specific capacity and energy density of the materials.[43] Additional considerations include the utilization of more benign, affordable, and environmentally friendly materials, as well as conversion-type cathode systems, for which selected examples are illustrated in **Figure 1.8**.

Due to the limitation of lithium extraction from the $LiCoO_2$ crystalline phase, many alternative materials have been investigated to improve the phase stability and further increase the operating voltage and capacity of layered transition-metal-oxide-based cathodes of the stoichiometry $LiMO_2$ (with M = Ni/Co/Mn/Al). Thereby, ternary systems with varying compositions of nickel, manganese, and cobalt in lithium nickel manganese cobalt oxides (NMC, $LiNi_xMn_yCo_{1-x-y}O_2$) have been developed.[44] Each of the individual lithium metal oxides ($LiNiO_2$, $LiMnO_2$, $LiCoO_2$) exhibits problems of capacity fading and crystalline, chemical, or thermal instabilities. However, combined in the ternary phase, the materials show synergistic effects, resulting in their commercialization. In such materials, Nickel improves both operating voltage and capacity, cobalt and manganese assist in crystalline and cycling stability. Additionally, the high abundance of manganese adds sustainability and reduces the overall cost of the cathode material. Similar considerations apply to the alternative ternary system of nickel, cobalt, and aluminum in lithium nickel cobalt aluminum oxide (NCA, $LiNi_xCo_yAl_{1-x-y}O_2$). Together, both systems dominate EV applications, especially in the high-performance vehicles. This is mostly attributed to their optimized high energy density, cycle life, and stability.[45]

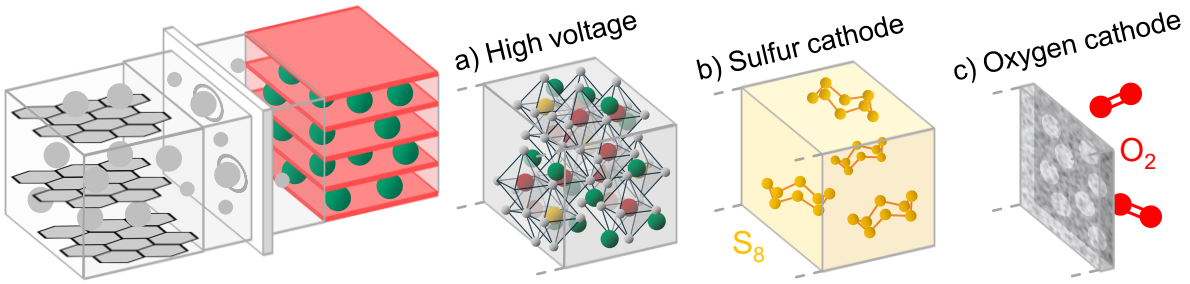


Figure 1.8. Illustration of different cathode technologies in lithium-based batteries.

An alternative to $LiMO_2$-derived cathode active materials like LCO, NMC, and NCA are spinel-type materials of the LiM_2O_4-stoichiometry. One of the earliest applied spinel-type materials was lithium magnesium oxide ($Li[Mn(III,IV)]_2O_4$, LMO).[46] In comparison to the aforementioned materials, $LiMn_2O_4$ is significantly cheaper due to the abundance of manganese, more environmentally friendly and non-toxic.[47] However, the material exhibits strong capacity fade under cycling which is mostly induced by manganese (Mn^{2+}) dissolution leading to both loss of active material and poisoning of the anode side.[43] Many efforts were made to stabilize the structure.[47] The LiM_2O_4 structure is also used as a fundamental motif for high-voltage cathode systems approaching 5 V (vs. Li/Li^+). One of the most prominent candidates is $LiNi_{0.5}Mn_{1.5}O_4$ (LMNO) with an operating voltage of 4.7 V and a theoretical specific capacity of 147 mAh g^{-1} (cf. **Figure 1.8**a).[47,48] Even though the specific energy of $LiNi_{0.5}Mn_{1.5}O_4$ is lower than in layered $LiMO_2$ alternatives, its low cost, stability, and flatter voltage profile encourage further research. However, an additional challenge for its commercialization is the lack of adequate electrolyte systems that can operate at such high cell voltages.[47,49] In all cases of ion-intercalating cathode systems, the potential energy density is limited by the comparably small gravimetric proportion of lithium in the host material (e.g., 7 wt% in $LiCoO_2$, or 4 wt% in $LiNi_{0.5}Mn_{1.5}O_4$). Lithium iron phosphate ($LiFePO_4$, or LFP) as a cathode active material was introduced by John Goodenough et al. in 1996. LFP offers high safety, longevity, and low cost over cobalt-based chemistries. After overcoming low conductivity hurdles with carbon coating in the early 2000s, LFP gained dominance in electric vehicles and stationary energy storage due to its stability, high charge rates, and cost-effectiveness.

Similar to anode materials, a shift to conversion-type materials promises a significant increase in the theoretical energy density. The most promising cathode systems are based on elemental sulfur (S_8) or atmospheric oxygen (O_2). Sulfur is a promising cathode material for lithium-sulfur batteries (LSBs) (**Figure 1.8**b). During battery operation, elemental sulfur is converted stepwise to the final discharge product, lithium sulfide (Li_2S). In total, this exhibits a theoretical specific capacity of 1675 mAh g^{-1} at an operating potential of around 2.1 V. Sulfur is abundant and has a surplus in annual production as a side product in fossil fuel purification, leading to low prices and around 6 Mto of sulfur that are put into stockpiles.[50,51] Based on the assumption that the entirety of surplus sulfur is used for battery capacity production at its theoretical specific capacity, an annual cathode capacity of 21 TWh (realistic estimation 12 TWh, at 60 % material utilization) could be realized. Compared to the cathode production capacity forecasted for 2028 of around 2-7 TWh, the potential for sulfur cathodes is imminent.[52,53] The main challenge of sulfur-based cathodes is a very prominent capacity fading due to the solubility of redox-intermediates (lithium polysulfides, LiPS, Li_2S_x) in common electrolytes. The dissolution and gradual depletion of sulfur towards the anode side is referred to as the shuttle effect (refer to the appendix for further information, Chapter 5.2.1.1). Furthermore, its very low electrical conductivity requires high amounts of conductive additives, reducing the potential energy density. Approaches to reduce

capacity fading and intermediate dissolution include the encapsulation in porous host materials,[54] the use of redox catalysts to mitigate the dissolution kinetically,[55] the incorporation of LiPS-blocking separators,[56] or the covalent attachment of sulfur to host materials on the cathode side.[51,57,58]

The use of oxygen as a cathode reactant in lithium-air/oxygen batteries (LABs) is one of the most promising concepts of high-energy storage systems due to its high theoretical specific capacity (**Figure 1.8**c). The theoretical specific capacity for oxygen in LABs is often reported as 3861 mAh g^{-1} at an operating potential of 2.96 V, which leads to a theoretical energy density of 11430 Wh kg^{-1} comparable to fossil fuels.[59] For the calculation, the mass of oxygen is not considered but is based solely on the theoretical capacity of lithium metal. In non-aqueous LABs, the reaction usually only reaches Li_2O_2, whereas aqueous systems proceed to Li_2O. Applying the same calculation as for LSBs to the oxygen cathode system leads to theoretical capacities of 3350 mAh g^{-1} or 1675 mAh g^{-1} for the discharge products of Li_2O and Li_2O_2, respectively. In comparison to the cathode systems described above, the design of the LAB cathode side significantly differs. While hermetically sealed cells are required to exclude reactive contaminants in the former, LAB utilize an open-cell approach. In this, the cathode side is designed to take up atmospheric oxygen through a perforated layer, as the cathode itself does not contain an oxygen reservoir. The main challenges associated with LABs are (1) the formulation of electrolytes that can withstand the oxidative environment, (2) the sluggish reduction of the discharge products during charging, (3) the clogging of the porous cathode matrix due to the precipitation of insoluble and insulating redox-products, and (4) possible cell poisoning by atmospheric carbon dioxide and humidity.[59] Therefore, the main focus for LAB research is the development of efficient redox catalysts,[60] stable electrolytes,[61,62] and oxygen-permeable membranes for encapsulation.[63]

1.2.3 Electrolyte Research

The first LIBs were already based on organic liquid solvents in combination with lithium salts using bulky anions (e.g., $LiClO_4$, $LiPF_6$) and are still used today.[25,26] Carbonate-, ester-, and ether-based systems are the most common classes of electrolyte solvents because of their capability of dissolving, dissociating lithium salts, and withstanding the operational potential of common cell chemistries. However, liquid electrolytes consist of a variety of compounds and additives to assist in interface stabilization, improve thermal and electrochemical stability, or improve capacity retention.[64] Commonly porous separators are soaked with liquid electrolytes to ensure electrode separation.[65] The main advantages of organic liquid electrolytes are associated with (1) the high ionic conductivity even at room temperature (10^{-3}–10^{-2} S cm^{-1}), (2) good wettability, (3) low interfacial resistances in contact with electrodes, and (4) easy and optimized manufacturing.[64,66,67] Despite their advantages, serious safety concerns due to their flammability, possible thermal runaway events, and rapid degradation at high potentials and temperatures promoted the research of new electrolyte systems. An overview of different electrolyte systems is given in **Table A2** in the appendix.[68] To address these limitations, gel-polymer electrolytes (GPEs) have been developed to retain the beneficial properties of liquid electrolytes in semi-solid systems with improved mechanical integrity and safety (**Figure 1.9**a). Instead of incorporating a liquid electrolyte into a porous membrane, physical or chemical polymer networks (e.g., based on PVDF, PMMA, PAN) are soaked with the electrolyte, which can significantly reduce the risk of electrolyte leaking.[69–71] Despite their advantages concerning mechanical safety aspects, the flammability of the electrolyte remains problematic.

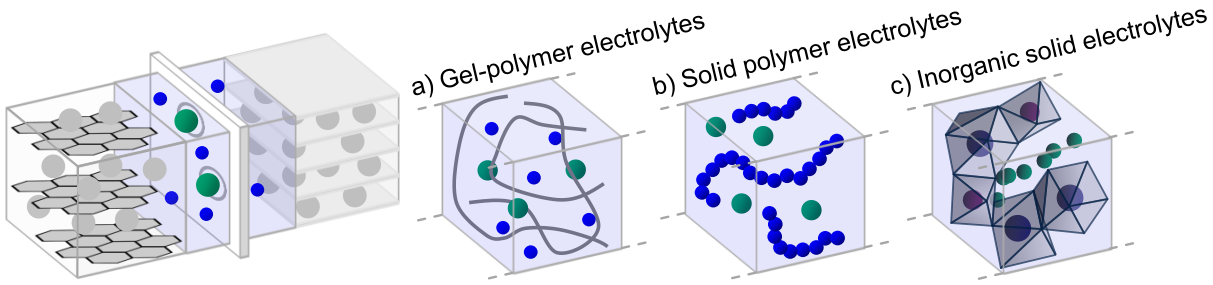


Figure 1.9. Illustration of different electrolyte technologies in lithium-based batteries.

Another type of electrolytes based on polymers was first initiated by the work of Wright et al, who reported on the ionic conductivity of alkali metal/poly(ethylene oxide) (PEO) complexes (**Figure 1.9**b).[72] In contrast to GPEs, the *solid polymer electrolytes* (SPEs) do not contain any solvent, but the polymer matrix dissolves the lithium salts itself. Due to the absence of organic solvents, the class of materials is also referred to as dry polymer electrolytes to emphasize the distinction from GPEs. To facilitate lithium salt dissolution and dissociation, the design principles of most SPEs are based on polar functional moieties (e.g., polyether, polyester) comparable to small molecule liquid electrolytes.[73,74] The main advantages of SPEs are (1) increased safety, (2) variability of physical properties by tailored polymer architecture, (3) increased mechanical stability compared to liquid electrolytes, and (4) easy manufacturing due to established polymer-based processing techniques.[75,76] The main drawback of SPEs is their low ionic conductivity at low temperatures. Depending on the electrolyte system, the critical threshold of 10^{-3} S cm^{-1} is only reached at elevated temperatures, impeding drop-in solutions in established lithium-battery manufacturing processes. Further details about the advantages, challenges, and prospects of SPEs are presented in Chapter 1.3.

The class of solid-state electrolytes (SSE, also solid inorganic electrolytes) stands in contrast to the electrolyte systems described above. While liquid- or polymer-based systems mostly rely on the coordination and dissociation of lithium salt and high ion diffusion constants to achieve appropriate ionic conductivity (cf. Chapter 1.3.2), SSE are based on solid-state materials like oxides, sulfides, or halides. Ions migrate through the materials by vacancy hopping, interstitial substitution within the crystalline lattice (**Figure 1.9**c). The most prominent candidates are based on garnets like $Li_7La_3Zr_2O_{12}$ (LLZO) and $Li_{6.4}La_3Zr_{1.4}Ta_{0.6}O_{12}$ (LLZTO), or argyrodites based on the motif of Li_6PS_5X (X = Cl, Br, I). The superior mechanical properties of SSE enable thinner device geometries, impede lithium dendrite formation, and improve battery safety. However, the mechanical rigidity can also result in contact/interface issues due to inappropriate material compliance during operation, especially in combination with electrode materials exhibiting large volume variations. Therefore, many battery systems require external pressurization to overcome elctrochemo-mechanical stresses.

1.3 Solid Polymer Electrolytes

1.3.1 Electrolytes – Roles and Requirements

Battery materials need to fulfill an intricate set of requirements, decided by their respective role within the operation of a battery. Considering the application, no material can be characterized by a single property but needs to be assessed by the accomplished trade-off between contradicting characteristics.[77] This chapter aims to highlight the main tasks of an electrolyte system in lithium-ion/-metal batteries, with each of the mentioned tasks opening a wide field of research. Some aspects are detailed in the following chapters.

- Ion transport – The ionic transport within the battery between the electrodes is the primary function of the electrolyte (cf chapter 1.3.2.1). Increasing ionic conductivity in an electrolyte system allows for higher charge and discharge rates. Typically, a room-temperature ionic conductivity of 1×10^{-3} S cm^{-1} is considered the minimum requirement for technical applications. This ionic conductivity should thereby be maintained over a wide range of temperatures.
- Ion Transference Number – Besides the magnitude of the total ionic conductivity, the effective contribution of lithium ions to the overall conductivity is decisive. The Li^+-ion transference number represents the proportion of conductivity correlated with lithium-ions exclusively (cf chapter 1.3.2.3). High Li^+ transference numbers and effective lithium conductivities can mitigate cell polarization and decrease internal resistance.
- Mechanical Properties – The mechanical resilience of the electrolyte layer is very important for the safety characteristics of a battery (cf chapter 1.3.4.1). The stable separation of the electrodes is paramount, as internal short circuits can result in serious safety concerns leading to thermal runaway. This especially applies to lithium metal anodes. Separation can be ensured by sufficient mechanical stability of a solid electrolyte or by additional separating membranes.
- Thermal Properties – During operation, a battery produces heat due to Joule heating, losses due to overpotentials, and side reactions. Especially for liquid organic electrolytes, their inherent inflammability and volatility restrict the thermal operation windows of a battery. Solid-state alternatives offer improved thermal stability and are typically leak-proof.
- Electrochemical Properties – Electrolytes are subjected to both highly reductive and oxidative environments at the anode and cathode, respectively. Electrolyte materials must therefore exhibit a high electrochemical stability window of 2.5 to 5 V (vs. Li/Li^+) depending on the cell chemistry (cf chapter 1.5.3). Electrolyte decomposition can result in gas generation and safety hazards.
- Interface Stabilization –The highly reductive environment at the anode leads to inevitable electrolyte decomposition. Decomposition products form a thin passivating layer, mostly consisting of diverse lithium-containing salt precipitates. This thin interfacial layer is hence referred to as solid electrolyte interface (SEI) and protects the electrolyte from further decomposition. The use of specialized SEI-forming additives helps to generate stable SEIs.

1.3.2 Ionic Conductivity in Polymer Electrolytes

1.3.2.1 Ionic Conductivity Mechanism

In classical theory, the conductivity of a system can be described by Eq. 1.17 for liquid-like transport.[21] The conductivity (σ) can be expressed as the sum of products of electrophoretic mobility (μ) and charge (q) as well as the number (n) of the ith ion species. While q and n are dependent on the specific salt, the mobility is also related to the surrounding electrolyte and the interaction between the ions and solvent molecules.

$$\sigma = \sum_i \mu_i \cdot q_i \cdot n_i \tag{1.17}$$

In dilute systems, the ion mobility is correlated to the ion diffusivity by the Einstein relation (Eq. 1.18). Ions with high diffusion coefficients (D) result in high ionic mobilities. Based on Stokes' law, the diffusion coefficient is also related to the viscosity of the electrolyte due to the frictional coefficient of the translational motion of ions as given by the Stokes-Einstein relation (Eq. 1.19). The frictional coefficient is dependent on the hydrodynamic radius of the solvated ion (r_i) and the viscosity (η) of the system. Under consideration of Eq. 1.18 and Eq. 1.19 it follows that the mobility is inversely proportional to the viscosity of the system ($\mu \propto \eta^{-1}$).[78]

$$D = \frac{\mu_i \cdot k_B \cdot T}{|q_i|} \tag{1.18}$$

$$D = \frac{k_B \cdot T}{6\pi \cdot \eta \cdot r_i} \tag{1.19}$$

with: k_B Boltzmann constant, T thermodynamic temperature.

The Nernst-Einstein equation correlates the diffusion coefficient with the molar conductivity at infinite dilution. Following Kohlrausch's law of independent migration of respective anions and cations, the molar conductivity (Λ_0) is given by Eq. 1.20. Together with Eq. 1.17 this suggests that for increasing the conductivity of the system, the addition of increasing amounts of salt would result in a linear increase in the conductivity. However, while the consideration of the molar conductivity is valid for many salts at low concentrations, ion-ion interactions, ion-pairing, or complexation result in deviations from the ideal molar conductivity, especially at high salt concentrations.

$$\Lambda_0 = \frac{q^2}{k_B \cdot T} \cdot (v_+ \cdot z_+^2 \cdot D_+ + v_- \cdot z_-^2 \cdot D_-) \tag{1.20}$$

with: v stoichiometric number, z ionic charge number.

For liquid-like ion transport, Eq. 1.19 and 1.20 imply that the molar conductivity is coupled to the viscosity of the electrolyte as described by the empirical Walden rule (Eq. 1.21).[79,80] Therefore, high molar conductivities can be achieved by minimizing the electrolyte viscosity.

$$\Lambda_0 \cdot \eta = constant \tag{1.21}$$

When considering polymers as the solvent for ion conduction, the macroscopic viscosity of the polymer (η_{macro}) depends on several factors, like molecular weight or chain entanglement.[81] For the consideration of ion conduction, the macroscopic viscosity would also relate to a vehicular transport in correlation to the entire polymer chain. Vehicular ion transport is depicted in **Figure 1.10**a. However, in polymer electrolytes, the ion conduction depends much more on the local viscosity (η_{micro}) of individual polymer segments (**Figure 1.10**b).[82]

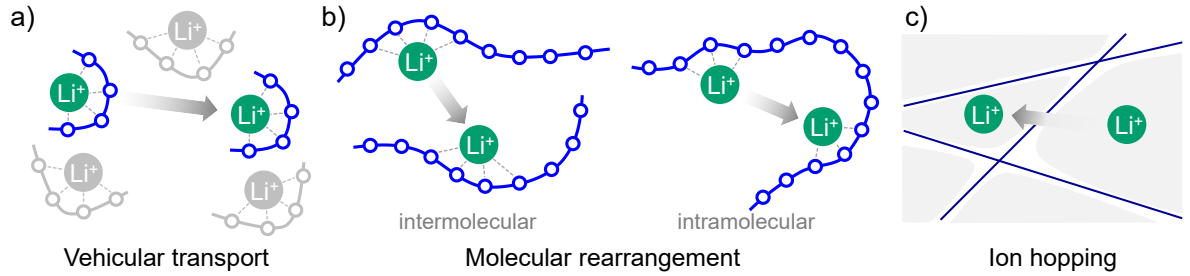


Figure 1.10. Schematic illustration of different transport modes of lithium ions. (a) At low molecular weights, the lithium ions can also be transported in a liquid-like vehicular manner, where the coordination persists, and the polymer/solvent-lithium-complex is translated through the electrolyte. (b) Exemplarily, in PEO-based electrolytes, the lithium ions are coordinated by ether oxygen atoms. At moderate and high molecular weights, the transport of lithium ions is correlated to structural rearrangements of the polymer backbone, resulting in either inter- or intra-chain hopping motions. Similar processes also occur in other non-PEO-based electrolytes. (c) In rigid polymer electrolytes, the ions are conducted by ion-hopping events in between free volume domains (gray shaded area) in the electrolyte.

According to Maxwell's relation, the η_{micro} is directly related to the structural relaxation time (τ_s) of the polymer. In this case, the molar conductivity is correlated to the molecular rearrangement of the polymer and is described by Eq. 1.22. This indicates that for systems where the conductivity is related to segmental rearrangement, a minimization of τ_s results in an increase of the conductivity.[83] This is especially the case in soft and highly flexible polymers

$$\Lambda_0 \cdot \tau_s = constant \qquad (1.22)$$

So far, the description of ion transport is valid for systems in which the conduction is coupled to the structural relaxation of the host material. This is the case for PEO-based materials and other soft polymers with low T_g like PCL. However, in relation to the structural relaxation time, higher ionic conductivities can also be obtained by decoupling the ion transport from polymer segmental mobility in alternative conduction mechanisms. Apart from ideal Walden behavior, ion transport can be more or less strongly coupled to the relaxation times (**Figure 1.11**). In the case, ion transport is less dominated by structural rearrangement, the ion conduction is referred to as super-ionic. Whereas sub-ionic is used to describe systems with low ionicity, resulting in more pronounced dependence on the structural relaxation.[84] Polymer electrolytes with decoupled, super-ionic properties usually utilize polymers with high glass transition temperatures. The relatively rigid polymers invoke chain packing disorder, creating free volume for ion transport by ion hopping processes (**Figure 1.10**c). Some examples include poly(polypropylene oxide), or certain copolymers of poly(vinyl ethyl carbonate).[7,8,85]

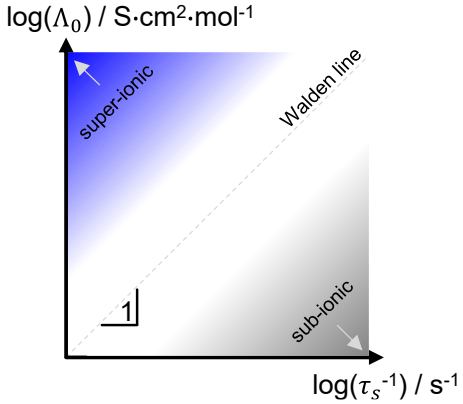


Figure 1.11. Schematic illustration of the ideal Walden behavior (dashed line) resulting in a direct correlation of molar conductivity and relaxation time. Deviations from the ideal line are categorized as super-ionic or sub-ionic for systems with decoupled or more strongly coupled conduction mechanisms.[85]

1.3.2.2 Temperature-Activation of Ion Transport

For glassy polymers with a decoupled ion transport mechanism and also crystalline inorganic electrolytes, the temperature-dependent ionic conductivity can be described by the Arrhenius relation (Eq. 1.23). The ionic conductivity depends on a pre-exponential factor (σ_0), the activation energy (E_A) of the specific transport mode (e.g., ion hopping processes) and the temperature (T). Therefore, the ionic conductivity can be increased by reducing the activation energy in more efficient transport processes or by increasing the temperature. For glassy super-ionic polymers, this could be achieved by increasing the fraction of free volume available for hopping processes.

$$\sigma = \sigma_0 \cdot exp\left(-\frac{E_A}{R \cdot T}\right) \tag{1.23}$$

Classical Arrhenius behavior usually cannot describe the temperature activation in commercial liquid electrolytes at low temperatures and also for systems relying on vehicular transport or structural rearrangement (**Figure 1.10**a+b). The ionic conductivity of liquid electrolytes is heavily dependent on the viscosity of the solvent, which increases at low temperatures, causing non-linear behavior in Arrhenius plots. In such systems, the temperature-dependent ionic conductivity is better described by the Vogel-Tammann-Fulcher (VTF) behavior, which is an expansion of an Arrhenius-type relation to account for the interdependence of ion conduction and structural rearrangement or increase in viscosity. The VTF equation was initially defined to describe the viscosity of organic glasses and supercooled liquids.[86–88] The Vogel temperature (T_0) refers to the temperature of the system at which the viscosity approaches infinity.[89] Commonly the glass transition temperature is used to describe the transition between the glassy and rubbery state caused by restricted structural mobility. Thereby, the T_g is defined as the temperature at which the structural relaxation times τ_s equals 100 seconds. Consequently, a viscosity approaching infinity is expected at even lower temperatures. For polymers, the Vogel temperature is commonly taken as roughly 50 K below the glass transition temperature. For the application as electrolyte, the ionic conductivity can be expressed by Eq. 1.24.

$$\sigma = \quad \sigma_{0,\mathrm{VTF}} \cdot exp\left[-\frac{E_{A,\mathrm{VTF}}}{R \cdot (T - T_0)}\right] \tag{1.24}$$

$$\sigma = \frac{1}{\sqrt{T}} \cdot \sigma_{0,\mathrm{VTF}} \cdot exp\left[-\frac{E_{A,\mathrm{VTF}}}{R \cdot (T - T_0)}\right] \tag{1.25}$$

In comparison to Eq. 1.24, the Vogel temperature, and an alternative pre-exponential factor ($\sigma_{0,VTF}$) and activation energy ($E_{A,VTF}$) are used. Thereby, $\sigma_{0,VTF}$ is mostly associated with the charge-carrier concentration and $E_{A,VTF}$ includes the segmental relaxation of the solvent/polymer. Depending on the system, an additional temperature-dependent factor can be introduced as shown in Eq. 1.25. However, the introduction of $T^{-0.5}$ was shown to only affect the value of the pseudo-activation energy without improving the qualitative representation of experimental data.[90] An increase in the ionic conductivity of VTF-activated electrolytes is accessible by a higher concentration of free charge carriers and by reducing the electrolyte's structural relaxation times and the glass transition temperature.

The Arrhenius and Vogel-Tammann-Fulcher behavior is compared in **Figure 1.12**. Identical activation energies and pre-exponential factors are assumed for the calculation of the respective ionic conductivity. For Arrhenius-activated processes, a linear temperature dependence can be observed. The activation energy is given by the slope of the linear dependence. For VTF-activated processes, the dependence on structural relaxation results in curved temperature-dependences of the ionic conductivity. The data is calculated for different glass transition temperatures. The Vogel temperature was taken as 50 K below the respective T_g. The curvature is increasingly pronounced for higher glass transition temperatures as the influence of reduced structural relaxation of the polymer increases. A visualization of the logarithmic conductivity against the the temperature according for the Vogel temperature enables the determination of the activation energy in VTF-activated electrolytes (**Figure 1.12**b).

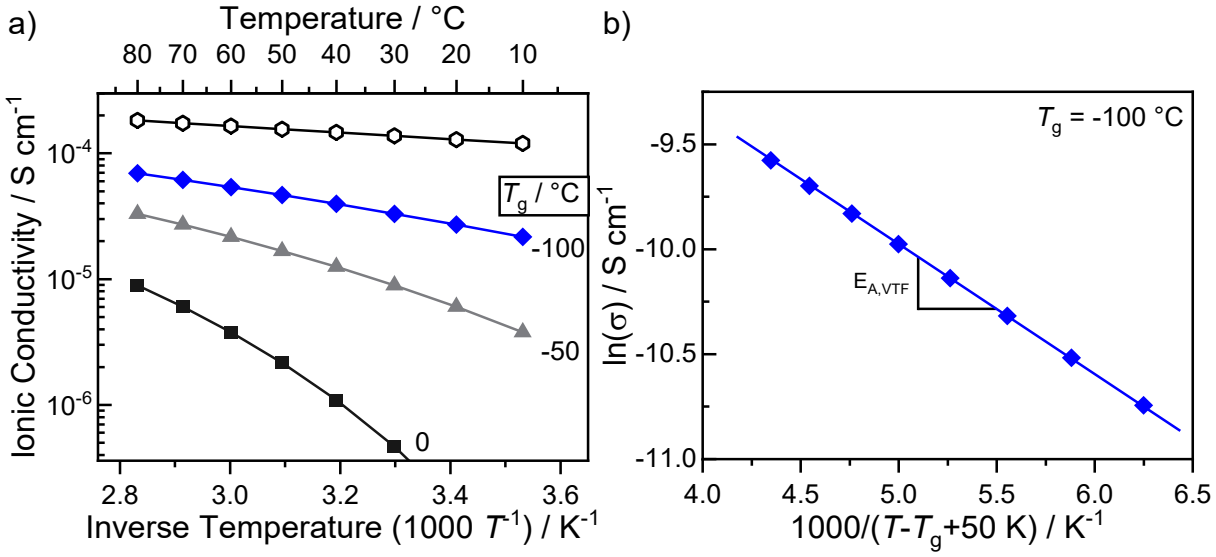


Figure 1.12. (a) Comparison of Arrhenius-type (hollow diamonds) and Vogel-Tamman-Fulcher-type activation of the calculated ionic conductivity in polymer electrolytes with different glass transition temperatures (color code: blue = better). The ionic conductivity values are calculated based on the assumption of an identical activation energy (E_A) and pre-exponential factor (σ_∞). The Vogel temperature (T_0) was taken as T_g–50 K. (b) Linearized data for the determination of the VTF activation energy ($E_{A,VTF}$).

1.3.2.3 Lithium Transference Number

Achieving high ionic conductivity (IC) in electrolytes can significantly influence the performance of battery power characteristics. Increased IC can allow for faster dis-/charging times and higher energy efficiency due to reduced internal cell resistances. In most battery

chemistries, a specific cation (i.e., lithium cations in lithium-based batteries) is relevant for electrochemical energy storage. At the electrodes, the de-/intercalation of lithium ions is the fundamental energy storage mechanism. Thus, the accompanying anion (e.g., $TFSI^-$, PF_6^-) does not partake in any energy-storing electrochemical reactions at the electrode. However, these anions contribute to the overall ionic conductivity of the electrolyte. Therefore, the general push towards higher ionic conductivities should be understood as the pursuit of increasing lithium-ion conductivity. The lithium transference number (LTN, t_+) is a measure of the proportion of lithium-ion conduction of the total ionic conductivity (Eq. 1.26).

$$\sigma_+ = \sigma_{\text{total}} \cdot t_+ \tag{1.26}$$

with: σ_+ lithium-ion conductivity, σ_{total} total ionic conductivity.

Besides the immediate effect of reduced cation conductivity, a low LTN can result in the formation of impeding ion concentration gradients. Such a gradient can impose additional resistive properties of the electrolyte by ion depletion at the electrode-electrolyte interface. This phenomenon will be discussed in Chapter 1.3.2.4. The t_+ of an electrolyte can be expressed by different fractional relations summarized in Eq. 1.27. The value of the LTN can vary between 0 and 1, whereby higher values represent a higher contribution of lithium cations.

$$t_+ = \frac{\mu_+}{\mu_+ + \mu_-} = \frac{D_+}{D_+ + D_-} = \frac{I_+}{I_+ + I_-} = \frac{\sigma_+}{\sigma_+ + \sigma_-} \tag{1.27}$$

with: μ = ion mobility, I = current, D = diffusion constant, $\sigma_\pm$ = ionic conductivity for cations or anions.

For the determination of t_+ different properties can be considered. In dilute systems, the ion mobilities and the related diffusion coefficients (by the Einstein relation Eq. 1.19) can be investigated. The self-diffusion coefficients (D_{self}) can be assessed by pulsed field gradient nuclear magnetic resonance (PFG-NMR) experiments.[91–93] Thereby, individual self-diffusion coefficients for lithium-ions and anions are accessible by ^{7}Li and, e.g., in the case of fluorine-containing salts, ^{19}F NMR measurements, which are exclusive to the respective ion species. Fluorine is commonly present in many Li-salts used in electrolyte systems. Anion structures without fluoride can also be investigated by ^{1}H- or ^{13}C-NMR correlations. Limitations of PFG-NMR measurements are that the determined diffusion coefficients do not represent the ion diffusion induced by an electric field, as present in typical electrochemical cells. To address this shortcoming, electrophoretic NMR (eNMR) experiments assess the diffusion characteristics and the electrophoretic mobility under an applied potential.[91,94,95] While PFG-NMR can be applied to various systems, eNMR is especially powerful for ion-containing systems like electrolytes.[96,97] For the evaluation, a potential is applied to an electrolyte, which is placed into a magnetic field exhibiting a magnetic field gradient in the direction of the electric field. Depending on the observation time, the ions drift according to the applied electric field. Based on the distance traveled, the ions are then located in a local magnetic field of a different strength compared to the initial location. This induces a phase shift of the NMR response, which is directly proportional to electrophoretic mobility.

Alternative to the many electrochemical protocols have also been proposed for investigating the LTN. Sørensen and Jacobsen (SJ-method) proposed one of the earliest electrochemical protocols. The evaluation uses lithium-symmetrical cells with thin electrolytes and requires impedance measurements at very low frequencies to extract the real part of the diffusion impedance (Z_d). The bulk resistance (R_b) of the electrolyte and the diffusion impedance are used to determine the LTN (Eq. 1.28).[98,99] However, the applicability is limited due to the extensive

measurement times, required temperature window, and the missing consideration of interfacial resistances at the electrolyte/electrode interface.

Additionally, to AC investigations conducted in the SJ-method, Watanabe implemented a DC polarization period before the impedance measurement in lithium-symmetrical cells.[100,101] Later on, Newman and coworkers further investigated the implications of DC polarization.[102,103] Polarization potentials range from a few millivolts up to several volts. During the polarization, an anion concentration gradient is invoked until an equilibrium state is established. In this state, the potential-induced current is equivalent to the reverse current caused by anion self-diffusion. The remaining current is therefore exclusively attributed to the lithium ions. The bulk and interface resistance obtained from impedance spectroscopy, the polarization potential, and the steady-state current are used to calculate the t_+ (Eq. 1.29).

Bruce and Vincent (BV-method) proposed the most frequently employed protocol for investigating the transference number (cf. Chapter 1.5.3.4). The setup and protocol are comparable to the W-method. However, only a small amplitude potential is used to polarize the cell (ΔV~10 mV). A continuous lithium flux is present through the electrolyte during the polarization period. However, depending on the direction of the electric field, anions are polarized to one electrode, resulting in a diminishing anion current over time. The consideration is similar to the W-method; however, both the initial (I_0) and the steady-state current (I_{SS}) are used for the calculation. The t_+ can be estimated by the current fraction of cation current to the total current observed at the beginning of the polarization period. Further, the polarization can induce additional resistances (R_0,R_{SS}) at the electrodes which are assessed by electrochemical impedance spectroscopy immediately before and after the polarization period, and are considered for the calculation of t_+ (Eq. 1.30).

$$t_+ = \frac{1}{1 - Z_\mathrm{d}(0) \cdot R_\mathrm{b}} \tag{1.28}$$

$$t_+ = \frac{R_b}{V/I_\mathrm{SS} - R_\mathrm{int}} \tag{1.29}$$

$$t_+ = \frac{I_\mathrm{SS} \cdot (\Delta V - I_0 \cdot R_0)}{I_0 \cdot (\Delta V - I_\mathrm{SS} \cdot R_\mathrm{SS})} \tag{1.30}$$

For many protocols, the assumption of fully dissociated salts and the consideration of electrolytes as dilute systems pose challenges for the investigation. These assumptions of dissociated salts typically do not hold true, especially at highly concentrated electrolytes, resulting in deviations.[97,104,105] Under certain conditions, negative transference numbers have been reported. For example, in PEO/LiTFSI electrolytes, negative diffusion coefficients could be observed due to the presence of negatively charged ion cluster formation.[106,107] An alternative approach to the effective lithium-ion conductivity (σ_+) is the consideration of the maximum/limiting current density that can be sustained during a dis-/charging step. The limiting current density (LCD) can be evaluated by DC methods (cf. Chapter 1.5.3.4). Thereby, the limitations and uncertainties associated with AC methods can be circumvented.[77] Fundamentally, the LCD is one of the most fundamental measures for the electrolyte application, as the AC conductivity fails to represent the performance on a device level. However, AC conductivity obtained from impedance spectroscopy is still an important material property.

1.3.2.4 Sand Equation

The limiting current density (LCD) describes the highest operational current density of a DC current through an electrochemical cell that can be sustained during prolonged charge or discharge processes. In general, this involves the current density, which is enabled by electrode processes as well as the ion transport characteristics of the electrolyte. Additional contributions can be present in porous materials and diffusion processes within the electrode materials. The active species must be present at the electrode surfaces to sustain electrochemical processes. Under DC current, i.e., during an electrolysis reaction, reactive species at the electrode surfaces are replenished from the bulk by diffusion and electromigration due to the applied field. While this results in stable overpotentials for prolonged electrochemical reactions at current densities below the LCD, diffusion limitations occur for current densities exceeding sustainable regimes. In 1901, Henry J. S. Sand formulated the empirical relationship between time and current density in diffusion-limited systems (Eq. 1.31), which is referred to as the Sand equation.[108]

$$j = \frac{1}{2} \cdot \frac{1}{\sqrt{\tau_{\text{Sand}}}} \cdot n \cdot F \cdot \sqrt{\pi \cdot D} \cdot c_0 \qquad (1.31)$$

with: j current density, τ_{Sand} Sand time, F Faraday constant, n number of electrons, D diffusion coefficient, c_0 initial concentration at the electrode surface.

The characteristic Sand time (τ_{Sand}) of a system describes the transition time after which the diffusion limitations result in a complete depletion of electrochemically active species at the electrode surface ($c_{electrode} = 0$). The transition duration is dependent on the applied current density, the diffusion coefficient, and the bulk concentration ($\tau_S \propto D \cdot c_0^2 \cdot j^{-2}$). In the beginning, the concentration of active species is still sufficient to sustain a current density above the limiting current density, but they are ultimately depleted at the Sand time. This stalls the electrochemical reaction at the electrode, leading to a significant increase in cell potential (**Figure 1.13**).

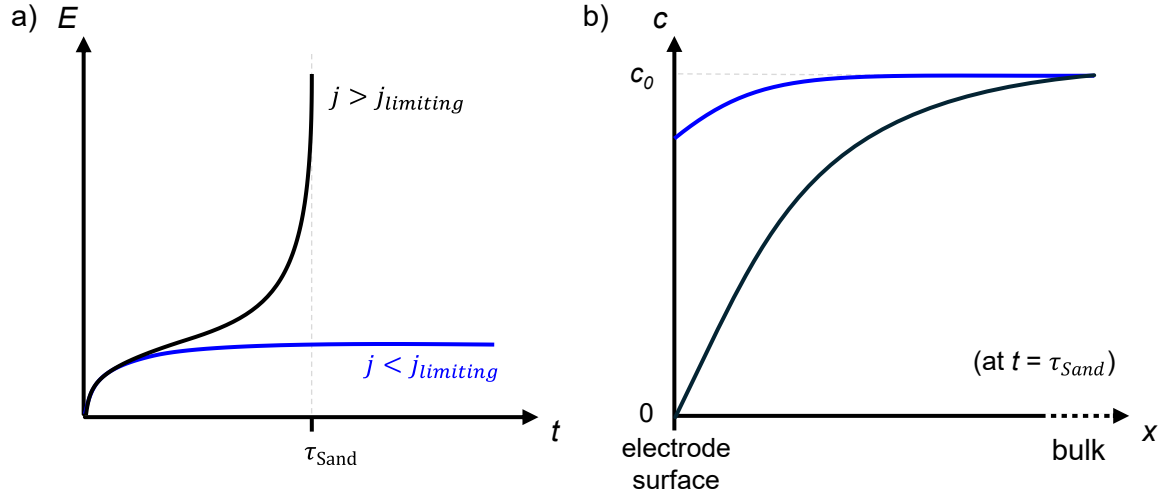


Figure 1.13. Schematic illustration of the (a) cell potential over time and the (b) active species concentration at the electrode surface at τ_{Sand}. Potential and concentration are given for a current density (black) above and (blue) below the limiting current density. After reaching the Sand time, the potential increases due to the depletion of active species at the electrode surface. Adapted and modified from reference.[109]

This phenomenon is especially relevant for the plating processes at lithium-metal electrodes in combination with solid polymer electrolytes of limited ionic conductivity, i.e., low lithium-ion diffusion. Therefore, the main aspect for increasing the limiting current density is to increase the conductive properties of electrolytes by, e.g., new polymer architectures, the incorporation of

additives, variation of the operating conditions, or optimizing electrolyte composition. Especially the bulk lithium salt concentration ($c_{0,Li}$) is an important factor in improving the LCD. It is directly correlated with the LCD ($j \propto c_0$) and can significantly influence the diffusion coefficient of the electrolyte system.[109] However, excessive lithium salt loading results in reduced ionic conductivity and ionic diffusivity. Additionally, the geometry of the applied electrolyte layer can directly influence the current density limitations. Increasing the electrolyte thickness is also demonstrated to decrease the limiting current density as the diffusion limitation is more pronounced for higher electrolyte thicknesses.[110] The incorporation of electrolytes into 3D scaffolds can induce tortuous pathways, which also result in reduced LCDs.

1.3.3 Ion-Coordinating Functional Groups in Polymer Electrolytes

Fundamentally, organic liquid electrolytes and solid polymer electrolytes are based on similar working principles. The host (organic solvent or polymer) needs to enable the dissolution and subsequent dissociation of a lithium salt within the electrolyte bulk. This is commonly achieved by combining highly polar functional groups (e.g., ether, carbonyl) in the host medium and Li-salts consisting of bulky and charge-delocalized anions (e.g., perchlorates, triflates, sulfonimides). A variety of organic solvents is used in typical organic liquid electrolytes. Most solvent systems are based on the combination of different cyclic or linear carbonates and esters, glyme-based (glycol diether) systems, or cyclic ethers.[64,66] They offer high dielectric constants and good solubility for lithium salts. Therefore, similar motifs are utilized in polymer electrolytes by introducing the respective functional groups into polymeric materials. Functional groups can be incorporated into the polymer backbone of linear homopolymers. However, more complex polymer architectures can be realized to tailor the materials' properties, which are discussed in the following chapter (see 1.3.4). In addition to carbonate- and ester-, and ether-based moieties present in liquid electrolytes, many different polar functional groups can be incorporated into polymer structures. **Figure 1.14** summarizes common functional groups capable of coordinating lithium ions.

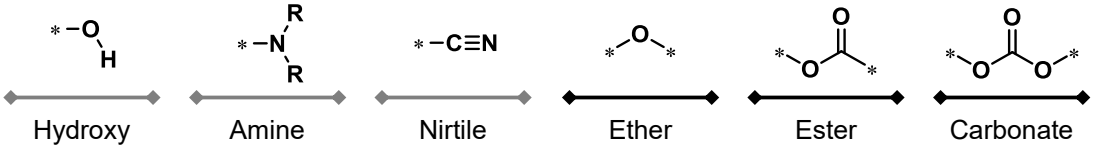


Figure 1.14. Overview of functional moieties used in polymers for solid polymer electrolytes. With ethers, esters, and carbonates being the dominant coordination moieties for SPEs.

Polyalcohols bearing multiple hydroxy groups show good compatibility with different lithium salts. The archetypal representative for polyalcohols is poly(vinyl alcohol) (PVA). It can form stable electrolyte films but suffers from solvent/moisture retention during standard drying procedures. Alternative dry, solvent-less processing methods result in low ionic conductivity in the range of 10^{-7} S cm^{-1} at 60 °C.[111] However, some reports suggest that the SEI formation on lithium metal anodes can be assisted by a thin PVA coating.[112] Besides oxygen-coordination, nitrogen in the form of amines or nitriles is explored for its application in SPEs. Amine groups show good compatibility and solubility in combination with common lithium salts.[113,114] A linear polymer incorporating the amine motif into the polymer main chain is poly(ethylene imine) (PEI), which consists of secondary amines connected by two methylene units. The remaining hydrogen can form intermolecular hydrogen bonds, resulting in semi-crystalline properties. Lithium salts can act as plasticizing agents to reduce crystallinity. Nevertheless, the ionic conductivity of PEI is below the accepted minimum ionic conductivity of 10^{-3} S cm^{-1}. By saturating the alkylation of

hydrogen in tertiary amines to form either linear or branched polymer architectures, crystallization can be suppressed, but simultaneously, the salt dissociation is reduced.[77,114] Alternatively, cyano-groups (or nitriles) exhibit high polarity and promote salt dissociation and find application as electrolyte additives or plastizisers.[115,116] The most common polymer containing cyano-groups, polyacrylonitrile (PAN), shows high thermal and electrochemical stability (4.5 V vs. Li/Li^+). However, its high glass transition temperature (T_g ~ 80 °C) and insolubility in solvents used for electrolyte preparation impose challenges for its application.[77,117]

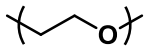
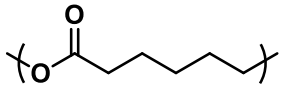
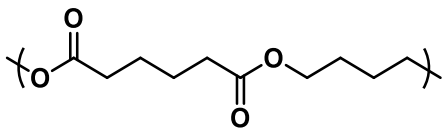
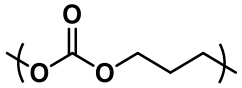
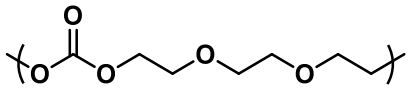
Compared to all other polymer materials, the most prominent and widely studied material is poly(ethylene oxide) (PEO), based on ether functional groups (**Figure 1.14**). PEO research was first sparked by the observations of ionic conductivity by Wright et al.[72] The most advantageous characteristics are the low glass transition temperature, high solubility of lithium salts, and a high degree of dissociation. The implications on the ionic conductivity are detailed in Chapter 1.3.2. In a PEO-matrix, the ion-coordination is facilitated by the free electron pairs of the ether oxygen atoms, and the ionic conductivity is around 1×10^{-3} S cm^{-1} at temperatures above 70 °C. While the efficient coordination is beneficial for the salt dissolution and dissociation, the strong interaction between the polymer matrix and lithium ions hinders efficient cation transport and results in low LTN and predominant anion-transport characteristics.[97] Further, the semi-crystalline nature of PEO limits the ionic conductivity below its melting temperature of around 65 °C, as the crystalline domains restrict ion conduction. The chemical structure of PEO is inherently fixed, rendering backbone modifications to influence physicochemical properties unfeasible. However, many different polymer architectures incorporating PEO segments have been investigated, which are discussed in the following chapter.[118–120]

Carbonyl coordination is utilized as an alternative motif to the dominating ether-oxygen coordination as in PEO. Carbonyl coordination is desirable because of the significantly weaker coordination strength, resulting in high LTN values (see **Table 1.1**). Like PEO, carbonyl-containing polymers can be prepared by ring-opening polymerization (ROP) techniques or alternatively by polycondensation reactions. A large variety of polymer structures can be realized by the choice of cyclic carbonates or esters and by the combination of different starting materials.[77,83] The structure of the resulting polymer is decisive for the physicochemical properties and can be tailored to manipulate key SPE characteristics such as the glass transition temperature, crystallinity, or coordination strength (see Chapter 1.3.4.1). Poly(ε-caprolactone) (PCL) is a common representative of polyester-based electrolyte systems. PCL shows thermal properties similar to PEO. Both polymers are semi-crystalline with comparable melting temperatures as well as glass transition temperatures (-50 to -60 °C). PCL also enables the use of high-voltage cathode systems due to its wider electrochemical stability window of over 4.8 V.[121,122] Further, PCL is biodegradable and exhibits high biocompatibility.[75,121] Despite these similarities of PEO and PCL, the ionic conduction properties differ because of the different nature of ion coordination between carbonyl/ether and lithium ions. Due to steric hindrance, the ion coordination of main-chain oxygen atoms adjacent to the ester is negligible.[123,124] The weak carbonyl-lithium interaction allows for a higher proportion of lithium ion conduction of the overall ionic conductivity.[83,96,123] Despite the overall conductivity of PCL-based electrolytes being lower than that of PEO, this results in comparable effective lithium ion conductivities. Another example for a material prepared by polycondensation of 1,4-butane diol and adipic acid is poly(butylene adipate) (PBA, mind the shared acronym with poly(butyl acrylate)).[125] The choice of diol and dicarboxylate yields a variety of further comparable polymer structures. PBA is also a semi-crystalline material, resulting in a

decreasing ionic conductivity at lower temperatures, but it can be plasticized by the addition of lithium salts.

Compared with polyesters, polycarbonates in general exhibit an even lower coordination strength between lithium ions and the carbonyl moiety. Similar to the previous systems, polycarbonates can be synthesized via ROP. Commonly, six-membered monomers, like trimethylene carbonate, are used, yielding the respective linear polymers. From trimethylene carbonate monomer, poly(trimethylene carbonate) (PTMC) is obtained; a material already established in biomedical applications, due to its biocompatibility and biodegradability. Changes in the polymer structure are accessible via chemically modified cyclic carbonates, to introduce, e.g., additional coordination sites or functional groups for post-polymerization modifications.[126–128] The use of polycarbonates as matrix material for electrolytes was explored much later than for PEO or PCL electrolytes. The first reports showed high electrochemical stability up to 5 V (vs. Li/Li^+) and demonstrated battery cycling in LFP half-cells. The electrolyte glass transition temperature of PTMC was significantly higher than for PEO or PCL, resulting in a lower ionic conductivity.[129] Another approach to obtain linear polycarbonates is the transesterification of, e.g., dimethyl carbonate (DMC) and linear diols. Longer and flexible diols can be utilized to reduce the glass transition temperature of the resulting polymer. Besides aliphatic linkers, more polar glymes can be used (di-, tri-, or oligoethylene glycols) to retain the hydrophilic character of PTMC. In poly(triethylene glycol carbonate) (PTEC), the glass transition temperature could be significantly reduced. However, the combination of carbonyl- and ether-coordination resulted in superimposed ion conduction characteristics with a transference number in between the individual polymers, PEO and polycarbonates.[130]

Table 1.1. Examples of chemical structures of linear polyethers, polyesters, and polycarbonates. The T_g and T_m refer to the polymer in the absence of added salt. The ionic conductivity represents the maximum value at their respective optimum salt concentration at a temperature of 60 °C.

Polymer structure	T_g °C	T_m °C	σ [a] S cm^{-1}	t_{Li^+} 1	ref
 poly(ethylene oxide)	-60	65	3×10^{-4}	0.1-0.2	[131]
 poly(ε-caprolactone)	-53	69	1×10^{-4}	0.54	[123]
 poly(butylene adipate)	-60	60	5×10^{-5}	n.a.	[125]
 poly(trimethylene carbonate)	-15	n.c.	1×10^{-6}	0.8	[129]
 poly(triethylene glycol carbonate)	-36	n.c.	4×10^{-5}	0.39	[130]

[a] = ionic conductivity at 60 °C, n.c. = non crystalline, n.a. = not available

1.3.4 Polymer Architectures

Beyond linear polymers, more complex polymer architectures provide additional means to tune critical characteristics of a polymer class for efficient ion transport. Polymer design aims at affecting conductivity-governing properties, including polymer crystallinity, segmental mobility, chain entanglement, or the ion-coordination environment.[132]

The closest resemblance to conventional linear polymers are linear polymers with modified monomeric units that introduce functional groups as short pendant side groups from the main polymer backbone (**Figure 1.15**). Functional pendant groups that can contribute directly to the ionic conductivity can be ester-, carbonate-, or ether-based.[104,133–137] Typically, the pendant moieties have more degrees of freedom and higher free volume to enable ion-coordination and conduction with less required segmental rearrangement. The increased flexibility can also result in reduced glass transition temperatures, improving VTF-based ion conduction (cf. 1.3.2.2). Anchoring lithium salt or the introduction of rigid units can also influence the transport characteristics or mechanical stability.[134,138]

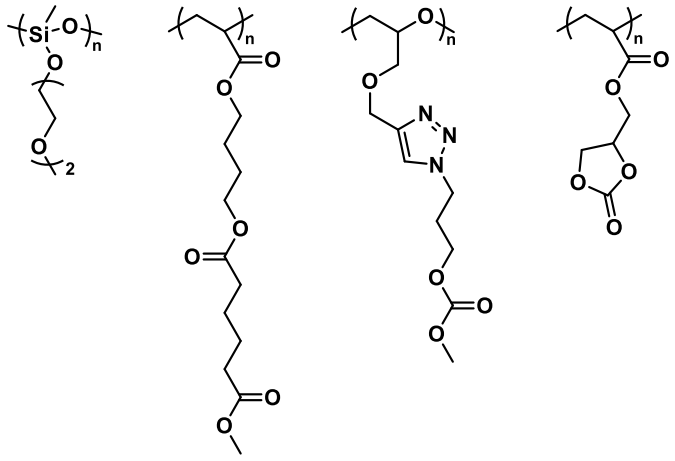
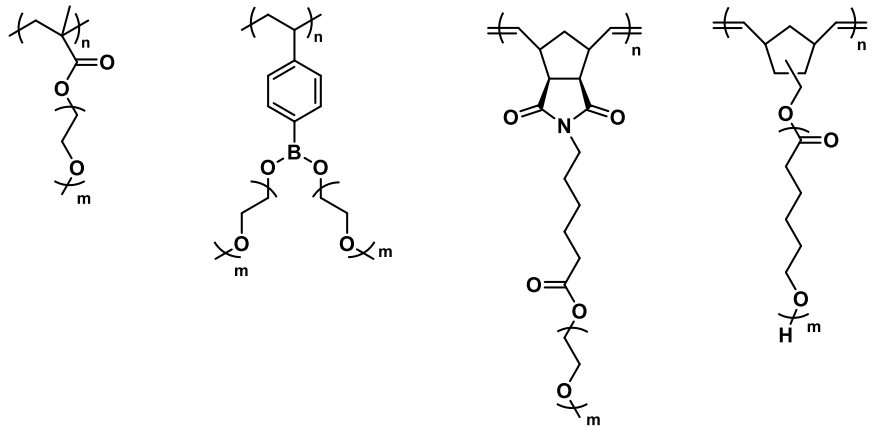


Figure 1.15. Polymer structures with linear polymer backbones and attached functional groups for ion coordination. (f.l.t.r) poly(methyl(diethylene glycol)siloxane) (PM(DEG)S), poly(butyl methyl adipate)acrylate (P(BMA)A), poly(3-(4-(glycidoxymethyl)-1*H*-1,2,3-triazol-1-yl)proyl methyl carbonate) (P(GPE-PMC)), poly((2-oxo-1,3-dioxolan-4-yl)methyl acrylate) (PDOA).[122,133,135,137]

In graft copolymers, macromolecules are tethered along a central polymer backbone. The polymer chemistry of the central backbone and the polymeric side chains can be selected independently (**Figure 1.16**). In this way, the local segmental dynamics of polymeric side chains and the polymer backbone can be decoupled. The concept of graft copolymers provides a vast platform for structural variation. The chemistry and properties of the individual domains can have a significant impact on the physicochemical properties of the resulting copolymer.[139] At very high grafting densities (i.e., number of side chains per repeating unit of the central backbone), the central backbone is elongated due to steric restrictions of the attached side chains in proximity to the central backbone. Polymers with a grafting density of at least one side chain per repeating unit are referred to as bottlebrush polymers.[140] This architecture further suppresses the

chain entanglement by effective elongation of the backbone, which can result in lowering the glass transition temperature. However, near the backbone, the side chains are densely packed, restricting their degrees of freedom and leading to a non-conductive dead zone.[141,142] Lithium ions are preferentially coordinated by oxygen atoms spaced further apart from the backbone, which show increased local dynamics. [142] At excessive molecular weights of the grafted moieties, the ionic conductivity can become limited by side chain crystallization or chain end entanglement that leads to inter-brush interlocking. Therefore, the ionic conductivity of the polymer electrolyte is governed by balancing the chemical structure, molecular weights, grafting density, molecular weight of the central backbone, and side chains. The central backbone is often based on more rigid polymer structures like polyacrylates,[143] polynorbornenes,[144–146] or polystyrene[147] with grafted side chains based on PEG[119,143,145–147] or other conductive motifs like PCL[148].



PMA-*graft*-PEG	PVBBA-*graft*-PEGME	PNDI-*graft*-PEGME	PNb-*graft*-PCL
9×10^{-5} S cm^{-1} (at 25 °C)	4×10^{-3} S cm^{-1} (at 100 °C)	3×10^{-5} S cm^{-1} (at 60 °C)	2×10^{-5} S cm^{-1} (at 40 °C)

Figure 1.16. Examples of polymer structures for graft copolymers used as solid polymer electrolytes. (f.l.t.r.) poly(methacrylate)-*graft*-poly(ethylene glycol)methyl ether (PMA-*graft*-PEGME), poly(4-vinylbenzeneboronic acid)-*graft*-poly(ethylene glycol)methyl ether (PVBBA-*graft*-PEGME, poly(norbornene carboxylic acid imide)-*graft*-poly(ethylene glycol)methyl ether (PNDI-*graft*-PEGME), poly(norbornene)-*graft*-poly(ε-caprolactone) (PNb-*graft*-PCL).[143,145,147] For PNb-*graft*-PCL refer to Chapter II.

Whereas grafted and bottlebrush polymers build on a linear central backbone, star-shaped or hyper-branched systems use multifunctional building blocks to create ramified polymer structures (**Figure 1.17**). Star-shaped systems typically rely on multifunctional core units from which polymer chains emanate.[120] The core unit can be coupled with preformed polymers in *grafting-to* strategies or act as a multifunctional initiator for *grafting-from* approaches. Living polymerization techniques enable the formation of defined block copolymers (**Figure 1.17**, top right). When using multifunctional monomers during the formation of the emanating chains, hyperbranched systems can be established. In the polycondensation reaction yielding *hb*-HSDP (**Figure 1.17**, bottom left), no distinct core unit can be defined, as trimethylolpropane is used in each equivalent polycondensation step. However, for *hb*-PEG (**Figure 1.17**, bottom left), the same unit is only used as the central core unit initiating the polymerization reaction. Further branching points are based on glycerol. Both systems can significantly decrease the polymer crystallinity by structural confinement. However, similar to bottlebrush polymer systems, this can also result in limited chain mobility in the inner domains of extended polymeric structures.

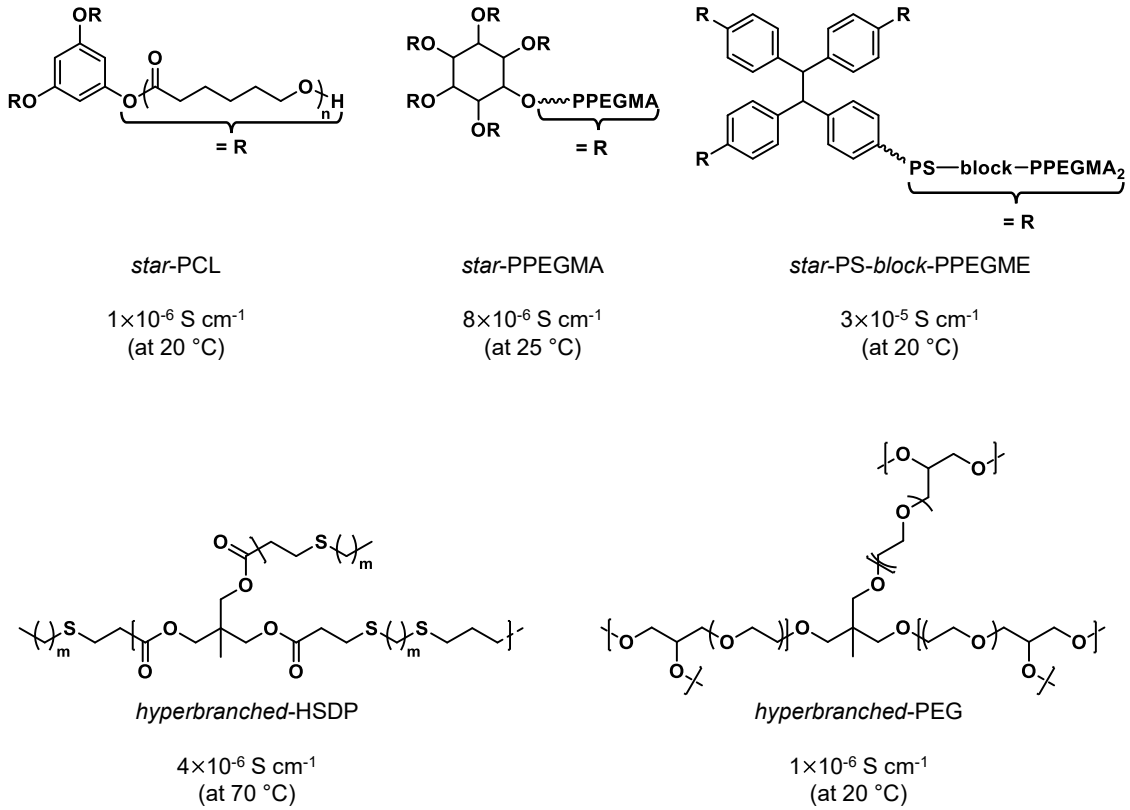


Figure 1.17. Examples of star-shaped polymer structures with a multifunctional central core and emanating linear polymer chains (top, f.l.t.r): *core*-phloroglucinol-*star*-poly(ε-caprolactone), *core*-inositol-*star*-poly(methacrylate)-*graft*-poly(ethylene glycol), *core*-1,1,2,2-tetraphenylethane-*star*-poly(styrene)-*block*-poly(methacrylate)-*graft*-poly(ethylene glycol). Exemplary hyperbranched polymer structures with multifunctional core units and additional branching points within the extending polymer structure (bottom, f.l.t.r): *hyperbranched*-(hexane-1,6-diylbis(sulfanediyl)dipropionate) and *hyperbranched*-poly(ethylene glycol). Hyperbranched systems are named after the propagating units between the branching points.[149–153]

1.3.4.1 Structure-Conductivity Correlations in Solid Polymer Electrolytes

Based on the fundamentals of ionic conduction in solid polymer electrolytes, three key parameters are highlighted for their importance in polymer design: The polymer crystallinity, glass transition temperature, and ion-coordinating motif. These aspects represent the fundamental considerations in design an concenpts of SPEs in later chapters and publications.

- Polymer Crystallinity

For polymer electrolytes with ion conductivity mechanisms relying on segmental motion and ion-hopping events between different coordination sites, as depicted in **Figure 1.10**b, the presented conduction mechanism is only valid for amorphous regions of the SPE. In crystalline domains, solvated ions are displaced into the remaining amorphous phase to establish crystalline structures, reducing the ion concentration accessible to ion transport processes. Further, due to the reduced flexibility of individual chains in the crystalline domain, their contribution to the bulk ionic conductivity is diminished. For these two reasons, polymer systems that suppress crystallization are required to reach high ionic conductivity (**Figure 1.18**). This can be accomplished by, e.g., the addition of plasticizers, crosslinking, or modification of the polymer architecture.[118,149,154] Linear poly(ethylene oxide) (PEO) has a melting point of around 65 °C, depending on the molecular weight and salt concentration.[143,155,156] This results in reduced ionic conductivities at low temperatures below the T_m. In a bottlebrush polymer architecture, shorter PEG side chains are grafted to a central polymer backbone. Poly(norbornene)-*graft*-poly(ethylene glycol) (PNb-*graft*-PEG) represents an example of a bottlebrush polymer detailed further in **Chapter II**. A reduced degree of freedom of the grafted side chains results in reduced crystallinity and, conversely, higher ionic conductivities at lower temperatures.

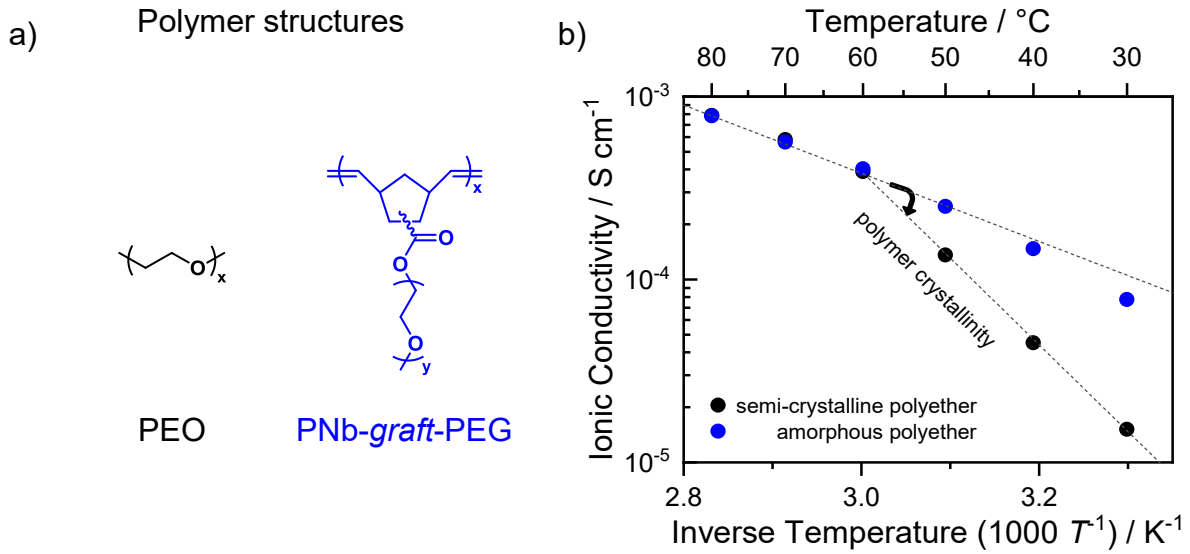


Figure 1.18. (a) Polymer structures used for the comparison of semi-crystalline and amorphous polymer electrolytes. (b) Comparison of the temperature-dependent ionic conductivity of a semi-crystalline and an amorphous polyether-based SPE at similar lithium salt concentrations (color code: blue = better). At high temperatures, both polymer matrices result in similar ionic conductivity. Below the melting point, crystalline domains form in the electrolyte, which do not partake in the ion conduction. This results in a significant reduction of the ionic conductivity compared to the amorphous polyether.[143,146]

- Coordinating Motif

As detailed in Chapter 1.3.2.3, the lithium transference number is an important parameter for determining effective lithium-ion conductivity based on measured bulk conductivities. For solid polymer electrolytes, the nature/strength of the coordinating motif in the polymer structure significantly impacts the contributions of anionic and cationic conductivities.[97,123,157] PEO-derived materials commonly exhibit a low LTN of around 0.2, indicating only 20 % contribution of Li-ion conductivity towards the total conductivity. In contrast, carbonyl-coordinating polymers like PCL or PTMC show higher LTN above 0.5.[158] The differences are mostly correlated to significantly weaker coordination strength for ester- or carbonate-based systems. When considering the LTN to determine the effective lithium ion conductivity (σ_{eff}) according to Eq. 1.26 different systems of vastly different LTN can be compared pragmatically. In **Figure 1.19**, two amorphous solid polymer electrolytes are compared concerning their total and effective conductivity.[136,146] Poly(norbornene)-*graft*-poly(ethylene glycol) utilizes ether-lithium coordination, whereas polymethyl(butyl methyl adipate)siloxane (PSi-BMA) coordinates to lithium via ester groups. The polymers reflect a common trend, that the total ionic conductivity is higher for PEO/PEG-based systems than for ester- or carbonate-based systems. However, the high LTN of PSi-BMA leads to a higher effective lithium ion conductivity. This emphasizes the importance of both high total ionic conductivity and the appropriate ion coordination strength to facilitate lithium-ion migration through the electrolyte.

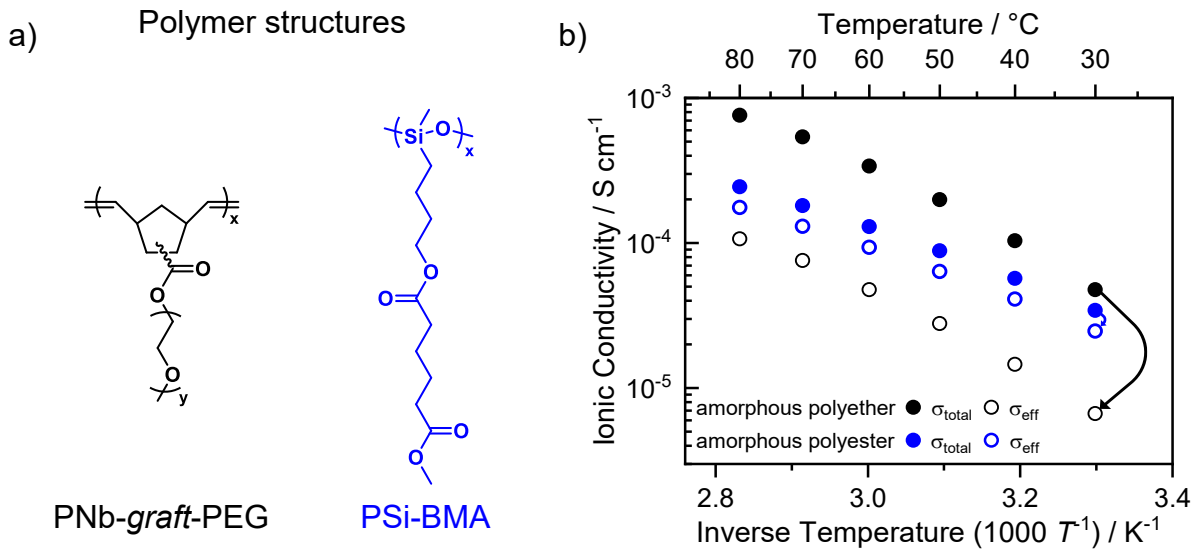


Figure 1.19. (a) Polymer structures used for the comparison of the total (σ_{total}) and effective (σ_{eff}) ionic conductivity of an amorphous polyether and polyester. (b) Temperature-dependent ionic conductivity and effective conductivity. (σ_{eff}) calculated by multiplying σ_{total} and the LTN. Lower LTNs for polyether-based materials, due to stronger coordination between ether-oxygen atoms to lithium ions, result in significant differences between σ_{total} and σ_{eff}. Data was taken from (black) Chapter III, and (blue) Chapter IV. [136,146,159]

- Glass Transition Temperature

The glass transition temperature of a polymer electrolyte system is decisive for its ion transport characteristics. The correlation of T_g and ionic conductivity, as well as the fundamentals of VTF-activated ion transport, are detailed in Chapter 1.3.2.2. Generally, the ionic conductivity of solid polymer electrolytes consisting of similar coordinating motifs can be correlated to the electrolyte glass transition temperature. Lower glass transition temperatures result in higher ionic conductivities, according to Eq. 1.24. In **Figure 1.20**a, three different polymers are compared, which all use butyl methyl adipate side chains as coordinating motifs.[122,136] They differ in polymer backbone: norbornene, acrylate, and siloxane. The choice of polymer backbone strongly influences the T_g of the side-chain functionalized polymer. However, it should be noted that the T_g of the electrolyte system is also influenced by other factors, e.g., the amount of lithium salt.

Lower salt loadings commonly result in lower glass transition temperatures. However, insufficient lithium concentrations result in lower ionic conductivities. Therefore, the glass transition temperature and lithium salt content must be optimized to achieve the best trade-off. For systems utilizing similar coordinating motifs, similar optimal lithium salt concentrations can be expected. In **Figure 1.20**b, the temperature-dependent ionic conductivities of the three polymers demonstrate the importance of the glass transition temperature of the electrolyte system under comparable experimental conditions.

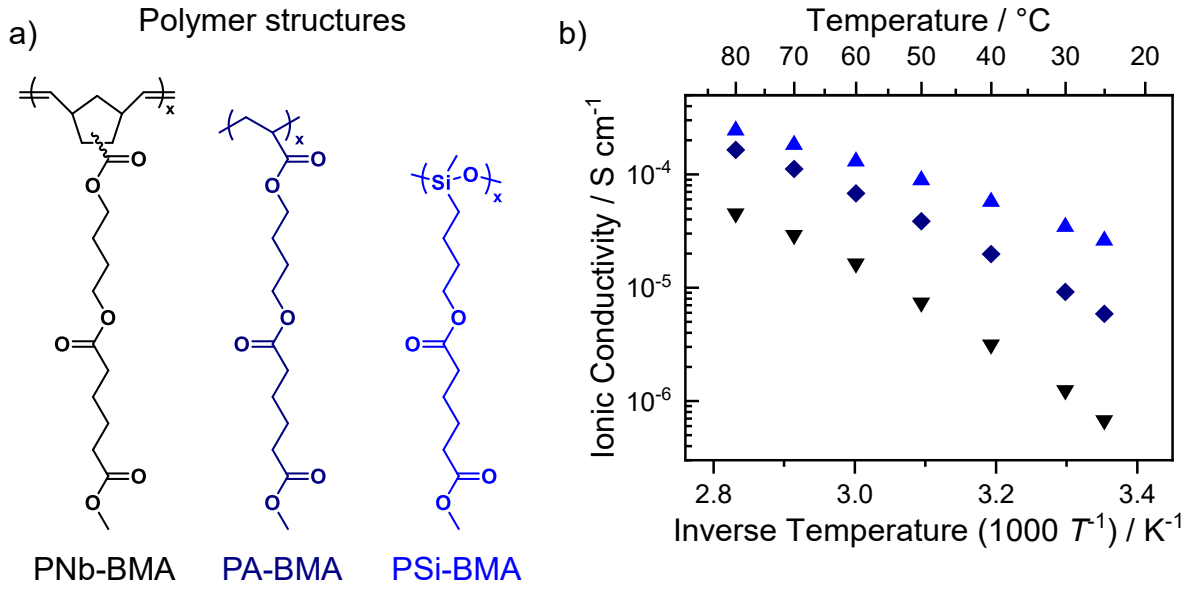


Figure 1.20. (a) Polymer structures are used for the comparison of the influence of the glass transition temperature. (b) Arrhenius plots of the temperature-dependent ionic conductivity for three similarly designed polymers. The polymer structures have an identical coordination motif as side chains but differ in the polymer backbone. The polymers are mixed with 20-25 wt% LiTFSI, and the resulting electrolyte glass transition temperatures are (blue) -67 °C, (marine) -40 °C, and (black) -29 °C. Data was taken from (black) Chapter II, (marine) reference[122], and (blue) Chapter IV.[136,159]

1.3.5 Mechanical Properties of Solid Polymer Electrolytes

The mechanical integrity of the separating electrolyte layer is of critical importance for the function of a battery. Without ensuring separation, the electrodes can short-circuit internally, leading to high current density discharges between the electrodes. However, besides just the separation of the electrodes, the mechanical properties exhibit an extensive influence on the battery operation and performance. As lithium metal electrodes are a promising high-energy density anode system, the risk of lithium dendrite formation poses imminent safety concerns. The general idea is to increase the mechanical properties of the contacting electrolyte to mitigate the formation of electrolyte-penetrating features. For an effective dendrite suppression, theoretical calculations by Monroe and Newman imply that the required shear modulus of an electrolyte should be double the shear modulus of the lithium metal electrode itself.[32,160] However, most polymer-based electrolyte systems do not meet that requirement but are very soft to allow for higher ionic conductivities. The quality of the electrolyte|electrode contact and interface is very important for the charge transfer reaction, as well as interface impedance during operation. In combination with electrode systems of high volume variation, a very rigid and non-compliant electrolyte can result in loss of contact and the formation of voids at the interface. Consequently, the current is localized to areas with maintained contact, which in turn increases thermal losses and contact resistance. Therefore, electrolytes of adequate compliance, as well as shear modulus, are required. In the following, different approaches are highlighted by selected studies and materials. The general concepts can be applied to different electrolyte systems and in combination to enable synergistic effects.

1.3.5.1 Membranes

The incorporation of porous separating membranes can support electrolytes with insufficient mechanical stability. In commercialized batteries, the dominant electrolyte systems are based on organic liquids. While their low viscosity evokes many advantages, like high ionic conductivity and excellent electrode wetting, they must be supported by a separating membrane. The most common membrane materials are based on single-layer or laminated polyolefin foils.[65,161] During manufacturing, the polymer sheets are stretched to generate the desired pore structure (**Figure 1.21**a). The membrane porosity is typically around 30-50 %, and the thickness is around 20 µm. Some multilayer membranes offer limited safety measures. Upon heating beyond the operational window of the battery, the porous structure collapses and prevents further mass/ion transport through the membrane.[162] Common alternatives to stretched membranes are nonwoven products produced from fibers (**Figure 1.21**b). Due to the manufacturing process, the resulting pore structure is less defined than those for stretched membranes. They can be prepared by wet-laid, dry-laid, or by electrospinning techniques.[163] The main challenge is the preparation of thin fiber mats with comparable thicknesses and physical properties to stretched microporous membranes.[161] Track-etched membranes have emerged as another class of tunable and defined separators. They can be produced from a wide variety of polymer foils with well-defined pore size and vertical alignment throughout the entire film thickness (**Figure 1.21**c). Thereby, the use of mechanically stable base films (e.g., polyimide, polyethylene terephthalate, polycarbonate) allows for thin membranes below 10 µm.[122,146,164] Additional surface modifications and coatings can be utilized to improve electrolyte compatibility. Park et al. introduced a thin polyvinylpyrrolidone layer on the foil and pore surfaces to improve wettability, ionic conductivity,

lithium transference numbers, and decrease the contact resistances and overpotentials in cycling experiments of symmetrical lithium cells.[165]

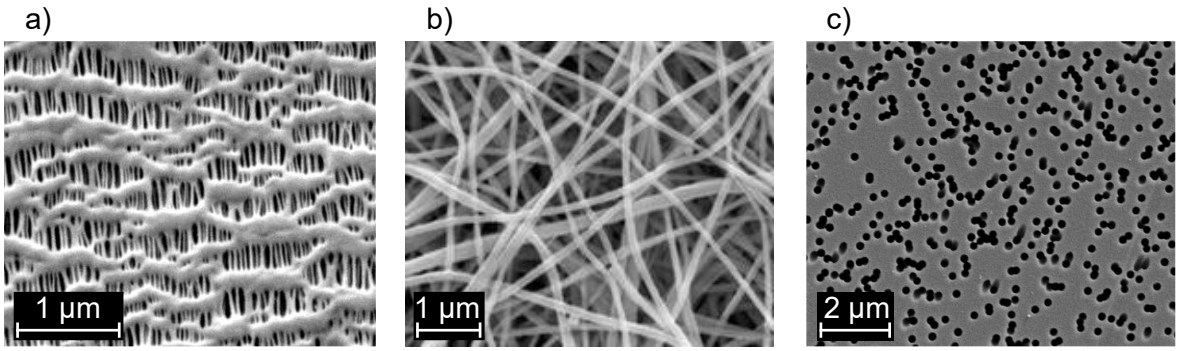


Figure 1.21. Examples of optical images of a) stretched polyolefin membrane,[161] b) PVDF nonwoven mat,[163] and c) track-etched polyimide membrane.[146] The pore structure differs for the different manufacturing processes.

1.3.5.2 Polymer-Based Approaches to Increase the Mechanical Stability

Membrane-supported systems offer practical stabilization of electrolytes with insufficient mechanical strength. However, they introduce additional layers, cost and structural complexity. Therefore, the following chapter focuses on strategies to enhance the mechanical robustness of all-polymer electrolytes for different polymer architectures. This chapter focuses on approaches using linear polymers (**Figure 1.22**) as well as the application of crosslinking to yield 3D network electrolytes (**Figure 1.23**).

Blend polymer electrolytes follow a simple and adaptable strategy for improving the mechanical stability by mixing soft ion-conducting polymers with rigid polymers (**Figure 1.22**a). Blends are commonly prepared by solution- or melt-based mixing processes. For the selection of polymer constituents, a wide variety of polymers is accessible. The properties of the resulting blend can be tuned by adjusting the proportion of the complementary polymer species. The composition of the polymer components varies significantly between studies, depending on the focus on mechanical stabilization or ionic conductivity. Examples of polymer combinations include $PCL_{83mol\%}$-$PVDF_{17mol\%}$,[166] $PEG_{90wt\%}$-$PNb_{10wt\%}$,[146] $PEO_{33wt\%}$-PVdF-$HFP_{66wt\%}$,[167] $PEO_{90mol\%}$-$PVP_{10mol\%}$,[168] or $PEO_{50wt\%}$-$PMMA_{50wt\%}$.[169]

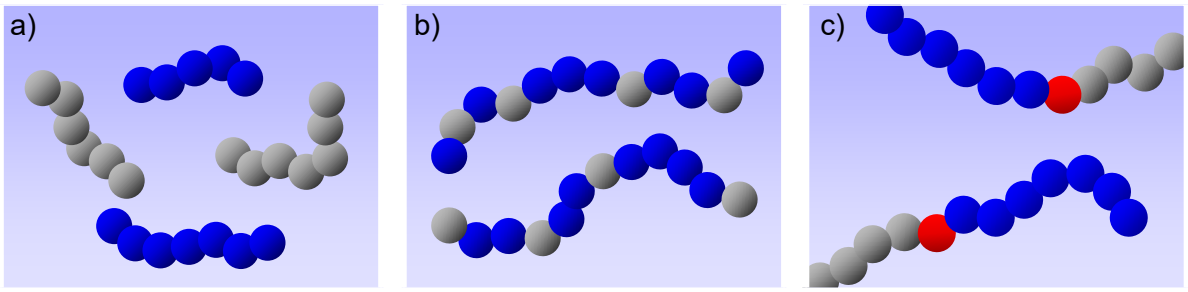


Figure 1.22. Schematic representation of different types of non-crosslinked approaches to increase mechanical stability. Color code: (blue) contributing to ion conduction, (gray) non-conducting, hard or solid phase for mechanical stability, (red) connection points in block copolymers. A) a polymer blend, b) statistical/random copolymer and c) a block copolymer.

Despite the straightforward preparation, the weak entropy contribution from long chains and unfavorable enthalpy (energy of mixing) typically results in thermodynamic incompatibility. Incompatibility can result in macrophase separation or demixing into single-component phases of the individual polymers. The thermodynamically driven phase separation results in

heterogeneous regions of ionically conductive and rigid non-conducting polymer domains, which can result in tortuous conduction pathways impeding efficient ion-transport. The use of compatibilizers or short block copolymers can improve the miscibility of blend electrolytes, but introduce additional complexity.[169]

Beyond physical blending of different polymers, the integration of complementary properties into a single macromolecular structure can be achieved by the copolymerization of complementary monomers. Depending on the selected monomers and the applied polymerization technique, different polymer architectures from the two extremes of random/statistical and block copolymers can be realized. On the one hand, the random copolymerization of contrasting polymers can be used to reinforce solid polymer electrolytes. Mechanically stabilizing monomers are integrated statistically into the ion-conducting backbone (**Figure 1.22**b). Besides affecting the mechanical properties, this can further lead to reduced polymer crystallinity of semi-crystalline ion-conducting segments. However, the ion-coordination can be compromised by the rigid and often non-polar monomer units. Systems obtained from statistical copolymerization include poly(methyl methacrylate-co-(2-oxo-1,3-dioxolan-4-yl)methacrylate),[137] poly(glycidyl methacrylate-co-(oligo(ethylene glycol)methacrylate),[170] or poly(vinylidene flouride-co-(2-oxo-1,3-dioxolan-4-yl)methyl-2-(trifluoromethyl)acrylate).[171] While the studies mentioned good mechanical properties, no direct investigation of rheological characteristics has been performed.[170,171] Alternatively to copolymerization, a random distribution can also be realized by the random attachment of different functional groups in post-polymerization techniques. The system of poly(glycidyl propargyl ether) could be sequentially modified by click reactions with different functional azides. In this, benzyl-azide and LiTFSI-azide introduced rigid and high T_g contributions, whereas OEG-azides provided ion-conducting domains. Due to the sequential click reaction, the three different pendant groups were distributed randomly along the glycidol-based polymer backbone.[134]

On the other hand, unlike random copolymers, block copolymers are constituted of covalently connected segments, each composed of different monomer types (**Figure 1.22**c). The separation of unlike monomers into distinct blocks induces incompatibility between different segments of a single macromolecule. Similar to polymer blends, the incompatible segments demix. However, for block copolymers, the covalent connection prevents macrophase separation and leads to microphase separation and well-defined microstructures depending on thermodynamic parameters and composition. Depending on the molecular weight and volume fraction of the individual segments, as well as the degree of incompatibility (quantified through the Flory-Huggins-parameter χ), the microphase separation can result in the controlled formation of nanostructures such as spherical, cylindrical, or lamellar morphologies.[172,173] The segregation into microdomains decouples the contradicting requirements of mechanical reinforcement and ion transport without the disadvantage of macrophase separation as in blends.

Due to the advantages of the block copolymer architecture, many different polymer systems have been investigated.[174] Linear AB diblock copolymers are the simplest case, where one ion-conducting block is connected to another mechanically robust block. Singh et al. synthesized a series of linear AB copolymers based on poly(styrene)-*block*-poly(ethylene oxide) and investigated the influence on morphology, mechanical properties, and ionic conductivity. The

block copolymerization resulted in stable microphase separation. They found that the ionic conductivity scales linearly with the volume fraction of the PEO domain.[175]

Poly(styrene)-*block*-poly(ethylene oxide)-*block*-poly(styrene) ABA triblock copolymers were investigated independently by different research groups.[176,177] They found that, irrespective of the volume fraction and molecular weight of the PEO segment, the EO units at the PS/PEO interface do not contribute to the ionic conductivity. They attributed the phenomenon to the restricted mobility of the EO units when covalently connected to PS segments.[176] While this effect limits the ionic conductivity for short PEO segments, high molecular weight PEO systems are restricted by polymer crystallization, limiting the viability of such linear systems. With respect to high-mass polymers, Devaux et al. demonstrated the beneficial effects of comb-type polymer architectures. They showed that the melting temperature and the crystallinity were less affected in comb-PEO than in linear PEO counterparts.[178]

This also advanced toward bottlebrush polymer electrolyte systems as described in Chapter 1.3.4. Different polymer systems incorporate bottlebrush block copolymer segments with reinforcing hard segments. Polymer systems can be based on different architectures, including poly(styrene)-*block*-poly(styrene)-*graft*-poly(ethylene oxide) or poly(norbornene)-*block*-poly(norbornene)-*graft*-poly(ethylene glycol).[146,179] Alternatively, the rigid polymer segment can also be introduced in a bottlebrush architecture, leading to all-bottlebrush block copolymers. Gai et al. synthesized a series of poly((norbornene)-*graft*-poly(styrene))-*block*-poly((norbornene)-*graft*-poly(ethylene glycol)) and found disordered, lamellar, or cylindrical nanostructures, based on the composition and molecular weight of the grafted polymer chains.[180] Bates et al. reported on ABA-type bottlebrush block copolymers using the same norbornene-based backbone motif. They obtained well-defined hexagonally aligned cylindrical nanostructures. The ionic conductivity of the ABA block copolymer and the equivalent PEO-bottlebrush homopolymer was around 3×10^{-5} S cm^{-1} at 60 °C, despite the PEO volume fraction in the ABA block copolymer being only 75 vol%.[145] The high variability of both the central backbone, grafted polymer side chains, and the restriction of macrophase separation offers a wide scope for architectural optimization within one material.

Alternatively, the formation or utilization of crosslinking and 3D polymer electrolytes offers tremendous potential to enhance the mechanical robustness as well as structural integrity (**Figure 1.23**). At elevated operating temperatures, linear materials are susceptible to thermoplastic deformation or can show creeping as a consequence of pressure, which can ultimately result in internal shorting of a battery. In contrast to linear polymers, the covalent crosslinking points or network nodes in 3D materials result in improved deformation resistance. Additionally, the crosslinking can result in reduced or suppressed crystallinity due to restricted chain mobility.[149,181]

Chemical crosslinking of linear polymers can be achieved by harsh ionizing radiation, milder photo-assisted crosslinking, or functional groups used for curing reactions.[149,181–183] Usually, a small amount of chemical crosslinking is sufficient to obtain 3D-stable materials (**Figure 1.23**a). For example, benzophenone can be used as a UV-photo crosslinker and has been applied in PEO- as well as PCL-based systems. [149,181] The crosslinking is achieved by hydrogen abstraction from the polymer backbone or side chains, followed by inter-polymer recombination reactions.[181] This approach is broadly applicable to a variety of polymers, as it does not require specific functional groups within the polymer structure. The advantage of UV-induced crosslinking is that the

electrolyte can be formulated, preshaped, and dried in the desired dimensions before it is cured by UV radiation to form stable and self-standing electrolyte membranes. However, excessive crosslinking is possible and can lead to significantly restricted flexibility. For example, Chen et al. prepared 3-armed PCL-based star polymer electrolytes and used benzophenone as a crosslinker to enhance the mechanical stability. The star polymers exhibited crystalline behavior, which was entirely suppressed upon crosslinking, resulting in a twofold increase in the room temperature ionic conductivity. Rheological measurements showed a shift from viscous-dominated to elastic-dominated behavior and a significant increase in the storage modulus.

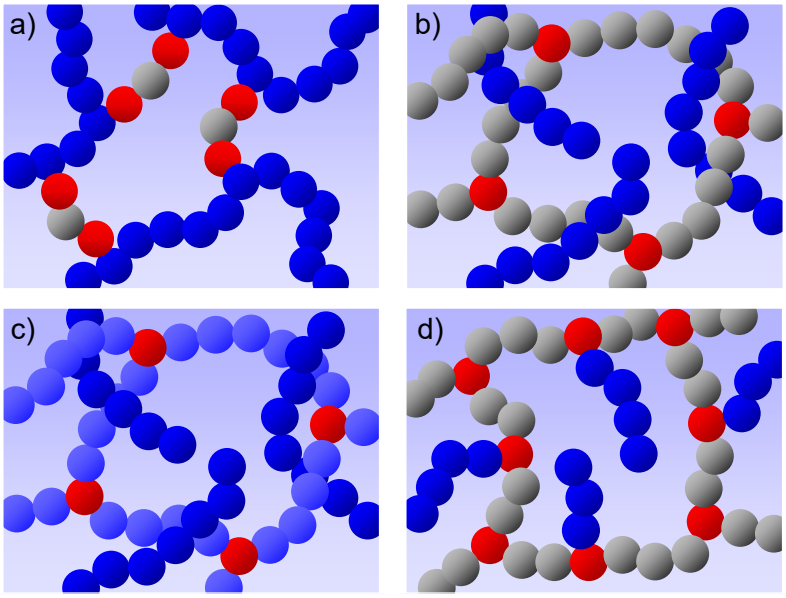


Figure 1.23. Schematic representation of different types of crosslinked or network polymer electrolytes. Color code: (blue) contributing to ion conduction, (gray) network-forming phase for mechanical stability, (light blue) ion-conducting network-forming phase, (red) crosslinking or branching point in networks. a) Linear polymer crosslinked via chemical crosslinking during a curing step, b) semi-interpenetrating network formed by a scaffold of crosslinked hard segments soaked or impregnated with an ion-conducting polymer without a covalent connection between the two constituents, c) semi-interpenetrating network formed by a scaffold of ion-conducting segments soaked or impregnated with another ion-conducting polymer, d) graft network consisting of a polymer network scaffold with covalently attached ion-conducting segments.

Although chemical crosslinking enables the formation of 3D networks, the approach can lack precision, resulting in a statistical distribution of crosslinking sites and limited control over the resulting network structure. Alternatively, network materials can be synthesized and tailored by polymer architecture design. Multivalent monomers or macromonomers can be used for the preparation of polymer networks with control over the degree of crosslinking, the distribution of crosslinking sites, and the mesh size. This approach can be applied to polymer electrolytes by the utilization of telechelics and polyfunctional precursors based on ion-coordinating motifs described in Chapter 1.3.3.[33,184–186] Typically, the bulk of the material is composed mostly of the telechelic polymer, as the proportion of network-forming sites is low to prevent excessive crosslinking. As a result, the electrolytes can retain polymer flexibility, ion transport characteristics, and increased mechanical stability. Telechelic diacrylates are commonly used for the preparation of network polymer electrolytes. For example, Jalbert et al used bifunctional acrylate-terminated polycaprolactone to obtain mechanically robust network electrolytes with a Young's modulus of 5.5×10^6 Pa.[186] Alternatively, epoxy resins are often used as network-forming materials that are based on the addition reaction between the epoxides and amines. The epoxide

groups can either be incorporated as end groups in telechelic polymers in combination with polyfunctional amine hardeners or *vice versa*.[185] Further, amine- or epoxide-bearing monomers can be built into the polymer backbone by copolymerization.[184] The properties of the resulting network can be tailored by, e.g., variation of the telechelic molecular weight, the valency of the curing agent, or the content of functional monomer in the polymer backbone.

The incorporation of dedicated network structures can significantly improve the mechanical stability of the resulting material. Networks can be categorized based on the number and connection pattern. While the systems described above form simple polymer networks, more intricate structures can be classified as interpenetrating networks, semi-interpenetrating networks, or graft networks. Interpenetrating networks (IPNs) are formed by two individual and intertwined networks. The networks can be formed simultaneously, side by side, or in succession, where one network is formed and the second network is then formed within the existing network structure. The structures are not connected by any covalent bond. However, demixing is entirely suppressed due to the interlocking interpenetration. Different polymer types can be used to form the individual network structures to introduce desired material properties. A network formed by a hard segment can provide mechanical stability, whereas a second complementary network can provide ionic conductivity to an interpenetrating network electrolyte. Goujon et al. prepared an interpenetrating network electrolyte in a two-step process. First, nitrile butadiene rubber (NBR) is thermally crosslinked, resulting in stable NBR films. Secondly, the pre-formed network is soaked with a poly(ethylene glycol) monomethyl ether methacrylate-based monomer, which is polymerized within the NBR-network to yield an interpenetrating network structure. The mechanical properties could be significantly increased with a maximum stress at break of 0.3 MPa to 1.0 MPa for the individual PEO-network and the interpenetrating network, respectively. However, the ionic conductivity was reduced in the interpenetrating network electrolyte due to restricted chain mobility of the PEO segments.[187] Alternatively, two soft/ion-conducting polymer networks can be formed to benefit from the increased mechanical stability by the network formation without significant restriction of the polymer chain flexibility. Guan et al. first prepared a PEO-based polymer network and soaked the structure with another formulation of PEO-based precursors to establish the second interpenetrating network.[188] They could increase the mechanical stability in compression stress-strain curves while also achieving high ionic conductivities of up to 1.9×10^{-4} S cm^{-1} at room temperature. However, the network was applied as a gel polymer electrolyte in combination with a liquid electrolyte.

In semi-interpenetrating networks (sIPNs), a polymer-based 3D scaffold is soaked or penetrated with another polymer that does not form a secondary network (**Figure 1.23**b). Thereby, the second polymer is only dissolved into the network structure. As for interpenetrating networks, neither the network nor dissolved polymer is connected to the other by any covalent bonds. This enables higher degrees of flexibility for the non-crosslinked polymer, but can also result in gradual demixing in highly incompatible combinations of polymer and network polymer. The 3D scaffold provides mechanical stability, whereas the incorporated polymer phase offers 3D ion diffusion pathways throughout the sIPN structure. The 3D network can be formed by non-ion-conducting and ion-conducting polymer structures. When using ion-conducting crosslinkers, the ionic conductivity of the electrolyte bulk can be retained while introducing mechanical stability due to the sIPN structure (**Figure 1.23**c). PEG/-PEO-based crosslinkers are commonly used to establish the 3D scaffold in combination with different electrolyte systems.[189,190] In an early study, Min et al. used 3D networks derived from the crosslinking of

poly(ethylene glycol)dimethacrylate. The sIPN-structure is formed *in situ* in the presence of the secondary polymer phase. The impregnated polymer electrolyte consisted of poly(siloxane-*graft*-allyl cyanide), low molecular weight PEGMDE, and LiTFSI. They achieved an ionic conductivity of 7×10^{-4} S cm^{-1} at 30 °C for the sIPN composition of 40 wt% network, 10 wt% poly(siloxane-*graft*-allyl cyanide), and 50 wt% PEGDME.[189] In a recent study, Homann et al. used a similar approach to investigate the influence of the mechanical properties on the lithium plating during charging. Instead of low molecular weight plasticizers, they used high molecular weight PEO as the impregnating phase. While non-crosslinked PEO-electrolytes showed distinct voltage fluctuations during charging, the phenomenon could be eliminated by the introduction of a 3D network derived from PEGDMA. The polymer composition of the sIPN-electrolyte was 31 % network and 69 % linear PEO. The ionic conductivity of the electrolyte was reduced by one order of magnitude when compared to the non-crosslinked PEO-electrolyte. However, the compressive stability could be increased from 0.02 MPa to 0.68 MPa. Moreover, the detrimental voltage fluctuations could be effectively suppressed, marking the importance of sufficient mechanical stability for the electrolyte.

The group of Li established a framework of comb-chain crosslinked electrolytes. The polymer network systems combine linear precursor polymers with pendant epoxy groups with telechelic PEG-diamines.[191] The resulting network properties can be tailored by the degree of functionalization of the epoxy-containing precursor as well as the molecular weight of the PEG-telechelics. They found that a high grafting density and high molecular weight of the PEG segments resulted in the highest ionic conductivity. Contrarily, the highest mechanical stability could be obtained for lower grafting density and low molecular weight PEG segments. In subsequent studies, they substituted some proportion of the PEG-telechelic with monofunctional PEG-amines, resulting in grafted network structures (**Figure 1.23**d). The overall structure is comparable to the comb-chain crosslinked electrolytes, but the fraction of dangling or grafted PEG-chains increases the ionic conductivity due to a higher degree of flexibility. The Young's modulus of the graft network structures decreased with an increasing proportion of dangling PEG chains. However, lithium plating and stripping experiments indicated that the compliance of the electrolyte systems resulted in enhanced cycling stability.[192] Alternatively, the copolymerization of linear telechelics with polymerizable chain ends with monofunctional macromonomers also yields graft network electrolytes with dangling polymer chains within the network.[193,194]

1.3.5.3 Composite Polymer Electrolytes

In addition to the described polymer architecture-based strategies, the formulation of composite polymer electrolytes (CPEs) represents an alternative approach to designing solid-state electrolytes with immproved mechanical properties. Rather than relying on chemical modifications of the polymer structures themselves, this concept involves the incorporation of nanoscale filler materials into the polymer matrix (**Figure 1.24**). The resulting composite materials commonly combine polymeric and inorganic components. The development of nanocomposite electrolytes is motivated by the complementary properties of polymers and inorganic materials.[195] While polymers provide excellent electrode wetting and low interfacial resistances, inorganic phases offer rigidity and mechanical integrity but suffer from interfacial contact issues. Importantly, polymer-based approaches described in the previous sections and the application of nanocomposite design strategies are not mutually exclusive. Both approaches can be combined synergistically to tailor mechanical and electrochemical properties.

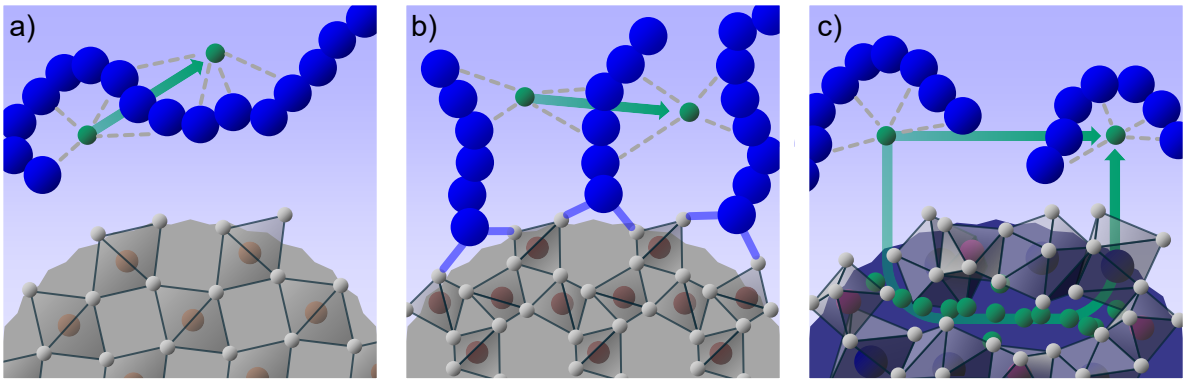


Figure 1.24. Schematic representation of different types of nanocomposite electrolytes. Color code: (blue) contributing to ion conduction, (gray) non-conducting, hard or solid phase for mechanical stability, and (green) conduction pathways. a) Physical mixing of inert TiO_2 nanoparticles and polymer matrix.[131,146] b) SiO_2 nanoparticles with surface-grafted polymer chains.[196] c) LLZO solid-state electrolyte in combination with solid polymer electrolytes. The ion transport can be facilitated by both constituents.[197]

Generally, nanofillers are categorized as either *passive* or *active* filler materials with respect to their contribution to the ionic conductivity of the resulting composite material.[195,198] Passive fillers do not show any intrinsic ionic conductivity through conduction pathways within the nanofiller material. The most common passive fillers are based on oxide ceramics like Al_2O_3, SiO_2, or TiO_2.[131,146,195,199] Nevertheless, passive fillers can improve the electrochemical properties of the electrolyte system due to secondary effects, as well as the mechanical and thermal properties of the electrolyte system.[200] Two main effects influence the electrochemical properties: 1) plasticizing effects and 2) interfacial polymer-nanofiller interactions. The incorporation of nanoparticles interferes with the arrangement of polymer chains and can result in lowering the degree of crystallinity. The resulting increase of the amorphous fraction can enhance ion transport. Besides structural effects, nanofillers can interact with the host polymer and lithium salts via Lewis acid-base interactions. Especially, the nanofiller-anion interaction can result in anion fixation and thus increase the lithium transference number. High surface polarity can also improve the salt dissociation, leading to higher concentration of free charge carriers and improved ionic conductivity and lower activation energies.[131,133,195] In the simplest form, nanocomposite electrolytes are prepared by combining a passive nanofiller and a polymer electrolyte using various means of formulation protocols to create homogeneous dispersions(**Figure 1.24**a). In solvent-assisted protocols, the constituents are dissolved in a suitable solvent by high-intensity stirring or ultrasonication to decrease nanofiller agglomeration in the electrolyte bulk. The solvent is then removed to yield dry and uniform composite films. Alternatively, solvent-free techniques include melt blending or mechanical milling.[201] The advantage of solvent-free protocols is the elimination of residual solvent within the electrolyte, which can lead to interfacial issues at the electrodes, the electrochemical stability of the electrolyte bulk, and the formation of detrimental decomposition products.[202]

Although unmodified passive nanofillers are readily available and inexpensive, they tend to agglomerate and can lack interfacial compatibility with the polymer matrix. Therefore, polymer-grafted nanofillers have emerged to enhance compatibility and improve the homogeneity of the filler dispersion throughout the composite electrolyte (**Figure 1.24**b). The grafted polymer corona around the nanoparticles offers design flexibility, as polymer chemistry, molecular weight, and grafting density can be adjusted. Some examples for polymer-grafted nanoparticles are

Jeffamine@SiO_2,[194] PEO@POSS,[203] PEO@SiO_2.[204] In addition to surface-grafted polymer chains, further motifs like surface-anchored anions or anion acceptors can be used to improve the lithium transference number of the CPE.[196,205] Notably, the central core can also be formed by polymeric materials. In different studies, Glynos et al. reported on different systems based on polystyrene nanoparticles with grafted polymer chains, either based on high T_g poly(methyl methacrylate) (PMMA) or ion-conducting PEG. After the addition of the polymer-based fillers to PEG-based electrolyte systems, they could maintain comparable ionic conductivities while improving the storage modulus by around 4 orders of magnitude.[206–208]

Active fillers, on the other hand, are typically nanoscale variants of inorganic solid-state electrolyte materials. In addition to the interactions described for passive nanofillers, active ceramic fillers such as garnet-type (LLZO), or NASICON-type (LLTO) electrolytes can contribute to the ion conduction by their intrinsic ionic conductivity and conduction pathways within the solid phase (**Figure 1.24**c).[195,198] PEO is the most common polymer matrix for the formation of CPE systems with active fillers in e.g., PEO:LLZO or PEO:LATP.[209,210] While the ionic conductivity of typical inorganic ion conductors is significantly higher than in SPEs, the effect on the overall ionic conductivity of the CPE reported is marginal. The critical challenge in CPEs is the charge transfer between the polymer matrix and the active fillers.[210] Commonly, the transition from the polymer electrolyte to the solid electrolyte phase is unfavored, resulting in an ionic conductivity governed by the polymer matrix. As an alternative to spherical nanofillers, different nanofiller morphologies are employed (e.g., nanorods, nanowires, nanosheets) to create extended and more continuous ion-conduction pathways. This results in a reduction of interfacial boundaries (i.e., the required number of phase transitions) and facilitates efficient charge transport. Further, grafting active nanofillers with ion-conducting polymers can improve the charge transfer characteristics and result in improved CPE ionic conductivities.[211]

1.4 Chemistry of Polymerization

1.4.1 Ring-Opening Metathesis Polymerization

Olefin metathesis is a versatile class of reactions in organic and polymer chemistry. For their significant efforts Grubbs[212–216], Chauvin[217], and Schrock[218,219] were rewarded with the Nobel Prize for chemistry in the year 2005.[220] Their contribution to the development led to a wide field of application and utilization.[221] The term metathesis translates to a *change in position*. In this, individual constituents of carbon-carbon double bonds can be rearranged in reaction products that retain sp^2 hybridization, hence the double bond of carbon atoms. The first metathesis catalysts were derived from early transition metal-alkylidene complexes based on Titanium, Molybdenum, Tantalum, and Tungsten.[220,222–224] Grubbs established the use of late transition metal-alkylidenes complexes based on Ruthenium (**Figure 1.25**a).[212–216] Synthetic and systematic efforts led to a versatile class of Ru-based catalyst systems tolerant towards many functional groups.

Generally, olefin metathesis is an equilibrium reaction and therefore unsuitable for polymerization reactions. However, for strained cyclic olefins, the metathesis reaction can be applied in the ring-opening metathesis polymerization (ROMP) to synthesize macromolecular structures. The driving force for polymerization is the relief of ring-strain during ring-opening, favoring linear reaction products. The reactivity scales with ring strain and includes systems like cyclobutene, norbornene, or cis-cyclooctene (**Figure 1.25**b).[225] The [2.2.1] bicyclic norbornene system exhibits a high ring strain and many possible substitution patterns, establishing a versatile platform for functional materials (**Figure 1.25**c).

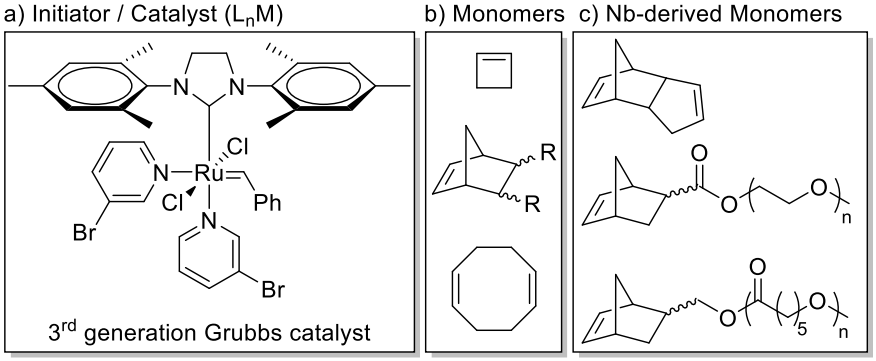


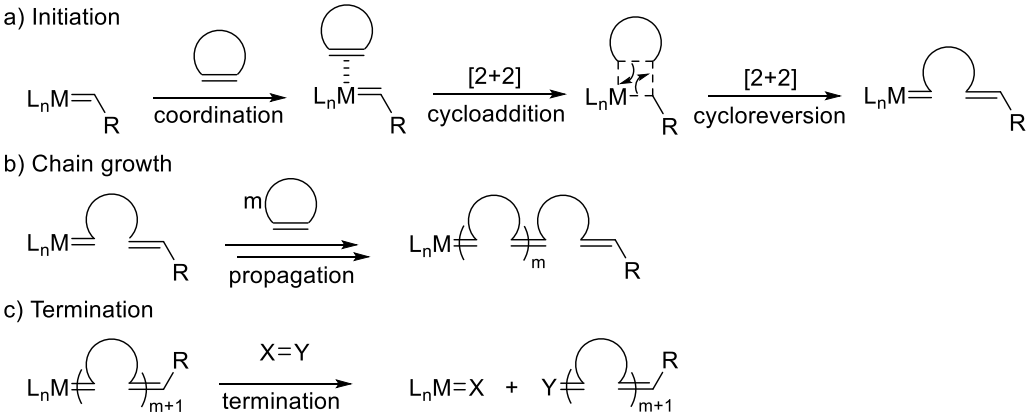
Figure 1.25. (a) Chemical structure of the 3rd generation Grubbs catalyst suitable for living and controlled ROMP.[215] (b) Generally, monomers applicable to ROMP exhibit a strained ring motif. Chemical structures represent examples of ring systems. The tolerance toward various functional groups offers the possibility of polymerizing many functionalized monomers.[221] (c) Functional monomers based on norbornene (Nb).[143,146,226]

The general mechanism for olefin metathesis reactions was proposed by Chauvin et al. in 1974. In a ROMP, olefin metathesis facilitates the three fundamental steps of polymerization: initiation, chain-growth, and termination (**Scheme 1.1**).[221] The initiation step involves coordinating a cyclic olefin to a transition metal-alkylidene (L_nM=CHR) complex. A [2+2] cycloaddition leads to a 4-membered metallacyclobutane intermediate, which subsequently results in the insertion of the monomer by a [2+2] cycloreversion (**Scheme 1.1**a). Especially for state-of-the-art ROMP catalysts, the initiation step proceeds at significantly higher rates than the subsequent propagation (rate of initiation $k_i >> k_p$ rate of propagation). This results in *controlled polymerization* characteristics, that can be utilized to achieve defined molecular weights and narrow molecular weight

distributions. The ROMP polymerization follows a chain-growth mechanism in which each catalyst initiates an individual polymer chain. The catalyst remains at the growing polymer chain end during the polymerization reaction without dissociation. Thereby, each chain growth step proceeds according to the general procedures or monomer coordination followed by cycloaddition and cycloreversion (**Scheme 1.1**b). This results in a carbon-carbon double bond containing a polymer backbone. The chain growth persists until the monomer is consumed, and a quantitative conversion is achieved, after which the catalyst remains active at the polymer chain end, enabling *living polymerization* characteristics. Therefore, the number-averaged molecular weight (M_n) of the polymer is given by Eq. 1.32 and can be adjusted and calculated by the ratio of monomer ($[M]_0$) and catalyst ($[I]_0$) and the molecular weight of the repeating unit (M_{RU}).

$$M_n = [M]_0/[I]_0 \cdot M_{RU} \tag{1.32}$$

After complete monomer consumption, the polymerization can be reinitiated by the addition of further equivalents of monomer. This opens the possibility to synthesize defined block copolymers. The chain termination is achieved by the addition of terminating agents after quantitative monomer conversion (**Scheme 1.1**c). The insertion of a terminating agent (X=Y) results in the cleavage of the catalyst from the polymer chain and the irreversible formation of an inactive metal alkylidene complex ($L_nM{=}X$). Most commonly, ethyl vinyl ether (EVE) is used as a simple and effective terminating agent. Functional terminating agents open the possibility of establishing defined chain end groups.[227]



Scheme 1.1. Schematic illustration of the general mechanism consisting of (a) initiation, (b) chain growth, and (c) terminating step. Monomer or olefin insertion proceeds via a [2+2] cycloaddition and -inversion. Terminating agents are used to irreversibly deactivate and detach the catalyst from the formed polymer chain.

Notably, the double bonds of the formed polymer backbone are prone to partake in the catalytic cycle, resulting in side reactions. This effect is less dominant for monomers with sterically demanding substituents, as the coordination is suppressed thermodynamically or sterically. Intramolecular backbiting reactions result in the elimination of macrocycles. Intermolecular reactions lead to broadened molecular weight distributions by redistributing the active propagating side between different polymers.[221,228] Deviations from the controlled polymerization characteristics are specifically aimed at using chain transfer agents (CTAs). Thereby, the molecular weight of the resulting polymer can be tuned as the propagating site is utilized to initiate a new polymer chain. The choice of functional CTAs enables the introduction of defined polymer end groups.[228–230]

1.5 Methods

1.5.1 Electrochemical Impedance Spectroscopy

Electrochemical impedance spectroscopy (EIS) is a powerful, versatile, and non-destructive characterization method finding application in the research for, e.g., batteries, fuel cells, or capacitors, where diverse bulk and interfacial processes, as well as complex resistances and capacitances are involved. The method is applied to observe, understand, identify, and analyze the different processes. In the context of batteries, EIS can be used to study the ionic conductivity of an electrolyte, charge transfer resistances at the electrodes, the development of passivating and resistive interfaces during battery operation, the determination of the current state-of-charge (SoC), state-of-health (SoH), or aging processes.[231–233]

In electrical conductors, the observed current (I) through the conductor is proportional to the applied potential (U) and is described by Ohm's law (Eq. 1.33). The proportionality factor is the electrical resistance (R), which describes the opposition to the flow of electrical current. For a resistor, this proportionality is independent of applied potential and invariant on the excitation frequency in alternating current (AC) measurements.

$$R = \frac{U}{I} \tag{1.33}$$

EIS investigates the frequency-dependent opposition to an alternating current, which is referred to as impedance Z ([Z] = ohm, Ω). The impedance is constituted by the frequency-independent resistance R and frequency-dependent contributions (e.g., capacitors or inductors), summarized as reactance X. For EIS experiments using a small sinusoidal excitation, there are two distinct modes where either a sinusoidal potential (potentiostatic EIS, PEIS) or a sinusoidal current (galvanostatic EIS, GEIS) is applied. The frequency (f) of the applied excitation is varied from a few MHz to mHz, depending on the observed system, measurement hardware, and intended experiment duration. In a PEIS measurement, a small excitation potential below the thermal voltage ($V_T \equiv RT/F \equiv kT/e \approx 25$ mV at 25 °C) is applied to warrant the linearity of the system.[234] Then a sinusoidal excitation potential $U(t)$ is applied, and the corresponding current response $I(t)$ is monitored (Eq. 1.34). The frequency f is converted to angular frequency ω ($\omega = 2\pi f$). The sinusoidal signals can be expressed as complex numbers following Euler's formula (Eq. 1.35 or 1.36).

$$U(t) = U_0 \cdot \sin(\omega t + \varphi_U) \qquad I(t) = I_0 \cdot \sin(\omega t + \varphi_I) \tag{1.34}$$

$$U(t) = U_0 \cdot e^{i(\omega t + \varphi_U)} \qquad I(t) = I_0 \cdot e^{i(\omega t + \varphi_I)} \tag{1.35}$$

$$U(t) = U_0 \cdot e^{i(\omega t)} \cdot e^{i\varphi_U} \qquad I(t) = I_0 \cdot e^{i(\omega t)} \cdot e^{i\varphi_I} \tag{1.36}$$

with angular frequency (ω) = $2\pi f$, φ = phase shift, $\hat{U}$ = complex potential, and $\hat{I}$ = complex current.

At a given frequency, the voltage and current can be represented as sinusoidal signals (**Figure 1.26**, right). Under the premise that the response is time-invariant and the angular frequency is constant the time-dependent contribution ($e^{i(\omega t)}$) can be omitted from Eq. 1.36. The sinusoidal signal of both voltage and current can be represented as phasors ($\tilde{U}$ and $\tilde{I}$) in the complex plane of a certain magnitude (U_0 and I_0) and phase angle (φ_U and φ_I) (Eq. 1.37, **Figure 1.26**, left).

$$\tilde{U} = U_0 \cdot e^{i\varphi_U} \qquad \tilde{I} = I_0 \cdot e^{i\varphi_I} \tag{1.37}$$

If the observed system behaves like an ideal ohmic resistor, the voltage and current signals are in phase, resulting in identical maxima and minima positions in the voltage and current signals (**Figure 1.26**, right). The magnitude of the phasors is accessible as the maximum sinusoidal signal heights, respectively.

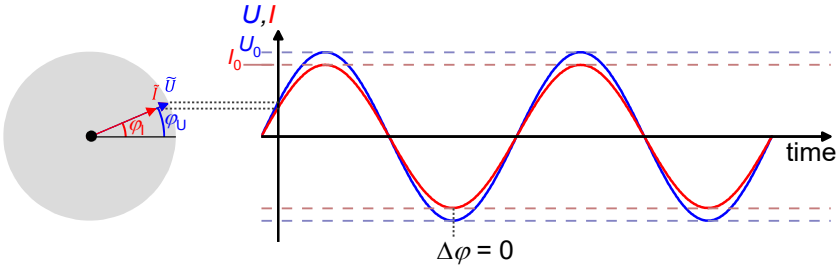


Figure 1.26. Illustration of the current response for an arbitrary frequency of an ohmic system. (left) Complex representation of the sinusoidal voltage and current signals as phasors in the frequency-domain with a certain magnitude (U_0 and I_0) and phase shift (φ_U and φ_I). The ohmic behavior results in identical phase shifts for current and voltage. (right) Sinusoidal time-dependent voltage $U(t)$ and current $I(t)$ signals. Adapted and modified from reference.[235]

The frequency-dependent impedance ($Z(\omega)$) can be expressed in an Ohm's law-like relation (Eq. 38) with $Z(\omega)$ as the proportionality factor between the excitation and response magnitude of the system. Note that this expression is given for a specific angular frequency; however, for an ideal resistor, this relation is independent of the applied excitation frequency. For an ideal resistor, as displayed in **Figure 1.26** the difference in the observed phase shifts (φ_U and φ_I) is zero identical resulting in the purely ohmic relation of voltage and current (Eq. 1.39). In that case, $Z(\omega)$ and R are interchangeable and valid independent of the observed angular frequency.

$$Z(\omega) = \frac{\tilde{U}}{\tilde{I}} = \frac{U_0}{I_0} \cdot e^{i(\varphi_U - \varphi_I)} = |Z| e^{i(\Delta\varphi)} \tag{1.38}$$

$$Z(\omega) = \frac{U_0}{I_0} \cdot 1 = R \tag{1.39}$$

Similar considerations can be applied to non-ohmic systems (**Figure 1.27**). The fundamental principle, including the complex representation by phasors, remains the same. The non-ohmic behavior results in a frequency-dependent relation and varying phase shifts between the excitation and response signals. Depending on the contributions, e.g., capacitive or inductive behavior, the phase shift can be negative ($\Delta\varphi$<0°), or positive ($\Delta\varphi$>0°), respectively. The frequency-dependent impedance is therefore described by Eq. 1.40.

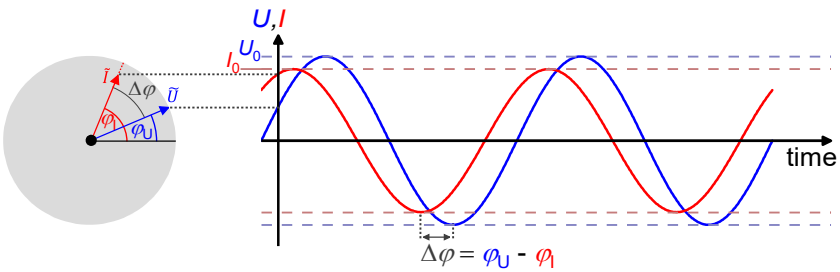


Figure 1.27. Illustration of the (red) current response for (blue) an arbitrary frequency of a non-ohmic system showing capacitive behavior. (left) Complex representation of the sinusoidal voltage and current signals as phasors ($\tilde{U}$ and $\tilde{I}$) with a certain magnitude (U_0 and I_0) and phase shift (φ_U and φ_I). The capacitive behavior induces a phase shift between the current response and the applied voltage. (right) Sinusoidal time-dependent voltage $U(t)$ and current $I(t)$ signals showing a phase shift $\Delta\varphi$. Adapted and modified from reference.[235,236]

The phasors can be visualized in the complex plane. As the frequency-dependent term is omitted in the phasor representation, the vectors are static in the complex plane with their respective magnitude and phase shift (**Figure 1.28**). The corresponding visualization of the impedance $Z(\omega)$ at a specific frequency is then given by the ratio $|Z| = I_0/U_0$ and the phase shift $\Delta\varphi$ between both phasors (**Figure 1.28**, right). The real (Z') and imaginary (Z'') components of the impedance are accessible as the x- and y-axis intercepts (Eq. 1.41), respectively.

$$Z(\omega) = |Z|\cos(\varphi) + |Z|(i\sin(\varphi)) \tag{1.40}$$

$$Z(\omega) = Z' + iZ'' \tag{1.41}$$

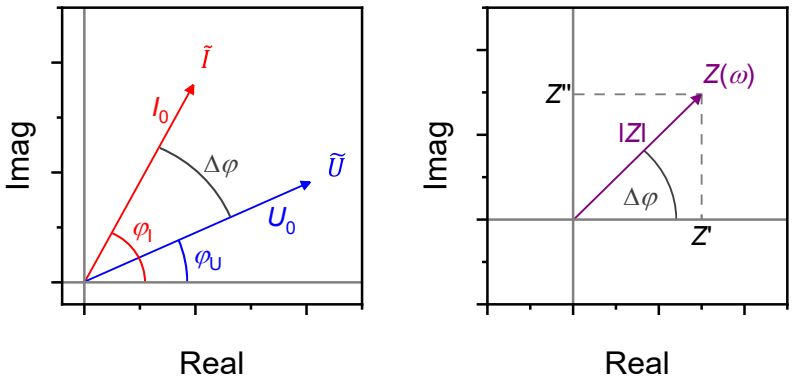


Figure 1.28. (left) Phasor diagram of the potential and current phasors in the complex plane. (right) The corresponding complex representation of the impedance as a vector of the magnitude $|Z|$ and the phase angle $\Delta\varphi$. Adapted and modified from literature.[234]

In electrochemical impedance spectroscopy, this consideration is performed at different excitation frequencies. The complex response highly depends on the applied frequency and the specific device under test. The electrochemical impedance of a system is commonly expressed by equivalent circuit models (ECMs). Therefore, different fundamental and ideal (also referred to as lumped) elements are connected in series or parallel. A summary of these elements, their symbols, and their respective frequency-dependent impedance is given in **Table 1.2**. A more detailed introduction and description of ECMs is provided in **Chapter 1.5.2**.

Table 1.2. Overview of typical elements used in the formulation and reconstruction of EIS data.[20,237]

Element	Resistor – R	Capacitor – C	Inductance – L	Warburg – Z_W
Symbol				
Impedance	R	$1/(i\omega C)$	$i\omega L$	$\frac{A_W\cdot\sqrt{2}}{\sqrt{i\omega}}$ [a]
Angle / °	0 [b]	-90 [b]	90 [b]	45 [c]

With A_W as the Warburg coefficient (dependent on: diffusion coefficients, concentrations, surface areas, temperature); [a] for a semi-infiniteWarburg element, [b] phase angle between voltage and current; [c] angle in the Nyquist plot representation.

In **Figure 1.29** a simulated frequency-dependent response of a system is presented, which comprises a series resistance (R_0), a parallel element of a resistance (R_1), and a capacitance (C_1) referred to as an RC-element. The combined equivalent circuit model is then $-R_0\text{-}R_1C_1-$ (depicted in **Figure 1.29**, left). Corresponding impedance data is commonly displayed in a Nyquist plot (**Figure 1.29**, left) or a Bode plot (**Figure 1.29**, right). In a Nyquist plot, each data point represents the complex impedance (similar to **Figure 1.28**) for a specific measurement frequency. In **Figure 1.29** (left), the vector for the magnitude of the impedance $|Z|$ and the phase shift $\Delta\varphi$ is exemplarily

shown for a specific excitation frequency. For the R(RC) equivalent circuit depicted in **Figure 1.29**, the high-frequency domain is accessible towards low values of the real component (at $Z' \rightarrow 0$) and the low-frequency domain appears at higher values (at $Z' \rightarrow \infty$). Therefore, the complex impedance $Z(\omega)$ is indirectly represented by the individual real and imaginary components. In the Bode-plot, the magnitude of the log impedance |Z| and the phase angle $\Delta\varphi$ between voltage and current are plotted as a function of the log excitation frequency. In this representation, real and imaginary components are not accessible directly but can be deconvoluted from the magnitude and the phase shift in accordance to Eq. 1.40.

For the defined ECM the frequency-dependent behavior can be described as follows. At high frequencies, the capacitive element dominates the RC-element and acts as a short circuit. Therefore, the total impedance is given only by the frequency-independent series resistance $Z(\omega) \rightarrow R_0$. At low frequencies the capacitive element acts as an open circuit, resulting in a predominantly real impedance composed of the sum of frequency-independent resistors $Z(\omega) \rightarrow R_0 + R_1$. In the frequency range between high and low measurement frequencies, the capacitive element results in a complex response of an imaginary contribution at a phase shift ($\Delta\varphi \neq 0$ °). This complex behavior of an RC element commonly translates to a semi-circle-shaped response in the complex plane in a Nyquist plot.

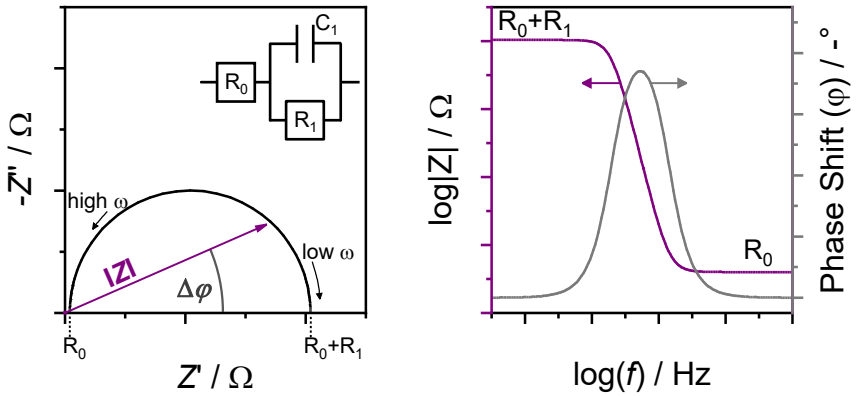


Figure 1.29. (left) Nyquist representation of the complex impedance for the equivalent circuit (R_0-R_1C_1). The series resistance (R_0) and the combined resistance of R_0+R_1 can be estimated from the high-frequency x-intercept and the low-frequency intercept, respectively. The frequency is not depicted in the Nyquist representation. However, each data point represents the impedance amplitude ($|Z|$) and phase shift (φ) at a given measurement frequency. (right) In the Bode representation, the impedance amplitude and phase shift are plotted as a function of the measurement frequency. Plateaus of $|Z|$ at low/negligible φ correspond to the real part of the ohmic resistances (R_0 and R_0+R_1).

Electrochemical impedance spectroscopy is one of the most powerful tools for the investigation and characterization of batteries. It is non-destructive and can be applied to evaluate critical parameters on the battery cell level as: state-of-charge (SoC), state-of-health (SoH), and internal temperature (IT).[231,233,238–240] Also on the material level, individual parameters and characteristics can be evaluated, like the ionic conductivity of an electrolyte, interface impedance, the stability of interphases, or diffusion processes in the electrodes. Depending on the figure of interest, different cell geometries are applied to investigate individual contributions. A schematic representation of common cell geometries and corresponding ECMs is depicted in **Figure 1.30**. Note that the illustrated equivalent circuits and corresponding Nyquist plots are highly simplified. Individual contributions can overlap and be indistinguishable. Therefore, the formulation of definitive and comprehensive ECMs for real battery systems is often very complex,

as most processes exhibit broad resistive and capacitive contributions due to inhomogeneities in the device structure, local electric fields, or concentration gradients (cf. chapter 1.5.2). Generally, processes comprising charge-transfer reactions and conductive processes like ionic conduction are reflected in the real part of the impedance. Conversely, processes originating from polarization phenomena at the electrodes (anode|electrolyte, electrolyte|cathode), like double-layer capacitance or space charge regions, contribute to the imaginary part of the impedance. Also, the electrolyte can exhibit a capacitive behavior, which is not observed in liquid electrolytes but in solid polymer electrolytes. The capacitive behavior can be described as a geometric capacity originating from the displacement of ionic charge due to molecular rearrangement. The Warburg impedance reflects diffusion-limited processes, especially at low frequencies, which manifests in a linear slope of 45 ° in a Nyquist representation. Inductive effects are commonly not associated with electrochemical processes during the operation of a battery cell; however, they can appear at high frequencies due to effects in the metallic cell housing and cables of the setup.

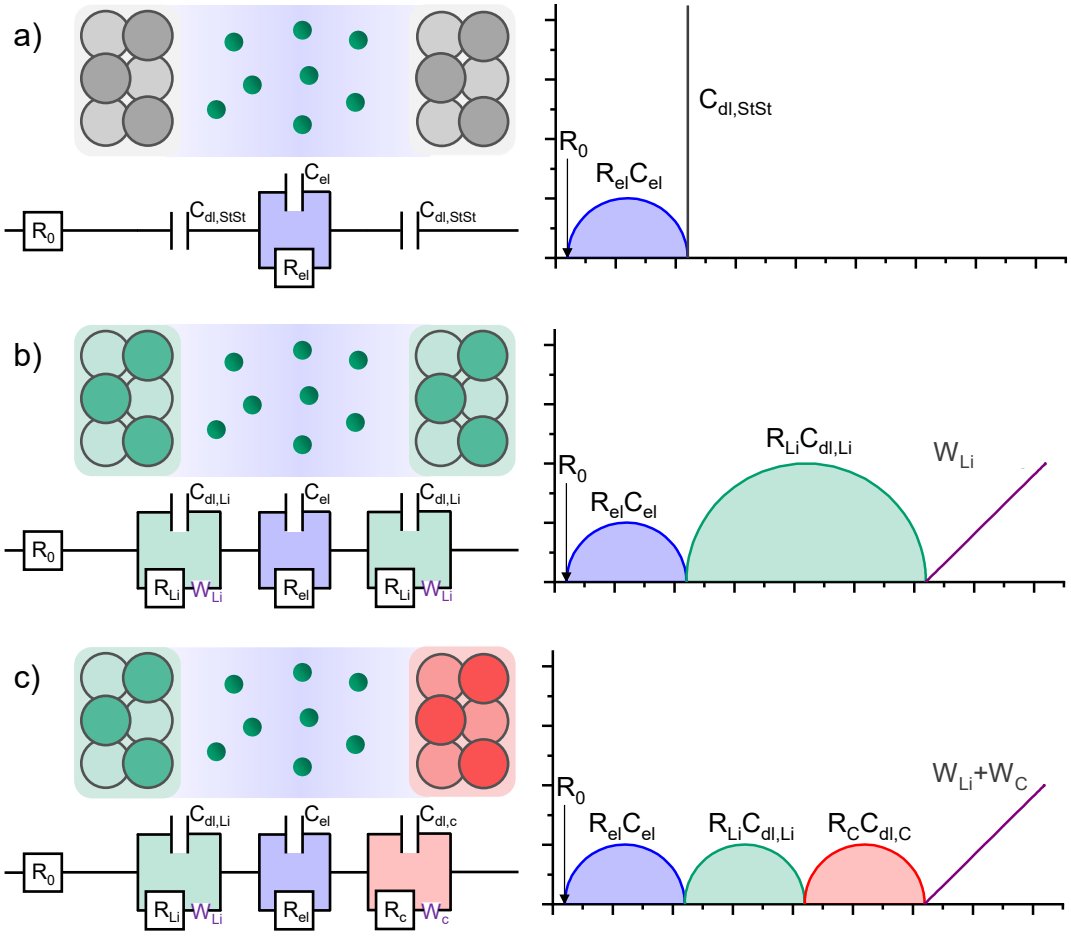


Figure 1.30. Schematic and simplified representation of common cell geometries in battery research (gray: stainless steel, StSt; green: lithium, Li; red: cathode, C). All geometries include a series resistance R_0 in the high-frequency regime due to the intrinsic resistances of the cell setup and connecting cables. a) For the determination of the ionic conductivity of the electrolyte, symmetrical ion-blocking stainless steel electrodes are used. b) Lithium symmetrical geometries can be utilized to evaluate the stability and compatibility of electrolytes as well as interface processes at the lithium electrodes under cycling conditions. c) Lithium-cathode half or full cells represent operational devices. Due to diffusion limitations at the interfaces, a Warburg diffusion is present for Li||Li and Li||cathode geometries. Adapted and reproduced from reference.[233,240,241]

1.5.2 Impedance Data Evaluation

The recorded impedance data is particular to the device under test and its frequency-dependent opposition to the applied and modulated excitation. For complex systems with different and interacting contributions, the corresponding response can result in superimposed and indistinct data. The corresponding data evaluation can require extensive fitting routines to access physically meaningful results, especially for increasingly complex systems. In this context, two alternative approaches can be distinguished for evaluating impedance data.

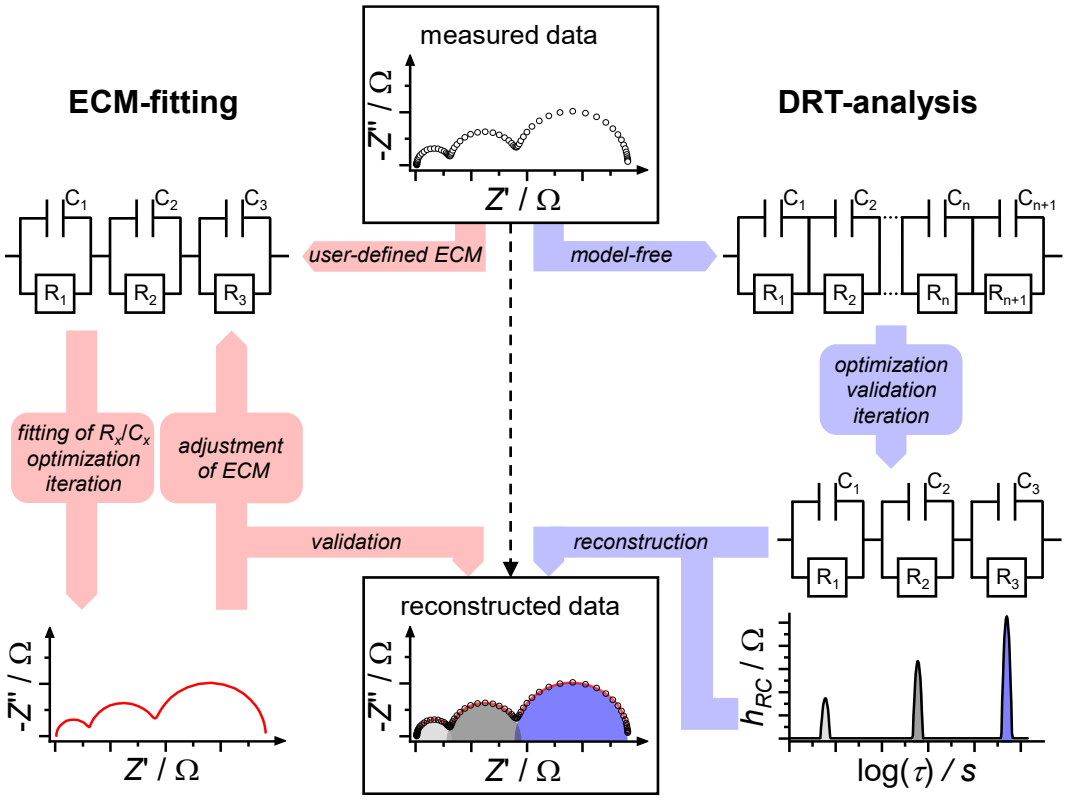
1.5.2.1 Equivalent Circuit Fitting

The most common approach is the equivalent circuit model (ECM)-fitting.[231,233,242] A schematic representation of an ECM fitting routine is presented in **Scheme 1.2** (left). ECM fitting is a parametric procedure, requiring a user-defined equivalent circuit formulated by the combination of equivalent elements shown in **Table 1.2**. The ECM is formulated to represent electrochemical processes in a specific system. It must be taken care that the choice of elements represents physically meaningful contributions to the device under test. The simplest ECM, consisting of the fewest elements possible, should be employed. Thereby, the model should still contain the complete physical and chemical meaning of a given system.[242] *A priori* knowledge and an understanding of the system and fundamental processes are required to select appropriate equivalent circuit models. For many (battery-related) systems, reference ECMs are available in literature, textbooks, or handbooks, which can serve as an initial starting point for specific systems.[234–236,240,242–246] An equivalent circuit model can be represented by a mathematical expression for the frequency-dependent impedance of the system. The total impedance of individual impedance contributions (i.e., different RC elements) in series can be calculated as their sum (Eq. 1.42). Then, Eq. 1.43 describes the generic ECM depicted in **Scheme 1.2**, consisting of three (RC) elements connected in series. Complex non-linear least square fitting routines are employed to compensate for the different contributions and result in the best possible fits for a given combination of experimental data and chosen ECM. The fit quality is also dependent on the selection of appropriate initial fit parameters.

$$Z_{total} = Z_1 + Z_2 + Z_3 \tag{1.42}$$

$$Z_{total} = \frac{1}{C_1 j\omega + \frac{1}{R_1}} + \frac{1}{C_2 j\omega + \frac{1}{R_2}} + \frac{1}{C_3 j\omega + \frac{1}{R_3}} \tag{1.43}$$

Both experimental data and fit need to be validated to ensure that the model represents all of the system characteristics. Adjustments in the ECM can be necessary to achieve matching fit results and representation of the processes in the system. The main challenge of the ECM fitting approach is selecting specific ECMs for a given system because different ECMs can fit the same experimental data equally well.[244,247–249] Further, the quality of the experimental data is very decicive to reducing the fitting procedure's ambiguity. Inhomogeneous processes, especially for rough interfaces or porous electrodes, can be difficult to represent in a definitive model. However, the simplicity of EC modeling and fitting for well-understood systems results in its wide application for impedance data evaluation.



Scheme 1.2. Illustration of different evaluation techniques for electrochemical impedance spectroscopy data as an example. (left) Impedance data can be fitted with user-defined electric equivalent circuits. This approach usually requires an understanding of the underlying processes and contributions, as missing or superfluous constituents in the ECC can result in misinterpretation of the spectra. (right) The distribution of relaxation times (DRT) analysis offers a model-free approach for which no *a priori* knowledge is required. The frequency-dependent data is transduced to the time domain, where characteristic relaxation times (τ) represent the individual contributions. This information can be used to reconstruct the corresponding EEC and data fit.

1.5.2.2 Distribution of Relaxation Times Analysis

An alternative to ECM fitting is the distribution of relaxation times (DRT) analysis. The DRT analysis is a non-parametric mathematical approach to the evaluation of impedance data. Therefore, the evaluation is mostly model-free and only requires a minimum of *a priori* knowledge about the system. The concept of distributed relaxation times was first proposed in the 1900s by Schweidler and expanded ever since.[250–252] The fundamental concept of the DRT analysis is the transformation of the impedance data in the frequency domain into the time domain. This is mathematically achieved by mapping the impedance data with an infinite series of RC elements of different distribution times (τ) as shown in Eq. 1.44.

$$\tau = R \cdot C \tag{1.44}$$

In its simplest and historical form, this can only be performed on impedance data showing exclusively resistive-capacitive behavior in combination with an ohmic resistor in series (R_o).[250,253] Modeling of other lumped elements or resistive-inductive behavior is not accessible. This leads to Eq. 1.45 for the description of the frequency-dependent impedance ($Z_{DRT}(\omega)$) by the DRT model. The term $\frac{h_{RC}(\tau)}{1+j\omega\tau}$ represents the resistive-capacitive behavior for a specific relaxation time.

$$Z_{\mathrm{DRT}}(\omega) = R_0 + \int_0^{\infty} \frac{h_{\mathrm{RC}}(\tau)}{1 + j\omega\tau} d\tau \tag{1.45}$$

For its mathematical computation, the infinite integral requires discretization, resulting in a finite sum (Eq. 1.46). Thereby, the number of time constants (n) should be large in comparison to the expected number of electrochemical processes in the system. Experimental impedance data covers a defined frequency range with a finite number of frequency steps between the frequency boundaries. This can result in mathematical artifacts in the corresponding DRT function. The extension of the domain of time constants beyond the experimental boundaries was demonstrated to reduce such phenomena and improve data quality. The resulting DRT function itself is only valid for the experimental frequency domain.[253,254]

$$Z_{\mathrm{DRT}}(\omega) = R_0 + \sum_{x=1}^{n} \frac{h_{RC}(\tau_x)}{1 + j\omega\tau_x} \tag{1.46}$$

Due to its restriction to resistive capacitive behaviors in combination with an ohmic resistor, the imaginary component of the impedance should converge to zero. However, especially for the investigation of batteries, inductive and capacitive contributions are commonly observed. For the application of the DRT analysis, these contributions need to be removed in a pre-processing step. Alternatively, the historical DRT model has been extended to represent contributions beyond resistive-capacitive behavior. In the extended DRT (eDRT), lumped elements like inductors and capacitors can be considered, which is mathematically described as Eq. 1.47.[253,255]

$$Z_{\mathrm{eDRT}}(\omega) = R_0 + \sum_{x=1}^{n} \frac{h_{\mathrm{RC}}(\tau_x)}{1 + j\omega\tau_x} + j\omega L_0 + \frac{1}{j\omega C_0} \tag{1.47}$$

Further development contributed to the generalization of the DRT (generalized DRT, gDRT), also representing frequency-dependent resistive-inductive contributions (RI) (Eq. 1.48).[253,256] This enables a truly model-free approach for the analysis of impedance spectra, as no pre-processing and removal of resistive-inductive contributions is required compared to eDRT.

$$Z_{\mathrm{gDRT}}(\omega) = R_0 + \sum_{x=1}^{n} \frac{h_{\mathrm{RC}}(\tau_x)}{1 + j\omega\tau_x} + j\omega L_0 + \frac{1}{j\omega C_0} + \sum_{x=1}^{n} \frac{j\omega\tau_x \cdot h_{\mathrm{RI}}(\tau_x)}{1 + j\omega\tau_x} d\tau \tag{1.48}$$

Analyzing impedance data by any form of DRT leads to a distribution function as exemplarily displayed in **Scheme 1.2** (right). Individual peaks correspond to distinct processes in the system under investigation. The ability to distinguish between different processes without *a priori* knowledge is one of the main advantages of the DRT analysis. Based on their relaxation time, different peaks can be assigned to various physico-electrochemical phenomena, including charge transfer reactions, ionic conductivity, or yield information concerning interface properties.[232,257,258] Based on the relaxation times and the corresponding polarization, the impedance data can be reconstructed. The main challenge involved in the DRT analysis is the mathematical optimization algorithm. Due to a limited number of experimental data points, the optimization problem is ill-posed and ill-conditioned, meaning that the problem cannot be solved analytically and that no unique solution can be obtained. To address this problem, Tikhonov regularization is commonly employed.[253,254,259,260]

1.5.3 Electrochemical Measurements in Material-focused Battery Research

For the investigation of individual processes or contributions, different cell geometries are commonly applied in battery research. Depending on the cell setup, certain processes can be suppressed, enabling the isolated examination of underlying processes. For electrochemical measurements, external electrode leads are connected to a test cell. The *working electrode* (*WE*) represents the electrode at which the reaction of interest is occurring and observed. The redox processes at the *WE* are compensated at the *counter electrode* (*CE*) to hold charge neutrality. The potential of the *WE* is controlled by a *reference electrode* (*RE*).[20] In a three-electrode setup, each electrode is an individual constituent of the electrochemical cell. In some cases, referred to as two-electrode setup, one single electrode functions as both *RE* and *CE*. For accurate measurements, the *RE* should be non-polarizable, reproducible, and reliable.[261–263] In lithium-based battery research, the most common *RE* in two-electrode setups are metallic lithium electrodes or $Li_4Ti_5O_{12}$ (LTO) and $LiFePO_4$ (LFP) at a state-of-charge in the middle of their respective potential plateaus. This allows for stable potentials during the use as *RE*.[263] While an additional *RE* can significantly improve the experimental quality, its use requires additional experimental complexity and complementary cell setups. Therefore, metallic lithium is often used as a combined electrode (*RE*/*CE*). This approach was shown to be reasonable under current-less or sufficiently low current density conditions.[264,265] In this work, CR2032 coin cells were used for all electrochemical experiments, which only allow for the connection of two electrode leads. Lithium is used as a combined *RE* and *CE* in non-symmetrical lithium cells. Electrode potentials are therefore reported against the redox couple of lithium (*E* vs. Li/Li^+). In lithium- or stainless steel-symmetrical cells, the designated function of either electrode is determined by the external connection or the conducted experiment. The following section is used to briefly summarize and portray applied characterization methods and their implications. The methods presented mainly focus on investigating material properties and their applicability in lithium-metal half-cell batteries. Beyond this, many other characterization methods are employed on the battery cell or pack level, comprising, for example, the investigation of state-of-charge (SoC), state-of-health (SoH), aging processes, or torture testing.[238,266,267] However, those methods are not directly relevent here.

1.5.3.1 Symmetrical Stainless-Steel Configuration

The *ionic conductivity* (IC), also denoted as σ, is one of the most predefined indicators for any electrolyte system. High IC is desirable for achieving high charging/discharging rates and to reduce losses due to internal resistances. In polymer electrolytes, the opposition to electrical current is frequency-dependent; hence, electrochemical impedance spectroscopy is commonly applied for its investigation. Though there are some reports of DC ionic conductivity, which is obtained from DC polarization experiments in lithium-symmetrical cells.[268,269] The disadvantage of this approach is that the conductivity is superimposed with polarization effects at the electrodes and charge transfer resistances. For EIS experiments, the cell setup commonly utilized a symmetrical stainless steel electrode configuration (StSt) (**Figure 1.31**a). StSt is considered an ion-blocking electrode without charge transfer reactions at the electrodes. The described cell setup for EIS experiments allows for an isolated evaluation of the ionic conductivity. For ideal systems, the frequency-dependent behavior of the electrolyte results in one semicircle in EIS measurements corresponding to the ohmic and capacitive behavior of the polymer electrolyte

(**Figure 1.31**b). Additionally, at very high frequencies, the ohmic series resistance (R_o) can be extracted from the x-intercept. The adjacent RC contribution of typical polymer electrolytes can be observed at moderate to high frequencies, while the StSt electrodes act as plate capacitors ($C_{dl,StSt}$) at low frequencies. In real measurements, the capacitive behavior of the StSt electrode comprises some resistive contribution in parallel to the capacitive behavior ($RC_{dl,StSt}$), resulting in a tilted response which is not to be mistaken as a Warburg impedance, as there are no charge transfer processes and diffusion-limited processes.

1.5.3.2 Symmetrical Stainless-Steel Configuration

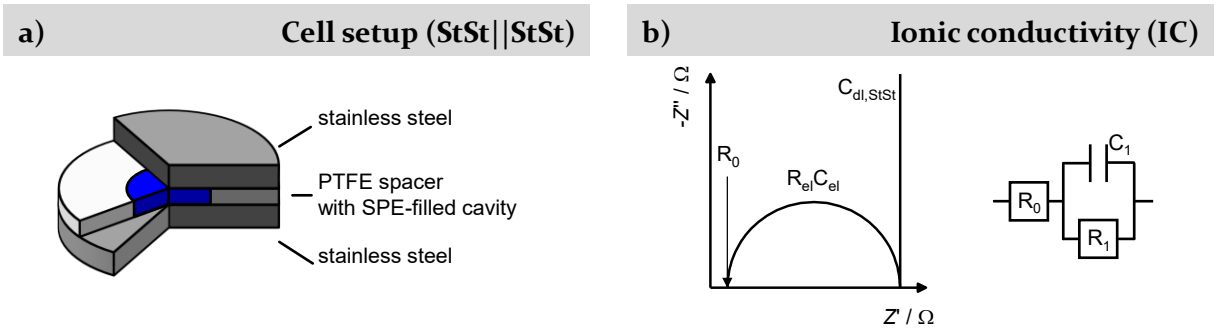


Figure 1.31. (a) Symmetrical StSt electrode configuration with a PTFE spacer of defined thickness and cavity diameter. (b) Nyquist plot for the evaluation of the IC for an R(RC) ECM.

The electrolyte bulk resistance (R_{el}) is accessible from the real part of the RC-element. The ionic conductivity (σ) can be calculated from the electrolyte bulk resistance (R_{el}) and the electrolyte geometry (A: area, l: thickness) (Eq. 1.49).[20] The IC is usually evaluated across different temperatures to evaluate the ionic conductivity at different application conditions.

$$\sigma = \frac{l}{R_{el} \cdot A} \tag{1.49}$$

1.5.3.3 Lithium-Stainless-Steel Configuration

The electrochemical stability window (ESW) of an electrolyte describes the potential range in which the electrolyte can be applied without showing oxidative decomposition processes. The ESW gives an indication of which cathode chemistries can be applied in combination with the electrolyte and lithium-based anodes. High-voltage cathode chemistries require oxidative stabilities above 4.5 V, while other systems, e.g., sulfur or LFP, operate at more moderate potentials of 2.3 V or 3.4 V, respectively. *Linear sweep voltammetry* (LSV) is a well-established method to evaluate the ESW of an electrolyte. The cell setup consists of lithium as reference (*RE*) and counter (*CE*) electrode, and StSt as working (*WE*) electrode (**Figure 1.32**a). The potential is increased from a starting point (E_o) to a cut-off potential ($E_{cut\text{-}off}$). E_o is commonly either set to -0.5 V or to the open circuit potential (E_{OCV}) of the cell. In the first case, at around 0 V, the stripping of lithium can be observed, followed by a flat plateau of a very low current density. In this regime, the electrolyte is stable without any decomposition. As StSt is ion-blocking, there are no charge transfer processes, which would induce a DC current through the cell. The oxidative stability is evaluated from the increase in the current response at highly oxidative potentials (**Figure 1.32**b). The decomposition potential (E_d) can be determined geometrically as the intercept of the stability plateau and the faradaic current ($E_{d,geo}$). For different electrolyte systems, the current density increase can feature multiple decomposition steps and peaks. This can cause difficulties in defining accurate tangents for geometrical evaluation. Alternatively, the threshold decomposition

potential ($E_{d,thresh}$) can be evaluated as the potential at which an arbitrarily defined threshold current density (usually j = 0.1 mA cm^{-2}) is exceeded.[270]

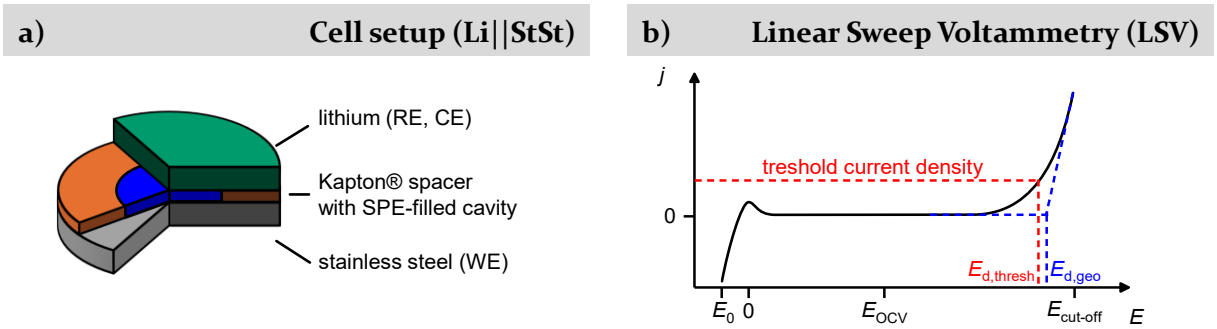


Figure 1.32. (a) Lithium||StSt electrode configuration with a Kapton® spacer of defined thickness and cavity diameter. (b) Schematic plot of the current density against the applied potential. The geometric- and threshold-based evaluation is indicated in blue and red, respectively.

Even though LSV is widely used across the literature, the method poses some inherent problems for the determination of an accurate stability window. First, the evaluation of the decomposition potentials is highly ambiguous and depends on arbitrary threshold limits or user-defined geometric approaches.[271] Further, the current density response can be influenced by the applied scan rate, or it can be dependent on the ionic conductivity and thickness of the electrolyte.[272,273] Lastly, the measurement is conducted with inert StSt electrodes as the *WE*, which neglects any influence of the cathode material on the electrolyte decomposition. Therefore, LSV can be used to approximate the ESW under inert conditions, but the electrochemical stability in anode|electrolyte|cathode geometries or under operating conditions needs to be evaluated using alternative approaches.[273] This will be discussed in the following sections.

1.5.3.4 Symmetrical Lithium Configuration

The formation and stability of the lithium|electrolyte interface layer are crucial for the longevity of a battery. Upon contact between lithium and electrolyte, the highly reductive nature of metallic lithium leads to the formation of decomposition products on the lithium surface. This involves the reduction of lithium salts or the electrolyte matrix and the formation of a mostly inorganic layer of lithium carbonates, lithium fluoride, or lithium oxide. The so-formed layer then protects the electrolyte from further decomposition. However, its stability is critical as the exposure of pristine lithium metal will consume more of the electrolyte material. Lithium-symmetrical cells (Li||Li) are commonly employed to investigate the compatibility and stability of the lithium|electrolyte interface (**Figure 1.33**a). Utilizing the Li||Li setup, the observed electrode properties, processes, and reversibility resemble the characteristics of later lithium anodes in full-/half-cells.

The reversibility and cycling stability can be evaluated in *lithium plating and stripping* (LPS) experiments in a Li||Li electrode setup. Thereby, a galvanostatic bias is applied to the lithium-symmetrical cell, which results in a lithium transfer from one electrode to the other. The bias is maintained for a defined duration after which the potential is inverted. Due to charge transfer reaction, the resistance of the electrolyte and the presence of resistive interlayers, the bias results in a potential response described as the overpotential (ΔE) to drive the DC current. Despite the cell being symmetric, the overpotential for the individual biases (I^+, I^-, cf. **Figure 1.33**b) can result in different magnitudes of overpotentials (ΔE^+, ΔE^-). The potential profile and the increase or decrease of ΔE can give information about several aspects of cycling stability of the interfaces. This comprises the formation of lithium dendrites or interfaces, as well as information about

capacity/lithium losses.[274–276] Simplified extreme cases of overpotential development over extended cycling experiments are depicted above in **Figure 1.33**b.

Besides the isolated investigation of the lithium|electrolyte interphase, additional information about the electrolyte is accessible using Li||Li cell setups. These include ion transport properties, which are related to and/or dependent on charge transfer reactions at the interfaces. As stated above, the ionic conductivity of an electrolyte is deciding for accessible charging/discharging rates in a battery application. The IC is to be understood as an isolated baseline for the electrolyte. However, under operational conditions, charge transfer processes need to be considered. Li-symmetrical cells can be used to evaluate the current density stability limit, described as the limiting current density (LCD). The LCD is the highest sustainable current density for charging or discharging, based only on the lithium|electrolyte combination.[275,277] Additional limiting contributions of the cathode are not considered here. Target LCD for technical applications like electric vehicles is 3 to 10 mA cm^{-2}.[277,278]

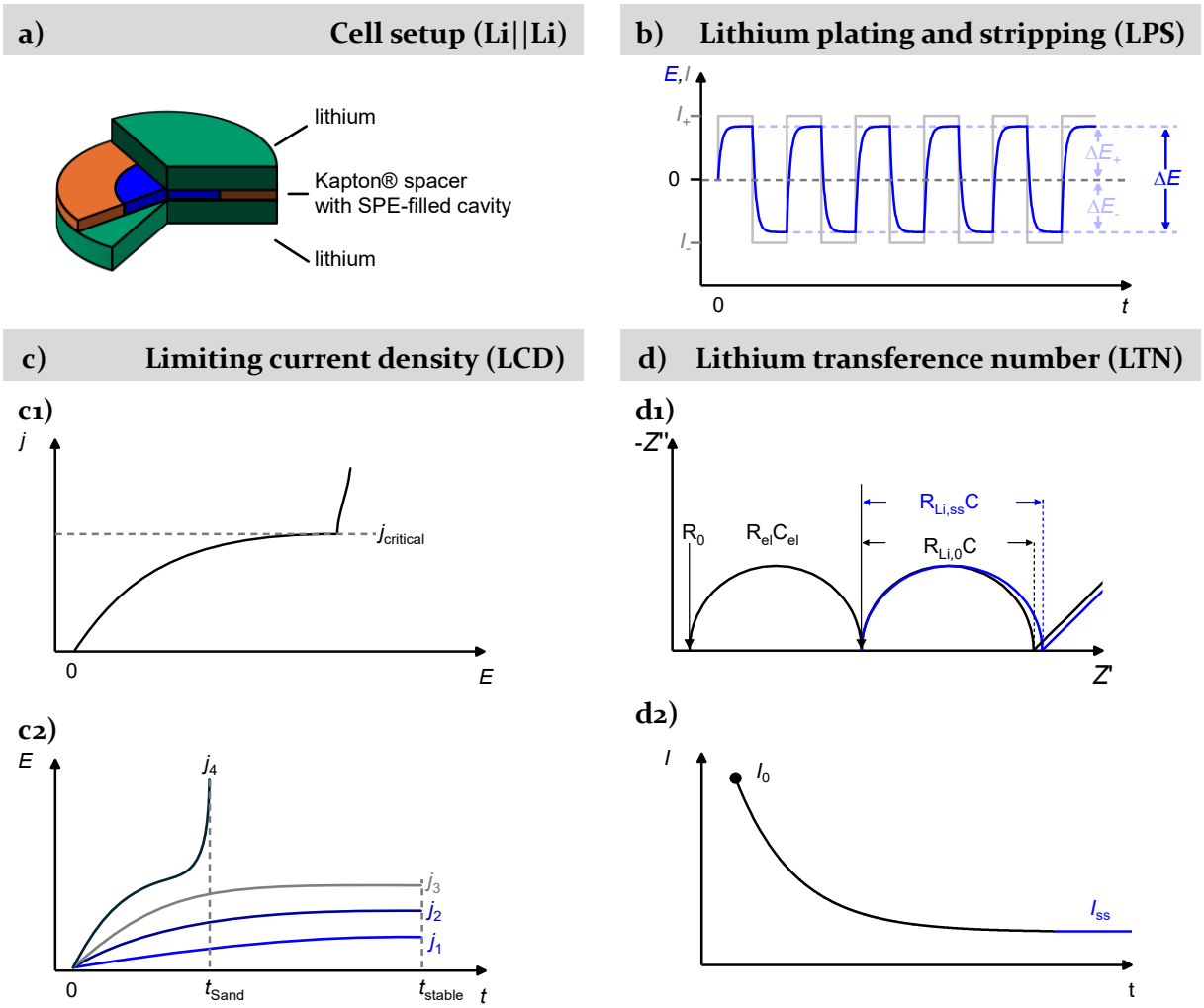


Figure 1.33. (a) Symmetrical Li electrode configuration with an electrolyte-filled Kapton® spacer of defined thickness and cavity diameter. Schematic illustration of (b) lithium plating and stripping profiles under the application of a DC bias, (c1) the current density variation for the evaluation of the critical current density, (c2) potential sweep experiments for the evaluation of the critical current density, (d1) Nyquist plots of (black) initial and (blue) final impedance spectra for before and after the polarization period, (d2) chronoamperometric polarization experiment for the evaluation of the lithium transference number.

Two possible evaluation methods are depicted in **Figure 1.33**c1,c2. In the first case, the LCD is examined voltammetrically by the application of a modulated potential (**Figure 1.33**c1). While the potential is increasing, the corresponding current density response also increases until it tapers off due to charge transfer limitations or the resistance of the electrolyte. The plateau indicates the limit of sustainable current ($j_{critical}$) for the lithium|electrolyte combination. At higher potential, irreversible processes result in sharply increasing or fluctuating current density responses. Alternatively, the LCD can be evaluated by applying incrementally increasing current densities (j_1, j_2, ...) for a defined time interval (t_{stable}) after which an equilibrated steady state should be reached (**Figure 1.33**c2). When exceeding the critical current density (j_4), polarization and ion-depletion processes result in a sharp increase in observed overpotential. The time required for the transition in the unstable state is the Sand time (t_{Sand}) (cf. 1.3.2.4). This approach can allow for an accurate evaluation of the LCD, as t_{stable} can be defined following typical durations of a battery charge cycle, representing operational conditions.

Lastly, Li-symmetrical cells can be utilized to investigate the *lithium transference number* of an electrolyte. The lithium transference number (LTN or t_{Li^+}) describes the current fraction conducted by lithium ions in comparison to the total current by both anions (I_{TFSI^-}) and lithium ions (I_{Li^+}) (Eq. 1.50). Over the past, several different evaluation methods have been developed, spanning from NMR studies to electrochemical protocols.[94,96,97,99,279–282]

$$LTN = \frac{I_{Li^+}}{I_{Li^+} + I_{TFSI^-}} \tag{1.50}$$

The Bruce and Vincent method is one LTN determination method proposed in 1987 by Evans et al.[279] The evaluation considers the lithium charge transfer resistance at the electrode interfaces, and the current response to an applied potential bias. The evaluation protocol consists of two electrochemical impedance spectra in combination with an intermittent polarization phase. In the first EIS measurement, the equilibrium state and the initial charge transfer resistance ($R_{Li,0}$) are determined (**Figure 1.33**d1). Afterward, the current response is evaluated in a chronoamperometric (CA) phase under the application of a small potential ($\Delta V \approx 10$ mV).[283] The current response usually represents an asymptotic decay with an initial current (I_0), which reaches a steady-state current (I_{ss}). During the polarization phase, ions translate through the electrolyte governed by their charge and the direction of the applied E field. Thereby, lithium ions are continuously transported between the electrodes, being oxidized at one electrode and reduced at the other electrode, respectively. Contrarily, the anions are polarized and accumulate at one electrode. Starting from the equilibrium state, anions are homogeneously dispersed across the electrolyte and can contribute to the ionic conductivity. During the transition to the polarized steady-state, the mobility of the anions reduces, and the contribution to the current diminishes. Therefore, the steady-state current (I_{ss}) is only attributed to the lithium-ion conduction (**Figure 1.33**d2). The ratio of steady-state current to initial current can give a first approximation for the LTN (Eq. 1.51)

$$LTN \approx \frac{I_{ss}}{I_0} \tag{1.51}$$

The final EIS experiment is performed immediately after the CA phase to evaluate the influence of the polarization on the charge transfer processes at the lithium interfaces ($R_{Li,ss}$). Considering the different parameters, the LTN (t_{Li^+}) can be calculated by Eq. 1.52). An alternative calculation is expanded to also consider the initial and steady-state electrolyte bulk resistances

(R_{el}) described as T_{Li^+} (Eq. 1.53).[270,284] However, the bulk resistance is mostly unaffected by the polarization, resulting in similar results.

$$t_{Li^+} = \frac{I_{ss} \cdot (\Delta V - I_0 R_{Li,0})}{I_0 \cdot (\Delta V - I_{ss} R_{Li,ss})} \tag{1.52}$$

$$T_{Li^+} = \frac{I_{ss} \cdot R_{el,ss} \cdot (\Delta V - I_0 R_{Li,0})}{I_0 \cdot R_{el,0} \cdot (\Delta V - I_{ss} R_{Li,ss})} \tag{1.53}$$

1.5.3.5 Lithium-Cathode Configuration

Ultimately, assessing battery cycling characteristics in half- and full-cell configurations is vital for understanding electrochemical stability, cycling reversibility, and capacity behavior under different charge and discharge conditions. Both half- and full-cell geometries comprise an anode and electrolyte in combination with a cathode to form a battery (**Figure 1.34**a). This cell setup is often referred to as both half- and full-cells in the literature. However, the terms differentiate between battery cells with a substantial capacity excess of one electrode and battery cells of balanced electrode capacities for half- and full-cells, respectively.[264] In half-cells, the observed capacities are limited by the electrode of lower capacity, and the influence of the excess electrode on the characteristics is reduced.

In typical lab-scale cycling experiments, batteries are charged and discharged under a constant current (galvanostatically) for the entire capacity (**Figure 1.34**b). For a given cathode||anode combination, defined potential cut-offs ($E_{ch,cut\text{-}off}$ or $E_{dch,cut\text{-}off}$) are imposed depending on the redox potential (E_{OCV}), the voltage profile, and the electrochemical stability. During charging and discharging, charge transfer resistances, the electrolytes' ionic conductivity, or diffusion limitations result in overpotentials (η_{ch} and η_{dch}). The determined charge (C_{ch}) and discharge (C_{dch}) capacity represent the amount of transported and stored charges up to the individual cut-off potential. The efficiency for a charge/discharge cycle is given by the Coulombic efficiency (CE), which describes the ratio of retrieved discharge capacity and the formerly introduced charge capacity (Eq. 1.54).

$$\mathrm{CE} = \frac{C_{\mathrm{dch}}}{C_{\mathrm{ch}}} \tag{1.54}$$

The battery characteristics and performances are usually investigated over a large number of charge/discharge cycles. During extended cycling experiments, the battery capacity declines gradually. The percentage of remaining discharge capacity ($C_{dch,n}$) after n-cycles in comparison to the initial (or maximum) discharge capacity ($C_{dch,o}$) is referred to as capacity retention (CR, Eq. 1.55). During the initial cycles, the capacity degradation is most prominent due to the formation of the SEI. After a stable equilibrium state is reached, the decline of discharge capacity is significantly reduced.

$$\mathrm{CR} = \frac{C_{dch,n}}{C_{dch,0}} \cdot 100\ \% \tag{1.55}$$

The battery performance, accessible capacities, and overpotentials are studied under different cycling conditions. Two critical parameters are the cycling temperature and the applied cycling rate (**Figure 1.34**c,d). Higher temperatures accelerate kinetically limited processes like ion migration within the electrode active materials and can also improve ion conduction and charge

transfer reactions. At lower temperatures, accessible capacities can be significantly reduced. Similar phenomena can be observed for increasing cycling rates. The cycling rate is commonly reported as a C-rate, expressing the cycling rate with respect to the electrode capacity. Ecamples of C-rates and corresponding charging times are listed in **Table 1.3**.

Table 1.3. Calculated charging times and current densities at different C-rates for a model system of a battery consisting of an active electrode area of 1 cm^2 and an areal capacity of 2 mAh cm^{-2}.

C-rate	0.1 C	1 C	2 C
charging time	10 h	1 h	0.5 h
current density	0.2 mA cm^{-2}	2.0 mA cm^{-2}	4.0 mA cm^{-2}

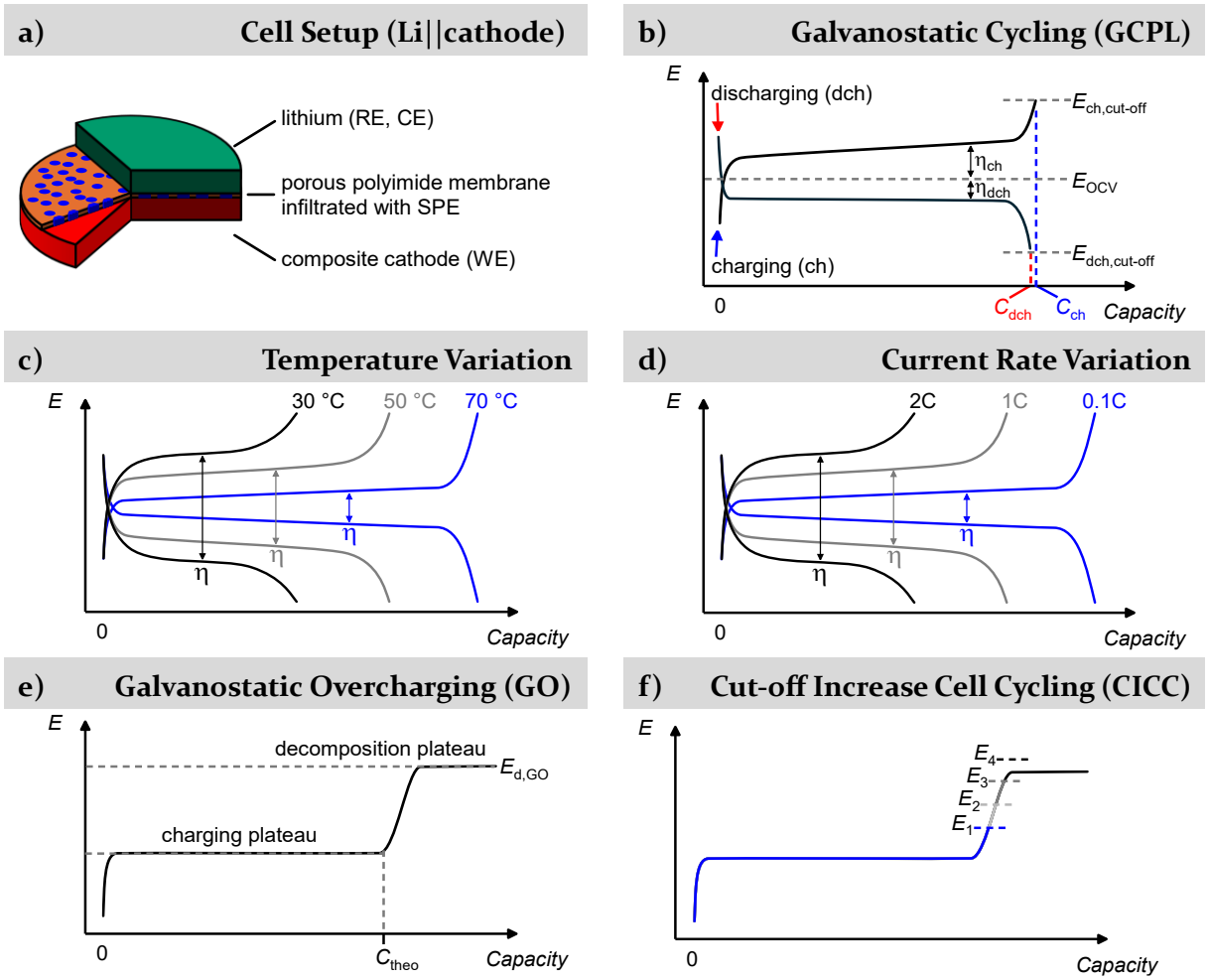


Figure 1.34. (a) Lithium||cathode electrode configuration with an electrolyte-soaked polyimide-based membrane. Alternatively, a Kapton® spacer, as displayed for lithium-symmetrical cells, was used. (b) Schematic representation of cell potential vs. capacity for a Li||LFP-based battery. The cell is charged and discharged to defined cut-off potentials ($E_{ch/dch,cut-off}$). The charge and discharge capacity ($C_{ch/dch}$) are evaluated at the respective cut-off potential. Internal processes result in overpotentials ($\eta_{ch/dch}$) around the open circuit potential. (c,d) Influence of different cycling conditions on accessible capacities and total overpotentials between charge and discharge curves. (e+f) Evaluation methods for the oxidative stability of an electrolyte under operational conditions. (e) Schematic charging profile during a galvanostatic overcharging to evaluate the decomposition potential ($E_{d,GO}$). (f) Schematic charging profiles for incrementally increasing cut-off potentials to evaluate the highest stable discharge potential. The discharge cycles, which are performed after each charge, are omitted for clarity.

Besides evaluating the cycling characteristics under different conditions, the anode||cathode cell geometry can also be used to assess the electrochemical stability of electrolyte materials under representative cycling conditions. While the isolated oxidative stability can be probed in LSV experiments, the method neglects the influence of the cathode and active materials. *Galvanostatic overcharging* (GO) or *cut-off increase cell cycling* (CICC) evaluate the ESW in a battery setup. In a typical cycling experiment, as displayed in **Figure 1.34**b, cut-off limits prevent the decomposition of battery components due to excessive cell potentials. In GO experiments, the battery is galvanostatically charged without a defined potential cut-off (**Figure 1.34**e). At first, the cell potential increases due to the applied current until the potential is sufficient to oxidatively decompose internal battery components. The decomposition processes result in a secondary decomposition plateau ($E_{d,GO}$). Especially for organic- or polymer-based electrolytes, the decomposition is attributed to the electrolyte itself. Alternatively, the decomposition potential can be assessed by charging the battery to incrementally increasing cut-off potentials (**Figure 1.34**f, E_1 – E_4). One or more charge/discharge cycles can be performed for each cut-off potential. Discharge curves are not presented in **Figure 1.34**f as the oxidative stability during charging is evaluated. As long as the battery is charged to cut-off potentials below the decomposition potential ($E_x < E_d$), stable charging capacities are observed. Once a cut-off potential greater than the decomposition potential is reached ($E_x > E_d$), oxidative decomposition processes result in a secondary charging plateau or fluctuating cell potential.

1.6 References

(1) Lüthi, D.; Le Floch, M.; Bereiter, B.; Blunier, T.; Barnola, J.-M.; Siegenthaler, U.; Raynaud, D.; Jouzel, J.; Fischer, H.; Kawamura, K.; Stocker, T. F. High-Resolution Carbon Dioxide Concentration Record 650,000–800,000 Years before Present. *Nature* **2008**, *453* (7193), 379–382. https://doi.org/10.1038/nature06949.

(2) *Carbon Dioxide Peaks near 420 Parts per Million at Mauna Loa Observatory*; NOAA Research, 2021. https://research.noaa.gov/coronavirus-response-barely-slows-rising-carbon-dioxide/ (accessed 2025-05-30).

(3) Nahar, S. N. Solar Irradiance of the Earth's Atmosphere. In *Climate Change and Food Security in South Asia*; Lal, R., Sivakumar, M. V. K., Faiz, S. M. A., Mustafizur Rahman, A. H. M., Islam, K. R., Eds.; Springer Netherlands: Dordrecht, 2011; pp 31–42. https://doi.org/10.1007/978-90-481-9516-9_3.

(4) The CenCO2PIP Consortium. Toward a Cenozoic History of Atmospheric CO2. *Science* **2023**, *382* (6675), eadi5177. https://doi.org/10.1126/science.adi5177.

(5) International Energy Agency (IEA). *World Energy Outlook 2024*.

(6) International Energy Agency. World Energy Statistics and Balances, 2025. https://www.iea.org/data-and-statistics/data-product/world-energy-statistics-and-balances.

(7) BP. Statistical Review of World Energy 2019: Full Report. *Statistical Review of World Energy* **2019**, *68th Edition*.

(8) BP. Statistical Review of World Energy 2022. **2022**, No. 71.

(9) United Nations; UNFFCCC. The Paris Agreement, 2015. https://unfccc.int/process-and-meetings/the-paris-agreement (accessed 2026-02-08).

(10) Lu, X.; McElroy, M. B.; Kiviluoma, J. Global Potential for Wind-Generated Electricity. *Proceedings of the National Academy of Sciences* **2009**, *106* (27), 10933–10938. https://doi.org/10.1073/pnas.0904101106.

(11) de Castro, C.; Mediavilla, M.; Miguel, L. J.; Frechoso, F. Global Solar Electric Potential: A Review of Their Technical and Sustainable Limits. *Renewable and Sustainable Energy Reviews* **2013**, *28*, 824–835. https://doi.org/10.1016/j.rser.2013.08.040.

(12) Korfiati, A.; Gkonos, C.; Veronesi, F.; Gaki, A.; Grassi, S.; Schenkel, R.; Volkwein, S.; Raubal, M.; Hurni, L. Estimation of the Global Solar Energy Potential and Photovoltaic Cost with the Use of Open Data. *International Journal of Sustainable Energy Planning and Management* **2016**, 17-30 Pages. https://doi.org/10.5278/IJSEPM.2016.9.3.

(13) European Association for Storage of Energy. *Energy Storage Targets 2030 and 2050 - Ensuring Europe's Energy Security in a Renewable Energy System*.

(14) European Commission. *Energy Storage - Underpinning a Decarbonised and Secure EU Energy System*; SWD(2023) 57 final; Brüssel, 2023.

(15) European Environment Agency. *Annual European Union Greenhouse Gas Inventory 1990-2023 and Inventory Document 2025*; EEA/PUBL/2025/024; European Commission, DG Climate Action, European Environment Agency, 2025; p 537. https://www.eea.europa.eu/en/analysis/publications/annual-european-union-greenhouse-gas-inventory-2025 (accessed 2025-05-31).

(16) *Lithium Cobalt Oxide - LiCoO2 - Conduction animation*. ChemTube3D. https://www.chemtube3d.com/lib_lco-2/ (accessed 2025-06-20).

(17) *The Nobel Prize in Chemistry 2019*. NobelPrize.org. https://www.nobelprize.org/prizes/chemistry/2019/summary/ (accessed 2024-10-07).

(18) Brédas, J.-L.; Buriak, J. M.; Caruso, F.; Choi, K.-S.; Korgel, B. A.; Palacín, M. R.; Persson, K.; Reichmanis, E.; Schüth, F.; Seshadri, R.; Ward, M. D. An Electrifying Choice for the 2019 Chemistry Nobel Prize: Goodenough, Whittingham, and Yoshino. *Chem. Mater.* **2019**, *31* (21), 8577–8581. https://doi.org/10.1021/acs.chemmater.9b04345.

(19) Panero, S. Electrochemical Theory | Thermodynamics. In *Encyclopedia of Electrochemical Power Sources*; Garche, J., Ed.; Elsevier: Amsterdam, 2009; pp 1–7. https://doi.org/10.1016/B978-044452745-5.00033-2.

(20) *Electrochemical Dictionary*; Bard, A. J., Inzelt, G., Scholz, F., Eds.; Springer Berlin Heidelberg: Berlin, Heidelberg, 2012. https://doi.org/10.1007/978-3-642-29551-5.

(21) Kurzweil, P. *Angewandte Elektrochemie: Grundlagen, Messtechnik, Elektroanalytik, Energiewandlung, technische Verfahren*; Springer Fachmedien Wiesbaden: Wiesbaden, 2020. https://doi.org/10.1007/978-3-658-32421-6.

(22) International Electrotechnical Commission. *International Electrotechnical Vocabulary 131-12-22*. https://www.electropedia.org/iev/iev.nsf/display?openform&ievref=131-12-22 (accessed 2024-10-10).

(23) Abens, S. G.; Mahy, T. X.; Merz, W. *Development of High Energy Denisty Primatry Batteries 200 Wh per Pount Total Battery Weight Minimum*; N66 29446; National Aeronautics and Space Administration, 1965.

(24) Besenhard, J. O.; Eichinger, G. High Energy Density Lithium Cells: Part I. Electrolytes and Anodes. *Journal of Electroanalytical Chemistry and Interfacial Electrochemistry* **1976**, *68* (1), 1–18. https://doi.org/10.1016/S0022-0728(76)80298-7.

(25) Whittingham, M. S. Chemistry of Intercalation Compounds: Metal Guests in Chalcogenide Hosts. *Progress in Solid State Chemistry* **1978**, *12* (1), 41–99. https://doi.org/10.1016/0079-6786(78)90003-1.

(26) Mizushima, K.; Jones, P. C.; Wiseman, P. J.; Goodenough, J. B. LixCoO2 (0<x<-1): A New Cathode Material for Batteries of High Energy Density. *Materials Research Bulletin* **1980**, *15* (6), 783–789. https://doi.org/10.1016/0025-5408(80)90012-4.

(27) Yoshino, A.; Sanechika, K.; Nakajima, T. Secondary Battery. US4668595A, May 26, 1987. https://patents.google.com/patent/US4668595A/en (accessed 2025-06-15).
(28) Cao, S.; Song, S.; Xiang, X.; Hu, Q.; Zhang, C.; Xia, Z.; Xu, Y.; Zha, W.; Li, J.; Gonzale, P. M.; Han, Y.-H.; Chen, F. Modeling, Preparation, and Elemental Doping of Li7La3Zr2O12 Garnet-Type Solid Electrolytes: A Review. *J. Korean Ceram. Soc* **2019**, *56* (2), 111–129. https://doi.org/10.4191/kcers.2019.56.2.01.
(29) Chen, Y.; Sun, Y.; Huang, X. Origin of the Ni/Mn Ordering in High-Voltage Spinel LiNi0.5Mn1.5O4: The Role of Oxygen Vacancies and Cation Doping. *Computational Materials Science* **2016**, *115*, 109–116. https://doi.org/10.1016/j.commatsci.2016.01.005.
(30) Asenbauer, J.; Eisenmann, T.; Kuenzel, M.; Kazzazi, A.; Chen, Z.; Bresser, D. The Success Story of Graphite as a Lithium-Ion Anode Material – Fundamentals, Remaining Challenges, and Recent Developments Including Silicon (Oxide) Composites. *Sustainable Energy & Fuels* **2020**, *4* (11), 5387–5416. https://doi.org/10.1039/D0SE00175A.
(31) Zhang, H.; Yang, Y.; Ren, D.; Wang, L.; He, X. Graphite as Anode Materials: Fundamental Mechanism, Recent Progress and Advances. *Energy Storage Materials* **2021**, *36*, 147–170. https://doi.org/10.1016/j.ensm.2020.12.027.
(32) Monroe, C.; Newman, J. The Impact of Elastic Deformation on Deposition Kinetics at Lithium/Polymer Interfaces. *J. Electrochem. Soc.* **2005**, *152* (2), A396. https://doi.org/10.1149/1.1850854.
(33) Khurana, R.; Schaefer, J. L.; Archer, L. A.; Coates, G. W. Suppression of Lithium Dendrite Growth Using Cross-Linked Polyethylene/Poly(Ethylene Oxide) Electrolytes: A New Approach for Practical Lithium-Metal Polymer Batteries. *J. Am. Chem. Soc.* **2014**, *136* (20), 7395–7402. https://doi.org/10.1021/ja502133j.
(34) Zheng, Y.; Li, X.; Fullerton, W. R.; Li, C. Y. Decoupling the Modulus and Toughness Effects of Solid Polymer Electrolytes in All-Solid-State Lithium Batteries. *ACS Appl. Energy Mater.* **2021**, *4* (12), 14093–14101. https://doi.org/10.1021/acsaem.1c02857.
(35) Ma, D.; Cao, Z.; Hu, A. Si-Based Anode Materials for Li-Ion Batteries: A Mini Review. *Nano-Micro Lett.* **2014**, *6* (4), 347–358. https://doi.org/10.1007/s40820-014-0008-2.
(36) Rahman, Md. A.; Song, G.; Bhatt, A. I.; Wong, Y. C.; Wen, C. Nanostructured Silicon Anodes for High-Performance Lithium-Ion Batteries. *Advanced Functional Materials* **2016**, *26* (5), 647–678. https://doi.org/10.1002/adfm.201502959.
(37) Shen, T.; Yao, Z.; Xia, X.; Wang, X.; Gu, C.; Tu, J. Rationally Designed Silicon Nanostructures as Anode Material for Lithium-Ion Batteries. *Advanced Engineering Materials* **2018**, *20* (1), 1700591. https://doi.org/10.1002/adem.201700591.
(38) Goriparti, S.; Miele, E.; de Angelis, F.; Di Fabrizio, E.; Proietti Zaccaria, R.; Capiglia, C. Review on Recent Progress of Nanostructured Anode Materials for Li-Ion Batteries. *Journal of Power Sources* **2014**, *257*, 421–443. https://doi.org/10.1016/j.jpowsour.2013.11.103.
(39) Neudecker, B. J.; Dudney, N. J.; Bates, J. B. "Lithium-Free" Thin-Film Battery with In Situ Plated Li Anode. *J. Electrochem. Soc.* **2000**, *147* (2), 517. https://doi.org/10.1149/1.1393226.
(40) Yao, W.; Zou, P.; Wang, M.; Zhan, H.; Kang, F.; Yang, C. Design Principle, Optimization Strategies, and Future Perspectives of Anode-Free Configurations for High-Energy Rechargeable Metal Batteries. *Electrochem. Energ. Rev.* **2021**, *4* (3), 601–631. https://doi.org/10.1007/s41918-021-00106-6.
(41) Huang, W.-Z.; Zhao, C.-Z.; Wu, P.; Yuan, H.; Feng, W.-E.; Liu, Z.-Y.; Lu, Y.; Sun, S.; Fu, Z.-H.; Hu, J.-K.; Yang, S.-J.; Huang, J.-Q.; Zhang, Q. Anode-Free Solid-State Lithium Batteries: A Review. *Advanced Energy Materials* **2022**, *12* (26), 2201044. https://doi.org/10.1002/aenm.202201044.
(42) Whittingham, M. S. History, Evolution, and Future Status of Energy Storage. *Proceedings of the IEEE* **2012**, *100* (Special Centennial Issue), 1518–1534. https://doi.org/10.1109/JPROC.2012.2190170.
(43) Goodenough, J. B. Cathode Materials: A Personal Perspective. *Journal of Power Sources* **2007**, *174* (2), 996–1000. https://doi.org/10.1016/j.jpowsour.2007.06.217.
(44) Xia, Y.; Zheng, J.; Wang, C.; Gu, M. Designing Principle for Ni-Rich Cathode Materials with High Energy Density for Practical Applications. *Nano Energy* **2018**, *49*, 434–452. https://doi.org/10.1016/j.nanoen.2018.04.062.
(45) Camargos, P. H.; dos Santos, P. H. J.; dos Santos, I. R.; Ribeiro, G. S.; Caetano, R. E. Perspectives on Li-Ion Battery Categories for Electric Vehicle Applications: A Review of State of the Art. *International Journal of Energy Research* **2022**, *46* (13), 19258–19268. https://doi.org/10.1002/er.7993.
(46) Thackeray, M. M.; David, W. I. F.; Bruce, P. G.; Goodenough, J. B. Lithium Insertion into Manganese Spinels. *Materials Research Bulletin* **1983**, *18* (4), 461–472. https://doi.org/10.1016/0025-5408(83)90138-1.
(47) Huang, Y.; Dong, Y.; Li, S.; Lee, J.; Wang, C.; Zhu, Z.; Xue, W.; Li, Y.; Li, J. Lithium Manganese Spinel Cathodes for Lithium-Ion Batteries. *Advanced Energy Materials* **2021**, *11* (2), 2000997. https://doi.org/10.1002/aenm.202000997.
(48) Jobst, N. M. About the Voltage Characteristics of Highly Lithiated Manganese Based Spinel Type Cathode Materials for Lithium Ion Batteries, Universität Ulm, Ulm, 2023.
(49) Liu, D.; Zhu, W.; Trottier, J.; Gagnon, C.; Barray, F.; Guerfi, A.; Mauger, A.; Groult, H.; M. Julien, C.; B. Goodenough, J.; Zaghib, K. Spinel Materials for High-Voltage Cathodes in Li-Ion Batteries. *RSC Advances* **2014**, *4* (1), 154–167. https://doi.org/10.1039/C3RA45706K.
(50) Kutney, G. *Sulfur: History, Technology, Applications & Industry*, Third edition.; ChemTec Publishing: Toronto, Ontario, 2023.
(51) Chung, W. J.; Griebel, J. J.; Kim, E. T.; Yoon, H.; Simmonds, A. G.; Ji, H. J.; Dirlam, P. T.; Glass, R. S.; Wie, J. J.; Nguyen, N. A.; Guralnick, B. W.; Park, J.; Somogyi, A.; Theato, P.; Mackay, M. E.; Sung, Y.-E.; Char, K.; Pyun, J. The Use of Elemental Sulfur as an Alternative Feedstock for Polymeric Materials. *Nature chemistry* **2013**, *5* (6), 518–524. https://doi.org/10.1038/nchem.1624.

(52) *World Energy Investment 2023*; International Energy Agency, IEA, 2023.
(53) Hettesheimer, Dr. T.; Neef, Dr. C.; Inclán, I. R.; Link, S.; Schmaltz, Dr. T.; Schuckert, F.; Stephan, Dr. A.; Stephan, M.; Thielmann, Dr. A.; Weymann, Dr. L.; Wicke, T. *Lithium-Ion Battery Roadmap – Industrialization Perspectives Toward 2030*; Fraunhofer Institute for Systems and Innovation Research ISI: Karlsruhe, 2023. 10.24406/publica-2153.
(54) Li, J.; Gao, L.; Pan, F.; Gong, C.; Sun, L.; Gao, H.; Zhang, J.; Zhao, Y.; Wang, G.; Liu, H. Engineering Strategies for Suppressing the Shuttle Effect in Lithium–Sulfur Batteries. *Nano-Micro Lett.* **2023**, *16* (1), 12. https://doi.org/10.1007/s40820-023-01223-1.
(55) Chen, Y.; Gao, X.; Su, D.; Wang, C.; Wang, G. Accelerating Redox Kinetics of Lithium-Sulfur Batteries. *Trends in Chemistry* **2020**, *2* (11), 1020–1033. https://doi.org/10.1016/j.trechm.2020.09.001.
(56) Chen, L.; Yu, H.; Li, W.; Dirican, M.; Liu, Y.; Zhang, X. Interlayer Design Based on Carbon Materials for Lithium–Sulfur Batteries: A Review. *J. Mater. Chem. A* **2020**, *8* (21), 10709–10735. https://doi.org/10.1039/D0TA03028G.
(57) Liu, X.; Xu, N.; Qian, T.; Liu, J.; Shen, X.; Yan, C. Stabilized Lithium-Sulfur Batteries by Covalently Binding Sulfur onto the Thiol-Terminated Polymeric Matrices. *Small (Weinheim an der Bergstrasse, Germany)* **2017**, *13* (44). https://doi.org/10.1002/smll.201702104.
(58) Gomez, I.; Mecerreyes, D.; Blazquez, J. A.; Leonet, O.; Ben Youcef, H.; Li, C.; Gómez-Cámer, J. L.; Bondarchuk, O.; Rodriguez-Martinez, L. Inverse Vulcanization of Sulfur with Divinylbenzene: Stable and Easy Processable Cathode Material for Lithium-Sulfur Batteries. *Journal of Power Sources* **2016**, *329*, 72–78. https://doi.org/10.1016/j.jpowsour.2016.08.046.
(59) *The Lithium Air Battery: Fundamentals*; Imanishi, N., Luntz, A. C., Bruce, P., Eds.; Springer New York: New York, NY, 2014. https://doi.org/10.1007/978-1-4899-8062-5.
(60) Lu, Y.-C.; Gasteiger, H. A.; Parent, M. C.; Chiloyan, V.; Shao-Horn, Y. The Influence of Catalysts on Discharge and Charge Voltages of Rechargeable Li–Oxygen Batteries. *Electrochem. Solid-State Lett.* **2010**, *13* (6), A69. https://doi.org/10.1149/1.3363047.
(61) Lai, J.; Xing, Y.; Chen, N.; Li, L.; Wu, F.; Chen, R. Electrolytes for Rechargeable Lithium–Air Batteries. *Angewandte Chemie International Edition* **2020**, *59* (8), 2974–2997. https://doi.org/10.1002/anie.201903459.
(62) Balaish, M.; Kraytsberg, A.; Ein-Eli, Y. A Critical Review on Lithium–Air Battery Electrolytes. *Phys. Chem. Chem. Phys.* **2014**, *16* (7), 2801. https://doi.org/10.1039/c3cp54165g.
(63) Zou, X.; Lu, Q.; Liao, K.; Shao, Z. Towards Practically Accessible Aprotic Li-Air Batteries: Progress and Challenges Related to Oxygen-Permeable Membranes and Cathodes. *Energy Storage Materials* **2022**, *45*, 869–902. https://doi.org/10.1016/j.ensm.2021.12.031.
(64) Blomgren, G. E. Liquid Electrolytes for Lithium and Lithium-Ion Batteries. *Journal of Power Sources* **2003**, *119–121*, 326–329. https://doi.org/10.1016/S0378-7753(03)00147-2.
(65) Zhang, S. S. A Review on the Separators of Liquid Electrolyte Li-Ion Batteries. *Journal of Power Sources* **2007**, *164* (1), 351–364. https://doi.org/10.1016/j.jpowsour.2006.10.065.
(66) Xu, K. Nonaqueous Liquid Electrolytes for Lithium-Based Rechargeable Batteries. *Chem. Rev.* **2004**, *104* (10), 4303–4418. https://doi.org/10.1021/cr030203g.
(67) Hubble, D.; Emory Brown, D.; Zhao, Y.; Fang, C.; Lau, J.; D. McCloskey, B.; Liu, G. Liquid Electrolyte Development for Low-Temperature Lithium-Ion Batteries. *Energy & Environmental Science* **2022**, *15* (2), 550–578. https://doi.org/10.1039/D1EE01789F.
(68) Golubkov, A. W.; Fuchs, D.; Wagner, J.; Wiltsche, H.; Stangl, C.; Fauler, G.; Voitic, G.; Thaler, A.; Hacker, V. Thermal-Runaway Experiments on Consumer Li-Ion Batteries with Metal-Oxide and Olivin-Type Cathodes. *RSC Adv* **2014**, *4* (7), 3633–3642. https://doi.org/10.1039/C3RA45748F.
(69) Song, J. Y.; Wang, Y. Y.; Wan, C. C. Review of Gel-Type Polymer Electrolytes for Lithium-Ion Batteries. *Journal of Power Sources* **1999**, *77* (2), 183–197. https://doi.org/10.1016/S0378-7753(98)00193-1.
(70) Manuel Stephan, A. Review on Gel Polymer Electrolytes for Lithium Batteries. *European Polymer Journal* **2006**, *42* (1), 21–42. https://doi.org/10.1016/j.eurpolymj.2005.09.017.
(71) Ahmed, M. S.; Islam, M.; Raut, B.; Yun, S.; Kim, H. Y.; Nam, K.-W. A Comprehensive Review of Functional Gel Polymer Electrolytes and Applications in Lithium-Ion Battery. *Gels* **2024**, *10* (9), 563. https://doi.org/10.3390/gels10090563.
(72) Wright, P. V. Electrical Conductivity in Ionic Complexes of Poly(Ethylene Oxide). *British Polymer Journal* **1975**, *7* (5), 319–327. https://doi.org/10.1002/pi.4980070505.
(73) Shriver, D. F. Polymer Electrolytes I: General Principles. In *Solid State Electrochemistry*; Bruce, P. G., Ed.; Cambridge University Press, 1994; pp 95–118. https://doi.org/10.1017/CBO9780511524790.006.
(74) Long, L.; Wang, S.; Xiao, M.; Meng, Y. Polymer Electrolytes for Lithium Polymer Batteries. *Journal of Materials Chemistry A* **2016**, *4* (26), 10038–10069. https://doi.org/10.1039/C6TA02621D.
(75) Ngai, K. S.; Ramesh, S.; Ramesh, K.; Juan, J. C. A Review of Polymer Electrolytes: Fundamental, Approaches and Applications. *Ionics* **2016**, *22* (8), 1259–1279. https://doi.org/10.1007/s11581-016-1756-4.
(76) Jr, D. T. H.; Balsara, N. P. Polymer Electrolytes. *Annual Review of Materials Research* **2013**, *43* (Volume 43, 2013), 503–525. https://doi.org/10.1146/annurev-matsci-071312-121705.
(77) Brandell, D.; Mindemark, J.; Hernández, G. *Polymer-Based Solid-State Batteries*; De Gruyter: Berlin [Germany] ; Boston [MA], 2021.
(78) Wang, Y.; Fan, F.; Agapov, A. L.; Saito, T.; Yang, J.; Yu, X.; Hong, K.; Mays, J.; Sokolov, A. P. Examination of the Fundamental Relation between Ionic Transport and Segmental Relaxation in Polymer Electrolytes. *Polymer* **2014**, *55* (16), 4067–4076. https://doi.org/10.1016/j.polymer.2014.06.085.

(79) Walden, P. Über Organische Lösungs- Und Ionisierungsmittel: III. Teil: Innere Reibung Und Deren Zusammenhang Mit Dem Leitvermögen. *Zeitschrift für Physikalische Chemie* **1906**, *55U* (1), 207–249. https://doi.org/10.1515/zpch-1906-5511.
(80) Sasabe, H.; Saito, S. Relationship between Ionic Mobility and Segmental Mobility in Polymers in the Liquid State. *Polym J* **1972**, *3* (5), 624–630. https://doi.org/10.1295/polymj.3.624.
(81) Devaux, D.; Bouchet, R.; Glé, D.; Denoyel, R. Mechanism of Ion Transport in PEO/LiTFSI Complexes: Effect of Temperature, Molecular Weight and End Groups. *Solid State Ionics* **2012**, *227*, 119–127. https://doi.org/10.1016/j.ssi.2012.09.020.
(82) Yang, H.; Wu, N. Ionic Conductivity and Ion Transport Mechanisms of Solid-State Lithium-Ion Battery Electrolytes: A Review. *Energy Science & Engineering* **2022**, *10* (5), 1643–1671. https://doi.org/10.1002/ese3.1163.
(83) Mindemark, J.; Lacey, M. J.; Bowden, T.; Brandell, D. Beyond PEO—Alternative Host Materials for Li + -Conducting Solid Polymer Electrolytes. *Progress in Polymer Science* **2018**, *81*, 114–143. https://doi.org/10.1016/j.progpolymsci.2017.12.004.
(84) Wang, Y.; Chen, W.; Zhao, Q.; Jin, G.; Xue, Z.; Wang, Y.; Mu, T. Ionicity of Deep Eutectic Solvents by Walden Plot and Pulsed Field Gradient Nuclear Magnetic Resonance (PFG-NMR). *Physical Chemistry Chemical Physics* **2020**, *22* (44), 25760–25768. https://doi.org/10.1039/D0CP01431A.
(85) Wang, Y.; Sokolov, A. P. Design of Superionic Polymer Electrolytes. *Current Opinion in Chemical Engineering* **2015**, *7*, 113–119. https://doi.org/10.1016/j.coche.2014.09.002.
(86) Garca-Coln, L. S.; Del Castillo, L. F.; Goldstein, P. Theoretical Basis for the Vogel-Fulcher-Tammann Equation. *Phys. Rev. B* **1989**, *40* (10), 7040–7044. https://doi.org/10.1103/PhysRevB.40.7040.
(87) Tammann, G.; Hesse, W. Die Abhängigkeit Der Viscosität von Der Temperatur Bie Unterkühlten Flüssigkeiten. *Zeitschrift für anorganische und allgemeine Chemie* **1926**, *156* (1), 245–257. https://doi.org/10.1002/zaac.19261560121.
(88) Fulcher, G. S. Analysis of Recent Measurements of the Viscosity of Glasses. *Journal of the American Ceramic Society* **1925**, *8* (6), 339–355. https://doi.org/10.1111/j.1151-2916.1925.tb16731.x.
(89) H. Vogel. Das Temperaturabhängigkeitsgesetz Der Viskosität von Flüssigkeiten. *Physikalische Zeitschrift* **1921**, *22*.
(90) Diederichsen, K. M.; Buss, H. G.; McCloskey, B. D. The Compensation Effect in the Vogel–Tammann–Fulcher (VTF) Equation for Polymer-Based Electrolytes. *Macromolecules* **2017**, *50* (10), 3831–3840. https://doi.org/10.1021/acs.macromol.7b00423.
(91) Bhattacharja, S.; Smoot, S. W.; Whitmore, D. H. Cation and Anion Diffusion in the Amorphous Phase of the Polymer Electrolyte (PEO) 8LiCF3SO3. *Solid State Ionics* **1986**, *18–19*, 306–314. https://doi.org/10.1016/0167-2738(86)90132-3.
(92) Saunier, J.; Gorecki, W.; Alloin, F.; Sanchez, J. Y. NMR Study of Cation, Anion, and Solvent Mobilities in Macroporous Poly(Vinylidene Fluoride). *J. Phys. Chem. B* **2005**, *109* (7), 2487–2492. https://doi.org/10.1021/jp048717m.
(93) Zhao, J.; Wang, L.; He, X.; Wan, C.; Jiang, C. Determination of Lithium-Ion Transference Numbers in LiPF6–PC Solutions Based on Electrochemical Polarization and NMR Measurements. *J. Electrochem. Soc.* **2008**.
(94) Holz, M.; Lucas, O.; Müller, C. NMR in the Presence of an Electric Current. Simultaneous Measurements of Ionic Mobilities, Transference Numbers, and Self-Diffusion Coefficients Using an NMR Pulsed-Gradient Experiment. *Journal of Magnetic Resonance (1969)* **1984**, *58* (2), 294–305. https://doi.org/10.1016/0022-2364(84)90218-X.
(95) Zhang, Z.; Madsen, L. A. Observation of Separate Cation and Anion Electrophoretic Mobilities in Pure Ionic Liquids. *The Journal of Chemical Physics* **2014**, *140* (8), 084204. https://doi.org/10.1063/1.4865834.
(96) Rosenwinkel, M. P.; Andersson, R.; Mindemark, J.; Schönhoff, M. Coordination Effects in Polymer Electrolytes: Fast Li+ Transport by Weak Ion Binding. *J. Phys. Chem. C* **2020**, *124* (43), 23588–23596. https://doi.org/10.1021/acs.jpcc.0c08369.
(97) Rosenwinkel, M. P.; Schönhoff, M. Lithium Transference Numbers in PEO/LiTFSA Electrolytes Determined by Electrophoretic NMR. *J. Electrochem. Soc.* **2019**, *166* (10), A1977. https://doi.org/10.1149/2.0831910jes.
(98) Ravn Sørensen, P.; Jacobsen, T. Conductivity, Charge Transfer and Transport Number—an *Ac*-Investigation of the Polymer Electrolyte LiSCN-Poly(Ethyleneoxide). *Electrochimica Acta* **1982**, *27* (12), 1671–1675. https://doi.org/10.1016/0013-4686(82)80162-X.
(99) Bublil, S.; Peta, G.; Fayena-Greenstein, M.; Alon-Yehezkel, H.; Raskin, O.; Elias, Y.; Aurbach, D. Electrochemical Methods of Transference Number Determination for Polymer Electrolyte Systems: A Comparative Study. *J. Electrochem. Soc.* **2022**, *169* (11), 110523. https://doi.org/10.1149/1945-7111/ac9f75.
(100) Watanabe, M.; Rikukawa, M.; Sanui, K.; Ogata, N. Evaluation of Ionic Mobility and Transference Number in a Polymeric Solid Electrolyte by Isothermal Transient Ionic Current Method. *Journal of Applied Physics* **1985**, *58* (2), 736–740. https://doi.org/10.1063/1.336191.
(101) Watanabe, M.; Nagano, S.; Sanui, K.; Ogata, N. Estimation of Li+ Transport Number in Polymer Electrolytes by the Combination of Complex Impedance and Potentiostatic Polarization Measurements. *Solid State Ionics* **1988**, *28–30*, 911–917. https://doi.org/10.1016/0167-2738(88)90303-7.
(102) Doyle, M.; Newman, J. Analysis of Transference Number Measurements Based on the Potentiostatic Polarization of Solid Polymer Electrolytes. *J. Electrochem. Soc.* **1995**, *142* (10), 3465. https://doi.org/10.1149/1.2050005.
(103) Balsara, N. P.; Newman, J. Relationship between Steady-State Current in Symmetric Cells and Transference Number of Electrolytes Comprising Univalent and Multivalent Ions. *J. Electrochem. Soc.* **2015**, *162* (14), A2720–A2722. https://doi.org/10.1149/2.0651514jes.

(104) Kunze, M.; Karatas, Y.; Wiemhöfer, H.-D.; Schönhoff, M. Correlations of Ion Motion and Chain Motion in Salt-in-Polysiloxane-g-Oligoether Electrolytes. *Macromolecules* **2012**, *45* (20), 8328–8335. https://doi.org/10.1021/ma3014405.
(105) Gouverneur, M.; Kopp, J.; Wüllen, L. van; Schönhoff, M. Direct Determination of Ionic Transference Numbers in Ionic Liquids by Electrophoretic NMR. *Phys. Chem. Chem. Phys.* **2015**, *17* (45), 30680–30686. https://doi.org/10.1039/C5CP05753A.
(106) Pesko, D. M.; Timachova, K.; Bhattacharya, R.; Smith, M. C.; Villaluenga, I.; Newman, J.; Balsara, N. P. Negative Transference Numbers in Poly(Ethylene Oxide)-Based Electrolytes. *J. Electrochem. Soc.* **2017**, *164* (11), E3569–E3575. https://doi.org/10.1149/2.0581711jes.
(107) Villaluenga, I.; Pesko, D. M.; Timachova, K.; Feng, Z.; Newman, J.; Srinivasan, V.; Balsara, N. P. Negative Stefan-Maxwell Diffusion Coefficients and Complete Electrochemical Transport Characterization of Homopolymer and Block Copolymer Electrolytes. *J. Electrochem. Soc.* **2018**, *165* (11), A2766. https://doi.org/10.1149/2.0641811jes.
(108) Sand, H. J. S. On the Concentration at the Electrodes in a Solution, with Special Reference to the Liberation of Hydrogen by Electrolysis of a Mixture of Copper Sulphate and Sulphuric Acid. *The London, Edinburgh, and Dublin Philosophical Magazine and Journal of Science* **1901**, *1* (1), 45–79. https://doi.org/10.1080/14786440109462590.
(109) Stolz, L.; Homann, G.; Winter, M.; Kasnatscheew, J. The Sand Equation and Its Enormous Practical Relevance for Solid-State Lithium Metal Batteries. *Materials Today* **2021**, *44*, 9–14. https://doi.org/10.1016/j.mattod.2020.11.025.
(110) Stolz, L.; Homann, G.; Winter, M.; Kasnatscheew, J. Kinetical Threshold Limits in Solid-State Lithium Batteries: Data on Practical Relevance of Sand Equation. *Data in Brief* **2021**, *34*, 106688. https://doi.org/10.1016/j.dib.2020.106688.
(111) MacFarlane, D. R.; Zhou, F.; Forsyth, M. Ion Conductivity in Amorphous Polymer/Salt Mixtures. *Solid State Ionics* **1998**, *113–115*, 193–197. https://doi.org/10.1016/S0167-2738(98)00373-7.
(112) Liu, G.; Li, Y.; Zhang, L.; Tao, H.; Yang, X. In Situ Construction of PVA/LiF Composite Artificial Protective Layer to Assist Dendrite-Free Li Metal Anode. *Applied Surface Science* **2023**, *620*, 156809. https://doi.org/10.1016/j.apsusc.2023.156809.
(113) Chiang, C. K.; Davis, G. T.; Harding, C. A.; Takahashi, T. Polymeric Electrolyte Based on Poly(Ethylene Imine) and Lithium Salts. *Solid State Ionics* **1986**, *18–19*, 300–305. https://doi.org/10.1016/0167-2738(86)90131-1.
(114) Tanaka, R.; Fujita, T.; Nishibayashi, H.; Saito, S. Ionic Conduction in Poly(Ethylenimine)-and Poly(N-Methylethylenimine)-Lithium Salt Systems. *Solid State Ionics* **1993**, *60* (1), 119–123. https://doi.org/10.1016/0167-2738(93)90284-A.
(115) Nanini-Maury, E.; Świątowska, J.; Chagnes, A.; Zanna, S.; Tran-Van, P.; Marcus, P.; Cassir, M. Electrochemical Behavior of Sebaconitrile as a Cosolvent in the Formulation of Electrolytes at High Potentials for Lithium-Ion Batteries. *Electrochimica Acta* **2014**, *115*, 223–233. https://doi.org/10.1016/j.electacta.2013.10.087.
(116) Fan, L.-Z.; Hu, Y.-S.; Bhattacharyya, A. J.; Maier, J. Succinonitrile as a Versatile Additive for Polymer Electrolytes. *Advanced Functional Materials* **2007**, *17* (15), 2800–2807. https://doi.org/10.1002/adfm.200601070.
(117) Hu, P.; Chai, J.; Duan, Y.; Liu, Z.; Cui, G.; Chen, L. Progress in Nitrile-Based Polymer Electrolytes for High Performance Lithium Batteries. *Journal of Materials Chemistry A* **2016**, *4* (26), 10070–10083. https://doi.org/10.1039/C6TA02907H.
(118) Xue, Z.; He, D.; Xie, X. Poly(Ethylene Oxide)-Based Electrolytes for Lithium-Ion Batteries. *Journal of Materials Chemistry A* **2015**, *3* (38), 19218–19253. https://doi.org/10.1039/C5TA03471J.
(119) Kim, D.-W.; Park, J.-K.; Gong, M.-S.; Song, H.-Y. Effect of Grafting Degree and Side PEO Chain Length on the Ionic Conductivities of NBR-g-PEO Based Polymer Electrolytes. *Polymer Engineering & Science* **1994**, *34* (17), 1305–1313. https://doi.org/10.1002/pen.760341702.
(120) Lapienis, G. Star-Shaped Polymers Having PEO Arms. *Progress in Polymer Science* **2009**, *34* (9), 852–892. https://doi.org/10.1016/j.progpolymsci.2009.04.006.
(121) Fonseca, C. P.; Rosa, D. S.; Gaboardi, F.; Neves, S. Development of a Biodegradable Polymer Electrolyte for Rechargeable Batteries. *Journal of Power Sources* **2006**, *155* (2), 381–384. https://doi.org/10.1016/j.jpowsour.2005.05.004.
(122) Rosenbach, D.; Krimalowski, A.; Erabhoina, H.; Thelakkat, M. Solid Polymer Electrolytes from Polyesters with Diester Sidechains for Lithium Metal Batteries. *Journal of Materials Chemistry A* **2022**, *10* (16), 8932–8947. https://doi.org/10.1039/D2TA00800A.
(123) Eriksson, T.; Gudla, H.; Manabe, Y.; Yoneda, T.; Friesen, D.; Zhang, C.; Inokuma, Y.; Brandell, D.; Mindemark, J. Carbonyl-Containing Solid Polymer Electrolyte Host Materials: Conduction and Coordination in Polyketone, Polyester, and Polycarbonate Systems. *Macromolecules* **2022**, *55* (24), 10940–10949. https://doi.org/10.1021/acs.macromol.2c01683.
(124) Mindemark, J.; Imholt, L.; Montero, J.; Brandell, D. Allyl Ethers as Combined Plasticizing and Crosslinkable Side Groups in Polycarbonate-Based Polymer Electrolytes for Solid-State Li Batteries. *Journal of Polymer Science Part A: Polymer Chemistry* **2016**, *54* (14), 2128–2135. https://doi.org/10.1002/pola.28080.
(125) Perz, V.; Bleymaier, K.; Sinkel, C.; Kueper, U.; Bonnekessel, M.; Ribitsch, D.; Guebitz, G. M. Data on Synthesis of Oligomeric and Polymeric Poly(Butylene Adipate-Co-Butylene Terephthalate) Model Substrates for the Investigation of Enzymatic Hydrolysis. *Data in Brief* **2016**, *7*, 291–298. https://doi.org/10.1016/j.dib.2016.02.029.
(126) Pratt, R. C.; Nederberg, F.; Waymouth, R. M.; Hedrick, J. L. Tagging Alcohols with Cyclic Carbonate: A Versatile Equivalent of (Meth)Acrylate for Ring-Opening Polymerization. *Chem. Commun.* **2007**, No. 1, 114–116. https://doi.org/10.1039/B713925J.

(127) Mindemark, J.; Bowden, T. Synthesis and Polymerization of Alkyl Halide-Functional Cyclic Carbonates. *Polymer* **2011**, *52* (25), 5716–5722. https://doi.org/10.1016/j.polymer.2011.10.027.
(128) Tempelaar, S.; Mespouille, L.; Coulembier, O.; Dubois, P.; Dove, A. P. Synthesis and Post-Polymerisation Modifications of Aliphatic Poly(Carbonate)s Prepared by Ring-Opening Polymerisation. *Chem. Soc. Rev.* **2013**, *42* (3), 1312–1336. https://doi.org/10.1039/C2CS35268K.
(129) Sun, B.; Mindemark, J.; Edström, K.; Brandell, D. Polycarbonate-Based Solid Polymer Electrolytes for Li-Ion Batteries. *Solid State Ionics* **2014**, *262*, 738–742. https://doi.org/10.1016/j.ssi.2013.08.014.
(130) He, W.; Cui, Z.; Liu, X.; Cui, Y.; Chai, J.; Zhou, X.; Liu, Z.; Cui, G. Carbonate-Linked Poly(Ethylene Oxide) Polymer Electrolytes towards High Performance Solid State Lithium Batteries. *Electrochimica Acta* **2017**, *225*, 151–159. https://doi.org/10.1016/j.electacta.2016.12.113.
(131) Erabhoina, H.; Rosenbach, D.; Mohanraj, J.; Thelakkat, M. Solid Polymer Nanocomposite Electrolytes with Improved Interface Properties towards Lithium Metal Battery Application at Room Temperature. *Electrochimica Acta* **2021**, *387*, 138455. https://doi.org/10.1016/j.electacta.2021.138455.
(132) Wang, J.; Li, S.; Zhao, Q.; Song, C.; Xue, Z. Structure Code for Advanced Polymer Electrolyte in Lithium-Ion Batteries. *Advanced Functional Materials* **2021**, *31* (12), 2008208. https://doi.org/10.1002/adfm.202008208.
(133) Krimalowski, A.; Rosenbach, D.; Erabhoina, H.; Thelakkat, M. Versatile Solid Polymer Electrolytes from Clickable Poly(Glycidyl Propargyl Ether) for Lithium Metal Batteries. *Journal of Energy Storage* **2023**, *65*, 107348. https://doi.org/10.1016/j.est.2023.107348.
(134) Krimalowski, A.; Thelakkat, M. Sequential Co-Click Reactions with Poly(Glycidyl Propargyl Ether) toward Single-Ion Conducting Electrolytes. *Macromolecules* **2019**, *52* (11), 4042–4051. https://doi.org/10.1021/acs.macromol.9b00206.
(135) Oh, B.; Vissers, D.; Zhang, Z.; West, R.; Tsukamoto, H.; Amine, K. New Interpenetrating Network Type Poly(Siloxane-g-Ethylene Oxide) Polymer Electrolyte for Lithium Battery. *Journal of Power Sources* **2003**, *119–121*, 442–447. https://doi.org/10.1016/S0378-7753(03)00187-3.
(136) Petry, J.; Dietel, M.; Thelakkat, M. Semi-Interpenetrating Network Electrolytes Utilizing Ester-Functionalized Low Tg Polysiloxanes in Lithium-Metal Batteries. *Adv. Energy Mater.* **2024**, *n/a* (n/a), 2403531. https://doi.org/10.1002/aenm.202403531.
(137) Britz, J.; Meyer, W. H.; Wegner, G. Blends of Poly(Meth)Acrylates with 2-Oxo-(1,3)Dioxolane Side Chains and Lithium Salts as Lithium Ion Conductors. *Macromolecules* **2007**, *40* (21), 7558–7565. https://doi.org/10.1021/ma0714619.
(138) Meziane, R.; Bonnet, J.-P.; Courty, M.; Djellab, K.; Armand, M. Single-Ion Polymer Electrolytes Based on a Delocalized Polyanion for Lithium Batteries. *Electrochimica Acta* **2011**, *57*, 14–19. https://doi.org/10.1016/j.electacta.2011.03.074.
(139) Butzelaar, A. J.; Liu, K. L.; Röring, P.; Brunklaus, G.; Winter, M.; Theato, P. A Systematic Study of Vinyl Ether-Based Poly(Ethylene Oxide) Side-Chain Polymer Electrolytes. *ACS Appl. Polym. Mater.* **2021**, *3* (3), 1573–1582. https://doi.org/10.1021/acsapm.0c01398.
(140) Xie, G.; Martinez, M. R.; Olszewski, M.; Sheiko, S. S.; Matyjaszewski, K. Molecular Bottlebrushes as Novel Materials. *Biomacromolecules* **2019**, *20* (1), 27–54. https://doi.org/10.1021/acs.biomac.8b01171.
(141) Ji, X.; Xiao, L.-L.; Zhang, Y.; Yue, K.; Zhou, X.; Guo, Z.-H. Unveiling the Side-Chain Effect on Ionic Conductivity of Poly(Ethylene Oxide)-Based Polymer-Brush Electrolytes. *ACS Appl. Energy Mater.* **2022**, *5* (7), 8410–8418. https://doi.org/10.1021/acsaem.2c00962.
(142) Bennington, P.; Deng, C.; Sharon, D.; A. Webb, M.; Pablo, J. J. de; F. Nealey, P.; N. Patel, S. Role of Solvation Site Segmental Dynamics on Ion Transport in Ethylene-Oxide Based Side-Chain Polymer Electrolytes. *Journal of Materials Chemistry A* **2021**, *9* (15), 9937–9951. https://doi.org/10.1039/D1TA00899D.
(143) Rosenbach, D.; Mödl, N.; Hahn, M.; Petry, J.; Danzer, M. A.; Thelakkat, M. Synthesis and Comparative Studies of Solvent-Free Brush Polymer Electrolytes for Lithium Batteries. *ACS Applied Energy Materials* **2019**, *2* (5), 3373–3388. https://doi.org/10.1021/acsaem.9b00211.
(144) An, S. Y.; Wu, X.; Zhao, Y.; Liu, T.; Yin, R.; Ahn, J. H.; Walker, L. M.; Whitacre, J. F.; Matyjaszewski, K. Highly Conductive Polyoxanorbornene-Based Polymer Electrolyte for Lithium-Metal Batteries. *Advanced Science* **2023**, *10* (27), 2302932. https://doi.org/10.1002/advs.202302932.
(145) Bates, C. M.; Chang, A. B.; Momčilović, N.; Jones, S. C.; Grubbs, R. H. ABA Triblock Brush Polymers: Synthesis, Self-Assembly, Conductivity, and Rheological Properties. *Macromolecules* **2015**, *48* (14), 4967–4973. https://doi.org/10.1021/acs.macromol.5b00880.
(146) Petry, J.; Erabhoina, H.; Dietel, M.; Thelakkat, M. Comparative Study of the Mechanical Reinforcement by Blending, Filling, and Block Copolymerization in Bottlebrush Polymer Electrolytes. *ACS Appl. Polym. Mater.* **2024**, *6* (9), 5109–5120. https://doi.org/10.1021/acsapm.4c00161.
(147) Çelik, S. Ü.; Bozkurt, A. Polymer Electrolytes Based on the Doped Comb-Branched Copolymers for Li-Ion Batteries. *Solid State Ionics* **2010**, *181* (21–22), 987–993. https://doi.org/10.1016/j.ssi.2010.05.039.
(148) Eissa, A. M.; Khosravi, E. Comb-Like Graft Copolymers of Poly(Oxa)Norbornene: Efficient Synthesis Using a Combination of ROMP and Click Chemistry. *Macromolecular Chemistry and Physics* **2015**, *216* (9), 964–976. https://doi.org/10.1002/macp.201400604.
(149) Chen, Y.-H.; Hsieh, Y.-C.; Liu, K. L.; Wichmann, L.; Thienenkamp, J. H.; Choudhary, A.; Bedrov, D.; Winter, M.; Brunklaus, G. Green Polymer Electrolytes Based on Polycaprolactones for Solid-State High-Voltage Lithium Metal Batteries. *Macromolecular Rapid Communications* **2022**, *43* (20), 2200335. https://doi.org/10.1002/marc.202200335.

(150) Niitani, T.; Amaike, M.; Nakano, H.; Dokko, K.; Kanamura, K. Star-Shaped Polymer Electrolyte with Microphase Separation Structure for All-Solid-State Lithium Batteries. *J. Electrochem. Soc.* **2009**, *156* (7), A577. https://doi.org/10.1149/1.3129245.
(151) Wang, B.; Lou, H.; Xu, H.; Zhao, J.; Wang, Q.; Shi, Q.; Deng, Y. High Voltage, Solvent-Free Solid Polymer Electrolyte Based on a Star-Comb PDLLA–PEG Copolymer for Lithium Ion Batteries. *RSC Adv.* **2018**, *8* (12), 6373–6380. https://doi.org/10.1039/C7RA13664A.
(152) Petry, J.; Dan, K.; Nag, A.; Thelakkat, M.; Ghosh, S. Easily Accessible Linear and Hyperbranched Polyesters as Solid Polymer Electrolytes. *European Polymer Journal* **2024**, *210*, 112965. https://doi.org/10.1016/j.eurpolymj.2024.112965.
(153) Lee, S.-I.; Schömer, M.; Peng, H.; Page, K. A.; Wilms, D.; Frey, H.; Soles, C. L.; Yoon, D. Y. Correlations between Ion Conductivity and Polymer Dynamics in Hyperbranched Poly(Ethylene Oxide) Electrolytes for Lithium-Ion Batteries. *Chem. Mater.* **2011**, *23* (11), 2685–2688. https://doi.org/10.1021/cm103696g.
(154) Xi, G.; Xiao, M.; Wang, S.; Han, D.; Li, Y.; Meng, Y. Polymer-Based Solid Electrolytes: Material Selection, Design, and Application. *Advanced Functional Materials* **2021**, *31* (9), 2007598. https://doi.org/10.1002/adfm.202007598.
(155) Stolz, L.; Röser, S.; Homann, G.; Winter, M.; Kasnatscheew, J. Pragmatic Approaches to Correlate between the Physicochemical Properties of a Linear Poly(Ethylene Oxide)-Based Solid Polymer Electrolyte and the Performance in a High-Voltage Li-Metal Battery. *J. Phys. Chem. C* **2021**, *125* (33), 18089–18097. https://doi.org/10.1021/acs.jpcc.1c03614.
(156) Judez, X.; Zhang, H.; Li, C.; González-Marcos, J. A.; Zhou, Z.; Armand, M.; Rodriguez-Martinez, L. M. Lithium Bis(Fluorosulfonyl)Imide/Poly(Ethylene Oxide) Polymer Electrolyte for All Solid-State Li–S Cell. *J. Phys. Chem. Lett.* **2017**, *8* (9), 1956–1960. https://doi.org/10.1021/acs.jpclett.7b00593.
(157) Eriksson, T.; Mace, A.; Mindemark, J.; Brandell, D. The Role of Coordination Strength in Solid Polymer Electrolytes: Compositional Dependence of Transference Numbers in the Poly(ε-Caprolactone)–Poly(Trimethylene Carbonate) System. *Phys. Chem. Chem. Phys.* **2021**, *23* (45), 25550–25557. https://doi.org/10.1039/D1CP03929F.
(158) Andersson, R.; Hernández, G.; Mindemark, J. Quantifying the Ion Coordination Strength in Polymer Electrolytes. *Physical Chemistry Chemical Physics* **2022**, *24* (26), 16343–16352. https://doi.org/10.1039/D2CP01904C.
(159) Dietel, M. Synthesis and Electrochemical Studies of Diester-Functionalized Polysiloxane Elastomers as Solid Electrolytes for Lithium Metal Batteries, 2023.
(160) Monroe, C.; Newman, J. Dendrite Growth in Lithium/Polymer Systems : A Propagation Model for Liquid Electrolytes under Galvanostatic Conditions. *J. Electrochem. Soc.* **2003**, *150* (10), A1377. https://doi.org/10.1149/1.1606686.
(161) Arora, P.; Zhang, Z. (John). Battery Separators. *Chem. Rev.* **2004**, *104* (10), 4419–4462. https://doi.org/10.1021/cr020738u.
(162) Orendorff, C. J. The Role of Separators in Lithium-Ion Cell Safety. *Interface magazine* **2012**, *21* (2), 61–65. https://doi.org/10.1149/2.f07122if.
(163) Russo, F.; Ursino, C.; Avruscio, E.; Desiderio, G.; Perrone, A.; Santoro, S.; Galiano, F.; Figoli, A. Innovative Poly (Vinylidene Fluoride) (PVDF) Electrospun Nanofiber Membrane Preparation Using DMSO as a Low Toxicity Solvent. *Membranes* **2020**, *10* (3), 36. https://doi.org/10.3390/membranes10030036.
(164) Wan, J.; Xie, J.; Kong, X.; Liu, Z.; Liu, K.; Shi, F.; Pei, A.; Chen, H.; Chen, W.; Chen, J.; Zhang, X.; Zong, L.; Wang, J.; Chen, L.-Q.; Qin, J.; Cui, Y. Ultrathin, Flexible, Solid Polymer Composite Electrolyte Enabled with Aligned Nanoporous Host for Lithium Batteries. *Nat. Nanotechnol.* **2019**, *14* (7), 705–711. https://doi.org/10.1038/s41565-019-0465-3.
(165) Eun Park, S.; Shin, K.; Hyuk Yang, J.; Keun Park, B.; Yeun Kim, S.; Kim, H.-S.; Park, M.-S.; Jae Kim, K. Track-Etched Polyimide Separator Decorated with Polyvinylpyrrolidone for Self-Assembling a Robust Protective Layer on Lithium-Metal Anode. *Chemical Engineering Journal* **2022**, *445*, 136801. https://doi.org/10.1016/j.cej.2022.136801.
(166) Pei, D.; Li, Y.; Huang, S.; Liu, M.; Hong, J.; Hou, S.; Jin, H.; Cao, G. Polycaprolactone-Poly(Vinylidene Fluoride) Blended Composite Polymer Electrolyte with Enhanced High Power Performance and Interfacial Stability for All-Solid-State Li Metal Batteries. *Chemical Engineering Journal* **2023**, *461*, 141899. https://doi.org/10.1016/j.cej.2023.141899.
(167) Prabakaran, P.; Manimuthu, R. P.; Gurusamy, S.; Sebasthiyan, E. Plasticized Polymer Electrolyte Membranes Based on PEO/PVdF-HFP for Use as an Effective Electrolyte in Lithium-Ion Batteries. *Chin J Polym Sci* **2017**, *35* (3), 407–421. https://doi.org/10.1007/s10118-017-1906-9.
(168) B, J.; Km, A.; M, M.; V.s, P.; S., J. Development of a Novel Type of Solid Polymer Electrolyte for Solid State Lithium Battery Applications Based on Lithium Enriched Poly (Ethylene Oxide) (PEO)/Poly (Vinyl Pyrrolidone) (PVP) Blend Polymer. *Electrochimica Acta* **2017**, *235*, 210–222. https://doi.org/10.1016/j.electacta.2017.03.118.
(169) Sengwa, R. J.; Dhatarwal, P.; Choudhary, S. Role of Preparation Methods on the Structural and Dielectric Properties of Plasticized Polymer Blend Electrolytes: Correlation between Ionic Conductivity and Dielectric Parameters. *Electrochimica Acta* **2014**, *142*, 359–370. https://doi.org/10.1016/j.electacta.2014.07.120.
(170) Yao, W.; Zhang, Q.; Qi, F.; Zhang, J.; Liu, K.; Li, J.; Chen, W.; Du, Y.; Jin, Y.; Liang, Y.; Liu, N. Epoxy Containing Solid Polymer Electrolyte for Lithium Ion Battery. *Electrochimica Acta* **2019**, *318*, 302–313. https://doi.org/10.1016/j.electacta.2019.06.069.
(171) Boujioui, F.; Zhuge, F.; Damerow, H.; Wehbi, M.; Améduri, B.; Gohy, J.-F. Solid Polymer Electrolytes from a Fluorinated Copolymer Bearing Cyclic Carbonate Pendant Groups. *J. Mater. Chem. A* **2018**, *6* (18), 8514–8522. https://doi.org/10.1039/C8TA01409D.

(172) Bates, F. S. Polymer-Polymer Phase Behavior. *Science (New York, N.Y.)* **1991**, *251* (4996), 898–905. https://doi.org/10.1126/science.251.4996.898.
(173) Matsen, M. W.; Bates, F. S. Origins of Complex Self-Assembly in Block Copolymers. *Macromolecules* **1996**, *29* (23), 7641–7644. https://doi.org/10.1021/ma9607446.
(174) Phan, T. N. T.; Issa, S.; Gigmes, D. Poly(Ethylene Oxide)-Based Block Copolymer Electrolytes for Lithium Metal Batteries. *Polymer International* **2019**, *68* (1), 7–13. https://doi.org/10.1002/pi.5677.
(175) Singh, M.; Odusanya, O.; Wilmes, G. M.; Eitouni, H. B.; Gomez, E. D.; Patel, A. J.; Chen, V. L.; Park, M. J.; Fragouli, P.; Iatrou, H.; Hadjichristidis, N.; Cookson, D.; Balsara, N. P. Effect of Molecular Weight on the Mechanical and Electrical Properties of Block Copolymer Electrolytes. *Macromolecules* **2007**, *40* (13), 4578–4585. https://doi.org/10.1021/ma0629541.
(176) Bouchet, R.; Phan, T. N. T.; Beaudoin, E.; Devaux, D.; Davidson, P.; Bertin, D.; Denoyel, R. Charge Transport in Nanostructured PS–PEO–PS Triblock Copolymer Electrolytes. *Macromolecules* **2014**, *47* (8), 2659–2665. https://doi.org/10.1021/ma500420w.
(177) Beaudoin, E.; Phan, T. N. T.; Robinet, M.; Denoyel, R.; Davidson, P.; Bertin, D.; Bouchet, R. Effect of Interfaces on the Melting of PEO Confined in Triblock PS-b-PEO-b-PS Copolymers. *Langmuir* **2013**, *29* (34), 10874–10880. https://doi.org/10.1021/la401889h.
(178) Devaux, D.; Glé, D.; Phan, T. N. T.; Gigmes, D.; Giroud, E.; Deschamps, M.; Denoyel, R.; Bouchet, R. Optimization of Block Copolymer Electrolytes for Lithium Metal Batteries. *Chemistry of Materials* **2015**, *27* (13), 4682–4692. https://doi.org/10.1021/acs.chemmater.5b01273.
(179) Butzelaar, A. J.; Röring, P.; Mach, T. P.; Hoffmann, M.; Jeschull, F.; Wilhelm, M.; Winter, M.; Brunklaus, G.; Théato, P. Styrene-Based Poly(Ethylene Oxide) Side-Chain Block Copolymers as Solid Polymer Electrolytes for High-Voltage Lithium-Metal Batteries. *ACS Appl. Mater. Interfaces* **2021**, *13* (33), 39257–39270. https://doi.org/10.1021/acsami.1c08841.
(180) Gai, Y.; Song, D.-P.; Yavitt, B. M.; Watkins, J. J. Polystyrene- Block -Poly(Ethylene Oxide) Bottlebrush Block Copolymer Morphology Transitions: Influence of Side Chain Length and Volume Fraction. *Macromolecules* **2017**, *50* (4), 1503–1511. https://doi.org/10.1021/acs.macromol.6b01415.
(181) Rupp, B.; Schmuck, M.; Balducci, A.; Winter, M.; Kern, W. Polymer Electrolyte for Lithium Batteries Based on Photochemically Crosslinked Poly(Ethylene Oxide) and Ionic Liquid. *European Polymer Journal* **2008**, *44* (9), 2986–2990. https://doi.org/10.1016/j.eurpolymj.2008.06.022.
(182) Maccallum, J. R.; Smith, M. J.; Vincent, C. A. The Effects of Radiation-Induced Crosslinking on the Conductance of $LiClO_4$·PEO Electrolytes. *Solid State Ionics* **1984**, *11* (4), 307–312. https://doi.org/10.1016/0167-2738(84)90022-5.
(183) Tian, G.; Zhao, Z.; Zinkevich, T.; Elies, K.; Scheiba, F.; Ehrenberg, H. A Crosslinked Polyethyleneglycol Solid Electrolyte Dissolving Lithium Bis(Trifluoromethylsulfonyl)Imide for Rechargeable Lithium Batteries. *ChemSusChem* **2019**, *12* (20), 4708–4718. https://doi.org/10.1002/cssc.201901587.
(184) Daigle, J.-C.; Asakawa, Y.; Vijh, A.; Hovington, P.; Armand, M.; Zaghib, K. Exceptionally Stable Polymer Electrolyte for a Lithium Battery Based on Cross-Linking by a Residue-Free Process. *Journal of Power Sources* **2016**, *332*, 213–221. https://doi.org/10.1016/j.jpowsour.2016.09.139.
(185) Andrews, W. T.; Liebig, A.; Cook, J.; Marsh, P.; Ciocanel, C.; Lindberg, G. E.; Browder, C. C. Development of a PEO-Based Lithium Ion Conductive Epoxy Resin Polymer Electrolyte. *Solid State Ionics* **2018**, *326*, 150–158. https://doi.org/10.1016/j.ssi.2018.09.013.
(186) Jalbert, P.-M.; Commarieu, B.; Daigle, J.-C.; Claverie, J. P.; Zaghib, K. A 3D Network Based on Poly(ε-Caprolactone) Macromonomers as Polymer Electrolyte for Solid State Lithium Metal Batteries. *J. Electrochem. Soc.* **2020**, *167* (8), 080527. https://doi.org/10.1149/1945-7111/ab8de0.
(187) Goujon, L. J.; Khaldi, A.; Maziz, A.; Plesse, C.; Nguyen, G. T. M.; Aubert, P.-H.; Vidal, F.; Chevrot, C.; Teyssié, D. Flexible Solid Polymer Electrolytes Based on Nitrile Butadiene Rubber/Poly(Ethylene Oxide) Interpenetrating Polymer Networks Containing Either LiTFSI or EMITFSI. *Macromolecules* **2011**, *44* (24), 9683–9691. https://doi.org/10.1021/ma201662h.
(188) Guan, T.; Rong, Z.; Cheng, F.; Zhang, W.; Chen, J. UV-Cured Interpenetrating Networks of Single-Ion Conducting Polymer Electrolytes for Rechargeable Lithium Metal Batteries. *ACS Appl. Energy Mater.* **2020**, *3* (12), 12532–12539. https://doi.org/10.1021/acsaem.0c02483.
(189) Min, K. H.; Kim, D. B.; Kang, Y. K.; Suh, D. H. Ionic Conductivity and Morphology of Semi-Interpenetrating-Type Polymer Electrolyte Entrapping Poly(Siloxane-g-Allyl Cyanide). *Journal of Applied Polymer Science* **2008**, *107* (3), 1609–1615. https://doi.org/10.1002/app.27276.
(190) Homann, G.; Stolz, L.; Winter, M.; Kasnatscheew, J. Elimination of "Voltage Noise" of Poly (Ethylene Oxide)-Based Solid Electrolytes in High-Voltage Lithium Batteries: Linear versus Network Polymers. *iScience* **2020**, *23* (6), 101225. https://doi.org/10.1016/j.isci.2020.101225.
(191) Li, X.; Zheng, Y.; Duan, Y.; Shang, M.; Niu, J.; Li, C. Y. Designing Comb-Chain Crosslinker-Based Solid Polymer Electrolytes for Additive-Free All-Solid-State Lithium Metal Batteries. *Nano Lett.* **2020**, *20* (9), 6914–6921. https://doi.org/10.1021/acs.nanolett.0c03033.
(192) Fullerton, W. R.; Li, C. Y. Compliant Solid Polymer Electrolytes (SPEs) for Enhanced Anode-Electrolyte Interfacial Stability in All-Solid-State Lithium–Metal Batteries (LMBs). *ACS Appl. Polym. Mater.* **2024**, *6* (13), 7468–7477. https://doi.org/10.1021/acsapm.4c00806.
(193) Wang, Y.; Zhang, Y.; Hou, H. Multifunctional Macromolecular Design as a Self-Standing Electrolyte for High-Temperature Single-Ion Lithium Batteries. *Journal of Applied Electrochemistry* **2017**, *47* (2), 237–248. https://doi.org/10.1007/s10800-016-1029-y.

(194) Hu, J.; Wang, W.; Zhou, B.; Feng, Y.; Xie, X.; Xue, Z. Poly(Ethylene Oxide)-Based Composite Polymer Electrolytes Embedding with Ionic Bond Modified Nanoparticles for All-Solid-State Lithium-Ion Battery. *Journal of Membrane Science* **2019**, *575*, 200–208. https://doi.org/10.1016/j.memsci.2019.01.025.
(195) Fan, P.; Liu, H.; Marosz, V.; Samuels, N. T.; Suib, S. L.; Sun, L.; Liao, L. High Performance Composite Polymer Electrolytes for Lithium-Ion Batteries. *Advanced Functional Materials* **2021**, *31* (23), 2101380. https://doi.org/10.1002/adfm.202101380.
(196) Lago, N.; Garcia-Calvo, O.; Lopez del Amo, J. M.; Rojo, T.; Armand, M. All-Solid-State Lithium-Ion Batteries with Grafted Ceramic Nanoparticles Dispersed in Solid Polymer Electrolytes. *ChemSusChem* **2015**, *8* (18), 3039–3043. https://doi.org/10.1002/cssc.201500783.
(197) Zheng, J.; Tang, M.; Hu, Y.-Y. Lithium Ion Pathway within Li7La3Zr2O12-Polyethylene Oxide Composite Electrolytes. *Angewandte Chemie International Edition* **2016**, *55* (40), 12538–12542. https://doi.org/10.1002/anie.201607539.
(198) Boaretto, N.; Meabe, L.; Martinez-Ibañez, M.; Armand, M.; Zhang, H. Review—Polymer Electrolytes for Rechargeable Batteries: From Nanocomposite to Nanohybrid. *J. Electrochem. Soc.* **2020**, *167* (7), 070524. https://doi.org/10.1149/1945-7111/ab7221.
(199) Judez, X.; Piszcz, M.; Coya, E.; Li, C.; Aldalur, I.; Oteo, U.; Zhang, Y.; Zhang, W.; Rodriguez-Martinez, L. M.; Zhang, H.; Armand, M. Stable Cycling of Lithium Metal Electrode in Nanocomposite Solid Polymer Electrolytes with Lithium Bis (Fluorosulfonyl)Imide. *Solid State Ionics* **2018**, *318*, 95–101. https://doi.org/10.1016/j.ssi.2017.07.021.
(200) Wang, W.; Alexandridis, P. Composite Polymer Electrolytes: Nanoparticles Affect Structure and Properties. *Polymers* **2016**, *8* (11), 387. https://doi.org/10.3390/polym8110387.
(201) Kamal, A.; Ashmawy, M.; S, S.; Algazzar, A. M.; Elsheikh, A. H. Fabrication Techniques of Polymeric Nanocomposites: A Comprehensive Review. *Proceedings of the Institution of Mechanical Engineers, Part C: Journal of Mechanical Engineering Science* **2022**, *236* (9), 4843–4861. https://doi.org/10.1177/09544062211055662.
(202) Liu, C.; Sacci, R. L.; Sahore, R.; Veith, G. M.; Dudney, N. J.; Chen, X. C. Polyacrylonitrile-Based Electrolytes: How Processing and Residual Solvent Affect Ion Transport and Stability. *Journal of Power Sources* **2022**, *527*, 231165. https://doi.org/10.1016/j.jpowsour.2022.231165.
(203) Pan, Q.; Smith, D. M.; Qi, H.; Wang, S.; Li, C. Y. Hybrid Electrolytes with Controlled Network Structures for Lithium Metal Batteries. *Advanced Materials* **2015**, *27* (39), 5995–6001. https://doi.org/10.1002/adma.201502059.
(204) Lin, D.; Liu, W.; Liu, Y.; Lee, H. R.; Hsu, P.-C.; Liu, K.; Cui, Y. High Ionic Conductivity of Composite Solid Polymer Electrolyte via In Situ Synthesis of Monodispersed SiO2 Nanospheres in Poly(Ethylene Oxide). *Nano Lett.* **2016**, *16* (1), 459–465. https://doi.org/10.1021/acs.nanolett.5b04117.
(205) Shim, J.; Kim, D.-G.; Kim, H. J.; Lee, J. H.; Lee, J.-C. Polymer Composite Electrolytes Having Core–Shell Silica Fillers with Anion-Trapping Boron Moiety in the Shell Layer for All-Solid-State Lithium-Ion Batteries. *ACS Appl. Mater. Interfaces* **2015**, *7* (14), 7690–7701. https://doi.org/10.1021/acsami.5b00618.
(206) Glynos, E.; Papoutsakis, L.; Pan, W.; Giannelis, E. P.; Nega, A. D.; Mygiakis, E.; Sakellariou, G.; Anastasiadis, S. H. Nanostructured Polymer Particles as Additives for High Conductivity, High Modulus Solid Polymer Electrolytes. *Macromolecules* **2017**, *50* (12), 4699–4706. https://doi.org/10.1021/acs.macromol.7b00789.
(207) Glynos, E.; Petropoulou, P.; Mygiakis, E.; Nega, A. D.; Pan, W.; Papoutsakis, L.; Giannelis, E. P.; Sakellariou, G.; Anastasiadis, S. H. Leveraging Molecular Architecture To Design New, All-Polymer Solid Electrolytes with Simultaneous Enhancement in Modulus and Ionic Conductivity. *Macromolecules* **2018**, *51* (7), 2542–2550. https://doi.org/10.1021/acs.macromol.7b02394.
(208) Glynos, E.; Pantazidis, C.; Sakellariou, G. Designing All-Polymer Nanostructured Solid Electrolytes: Advances and Prospects. *ACS Omega* **2020**, *5* (6), 2531–2540. https://doi.org/10.1021/acsomega.9b04098.
(209) Li, Z.; Huang, H.-M.; Zhu, J.-K.; Wu, J.-F.; Yang, H.; Wei, L.; Guo, X. Ionic Conduction in Composite Polymer Electrolytes: Case of PEO:Ga-LLZO Composites. *ACS Appl. Mater. Interfaces* **2019**, *11* (1), 784–791. https://doi.org/10.1021/acsami.8b17279.
(210) Boaretto, N.; Ghorbanzade, P.; Perez-Furundarena, H.; Meabe, L.; López del Amo, J. M.; Gunathilaka, I. E.; Forsyth, M.; Schuhmacher, J.; Roters, A.; Krachkovskiy, S.; Guerfi, A.; Armand, M.; Martinez-Ibañez, M. Transport Properties and Local Ions Dynamics in LATP-Based Hybrid Solid Electrolytes. *Small* **2024**, *20* (10), 2305769. https://doi.org/10.1002/smll.202305769.
(211) Ranque, P.; Zagórski, J.; Accardo, G.; Orue Mendizabal, A.; López del Amo, J. M.; Boaretto, N.; Martinez-Ibañez, M.; Arrou-Vignod, H.; Aguesse, F.; Armand, M.; Devaraj, S. Enhancing the Performance of Ceramic-Rich Polymer Composite Electrolytes Using Polymer Grafted LLZO. *Inorganics* **2022**, *10* (6), 81. https://doi.org/10.3390/inorganics10060081.
(212) Nguyen, S. T.; Grubbs, R. H.; Ziller, J. W. Syntheses and Activities of New Single-Component, Ruthenium-Based Olefin Metathesis Catalysts. *J. Am. Chem. Soc.* **1993**, *115* (21), 9858–9859. https://doi.org/10.1021/ja00074a086.
(213) Scholl, M.; Ding, S.; Lee, C. W.; Grubbs, R. H. Synthesis and Activity of a New Generation of Ruthenium-Based Olefin Metathesis Catalysts Coordinated with 1,3-Dimesityl-4,5-Dihydroimidazol-2-Ylidene Ligands. *Org. Lett.* **1999**, *1* (6), 953–956. https://doi.org/10.1021/ol990909q.
(214) Sanford, M. S.; Love, J. A.; Grubbs, R. H. Mechanism and Activity of Ruthenium Olefin Metathesis Catalysts. *J. Am. Chem. Soc.* **2001**, *123* (27), 6543–6554. https://doi.org/10.1021/ja010624k.
(215) Choi, T.-L.; Grubbs, R. H. Controlled Living Ring-Opening-Metathesis Polymerization by a Fast-Initiating Ruthenium Catalyst. *Angewandte Chemie International Edition* **2003**, *42* (15), 1743–1746. https://doi.org/10.1002/anie.200250632.
(216) Grubbs, R. H. Olefin Metathesis. *Tetrahedron* **2004**, *60* (34), 7117–7140. https://doi.org/10.1016/j.tet.2004.05.124.

(217) Jean-Louis Hérisson, P.; Chauvin, Y. Catalyse de transformation des oléfines par les complexes du tungstène. II. Télomérisation des oléfines cycliques en présence d'oléfines acycliques. *Die Makromolekulare Chemie* **1971**, *141* (1), 161–176. https://doi.org/10.1002/macp.1971.021410112.
(218) Schrock, R. R. Alkylcarbene Complex of Tantalum by Intramolecular .Alpha.-Hydrogen Abstraction. *J. Am. Chem. Soc.* **1974**, *96* (21), 6796–6797. https://doi.org/10.1021/ja00828a061.
(219) Schrock, R. R. Living Ring-Opening Metathesis Polymerization Catalyzed by Well-Characterized Transition-Metal Alkylidene Complexes. **1990**.
(220) Casey, C. P. 2005 Nobel Prize in Chemistry. Development of the Olefin Metathesis Method in Organic Synthesis. *J. Chem. Educ.* **2006**, *83* (2), 192. https://doi.org/10.1021/ed083p192.
(221) Bielawski, C. W.; Grubbs, R. H. Living Ring-Opening Metathesis Polymerization. *Progress in Polymer Science* **2007**, *32* (1), 1–29. https://doi.org/10.1016/j.progpolymsci.2006.08.006.
(222) Wengrovius, J. H.; Schrock, R. R.; Churchill, M. R.; Missert, J. R.; Youngs, W. J. Multiple Metal-Carbon Bonds. 16. Tungsten-Oxo Alkylidene Complexes as Olefins Metathesis Catalysts and the Crystal Structure of W(O)(CHCMe3(PEt3)Cl2. *J. Am. Chem. Soc.* **1980**, *102* (13), 4515–4516. https://doi.org/10.1021/ja00533a035.
(223) Tebbe, F. N.; Parshall, G. W.; Ovenall, D. W. Titanium-Catalyzed Olefin Metathesis. *J. Am. Chem. Soc.* **1979**, *101* (17), 5074–5075. https://doi.org/10.1021/ja00511a053.
(224) Kress, J. R. M.; Russell, M. M.; Wesolek, M. Tungsten(v1) and Molybdenum(v1) Oxo-Alkyl Species. Their Role in the Metathesis of Olefins.
(225) Benson, S. W.; Cruickshank, F. R.; Golden, D. M.; Haugen, G. R.; O'Neal, H. E.; Rodgers, A. S.; Shaw, R.; Walsh, R. Additivity Rules for the Estimation of Thermochemical Properties. *Chem. Rev.* **1969**, *69* (3), 279–324. https://doi.org/10.1021/cr60259a002.
(226) Kovačič, S.; Slugovc, C. Ring-Opening Metathesis Polymerisation Derived Poly(Dicyclopentadiene) Based Materials. *Materials Chemistry Frontiers* **2020**, *4* (8), 2235–2255. https://doi.org/10.1039/D0QM00296H.
(227) Leitgeb, A.; Wappel, J.; Slugovc, C. The ROMP Toolbox Upgraded. *Polymer* **2010**, *51* (14), 2927–2946. https://doi.org/10.1016/j.polymer.2010.05.002.
(228) Mulhearn, W. D.; Register, R. A. Synthesis of Narrow-Distribution, High-Molecular-Weight ROMP Polycyclopentene via Suppression of Acyclic Metathesis Side Reactions. *ACS Macro Lett.* **2017**, *6* (2), 112–116. https://doi.org/10.1021/acsmacrolett.6b00969.
(229) Mandal, M.; Huang, G.; Kohl, P. A. Anionic Multiblock Copolymer Membrane Based on Vinyl Addition Polymerization of Norbornenes: Applications in Anion-Exchange Membrane Fuel Cells. *Journal of Membrane Science* **2019**, *570–571*, 394–402. https://doi.org/10.1016/j.memsci.2018.10.041.
(230) Stoddart, A. Catalytic Living ROMP. *Nat. Synth* **2023**, *2* (1), 3–3. https://doi.org/10.1038/s44160-022-00222-1.
(231) Santoni, F.; De Angelis, A.; Moschitta, A.; Carbone, P.; Galeotti, M.; Cinà, L.; Giammanco, C.; Di Carlo, A. A Guide to Equivalent Circuit Fitting for Impedance Analysis and Battery State Estimation. *Journal of Energy Storage* **2024**, *82*, 110389. https://doi.org/10.1016/j.est.2023.110389.
(232) Jossen, A. Fundamentals of Battery Dynamics. *Journal of Power Sources* **2006**, *154* (2), 530–538. https://doi.org/10.1016/j.jpowsour.2005.10.041.
(233) Middlemiss, L. A.; Rennie, A. J. R.; Sayers, R.; West, A. R. Characterisation of Batteries by Electrochemical Impedance Spectroscopy. *Energy Reports* **2020**, *6*, 232–241. https://doi.org/10.1016/j.egyr.2020.03.029.
(234) *Impedance Spectroscopy: Theory, Experiment, and Applications*, 2nd ed.; Barsoukov, E., Macdonald, J. R., Eds.; Wiley-Interscience: Hoboken, N.J, 2005.
(235) Lazanas, A. Ch.; Prodromidis, M. I. Electrochemical Impedance Spectroscopy—A Tutorial. *ACS Meas. Sci. Au* **2023**, *3* (3), 162–193. https://doi.org/10.1021/acsmeasuresciau.2c00070.
(236) Choi, W.; Shin, H.-C.; Kim, J. M.; Choi, J.-Y.; Yoon, W.-S. Modeling and Applications of Electrochemical Impedance Spectroscopy (EIS) for Lithium-Ion Batteries. *J. Electrochem. Sci. Technol* **2020**, *11* (1), 1–13. https://doi.org/10.33961/jecst.2019.00528.
(237) Lasia, A. *Electrochemical Impedance Spectroscopy and Its Applications*; Springer New York: New York, NY, 2014. https://doi.org/10.1007/978-1-4614-8933-7.
(238) Carthy, K. M.; Gullapalli, H.; Ryan, K. M.; Kennedy, T. Review—Use of Impedance Spectroscopy for the Estimation of Li-Ion Battery State of Charge, State of Health and Internal Temperature. *J. Electrochem. Soc.* **2021**, *168* (8), 080517. https://doi.org/10.1149/1945-7111/ac1a85.
(239) Hu, W.; Peng, Y.; Wei, Y.; Yang, Y. Application of Electrochemical Impedance Spectroscopy to Degradation and Aging Research of Lithium-Ion Batteries. *J. Phys. Chem. C* **2023**, *127* (9), 4465–4495. https://doi.org/10.1021/acs.jpcc.3c00033.
(240) Gaberščček, M. Impedance Spectroscopy of Battery Cells: Theory versus Experiment. *Current Opinion in Electrochemistry* **2022**, *32*, 100917. https://doi.org/10.1016/j.coelec.2021.100917.
(241) Westerhoff, U.; Kurbach, K.; Lienesch, F.; Kurrat, M. Analysis of Lithium-Ion Battery Models Based on Electrochemical Impedance Spectroscopy. *Energy Technology* **2016**, *4* (12), 1620–1630. https://doi.org/10.1002/ente.201600154.
(242) Vadhva, P.; Hu, J.; Johnson, M. J.; Stocker, R.; Braglia, M.; Brett, D. J. L.; Rettie, A. J. E. Electrochemical Impedance Spectroscopy for All-Solid-State Batteries: Theory, Methods and Future Outlook. *ChemElectroChem* **2021**, *8* (11), 1930–1947. https://doi.org/10.1002/celc.202100108.
(243) Talian, S. D.; Brutti, S.; Navarra, M. A.; Moškon, J.; Gaberscek, M. Impedance Spectroscopy Applied to Lithium Battery Materials: Good Practices in Measurements and Analyses. *Energy Storage Materials* **2024**, 103413. https://doi.org/10.1016/j.ensm.2024.103413.

(244) Ciucci, F. Modeling Electrochemical Impedance Spectroscopy. *Current Opinion in Electrochemistry* **2019**, *13*, 132–139. https://doi.org/10.1016/j.coelec.2018.12.003.
(245) Plett, G. L. *Battery Management Systems: Battery Modeling. Volume 1*; Artech House: Boston : London, 2015.
(246) Nejad, S.; Gladwin, D. T.; Stone, D. A. A Systematic Review of Lumped-Parameter Equivalent Circuit Models for Real-Time Estimation of Lithium-Ion Battery States. *Journal of Power Sources* **2016**, *316*, 183–196. https://doi.org/10.1016/j.jpowsour.2016.03.042.
(247) Ciucci, F. Revisiting Parameter Identification in Electrochemical Impedance Spectroscopy: Weighted Least Squares and Optimal Experimental Design. *Electrochimica Acta* **2013**, *87*, 532–545. https://doi.org/10.1016/j.electacta.2012.09.073.
(248) Meddings, N.; Heinrich, M.; Overney, F.; Lee, J.-S.; Ruiz, V.; Napolitano, E.; Seitz, S.; Hinds, G.; Raccichini, R.; Gaberšček, M.; Park, J. Application of Electrochemical Impedance Spectroscopy to Commercial Li-Ion Cells: A Review. *Journal of Power Sources* **2020**, *480*, 228742. https://doi.org/10.1016/j.jpowsour.2020.228742.
(249) Macdonald, D. D. Reflections on the History of Electrochemical Impedance Spectroscopy. *Electrochimica Acta* **2006**, *51* (8), 1376–1388. https://doi.org/10.1016/j.electacta.2005.02.107.
(250) v. Schweidler, E. R. Studien Über Die Anomalien Im Verhalten Der Dielektrika. *Annalen der Physik* **1907**, *329* (14), 711–770. https://doi.org/10.1002/andp.19073291407.
(251) Ivers-Tiffée, E.; Weber, A. Evaluation of Electrochemical Impedance Spectra by the Distribution of Relaxation Times. *Journal of the Ceramic Society of Japan* **2017**, *125* (4), 193–201. https://doi.org/10.2109/jcersj2.16267.
(252) Kobayashi, K.; Suzuki, T. S. Distribution of Relaxation Time Analysis for Non-Ideal Immittance Spectrum: Discussion and Progress. *J. Phys. Soc. Jpn.* **2018**, *87* (9), 094002. https://doi.org/10.7566/JPSJ.87.094002.
(253) Plank, C.; Rüther, T.; Jahn, L.; Schamel, M.; Schmidt, J. P.; Ciucci, F.; Danzer, M. A. A Review on the Distribution of Relaxation Times Analysis: A Powerful Tool for Process Identification of Electrochemical Systems. *Journal of Power Sources* **2023**, 233845. https://doi.org/10.1016/j.jpowsour.2023.233845.
(254) Hahn, M.; Schindler, S.; Triebs, L.-C.; Danzer, M. A. Optimized Process Parameters for a Reproducible Distribution of Relaxation Times Analysis of Electrochemical Systems. *Batteries* **2019**, *5* (2), 43. https://doi.org/10.3390/batteries5020043.
(255) Hahn, M.; Rosenbach, D.; Krimalowski, A.; Nazarenus, T.; Moos, R.; Thelakkat, M.; Danzer, M. A. Investigating Solid Polymer and Ceramic Electrolytes for Lithium-Ion Batteries by Means of an Extended Distribution of Relaxation Times Analysis. *Electrochimica Acta* **2020**, *344*, 136060. https://doi.org/10.1016/j.electacta.2020.136060.
(256) Danzer, M. A. Generalized Distribution of Relaxation Times Analysis for the Characterization of Impedance Spectra. *Batteries* **2019**, *5* (3), 53. https://doi.org/10.3390/batteries5030053.
(257) Lu, Y.; Zhao, C.-Z.; Huang, J.-Q.; Zhang, Q. The Timescale Identification Decoupling Complicated Kinetic Processes in Lithium Batteries. *Joule* **2022**, *6* (6), 1172–1198. https://doi.org/10.1016/j.joule.2022.05.005.
(258) Markus Hahn. Diskrete Elektrochemische Modellierung Für Elektrodendesign Und Laderegelung von Lithium-Ionen-Batterien, Univeristät Bayreuth, Bayreuth, 2022.
(259) Ciucci, F.; Chen, C. Analysis of Electrochemical Impedance Spectroscopy Data Using the Distribution of Relaxation Times: A Bayesian and Hierarchical Bayesian Approach. *Electrochimica Acta* **2015**, *167*, 439–454. https://doi.org/10.1016/j.electacta.2015.03.123.
(260) Wan, T. H.; Saccoccio, M.; Chen, C.; Ciucci, F. Influence of the Discretization Methods on the Distribution of Relaxation Times Deconvolution: Implementing Radial Basis Functions with DRTtools. *Electrochimica Acta* **2015**, *184*, 483–499. https://doi.org/10.1016/j.electacta.2015.09.097.
(261) Blyr, A.; Sigala, C.; Amatucci, G.; Guyomard, D.; Chabre, Y.; Tarascon, J.-M. Self-Discharge of LiMn2 O 4/C Li-Ion Cells in Their Discharged State: Understanding by Means of Three-Electrode Measurements. *J. Electrochem. Soc.* **1998**, *145* (1), 194. https://doi.org/10.1149/1.1838235.
(262) Dollé, M.; Orsini, F.; Gozdz, A. S.; Tarascon, J.-M. Development of Reliable Three-Electrode Impedance Measurements in Plastic Li-Ion Batteries. *J. Electrochem. Soc.* **2001**, *148* (8), A851. https://doi.org/10.1149/1.1381071.
(263) La Mantia, F.; Wessells, C. D.; Deshazer, H. D.; Cui, Y. Reliable Reference Electrodes for Lithium-Ion Batteries. *Electrochemistry Communications* **2013**, *31*, 141–144. https://doi.org/10.1016/j.elecom.2013.03.015.
(264) Nölle, R.; Beltrop, K.; Holtstiege, F.; Kasnatscheew, J.; Placke, T.; Winter, M. A Reality Check and Tutorial on Electrochemical Characterization of Battery Cell Materials: How to Choose the Appropriate Cell Setup. *Materials Today* **2020**, *32*, 131–146. https://doi.org/10.1016/j.mattod.2019.07.002.
(265) Bard, A. J.; Faulkner, L. R. *Electrochemical Methods: Fundamentals and Applications*, 2nd ed.; Wiley: New York, 2001.
(266) Jaguemont, J.; Bardé, F. A Critical Review of Lithium-Ion Battery Safety Testing and Standards. *Applied Thermal Engineering* **2023**, *231*, 121014. https://doi.org/10.1016/j.applthermaleng.2023.121014.
(267) Chen, Y.; Kang, Y.; Zhao, Y.; Wang, L.; Liu, J.; Li, Y.; Liang, Z.; He, X.; Li, X.; Tavajohi, N.; Li, B. A Review of Lithium-Ion Battery Safety Concerns: The Issues, Strategies, and Testing Standards. *Journal of Energy Chemistry* **2021**, *59*, 83–99. https://doi.org/10.1016/j.jechem.2020.10.017.
(268) Watanabe, M.; Kanba, M.; Nagaoka, K.; Shinohara, I. Ionic Conductivity of Hybrid Films Based on Polyacrylonitrile and Their Battery Application. *Journal of Applied Polymer Science* **1982**, *27* (11), 4191–4198. https://doi.org/10.1002/app.1982.070271110.
(269) Guo, X.; Ju, Z.; Qian, X.; Liu, Y.; Xu, X.; Yu, G. A Stable Solid Polymer Electrolyte for Lithium Metal Battery with Electronically Conductive Fillers. *Angewandte Chemie International Edition* **2023**, *62* (7), e202217538. https://doi.org/10.1002/anie.202217538.

(270) Aldalur, I.; Martinez–Ibañez, M.; Piszcz, M.; Zhang, H.; Armand, M. Self–Standing Highly Conductive Solid Electrolytes Based on Block Copolymers for Rechargeable All–Solid–State Lithium–Metal Batteries. *Batteries & Supercaps* **2018**, *1* (4), 149–159. https://doi.org/10.1002/batt.201800048.
(271) Xu, K.; Ding, M. S.; Richard Jow, T. A Better Quantification of Electrochemical Stability Limits for Electrolytes in Double Layer Capacitors. *Electrochimica Acta* **2001**, *46* (12), 1823–1827. https://doi.org/10.1016/S0013-4686(01)00358-9.
(272) Mousavi, M. P. S.; Dittmer, A. J.; Wilson, B. E.; Hu, J.; Stein, A.; Bühlmann, P. Unbiased Quantification of the Electrochemical Stability Limits of Electrolytes and Ionic Liquids. *J. Electrochem. Soc.* **2015**, *162* (12), A2250. https://doi.org/10.1149/2.0271512jes.
(273) Hernández, G.; Johansson, I. L.; Mathew, A.; Sångeland, C.; Brandell, D.; Mindemark, J. Going Beyond Sweep Voltammetry: Alternative Approaches in Search of the Elusive Electrochemical Stability of Polymer Electrolytes. *J. Electrochem. Soc.* **2021**, *168* (10), 100523. https://doi.org/10.1149/1945-7111/ac2d8b.
(274) Maslyn, J. A.; McEntush, K. D.; Harry, K. J.; Frenck, L.; Loo, W. S.; Parkinson, D. Y.; Balsara, N. P. Preferential Stripping of a Lithium Protrusion Resulting in Recovery of a Planar Electrode. *J. Electrochem. Soc.* **2020**, *167* (10), 100553. https://doi.org/10.1149/1945-7111/ab9d62.
(275) Kasemchainan, J.; Zekoll, S.; Spencer Jolly, D.; Ning, Z.; Hartley, G. O.; Marrow, J.; Bruce, P. G. Critical Stripping Current Leads to Dendrite Formation on Plating in Lithium Anode Solid Electrolyte Cells. *Nat. Mater.* **2019**, *18* (10), 1105–1111. https://doi.org/10.1038/s41563-019-0438-9.
(276) Tewari, D.; Rangarajan, S. P.; Balbuena, P. B.; Barsukov, Y.; Mukherjee, P. P. Mesoscale Anatomy of Dead Lithium Formation. *J. Phys. Chem. C* **2020**, *124* (12), 6502–6511. https://doi.org/10.1021/acs.jpcc.9b11563.
(277) Lu, Y.; Zhao, C.-Z.; Yuan, H.; Cheng, X.-B.; Huang, J.-Q.; Zhang, Q. Critical Current Density in Solid-State Lithium Metal Batteries: Mechanism, Influences, and Strategies. *Advanced Functional Materials* **2021**, *31* (18), 2009925. https://doi.org/10.1002/adfm.202009925.
(278) Advanced Research Projects Agency – Energy (ARPA-E). *Integration and Optimization of Novel Ion Conducting Solids (Ionics)*; U.S. Department of Energy, 2016.
(279) Evans, J.; Vincent, C. A.; Bruce, P. G. Electrochemical Measurement of Transference Numbers in Polymer Electrolytes. *Polymer* **1987**, *28* (13), 2324–2328. https://doi.org/10.1016/0032-3861(87)90394-6.
(280) Zugmann, S.; Gores, H. J. Transference Numbers of Ions in Electrolytes. In *Encyclopedia of Applied Electrochemistry*; Kreysa, G., Ota, K., Savinell, R. F., Eds.; Springer: New York, NY, 2014; pp 2086–2091. https://doi.org/10.1007/978-1-4419-6996-5_501.
(281) Zugmann, S.; Fleischmann, M.; Amereller, M.; Gschwind, R. M.; Wiemhöfer, H. D.; Gores, H. J. Measurement of Transference Numbers for Lithium Ion Electrolytes via Four Different Methods, a Comparative Study. *Electrochimica Acta* **2011**, *56* (11), 3926–3933. https://doi.org/10.1016/j.electacta.2011.02.025.
(282) Aihara, Y.; Bando, T.; Nakagawa, H.; Yoshida, H.; Hayamizu, K.; Akiba, E.; Price, W. S. Ion Transport Properties of Six Lithium Salts Dissolved in γ-Butyrolactone Studied by Self-Diffusion and Ionic Conductivity Measurements. *J. Electrochem. Soc.* **2003**, *151* (1), A119. https://doi.org/10.1149/1.1630592.
(283) Hiller, M. M.; Joost, M.; Gores, H. J.; Passerini, S.; Wiemhöfer, H.-D. The Influence of Interface Polarization on the Determination of Lithium Transference Numbers of Salt in Polyethylene Oxide Electrolytes. *Electrochimica Acta* **2013**, *114*, 21–29. https://doi.org/10.1016/j.electacta.2013.09.138.
(284) Abraham, K. M.; Jiang, Z.; Carroll, B. Highly Conductive PEO-like Polymer Electrolytes. *Chem. Mater.* **1997**, *9* (9), 1978–1988. https://doi.org/10.1021/cm9700075a.

2 Synopsis

2.1 Objective of the Thesis

Solid polymer electrolytes (SPEs) have long been regarded as promising electrolyte systems to replace liquid electrolytes in next-generation batteries. The main advantages comprise improved safety and compatibility with high-energy-density, conversion-type electrode materials. Additionally, their solvent-free composition can contribute to enhanced thermal stability, reduced electrolyte leakage risks, and the formation of more robust electrolyte/electrode interfaces, which is especially relevant for lithium-metal-based battery systems. Despite this potential, SPEs are limited by high degrees of polymer crystallinity at moderate operating temperatures, due to restricted segmental mobility, which has detrimental effects on the ionic conductivity. This negative impact of polymer crystallinity confines the applicability of SPEs to temperatures above the melting point of the electrolyte. Improving low-temperature conductivity typically requires the reduction of the polymer crystallinity and lowering the glass transition temperature to achieve higher chain flexibility. However, this results in insufficient mechanical properties for the application as solid-state electrolytes. Accordingly, SPE research is fundamentally governed by the trade-off between flexible, ion-conducting polymer segments and the structural rigidity required to establish dimensionally stable electrolytes to ensure the operability of the battery.

In view of these considerations, this work addresses the conundrum between the ionic conductivity and the mechanical stability in SPEs following overarching questions:

1. How can the selection of the polymer backbone, side chain chemistry, and macromolecular architecture of the polymer matrix in SPEs influence the polymer crystallinity, the glass transition temperature, and the polymer-ion interaction, particularly concerning their influence on the fundamental bulk properties of the electrolyte materials?
2. Which of the available reinforcement strategies, including blending, nanocomposite formation, block copolymerization, and network integration, offer beneficial or synergistic effects and can enable soft, low T_g materials? In this context, the central question is whether mechanical stabilization can be introduced in such a way that the mechanically reinforcing component increases the modulus and structural integrity without disrupting the ion-transport characteristics of the polymer electrolyte.
3. How do the bulk material properties resulting from molecular and architectural variations in solid polymer electrolytes influence their electrochemical response in different types of electrochemical analysis, ranging from the determination of the ionic conductivity to comprehensive cycling experiments in battery applications?

To address these questions, this thesis pursues a comprehensive investigation beginning with the monomer and polymer design, synthesis, and detailed characterization. Different ion-coordinating motifs are integrated into a range of polymer architectures, including linear, hyperbranched, block copolymer, or bottlebrush-type systems. Their influence on key parameters like polymer crystallinity, glass transition temperature, melting behavior, and the ion-coordination is systematically investigated to establish structure-property relationships relevant for ionic conductivity. The scope is subsequently expanded to evaluate different design strategies

to improve the mechanical properties in soft and low T_g polymer systems. In this context, blending, filling, block copolymerization, and semi-interpenetrating networks are integrated and evaluated with the intention to balance the contradicting parameters of ion-transport and mechanical integrity. Ultimately, these electrolyte systems are applied in electrochemical cells to assess the impact of the material properties on the ionic conductivity, electrochemical stability, interfacial properties, and cycling characteristics at the device level. Thereby, the thesis links macromolecular design with application-relevant battery metrics and evaluates whether material properties observed in bulk characterization are retained under operating conditions.

Following this approach, this dissertation aims to extend the understanding of the interplay between polymer design, the resulting material properties, and their subsequent impact on electrochemical characteristics when applied as solid polymer electrolytes. The comprehensive workflow, starting with material design and ending in cell-level characterization, establishes a systematic foundation and guiding principles for the rational design of next-generation SPE systems. By the combination of fundamental structure-property analysis and electrochemical validation in battery applications, this work is intended to provide design rules for polymer electrolyte systems that tackle the optimization problem between ionic conductivity and mechanical stability.

2.2 Overview of this Thesis

Ever since its ion-conducting properties have been observed in PEO, it has become the benchmark material for SPEs because of its high compatibility with many common lithium salts and material availability due to its commercialization in many fields of application. However, its strong coordination of lithium significantly limits the mobility of cations, resulting in predominant anion-conduction. The consequence is the development of ion-concentration gradients throughout the electrolyte bulk, which negatively impacts electrochemical performance and cycling stability. The crystallization tendency in high molecular weight PEO further inhibits the application at moderate temperatures, due to restricted chain segment mobility. Therefore, research was extended to other coordination motifs, especially carbonyl-coordination in esters or carbonates. The coordination of lithium ions to carbonyl oxygen is significantly weaker and enables predominant cation-conduction. Additionally, the carbonyl motif can be integrated into a polymer structure more flexibly than the ethylene oxide repeating unit (-CH_2CH_2O-). The variability of the spacer in between different coordinating groups offers potential for optimizing the chemical structure. However, the overall magnitude of ionic conductivity is commonly lower than for PEO-based systems. The most comparable and archetypal ester-representative of PEO is poly(ε-caprolactone) (PCL). Similar to PEO, the semi-crystalline nature of PCL results in a drop of ionic conductivity below its melting temperature.

In the following, the four chapters of this thesis are briefly introduced to highlight the architectural considerations and variations in light of the challenges of polymer-based electrolyte systems. Afterwards, the results of the individual chapters are detailed to contextualize the research questions and the results of the conducted investigations.

In the first two chapters, ester-based coordination motifs are integrated into polymers of different macromolecular architectures to increase polymer flexibility and reduce polymer crystallinity. In **Chapter I,** ester-containing linear and hyperbranched polymers are prepared by a thiol-arylate Michael polyaddition reaction. The hyperbranched architecture is well-known for its reduction of polymer crystallinity, which can improve the low-temperature ionic conductivity. In total, four different materials (linear-short dithiol, linear-long dithiol, hyperbranched-short dithiol, and hyperbranched-long dithiol) are investigated as solid polymer electrolytes. In **Chapter II,** linear PCL is compared with norbornene-derived polymers equipped with short ester-based pendant groups or grafted PCL side chains. The polymer electrolytes are compared at a wide range of salt concentrations to determine the impact of the architectural variation on lithium-ion coordination, polymer crystallinity, and glass transition temperature.

The third and fourth chapters extend to scope to the mechanical reinforcement of soft polymer electrolytes. These chapters introduce different approaches to balance the ionic conductivity with mechanical integrity and support of soft polymer electrolyte systems. In **Chapter III,** a norbornene-based bottlebrush polymer with grafted PEG side chains is used as a model system to investigate the influence of established reinforcement strategies. The low viscosity polymer electrolyte is combined with either a high T_g polymer, with TiO_2 nanoparticles by homogenously mixing, or is block copolymerized with a high T_g polymer segment. The different strategies are compared regarding morphological homogeneity and electrochemical characteristics. In **Chapter IV**, a polysiloxane-based polymer with pendant diester groups is synthesized to achieve extremely low glass transition temperatures. However, the polymer exhibits very soft mechanical

behavior and therefore requires additional mechanical reinforcement. The low-viscosity property of the polysiloxane-derived system is addressed by combining the soft polymer with a network-forming polymer to yield a semi-interpenetrating network electrolyte. The effects of network integration are evaluated concerning the mechanical properties and the resulting electrochemical characteristics.

Figure 2.1 schematically summarizes the individual chapters. **Chapters I** and **Chapter II** mainly focus on the architectural variation of ester-containing polymers. **Chapters III** and **Chapter IV** apply different reinforcement strategies to ether- and ester-based soft polymers to increase their mechanical stability.

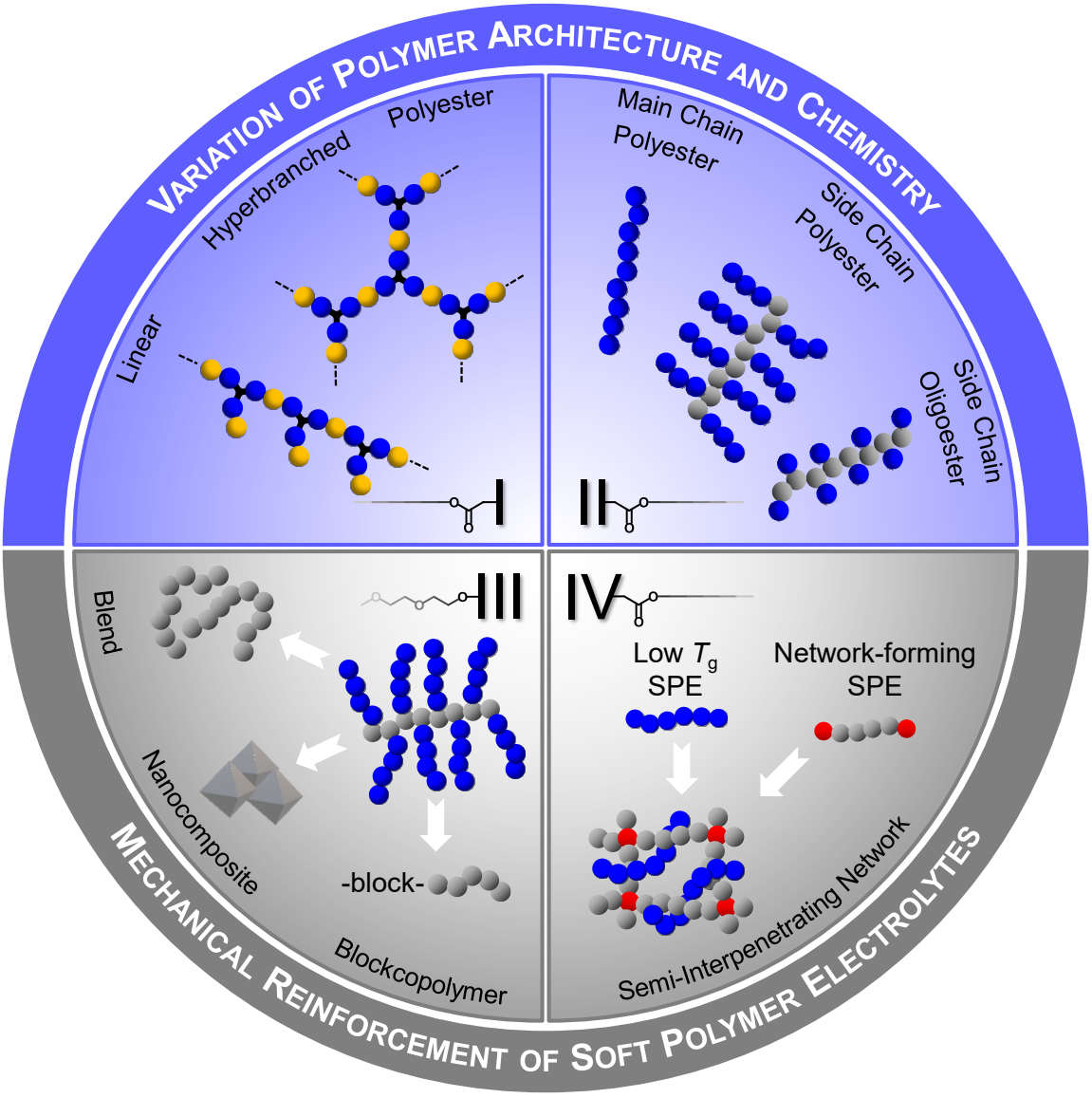


Figure 2.1. Graphical overview of this thesis comprising the four main chapters. **Chapter I** and **Chapter II** investigate different polymer architectures. In **Chapter III,** the influence of established reinforcement strategies in combination with a PEG-based bottlebrush is evaluated. In **Chapter IV,** a low T_g polysiloxane is combined with a network-forming SPE in semi-interpenetrating networks to improve the structural integrity. The depicted functional groups in the center indicate the investigated ion-coordinating motif of the different chapters.

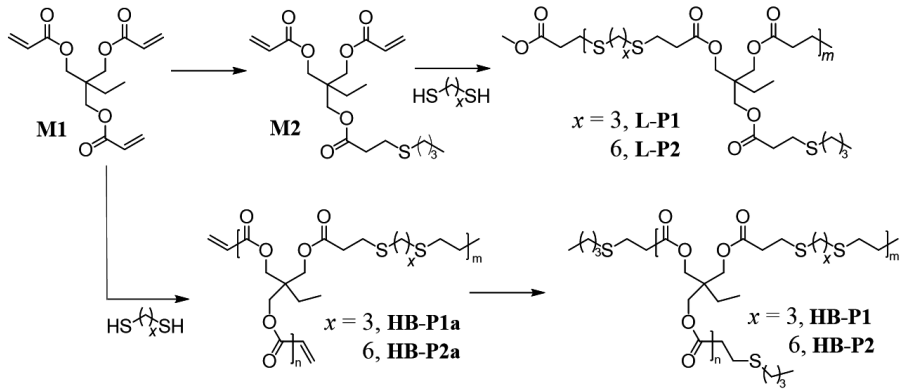
Chapter I **Easily Accessible Linear and Hyperbranched Polyesters as Solid Polymer Electrolytes**

Published as: *Eur. Polym. J.* **2024**, 210, 112965

The representation is subject to reformatting and recomposition without changing the content of the underlying work.

Linear and hyperbranched polymer architectures are investigated for their application as SPE to address research questions 1 and 3 of this thesis. The performed analysis spans from the characterization of the polymer crystallinity, the determination of the glass transition temperature and electrochemical stability, to the investigation of the temperature-dependent ionic conductivity.

The polymers are prepared by a thiol-acrylate Michael polyaddition in different stoichiometries of the functional groups to establish the desired polymer architectures. Linear polymers (**L-P1**, **L-P2**) and hyperbranched polymers (**HP-P1**, **HP-P2**) were prepared using monomer combinations with a functional group stoichiometry of A2+B2 and A3+B2, respectively (**Scheme 2.1**). Trimethylolpropane triacrylate (**M1**) was used as trifunctional monomer. Selective capping of one hydroxy-group yields the bifunctional monomer **M2** which enabled the polymerization towards linear architectures. α-ω-Dithiols with propyl or hexyl spacers were used as the second monomers. α-ω-Dithiols with three or six methylene units were used during the polymerization to alter the chain flexibility and spacing between carbonyl coordinating units.



Scheme 2.1. Synthesis of the linear (L-P1, L-P2) and hyperbranched (HB-P1, HB-P2) polymers. M1 is selectively capped at one acrylate unit to yield an A2-type monomer (M2). Subsequent polyaddition results in linear polymers. Using M1 without capping as an A3-type monomer results in hyperbranched polymers. Depending on the choice of α-ω-dithiols, two different linear as well as hyperbranched polymers are synthesized. Scheme adapted from publication.

The four synthesized polymers showed comparable molecular weights of around 5000-6300 g mol^{-1} and demonstrated thermally stable properties up to a temperature of around 300 °C, above which a significant decomposition could be observed (**Figure 2.2**a). The polymers showed amorphous properties without any additional plasticizing agents. In comparison, linear PCL benchmark materials exhibit strong crystallization behavior, requiring significant plasticization to achieve amorphous electrolyte properties. The linear and hyperbranched polymers with hexyl spacers (L-P2 and HB-P2) exhibited a glass transition temperature of -51 °C, which was around 5 °C lower than for their respective counterparts using shorter propyl spacers (L-P1 and HB-P1). After the addition of lithium salts to yield the respective polymer electrolytes, the glass transition temperature increased by around 10 K, which is a common effect observed in polymer-based

electrolyte systems (**Figure 2.2**b). The electrochemical stability of the electrolytes was investigated by linear sweep voltammetry, showing initial decomposition onset above 3.7 V and more pronounced decomposition currents above 4.4 V. While high voltage cathode systems, as described above, require higher electrochemical stability, the materials could be suitable for low voltage cathode systems like sulfur or lithium iron phosphate.

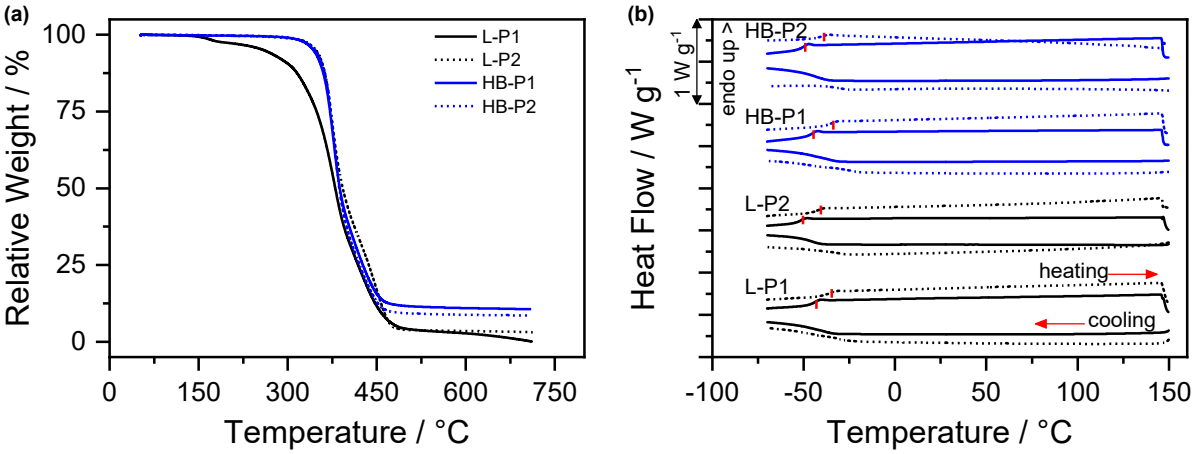


Figure 2.2. Thermogravimetric analysis and differential scanning calorimetry of the (black lines) linear polymers L-P1 and L-P2, and (blue lines) hyperbranched polymers HB-P1 and HB-P2. (a) Thermal decomposition curves at a heating rate of 10 K min^{-1} under a nitrogen atmosphere. (b) Thermal transitions of the (solid lines) pristine polymers and (dotted lines) corresponding electrolytes at a C=O/Li ratio of 10. The second cooling and heating cycle is shown for all samples. The glass transition temperatures of the pristine polymers and electrolytes are marked with red indicators and were determined from the second heating curves. Figure adapted from publication.

The temperature-dependent ionic conductivity is evaluated at a C=O/Li ratio of 10, which amounts to 14-15 wt% and 12-14 wt% of lithium salt for polymers using the shorter and longer alkyl spacers, respectively. Due to the amorphous polymer characteristics, the plasticizing effects of the lithium salt do not come into play. The temperature dependence of the ionic conductivity shows typical quasi-linear behavior without a crystallization-induced conductivity drop at lower temperatures. Commonly, the ionic conductivity is strongly related to the electrolyte's glass transition temperature. Based on thermal characterization, the polymers with longer alkyl spacers (L-P2, HB-P2) could be expected to show higher ionic conductivity. However, independent of the alkyl spacers, the linear polymers showed slightly increased ionic conductivity over the hyperbranched counterparts. This finding exemplifies the importance of polymer architecture and the interplay with the thermal properties and ion-coordination sites in SPEs. In hyperbranched polymers, the constitutional units can exhibit reduced flexibility, resulting in lower ionic conductivity. Comparing both linear polymers, the lower T_g leads to slightly better low temperature conductivity (L-P1: 2.3×10^{-7} S cm^{-1}; L-P2: 2.6×10^{-7} S cm^{-1}). L-P1 is then compared to linear PCL-based electrolyte systems at a comparable salt concentration. While the PCL-system shows significantly higher ionic conductivities above the electrolytes' melting point, the strong crystallization tendency results in significantly reduced low-temperature ionic conductivity. Despite the overall lower ionic conductivity of L-P2, the importance of amorphous polymer characteristics for low-temperature performance is obvious.

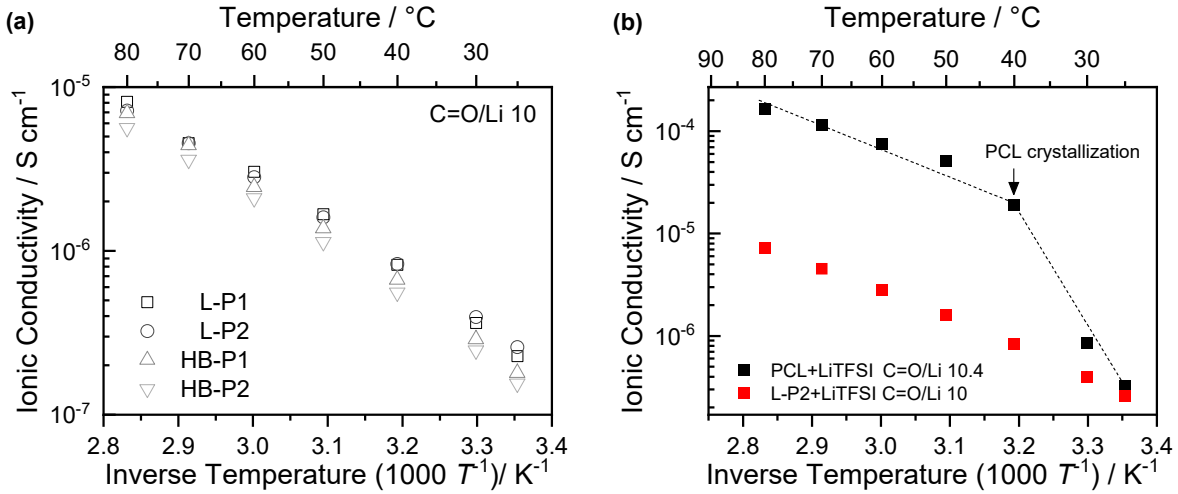


Figure 2.3. Arrhenius plots of the temperature-dependent ionic conductivity (80 °C–25 °C) for (a) the synthesized polymers at a C=O/Li ratio of 10. (b) Comparison of (red) L-P2 and (black) linear PCL at a comparable C=O/Li ratio. The dotted line is a guide to the eye. Figure adapted and recomposed from publication.

In summary, this chapter highlights the importance of macromolecular architecture besides the molecular spacing and choice of coordination motifs. Notably, both, the synthesized linear and hyperbranched polymer architectures resulted in amorphous electrolyte materials, which is particularly relevant for the low-temperature ionic conductivity by preventing crystallization-induced conductivity drops. This aspect is central to research question 1, as it demonstrates that polymer architecture is not only relevant for modulating the fundamental bulk properties of the electrolyte materials, but also for enabling amorphous low-T_g polymer systems within this material class. Regarding research question 3, this work highlights that electrochemical behavior in polyester-based SPEs is influenced not only by bulk properties such as the glass transition temperature but also by the underlying polymer architecture. While both linear and hyperbranched systems provided amorphous low-T_g materials, which are beneficial for low-temperature ion transport, the observed conductivity differences show that architecture remains a decisive factor. The relevance of this amorphous character becomes especially apparent in comparison to linear PCL-based electrolytes, where crystallization causes a decrease in ionic conductivity at lower temperatures. This suggests that the accessibility of the coordinating groups, in addition to the general thermal properties of the polymer matrix, contributes significantly to the resulting electrochemical response. Accordingly, the study emphasizes that correlations between bulk properties and electrochemical performance must also account for architecture-dependent differences in the local coordination environment.

Chapter II **Synthesis and Comparison of Linear, Side Chain, and Grafted Polyester-based Architectures as Solid Polymer Electrolytes**
Prepared for submission

Ester-based coordination sites are integrated into linear main chain polyesters, side chain polyesters, and side chain oligoester polymer architectures. The materials are investigated for their application as SPE to address research questions 1 and 3 of this thesis. The performed analysis includes the characterization of the polymer crystallinity, thermal transitions, ion-coordination, and the investigation of the temperature-dependent ionic conductivity across a wide range of salt concentrations.

Therefore, two norbornene-based monomers were prepared and subsequently polymerized *via* ring-opening metathesis polymerization. Grafted polyester side chains led to a bottlebrush polymer with a central norbornene-based backbone and grafted poly(ε-caprolactone) side chains (PNb-*graft*-PCL). Short adipate-based ester groups were introduced into another norbornene-based polymer to yield PNb-BMA. Both polymers were compared to the linear benchmark polyester poly(ε-caprolactone) (PCL).

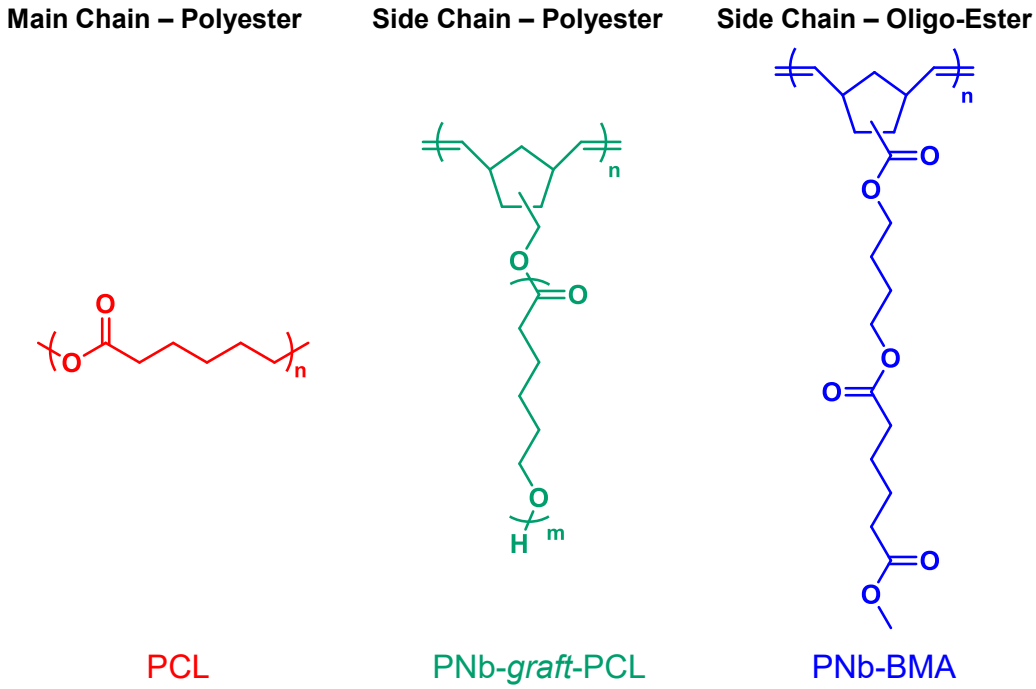


Figure 2.4. Chemical structures of the three electrolyte systems investigated using different polymer architectures. (red) Linear poly(ε-caprolactone), (green) polynorbornene-based bottlebrush polymer with linear PCL side chains (PNb-*graft*-PCL), (blue) polynorbornene-based backbone with short oligoester (PNb-BMA).

The three polymers and LiTFSI are used to formulate solid polymer electrolytes across a wide range of salt concentrations (C=O/Li 2.5 – 100, or ca. 50 – 2 wt%). The thermal properties of the polymers and corresponding electrolytes show a strong crystallization tendency for linear PCL and the bottlebrush PNb-*graft*-PCL. While the melting enthalpies are only marginally influenced by the bottlebrush architecture, the melting temperatures are decreased by 10 to 15 °C, indicating smaller crystallite sizes. On the other hand, pristine PNb-BMA and electrolytes at all salt

concentrations are amorphous. However, the T_g of PNb-BMA is significantly increased compared to the other polymer systems. For the pristine polymer, the T_g of PNb-BMA is around 20 °C higher than for the PCL-based materials. For PNb-BMA, the norbornene polymer backbone showed a significant influence on the T_g, whereas the bottlebrush polymer architecture is more dependent on the PCL rather than the norbornene polymer backbone.

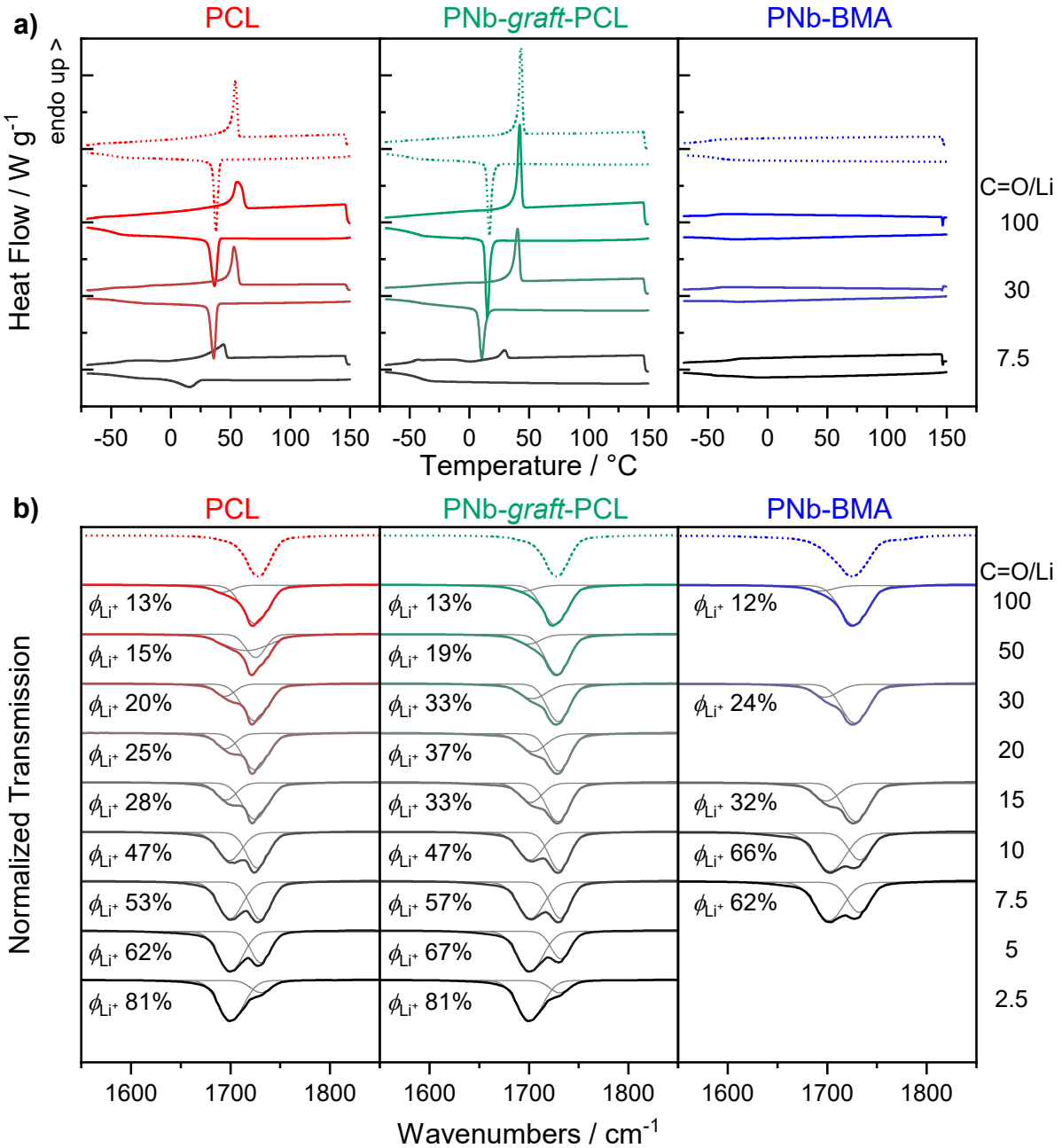


Figure 2.5. (a) Differential scanning calorimetry (second heating and cooling curve, 10 K min^{-1}, -70 °C – 150 °C) of the (dotted lines) pristine polymers and corresponding (solid lines) electrolyte at different salt concentrations for PCL, PNb-*graft*-PCL, and PNb-BMA. (b) Transmission FT-IR spectra of the (dashed lines) pristine polymers (red) PCL, (green) PNb-*graft*-PCL, (blue) PNb-BMA, and (solid lines) corresponding electrolytes at different C=O/Li ratios from 100 to 2.5. (gray lines) Double-peak Gaussian peak fits for non-coordinating carbonyl peaks, ν(C=O) at 1730 cm^{-1} and coordinating carbonyl peaks, ν(C=O---Li) at 1705 cm^{-1}. The fraction of coordinated carbonyl groups (ϕ_{Li}+) is calculated as the ratio of $A_{\nu(C=O---Li)}/(A_{\nu(C=O)}+A_{\nu(C=O---Li)})$.

The effect of salt concentration on the ion-coordination is investigated by IR spectroscopy. The region of the carbonyl stretching vibration between 1600 and 1800 cm^{-1} gives insight into the fraction of coordinating and non-coordinating carbonyl moieties (**Figure 2.5**b). Besides the non-coordinating peak at around 1730 cm^{-1}, a secondary peak at lower wavenumbers appears upon the addition of lithium salt. With increasing salt concentration, the fraction of coordinating carbonyl units (ϕ_{Li^+}) increases for the three electrolyte systems. At low salt concentrations (i.e., high C=O/Li ratios) ϕ_{Li^+} is comparable for the three systems. However, at higher salt concentrations, the coordination is higher for PNb-BMA, which indicates better accessibility of the coordination sites.

Lastly, the effects of the polymer architecture and salt concentration on the ionic conductivity are evaluated. Therefore, the temperature-dependent ionic conductivity is determined in the temperature range of 25 to 80 °C. The salt concentration showed a strong influence on the achieved ionic conductivity for each system. A representative overview is given for a temperature of 40 °C (**Figure 2.6**a). Very low and excessively high salt concentrations lead to limited ionic conductivity. Especially for the semi-crystalline materials (PCL and PNb-*graft*-PCL), the low temperature conductivity is limited by polymer crystallization. The maximum ionic conductivity could be observed in the range of C=O/Li 7.5 to 10. This agrees well with the findings from IR spectroscopy, where the ϕ_{Li^+} was around 50 % for PCL and PNb-*graft*-PCL. Vogel-Tamman-Fulcher analysis was used to determine the exponential prefactor (A) and activation energy (B) for the electrolyte systems. At low salt concentrations, A is mostly reduced due to a limited number of charge carriers (**Figure 2.11**b). However, at high salt concentrations, the activation energy increases, especially for PCL and PNb-*graft*-PCL. The activation energy of PNb-BMA-based electrolytes is not influenced by the salt concentration but is mostly limited by the higher T_g of the electrolyte systems.

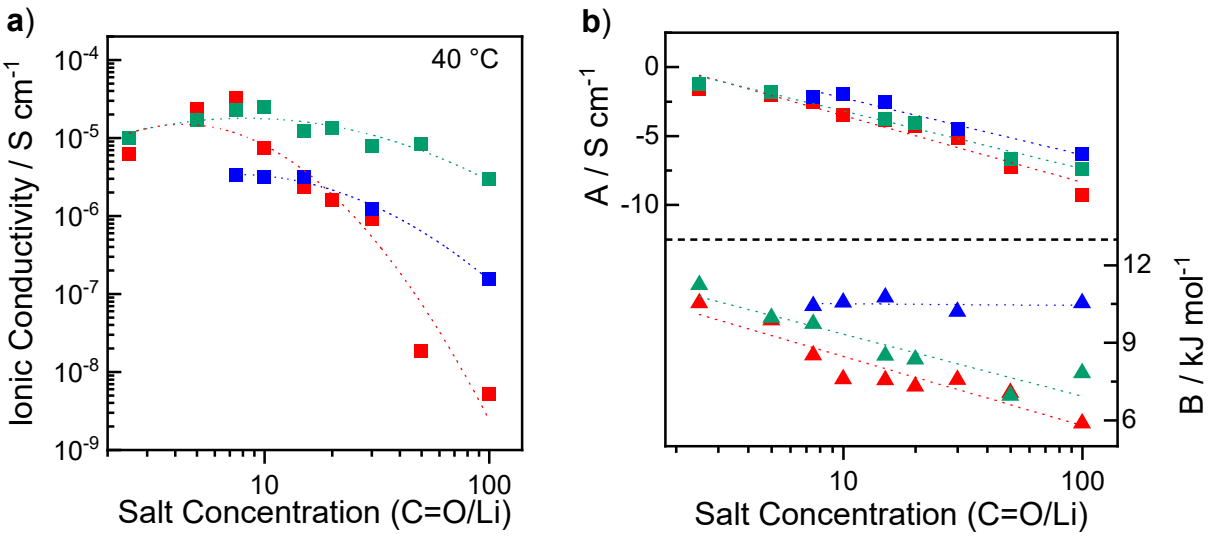


Figure 2.6. Evaluation of the ionic conductivity for (red) PCL-based, (green) PNb-*graft*-PCL-based, and (blue) PNb-BMA-based electrolytes at different LiTFSI salt concentrations. The dotted lines in all subfigures represent guidelines for the eyes. (a) Salt concentration-dependent ionic conductivity at 40 °C. (b) Salt concentration-dependent VTF-fit parameters (A) and calculated pseudo-activation energy (B).

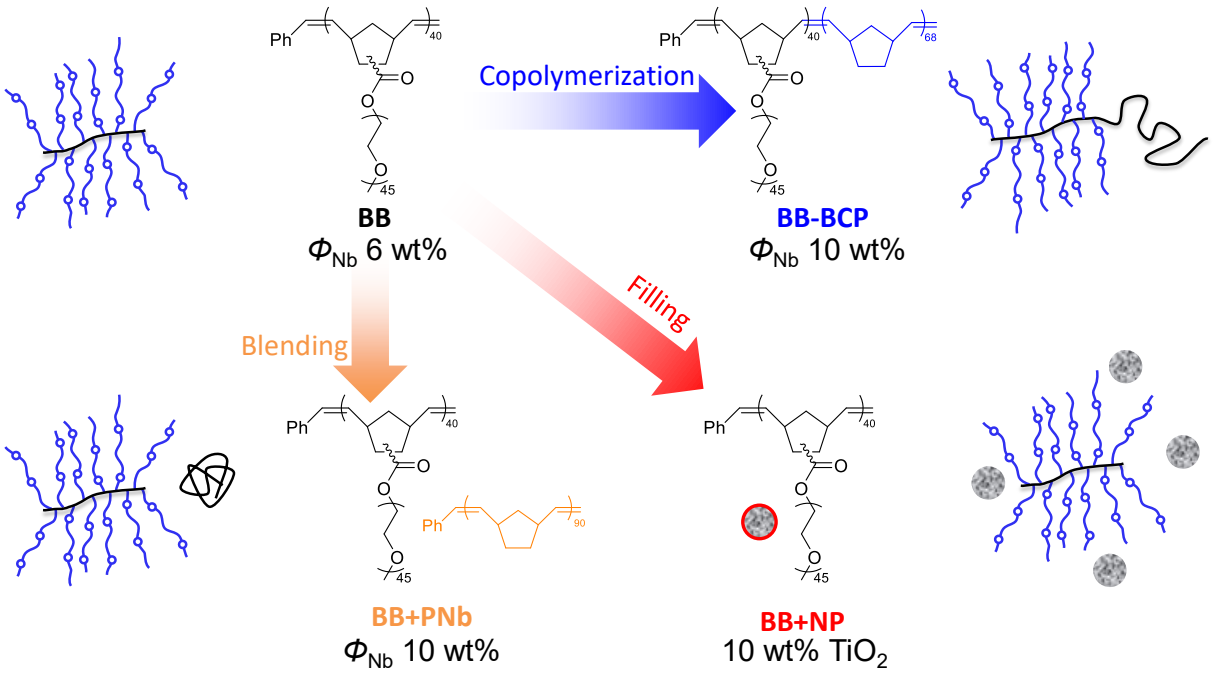
In conclusion, this chapter addresses research questions 1 and 3 in polymer systems with relocated ester-coordinating motifs from the polymer main chain into grafted polyester side chains or short pendant oligo-ester groups. The influences on the fundamental bulk and electrochemical properties of polyester-based solid polymer electrolytes are investigated. The comparison demonstrates that polymer architecture strongly affects glass transition temperature, melting behavior, polymer crystallinity, and the accessibility of the coordinating groups. These factors are directly reflected in the temperature- and salt-dependent ionic conductivity of the three systems. Among the investigated systems, the bottlebrush architecture provided the most balanced combination of favorable thermal transitions, ion coordination, and ionic conductivity.

Chapter III **Comparative Study of the Mechanical Reinforcement by Blending, Filling, and Block Copolymerization in Bottlebrush Polymer Electrolytes**
Published as: *ACS Appl. Polym. Mater.* **2024**, 6, 5109–5120

The representation is subject to reformatting and recomposition without changing the content of the underlying work.

This chapter addresses research questions 1 to 3 in a comparative study applying different reinforcement strategies to soft bottlebrush polymer systems. The bottlebrush polymer architecture provides improved chain segment mobility, lowered glass transition and melting temperatures, reduced polymer crystallinity, and improved low-temperature ionic conductivity when compared to equivalent linear polymers of similar total molecular weight. However, the bottlebrush copolymers show reduced mechanical stability. In this chapter, the drawback of limited mechanical stability is addressed by applying three reinforcement strategies to norbornene-based (Nb-based) bottlebrush copolymers with grafted poly(ethylene glycol) (PEG) side chains (**Scheme 2.2**). The effects on fundamental electrochemical properties, as well as on lithium compatibility and battery cycling, are investigated.

The bottlebrush polymer is prepared by ring-opening metathesis polymerization (ROMP) using norbornene-terminated poly(ethylene glycol) as macromonomer. The grafting-through approach ensures quantitative grafting density, while the living and controlled characteristics of ROMP enable the synthesis of polymers with defined and narrowly distributed molecular weight distributions. The bottlebrush polymer (PNb-*graft*-PEG, BB) is used as a reference material and as the basis material for different reinforcement strategies. First, the bottlebrush polymer is combined with a high T_g polynorbornene homopolymer (PNb) in a polymer blend (BB+PNb). Secondly, TiO_2 nanoparticles fillers are dispersed in the polymer matrix (BB+NP), following established polymer filling approaches. Lastly, the living characteristics of the ROMP are utilized to synthesize a defined bottlebrush block copolymer (BB-BCP).



Scheme 2.2. Illustration of the investigated materials and composites based on a polynorbornene-*graft*-poly(ethylene glycol) bottlebrush (BB) polymer. By blending, filling, and copolymerization, three different reinforcement strategies are implemented.

The amount of the reinforcing constituent is controlled to be around 10 wt% (for PNb homopolymer in a blend, TiO_2 nanoparticles in the nanocomposite, and PNb segment in the bottlebrush block copolymer).

In comparison to the pristine bottlebrush polymer, the polymer crystallization is reduced for each of the three strategies (**Figure 2.7**). The lowest melting enthalpy is achieved for the bottlebrush block copolymer (BB-BCP) with only 80 % compared to the BB. While the second polymer segment only constitutes around 4-5 wt% the crystallization is effectively suppressed. In a polymer blend of similar overall composition (BB+PNb), the transition enthalpy is only marginally reduced. After the addition of lithium bis(trifluoromethanesulfonyl)imide at a O/Li ratio of 16, only the blend electrolyte showed recrystallization and melting transitions at reduced enthalpies.

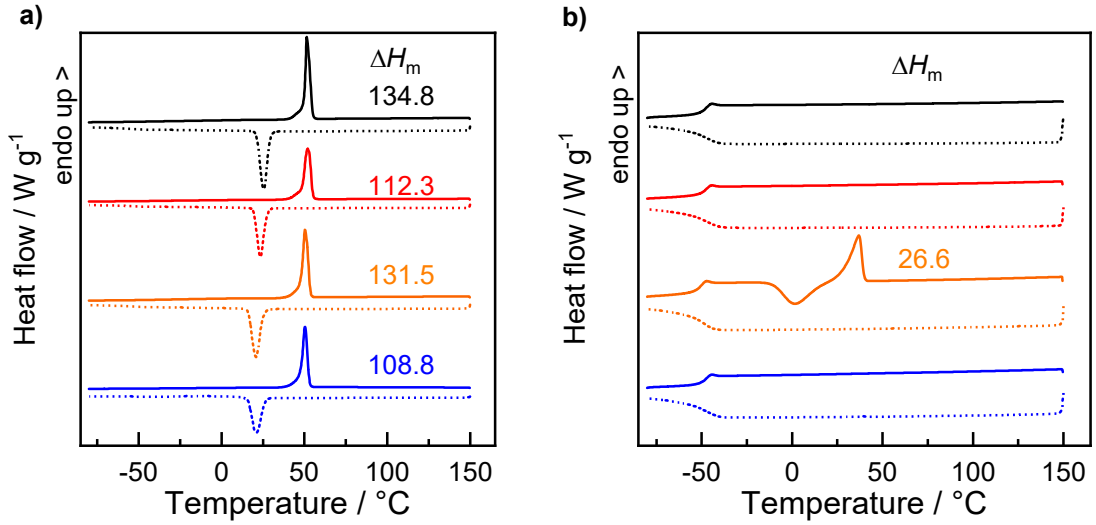


Figure 2.7. Differential scanning calorimetry (10 K min^{-1}, -70 °C – 150 °C), (solid lines) heating curves and (dotted lines) cooling curves of (black) BB and (red) BB+NP and (orange) BB+PNb, and (blue) BB-BCP. (a) Synthesized polymers without Li-salt and (b) the respective electrolyte system at an O/Li ratio of 16 using LiTFSI as Li-salt. Figure adapted and recomposed from publication.

The mechanical properties of the electrolytes were determined in rheological experiments without lithium salt (**Figure 2.8**a). Compared to the BB polymer, the mechanical reinforcement by all of the three reinforcement strategies is evident as both storage (*G'*) and loss (*G"*) modulus could be increased. While the BB, BB+PNb, and BB+NP show decreasing *G'* at high strain, the BB-BCP shows an extended linear viscoelastic regime. At low strain, the blend and nanocomposite show predominantly elastic behavior, whereas the block copolymer shows predominantly viscous characteristics. However, both moduli are the highest for BB-BCP, and the viscous characteristics can help in keeping an intimate contact with the electrodes, demonstrating the advantages of the polymer architecture. The ionic conductivity of the corresponding electrolyte systems is investigated at an O/Li ratio of 16 (**Figure 2.8**b). The addition of nanoparticles (BB+NP) does not influence the ionic conductivity of the resulting nanocomposite electrolyte. The residual thermal transitions for the blend systems result in a conductivity drop below 40 °C. The threshold conductivity of 1×10^{-3} S cm^{-1} is only surpassed by BB-BCP, showing an increased ionic conductivity across the whole temperature range. The room temperature ionic conductivity of BB-BCP was

7×10^{-5} S cm^{-1}, showing no crystallization-induced drop of the ionic conductivity as observed for BB+PNb and linear PEO-based polymer electrolytes. Despite the compositional similarity of BB+PNb-16 and BB-BCP-16, the architectural differences result in contrasting thermal and electrochemical properties. Interestingly, the ionic conductivity of the BB-BCP is even higher than for the BB, even though the fraction of ion-conducting phase is lowered due to the PNb polymer segment in BB-BCP. Due to the semi-crystalline properties of BB+PNb, the system is not investigated further.

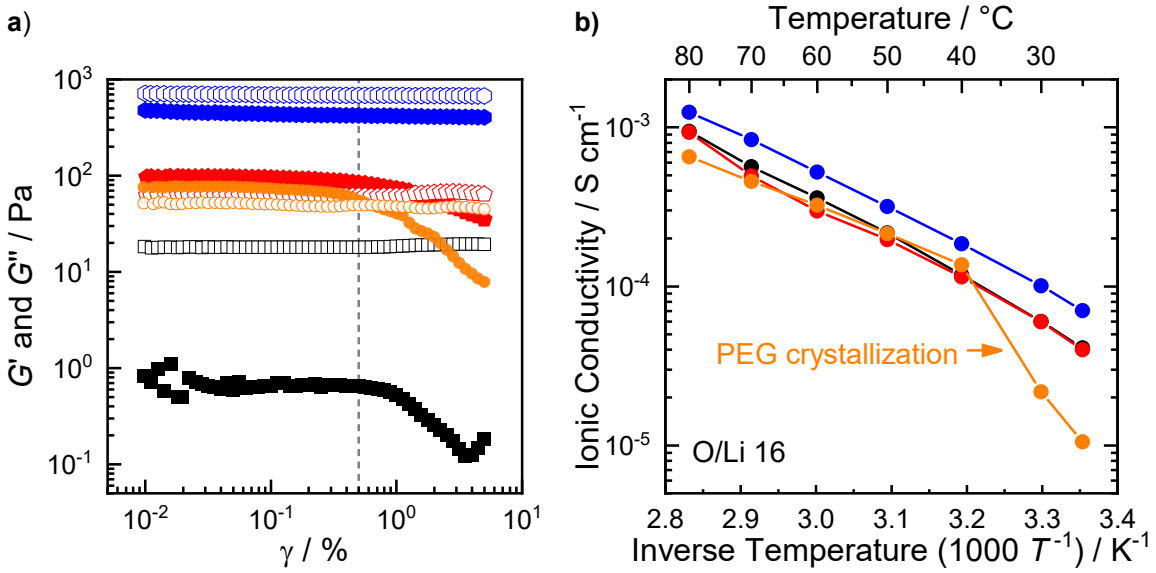


Figure 2.8. Rheological measurements and temperature-dependent ionic conductivity for (black) BB, (orange) BB+PNb, (red) BB+NP, and (blue) BB-BCP. (a) Complex shear strain (γ^*) measurements (1 Hz, 60 °C) showing the storage (G') and loss (G'') modulus of the materials (G' filled symbols, G'' hollow symbols). The grey dotted lines show the intersection of G' and G'' where the transition occurs. (b) Arrhenius plots of temperature-dependent ionic conductivity (80 °C – 25 °C) at O/Li 16. Figure adapted and recomposed from publication.

The influence on the electrochemical stability is investigated in different test cell configurations. In linear sweep voltammetry (LSV), an inert stainless steel electrode is used as the working electrode. At high potentials (against Li/Li$^+$), oxidative processes result in material decomposition (**Figure 2.9**a). The determined electrochemical stability of around 5 V suggests excellent compatibility with high-voltage electrode systems. However, this method neglects the influence of the cathode materials. Therefore, we also investigated the electrochemical stability in battery half-cells (Li||LFP configuration) applying cut-off increase cell cycling (CICC). In this method, a battery is cycled with increasing cut-off potentials during charging (**Figure 2.9**b). Similar to LSV, high cut-off potentials result in material composition that can be observed by decreasing accessible specific capacities. For the electrolyte systems, stable cycling could be observed until a cut-off potential of 4.4 V. A further increase to 4.6 V resulted in material decomposition and deterioration of the specific capacity. The discrepancy between results from LSV and CICC experiments highlights the importance of the electrolyte-cathode interaction for the consideration of electrochemical stability and applicability in battery cells.

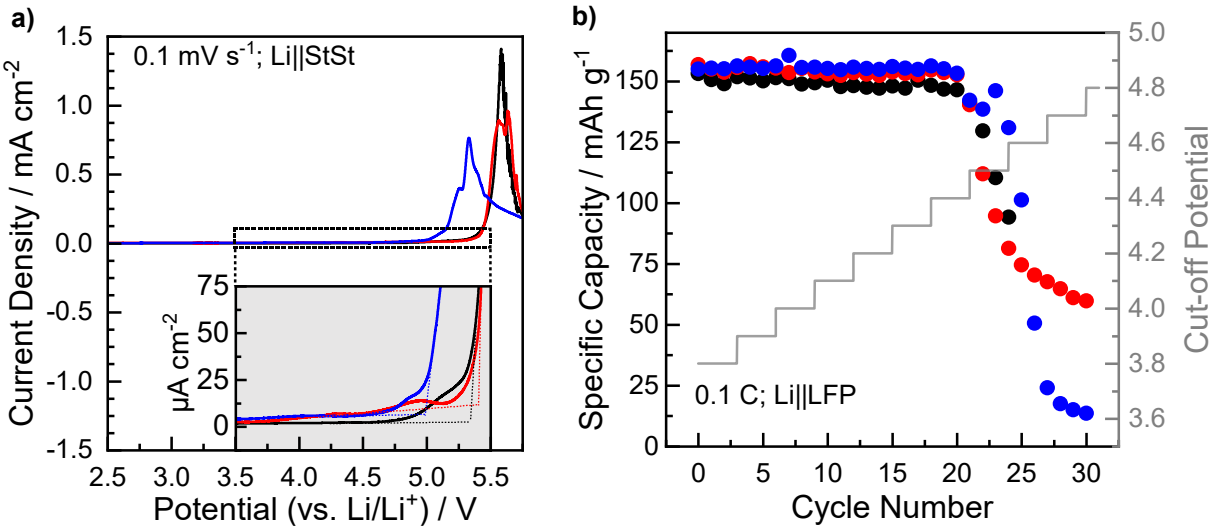


Figure 2.9. Determination of electrochemical stability. (a) Linear sweep voltammetry measurements at a sweep rate of 0.1 mV s^{-1} using Li|SPE|StSt cells at 70 °C. The inset shows a magnification of the recorded current response between 3.5 V and 5.5 V. Figure adapted and recomposed from publication. Cut-off increase cell cycling measurements using Li|SPE|LFP in a cut-off potential range of 3.8 – 4.8 V and increments of 0.1 V at 70 °C. For each cut-off potential, three charge/discharge cycles were performed. Figure adapted and recomposed from publication.

The lithium compatibility is further investigated in lithium plating and stripping (LPS) experiments in symmetrical Li||Li cells (**Figure 2.10**a). Intermittent impedance analysis during lithium plating and stripping experiments showed low charge transfer resistances for over 200 cycles for BB-16 and BB-BCP-16, while the BB+NP-16 showed steadily increasing charge transfer resistances and overpotentials. In battery half-cells, the highest accessible discharge capacities (159 mAh g^{-1}) and the highest capacity retention in comparison to the initial discharge capacity of 88 % after 50 cycles were achieved with the BB-BCP system (**Figure 2.10**b).

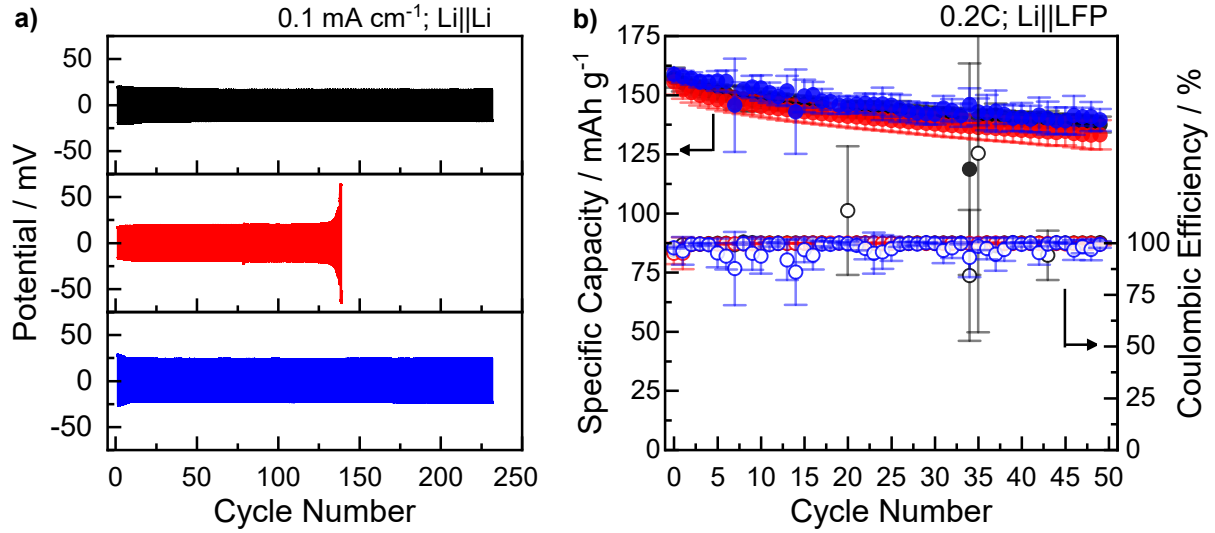


Figure 2.10. Lithium plating and stripping (LPS) cycling data in Li|SPE|Li cells and galvanostatic battery cycling in Li|SPE|LFP cells for (black) BB-16, (red) BB+NP-16, and (blue) BB-BCP-16. (a) LPS cycling data at 70 °C. The cycling was performed for 1 h per half cycle at 0.1 mA cm^{-2}. (b) Overview of (solid spheres) discharge capacity and (circles) coulombic efficiency over 50 cycles at 0.2 C. Figure adapted and recomposed from publication.

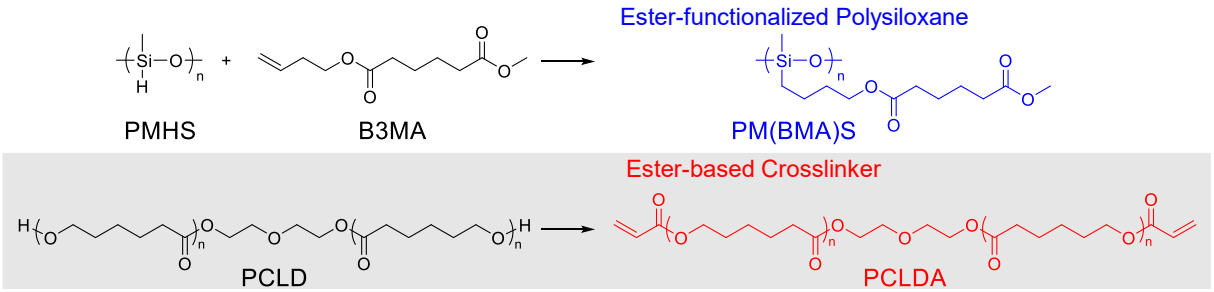
In summary, this chapter highlights the importance of polymer architecture on fundamental bulk properties, the mechanical stability of the electrolyte system, and the effects on the applicability in battery cells, addressing research questions 1 to 3. Concerning research question 1, the results demonstrate that the polymer architecture and the reinforcement strategy can have a significant impact on the polymer crystallinity, thermal transitions, and morphological homogeneity. In particular, the comparison of BB and BB-BCP reveals that materials of similar composition can result in significantly different properties. In relation to research question 2, the study shows that blending, filling, and block copolymerization can provide mechanical stabilization. Block copolymerization resulted in the highest moduli while also increasing the ionic conductivity of the electrolyte system. Addressing research question 3, this chapter demonstrates that the effects of the different approaches are reflected in electrochemical behavior, with the highest specific discharge capacities and capacity retention being observed for the bottlebrush block copolymer. The results underline the importance of polymer architecture and appropriate reinforcement strategies to obtain balanced electrochemical and mechanical properties in soft polymer electrolytes.

Chapter IV **Semi-Interpenetrating Network Electrolytes Utilizing Ester-Functionalized Low T_g Polysiloxanes in Lithium-Metal Batteries**
Published as: *Adv. Energy Mater.* **2024**, 15, 2403531

The representation is subject to reformatting and recomposition without changing the content of the underlying work.

Research questions 1 to 3 are investigated through the development of an ester-functionalized polysiloxane-based solid polymer electrolyte and its stabilization by the incorporation of a semi-interpenetrating network architecture. The chapter first considers how the combination of a low-T_g polysiloxane backbone with ester-based coordinating side chains affects the fundamental bulk properties of the electrolyte system, including thermal behavior and lithium-ion coordination. Secondly, the mechanical limitations of the soft electrolyte are addressed by the incorporation of the polymer electrolyte into a polyester-based network. Finally, the influence of these structural and mechanical modifications on the electrochemical response is investigated in different electrochemical analyses, including ionic conductivity, lithium compatibility, and battery cycling in lithium-metal cells.

The ester-functionalized polysiloxane is prepared by a hydrosilylation reaction between a poly(methylhydro)siloxane (PMHS) precursor polymer and but-3-en-methyl adipate (BMA) (**Scheme 2.3**, top). While the adipinic ester groups of the BMA motif provide carbonyl-based ion coordination sites, the polysiloxane backbone leads to an exceptionally low glass transition temperature for the resulting poly(methyl-[butyl-4-{methyl adipate}])siloxane of -76 °C. The network former poly(caprolactone)-diacrylate (PCLDA) is synthesized by an esterification reaction starting from commercially available poly(caprolactone)-diol (PCLD) (**Scheme 2.3**, bottom).



Scheme 2.3. Reaction scheme for the synthesis of (top) the siloxane-based polymer electrolyte PM(BMA)S and (bottom) the polycaprolactone-based network former PCLDA. Figure adapted from publication.

At first, the PM(BMA)S is individually characterized at different salt concentrations without the incorporation of the network structure. Thereby, fundamental properties like ion-coordination, thermal properties, and the ionic conductivity of the electrolyte system can be investigated and optimized first and subsequently transferred to the semi-interpenetrating network architecture. The PM(BMA)S is combined with LiTFSI at salt concentrations between 10 wt% and 50 wt%. In ester-based electrolyte systems, the carbonyl moieties are predominantly responsible for ion coordination. In FTIR measurements, the carbonyl band gives insight into the fraction of coordinating and non-coordinating carbonyl moieties (**Figure 2.11**a). At a salt content of 20 wt%, approximately half of the carbonyl sites are participating in salt coordination. This

correlates to efficient ion transport, resulting in the highest ionic conductivity at elevated and room temperatures. Additionally, the system's glass transition temperature influences the ionic conductivity following Vogel-Tamman-Fulcher (VTF) theory. At salt concentrations below the optimum loading, the ionic conductivity is reduced by a limited number. Conversely, excessive salt concentrations above a certain loading lead to decreased ionic conductivity by increasing the T_g of the electrolyte system (**Figure 2.11**b).

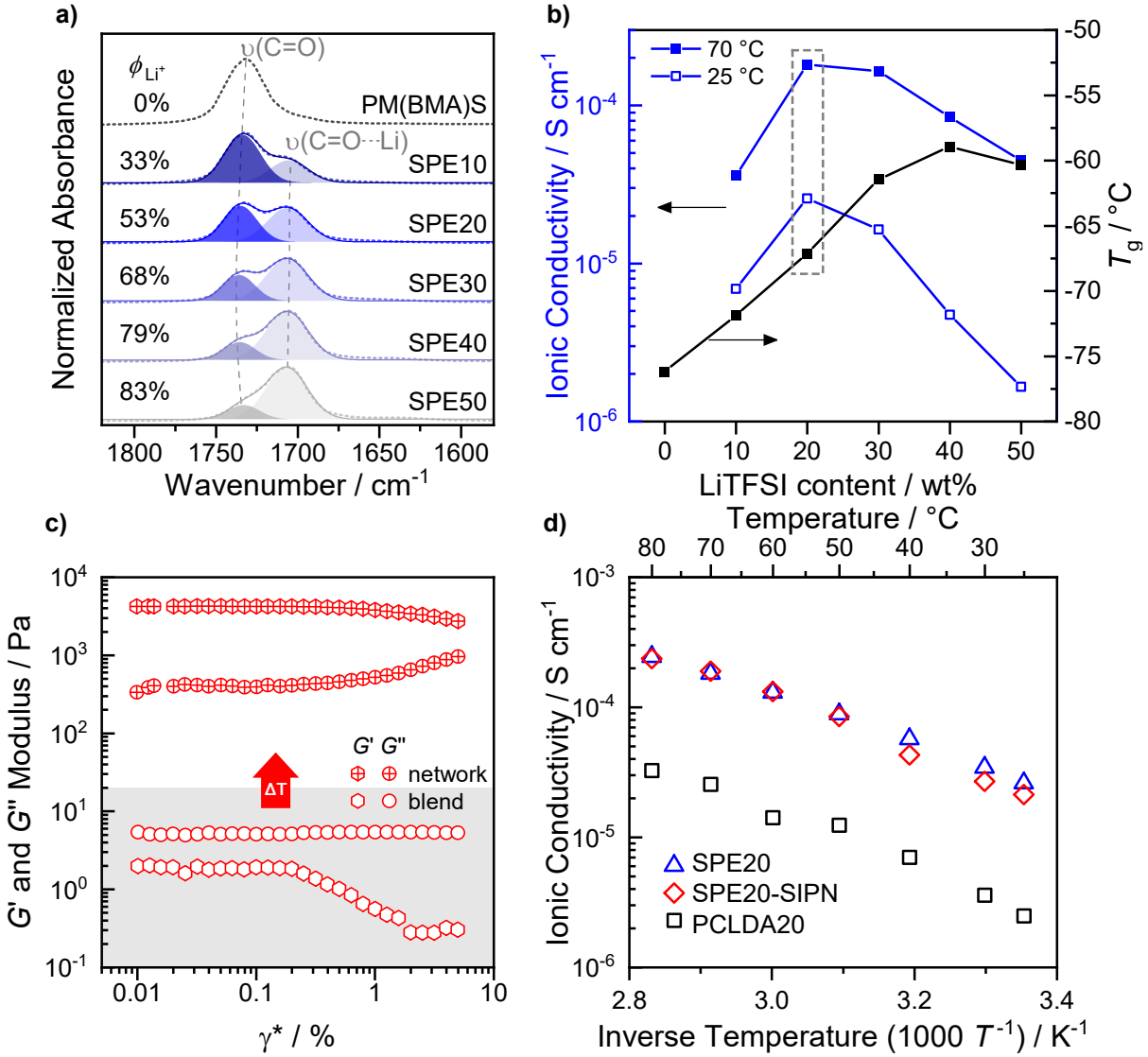


Figure 2.11. (a) (dotted lines) recorded FT-IR spectra, (solid lines) cumulative fit, (dark shared area) fit for ν(C=O)-peak at 1730 cm^{-1}, and (light shaded area) fit for ν(C=O---Li)-peak at 1705 cm^{-1}. (b) LiTFSI salt concentration variation between 10 and 50 wt%. (blue) Ionic conductivity at (squares) 70 °C, (hollow squares) 25 °C. (black) The glass transition temperature of the solid polymer electrolytes. Solid lines in (b) are a guide to the eye. (c) Rheological strain sweep measurement at 1 Hz and 60 °C of (hollow symbols) the blend of PM(BMA)S and PCLDA (hashed symbols) the obtained network. (d) Temperature-dependent ionic conductivity of the SPE20, the crosslinked electrolyte (SPE20-SIPN), and the PCLDA20. Figure adapted and recomposed from publication.

The PM(BMA)S of polymer is then stabilized by its incorporation into a network structure using the PCLDA network former. The rheological experiments were performed using the non-crosslinked blend of PM(BMA)S and PCLDA that is subsequently crosslinked to form the semi-interpenetrating architecture (**Figure 2.11**c). The blend showed predominantly viscous behavior ($G' < G''$). After crosslinking, the resulting network showed predominantly elastic behavior ($G' > G''$) at an increase of the storage modulus by more than three orders of magnitude. The ionic conductivity of the resulting SPE20-SIPN only showed marginally reduced ionic conductivity at low temperatures (**Figure 2.11**d). The network-former itself is also contributing to the ion transport in the electrolyte bulk. Despite the ionic conductivity of the network former is significantly lower, the ion-coordinating groups help in maintaining the ionic conductivity of the poly(siloxane)-based electrolyte system.

The improved mechanical stability has a profound influence on the interfacial stability against lithium metal electrodes as well as the cycling stability in battery cells. Against lithium electrodes in lithium plating and stripping experiments, stable charge transfer resistances could be observed (**Figure 2.12**a). This is also observed in battery cycling experiments, where the mechanical stability of the SPE20-SIPN resulted in stable cycling profiles (**Figure 2.12**b). The SPE20 and SPE20-SIPN were combined with TiO_2 nanoparticles to form nanocomposite electrolyte systems (SPE20-N10, SPE20-N10-SIPN). For SPE20-N10 the mechanical support of the nanoparticles is not sufficient to enable stable cycling profiles. The electrolyte showed severe voltage fluctuations during charge. For SPE20-N10-SIPN, the resulting cycling profiles showed reduced overpotentials and higher specific discharge capacity compared to SPE20-SIPN. Battery cycling is performed for over 200 cycles at 0.1 C at 30 °C and 0.3C at 40 °C, delivering stable discharge capacities of 66 mAh g^{-1} and 40 mAh g^{-1}, respectively.

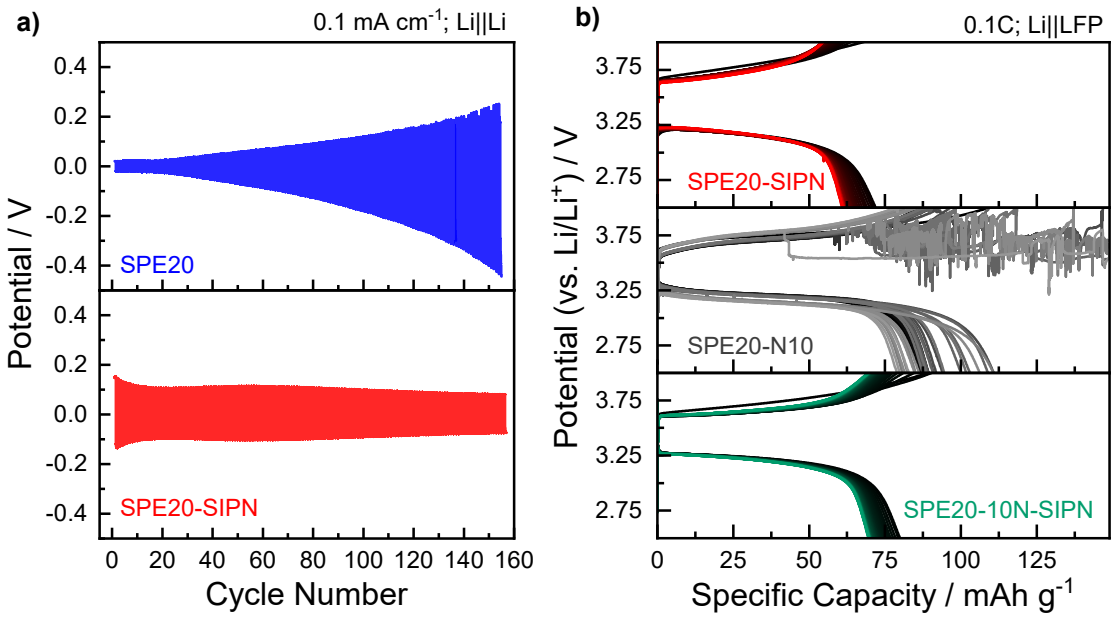


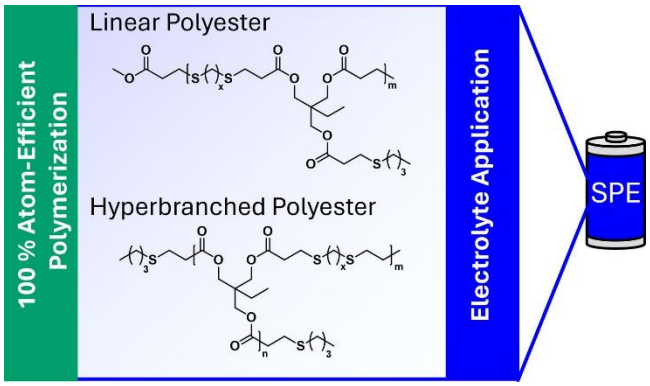
Figure 2.12. Lithium plating and stripping (LPS) cycling data in Li|SPE|Li cells and galvanostatic battery cycling in Li|SPE|LFP cells for (blue) SPE20, (red) SPE20-SIPN, (gray) SPE20-N10, (green) SPE20-N10-SIPN. (a) Lithium plating/stripping cycling data (electrolyte thickness 136 µm, diameter 4 mm) at 70°C using a half cycle time of 1h and a current density of 0.1 mA cm^{-1}. (b) Charge and discharge profiles (electrolyte thickness ~7 µm, diameter 12 mm) for the three systems, for cycles 0 to 50. Figure adapted and recomposed from publication.

Overall, this chapter addresses research questions 1 to 3 through the development of a low-T_g ester-functionalized polysiloxane electrolyte and its stabilization in a semi-interpenetrating network architecture. In relation to research question 1, the results show that the selected polymer backbone and side-chain functionality enable an amorphous electrolyte system with a low glass transition temperature and good compatibility with lithium salts. In relation to research question 2, the study shows that the mechanical stability of this soft electrolyte can be significantly improved by incorporation into a polyester-based network structure, while the ionic conductivity is largely retained. In relation to research question 3, the resulting differences between the non-crosslinked and crosslinked electrolyte systems are reflected in electrochemical experiments. Particularly in lithium compatibility and battery cycling behavior, the enhanced mechanical properties enabled stable cycling characteristics. The results demonstrate that network integration is a suitable strategy to mechanically stabilize very soft ester-based electrolytes and to improve their cyclability and applicability in lithium-metal batteries.

3 Individual Contributions to Joint Publications

The individual contributions of participating authors in joint publications are detailed in the following section.

CHAPTER I **Easily accessible linear and hyperbranched polyesters as solid polymer electrolytes**

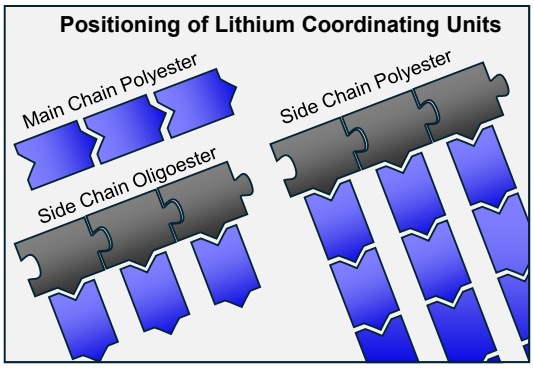


Copyright 2024 Elsevier Ltd. All rights reserved.

Published as: *Eur. Polym. J.* **2024**, 210, 112965 by Jannik Petry, Krishna Dan, Atish Nag, Mukundan Thelakkat and Suhrit Ghosh*.
The article was published with shared first authorship between Krishna Dan, Atish Nag, and myself.

Jannik Petry – I received the synthesized polymer materials and conducted their thermal characterization. I performed electrolyte formulation, temperature-dependent ionic conductivity measurements, distribution of relaxation times analysis, and linear sweep voltammetry experiments. Figures and article sections covering these experiments were visualized and written by myself.
Krishna Dan – performed partial polymer synthesis, ^{1}H NMR spectroscopy, size exclusion chromatography, and contributed to the article sections covering these aspects.
Atish Nag – performed partial polymer synthesis, ^{1}H NMR spectroscopy, size exclusion chromatography, and contributed to the article sections covering these aspects.
Mukundan Thelakkat – conceptualized and supervised the project.
Suhrit Ghosh – conceptualized and supervised the project.
All authors proofread the final manuscript.

CHAPTER II Synthesis and Comparison of Linear, Branched, and Grafted Polyester-based Architectures as Solid Polymer Electrolytes

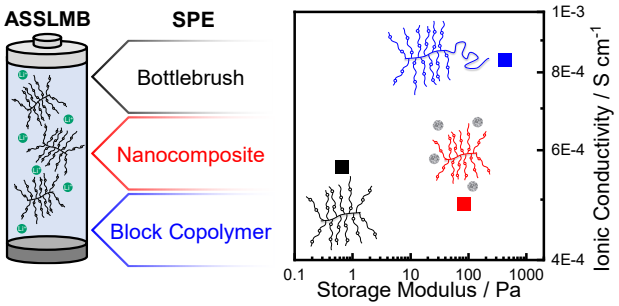


Prepared for submission by Jannik Petry, Marcel Sticher, Gabriele Caputo and Mukundan Thelakkat*.

Jannik Petry – I conceptualized the project and synthesized the polymer materials, conducted ^{1}H NMR spectroscopy, size exclusion chromatography, and thermal characterization. I formulated electrolyte compositions and performed and evaluated the temperature-dependent ionic conductivity measurements and FTIR lithium coordination analysis.
Marcel Sticher – synthesized a norbornene-based macromonomer, performed ^{1}H NMR spectroscopy, and size exclusion chromatography as part of a practical under my supervision.
Gabriele Caputo – synthesized a norbornene-based monomer and performed ^{1}H NMR spectroscopy as a student assistant under my supervision.
Mukundan Thelakkat – supervised the project.
All authors proofread the prepared manuscript.

CHAPTER III

Comparative Study of the Mechanical Reinforcement by Blending, Filling, and Block Copolymerization in Bottlebrush Polymer Electrolytes

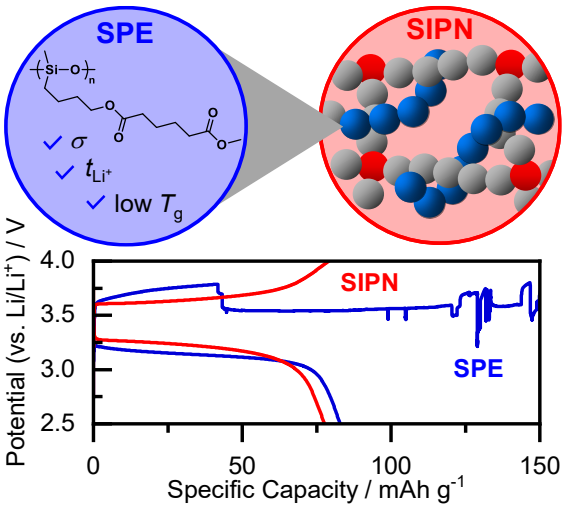


Copyright 2024 The Authors. Published by American Chemical Society

Published as: *ACS Appl. Polym. Mater.* **2024**, 6, 5109–5120 by Jannik Petry, Harimohan Erabhoina, Markus Dietel, and Mukundan Thelakkat*.

Jannik Petry – I synthesized the polymer materials and performed and evaluated ^{1}H NMR spectroscopy, thermal characterization, size exclusion chromatography, linear sweep voltammetry experiments, galvanostatic overcharging experiments, cutoff increase cell cycling, and distribution of relaxation times analysis. I visualized the data and wrote the manuscript.
Harimohan Erabhoina – recorded SEM images, supervised and performed electrochemical experiments, prepared composite cathodes, and fabricated battery test cells.
Markus Dietel – assembled electrochemical test cells, and performed temperature-dependent ionic conductivity measurements, transference number determination, and lithium plating and stripping experiments as part of a practical under my supervision.
Mukundan Thelakkat – conceptualized and supervised the project.
All authors proofread the final manuscript.

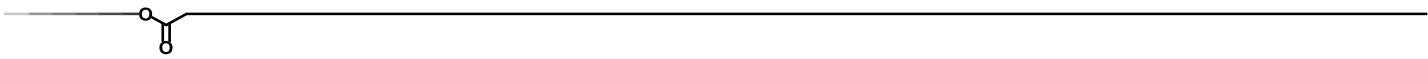
CHAPTER IV Semi-Interpenetrating Network Electrolytes Utilizing Ester-Functionalized Low T_g Polysiloxanes in Lithium-Metal Batteries



Copyright 2024, Advanced Energy Materials published by Wiley VCH GmbH

Published as: *Adv. Energy Mater.* 2024, 15, 2403531 by Jannik Petry, Markus Dietel, and Mukundan Thelakkat*.

Jannik Petry – I conceptualized the project and designed the polymer materials. I performed and evaluated temperature-dependent ionic conductivity measurements, fabricated and optimized composite cathodes, and performed galvanostatic overcharging and battery cycling experiments. I visualized the data and wrote the manuscript.
Markus Dietel – synthesized the polymer materials, performed and evaluated ^{1}H NMR spectroscopy, thermal characterization, temperature-dependent ionic conductivity measurements, transference number determinations, distribution of relaxation times analysis, and lithium plating and stripping experiments as part of his Master's thesis under my supervision.
Mukundan Thelakkat – supervised the project.
All authors proofread the final manuscript.



I Easily Accessible Linear and Hyperbranched Polyesters as Solid Polymer Electrolytes

Jannik Petry[a,1], Krishna Dan[b,1], Atish Nag[b,1], Mukundan Thelakkat[a,c,d], and Suhrit Ghosh[b,*]

[a] Applied Functional Polymers, University of Bayreuth, Universitätsstraße 30, 95447 Bayreuth, Germany
[b] School of Applied and Interdisciplinary Sciences, Indian Association for the Cultivation of Science, 2A and 2B Raja S. C. Mullick Road, Kolkata 700032, India
[c] Bavarian Polymer Institute (BPI), University of Bayreuth, Universitätsstraße 30, 95447 Bayreuth, Germany
[d] Bavarian Center for Battery Technology (BayBatt), University of Bayreuth, Universitätsstraße 30, 95447 Bayreuth, Germany
[1] contributed equally

* Corresponding Author
E-mail: psusg2@iacs.res.in

Reproduced with permission from European Polymer Journal 2024, 210, 112965,
Copyright 2024 Elsevier

I.1 Abstract

Herein we report synthesis, characterization, thermal properties, ionic conductivity and oxidative stability of novel linear and hyperbranched polyesters. Tri-acrylate ester of commercially available 1,1,1-Tris(hydroxymethyl)propane (M1) was used as the primary building block for the synthesis of linear and hyperbranched polymers. A3 + B2 type polycondensation between M1 and dithiols of two different chain lengths (C3, C6) by 100 % atom efficient thiol-acrylate Michael addition reaction, followed by consumption of the unreacted acrylate esters (in the linear or terminal units) with 1-butane thiol produced two hyperbranched polymer namely HB-P1 and HB-P2. For synthesis of linear analogues, one of the equivalent acrylate esters was reacted first with 1-butane thiol and the resulting di-acrylate monomer was polymerized with the C3 and C6-dithiols, producing linear polymers L-P1 and L-P2. All the polymers showed molecular weight (M_n) in the range of 5000–6000 g mol^{-1} with low dispersity. TGA analysis revealed sufficient thermal stability of the polymers for the application as solid polymer electrolyte. All the polymers are amorphous, showing only a glass transition in the range of ~ -45 °C (C3 spacer) to 50 ◦C (C6 spacer) and no crystallization peak. In presence of lithium bis(trifluoromethanesulfonyl) imide (LiTFSI) salt the T_g increased by ~ 10 °C. Solid polymer electrolytes were prepared by incorporating LiTFSI at a molar ratio of polymer carbonyl units to lithium of C=O/Li of 10 and ionic conductivity (σ) was evaluated by electrochemical impedance spectroscopy (EIS). Moderate values in the range of 10^{-7} S cm^{-1} were obtained at 25 °C with slightly higher values for the linear polymers. The ionic conductivity increased up to ~ 2 orders of magnitude at higher temperatures. The oxidative stability of the polymer electrolytes against lithium-metal electrodes revealed onset potential for the first degradation in the range of 3.8 V, indicating moderate stability that might be suitable for testing applications in all-solid-state lithium-metal batteries using sulfur or lithium iron phosphate cathodes.

I.2 Introduction

Lithium-ion batteries (LIB) are of high demand to meet sharply increasing need for energy storage technologies suitable for electric vehicles or other electronics.[1,2] Conventionally, such batteries contain flammable liquid electrolytes, which is not desirable due to the growth of Li dendrite and serious safety-related concerns if used in combination with metallic lithium anodes.[3] Hence, there is a tremendous research interest in solid polymer electrolytes (SPE) for all solid-state battery application and till date, poly(ethylene oxide) (PEO) is considered to be the benchmark candidate as solid polymer electrolyte for LIB.[4–7] High degree of crystallinity, low ionic conductivity at room temperature, low lithium transport number, and not so high electrochemical stability are major drawbacks of PEO.[8] To address these issues, in the recent past other synthetic polymers "beyond PEO" have been explored as solid electrolyte for LIB.[9–13] Amongst them, polyesters are particularly promising considering weak Li coordination resulting in high lithium transport number compared to PEO. From a few recent reports, including recent work by our group, it is evident that some of the pressing problems in the solid polymer electrolytes may be addressed by appropriate structural fine-tuning in easily accessible polyester scaffolds, which also offer the additional advantage of biodegradability.[14–19] Inspired by these recent promising results, we wanted to explore new polyesters for LIB. Polyesters are generally synthesized by transesterification reaction, which requires high temperature and continuous removal of the volatile alcohol to push the reaction in the forward direction. This may not be the ideal scenario for exploring functional polymers in which structure–property relationship studies often requires comparing the properties of a series of polymers. Hence, mild and versatile synthetic methods may enhance the scope of polyesters in solid polymer electrolyte of other applications.[20] We had established a methodology for synthesis of polyesters by thiol-acrylate Michael addition reaction between diacrylate and dithiol monomers.[21] Although it produces polyesters with a sulphur atom present at the β-position to the ester group in every repeating unit, the polymerization reaction undergoes at room temperature and the reaction is 100 % atom efficient as there is no byproduct during the reaction. In this manuscript, we report synthesis of linear and hyperbranched polyesters (L-P1, L-P2, HB-P1, HB-P2, Scheme 1) by thiol-acrylate Michael addition reaction and study the effect of structural nuances on thermal properties, lithium-ion conductivity, and electrochemical stability.

I.2 Experimental

I.2.1 Materials and methods

Solvents and reagents were purchased from commercial sources and purified by prescribed protocols. Trimethylolpropane triacrylate (M1), 1-butanethiol, 1,3-propanedithiol, 1,6-hexanedithiol, methyl-acrylate, Me_2PPh, acetonitrile (99.8 %, anhydrous) and lithium bis(trifluoromethane)sulfonimide (LiTFSI, 99.9 % ^{19}F NMR) were purchased from Sigma Aldrich. The Li-salt was dried at 60 °C under vacuum overnight before storing in an Ar-filled glovebox. Chloroform (99 %) was retrieved from VWR chemicals. CR2032-type coin cell parts (cases, stainless steel (StSt) spacers (500 µm thickness), stainless steel wave springs) were bought from PI-KEM limited. Teflon® sheets (500 µm thickness) and Kapton® sheets (135 µm thickness) were purchased from Goodfellow Cambridge Ltd. Lithium metal ribbon (purity 99.9 %, thickness 380 µm, width 23 mm) was retrieved from Sigma Aldrich, lithium electrodes were punched from the

ribbon using a 14 mm diameter punching die inside the glovebox. Spectroscopic grade solvents were used for all physical studies. ^{1}H NMR spectra were recorded in a Bruker DPX-400 MHz spectrometer the peak positions were calibrated using TMS as an internal standard. Molecular weight of the polymer was estimated in THF (1.0 mg mL^{-1}) solvent at 30 °C with respect to poly (methyl methacrylate) (PMMA) standards in a Waters GPC machine equipped with a 515 HPLC pump, Waters 2414 RI detector, and HSPgel HT 4.0/HSPgel HT 2.5 columns connected in a series.

I.2.2 Synthesis of L-P1

Monomer M2 (1 g, 2.6 mmol), propane-1,3-dithiol (308 mg, 2.8 mmol) and methyl acrylate (47 mg, 0.546 mmol) were dissolved in anhydrous and degassed dimethylacetamide (DMAc) and placed in an ice bath. To this reaction mixture Me_2PPh (0.03 mmol) was added and stirred at room temperature for 1 h under inert atmosphere. The polymer was collected by precipitation from cold excess diethyl ether and isolated as a colourless viscous liquid. Yield = 800 mg (~61 %). ^{1}H NMR ($CDCl_3$, 300 MHz, TMS): δ (ppm) = 4.05 (d, 6H), 3.69 (s, 6H), 2.75 (m, 6H), 2.64 (m, 12H), 1.85 (m, 1H), 1.50 (m, 6H), 0.91 (m, 6H). End group analysis from ^{1}H NMR revealed molecular weight of L-P1 to be 6500 g mol^{-1}. Molecular weight obtained from SEC in THF is 5500 g mol^{-1} ($Đ$ = 1.2).

I.2.3 Synthesis of L-P2

For the preparation of L-P2, the similar procedure as for the L-P1 synthesis was followed. In this case hexane dithiol was utilized for the thiol acrylate polymerization reaction. Yield = 900 mg (~64 %). ^{1}H NMR ($CDCl_3$, 300 MHz, TMS): δ (ppm) = 4.05 (d, 6H), 2.75 (t, 6H), 2.60 (t, 6H), 2.49 (t, 6H), 2.34 (t, 4H), 1.85 (m, 1H), 1.58 (b, 6H), 1.39 (b, 4H), 0.91 (m, 6H). End group analysis from ^{1}H NMR revealed molecular weight of L-P2 to be 7500 g mol^{-1}. Molecular weight obtained from SEC in THF is 5000 g mol^{-1} ($Đ$ = 1.2).

I.2.4 Synthesis of HB-P1a

Commercially available trimethylolpropane triacrylate (M1) (0.5 g, 1.68 mmol) and monomer propane dithiol (0.134 g, 1.2 mmol) were dissolved in 3 mL of degassed dimethylacetamide (DMAc) in inert atmosphere and was placed in an ice-bath. Then catalytic amount of Me_2PPh (0.03 mmol) was added under inert atmosphere to this reaction mixture and it was stirred for 2 h at rt. The reaction was subsequently stopped and the polymer (HB-P1a) was collected by precipitation from excess cold diethyl ether and isolated as highly viscous colourless liquid after drying under vacuum. Yield: 400 mg (~63 %). ^{1}H NMR ($CDCl_3$, 400 MHz) δ (ppm): 6.44 (d, 1H), 6.14 (m, 1H), 5.88 (d, 1H), 4.16–4.07 (m, 18H), 2.78 (b, 2H), 2.64 (b, 4H), 1.87 (b, 2H), 1.52 (b, 2H), 0.91 (b, 3H).

I.2.5 Synthesis of HB-P2a

For the preparation of HB-P2a, similar reaction procedure was followed as in the case of HB-P1a. Here, the hexane dithiol was used as the dithiol monomer for thiol acrylate polymerization reaction. Yield = 500 mg (~70 %). ^{1}H NMR ($CDCl_3$, 400 MHz) δ (ppm): 6.38 (d, 1H), 6.12 (m, 1H), 5.87 (d, 1H), 4.15–4.05 (m, 18H), 2.75 (b, 2H), 2.60 (b, 4H), 2.51 (b, 2H), 1.6 (b, 8H), 1.38 (b, 2H), 0.90 (b, 3H).

I.2.6 Synthesis of HB-P1

HB-P1a (0.3 g) and 1-butane thiol (0.435 g, 4.83 mmol) was dissolved in anhydrous THF under an inert atmosphere and placed in an ice bath. Subsequently, catalytic amount of Me2PPh (0.03 mmol) was added to this reaction mixture maintaining the inert atmosphere. The reaction mixture was stirred for 2 h at rt. The reaction was stopped then and the polymer(HB-P1) was isolated by precipitation from excess cold diethyl ether. The purified polymer was vacuum dried and collected as a colourless viscous liquid. Yield = 310 mg (~90 %). ^{1}H NMR ($CDCl_3$, 400 MHz) δ (ppm): 4.05 (s, 18H), 2.76 (b, 2H), 2.62 (b, 4H), 2.52 (b, 2H), 1.85 (b, 2H), 1.48 (b, 2H), 0.91 (b, 3H). Molecular weight (M_w) from SEC: 5500 g mol^{-1} ($Đ$ =1.18).

I.2.7 Synthesis of HB-P2

For the preparation of HB-P2, similar reaction procedure was followed as in the case of HB-P1. Yield = 420 mg (~95 %). ^{1}H NMR ($CDCl_3$, 400 MHz) δ (ppm): 4.08 (m, 18H), 2.78 (b, 2H), 2.63 (b, 2H), 2.54 (b, 2H), 1.61 (b, 8H), 1.41 (b, 2H), 0.94 (b, 3H). Molecular weight (M_w) from SEC: 6300 g mol^{-1} ($Đ$ = 1.25).

I.2.8 Thermogravimetric Analysis (TGA)

TGA thermograms were recorded on a Mettler Toledo TGA/DSC 3. Samples (ca. 5–10 mg) were placed in aluminum oxide ceramic crucibles (70 µL) and heated from 30 to 700 °C at a heating rate of 10 K min^{-1} under nitrogen atmosphere.

I.2.9 Differential Scanning Calorimetry (DSC)

DSC thermograms were obtained using a Mettler Toledo DSC 3. The samples were sealed in aluminum crucibles. The temperature program comprised two cycles of cooling down to -70 °C and subsequent heating up to 150 °C at a cooling/heating rate of 10 K min^{-1}. For the third cycle, a cooling/ heating rate of 40 K min^{-1} was chosen. Glass transition temperatures (T_g) are derived as inflection points of the transition temperature in the second heating curve.

I.2.10 Electrochemical Measurements

Electrochemical measurements were conducted using a VMP300 potentiostat (BioLogic) equipped with EIS boards. Before any measurement coin cells were tempered at 70 °C at open-circuit voltage (OCV) for at least 12 h. The temperature was controlled using a climate chamber Vötsch VT4002.

I.2.11 Electrolyte Preparation

The electrolytes were prepared by dissolving the polymer in chloroform (ca. 0.75 mL per 100 mg of polymer). Lithium-bis(trifluoromethylsulfonyl)imide (LiTFSI) was weighed inside an argon-filled glovebox. The molar concentration of lithium salt was 10:1 with respect to the carbonyl groups of the polymer repeating unit to the number of lithium cations (C=O/Li 10). The LiTFSI is dissolved in acetonitrile (same amount of ACN as chloroform). The two solutions are combined and stirred for 1 h. Afterwards the electrolyte mixtures are dried in high vacuum at 80 °C for at least 15 h. After drying the electrolytes are transferred to a argon-filled glovebox for later use.

I.2.12 Ionic Conductivity

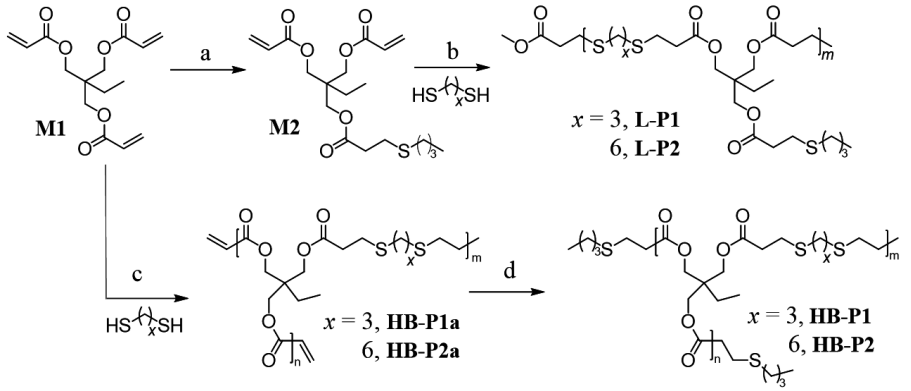
The ionic conductivity was evaluated by electrochemical impedance spectroscopy. For temperature-dependent ionic conductivity measurements, the temperature was controlled by a climate chamber (80 – 25 °C). For each temperature step, the impedance spectrum is recorded after an equilibration interval of 1.5 h. All electrochemical impedance spectroscopy (EIS) measurements were conducted in a frequency range of 3 MHz – 0.1 Hz using a sinusoidal excitation potential of 20 mV. EIS measurements were reconstructed by the extended distribution of relaxation times-(eDRT)-analysis using the software ec–idea provided by the Department of Electrical Energy Systems at the University of Bayreuth. Fitting parameters: Number of time constants: 159, 3-fold number of measured frequencies, extended upper time constant limit by 1 decade, extended lower time constant limit by 1 decade, regularization parameter: 0.1. The CR2032 coin cell setup consisted of lithium-blocking stainless steel electrodes and the respective electrolyte. The electrolyte geometry is ensured by a Telfon® spacer (500 µm thickness, diameter 16 mm, cavity diameter 3 mm). The spacer cavity is filled with electrolyte during cell preparation.

I.2.13 Linear Sweep Voltammetry

Linear sweep voltammograms were recorded at 70 °C and a scan rate of 0.1 mV s^{-1} between OCV (2.6 V vs. Li/Li+) and 6 V. The CR2032 coin cell setup consisted of a lithium electrode (as reference and counter electrode) and a stainless-steel electrode (as working electrode). The electrolyte geometry is ensured by a Kapton ® spacer (135 µm thickness, diameter 16 mm, cavity diameter 4 mm). The spacer cavity is filled with electrolyte during cell preparation.

I.3 Results and Discussion

Synthesis of the linear and hyperbranched polymers are shown in **Scheme I.1**. Tri-acrylate building block M1 was reacted with 1-butanethiol to produce the di-acrylate monomers M2 which was characterized by ^{1}H NMR (**Figure S.I.1**). M1 was chosen as the primary building block as it is readily available from commercial sources. Furthermore, the $-CH_2CH_3$ group attached to the central sp^3 hybridized carbon was anticipated to contribute to amorphous character of the resulting polymers with low glass transition temperature, which is desirable for the solid polymer electrolyte application. Polycondensation between M2 and 1,3-propane dithiol or 1,6-hexane dithiol in presence of Me_2PPh catalyst produced linear polyesters L-P1 and L-P2, respectively.



Scheme I.1. Synthesis of the linear and hyperbranched polymers studied in this paper. Reagents and conditions: (a) 1-butanethiol, Me_2PPh, THF, 0 ºC-rt, 1 h; (b) Methyl-acrylate, Me_2PPh, DMAc, 0 ºC-rt, 1 h; (c) Me_2PPh, DMAc, 0 ºC-rt, 2 h; (d) 1-butanethiol, Me_2PPh, THF, 0 ºC-rt, 2 h.

Little amount of methyl acrylate was used as the chain stopper to avoid presence of free thiols at the chain-ends. For solid polymer electrolyte applications, it is desirable that the polymers exhibit low glass transition temperature (T_g). This is precisely the reason why a monomer like M2 was chosen as it was anticipated that the pendant moieties would inhibit crystallization and help in achieving low T_g. L-P1 and L-P2 were synthesized to examine the effect of density of ester groups in the backbone on the ion conductivity as it would depend on the coordination of the ester carbonyl to the Li-ion. To examine the effect of linear and hyperbranched polymers of similar nature, monomer M1 was used to synthesize hyperbranched polymer by a A3+B2 condensation approach with the same two dithiols.[22–25] For the synthesis of the hyperbranched polymers, tri-acrylate monomer M1 was taken in little excess (M1: dithiol = 1.4: 1) to avoid the crosslinking-induced gelation during polymerization. This produced hyperbranched polymers HB-P1a and HB-P2a which were reacted with 1-butanethiol to consume the unreacted acrylate groups in the linear/dendritic units of the hyperbranched polymers producing HB-P1 and HB-P2 (Scheme 1). Representative ^{1}H NMR spectra of L-P2 and HB-P2 are shown in **Figure I.1**.

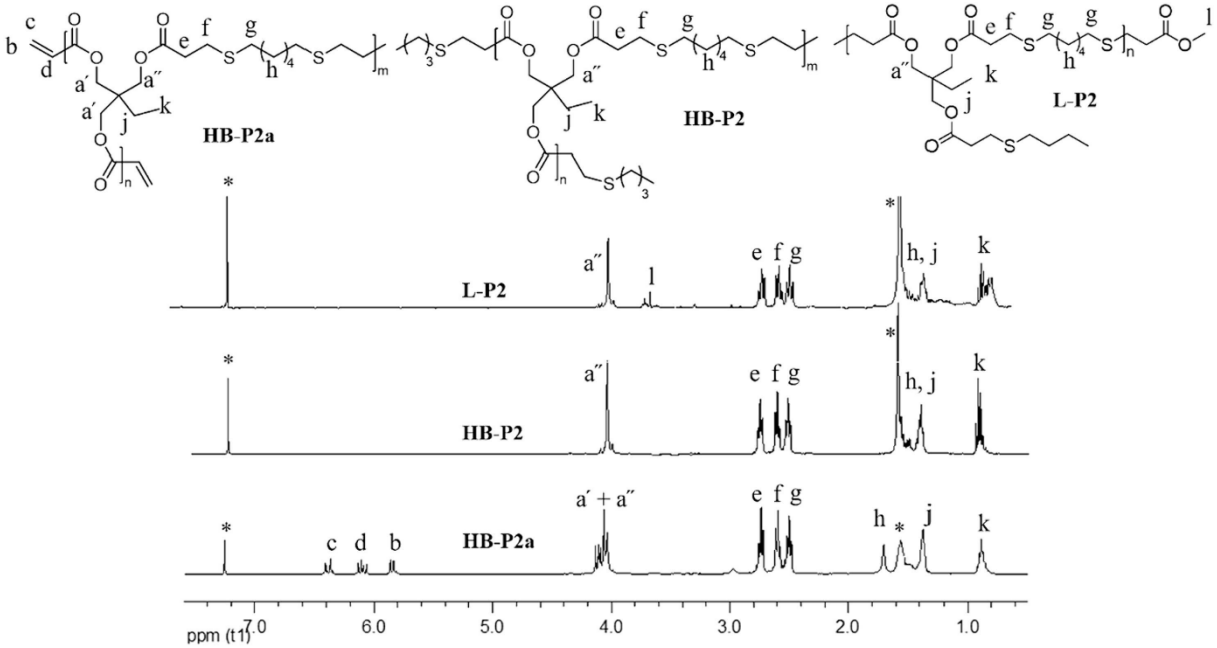


Figure I.1. Representative ^{1}H NMR spectra of a linear and hyperbranched polymer in $CDCl_3$. For the hyperbranched case, acrylate containing pre-polymer spectrum is also shown for comparison purposes. (* indicates residual solvent peaks).

For the linear polymer L-P2, a singlet appears at δ = 4.03 ppm, which can be assigned to H_a''(–CH_2 proton) adjacent to the ester group and three clear triplets appear at δ = 2.4–2.8 ppm which can be assigned to the methylene protons in the backbone (H_e, H_f, H_g, Figure 1). Other methylene protons appear in the up-field region (δ = 1.4–1.6 ppm, 0.8–1.0 ppm). For the hyperbranched polymer HB-P2a, multiple peaks appeared in the region of δ = 4.03 ppm, which can be assigned to difference in the chemical environment of the –OCH_2 protons (H_a', H_a'') adjacent to the ester groups in the dendritic, terminal and linear units of the polymer. From the integration of the peaks corresponding to linear (L), terminal (T) and dendritic (D) units, the degree of branching (DB) of HB-P1a and HB-P2a was estimated to be 0.59 and 0.62, respectively, using the following equation (**Eq. I.1**).

$$\mathrm{DB} = \frac{D + T}{D + T + L} \tag{I.1}$$

Peaks appearing in the region δ = 5.8–6.4 ppm can be assigned to the unreacted acrylate groups (in the linear and terminal units). After the polymer was treated with 1-butanethiol, in the resulting polymer HBP2, all the acrylate protons disappeared indicating complete consumption and interestingly multiple peaks appearing in the δ = 4.00 ppm region due to the $-OCH_2$ protons merged to almost a single peak similar to the linear polymer as in this case the difference in chemical environment of the different units in the hyperbranched polymer reduced significantly. Likewise, L-P1 and HB-P2 were also characterized by ^{1}H NMR spectra, which are shown in the supporting information (**Figure S.I.2-S.I.4**). Molecular weight of the polymers was estimated by size exclusion chromatography (**Figure S.I.5-S.I.6**), which revealed moderate values (M_n in the range of 5000–6000 g mol^{-1}, $Đ$ < 1.3) for all four polymers (**Table I.1**).

Table I.1. Overview of achieved molecular weights and polymer dispersity and thermal properties of the linear and hyperbranched polymers and corresponding electrolytes.

Polymer	M_n[a]	$Đ$[b]	$T_{d,onset}$	$T_{g,polymer}$[c,d]	$T_{g,electrolyte}$[c,e]
	g mol^{-1}		°C	°C	°C
L-P1	5500	1.20	329	-45	-36
L-P2	500	1.21	348	-51	-43
HB-P1	5500	1.18	349	-46	-36
HB-P2	6300	1.25	354	-51	-40

[a] determined from SEC: THF eluent, PMMA standards. [b] M_w/M_n. [c] determined from the second heating cycle at 10 K min^{-1}. [d] glass transition of the pristine polymer. [e] glass transition of the polymer electrolyte (mixture of polymer + LiTFSI) at a C=O/Li ratio of 10.

The synthesized polymers were evaluated for their potential as solid polymer electrolytes. The polymers were converted to solid polymer electrolytes by incorporating lithium bis(trifluoromethanesulfonyl) imide (LiTFSI) at a molar ratio of polymer carbonyl units to lithium of C=O/Li of 10. Given the variations in polymer architecture and chemical composition, this corresponded to salt concentrations ranging between 12 and 15 wt%, as detailed in **Table S.I.1**. As the molar ratio of carbonyl units to lithium ions can significantly influence ionic conduction within the polymer matrix, we opted for a consistent molar ratio rather than the same weight proportion.[17,26] Thermal properties were evaluated by thermogravimetric analysis and differential scanning calorimetry. Values are summarized in Table 1. The polymers showed sufficient thermal stability for the application in solid-state lithium-metal batteries. The polymers showed a thermal decomposition onset of around 300 °C. L-P1 showed an additional decomposition step starting at 160 °C, however terminal decomposition was comparable to the other three polymers (**Figure I.2**a). Further, the thermal transitions of the polymers and corresponding electrolytes were investigated. All of the pristine polymers only showed a glass transition (**Figure I.2**b).

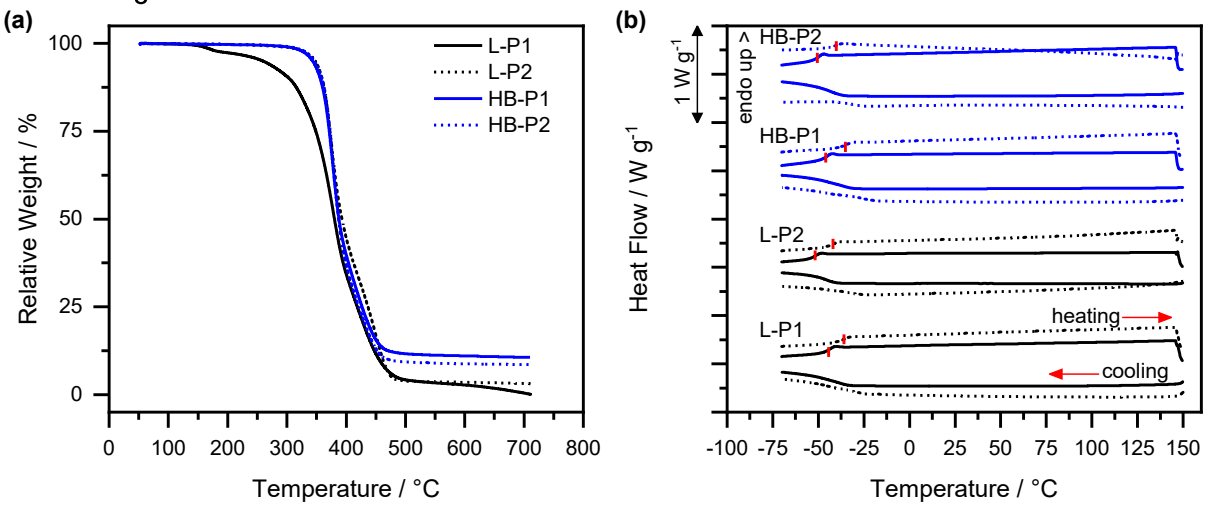


Figure I.2. Thermogravimetric analysis and differential scanning calorimetry of the (black lines) linear polymers L-P1 and L-P2, and (blue lines) hyperbranched polymers HB-P1 and HB-P2. (a) Thermal decomposition curves at a heating rate of 10 K min^{-1} under nitrogen atmosphere. (b) Thermal transitions of the (solid lines) pristine polymers and (dotted lines) corresponding electrolytes at a C=O/Li ratio of 10. The second cooling and heating cycle is shown for all samples. The glass transition temperature of the pristine polymers and electrolytes are marked with red indicators and were determined from the second heating curves.

The glass transition temperature (T_g) of the polymers with shorter spacer lengths (L-P1 and HB-P1) showed a comparable T_g of around 45 °C. With longer spacer lengths in L-P2 and HB-P2 the glass transition shifted to lower temperatures of about 50 °C. Further spacing of the ester groups is commonly resulting in lower glass transition temperatures. The rational design and choice of spacer units between ester moieties was investigated by Rosenbach et al.[17] By changing the number of methylene units the glass transition temperature could be incrementally tuned from +32 °C to -44 °C in methacrylate-based polymers with two ester groups as side chain modification.[17] Notably, both pristine polymers and corresponding electrolytes exhibited no melting/crystallization peaks. The addition of LiTFSI resulted in an increase of the T_g by around 10 °C in all cases, which is commonly observed for solid polymer electrolytes. This amorphous character is beneficial for the application as solid polymer electrolytes, as ion transport is usually observed in the amorphous polymer domains. The ionic conductivity (σ) was evaluated by electrochemical impedance spectroscopy (EIS) at different temperatures using ion-blocking stainless steel electrodes (StSt|electrolyte|StSt). The cell geometry enables the isolated evaluation of the ionic conductivity due to the absence of any charge-transfer processes. The recorded impedance data reveals one semi-circle corresponding to the ionic conductivity of the polymer electrolytes and non-ideal capacitive behavior attributed to the electrode interfaces towards high Z' values and is well represented by the employed eDRT analysis (**Figure I.3**a, **Figure S.I.7-10**). The evaluation of the Nyquist plots was performed by the extended distribution of relaxation times (eDRT) analysis.

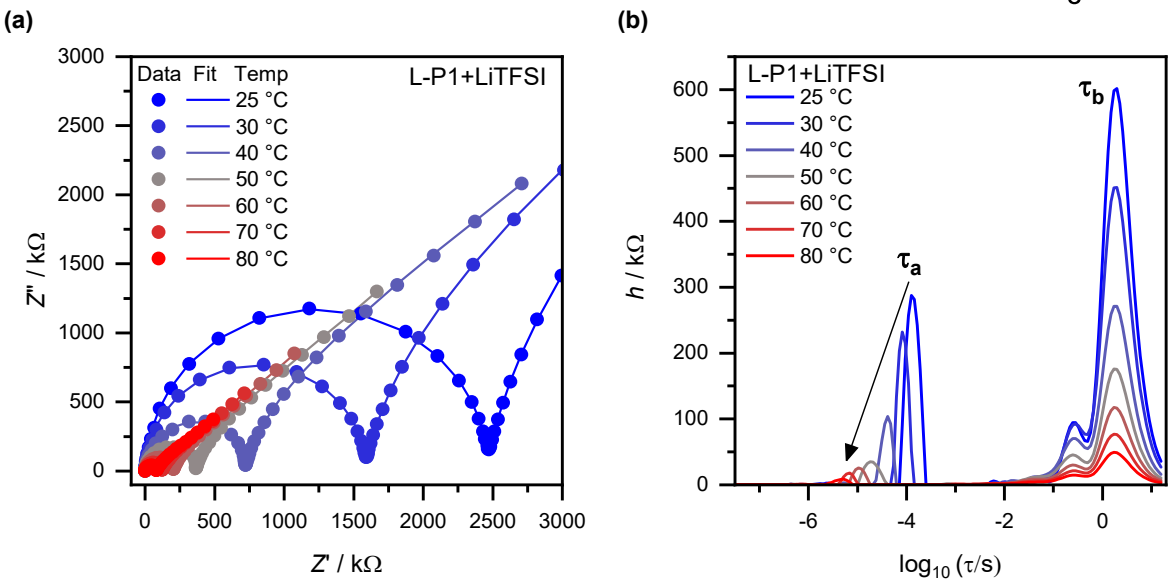


Figure I.3. (a) Exemplary Nyquist plot of temperature-dependent EIS measurements and eDRT fit for the L-P1 + LiTFSI (C=O/Li 10) electrolyte. (b) Extended distribution of relaxation times. The DRT results are represented by the absolute distribution function $h(\tau)$. τ_a and τ_b can be attributed to the ionic conductivity and capacitive behavior, respectively.

This enabled the evaluation of the EIS measurements without pre-defined equivalent circuits, as the analysis method uses no ab initio knowledge to reconstruct the impedance data.[27–29] Exemplary data is shown for L-P1 in **Figure I.3**b and in **Figure S.I.11-13** for the remaining polymer electrolytes. The two processes (ionic conductivity and capacitive behavior) occur at different relaxation times. The relaxation time constant of the ionic conductivity contribution (τ_a) is highly dependent on the temperature and shifts to faster relaxation times as well as exhibits decreasing ohmic polarization. On the other hand, the corresponding relaxation time constant of the capacitive behavior (τ_b) is not shifting with temperature. The determined values of the ionic conductivity are summarized in **Table I.2**.

Table I.2. Overview of the ionic conductivity and electrochemical stability of the polymers.

Polymer	σ @25 °C S cm^{-1}	σ @40 °C S cm^{-1}	$V_{d,LSV}$[a] V	$V_{d,LSV}$[b] V
L-P1	2.27×10^{-7}	4.54×10^{-6}	3.78	4.39
L-P2	2.58×10^{-7}	4.53×10^{-6}	3.72	4.53
HB-P1	1.79×10^{-7}	4.42×10^{-6}	3.74	4.51
HB-P2	1.54×10^{-7}	3.59×10^{-6}	n.d.	n.d.

[a] Potential of the first decomposition onset. [b] Potential of the second decomposition onset.

The ionic conductivity of all of the four materials was found to be relatively similar with σ@25 °C between 1.5×10^{-7} and 2.6×10^{-7} S cm^{-1} and σ@70 °C between 4.54×10^{-6} and 3.59×10^{-6} S cm^{-1}. Notably, the electrolytes of linear polymers (L-P1 and L-P2) have marginally higher ionic conductivity, especially at lower temperatures (**Figure I.4**a). Generally, the ionic conductivity can consist of intra- and interchain hopping events facilitated by low glass transition temperatures (or i.e. high polymer flexibility). Also, macroscopic polymer movements can contribute in a vehicular manner.[30,31] We hypothesize that the observed increase in ionic conductivity could originate from less restricted chain flexibility and higher polymer mobility provided in a linear polymer compared to hyperbranched polymer counterparts.

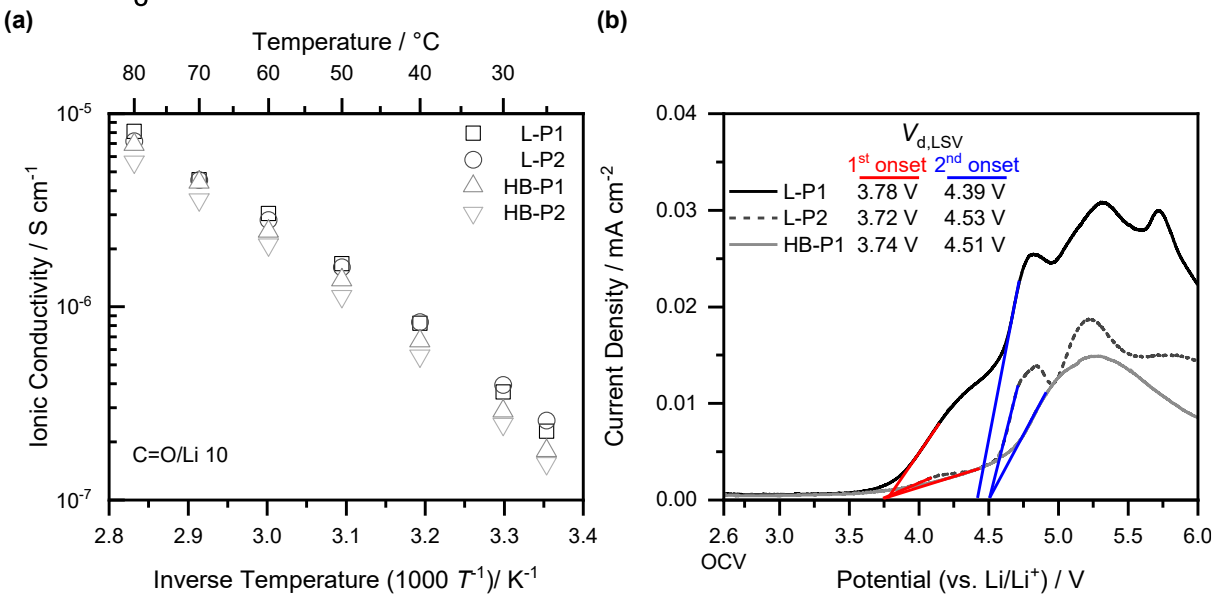


Figure I.4. (a) Arrhenius plots of the temperature-dependent ionic conductivity (80 °C–25 °C). (b) Linear sweep voltammograms in Li|electrolyte|StSt cells at a sweep rate of 0.1 mV s^{-1} from OCV to 6 V. (red) First decomposition onset and (blue) second decomposition onset.

The ionic conductivity values of L-P2 are compared to a polyester electrolyte consisting of linear poly(ε-caprolactone) (PCL) with a LiTFSI content of 19.5 wt% (C=O/Li = 10.4). The data for the whole temperature range of 25–80 °C is presented in **Figure S.I.14**. Similar to PEO, PCL is a semi-crystalline polymer with a melting point at about 50 °C. At high temperatures above the melting point of PCL, the ionic conductivity of PCL is higher than the values for the SPEs presented here. Below the melting point of PCL, its σ value decreases significantly by one order of magnitude and at 25 °C for a comparable salt concentration (C=O/Li = 10) similar ionic conductivities are obtained for L-P2 and PCL electrolytes; the σ values being 2.6×10^{-7} and 3.2×10^{-7} S cm^{-1}, respectively. Thus, the crystallization-induced decrease of the ionic conductivity in linear PCL emphasizes the necessity of amorphous polymers as presented here. In further experiments, the salt content in linear and hyperbranched polymer electrolytes can be optimized to increase the ionic conductivity of these systems. Lastly, we evaluated the oxidative stability of the polymer electrolytes against lithium-metal electrodes. The observed electrochemical stability windows were evaluated geometrically by fitting the oxidative current response (**Figure I.4**b). Thereby, we distinguished between the first and second degradation onset. The determined onset potentials for the first degradation step were 3.78, 3.72, and 3.74 V for the polymers L-P1, L-P2, and HB-P1, respectively. LSV was not performed for HB-P2. The observed electrochemical stability windows are relatively low, as high potential nickel-manganese-cobalt-oxide (NMC) cathodes operate at potentials above 4 V. However, the electrochemical stability may be adequate when paired with alternative cathode chemistries, such as in lithium-sulfur batteries (operating at around 2.3 V) or lithium–iron phosphate-cathodes (3.4 V). Consequently, the application of polymer electrolytes in such batteries could be of future interest.

I.4 Conclusion

In this manuscript, we have shown the synthesis of new polyester-based materials for potential use as solid polymer electrolytes (SPE) in batteries. Polymers reported herein are particularly interesting considering the synthetic ease of these polyesters by 100 % atom-efficient thiol-

acrylate Michael addition reaction, operating at room temperature. By choosing appropriate monomers, we could indeed make fully amorphous polyesters (linear or hyperbranched) with significantly low glass transition temperature, that is highly desirable for efficient ion conduction. However, in the present systems conductivity values were moderate, and oxidative stability of the polymer electrolytes against lithium-metal electrodes was just adequate. This underscores the need for further structural engineering with these new systems, which can be achieved easily due to the synthetic ease of this methodology. In further experiments, the salt content in linear and hyperbranched polymer electrolytes can be individually varied to obtain the optimum salt concentration towards best ionic conductivity of these systems. Furthermore, the different functional di-thiols could be of interest to introduce more ester or ether moieties for better ion coordination/conduction. Our studies indicate linear polymers to be better candidates than hyperbranched analogues for this application. Synthesis of new polyester analogues with even lower T_g, higher conductivity, and oxidative stability and in-depth mechanistic study of ion conduction in these materials are underway in our laboratory.

I.5 CRediT authorship contribution statement

Jannik Petry: Writing – original draft, Visualization, Methodology, Investigation. **Krishna Dan:** Writing – original draft, Investigation. **Atish Nag**: Writing – original draft, Investigation. **Mukundan Thelakkat**: Writing – review & editing, Supervision, Conceptualization. **Suhrit Ghosh**: Writing – review & editing, Supervision, Funding acquisition, Conceptualization.

I.6 Declaration of competing interest

The authors declare that they have no known competing financial interests or personal relationships that could have appeared to influence the work reported in this paper.

I.7 Data availability

Data will be made available on request.

I.8 Acknowledgement

SG and MT thank the Alexander von Humboldt Foundation for facilitating collaborative research by sponsoring short-term visit. KD thanks DST-WOS-A (DST/WOS-A/CS-141/2021) for a research fellowship and funding. JP thanks the Deutsche Bundesstiftung Umwelt (grant no. 20021/714-242) for funding support. AN thanks CSIR, New Delhi for a research fellowship.

I.9 Appendix A. Supplementary material

Supplementary data to this article can be found online at https://doi.org/10.1016/j.eurpolymj.2024.112965.

I.10 References

(1) Goodenough, J. B.; Park, K.-S. The Li-Ion Rechargeable Battery: A Perspective. *J. Am. Chem. Soc.* **2013**, *135* (4), 1167–1176. https://doi.org/10.1021/ja3091438.

(2) Mindemark, J.; Lacey, M. J.; Bowden, T.; Brandell, D. Beyond PEO—Alternative Host Materials for Li + -Conducting Solid Polymer Electrolytes. *Progress in Polymer Science* **2018**, *81*, 114–143. https://doi.org/10.1016/j.progpolymsci.2017.12.004.

(3) Notter, D. A.; Gauch, M.; Widmer, R.; Wäger, P.; Stamp, A.; Zah, R.; Althaus, H.-J. Contribution of Li-Ion Batteries to the Environmental Impact of Electric Vehicles. *Environ. Sci. Technol.* **2010**, *44* (17), 6550–6556. https://doi.org/10.1021/es903729a.

(4) Jr, D. T. H.; Balsara, N. P. Polymer Electrolytes. *Annual Review of Materials Research* **2013**, *43* (Volume 43, 2013), 503–525. https://doi.org/10.1146/annurev-matsci-071312-121705.

(5) Zhao, Q.; Stalin, S.; Zhao, C.-Z.; Archer, L. A. Designing Solid-State Electrolytes for Safe, Energy-Dense Batteries. *Nat Rev Mater* **2020**, *5* (3), 229–252. https://doi.org/10.1038/s41578-019-0165-5.

(6) Fenton, D. E.; Parker, J. M.; Wright, P. V. Complexes of Alkali Metal Ions with Poly(Ethylene Oxide). *Polymer* **1973**, *14* (11), 589. https://doi.org/10.1016/0032-3861(73)90146-8.

(7) Wright, P. V. Electrical Conductivity in Ionic Complexes of Poly(Ethylene Oxide). *British Polymer Journal* **1975**, *7* (5), 319–327. https://doi.org/10.1002/pi.4980070505.

(8) Armand, M. Polymer Solid Electrolytes - an Overview. *Solid State Ionics* **1983**, *9–10*, 745–754. https://doi.org/10.1016/0167-2738(83)90083-8.

(9) Florjańczyk, Z.; Zygadło-Monikowska, E.; Wieczorek, W.; Ryszawy, A.; Tomaszewska, A.; Fredman, K.; Golodnitsky, D.; Peled, E.; Scrosati, B. Polymer-in-Salt Electrolytes Based on Acrylonitrile/Butyl Acrylate Copolymers and Lithium Salts. *J. Phys. Chem. B* **2004**, *108* (39), 14907–14914. https://doi.org/10.1021/jp049195d.

(10) Wang, X.; Hao, X.; Xia, Y.; Liang, Y.; Xia, X.; Tu, J. A Polyacrylonitrile (PAN)-Based Double-Layer Multifunctional Gel Polymer Electrolyte for Lithium-Sulfur Batteries. *Journal of Membrane Science* **2019**, *582*, 37–47. https://doi.org/10.1016/j.memsci.2019.03.048.

(11) Kimura, K.; Yajima, M.; Tominaga, Y. A Highly-Concentrated Poly(Ethylene Carbonate)-Based Electrolyte for All-Solid-State Li Battery Working at Room Temperature. *Electrochemistry Communications* **2016**, *66*, 46–48. https://doi.org/10.1016/j.elecom.2016.02.022.

(12) Tominaga, Y. Ion-Conductive Polymer Electrolytes Based on Poly(Ethylene Carbonate) and Its Derivatives. *Polym J* **2017**, *49* (3), 291–299. https://doi.org/10.1038/pj.2016.115.

(13) Butzelaar, A. J.; Röring, P.; Mach, T. P.; Hoffmann, M.; Jeschull, F.; Wilhelm, M.; Winter, M.; Brunklaus, G.; Théato, P. Styrene-Based Poly(Ethylene Oxide) Side-Chain Block Copolymers as Solid Polymer Electrolytes for High-Voltage Lithium-Metal Batteries. *ACS Appl. Mater. Interfaces* **2021**, *13* (33), 39257–39270. https://doi.org/10.1021/acsami.1c08841.

(14) Wu, I.-D.; Chang, F.-C. Determination of the Interaction within Polyester-Based Solid Polymer Electrolyte Using FTIR Spectroscopy. *Polymer* **2007**, *48* (4), 989–996. https://doi.org/10.1016/j.polymer.2006.12.045.

(15) Fonseca, C. P.; Rosa, D. S.; Gaboardi, F.; Neves, S. Development of a Biodegradable Polymer Electrolyte for Rechargeable Batteries. *Journal of Power Sources* **2006**, *155* (2), 381–384. https://doi.org/10.1016/j.jpowsour.2005.05.004.

(16) Yu, X.; Hoffman, Z. J.; Lee, J.; Fang, C.; Gido, L. A.; Patel, V.; Eitouni, H. B.; Wang, R.; Balsara, N. P. A Practical Polymer Electrolyte for Lithium and Sodium Batteries: Poly(Pentyl Malonate). *ACS Energy Lett.* **2022**, *7* (11), 3791–3797. https://doi.org/10.1021/acsenergylett.2c02128.

(17) Rosenbach, D.; Krimalowski, A.; Erabhoina, H.; Thelakkat, M. Solid Polymer Electrolytes from Polyesters with Diester Sidechains for Lithium Metal Batteries. *Journal of Materials Chemistry A* **2022**, *10* (16), 8932–8947. https://doi.org/10.1039/D2TA00800A.

(18) Erabhoina, H.; Rosenbach, D.; Mohanraj, J.; Thelakkat, M. Solid Polymer Nanocomposite Electrolytes with Improved Interface Properties towards Lithium Metal Battery Application at Room Temperature. *Electrochimica Acta* **2021**, *387*, 138455. https://doi.org/10.1016/j.electacta.2021.138455.

(19) Rosenbach, D.; Mödl, N.; Hahn, M.; Petry, J.; Danzer, M. A.; Thelakkat, M. Synthesis and Comparative Studies of Solvent-Free Brush Polymer Electrolytes for Lithium Batteries. *ACS Applied Energy Materials* **2019**, *2* (5), 3373–3388. https://doi.org/10.1021/acsaem.9b00211.

(20) *A Versatile Step-Growth Polymerization Route to Functional Polyesters from an Activated Diester Monomer - Biswas - 2023 - Chemistry – A European Journal - Wiley Online Library*. https://chemistry-europe.onlinelibrary.wiley.com/doi/10.1002/chem.202203849 (accessed 2026-01-06).

(21) Dan, K.; Ghosh, S. One-Pot Synthesis of an Acid-Labile Amphiphilic Triblock Copolymer and Its pH-Responsive Vesicular Assembly. *Angew. Chem. Int. Ed.* **2013**, *52* (28), 7300–7305. https://doi.org/10.1002/anie.201302722.

(22) Kumar Gayen, A.; Singla, R.; Ramakrishnan, S. Hyperbranched Polymers: Growing Richer in Flavours with Time. *Chem. Commun.* **2024**, *60* (12), 1534–1545. https://doi.org/10.1039/D3CC05506J.

(23) Saha, A.; Ramakrishnan, S. Unimolecular Micelles and Reverse Micelles Based on Hyperbranched Polyethers—Comparative Study of AB2 + A-R and A2 + B3 + A-R Type Strategies. *J. Polym. Sci. A Polym. Chem.* **2009**, *47* (1), 80–91. https://doi.org/10.1002/pola.23122.

(24) Bej, R.; Rajdev, P.; Barman, R.; Ghosh, S. Hyperbranched Polydisulfides. *Polym. Chem.* **2020**, *11* (5), 990–1000. https://doi.org/10.1039/c9py01675a.
(25) Dan, K.; Uvais, M.; Koner, S.; Ghosh, S. Synthesis of pH-Responsive Hyperbranched Polyesters by Thiol-Acrylate Michael Addition Reaction and Versatile Post-Polymerization Functionalization. *Macromol. Rapid Commun.* **2025**, *46* (16), 2500269. https://doi.org/10.1002/marc.202500269.
(26) Rosenwinkel, M. P.; Andersson, R.; Mindemark, J.; Schönhoff, M. Coordination Effects in Polymer Electrolytes: Fast Li+ Transport by Weak Ion Binding. *J. Phys. Chem. C* **2020**, *124* (43), 23588–23596. https://doi.org/10.1021/acs.jpcc.0c08369.
(27) Plank, C.; Rüther, T.; Jahn, L.; Schamel, M.; Schmidt, J. P.; Ciucci, F.; Danzer, M. A. A Review on the Distribution of Relaxation Times Analysis: A Powerful Tool for Process Identification of Electrochemical Systems. *Journal of Power Sources* **2023**, 233845. https://doi.org/10.1016/j.jpowsour.2023.233845.
(28) Hahn, M.; Schindler, S.; Triebs, L.-C.; Danzer, M. A. Optimized Process Parameters for a Reproducible Distribution of Relaxation Times Analysis of Electrochemical Systems. *Batteries* **2019**, *5* (2), 43. https://doi.org/10.3390/batteries5020043.
(29) Hahn, M.; Rosenbach, D.; Krimalowski, A.; Nazarenus, T.; Moos, R.; Thelakkat, M.; Danzer, M. A. Investigating Solid Polymer and Ceramic Electrolytes for Lithium-Ion Batteries by Means of an Extended Distribution of Relaxation Times Analysis. *Electrochimica Acta* **2020**, *344*, 136060. https://doi.org/10.1016/j.electacta.2020.136060.
(30) Xu, H.; Xie, J.; Liu, Z.; Wang, J.; Deng, Y. Carbonyl-Coordinating Polymers for High-Voltage Solid-State Lithium Batteries: Solid Polymer Electrolytes. *MRS Energy & Sustainability* **2020**, *7* (1), 1. https://doi.org/10.1557/mre.2020.3.
(31) Yang, H.; Wu, N. Ionic Conductivity and Ion Transport Mechanisms of Solid-State Lithium-Ion Battery Electrolytes: A Review. *Energy Science & Engineering* **2022**, *10* (5), 1643–1671. https://doi.org/10.1002/ese3.1163.

I.11 Supporting Information

I.11.1 Synthesis of M2

Commercially available M1 (1 g, 3.37 mmol) was dissolved in anhydrous THF and placed in an ice bath under inert atmosphere. To this ice-cold solution, 1-butanethiol (243 mg, 2.7 mmol) and Me_2PPh (4.7 mg, 0.0337 mmol) were added dropwise and stirred at room temperature for 2 h. Subsequently, the reaction was stopped and the THF in the reaction mixture was evaporated. The crude product was purified by column chromatography using silica gel (60-120 mesh) as a stationary phase and 10 % DCM/hexane as eluent. (1 g, 77 % yield). ^{1}H-NMR ($CDCl_3$, 400 MHz, TMS): δ (ppm)= 6.42 (d, 2H), 6.12 (m, 2H), 5.85 (d, 2H), 4.17-4.10 (m, 6H), 2.74 (m, 2H), 2.61 (m, 2H), 2.52 (m, 2H), 1.62 (m, 1H,), 1.55 (m, 2H), 1.40 (m, 2H), 0.91 (t, 6H).

I.11.2 NMR spectroscopy

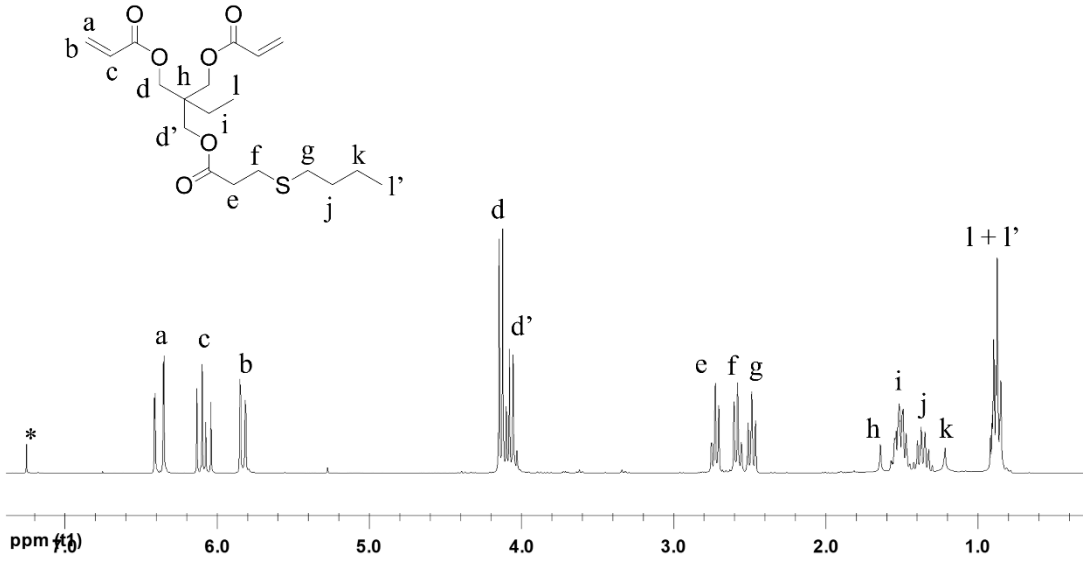


Figure S.I.1. ^{1}H-NMR of M2 in $CDCl_3$ (* indicates residual solvent peak).

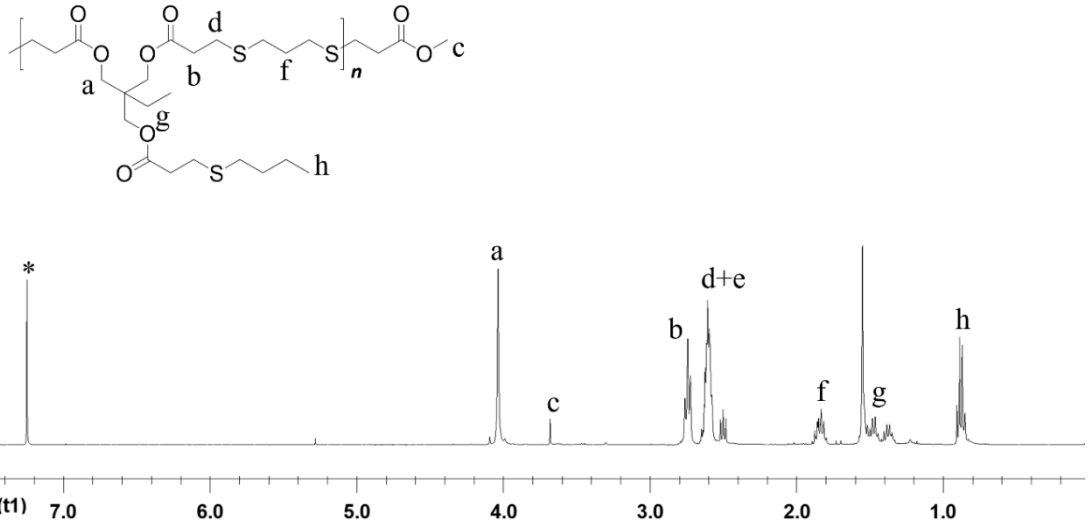


Figure S.I.2. ^{1}H-NMR of L-P1 (with peak assignment) in $CDCl_3$ (* indicates residual solvent peak).

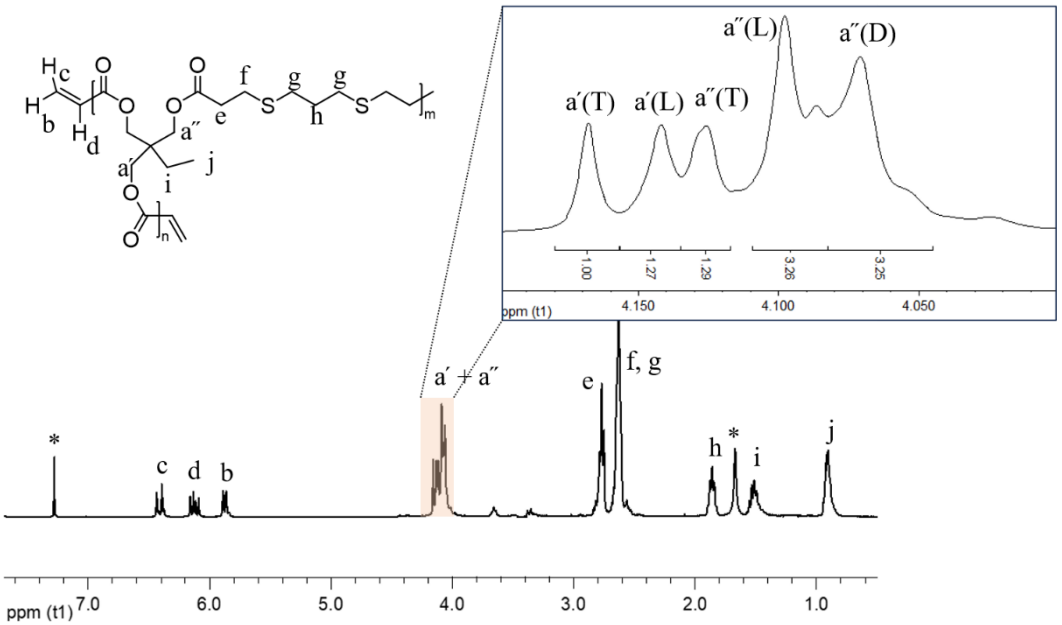


Figure S.I.3. ^{1}H-NMR of HB-P1a in $CDCl_3$. The highlighted part depicts different extents of methylene proton shift of triacrylate monomer after thiol-acrylate Michael addition reaction that results in linear, terminal and dendritic components, present in the HB-P1a polymer. Comparing the peak intensity, degree of branching could be estimated to be 0.59. Likewise, from the ^{1}H NMR spectra of HB-P2a (shown in Figure I.1), degree of branching was estimated to be 0.6. (* indicates residual solvent peak).

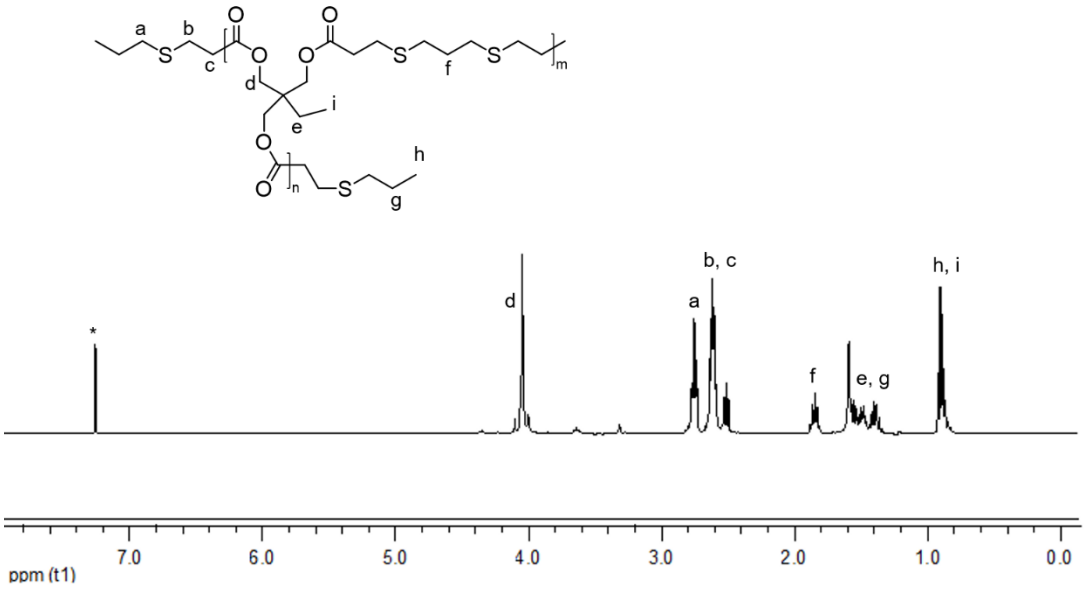


Figure S.I.4. ^{1}H-NMR of HB-P1 (with corresponding peak assigned) in $CDCl_3$ (* indicates residual solvent peak).

I.11.3 Molecular Weight Determination

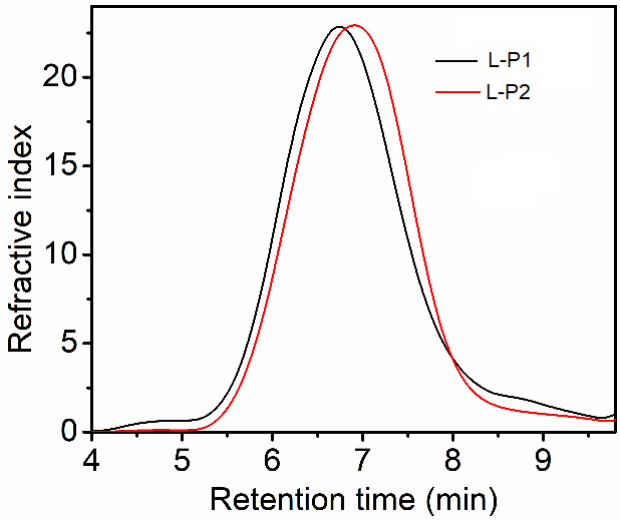


Figure S.I.5. GPC chromatogram of linear polyesters L-P1 and L-P2 in THF.

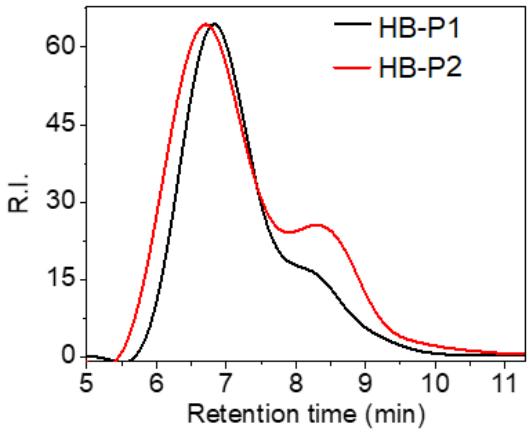


Figure S.I.6. Size exclusion chromatogram (SEC) of hyperbranched poly beta-thiopropionate ester HB-P1 and HB-P2 in THF.

I.11.4 Electrolyte Composition

The electrolytes were prepared by dissolving the polymer in chloroform (ca. 0.75 mL per 100 mg of polymer). Lithium-bis(trifluoromethanesulfonyl)imide (LiTFSI) was weighed inside an argon-filled glovebox. The molar concentration of lithium salt was 10:1 with respect to the carbonyl groups of the polymer repeating unit to the number of lithium cations (C=O/Li 10). The LiTFSI is dissolved in acetonitrile (the same amount of ACN as chloroform). The two solutions are combined and stirred for 1 h. Afterwards, the electrolyte mixtures are dried in high vacuum at 80 °C. After drying the electrolytes are transferred to an argon-filled glovebox for later use.

Table S.I.1. Electrolyte composition for L-P1, L-P2, HB-P1, and HB-P2-based electrolytes with LiTFSI.

Polymer	Polymer mg	LiTFSI mg	C=O/Li	LiTFSI content wt%	Solvent
L-P1	205.0	35.6	10	14.8	1.5 mL $CHCl_3$ + 1.5 mL ACN
L-P2	189.2	30.3	10	13.8	1.5 mL $CHCl_3$ + 1.5 mL ACN
HB-P1	275.7	46.2	10	14.4	2.0 mL $CHCl_3$ + 2.0 mL ACN
HB-P2	221.5	31.9	10	12.6	1.5 mL $CHCl_3$ + 1.5 mL ACN

I.11.5 Electrochemical Impedance Spectroscopy

The temperature-dependent ionic conductivity was evaluated by electrochemical impedance spectroscopy (EIS) at different temperatures between 25 °C and 80 °C. The experiments were conducted using coin-cells in StSt|electrolyte (thickness 500 µm, diameter 3 mm)|StSt configuration. The data is evaluated by extended distribution of relaxation times (eDRT) analysis. The figures below show exemplary data for each polymer electrolyte the respective polymer together with LiTFSI at a molar ratio between polymer carbonyl groups and lithium of 10 (C=O/Li 10).

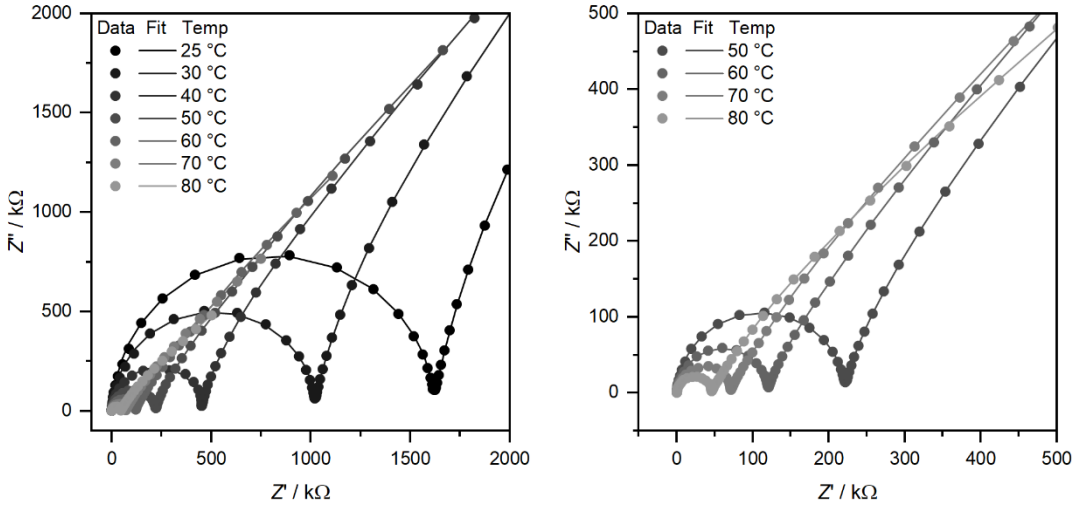


Figure S.I.7. L-P1 (left) Nyquist plot of temperature-dependent EIS measurements and eDRT fit for L-P1 + LiTFSI (C=O/Li 10) electrolytes (right) Enlargement of the measurements at 80 °C, 70 °C, and 60 °C.

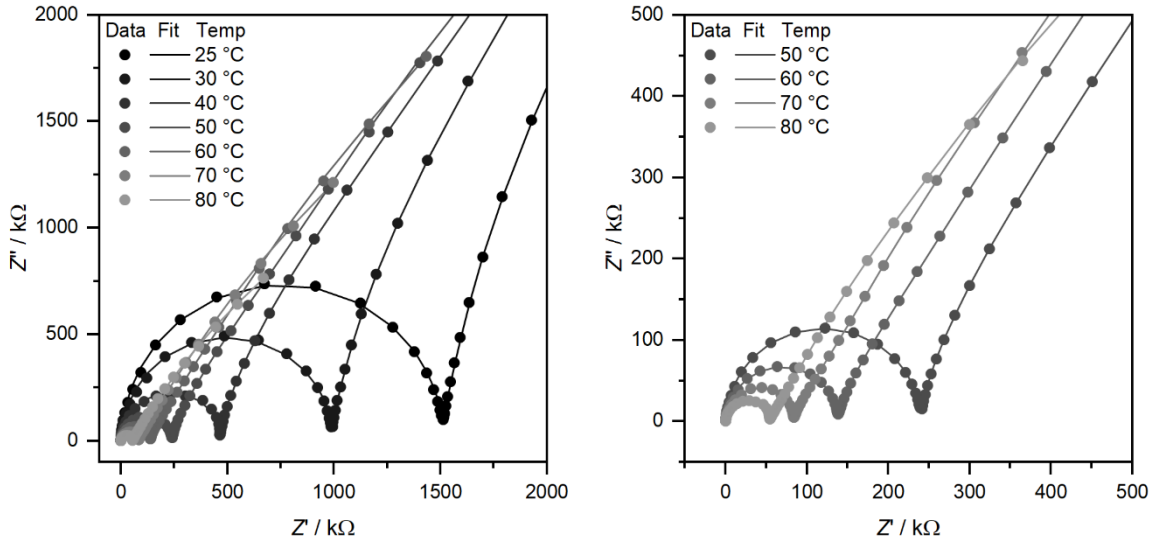


Figure S.I.8. L-P2 (left) Recorded electrochemical impedance spectra and eDRT fit for L-P2 + LiTFSI (C=O/Li 10) electrolytes. (right) Enlargement of the measurements at 80 °C, 70 °C, and 60 °C.

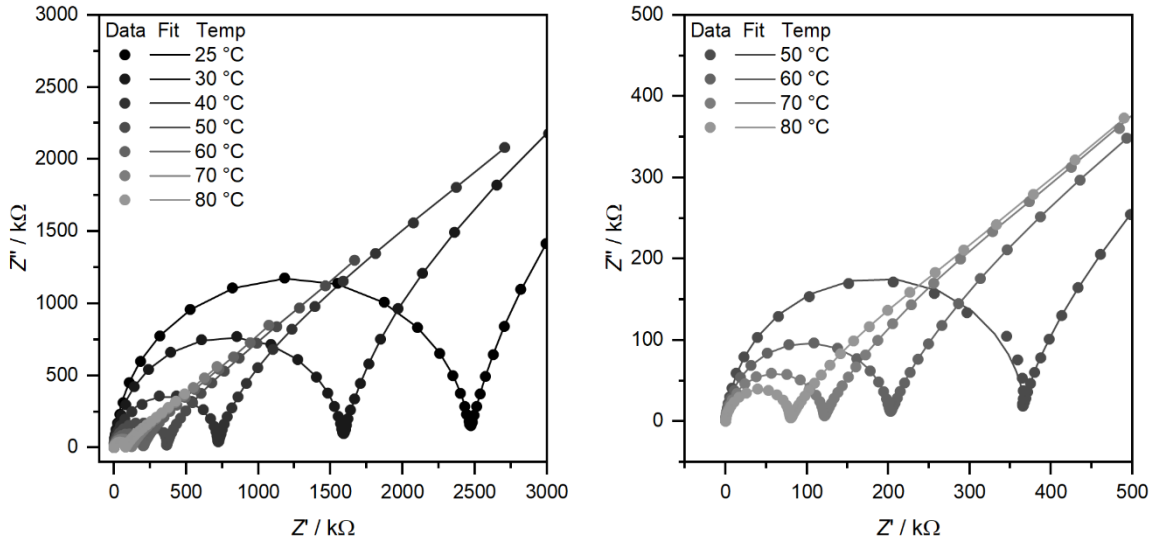


Figure S.I.9. HB-P1 (left) Recorded electrochemical impedance spectra and eDRT fit for HB-P1 + LiTFSI (C=O/Li 10) electrolytes. (right) Enlargement of the measurements at 80 °C, 70 °C, and 60 °C.

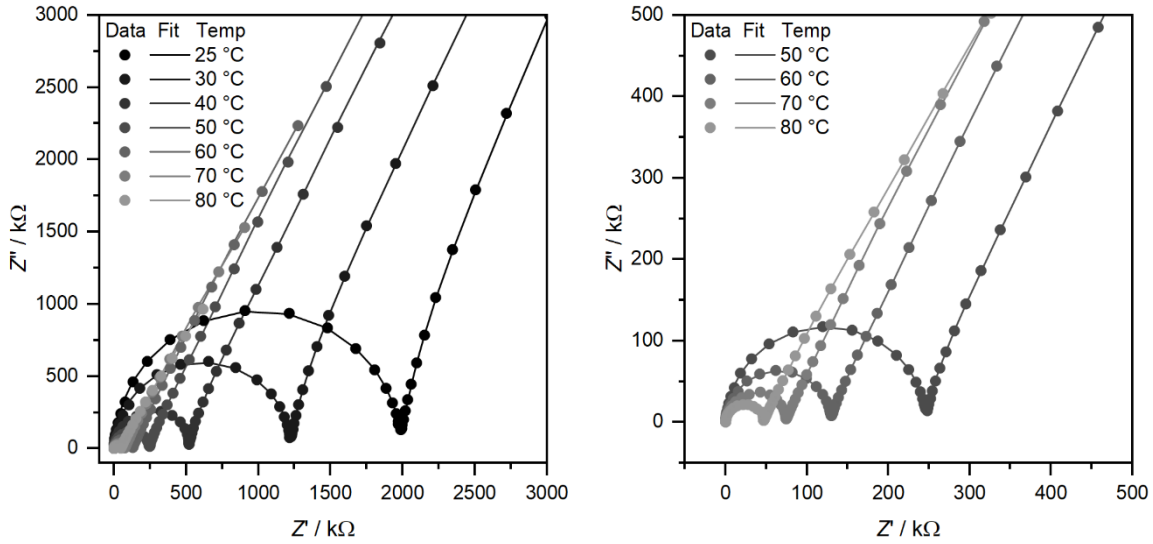


Figure S.I.10. HB-P2 (left) Recorded electrochemical impedance spectra and eDRT fit for HB-P2 + LiTFSI (C=O/Li 10) electrolytes. (right) Enlargement of the measurements at 80 °C, 70 °C, and 60 °C.

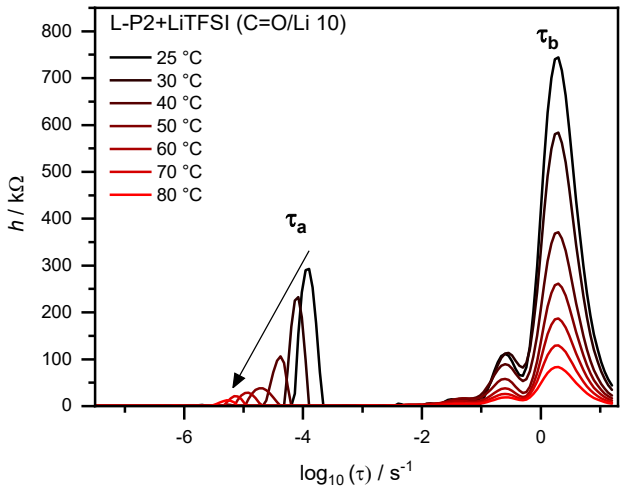


Figure S.I.11. Extended distribution of relaxation times for L-P2. The DRT results are represented by the absolute distribution function $h(\tau)$. τ_a and τ_b can be attributed to the ionic conductivity and capacitive behavior, respectively.

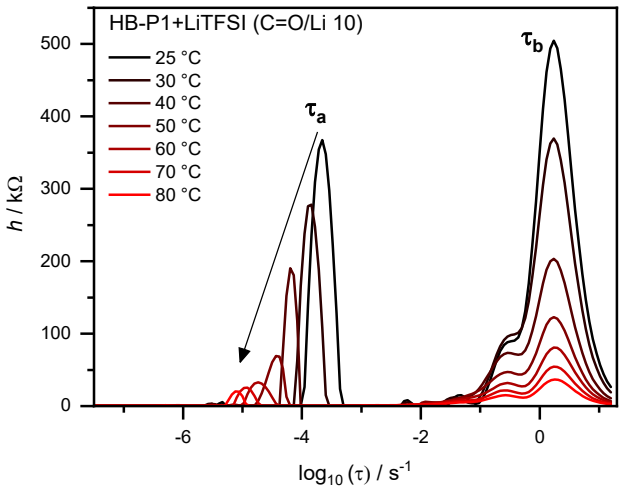


Figure S.I.12. Extended distribution of relaxation times for HB-P1. The DRT results are represented by the absolute distribution function $h(\tau)$. τ_a and τ_b can be attributed to the ionic conductivity and capacitive behavior, respectively.

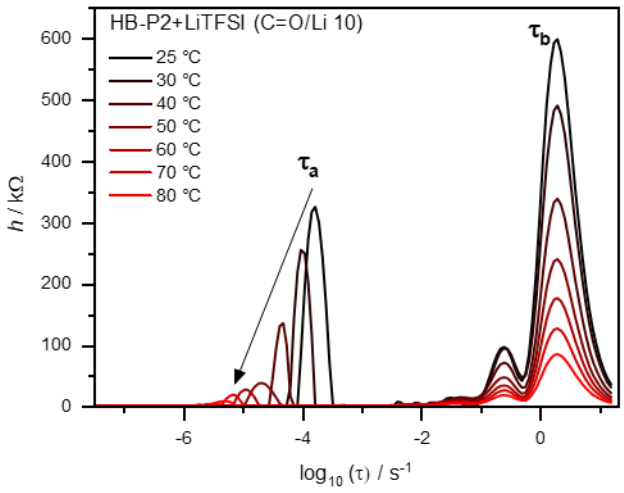


Figure S.I.13. Extended distribution of relaxation times for HB-P2. The DRT results are represented by the absolute distribution function $h(\tau)$. τ_a and τ_b can be attributed to the ionic conductivity and capacitive behavior, respectively.

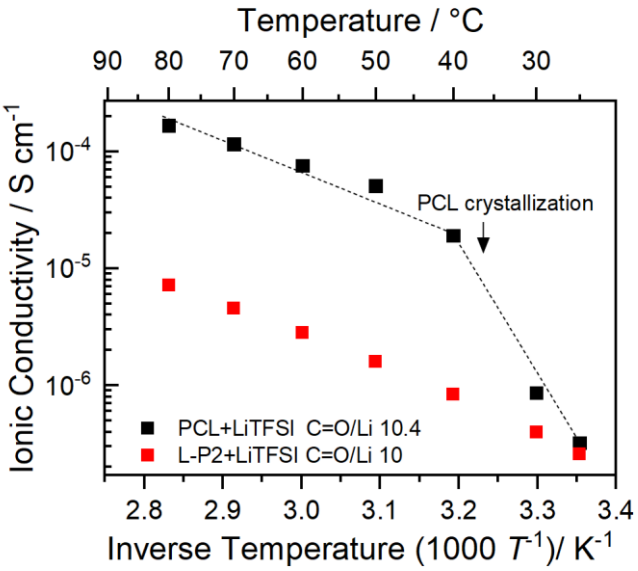
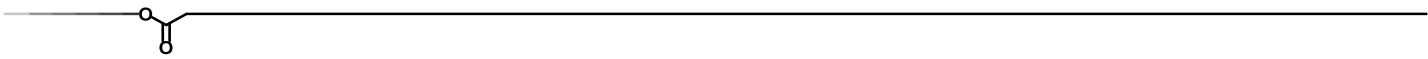


Figure S.I.14. Arrhenius plots of the temperature-dependent ionic conductivity (80 °C – 25 °C) for the electrolytes based on (red) L-P2+LiTFSI and (black) PCL+LiTFSI for comparable C=O/Li ratios. Below 40 °C the ionic conductivity of PCL is significantly reduced because of polymer crystallization. The dotted line is a guide to the eye. L-P2 does not exhibit a crystallization-induced drastic decrease because the polymer is completely amorphous without any thermal transitions besides the glass transition.



II Synthesis and Comparison of Main Chain, Side Chain, and Grafted Polyester-based Architectures as Solid Polymer Electrolytes

Jannik Petry[a], Marcel Sticher[a], Gabriele Caputo[a] and Mukundan Thelakkat*[abc]

[a] Applied Functional Polymers, University of Bayreuth, Universitätsstraße 30, 95447 Bayreuth, Germany
[b] Bavarian Polymer Institute (BPI), University of Bayreuth, Universitätsstraße 30, 95447 Bayreuth, Germany
[c] Bavarian Center for Battery Technology (BayBatt), University of Bayreuth, Universitätsstraße 30, 95447 Bayreuth, Germany

* Corresponding Author
E-mail: mukundan.thelakkat@uni-bayreuth.de

II.1 Abstract

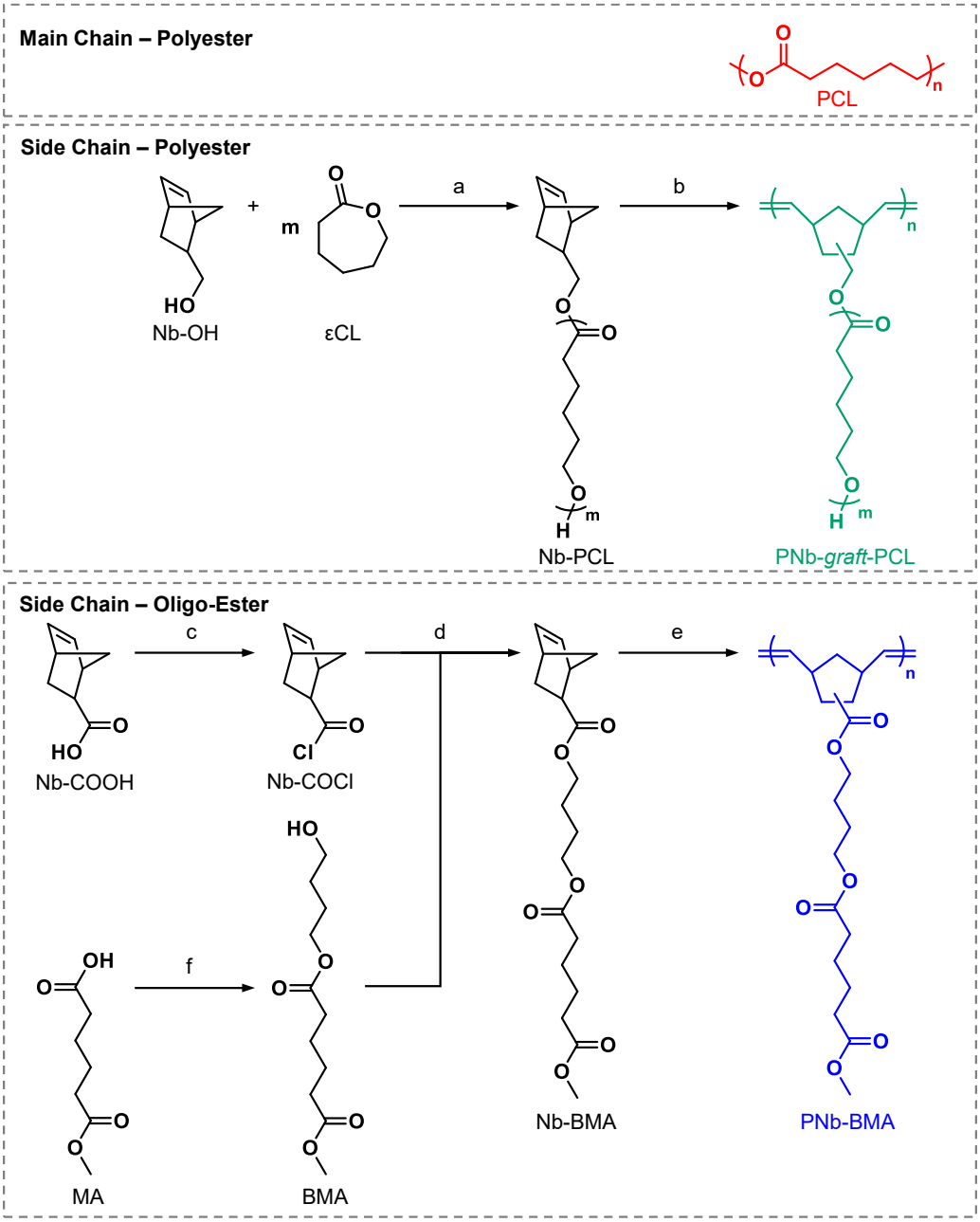
We synthesized two norbornene-based polymers with short ester-containing pendant groups (PNb-BMA) and grafted polyester side chains (PNb-*graft*-PCL) and evaluated and compared the architectural influences with benchmark polyester poly(ε-caprolactone) for their application as solid polymer electrolytes. The polymers are prepared by ring-opening metathesis polymerization using functionalized norbornene-based monomers. To ensure comparability between the different polymer systems, the molecular weight of the synthesized polymer materials was adjusted during synthesis. The polymers are combined with LiTFSI at a wide range of salt concentrations from C=O/Li 2.5 to 100. The thermal properties of the polymers and resulting electrolytes were investigated regarding their glass transition temperatures and polymer crystallinity. The correlation of polymer properties, ion coordination, and the temperature-dependent ionic conductivity is investigated by detailed IR spectroscopy, electrochemical impedance spectroscopy, and VTF analysis.

II.2 Introduction

In the field of solid polymer electrolytes, poly(ethylene oxide) (PEO) has long been the benchmark material due to its compatibility with many lithium salts, excellent salt dissociation, and low glass transition temperature.[1–4] However, its strong lithium ion coordination and conversely low lithium transference number (LTN) of 0.1-0.2, limited oxidative stability, and high degree of crystallinity limit its application in next-generation solid state batteries.[5–7] To overcome these challenges, various polymer architectures and additives have been investigated.[8–12] Going beyond PEOs' ether coordination, alternative coordination motifs are intensively investigated. Especially oxy-compounds, including esters and carbonates, are viable alternatives to the ether coordination, offering lower coordination strength, increased electrochemical stability, and superior molecular design flexibility.[13–15] The ester-based counterpart to well-established PEO is poly(ε-caprolactone) (PCL), showing significantly improved lithium transference numbers (0.5-0.7) and comparable glass transition temperatures. However, both polymers share their high degree of crystallinity and melting temperatures above the desired application temperature, leading to significant drops in ionic conductivity at moderate temperatures. In this study, we applied established architectural design strategies of PEO-based systems to the class of ester-based systems to influence physicochemical polymer properties and investigate the effects on the resultant electrochemical characteristics. As an alternative to ion-coordinating groups as structural constituents of a linear polymer main-chain, ion-coordinating moieties are incorporated as grafted side-chain constituents or pendant side groups. Therefore, we synthesized two norbornene-based polymers: 1) a polynorbornene with grafted poly(ε-caprolactone) in a bottlebrush polymer architecture and 2) a linear polynorbornene with short pendant oligo-ester side groups. The synthesized polymers are compared to commercially available linear PCL regarding their thermal properties, ion-coordination, and ionic conductivity across a wide range of salt concentrations.

II.3 Results and Discussion

The bottlebrush polymer was synthesized in a grafting-through approach to ensure a quantitative grafting density along the central polymer backbone (**Scheme II.1**, middle). At first, the corresponding macromonomer (Nb-PCL) was prepared by an organic base-assisted ring-opening polymerization. 5-Norbornen-2-methanol (Nb-OH) was used as the initiator and to establish the polymerizable moiety of the macromonomer. In a subsequent ring-opening metathesis polymerization (ROMP) using 3rd-generation Grubbs catalyst (G3), the macromomer was polymerized to yield the poly(norbornene)$_n$-*graft*-poly(ε-caprolactone)$_m$ (PNb-*graft*-PCL). Similar to the bottlebrush polymer, a norbornene-based monomer was used for the polymerization of poly(butyl-4-{methyl adipate])norbornene-2-carboxylate) (PNb-BMA) (**Scheme II.1**, middle). For the monomer synthesis, 5-norbornene-2-carboxylic acid (Nb-COOH) is converted to the corresponding acid chloride (Nb-COCl). The side chain is prepared by an esterification reaction of methyl adipate and 1,4-butane diol to yield 4-hydroxybutyl methyl adipate (BMA).[14] Subsequently, the Nb-COCl and BMA are combined in an esterification reaction to yield the corresponding norbornene-based monomer (Nb-BMA). Nb-BMA is polymerized using ROMP to form PNb-BMA. All of the reactions were monitored using ^{1}H NMR spectroscopy (**Figure S.II.1-4**). The molecular weights of the synthesized polymers were investigated by size-exclusion chromatography (SEC) and are stated in **Table II.1** and presented in **Figure S.II.5**.



Scheme II.1. Chemical structures of the polymer materials and synthetic routes for the synthesized polymers PNb-*graft*-PCL and PNb-BMA. degree of polymerization of the (n) polymer backbone and (m) of the grafted side chain. a) Toluene, RT, 5 h, TBD; b) G3, 15 °C, 1 h; c) $CHCl_3$, $SOCl_2$, reflux, 4h; d) DCM, pyridine, 3 h; e) DCM, G3, 1h; f) DCM, pyridine, 0°C, 15 h.

The stated molecular weight of the commercially available PCL was 80000 g mol^{-1}. Therefore, similar molecular weights were targeted during the ROMP by adjusting the monomer-to-initiator ratio. SEC experiments using a THF-based eluent (salt additive: 0.25 wt% TBAB) and PS calibration showed an increased molecular weight for the PCL and deviations between theoretical and experimental molecular weights of the synthesized materials (**Table II.1**). However, the chemical and structural distinctions of the polymer materials can induce experimental error using a relative molecular weight determination technique, like SEC. Especially for bottlebrush polymers, challenges for the exact determination of the molecular weight are reported in the literature.[16–18] The graft copolymer PNb-*graft*-PCL showed increased molecular weights compared

to the calculated molecular weight based on the ratio of monomer to initiator and the molar mass of the monomer. On the other hand, PNb-BMA showed lower molecular weight. However, both polymers showed narrower polydispersity than the commercial PCL reference. The thermal stability was evaluated by thermogravimetric analysis (**Table II.1**, **Figure S.II.6**). While the thermal stability of PCL and PNb-*graft*-PCL is significantly higher than that of PNb-BMA, all of the materials are sufficiently stable for their application in LMBs.

Table II.1. Overview of the determined molecular weights, thermal stability, and thermal transitions for the pristine materials and corresponding electrolytes.

		PCL	PNb-*graft*-PCL	PNb-BMA
$M_{n,theo}$[a]	g mol^{-1}	-	80000	80000
M_n[b]	g mol^{-1}	114000[b]	97600[c]	57500[b]
$Đ$[d]		1.48	1.12	1.25
$T_{d,5\%}$[d]	°C	383	351	229

[a] calculated based on $[M]_0/[I]_0 \cdot M_{monomer}$; [b] determined by SEC, eluent: THF+0.25 wt% TBAB, PS calibration; [c] eluent: $CHCl_3$, PS calibration; [d] M_w/M_n; [e] determined by TGA at a remaining sample weight of 95 %.

SPEs are formulated by combining the polymers with LiTFSI at different salt concentrations ranging from C=O/Li 100 to 2.5, corresponding to salt weight proportions between 2 wt% and 50 wt%, respectively. For PNb-BMA electrolytes, no homogeneous polymer-salt mixtures could be obtained at C=O/Li 5 and 2.5, showing non-dissolved salt residues after the mixing procedure. Based on results from PCL and PNb-*graft*-PCL, the salt concentrations of C=O/Li 50 and 20 were not investigated for PNb-BMA. For these systems, the results for ionic conductivity, ion coordination, and activation energies fell well into the general trends, which will be discussed in detail later. The thermal characteristics of the pristine polymers and SPEs were investigated by differential scanning calorimetry (DSC) (**Table II.2**, **Figure S.II.7**). However, some electrolytes showed only weak or no glass transitions in DSC experiments. The glass transition was then analyzed by dynamic mechanical analysis (DMA) (**Table II.2**, **Figure S.II.8**, **Figure S.II.9**).

Table II.2. Overview of the determined thermal transitions for the pristine materials and corresponding electrolytes.

	PCL			PNb-*graft*-PCL			PNb-BMA		
C=O/Li	T_g	T_m	ΔH_m	T_g	T_m	ΔH_m	T_g	T_m	ΔH_m
	°C	°C	J g^{-1}	°C	°C	J g^{-1}	°C	°C	J g^{-1}
-[a]	-66.4[b]	56.5	66.4	-69.3[b]	43.4	59.8	-47.2[b]	n.c.	n.c.
100	-61.5[b]	53.8	53.2	-69.6[b]	42.2	59.4	-45.5[c]	n.c.	n.c.
50	-55.8[c]	53.7	49.0	-60.3[b]	42.1	58.0	-	-	-
30	-50.5[c]	53.0	47.8	n.d.	40.5	51.1	-44.4[c]	n.c.	n.c.
20	-47.1[c]	53.7	40.2	-47.8[b]	39.6	41.6	-	-	-
15	-46.2[c]	51.6	45.4	-46.8[b]	38.5	41.5	-37.9[c]	n.c.	n.c.
10	-42.2[c]	49.8	35.7	-48.7[c]	33.8	29.6[d]	-28.7[c]	n.c.	n.c.
7.5	-41.4[c]	44.1	28.9[d]	-47.1[c]	29.7	7.8[d]	-29.0[c]	n.c.	n.c.
5	-46.4[c]	n.c.	n.c.	-41.3[c]	n.c.	n.c.	-	-	-
2.5	-31.9[c]	n.c.	n.c.	-41.2[c]	n.c.	n.c.	-	-	-

[a] polymer without added LiTFSI, [b] Determined by DMA from the second heating cycle at 10 K min^{-1}; [c] Determined by DSC from the second heating cycle at 10 K min^{-1}; [d] sample shows recrystallization during heating.

With increasing salt concentration, all of the SPE systems showed increasing glass transition temperatures. Compared to linear PCL, the bottlebrush polymer PNb-*graft*-PCL generally showed lower glass transition temperatures. Due to the bottlebrush architecture, the central high T_g norbornene backbone does not increase the system's overall T_g. The polymer elongation and reduced polymer entanglement for bottlebrush polymers induced the reduced transition temperatures. On the other hand, the short oligo-ester side chains in PNb-BMA are not sufficient to outweigh the high T_g of the norbornene polymer backbone. The T_g of PNb-BMA and its electrolytes are around 20 °C higher than for the other systems.

Nevertheless, the advantage of PNb-BMA is its entirely amorphous character at any salt concentration. The linear architecture of PCL and the grafted PCL side chains of PNb-*graft*-PCL induce semi-crystalline properties. The plasticizing effect of LiTFSI in SPEs leads to decreasing melting enthalpies (ΔH_m) with increasing salt concentration. At high salt concentrations (C=O/Li 5 and 2.5), the crystallization is suppressed, and the electrolytes show amorphous characteristics (**Figure S.II.7**). In the pristine state without salt, compared to linear PCL, the PNb-*graft*-PCL shows a slightly reduced melting enthalpy. The melting enthalpies are higher for PNb-*graft*-PCL at low salt concentrations (C=O/Li 100, 50, 30, 20) but lower at higher salt concentrations. However, expectedly, the observed enthalpies are in the same range for both polymers, as both are mostly constituted by linear PCL chains. The different polymer architectures result in significant differences in the melting temperatures. On average, the melting temperatures are reduced by more than 13 °C in the bottlebrush architecture. According to the Gibbs-Thomson effect, this indicates reduced crystallite sizes for PNb-*graft*-PCL.[19,20] Lowering the melting temperature in semi-crystalline materials can improve the low-temperature ionic conductivity, which is discussed in detail later.

In addition to the effects of salt concentration on the thermal properties of the SPEs, the ion-coordination is investigated by infrared (IR) spectroscopy in the carbonyl stretching region between 1600 and 1800 cm^{-1} (**Figure II.1**). The salt-free polymer materials showed a single peak at 1730-1735 cm^{-1} which is assigned to the stretching vibration ν(C=O) of non-coordinating carbonyl moieties. Upon the addition of LiTFSI, a secondary peak arises at lower wavenumbers (1690-1705 cm^{-1}) corresponding to carbonyl units contributing to lithium coordination. The individual peaks are deconvoluted by nonlinear double-peak Gaussian fitting (results in **Table S.II.1-3**). The individual peak areas of the two contributions ($A_{\nu(C=O)}$, $A_{\nu(C=O\cdots Li)}$) were used to calculate the fraction of coordinating carbonyl moieties (ϕ_{Li^+}). For all three polymers, ϕ_{Li^+} generally increased with increasing salt concentration. At very low salt concentrations, ϕ_{Li^+} was at around 12-13 % for all polymers and reached up to 81 % at high salt concentrations for PCL and PNb-*graft*-PCL. At comparable salt concentrations, PNb-*graft*-PCL showed slightly higher ϕ_{Li^+} values than linear PCL. This could indicate that carbonyls are more accessible in the bottlebrush polymer architecture and have more degrees of freedom to orient for ion coordination. Compared to the other systems at C=O/Li ratios of 7.5 and 10, PNb-BMA exhibited very high ϕ_{Li^+}. For the polyester side chains in PNb-*graft*-PCL, the ion-coordination of ester groups in the proximity of the central norbornene backbone is unfavorable, due to dense chain packing and steric hindrance.[21,22] This suggests that the short oligo-ester side chains in PNb-BMA are well accessible for ion-coordination.

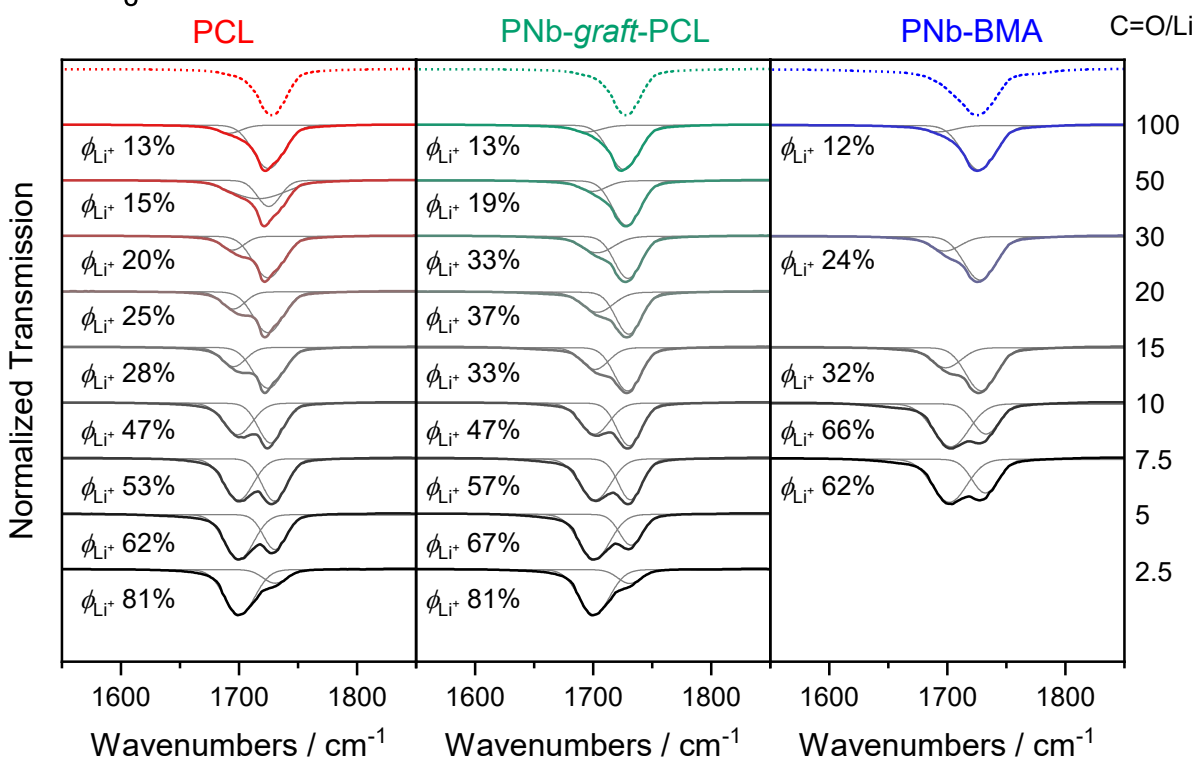


Figure II.1. Transmission FT-IR spectra of the (dashed lines) pristine polymers (red) PCL, (green) PNb-*graft*-PCL, (blue) PNb-BMA, and (solid lines) corresponding electrolytes at different C=O/Li ratios from 100 to 2.5. (gray lines) Double-peak Gaussian peak fits for non-coordinating carbonyl peaks, ν(C=O) at 1730 cm^{-1} and coordinating carbonyl peaks, ν(C=O---Li) at 1705 cm^{-1}. The fraction of coordinated carbonyl groups (ϕ_{Li^+}) is calculated as the ratio of $A_{\nu(C=O---Li)}/(A_{\nu(C=O)}+A_{\nu(C=O---Li)})$.

Finally, the ionic conductivity of the electrolyte systems was evaluated by electrochemical impedance spectroscopy (EIS) in symmetrical stainless steel test cells. For all of the electrolyte systems, the maximum of the ionic conductivity could be observed around a lithium salt concentration of C=O/Li 7.5 and 10 (**Figure II.2**a, all electrolyte systems **Figure S.II.10**). The ionic conductivity shows a distinct curvature across the temperature range instead of a linear Arrhenius-type temperature activation. The temperature-dependence of SPEs can be better described by the Vogel-Tammann-Fulcher (VTF) model, which takes into account the correlation between ionic conductivity and the segmental mobility of the polymer (Eq. II.1). The ionic conductivity is described by the prefactor *A*, which is mostly dependent on the salt/charge carrier concentration, the VTF pseudo-activation energy (*B*), and correlated to the material-dependent Vogel temperature (T_0). For polymer systems, T_0 is often approximated as $T_0 = T_g - 50$ °C. The VTF model underlines the importance of the glass transition temperature on the ionic conductivity even at application temperatures above the material's T_g.[14,23–26].

$$\sigma = A \cdot exp\left(-\frac{B}{R(T-T_0)}\right) \qquad \text{(II.1)}$$

In the VTF plots (**Figure S.II.11**), the ionic conductivity is plotted against the absolute temperature corrected by the individual T_0 of the polymer electrolyte systems. The resulting temperature-dependent ionic conductivities show linear temperature activation. From linear fits, the prefactor (*A*) and the pseudo activation energy (*B*) can be calculated (details in supporting information). The resulting parameters for the three electrolyte systems at the investigated salt concentrations are displayed in **Figure II.2**b. In accordance with its salt concentration

dependence, the prefactor *A* increases with increasing salt concentrations. The determined activation energies of PCL and PNb-*graft*-PCL are significantly lower than for PNb-BMA, especially at low salt concentrations. Additionally, the activation energy of PNb-BMA is similar across all salt concentrations from C=O/Li 7.5 to 100. On the other hand, the other systems show increasing activation energies at higher salt concentrations. This correlates to the increasing fraction of coordinating carbonyl moieties, as observed in FTIR measurements. At very high salt concentrations, the coordination sites are more occupied, impeding the ion-hopping events between different coordination sites. Additionally, at increasing salt concentrations, ion-pairing and quasi-ionic crosslinking of polymer segments are more pronounced, increasing the glass transition temperature and limiting segmental mobility. For PNb-BMA, the similarities between the activation energies are more correlated with the high T_g of the electrolyte systems. As the T_g is already higher for these systems, the ionic conductivity is less sensitive to the addition of higher salt concentrations but is dominated by the high T_g. The salt-dependent ionic conductivity reflects the combined influence of the ion-coordination environment, glass transition and melting temperatures, transition enthalpies, and the VTF parameters (**Figure II.2**c,d).

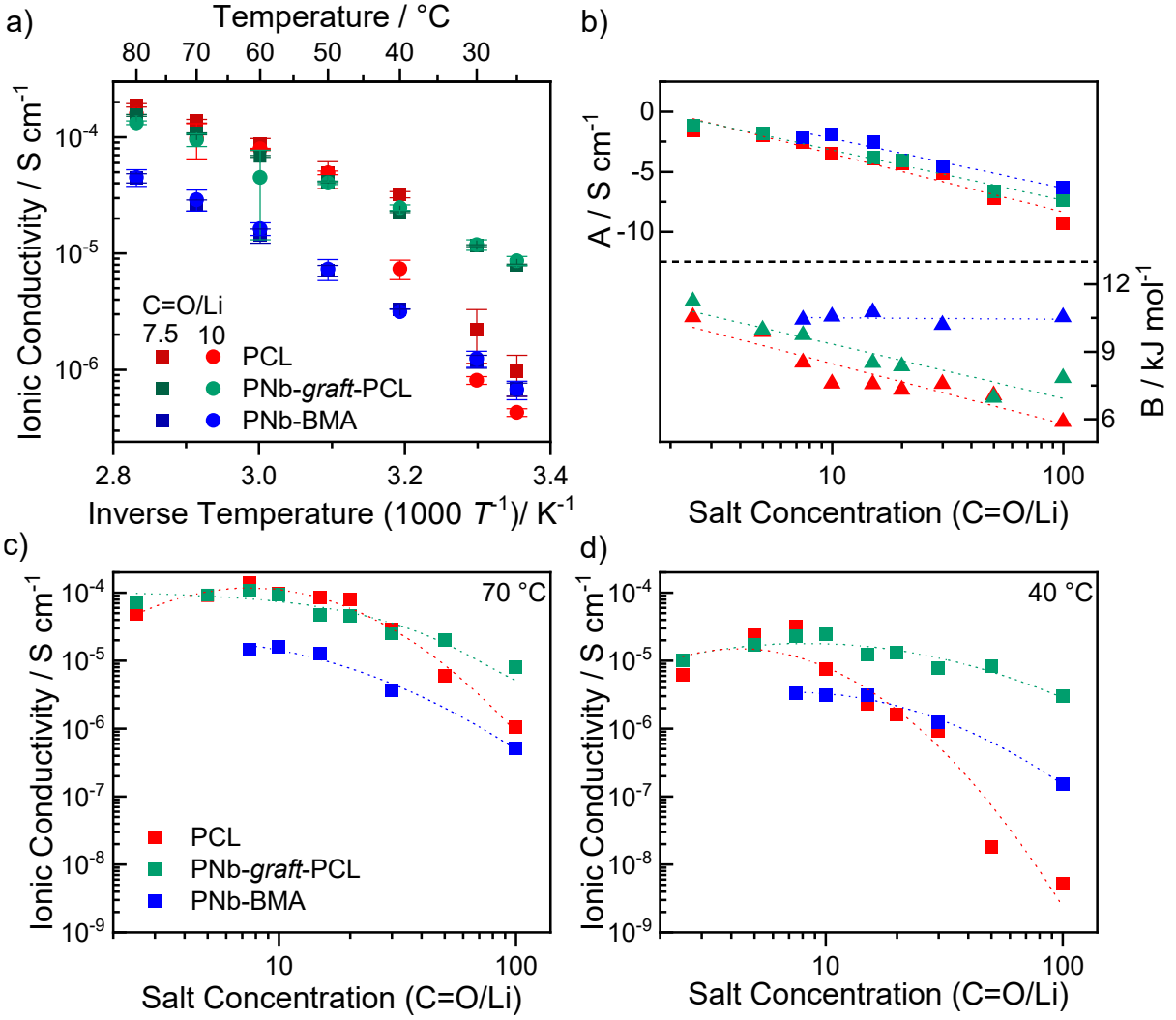


Figure II.2. Evaluation of the ionic conductivity for electrolyte systems based on (red) PCL, (green) PNb-*graft*-PCL, and (blue) PNb-BMA at different LiTFSI concentrations. (a) Arrhenius plots of the temperature-dependent ionic conductivity of SPEs. (b) Salt concentration-dependent VTF-fit parameters. (c+d) Salt concentration-dependent ionic conductivity at 70 °C and 40 °C. The dotted lines in all subfigures represent guidelines for the eyes.

At any temperature, the ionic conductivity of PCL and PNb-*graft*-PCL decreases at salt concentrations above C=O/Li 7.5, which can be attributed to the increasing activation energy, ion-pair formation, and occupation of the coordination sites. **Figure II.2**c shows the ionic conductivity at 70 °C, which is above the melting temperature of all electrolyte systems. Under these fully amorphous conditions, the ionic conductivity of PCL and PNb-*graft*-PCL is very comparable, whereas the ionic conductivity of PNb-BMA is significantly lower. Overall, PNb-*graft*-PCL shows a lower decline of the ionic conductivity at either very high (C=O/Li 2.5) or very low (C=O/Li > 30) salt concentrations. The more pronounced decline of PCL, especially at low salt concentrations, can be attributed to the higher glass transition and melting temperatures. However, the maximum conductivity could be observed for PCL at C=O/Li 7.5. Under these optimum conditions, the lower proportion of conducting PCL-phase in PNb-*graft*-PCL (94 wt% PCL) limits the ionic conductivity of the PNb-*graft*-PCL system.[7] At any salt concentration, the ionic conductivity of PNb-BMA was lower than for the other electrolyte systems. For PNb-BMA, both the non-conducting central norbornene backbone constitutes an even higher proportion, and the high glass transition temperatures limit the ionic conductivity. The results at 40 °C show a more pronounced decline of the ionic conductivity for linear PCL at low salt concentrations induced by the residual crystallinity for linear PCL (**Figure II.2**d). Although PNb-*graft*-PCL also showed crystalline behavior, the lower transition enthalpy and temperatures suppressed this decrease. The amorphous properties of PNb-BMA lead to a higher ionic conductivity than for semi-crystalline linear PCL at low salt concentrations.

II.4 Conclusion

In conclusion, we translated architectural design strategies known in PEO-based systems to ester-containing polymer electrolytes. We compared linear main-chain polyester (PCL) with side-chain polyesters (PNb-*graft*-PCL) and side-chain oligoesters (PNb-BMA). The relocation of the ester motif into grafted or pendant side chains resulted in different glass transition temperatures, melting behavior, crystallinity, and segmental mobility. FTIR analysis revealed a higher fraction of coordinating carbonyl moieties for PNb-*graft*-PCL and PNb-BMA at higher salt concentrations, indicating better accessibility than in linear PCL. The ionic conductivity is governed by the combined effects of ion coordination, thermal transitions, and the proportion of conducting phase. Overall, the bottlebrush architecture of PNb-*graft*-PCL showed the best balance under different salt concentrations and application temperatures. The reduced melting temperatures, low glass transition temperatures, and a balance between free and coordinating carbonyl moieties at moderate salt concentrations result in the best compromise for the ionic conductivity. The investigation of architectural influences highlights the importance of fundamental polymer properties on the materials' potential for application as a solid polymer electrolyte.

II.5 Supporting Information

Materials, experimental procedures, ^{1}H NMR spectra, thermogravimetry, differential scanning calorimetry, dynamic mechanical analysis, FTIR, and Arrhenius and VTF plots are provided in the supporting information.

II.6 Funding Sources and Acknowledgements

This work was supported by the Bavarian Ministry of State for Research and Arts under the SolTech project. JP was supported with a fellowship by the Deutsche Bundesstiftung Umwelt. (grant no.: 20021/714-242)

II.7 References

(1) Xue, Z.; He, D.; Xie, X. Poly(Ethylene Oxide)-Based Electrolytes for Lithium-Ion Batteries. *Journal of Materials Chemistry A* **2015**, *3* (38), 19218–19253. https://doi.org/10.1039/C5TA03471J.

(2) Hahn, M.; Rosenbach, D.; Krimalowski, A.; Nazarenus, T.; Moos, R.; Thelakkat, M.; Danzer, M. A. Investigating Solid Polymer and Ceramic Electrolytes for Lithium-Ion Batteries by Means of an Extended Distribution of Relaxation Times Analysis. *Electrochimica Acta* **2020**, *344*, 136060. https://doi.org/10.1016/j.electacta.2020.136060.

(3) Zhang, H.; Oteo, U.; Judez, X.; Eshetu, G. G.; Martinez-Ibañez, M.; Carrasco, J.; Li, C.; Armand, M. Designer Anion Enabling Solid-State Lithium-Sulfur Batteries. *Joule* **2019**, *3* (7), 1689–1702. https://doi.org/10.1016/j.joule.2019.05.003.

(4) Judez, X.; Zhang, H.; Li, C.; González-Marcos, J. A.; Zhou, Z.; Armand, M.; Rodriguez-Martinez, L. M. Lithium Bis(Fluorosulfonyl)Imide/Poly(Ethylene Oxide) Polymer Electrolyte for All Solid-State Li–S Cell. *J. Phys. Chem. Lett.* **2017**, *8* (9), 1956–1960. https://doi.org/10.1021/acs.jpclett.7b00593.

(5) Borodin, O.; Smith, G. D. Mechanism of Ion Transport in Amorphous Poly(Ethylene Oxide)/LiTFSI from Molecular Dynamics Simulations. *Macromolecules* **2006**, *39* (4), 1620–1629. https://doi.org/10.1021/ma052277v.

(6) Devaux, D.; Bouchet, R.; Glé, D.; Denoyel, R. Mechanism of Ion Transport in PEO/LiTFSI Complexes: Effect of Temperature, Molecular Weight and End Groups. *Solid State Ionics* **2012**, *227*, 119–127. https://doi.org/10.1016/j.ssi.2012.09.020.

(7) Rosenbach, D.; Mödl, N.; Hahn, M.; Petry, J.; Danzer, M. A.; Thelakkat, M. Synthesis and Comparative Studies of Solvent-Free Brush Polymer Electrolytes for Lithium Batteries. *ACS Applied Energy Materials* **2019**, *2* (5), 3373–3388. https://doi.org/10.1021/acsaem.9b00211.

(8) Zhang, X.; Daigle, J.-C.; Zaghib, K. Comprehensive Review of Polymer Architecture for All-Solid-State Lithium Rechargeable Batteries. *Materials* **2020**, *13* (11), 2488. https://doi.org/10.3390/ma13112488.

(9) Li, X.; Zheng, Y.; Duan, Y.; Shang, M.; Niu, J.; Li, C. Y. Designing Comb-Chain Crosslinker-Based Solid Polymer Electrolytes for Additive-Free All-Solid-State Lithium Metal Batteries. *Nano Lett.* **2020**, *20* (9), 6914–6921. https://doi.org/10.1021/acs.nanolett.0c03033.

(10) Homann, G.; Stolz, L.; Winter, M.; Kasnatscheew, J. Elimination of "Voltage Noise" of Poly (Ethylene Oxide)-Based Solid Electrolytes in High-Voltage Lithium Batteries: Linear versus Network Polymers. *iScience* **2020**, *23* (6), 101225. https://doi.org/10.1016/j.isci.2020.101225.

(11) Rupp, B.; Schmuck, M.; Balducci, A.; Winter, M.; Kern, W. Polymer Electrolyte for Lithium Batteries Based on Photochemically Crosslinked Poly(Ethylene Oxide) and Ionic Liquid. *European Polymer Journal* **2008**, *44* (9), 2986–2990. https://doi.org/10.1016/j.eurpolymj.2008.06.022.

(12) Bates, C. M.; Chang, A. B.; Momčilović, N.; Jones, S. C.; Grubbs, R. H. ABA Triblock Brush Polymers: Synthesis, Self-Assembly, Conductivity, and Rheological Properties. *Macromolecules* **2015**, *48* (14), 4967–4973. https://doi.org/10.1021/acs.macromol.5b00880.

(13) Mindemark, J.; Lacey, M. J.; Bowden, T.; Brandell, D. Beyond PEO—Alternative Host Materials for Li + -Conducting Solid Polymer Electrolytes. *Progress in Polymer Science* **2018**, *81*, 114–143. https://doi.org/10.1016/j.progpolymsci.2017.12.004.

(14) Rosenbach, D.; Krimalowski, A.; Erabhoina, H.; Thelakkat, M. Solid Polymer Electrolytes from Polyesters with Diester Sidechains for Lithium Metal Batteries. *Journal of Materials Chemistry A* **2022**, *10* (16), 8932–8947. https://doi.org/10.1039/D2TA00800A.
(15) Krimalowski, A.; Rosenbach, D.; Erabhoina, H.; Thelakkat, M. Versatile Solid Polymer Electrolytes from Clickable Poly(Glycidyl Propargyl Ether) for Lithium Metal Batteries. *Journal of Energy Storage* **2023**, *65*, 107348. https://doi.org/10.1016/j.est.2023.107348.
(16) Walsh, D. J.; Wade, M. A.; Rogers, S. A.; Guironnet, D. Challenges of Size-Exclusion Chromatography for the Analysis of Bottlebrush Polymers. *Macromolecules* **2020**, *53* (19), 8610–8620. https://doi.org/10.1021/acs.macromol.0c01357.
(17) Wang, Y.; Li, R.; Bian, Y.; Zhang, X.; Zhu, X. The Synthesis and Oligomerization of a Monofunctional Bottlebrush-Shaped Polymer Terminated with an Azide Group. *Polym. Chem.* **2019**, *10* (38), 5168–5171. https://doi.org/10.1039/C9PY00985J.
(18) Radzinski, S. C.; Foster, J. C.; Matson, J. B. Preparation of Bottlebrush Polymers via a One-Pot Ring-Opening Polymerization (ROP) and Ring-Opening Metathesis Polymerization (ROMP) Grafting-Through Strategy. *Macromolecular Rapid Communications* **2016**, *37* (7), 616–621. https://doi.org/10.1002/marc.201500672.
(19) Tammann, G. Über eine Methode zur Bestimmung der Abhängigkeit des Schmelzpunktes einer Kristallamelle von ihrer Dicke. *Z. Anorg. Allg. Chem.* **1920**, *110* (1), 166–168. https://doi.org/10.1002/zaac.19201100111.
(20) Lai, S. L.; Guo, J. Y.; Petrova, V.; Ramanath, G.; Allen, L. H. Size-Dependent Melting Properties of Small Tin Particles: Nanocalorimetric Measurements. *Phys. Rev. Lett.* **1996**, *77* (1), 99–102. https://doi.org/10.1103/PhysRevLett.77.99.
(21) Ji, X.; Xiao, L.-L.; Zhang, Y.; Yue, K.; Zhou, X.; Guo, Z.-H. Unveiling the Side-Chain Effect on Ionic Conductivity of Poly(Ethylene Oxide)-Based Polymer-Brush Electrolytes. *ACS Appl. Energy Mater.* **2022**, *5* (7), 8410–8418. https://doi.org/10.1021/acsaem.2c00962.
(22) Bennington, P.; Deng, C.; Sharon, D.; A. Webb, M.; Pablo, J. J. de; F. Nealey, P.; N. Patel, S. Role of Solvation Site Segmental Dynamics on Ion Transport in Ethylene-Oxide Based Side-Chain Polymer Electrolytes. *Journal of Materials Chemistry A* **2021**, *9* (15), 9937–9951. https://doi.org/10.1039/D1TA00899D.
(23) Diederichsen, K. M.; Buss, H. G.; McCloskey, B. D. The Compensation Effect in the Vogel–Tammann–Fulcher (VTF) Equation for Polymer-Based Electrolytes. *Macromolecules* **2017**, *50* (10), 3831–3840. https://doi.org/10.1021/acs.macromol.7b00423.
(24) Petry, J.; Dietel, M.; Thelakkat, M. Semi-Interpenetrating Network Electrolytes Utilizing Ester-Functionalized Low Tg Polysiloxanes in Lithium-Metal Batteries. *Adv. Energy Mater.* **2024**, *n/a* (n/a), 2403531. https://doi.org/10.1002/aenm.202403531.
(25) Tammann, G.; Hesse, W. Die Abhängigkeit Der Viscosität von Der Temperatur Bie Unterkühlten Flüssigkeiten. *Zeitschrift für anorganische und allgemeine Chemie* **1926**, *156* (1), 245–257. https://doi.org/10.1002/zaac.19261560121.
(26) Garca-Coln, L. S.; Del Castillo, L. F.; Goldstein, P. Theoretical Basis for the Vogel-Fulcher-Tammann Equation. *Phys. Rev. B* **1989**, *40* (10), 7040–7044. https://doi.org/10.1103/PhysRevB.40.7040.

II.8 Supporting Information

II.8.1 Materials

5-Norbornene-2-methanol (98 %, mixture of *endo* and *exo*), 5-norbornene-2-carboxylic acid (97 %, mixture of *endo* and *exo*), ε-caprolactone (97 %), 1,4-butanediol (99 %), 3rd generation Grubbs Catalyst, 1,5,7-Triazabicyclo[4.4.0]dec-5-en (98 %), ethyl vinyl ether (99 %), and diethyl ether (99.5 %, p.a.) were bought from Sigma Aldrich and used as received. Monomethyl adipate (97 %) was bought from abcr and used as received. DCM (99.8 %, extra dry over molecular sieve), THF (99.5 % extra dry over molecular sieve), pyridine (99.5 %, extra dry over molecular sieve) was bought from fisher scientific. Solvents for column chromatography and dialysis (hexane, ethyl acetate, methanol) were distilled at the department for Macromolecular Chemistry 1, University of Bayreuth. Silica 60 was retrieved from Macherey-Nagel for chromatography. Deuterated chloroform was purchased from Deutero. Coin cell parts were bought from MTI corporation.

II.8.2 Instrumentation

II.8.2.1 ^{1}H Nuclear Magnetic Resonance (NMR) Spectroscopy

A Bruker Avance AC250 spectrometer at a working frequency of 300 MHz was used to record ^{1}H NMR spectra. Chemical shifts were calibrated to 7.28 ppm for chloroform-d1. Chemical shifts are reported as ppm, coupling constants in Hz, and multiplicity are indicated as: s (singlet), d (doubled), t (triplet), m (multiplet).

II.8.2.2 Size exclusion Chromatography

SEC was measured utilizing a Waters 515 HPLC pump and THF with 0.25 wt % tetrabutylammonium bromide (TBAB) as eluent at a flow rate of 0.5 mL min–1. 100 µL of polymer solution (1–2 mg mL^{-1}) are injected by a 707 Waters autosampler into a column setup comprising a guard column (Agilent PLgel Guard MIXED-C, 5cm × 0.75 cm, particle size 5 µm) and two separation columns (Agilent PLgel MIXED-C, 30 cm × 0.75 cm, particle size 5 µm). Polymer size distributions were monitored by a Waters 414 refractive index detector. Polystyrene (PS) standard was used for calibration and 1,2-dichlorobenzene was used as an internal reference.

II.8.2.3 Thermogravimetric Analysis

TGA thermograms were recorded on a Mettler Toledo TGA/DSC 3. Samples (ca. 10 - 20 mg) were placed in aluminum oxide ceramic crucibles (70 µL) and heated from 30 to 700 °C at a heating rate of 10 K min^{-1} under nitrogen atmosphere.

II.8.2.4 Differential Scanning Calorimetry

DSC thermograms were obtained using a Mettler Toledo DSC 3. The samples were sealed within aluminum crucibles. The temperature program comprised two cycles of cooling down to –80 °C and subsequent heating up to 150 °C or 200 °C at a cooling/heating rate of 10 K min^{-1}. For the third cycle, a cooling/heating rate of 40 K min^{-1} was chosen. Glass transition temperatures (T_g) are derived as inflection points of the transition temperature and melting points (T_m) are obtained as the peak maximum of the melting peak in the second heating curve. For PMHS and PM(BMA)S a Netzsch 204F1 Phoenix system was used between -120 and-50 °C at a heating rate of 10K min^{-1}.

II.8.2.5 Scanning Electron Microscopy (SEM)

SEM analysis was conducted using a Zeiss Ultra plus equipped with a field emission gun. Samples were sputtered with platinum with a thickness of 2.8 nm.

II.8.2.6 Electrochemical Measurements

Electrochemical measurements were conducted using a VMP300 potentiostat (BioLogic) equipped with EIS boards. Electrochemical impedance spectroscopy was conducted in the frequency range of 3 MHz – 100 mHz using a sinusoidal excitation potential of 20 mV.

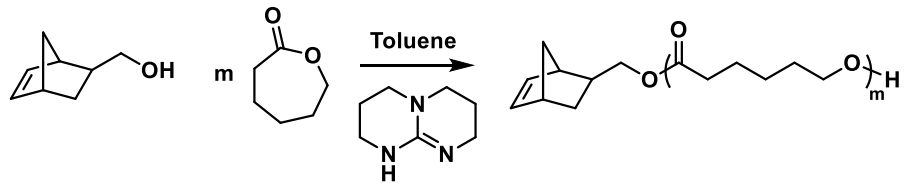
I.8.2.7 Electrolyte Preparation

The polymers were thoroughly dried before being transferred into an argon-filled glovebox. The electrolytes were prepared in the argon-filled glovebox by combining the desired amount of salt, polymer, and a magnetic stirring bar in a glass vial. The mixture was heated to 100 °C in custom-made aluminum blocks for homogeneous heat transfer under vigorous stirring for 24 h. For the preparation of test cells, electrolytes were heated above their melting point to facilitate the electrolyte handling.

II.8.3 Syntheses

4-hydroxybutyl methyl adipate was synthesized following published procedures.[1]

II.8.3.1 α-Norbornene-ω-hydroxy-poly(ε-caprolactone) (Nb-PCL)



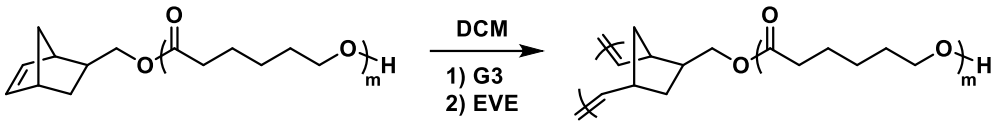
A 100 mL Schlenk flask equipped with a magnetic stirring bar and a septum was baked out at 650 °C under high vacuum. After cooling down to room temperature, 0.636 mL (652.8 mg, 5.26 mmol, 1 eq.) and 9.723 mL (10500.4 g, 92 mmol, 17.5 eq.) ε-caprolactone were dissolved in 46.5 mL anhydrous toluene. Afterwards, 64 mg (0.46 mmol) 1,5,7-triactabycyclo[4.4.0]dec-5-en (TBD) were added to the solution under vigorous stirring. After 5 h, the polymerization was terminated by the addition of benzoic acid. The reaction solution was concentrated under reduced pressure and precipitated in an eightfold excess of diethyl ether three times. The product was isolated by freeze-drying from benzene to yield a white solid.

Yield 3.3 g (73 %)

^{1}H-NMR (300 MHz, $CHCl_3$-d1): δ (ppm) = 6.22 – 5.82 (dd+q, 2H), 4.05 (t, 31H), 3.64 (t, 2H), 2.91 – 2.62 (m, 1.8H), 2.30 (t, 31H), 1.85-1.75 (m, 1.2H), 1.71 – 1.55 (m, 65H), 1.45 – 1.30 (m, 2H), 1.28-1.07 (m, 1.2H).

GPC M_n 4710 g mol^{-1}
M_w 5610 g mol^{-1}
M_p 4750 g mol^{-1}
$Đ$ 1.19
(eluent: $CHCl_3$, PS standards)

II.8.3.2 Poly(norbornene)-*graft*-poly(ε-caprolactone) (PNb-*graft*-PCL)



A 100 mL Schlenk flask equipped with a magnetic stirring bar and a septum was baked out at 650 °C under high vacuum. After cooling down to room temperature, 4.5 g (1.88 mmol, 40 eq.) Nb-PCL was added under argon counterflow and dissolved in 38.9 mL anhydrous DCM. The monomer solution was degassed by three freeze/pump/thaw cycles. The monomer solution was cooled to 15 °C. The 3rd-generation Grubbs catalyst was added from a stock solution. To prepare the stock solution, 55.3 mg of catalyst were dissolved in 2 mL anhydrous DCM inside an argon-filled glovebox. Of that stock solution, 1.5 mL (= 41.46 mg, 0.05 mmol, 1 eq. of catalyst) was added to the monomer solution by syringe under vigorous stirring. After 1 h, the polymerization was terminated by the addition of vinyl ethyl ether. The reaction solution was concentrated under reduced pressure and precipitated in an eightfold excess of diethyl ether three times. The grey product was dissolved in MeOH and dialyzed for three days. The dialysis fluid is exchanged every day. The solvent was removed under reduced pressure, and the grey solid was freeze-dried from benzene.

Yield 3.30 g (73 % %)

^{1}H-NMR (300 MHz, $CHCl_3$-d1): δ (ppm) = 5.58 – 4.92 (br, 2H), 4.32 – 3.92 (t, 31H), 3.65 – 3.55 (t, 3H), 3.35 – 1.1 (br, 7H), 2.35 - 2.2 (t, 31H), 1.72 – 1.52 (m, 67H), 1.45 – 1.36 (m, 33H).

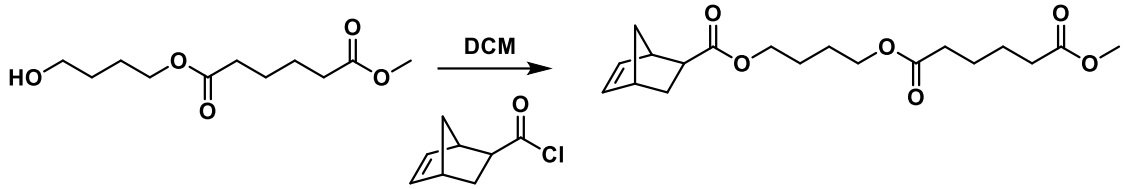
GPC M_n 97600 g mol^{-1}
M_w 110000 g mol^{-1}
M_p 126000 g mol^{-1}
$Đ$ 1.12
(eluent: $CHCl_3$, PS standards)

DSC T_m 43.4 °C
ΔH_m 59.8 J g^{-1}

DMA T_g -69.3 °C

TGA $T_{d,5\%}$ 351 °C

II.8.3.3 Butyl-4-{methyl adipate])norbornene-2-carboxylate (Nb-BMA)

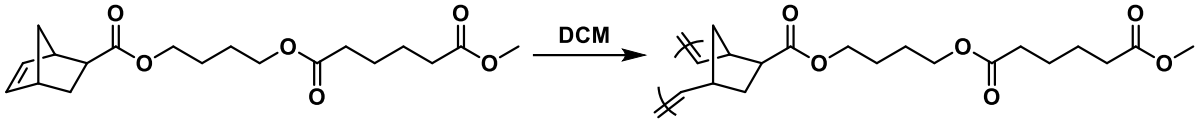


A 250 mL Schlenk flask equipped with a magnetic stirring bar and a septum was baked out at 650 °C under high vacuum. After cooling down to room temperature, 5000 mg (21.53 mmol, 1 eq.) 4-hydroxybutyl methyl adipate was dissolved in 55.6 mL anhydrous DCM. 2.085 mL (2043 mg, 25.83 mmol, 1.2 eq.) was added by syringe. 4213.9 mg (26.91 mmol, 1.25 eq.) 5-norbornene-2-carbonyl chloride (Nb-COCl) was added to the solution. After 3 h, a white precipitate formed. A small aliquot was taken from the reaction mixture to monitor the reaction progress in TLC (hexane:ethyl acetate, 8:2 v/v). 50 mL of hexane was added to the reaction solution, which caused more precipitate to form. The reaction solution was filtered, and the precipitate was washed with additional hexane two times. The organic phase was washed with DI water and subsequently dried using $NaSO_4$. The reaction solution was concentrated under reduced pressure. The product was isolated by column chromatography using neutral Alox as the stationary phase and a mixture of hexane:ethyl acetate (8:2 v/v) as eluent.

Yield 5.0 g (65.9 %)

^{1}H-NMR (300 MHz, $CHCl_3$-d1): δ (ppm) = 6.31 – 5.83 (dd+q, 2H), 4.16 – 3.97 (br, 4H), 3.67 (s, 3H), 3.33 – 2.80 (m, 2.7H), 2.33 (br, 4H), 2.22 (m, 0.3H), 1.98 – 1.85 (m, 1H), 1.80 – 1.61 (m, 8H), 1.55 – 1.13 (m, 3H).

II.8.3.4 Poly(butyl-4-{methyl adipate])norbornene-2-carboxylate (PNb-BMA)



A 100 mL Schlenk flask equipped with a magnetic stirring bar and a septum was baked out at 650 °C under high vacuum. After cooling down to room temperature, 3.5 g (9.93 mmol, 230 eq.) Nb-BMA was added under argon counterflow and dissolved in 38.9 mL anhydrous DCM. The monomer solution was degassed by three freeze/pump/thaw cycles. The monomer solution was cooled to 15 °C. The 3rd-generation Grubbs catalyst was added from a stock solution. To prepare the stock solution, 50.7 mg of catalyst was dissolved in 2 mL anhydrous DCM inside an argon-filled glovebox. Of that stock solution, 1.5 mL (= 38.2 mg, 0.04 mmol, 1 eq. of catalyst) was added to the monomer solution by syringe under vigorous stirring. After 1 h, the polymerization was terminated by the addition of vinyl ethyl ether. The reaction solution was concentrated under reduced pressure and precipitated in an eightfold excess of diethyl ether three times. The grey product was dissolved in MeOH and dialyzed for three days. The dialysis fluid is exchanged every day. The solvent was removed under reduced pressure, and the grey solid was freeze-dried from benzene.

Yield 3.04 g (86.9 %)

^{1}H-NMR (300 MHz, $CHCl_3$-d1): δ (ppm) = 5.27 (br, 2H), 4.10 (br, 4H), 3.66 (s, 3H), 3.21-1.35 (br, 7H), 2.33 (m, 4H), 1.85 – 1.52 (m, 8H).

GPC
M_n	57500	g mol^{-1}
M_w	72200	g mol^{-1}
M_p	86000	g mol^{-1}
$Đ$	1.25	

(eluent THF+0.25 wt% TBAB, PS calibration)

DSC
T_g	-47.2	°C
T_m	n.c.	°C
$ΔH_m$	n.c.	J g^{-1}

TGA $T_{d,5\%}$ 229 °C

II.8.4 ^{1}H NMR Spectroscopy

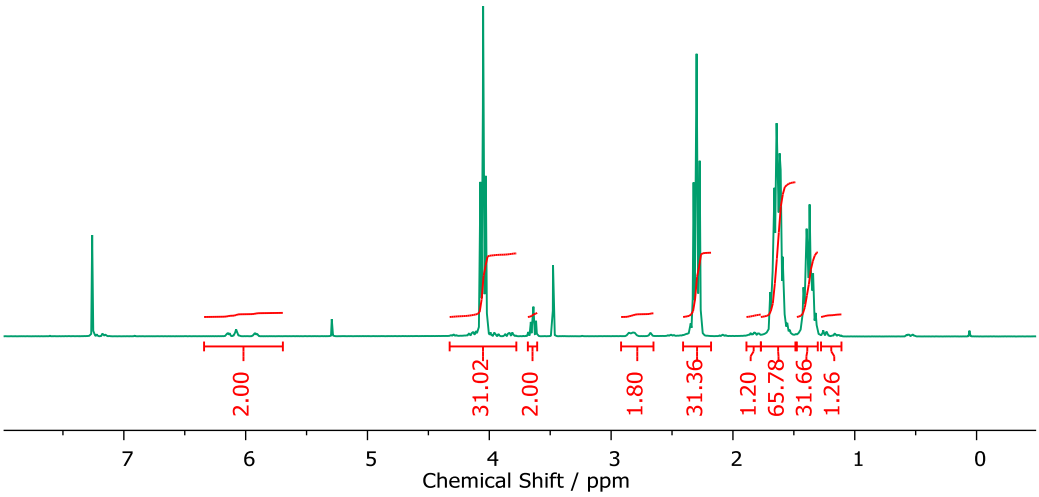


Figure S.II.1. ^{1}H NMR spectrum of Nb-PCL.

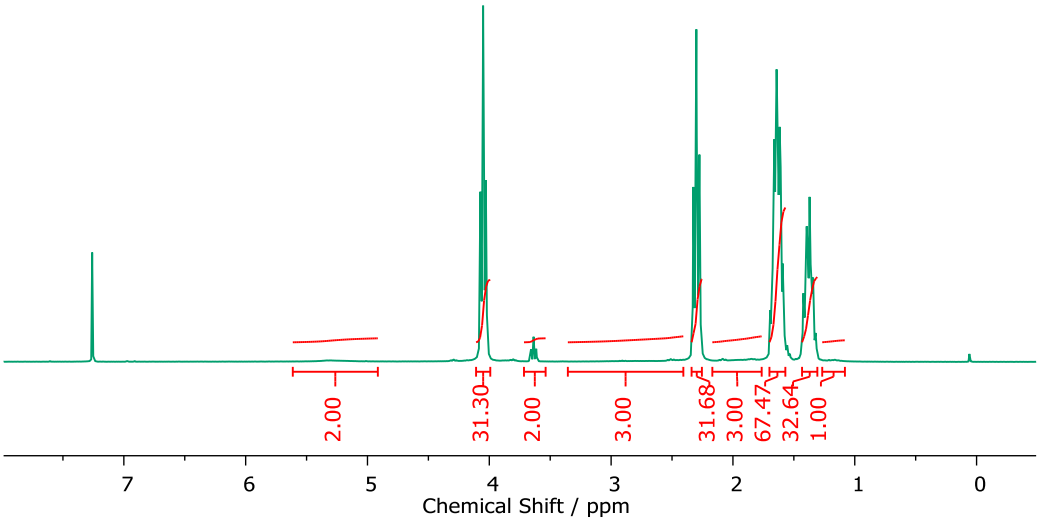


Figure S.II.2. ^{1}H NMR spectrum of PNb-*graft*-PCL.

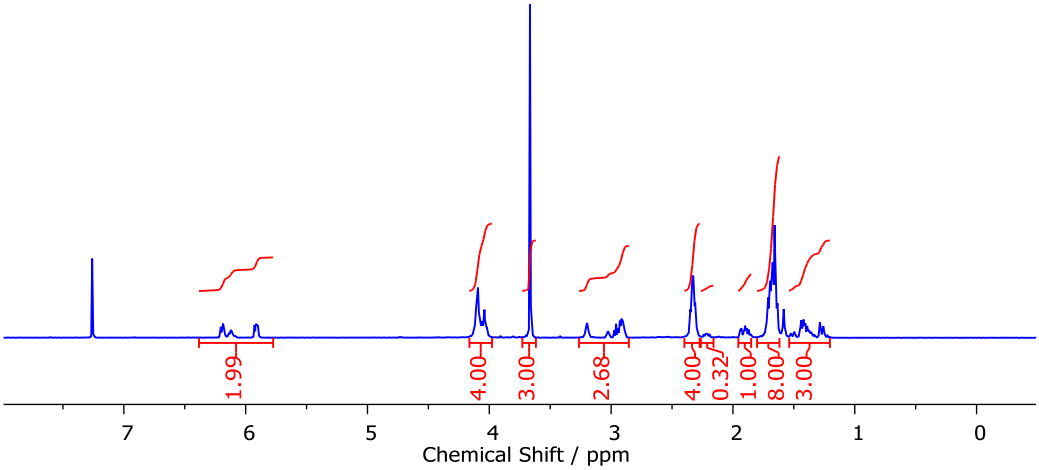


Figure S.II.3. ^{1}H NMR spectrum of Nb-BMA.

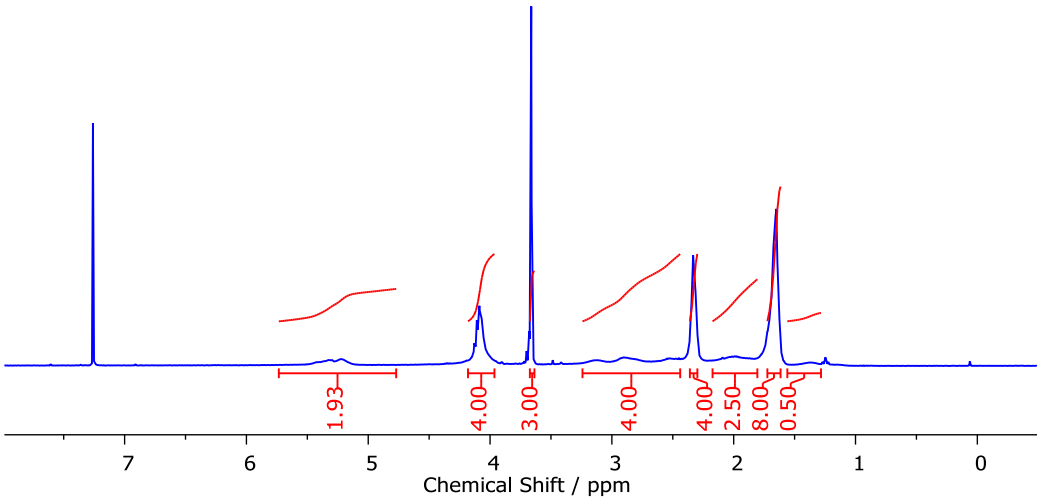


Figure S.II.4. ^{1}H NMR spectrum of PNb-BMA.

II.8.5 Molecular Weight Determination

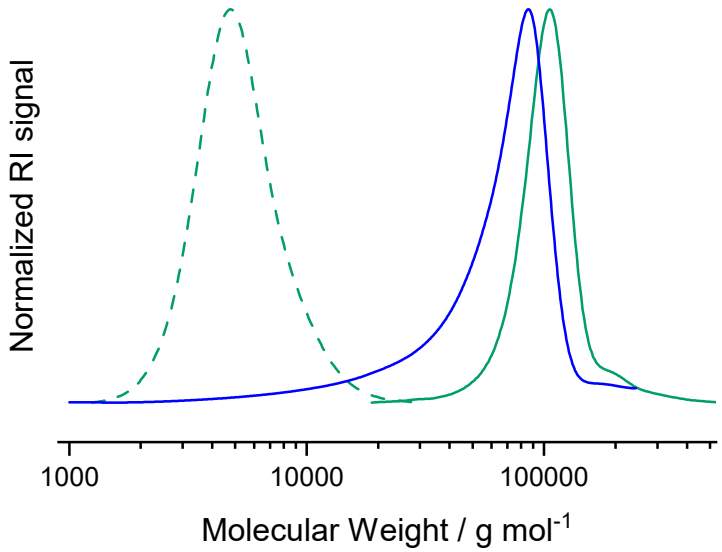


Figure S.II.5. SEC curves for the (green, dashed lines) Nb-PCL monomer, (green solid lines) PNb-*graft*-PCL bottlebrush polymer, and (blue) PNb-BMA.

II.8.6 Thermal Characterization –Thermal Stability

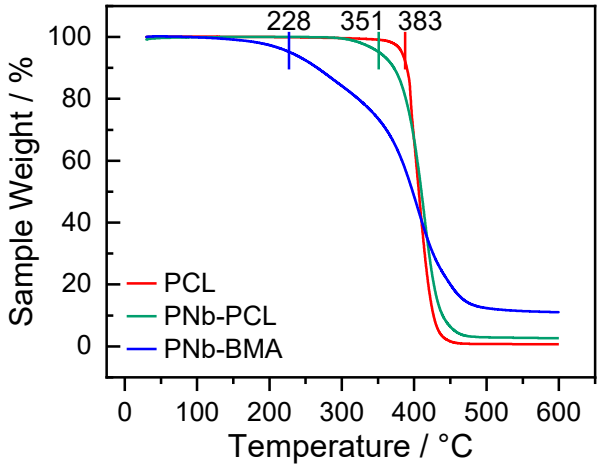


Figure S.II.6. Thermogravimetric analysis of pristine polymers (red) PCL, (green) PNb-*graft*-PCL, and (blue) PNb-BMA. Measurement is conducted from 30 °C to 600 °C at a heating rate of 10 K min^{-1} under nitrogen atmosphere.

II.8.7 Thermal Characterization – Thermal Transitions

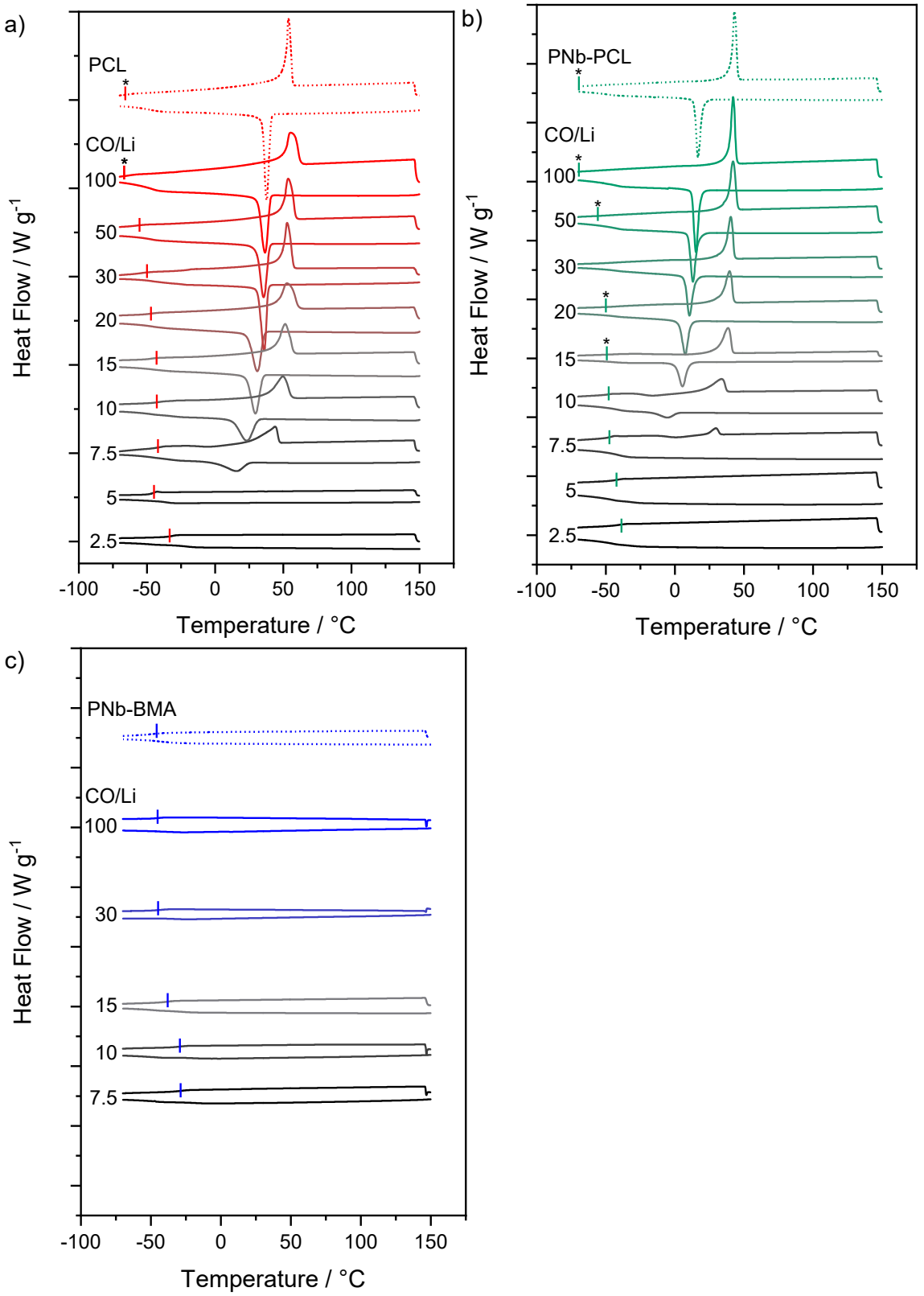


Figure S.II.7. Differential scanning calorimetry (second heating and cooling curve, 10 K min^{-1}, -70 °C – 150 °C) of the pristine polymers and corresponding electrolyte at different salt concentrations (a) PCL, (b) PNb-*graft*-PCL, and (c) PNb-BMA. The glass transition temperature is marked by the ticks. Ticks marked with * are taken from DMA measurements and not from the DSC measurements.

II.8.8 Thermal Characterization – Dynamical Mechanical Analysis

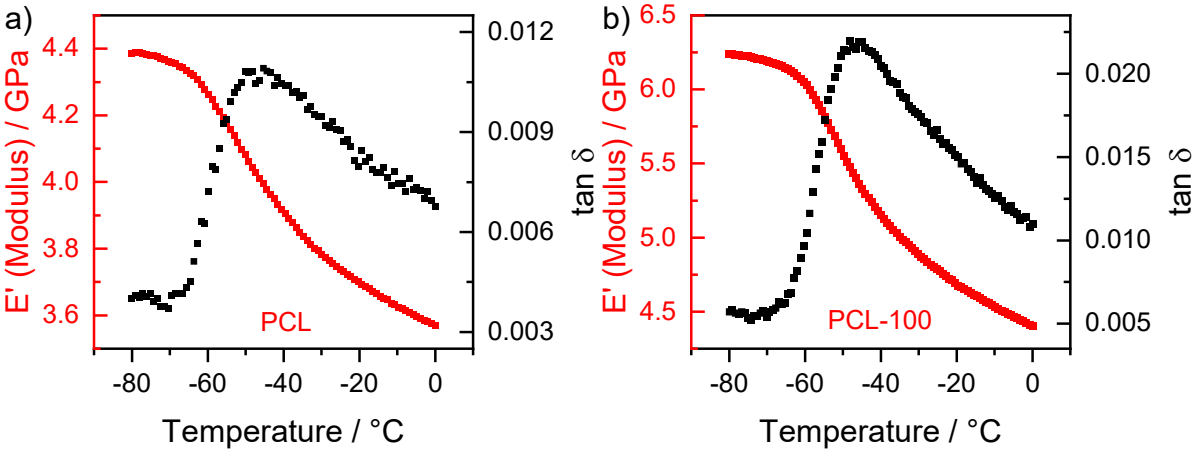


Figure S.II.8. DMA measurements of PCL and the PCL electrolyte at a C=O/Li ratio of 100. The data is taken from the second heating at a heating rate of 10 K min^{-1}

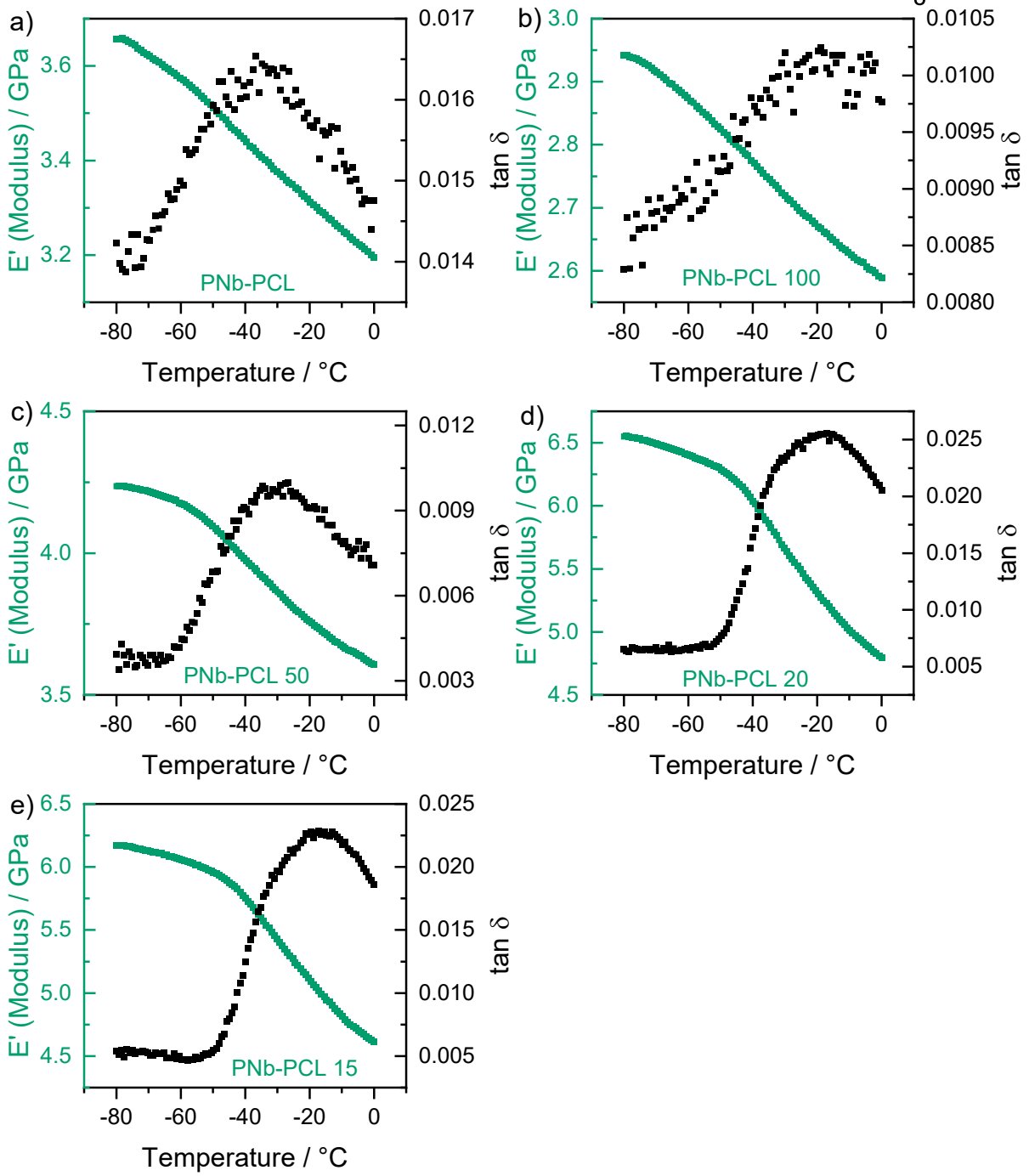


Figure S.II.9. DMA measurements of (a) PNb-*graft*-PCL and the (b-e) PNb-*graft*-PCL electrolyte at different C=O/Li ratios from 100 to 15. The data is taken from the second heating step at a heating rate of 10 K min^{-1}

II.8.9 Ion-Coordination – FTIR- Analysis

IR spectra were recorded using a PerkinElmer Spectrum 100 FT-IR spectrometer. IR data was recorded in total reflectance mode in the form of transmission information. The data was normalized to 0 to 1. The deconvolution process of the free and coordinating carbonyl moiety was performed by Gaussian nonlinear fitting by a Levenberg Marquardt iteration algorithm with 4 parameters for each peak. Fitting was performed using the following equation (Equation S.II.1).[1]

$$y = y_0 + \frac{A}{w \cdot \sqrt{\frac{\pi}{4 \cdot ln2}}} \cdot exp^{\left(-4 \cdot ln2 \frac{(x-x_c)^2}{w^2}\right)} \qquad \text{(Eq. S.II.1)}$$

With y_0 as y-axis offset, A as the area of the distribution function, w as the variance, and x_c as the center of the peak position.

Table S.II.1. Double/single Gaussian FTIR-analysis of the coordinating and non-coordinating carbonyl moiety of PCL at different salt concentrations.

PCL	Peak 1 (C=O)				Peak 2 (C=O---Li)				ϕ_{Li^+}
C=O/Li	y_0	x_c	A	w	y_0	x_c	A	w	%
100	0.984 ±0.001	1725.109 ±0.140	-30.486 ±0.305	26.008 ±0.27	0.984 ±0.001	1691.351 ±0.672	-4.565 ±0.286	21.137 ±1.190	13
50	0.992 ±0.002	1725.319 ±0.173	-13.619 ±0.692	19.350 ±0.494	0.992 ±0.002	1716.236 ±0.527	-23.388 ±0.716	47.397 ±0.977	15
30	0.984 ±0.002	1724.829 ±0.224	-28.794 ±0.462	25.612 ±0.402	0.984 ±0.002	1694.374 ±0.560	-7.383 ±0.434	19.813 ±0.907	20
20	0.983 ±0.002	1724.765 ±0.263	-27.833 ±0.531	25.170 ±0.451	0.983 ±0.002	1695.108 ±0.525	-9.275 ±0.506	20.043 ±0.819	25
15	0.983 ±0.002	1724.767 ±0.292	-27.767 ±0.589	25.175 ±0.473	0.983 ±0.002	1695.396 ±0.527	-10.774 ±0.568	20.793 ±0.786	28
10	0.977 ±0.002	1727.089 ±0.288	-23.188 ±0.639	21.509 ±0.399	0.977 ±0.002	1698.893 ±0.412	-20.796 ±0.653	24.429 ±0.609	47
7.5	0.978 ±0.001	1730.099 ±0.183	-24.235 ±0.422	21.136 ±0.290	0.978 ±0.001	1699.580 ±0.212	-27.860 ±0.437	24.854 ±0.361	53
5	0.970 ±0.002	1730.528 ±0.211	-18.383 ±0.410	19.446 ±0.35	0.97 ±0.002	1700.083 ±0.199	-30.255 ±0.438	25.166 ±0.365	62
2.5	0.983 ±0.001	1730.689 ±0.483	-7.538 ±0.371	20.452 ±0.75	0.983 ±0.001	1700.570 ±0.174	-31.311 ±0.389	25.594 ±0.297	81

Table S.II.2. Double/single Gaussian FTIR-analysis of the coordinating and non-coordinating carbonyl moiety of PNb-*graft*-PCL at different salt concentrations.

PNb-PCL	Peak 1 (C=O)				Peak 2 (C=O---Li)				ϕ_{Li^+}
C=O/Li	y_o	x_c	A	w	y_o	x_c	A	w	%
100	0.984 ±0.001	1726.359 ±0.088	-30.379 ±0.202	25.300 ±0.172	0.984 ±0.001	1694.151 ±0.640	-4.582 ±0.147	25.300 ±0.172	13
50	0.984 ±0.001	1728.517 ±0.080	-28.811 ±0.178	23.861 ±0.149	0.984 ±0.001	1699.46 6 ±0.358	-6.848 ±0.132	23.861 ±0.149	19
30	0.983 ±0.001	1729.583 ±0.280	-25.600 ±0.848	22.503 ±0.304	0.983 ±0.001	1703.331 ±1.037	-12.596 ±0.864	28.332 ±1.222	33
20	0.976 ±0.001	1730.282 ±0.282	-24.725 ±0.769	21.800 ±0.329	0.976 ±0.001	1703.696 ±0.778	-14.476 ±0.785	26.697 ±0.988	37
15	0.977 ±0.001	1729.331 ±0.110	-26.959 ±0.213	23.035 ±0.186	0.977 ±0.001	1701.614 ±0.227	-13.555 ±0.169	23.035 ±0.186	33
10	0.980 ±0.001	1730.759 ±0.166	-24.146 ±0.395	20.917 ±0.251	0.980 ±0.001	1701.138 ±0.266	-21.048 ±0.410	25.050 ±0.435	47
7.5	0.975 ±0.002	1731.642 ±0.202	-22.051 ±0.485	19.951 ±0.311	0.975 ±0.002	1701.774 ±0.255	-29.291 ±0.514	26.384 ±0.435	57
5	0.976 ±0.002	1732.185 ±0.220	-16.100 ±0.389	19.333 ±0.365	0.976 ±0.002	1701.135 ±0.19	-32.176 ±0.422	26.512 ±0.353	67
2.5	0.981 ±0.001	1731.077 ±0.476	-7.431 ±0.377	19.924 ±0.748	0.981 ±0.001	1700.977 ±0.179	-31.688 ±0.40	25.961 ±0.313	81

Table S.II.3. Double/single Gaussian FTIR-analysis of the coordinating and non-coordinating carbonyl moiety of PNb-BMA at different salt concentrations.

PNb-BMA	Peak 1 (C=O)				Peak 2 (C=O---Li)				ϕ_{Li^+}
C=O/Li	y_o	x_c	A	w	y_o	x_c	A	w	%
100	0.979 ±0.001	1727.264 ±0.097	-33.736 ±0.228	27.902 ±0.189	0.979 ±0.001	1692.301 ±0.745	-4.793 ±0.164	27.902 ±0.189	12
30	0.977 ±0.001	1728.198 ±0.126	-31.645 ±0.268	27.027 ±0.217	0.977 ±0.001	1698.268 ±0.377	-10.624 ±0.203	27.027 ±0.217	24
15	0.976 ±0.001	1728.889 ±0.325	-30.246 ±0.749	26.000 ±0.411	0.976 ±0.001	1698.836 ±0.696	-14.050 ±0.749	25.951 ±0.881	32
10	0.964 ±0.002	1733.017 ±0.492	-17.941 ±1.039	21.954 ±0.657	0.964 ±0.002	1703.212 ±0.517	-35.218 ±1.085	30.333 ±0.749	66
7.5	0.967 ±0.002	1732.379 ±0.4	-20.397 ±0.857	22.372 ±0.538	0.967 ±0.002	1702.006 ±0.421	-33.945 ±0.891	29.151 ±0.622	62

II.8.10 Arrhenius Plots

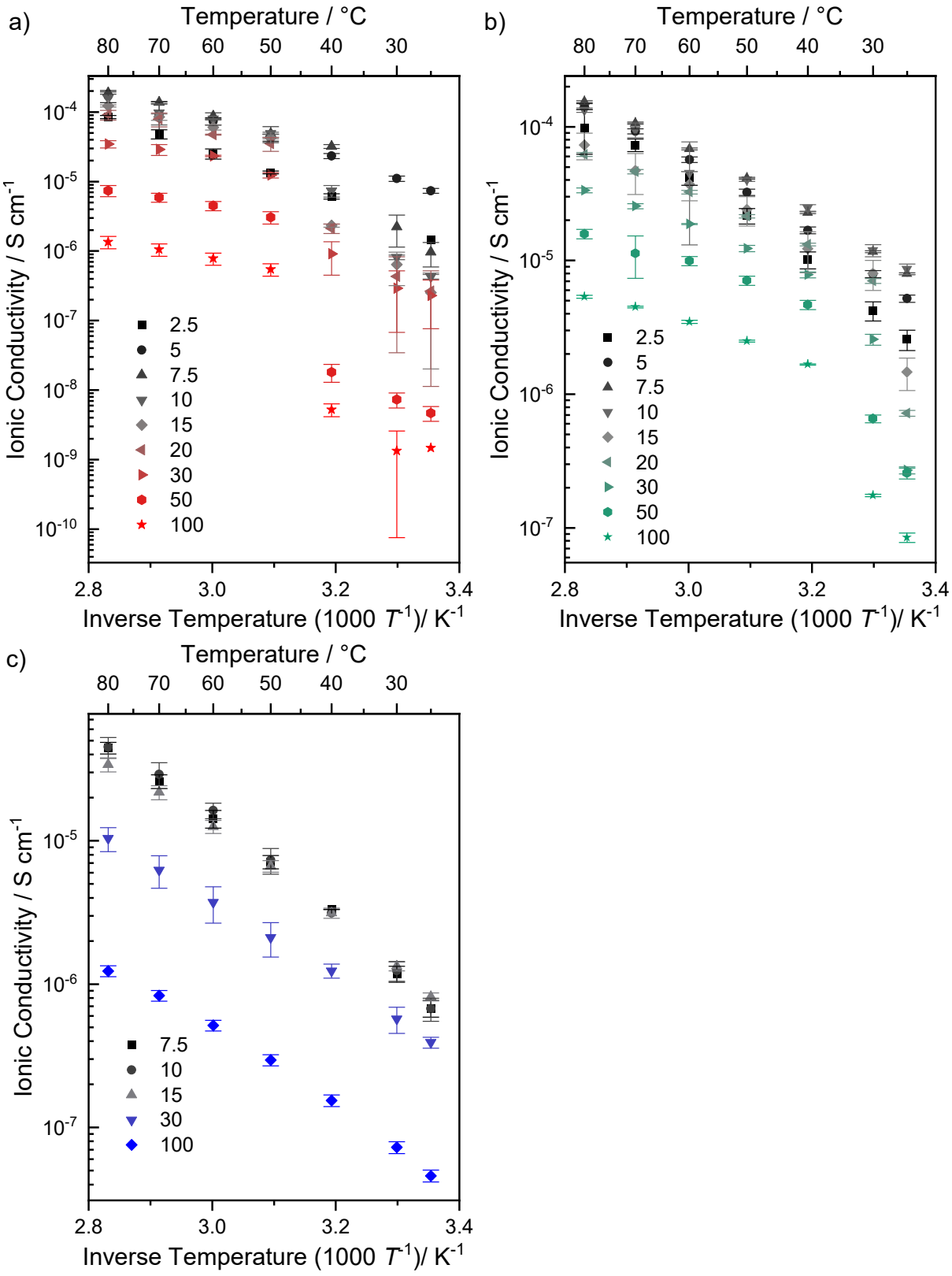


Figure S.II.10. Temperature-dependent ionic conductivity for (a)PCL, (b) PNb-*graft*-PCL, and (c) PNb-BMA at different salt concentrations.

II.8.11 VTF Analysis – Fits

The temperature-dependent ionic conductivity was fitted using **Equation II.1**. The equation was linearized to yield **Equation S.II.2**. The data for the temperature-dependent ionic conductivity for the three polymer electrolyte systems was plotted as ln(σ) vs. $1/(T\text{-}T_0)$ as depicted in **Figure S.II.11**. The pseudo-activation energy (B) was extracted from the slope.

$$ln(\sigma) = -\frac{B}{R} * \frac{1}{(T - T_0)} + ln(A) \qquad \text{(S.II.1)}$$

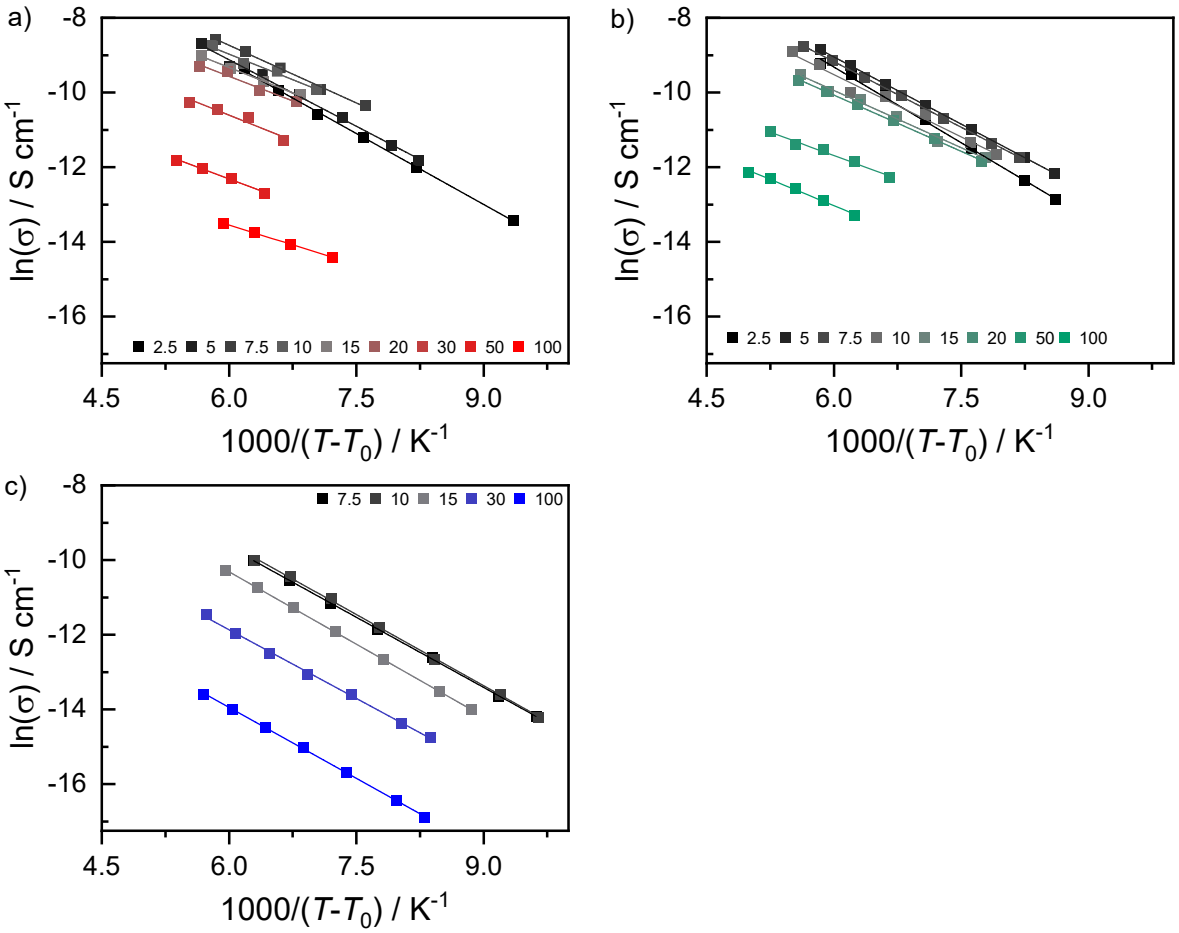
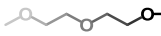


Figure S.II.11. VTF plots of the temperature-dependent ionic conductivity and linear VTF-fits for (a) PCL, (b) PNb-*graft*-PCL, and (c) PNb-BMA electrolyte systems at different salt concentrations. For each electrolyte system, only the ionic conductivity in the amorphous region is considered. For comparability, the axis scaling is consistent across the three sub-figures.

II.8.12 References – Supporting Information

(1) Rosenbach, D.; Krimalowski, A.; Erabhoina, H.; Thelakkat, M. Solid Polymer Electrolytes from Polyesters with Diester Sidechains for Lithium Metal Batteries. *Journal of Materials Chemistry A* **2022**, *10* (16), 8932–8947. https://doi.org/10.1039/D2TA00800A

(2) Petry, J.; Dietel, M.; Thelakkat, M. Semi-Interpenetrating Network Electrolytes Utilizing Ester-Functionalized Low Tg Polysiloxanes in Lithium-Metal Batteries. *Adv. Energy Mater.* **2024**, *n/a* (n/a), 2403531. https://doi.org/10.1002/aenm.202403531.



III Comparative Study of the Mechanical Reinforcement by Blending, Filling, and Block Copolymerization in Bottlebrush Polymer Electrolytes

Jannik Petry[a], Harimohan Erabhoina[a], Markus Dietel[a] and Mukundan Thelakkat*[abc].

[a] Applied Functional Polymers, University of Bayreuth, Universitätsstraße 30, 95447 Bayreuth, Germany
[b] Bavarian Polymer Institute (BPI), University of Bayreuth, Universitätsstraße 30, 95447 Bayreuth, Germany
[c] Bavarian Center for Battery Technology (BayBatt), University of Bayreuth, Universitätsstraße 30, 95447 Bayreuth, Germany

* Corresponding Author
E-mail: mukundan.thelakkat@uni-bayreuth.de

Reproduced with permission from ACS Applied Polymer Materials, 2024, 6, 5209-5120
Copyright 2024 The Authors, American Chemical Society

III.1 Abstract

Poly(ethylene glycol) (PEG)-based bottlebrush polymer electrolytes exhibit improved room-temperature ionic conductivity and reduced crystallinity compared to those of semicrystalline poly(ethylene oxide) (PEO). However, these graft copolymers suffer from low mechanical stability. Therefore, we synthesized a PEG-based bottlebrush polymer having a polynorbornene backbone using ring-opening metathesis polymerization, and it was mechanically reinforced using three strategies: (a) by blending with a polynorbornene (PNb) homopolymer, (b) filling with TiO_2 nanoparticles, or (c) via block copolymerization with a PNb segment. All three systems were converted to solid polymer electrolytes by adding LiTFSI, and their thermal, mechanical, and detailed electrochemical properties in symmetrical Li/SPE/Li cells over a large number of cycles are given. All solid-state lithium metal battery (Li/SPE/LFP) cells were fabricated, and charge/discharge cycles as well as the cycling behavior were comparatively studied. It was found that block copolymerization resulted in the highest storage modulus above 0.1 Hz and overall ionic conductivity (in the whole range of 25 to 80 °C) compared to those of the other two strategies. Furthermore, the highest accessible discharge capacities (159 mA h g^{-1}) and highest capacity retention of 88 % after 50 cycles were also achieved with the block copolymer concept.

III.2 Introduction

Rechargeable lithium-ion batteries (LIBs) are well-established in many fields of mobile energy storage. Coming from mostly small and mobile devices, LIBs have emerged into further fields of technological applications with complex requirement portfolios and challenges. These applications of batteries include electric vehicles/aviation or grid-based energy storage systems. Especially the mobility sector requires high energy densities to achieve extended driving ranges at moderate battery pack sizes and weights. The current state-of-the-art lithium-ion batteries utilize intercalating positive and negative electrode materials in combination with liquid electrolytes and a separator. The intercalating host materials constitute a large percentage of the entire battery cell, limiting the maximum energy density of the LIBs. Instead of using lithiated graphite as anode material, lithium metal promises a 10-fold increase in the specific capacity in lithium–metal batteries (LMBs). However, the currently employed liquid electrolytes from LIBs are not compatible with the lithium metal anode due to the formation of an unstable solid electrolyte interface (SEI) as well as the tendency to uncontrolled lithium plating and stripping (LPS) and subsequent formation of lithium dendrites resulting in cell shorting and thermal runaway, especially at high C-rates.[1,2] Hence, mechanically resilient solid electrolyte systems in the form of either inorganic or polymer-based ion conductors are required to overcome these challenges and enable the realization of efficient all-solid-state LMBs.[3] Within the field of polymer-based solid electrolytes, poly(ethylene oxide) (PEO) systems are the most studied.[4,5] In the PEO matrix, lithium ions are transported only in the amorphous polymer regions, as the ionic conductivity is linked to the polymer segmental mobility. The high degree of crystallinity of linear PEO hinders efficient ion conduction, especially at lower temperatures. Therefore, starting from the first report about the ionic mobility in a PEO matrix in the 1970s, different architectures were investigated to reduce the PEO crystallinity and to improve the ionic conductivity. Exemplary architectures are star-shaped/hyper-branched, block copolymers, or graft copolymers.[6–12] However, the reduction of crystallinity in such materials is very often accompanied by a decrease in mechanical stability, which can result in insufficient electrode separation and accelerated formation of lithium dendrites during prolonged charging and discharging. To overcome this, inorganic additives or the concept of block copolymers was introduced to obtain nanostructured materials with improved mechanical strength. Srinivasan et al. reported on lithium dendrite growth mechanisms in solid polymer electrolytes and various strategies adopted to decrease or prevent the same.[13] Recently, PEO-based materials were combined in blends with different polymers (e.g., PVdF-HFP and PVP),[14,15] inorganic nanoparticle (NP) fillers (e.g., TiO_2 and Al_2O_3),[16,17] or ion-conducting additives (e.g., LLZO and LGPS)[18,19] to suppress the polymer crystallization, increase the mechanical stability to avoid Li-dendrite growth, and influence the ion conduction through the electrolyte. Recently, Helms et al. demonstrated how to access either pressure-driven dendrite-blocking or density-driven dendrite-suppressing properties in solid electrolytes.[20] Besides adding mechanically reinforcing additives through mixing or blending, the components can also be covalently connected in the form of, e.g., surface-grafted nanoparticles or block copolymer architectures.[21–27] In block copolymers, the antagonistic properties of improving the ionic conductivity and mechanical properties can be addressed by rational design of the polymer architecture. The volume fraction of each segment can be varied and optimized during the polymer synthesis, enabling the optimization of both contributions within a single material.[10,28] The different natures of the constituents can result in nanostructured materials with ion-conducting domains and mechanically reinforcing domains, depending on the volume

fractions. The covalent connection prevents macrophase separation, which is commonly observed for blend systems with comparable constituents. In this regard, different polymer architectures were realized in the past, including linear block copolymers,[26] bottlebrush copolymers,[25] or a combination of bottlebrush and linear polymer segments.[29]

To study comparatively the effect of mechanical reinforcement using blending, filling, or block copolymerization, we first synthesized PEG-based bottlebrush as well as bottlebrush block copolymer host materials for SPEs. Here, we utilized the living and controlled ring-opening metathesis polymerization (ROMP) of norbornene derivatives for precise control over the polymer properties and composition. The morphological and mechanical properties are examined by scanning electron microscopy (SEM) and rheology. The materials are then combined with lithium bis(trifluoromethane)sulfonimide (LiTFSI) to obtain the electrolytes for electrochemical measurements, including ionic conductivity, lithium transport number, electrochemical stability window, lithium compatibility, and battery cycling using lithium iron phosphate-based cathodes. The purpose of this study is to compare and evaluate the three different approaches of mechanical reinforcement using amorphous SPEs under comparable experimental conditions to evaluate and understand the benefits and drawbacks of each strategy toward all-solid-state lithium–metal battery application. Interestingly, the BB-BCP exhibited by far the highest storage modulus and appreciably high ionic conductivities reaching 8.4×10^{-4} S cm^{-1} at 70 °C (similar to the nonreinforced SPE, BB-16).

III.3 Results and Discussion

III.3.1 Polymer Syntheses

Three different polymers were synthesized by ring-opening metathesis polymerization (ROMP) of norbornene (Nb) monomers using a third generation Grubbs catalyst (G3), as illustrated in **Figure III.1.** First, the polynorbornene homopolymer poly(Nb)$_{90}$ 1 and bottlebrush polymer poly(Nb)$_{40}$-graft-PEGME 2 (BB) were synthesized. The bottlebrush polymers were prepared using a grafting-through approach to ensure a quantitative grafting density.[33] For the synthesis of the bottlebrush polymer, a norbornene-based macromonomer was first prepared by Steglich esterification. For this, functionalized norbornene, Nb–COOH was esterified with commercially available monomethoxy PEG alcohol (M_n 2000 g mol^{-1};N_{PEG} 45) to obtain the Nb-PEGME macromonomer (^{1}H NMR spectra and SEC data are presented in **Figures S.III.1** and **S.IiI.2**). Finally, the bottlebrush block copolymer poly(Nb)-*graft*-PEGME-*block*-poly(Nb) 3 (BB-BCP) was prepared by sequential monomer addition of the Nb-PEGME macromonomer, followed by nonfunctionalized norbornene utilizing the living character of the ROMP. The block copolymer formation can be observed by the stepwise molecular weight increase in the SEC elugrams. Thus, the grafting through ROMP allowed us to keep the length of the BB backbone the same in both 2 and 3, for the sake of comparability. The length of the PEGME side chain and the number of repeating units of Nb in bottlebrush copolymer 2 and in BB-BCP 3 were selected on the basis of our earlier studies of polynorbornene graft copolymers for their suitability as solid polymer electrolytes.[33] The obtained polymer structures of 1–3 are confirmed by ^{1}H NMR spectroscopy (**Figures S.III.3–S.III.5**). The polymer composition of 3 was determined by ^{1}H NMR spectroscopy. Both polymer segments exhibit similar chemical shifts for the polymer backbone. Assuming that the relative peak intensity of PEG side chains and Nb-PEGME double bond protons remains constant during the polymerization, the total integral of double bond protons can be

attributed to the individual polymer segments (**Figure S.III.5**; **Table S.III.1**). Therefore, a polymer composition for BB-BCP 3 of poly(Nb)$_{40}$-*graft*-PEGME-*block*-poly(Nb)$_{68}$ could be determined.

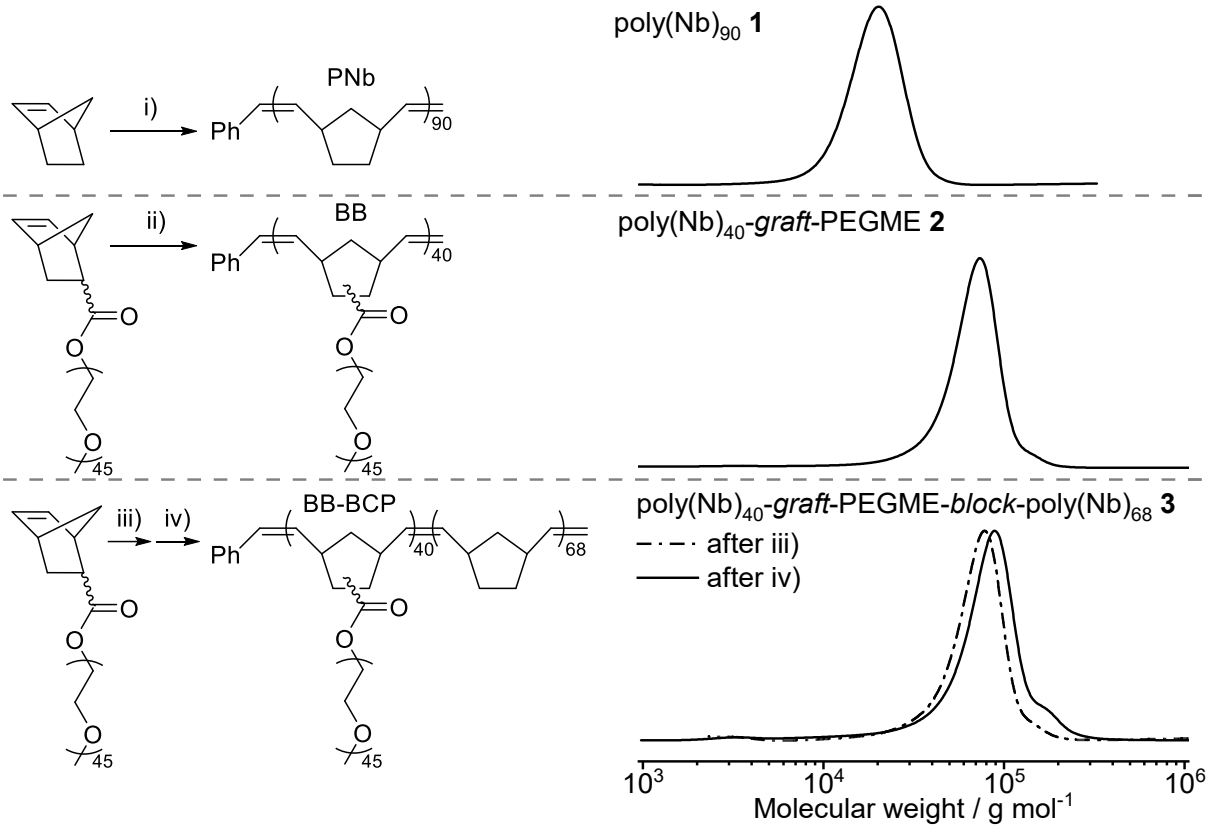


Figure III.1. Synthesis of norbornene-based polymers, poly(Nb)$_{90}$ (**1**) and poly(Nb)$_{40}$-graft-PEGME (**2**) and bottlebrush block copolymer poly(Nb)$_{40}$-*graft*-PEGME-*block*-poly(Nb)$_{68}$ (**3**) using different synthetic protocols: i) -10 °C, 30 min, ethyl vinyl ether (EVE); ii) 15 °C, 60 min, EVE; iii) 15 °C, 60 min; iv) norbornene, -10 °C, 30 min, EVE. SEC curves (eluent: THF + 0.25 wt% TBAB, PS calibration) show monomodal molecular weight distributions. A sequential increase of molecular weight can be observed for the block copolymerization in SEC.

The polymerizations proceeded until quantitative conversion, as determined by ^{1}H NMR spectroscopy, which is corroborated by the absence of monomer double bond protons after the respective reaction times. All polymers show defined molecular weights and narrow molecular weight distributions in the range of 1.1 to 1.2 (**Table III.1**). For each polymer, the theoretical molecular weight was calculated based on the monomer-to-initiator ratio assuming quantitative conversion. During the polymerization of norbornene monomers by ROMP, the monomer can be incorporated in two modes: cis- and trans-configuration. The predominant trans-configuration observed in the ^{1}H NMR spectra (**Figure S.III.3**) of poly(Nb)$_{90}$ results in a molecular weight overestimation by SEC.[34] Furthermore, the molecular weight determination of bottlebrush polymers by the means of SEC relies on a multitude of parameters as described in the literature.[35] Bottlebrush molecular weights are often underestimated because of their nonentangled and elongated polymer morphology.[25,36,37] In comparison to the first polymer segment, poly(Nb)$_{40}$-*graft*-PEGME, an increase in molecular weight can be observed for the block copolymer. The SEC curves of 2 and 3 show a slight shoulder at higher molecular weights which might be attributed to a small amount of chain coupling. The norbornene content in all the polymers was calculated

based on the NMR analysis of double bond signals arising from polymerized norbornene unit and the degree of polymerization in the respective polymer (for more details, refer to Supporting Information, **Table S.III.1**). For the homopolymers (1 + 2), the norbornene content is equivalent to the norbornene content of the monomers. For the bottlebrush block copolymer 3, a total norbornene content of 11 wt % was obtained corresponding to a composition of poly(Nb)$_{40}$-*graft*-PEGME-*block*-poly(Nb)$_{68}$. The poly(Nb)$_{68}$ polymer segment amounts to 7 wt % of the total polymer, and under consideration of bulk polymer densities, this is equivalent to a volume fraction (Φ_{Nb}) of around 8vol %.

Table III.1. Overview of synthesized polymers, calculated norbornene contents, theoretical and experimentally determined molecular weights, and polymerization conversions.

polymer	abbrev.	Φ_{Nb} / wt%	$M_{n,cal}$	$M_{n,SEC}$ [a]	$Đ$ [b]	p [c]
poly(Nb)$_{90}$ **1**	PNb	100	8500 [d]	18200	1.12	quant.
poly(Nb)$_{40}$-*graft*-PEGME **2**	BB	4	84800 [e]	63300	1.13	quant.
poly(Nb)$_{40}$-*graft*-PEGME-*block*-poly(Nb)$_{68}$ **3**	BB-BCP	11	91200 [f]	76300	1.17	quant.

[a] eluent THF + 0.25 wt% TBAB, PS calibration

[b] based on SEC results: M_w/M_n

[c] determined by ^{1}H NMR spectroscopy; quant: quantitative conversion

[d] calculated by [Nb]/[G3]*M_{Nb}

[e] calculated by [Nb-PEGME]/[G3]*$M_{Nb\text{-}PEGME}$

[f] calculated by [Nb-PEGME]/[G3]*$M_{Nb\text{-}PEGME}$+[Nb]/[G3]*M_{Nb}

III.3.2 Morphology and Mechanical Stability.

The pristine bottlebrush polymer BB and its reinforced counterparts (BB +PNb blend, BB+NP with TiO_2 fillers, and BB-BCP block copolymer) were characterized by oscillatory rheological measurements as well as SEM. SEM images (**Figure III.2**a) show a coherent and homogeneous polymer film morphology for BB and BB-BCP. For the polymer blend (BB+PNb), a macrophase separation of the immiscible polymer constituents could be observed. The differences between BB+PNb and BB-BCP substantiate the successful block copolymerization, as the covalent connection of the immiscible polymer segments prevents macroscopic segregation. Further, no ordered microstructures (i.e., microphase separation) are to be expected, as the second polymer segment (poly(Nb)$_{68}$) in BB-BCP 3 is not sufficient (7 wt % and 8 vol %) to establish an ordered microphase separation.[41,42] This difference in morphology between blend and block copolymers is particularly interesting to study the consequences for the ionic transport through the polymer matrix in solid polymer electrolytes, as the non-conducting macroscopic poly(Nb)$_{90}$ domains may obstruct the Li-ion transport pathways through the electrolyte and at the interfaces. The nanocomposite BB+NP shows a homogeneous distribution of the TiO_2 nanoparticles, which can be observed as bright spots throughout the polymer matrix. Frequency sweep measurements and a shear strain amplitude sweep are presented in **Figure III.2**b,c, respectively. We want to point out that all experiments have been conducted without the addition of LiTFSI salt because of the highly hygroscopic nature of the electrolyte mixtures under ambient conditions. In both experiments, the mechanical reinforcement for all the three cases is evident in comparison to the pristine bottlebrush polymer (BB), as the storage (G') and loss (G'') modulus could be increased by **three** orders of magnitude. In the frequency sweep measurements (**Figure III.2**b), both the

polymer blend and the polymer nanocomposite show elastic behavior at low frequencies, showing a gel point at around 1 Hz. The BB-BCP on the other hand shows viscous behavior across the entire frequency range (G′ < G″). Above frequencies of 0.1 Hz, G′ and G″ of the BB-BCP surpass those of BB+PNb and BB+NP. The difference can be attributed to the morphology of the materials. On the one hand, blend and nanocomposites exhibit phase-separated domains. On the other hand, the block copolymer, which lacks any phase separation, shows predominantly viscous behavior. Additionally, we conducted an amplitude sweep experiment at a selected frequency of 1Hz to assess the limits of the linear viscoelastic regime (**Figure III.2**c). Compared to BB, the storage modulus at 1 Hz could be increased from 0.6 to 73.7, 94.8, and 681.1 Pa for BB+PNb, BB+NP, and BB-BCP, respectively. This represents three orders of magnitude increase of the G′ from BB to BB-BCP. In contrast to the other two reinforced systems, BB-BCP shows a linear behavior of the G′ over the whole amplitude range of the measurement. BB, BB+PNb, and BB+NP showed a decrease in storage modulus above a critical shear strain amplitude, resulting in irreversible deformation of the systems. For example, the linear regime for BB ends at 0.7 %, whereas for BB+PNb, and BB+NP, the limits are 0.3 and 0.4 %, respectively. In this context, it is also to be noted that in the case of cross-linked and porous SPEs, remarkable dendrite growth resistance is observed even at low modulus (10^5 Pa), suggesting that a high-modulus SPE is not the only requirement for the control of dendrite proliferation.[38–40] The lithium electrolyte interface stability is part of **a** further examination in the following.

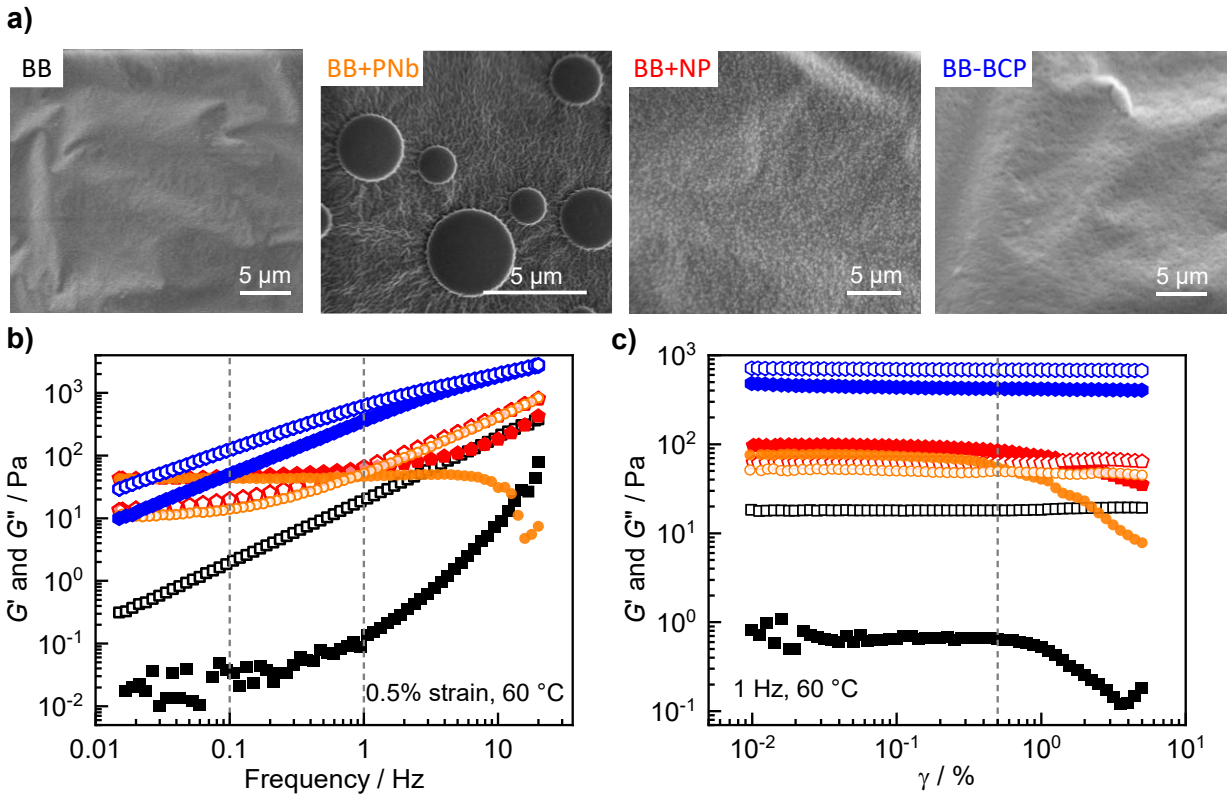


Figure III.2. (a) SEM images of the synthesized polymers (BB, BB-BCP), polymer nanocomposite (BB+NP), and polymer blend (BB+PNb). (b) Frequency sweep measurements (strain of 0.5 %, 60 °C) and (c) complex shear strain (γ*) measurements (1 Hz, 60 °C) showing the storage (G') and loss (G") modulus of the materials (G' filled symbols, G" hollow symbols): (black squares) BB, (orange circles) BB+PNb, (red pentagons) BB+NP, and (blue hexagons) BB-BCP. The grey dotted lines show the intersection of G' and G" where the transition occurs.

III.3.3 Thermal Characterization.

The thermal stability of the synthesized polymers, the reinforced systems, and electrolytes was characterized by TGA, and the temperature corresponding to a weight loss of 5 % ($T_{d,5\%}$) is given in **Table III.2**. The measured TGA curves are presented in **Figure S.III.6**. All of the systems are highly thermally stable. The PNb 1 shows the highest thermal stability with a $T_{d,5\%}$ of 425 °C, whereas the bottlebrush polymer 2 shows a $T_{d,5\%}$ of 376 °C. The incorporation of polynorbornene constituents in either polymer blend (BB+PNb) or the synthesized BB-BCP 3 shows increased thermal stability of 385 and 389 °C, respectively. On the other hand, the addition of aTiO_2 filler in the bottlebrush nanocomposite (BB+NP) resulted in a lower $T_{d,5\%}$ of 366 °C. The pristine polymers and mixtures were used as the matrix for the formulation of electrolytes by adding lithium bis(trifluoromethane sulfonyl)imide (LiTFSI) at an O/Li ratio of 16 (nomenclature being polymer matrix-16) (**Tables III.2** and **S.III.2**). Even though the thermal stability was slightly reduced by the Li-salt addition, all of the electrolytes are stable above 300 °C and sufficiently stable for applications in all-solid-state LMBs. Thermal transitions were evaluated by DSC (**Figure S.III.7**). The homopolymer PNb is fully amorphous with a T_g of 55 °C, whereas the bottlebrush systems exhibit crystallinity (T_{cr} and T_m) arising from PEG side chains. All electrolytes show similar glass transition temperatures (T_g) in the range of −47 to −51 °C, which can be attributed to the T_g of the PEG side chains. The PNb backbone does not influence the T_g of the side chains at a sufficient side chain length.[29] The T_g at 55 °C of PNb overlaps with the melting temperature (T_m) of the PEG segments in the bottlebrush systems. Therefore, the crystallization enthalpies (ΔH_{cr}) from cooling curves across the different systems are compared to understand the degree of crystallinity of each system. Across the pristine polymer matrices, blending (BB+PNb), filling (BB+NP), and block copolymerization (BB-BCP) decrease the transition enthalpy compared to that of the BB polymer.[30–32]

Table III.2. Overview of the thermal properties of synthesized polymers (**1-3**), formulated polymer mixtures (BB+NP, BB+PNb), and electrolytes (BB-16, BB+NP-16, BB+PNb-16, and BB-BCP-16).

abbreviation	composition	O/Li	$T_{d,5\%}$ °C	T_g °C	T_{cr} / T_m °C	ΔH_{cr} / ΔH_m J g^{-1}
PNb	**1**	-	425	55	-	-
BB	**2**	-	376	-	26 / 63	-124.5 / 134.8
BB-16	**2** + LiTFSI	16	365	-48	-	-
BB+PNb	**1** + **2** [a]	-	385	-	21 / 50	-117.7 / 131.5
BB+PNb-16	**1** + **2** + LiTFSI [a]	16	363	-51	2[b] / 37	-24.0[b] / 26.6
BB+NP	**2** + TiO_2 (10 wt%)	-	366	-	26 / 51	-103.4 / 112.3
BB+NP-16	**2** + TiO_2 (10 wt%) + LiTFSI	16	327	-48	-	-
BB-BCP	**3** [a]	-	389	-	21 / 50	-101.5 / 108.8
BB-BCP-16	**3** + LiTFSI [a]	16	358	-48	-	-

[a] total weight content of norbornene (Φ_{Nb}) in both BB+Nb and BB-BCP are equivalent.

[b] T_{cr} and recrystallization enthalpy (ΔH_{recr}) during 2nd heating step.

Interestingly, the crystallization enthalpy of the blend BB+PNb is closer to that of pristine bottlebrush polymer BB and is higher than for the block copolymer BB-BCP despite the similar norbornene content in both systems. This indicates that a possible macrophase separation in a

blend affects the crystallization of PEG in BB to a lesser extent than the polynorbornene segment in the BB-BCP, which is probably distributed more homogeneously throughout the entire system, reducing the crystallinity of the PEG domains more effectively. The crystallinity is further reduced by the addition of plasticizing LiTFSI in all cases. After salt addition, all of the electrolytes show no melting crystallization transition except for the polymer blend electrolyte (BB+PNb-16). However, the transition enthalpy is significantly reduced from 117.7 to 24 J g^{-1} for the blend electrolyte.

III.3.4 Electrochemical Characterization.

Besides mechanical stability of the electrolyte, the electrochemical stability window (ESW) and the ability to transport lithium ions are important properties of any electrolyte system. Therefore, the temperature-dependent ionic conductivity was determined by electrochemical impedance spectroscopy (EIS) in the temperature range between 80 and 25 °C in symmetrical blocking cells (StSt/SPE/StSt). For PNb-*graft*-PEGME (BB), three different salt concentrations (O/Li =12, 16, and 20) were evaluated (**Figure S.III.8**). Based on the results, an O/Li ratio of 16 was selected for all the electrolytes (polymer matrix-16). The addition of nanoparticles, polymers, or polymer segments could influence the optimum salt concentration. However, to ensure comparability, we selected the same O/Li ratio for all of the electrolyte systems. An overview of the determined ionic conductivities and further electrochemical properties is given in **Table III.3** The corresponding Nyquist plots for each electrolyte are given in **Figure S.III.9**. The Arrhenius plots for the BB-16, BB+PNb-16, BB+NP-16, and BB-BCP-16 electrolytes are displayed in **Figure III.3**a. The temperature-dependent ionic conductivity shows a distinct curvature across the temperature range, reflecting the interdependence of ionic mobility and the segmental motion of the polymer matrix, as described by the Vogel–Tamman–Fulcher (VFT) theory.[43] The electrolyte systems of BB-16 and the nanocomposite BB+NP-16 show a similar ionic conductivity (10^{-4} S cm^{-1})in the whole temperature range between 80 and 25 °C. In contrast to the other electrolyte systems, the blend electrolyte BB+PNb-16 shows a significant decrease of the ionic conductivity below 40 °C, which can be attributed to the macrophase separation and semi-crystalline properties of the blend electrolyte, as discussed above. Over the whole temperature range, the BB-BCP-16 electrolyte showed the highest ionic conductivity, with a value of up to 1.2×10^{-4} S cm^{-1} at 80 °C. The dilution of lithium conducting domains (PEG domains) with isolating domains (i.e., Nb domains) has been shown to reduce slightly the ionic conductivity, as reported earlier in comparisons of PEO homopolymers with PEO block copolymers.[26,44] Contrary to this trend, the introduction of 10 wt % norbornene segments in the block copolymer leads to an increase of the ionic conductivity. Despite the identical overall composition of blend BB+PNb-16 and block copolymer BB-BCP-16, the impact of incorporating small amounts of Nb is beneficial only for the block copolymer architecture and not for blending. Due to the observed macrophase separation and semicrystalline nature of the blend system leading to very low ionic conductivity at room temperature, the BB+PNb-16 electrolyte is not considered for battery applications and therefore not discussed further. The lithium transport number (t_{Li+}) was determined in symmetrical Li|SPE|Li cells in accordance with the Bruce and Vincent method.[45] The experimental data are summarized in the Supporting Information (**Figure S.III.10** and **Table S.III.3**). The BB-16 exhibits typical t_{Li+} values of 0.24 ± 0.01 for PEO/PEG-based materials. The addition of TiO_2 nanoparticles into the bottlebrush polymer resulted in a small increase of the lithium transport number (t_{Li+} = 0.29 ± 0.02), as described for comparable systems in the

literature.[16] Similarly, the BB-BCP-16 also showed a slight increase of the t_{Li+} to 0.27 ± 0.02 compared to the BB-16. However, all of the systems show t_{Li+} values in the same range, and the increases in BB+NP-16 and BBCP-16 are only marginal. The electrochemical stability can be probed by linear sweep voltammetry (LSV) using Li|SPE|StSt cells (**Figure III.3**b). The electrochemical stability in LSV experiments was evaluated geometrically as the transition from the faradaic to the non-faradaic regime by putting tangents and taking the x-intercept values. This is a simple and preliminary method, as discussed below. The recorded voltammograms show significant oxidative decomposition around 5 V (**Figure III.3**b). The determined potential of decomposition (V_d) is 5.3, 5.4, and 5.0 V for BB-16, BB+NP-16, and BB-BCP-16, respectively. The indicated electrochemical stability windows suggest sufficient oxidative stability against most cathode materials.

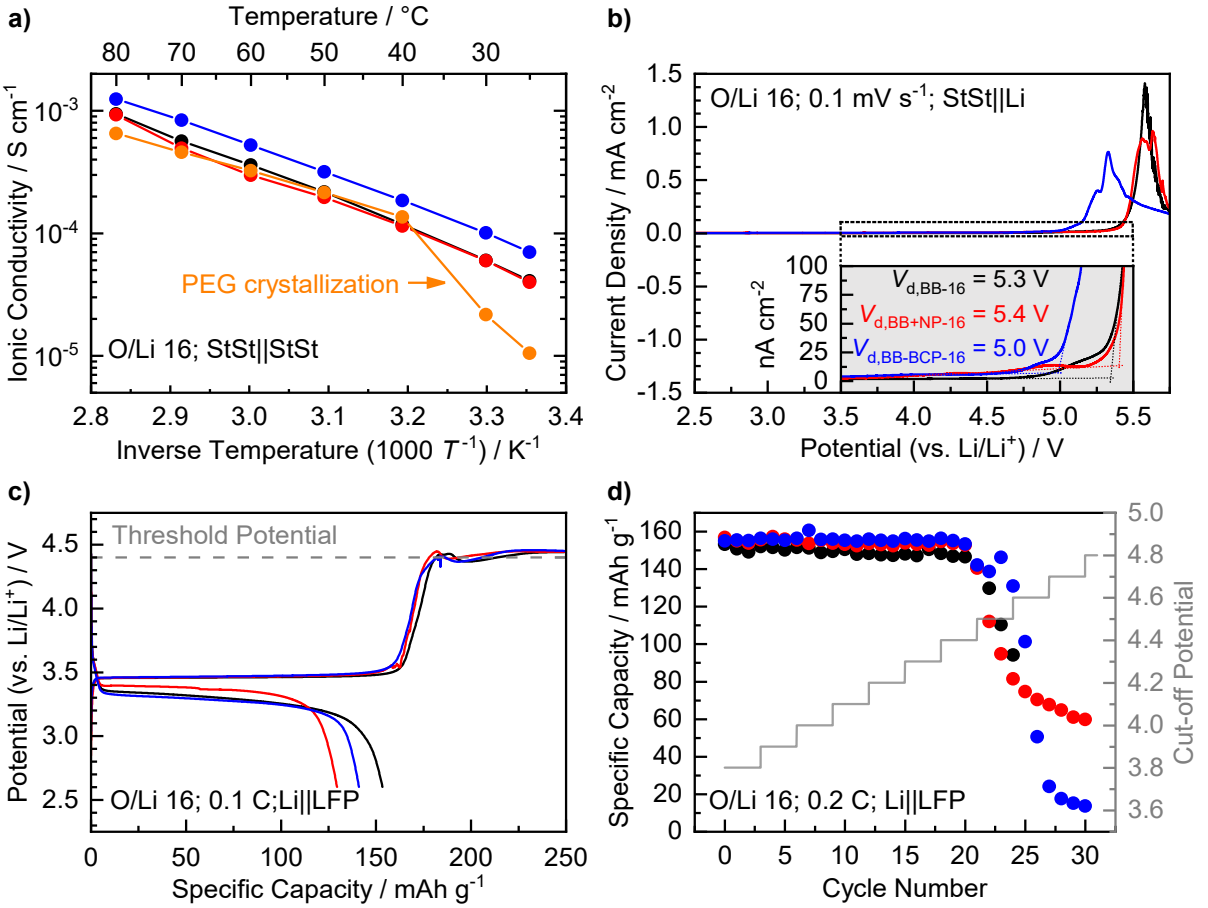


Figure III.3. For all plots (**a**-**d**): (black) BB-16, (red) BB+NP-16, (orange) BB+PNb-16, and (blue) BB-BCP-16. (**a**) Arrhenius plots of temperature-dependent ionic conductivity (80 °C – 25 °C). (**b**) Linear sweep voltammetry measurements at a sweep rate of 0.1 mV s^{-1} using Li|SPE|StSt cells at 70 °C. The inset shows a magnification of the recorded current response between 3.5 V and 5.5 V. (**c**) Galvanostatic overcharging experiments using Li|SPE|LFP cells at 70 °C. The displayed discharge curve corresponds to the first discharging process after the galvanostatic overcharging. (**d**) Cutoff increase cell cycling measurements in a cut-off potential range of 3.8 – 4.8 V and increments of 0.1 V at 70 °C. For each cut-off potential three charge/discharge cycles were performed.

However, LSV often results in an overestimation of the ESW as the influence of the cathode electrolyte interface is not accessible using such test cells. Therefore, the application under operational conditions of cells using a combination of Li–metal anode and representative cathode

is essential for the evaluation of the applicability in LMBs. For this, the electrochemical stability is investigated by galvanostatic overcharging (GO) as well as cutoff increase cell cycling (CICC) in Li|SPE|LFP test cells.[46,47] During galvanostatic overcharging, the cell is charged continuously without a cutoff limit, which is commonly set between 3.8 and 4.0 V for LFP cathodes. As can be observed in **Figure III.3**c, the charging profile shows a steep increase of the cell potential at 160 mAh g^{-1} as a consequence of the completed charging process. The second plateau at 4.4 V is attributed to the oxidative decomposition of the electrolyte. Similar effects can be observed in the CICC plot (**Figure III.3**d) of the electrochemical stability. During CICC measurements, the LMB is charged to an incrementally increased cutoff voltage starting from 3.8 V. For each cutoff potential, three individual cycles are performed. Until 4.3 V, all of the electrolytes show stable specific discharge capacities of around 150–160 mAh g^{-1}. However, when the batteries are charged to 4.4 V, the cells show decreasing or unstable discharge capacities for all of the electrolytes. Both GO and CICC measurements unambiguously revealed that the electrochemical stability determined by LSV is not necessarily representative for anode|SPE|cathode systems/half cell setups. The oxidative stability of these electrolytes is limited to potentials below 4.4 V, which can be attributed to the PEG-based constituents of the polymer matrices.[47]

Table III.3. Overview of the electrochemical properties and cycling performance of electrolytes BB-16, BB+NP-16, BB+PNb-16, and BB-BCP-16.

electrolyte	O/Li	σ / S cm^{-1}	σ / S cm^{-1}	t_{Li^+}	electrochemical stability / V		
		@25 °C	@70 °C	@70 °C	LSV [a]	GO [b]	CICC [c]
BB-16	16	4.1×10^{-5}	5.6×10^{-4}	0.24±0.01	5.3	4.4	4.4
BB+NP-16	16	3.9×10^{-5}	4.9×10^{-4}	0.29±0.02	5.4	4.4	4.4
BB-BCP-16	16	7.0×10^{-5}	8.4×10^{-4}	0.27±0.02	5.0	4.4	4.4

[a] Potential at x-intercept of two tangents.

[b] Potential of decomposition plateau attributed to electrolyte oxidation.

[c] Highest cut-off potential showing stable discharge capacity.

III.3.5 Cycling Performance in Li/SPE/Li and Li/SPE/LFP Cells.

In addition to fundamental electrochemical properties determined in the section above using various cell geometries, the lithium|electrolyte interface properties play a salient role in LMBs, especially to understand interface impedance at the solid electrolyte interface (SEI). Since the different electrolytes have vastly different mechanical properties, for a comparative study of interfaces in both symmetrical Li|SPE|Li cells as well as in Li|SPE|LFP cells over a large number of cycles and to achieve high ionic conductivity by reducing the thickness of the electrolyte, we used a porous (porosity: 28 %) track-etched poly(imide) membrane with a thickness of 7 µm (PI7) and diameter of 16 mm, which was infiltrated with different SPEs from both sides before cell fabrication. The membrane is decorated with vertically aligned conduction channels, as shown in SEM images (**Figures III.5e,f** and **S.III.13**), which provide low tortuosity and direct ion transport pathways as reported in literature. [50–52] The small pores of the membrane (diameter ~ 0.2 µm) were also shown to reduce the formation of lithium dendrites to some extent.[50–52] Symmetrical lithium cells enable the isolated evaluation of the reversibility and stability of the electrolytes employed at the Li interfaces. During galvanostatic cycling, the applied current density (0.1 mA cm^{-2}) causes an overpotential which is required to overcome the resistive behavior of the electrolyte and charge transfer processes at the interfaces. The applied current density during lithium plating-stripping (LPS) experiments was selected to be similar to the current density

applied in later battery cycling experiments of 0.2C; hence, this allows for the individual observation of Li|SPE interface processes in a comparable stress. All of the electrolytes show similar overpotentials during the LPS experiments (**Figure III.4**a–c). Magnified excerpts of the LPS measurements are given in **Figure S.III.11.** For all of the systems, no internal shorting caused by penetrating lithium dendrites could be observed, which would be observed as an instantaneous decrease of the overpotential toward 0 V. The electrolyte BB+NP-16 shows a slight increase of the overpotential in the first few cycles during equilibration and fluctuation, whereas the other electrolytes show a decrease in cell polarization and smooth plating and stripping behavior. For both BB-16 and BB-BCP-16, stable cycling could be observed over the 240 cycles (equivalent to 470 h) of cycling without a significant increase in cell polarization. For BB+NP-16, stable cycling could be achieved only until 140 cycles. In addition to the LPS data presented here, additional LPS experiments for BB+NP-16 are shown in the Supporting Information. All of the test cells of nanocomposites showed either cycling instabilities after only a few cycles or very high overpotentials. The voltage profile can provide insight into the cycling stability of the cell. However, a more in-depth analysis can be achieved by intermittent PEIS experiments (**Figure III.4**d–f). After every five full cycles, the galvanostatic cycling is briefly interrupted to conduct a PEIS measurement. The recorded PEIS spectra are analyzed by the generalized distribution of relaxation times (gDRT), which enables an ab initio reconstruction of impedance spectra based on the fundamental time constants of different processes (**Figure III.4**g–i).[16,48,49] The absolute distribution function $h(\tau)$ in DRT plots represents the corresponding impedance of process with a particular time constant. The recorded PEIS spectra and the conducted gDRT analysis confirm the trends deduced from the voltage profiles. While the diagonal straight lines at high Z′ in **Figure III.4**d–f can be attributed to diffusion limitations, the adjacent semicircle reflects the charge transfer resistance at the electrode–electrolyte interfaces. The electrolyte bulk resistance constitutes the small semicircles at low Z′ values (at very high frequencies).[49] For clarity, the impedance data of one of the systems BB-BCP-16 are enlarged at the high frequency part and shown in **Figure S.III.13**. The bulk (a), interface (b), and diffusion (c) contributions to impedance can be observed at different relaxation times in the absolute distribution function $h(\tau)$ displayed in **Figure III.4**g–i. BB-16 and BB-BCP-16 show a decrease in the interface resistance after the fifth cycle. After the equilibration, the spectra of the 125th and 230th cycles show similar impedance spectra indicating the formation of a stable SEI interface in these two cases. The decrease in the polarization of the interface contribution (b) further demonstrated the equilibration and subsequent stable cycling performance for BB-16 and BB-BCP-16. In contrast to these two electrolyte systems, the interface resistance of BB+NP-16 already shows a well-established SEI within the fifth cycle without any equilibration processes (**Figure III.4**e). The overall polarization of the interface contribution is also lower than for the other electrolytes systems. The beneficial effects of TiO_2 nanoparticle addition on the interface properties have been demonstrated in the literature.[16] However, the interface resistance slightly increased from the 5th to the 125th and 135th cycle. The PEIS measurements of the nanocomposite BB+NP-16 show a significant and continuous increase of the bulk contribution, indicated by the shift toward higher Z′ values. This increase can also be observed in the increase of the bulk contribution (a) in the absolute distribution function (**Figure III.4**h). In brief, the addition of nanoparticles in BB+NP-16 proved to be beneficial for the fast stable interface formation, but during prolonged cycling, the polymer matrix was affected negatively. The pristine bottlebrush BB-16 and block copolymer BB-BCP-16 electrolytes exhibited higher initial interface resistances, which decreased with cycling and led to stable cycling over the entire experiment duration.

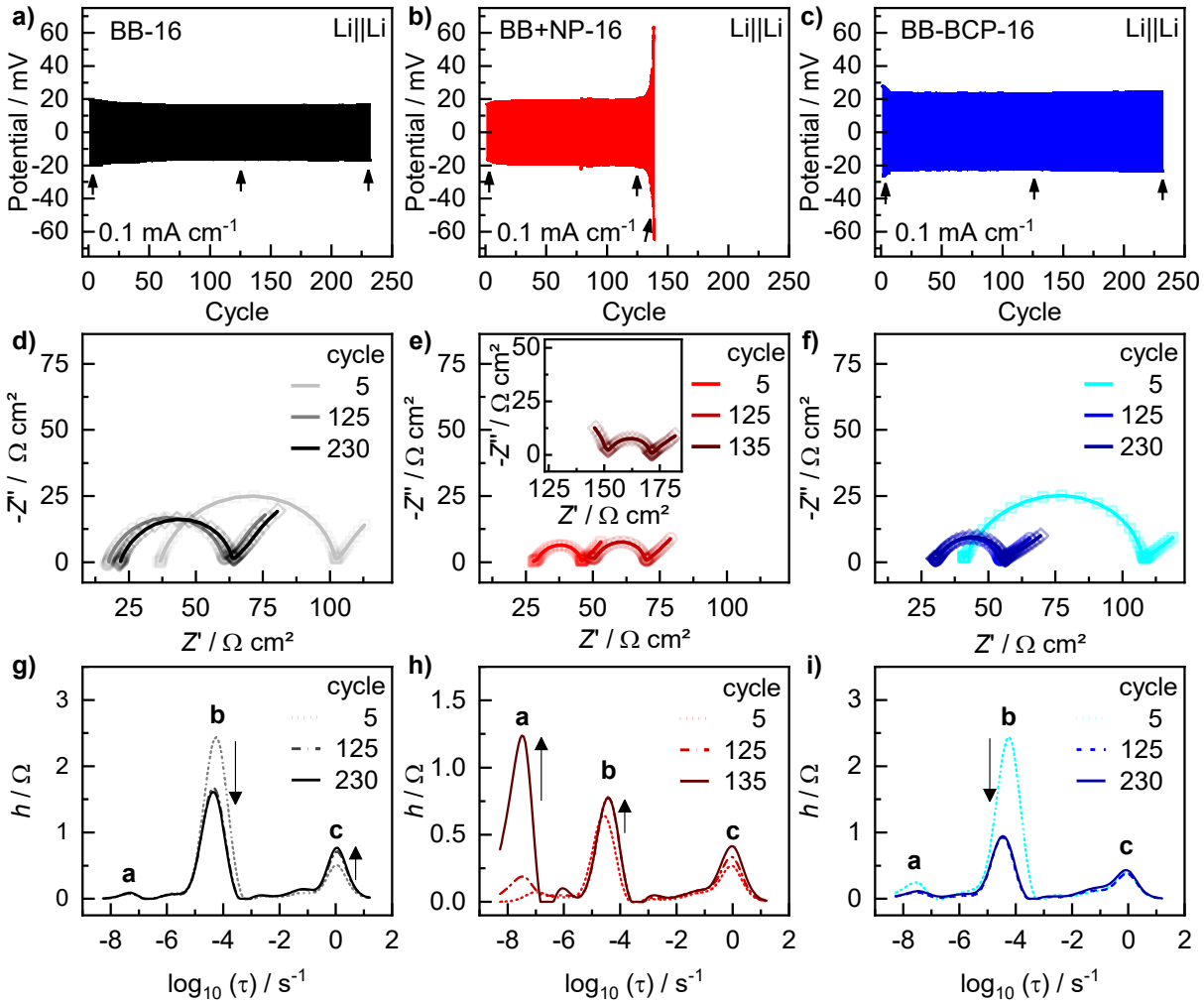


Figure III.4. Lithium plating and stripping (LPS) cycling data in Li/SPE/Li cells. For all plots (**a-i**): (black) BB-16, (red) BB+NP-16, and (blue) BB-BCP-16. (**a-c**) LPS cycling data at 70 °C. The cycling was performed for 1 h per half cycle at 0.1 mA cm^{-2}. Arrows indicate the specific cycles analyzed by PEIS and DRT. (**d-f**) PEIS measurements after the indicated number of LPS cycles (hollow symbols) data points, (solid lines) DRT fit. The impedance spectra are normalized to electrolyte area. (**g-i**) gDRT analysis of displayed PEIS measurements. The DRT results are represented by the absolute distribution function $h(\tau)$. Peaks **a**, **b**, and **c** can be attributed to ionic conductivity, interfacial resistance/processes, and diffusion at the electrodes, respectively.

Finally, the cycling performance of the different electrolytes was comparatively evaluated in all solid-state battery half-cells comprising lithium metal anodes and lithium iron phosphate-based (LFP) cathodes. The battery cycling was performed at 70 °C (since most of the studies of PEO-based electrolytes are given at elevated temperatures) at charging and discharging rates of 0.2C. The charge and discharge profiles (**Figure III.5**a–c) of the electrolytes exhibited a dominant plateau between 3.4– 3.5 V reminiscent of the LFP redox behavior. The cells with BB-BCP-16 showed slightly increased overpotentials during charge and discharge compared with the other electrolyte systems. The overpotential was evaluated as the voltage difference between the charge and discharge curve at a specific capacity of 100 mAh g^{-1}. The corresponding overpotentials during the first battery cycle were 106, 99, and 124 mV for BB-16, BB+NP-16, and BB-BCP-16, respectively. The trends for the overpotentials reflect the findings from the LPS experiments. The addition of TiO_2 nanoparticles in BB+NP-16 shows beneficial effects for the interface formation and charge

transfer at the electrodes, resulting in overall lower overpotentials. Compared to BB-16 the incorporation of the PNb segment in BB-BCP-16 led to an increase in the observed overpotential. This behavior can be attributed to the nonconducting poly(Nb)$_{68}$ polymer segment. Even though the bulk conductivity of the BB-BCP-16 electrolyte is increased compared to that of BB-16, the PNb domains can lead to a restriction of the current density at both electrode–electrolyte interfaces. All of the electrolyte systems showed high initial specific capacities under the applied cycling conditions. The specific capacities and Coulombic efficiencies in **Figure III.5**d represent the average of three battery cells per electrolyte system. In the following, only the average values are discussed. The initial discharge capacities were 157, 156, and 159 mAh g^{-1} for BB-16, BB+NP-16, and BB-BCP-16, respectively.

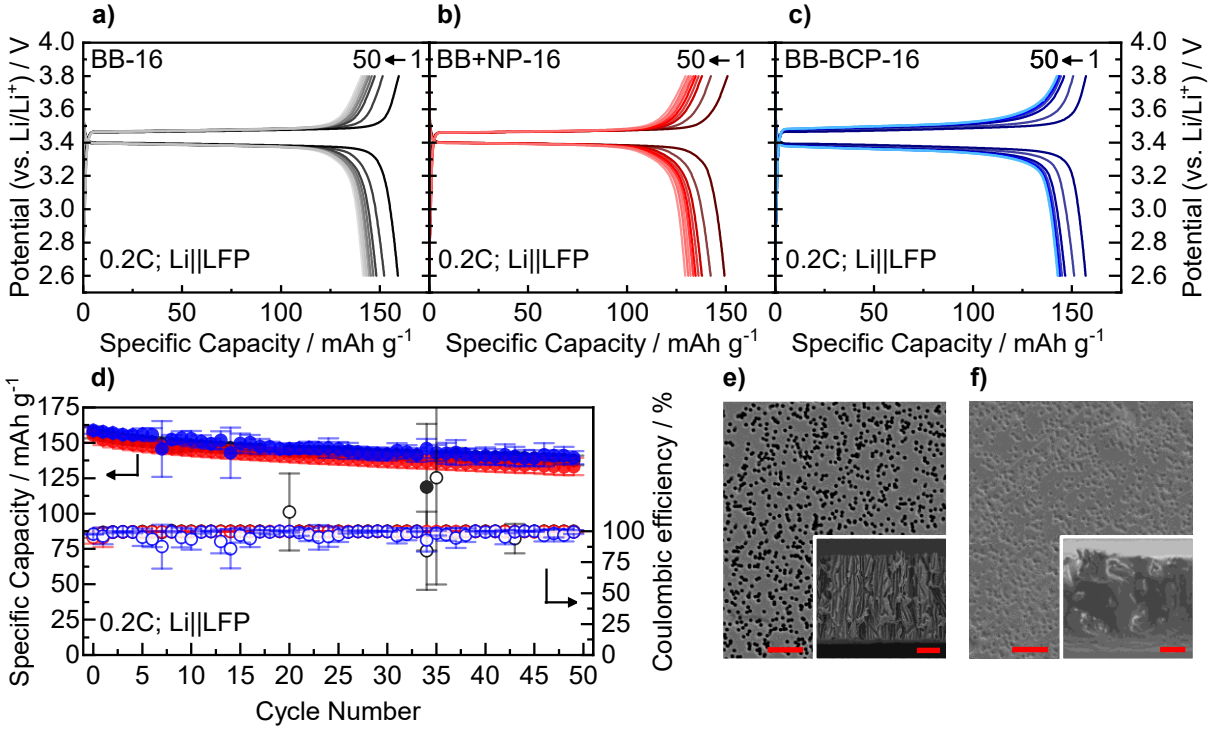


Figure III.5. Cycling performance of Li-metal batteries using Li|SPE|LFP cells. (**a**-**c**) Exemplary charge and discharge curves of cycles (cycle number represented by hue from dark to bright) 0, 10, 20, 25, 30, 35, 40, 45, and 50. (**d**) Overview of (spheres) discharge capacity and (circles) coulombic efficiency over 50 cycles at 0.2 C. Top view and cross-sectional (as inset) SEM images of (**e**) the pristine PI7 membrane and (**f**) the PI7 membrane filled with BB-BCP-16 electrolyte. The scale bar is equivalent to 2 µm in all cases.

The comparable discharge capacities demonstrate that the mechanical stability of soft bottlebrush polymer electrolytes can be enhanced without compromising the electrochemical performance of battery cells either by fillers or by the block copolymerization strategy. All the electrolyte systems showed comparable high capacity retention (CR) >85 % after 50 cycles. In detail, while BB-16 and BB-BCP-16 show similar CR values of 87.8 and 88.0 %, BB+NP-16 showed a retention of 85.3 %. The Coulombic efficiency (CE) represents the ratio of discharge capacity to charge capacity. For any battery application, a CE of 100 % is highly desirable to reduce efficiency losses during battery operation. Interestingly, after an equilibration phase of two cycles, BB+NP-16 showed a steady CE close to 100 % without significant fluctuations. This further proves the benefits of TiO_2 NP on the interface properties between lithium and electrolyte. BB-16 and BB-

BCP-16 showed fluctuations of the CE. The reduced CE and the fluctuations can be attributed to the so-called voltage noise phenomenon in solid polymer electrolytes.[53] The phenomenon describes voltage fluctuations during the charging process, which results in excessive charge without reaching the defined cutoff potential. This effect becomes increasingly prominent for thin electrolyte geometries. In this work, porous poly(imide) separators with a thickness of 7 µm (PI7) infiltrated with SPEs were used to reduce the SPE thickness and ensure electrode separation. This makes the cells especially prone to this effect. Homann et al. localize the origin of the voltage noise to be the Li|SPE interface and possible micro short circuits. In summary, all three strategies lead to cycling stability in Li|SPE|LFP cells and very high CE values, the fluctuations of which can be attributed to the general cell design.

III.4 Conclusion

We evaluated and compared different strategies of mechanical reinforcement of bottlebrush polymer electrolytes and their influence on all-solid-state LMBs. By employing ring-opening metathesis copolymerization, different norbornene-based polymers were synthesized. A bottlebrush (BB) polymer was combined with either PNb in a polymer blend (BB+PNb), or TiO_2 nanoparticles in a polymer nanocomposite (BB+NP), or in a block copolymer architecture with an additional norbornene segment (BB-BCP). Rheological amplitude sweep experiments showed an increase of the storage modulus by up to three orders of magnitude due to the blending of PNb and BB (BB+PNb) or addition of NP to the BB polymer (BB+NP). Interestingly, BB-BCP exhibited by far the highest storage modulus of 681 Pa. SEM images revealed a macrophase separation of the two polymers in the BB+PNb blend, while the other materials showed homogeneous morphologies. Electrolytes were formulated by a combination of these polymers and LiTFSI. The electrolytes BB-16 and BB+NP-16 showed congruent ionic conductivities reaching 8.4×10^{-4} S cm^{-1} at 70 °C. BB-BCP-16 showed an increase in ionic conductivity despite the nonconducting PNb polymer segments. The corresponding blend of the individual homopolymers (BB+PNb-16) showed residual crystallinity at the same Li-salt content resulting in reduced ionic conductivity at room temperature. High electrochemical stability of the materials was observed until 4.4 V, which is generally governed by the PEG-domain stability, as determined by GO and CICC measurements. The Li|SPE interface was investigated by LPS cycling experiments, revealing that all of the materials show excellent stability against lithium metal. However, the electrolyte was negatively affected by the TiO2 nanoparticles in BB+NP-16, leading to premature cell failure. Solvent-free Li|SPE|LFP battery cycling experiments showed high initial discharge capacities of over 150 mAh g^{-1} and stable cycling over 50 cycles for BB-16, BB-BCP-16, and BB+NP-16. The voltage noise phenomenon resulted in reduced Coulombic efficiencies for BB-16 and BB-BCP-16. This effect was not observed by the addition of nanoparticles in BB+NP-16. The increase of both ionic conductivity and mechanical stability paired with excellent electrochemical stability of the BB-BCP block copolymer system demonstrates that the incorporation of nonconducting polymer segments in a block copolymer strategy can contribute the most toward overall performance of bottlebrush polymer electrolytes compared to the blending and filling approaches.

III.5 Experimental Section

III.5.1 Polymer Synthesis

The macromonomer Nb-PEGME (poly(ethylene glycol) monomethyl ether-5-norbornene-2-carboxylate) was synthesized following published procedures.[33] The polymers poly(Nb)$_{90}$ 1, poly(Nb)$_{40}$-*graft*-PEGME 2, and poly(Nb)$_{40}$-*graft*-PEGME-*block*-poly(Nb)$_{68}$ 3 were prepared by ring-opening metathesis polymerization (ROMP) using a third-generation Grubbs catalyst (G3). Bottlebrush polymer segments of 2 and 3 were synthesized at 15 °C for 1 h. The polymerization of norbornene segments of 1 and 3 was conducted at –10 °C for 30 min. All polymerizations were terminated by the addition of EVE. For detailed synthetic procedures, refer to the Supporting Information.

III.5.2 Electrolyte Preparation

The polymers were dissolved in small amounts of acetonitrile. In the case of the polymer blend (BB+PNb-16) of poly(Nb)$_{90}$ 1 and poly(Nb)$_{40}$-*graft*-PEGME 2, the polymers were dissolved in a 1:1 (v/v) mixture of acetonitrile and toluene. For the polymer nanocomposite (BB+NP-16), 10 wt % of TiO_2 nanoparticles (P25) were added to the polymer solution. The polymer nanoparticle mixture was sonicated for 30 min to achieve a stable dispersion. To the polymer solutions, adequate amounts of lithium bis(trifluoromethane)sulfonimide (LiTFSI) were added to achieve the desired O/Li ratio. Polymer salt mixtures were prepared at a molar ratio of ether oxygen atoms to lithium cations (O/Li) of 16. All electrolyte mixtures were allowed to stir overnight and were subsequently dried in vacuo at 80 °C for 24 h. For detailed information about the electrolyte composition, see **Table S.III.2**.

III.5.3 Electrode Preparation

The cathodes consist of lithium iron phosphate (LFP) as active material, super P carbon (carbon black, CB) and conductive graphite (CG) as electron-conducting additives, and poly(vinylidene fluoride) (PVdF) as polymer binder. The weight ratio was adjusted to 80:5:5:10 wt % (LFP/CB/CG/PVdF). For the preparation, PVdF was dissolved in acetonitrile and a small amount of N-methyl pyrrolidone (NMP). The active material and carbon additives were added to the polymer solution, which was subsequently ball-milled for 2 h for homogenization. The resulting cathode slurry was applied to a carbon-coated aluminum current collector (thickness = 18 µm) by doctor blading. The cathodes were dried in vacuo at 60 °C for 24 h. The cathodes were calendared and cut into cathode discs (diameter 14 mm, area 1.54 cm^2). The active material loading of the resulting cathodes was ~3.3 mg cm^{-2} (0.561 mAh cm^{-2}).

III.5.4 Coin-Cell Fabrication

All electrochemical experiments were conducted using CR2032 coin-cell test cells. Ionic conductivity (IC) measurements were conducted in symmetrical stainless steel (StSt) cells as blocking electrodes (StSt|SPE|StSt). LSV was measured using StSt as the working electrode (WE) and lithium metal as the counter (CE) and reference electrode (RE) (StSt|SPE|Li). LPS and lithium transference number determination (LTN) were performed using symmetrical lithium cells (Li|SPE|Li). A Kapton spacer (thickness 130 µm; active area diameter: 4 mm) was used for IC and LSV measurements. During cell fabrication, the cavity of the Kapton separator was filled with the electrolyte. For LPS, lithium transference number (LTN), galvanostatic overcharging (GO),

cutoff increase cell cycling (CICC), and galvanostatic cycling with potential limitations (GCPL), a porous (porosity: 28 %) track-etched poly(imide) separator with a thickness of 7 µm (PI7) and diameter of 16 mm was used. The separator was infiltrated with SPE before cell fabrication (procedure described in Supporting Information).

III.5.5 Electrochemical Characterization

Before any measurement, coin cells were tempered at 70 °C at open-circuit voltage (OCV) for at least 12 h. All EIS measurements were conducted in a frequency range of 3 MHz–0.1 Hz by using a sinusoidal excitation potential of 20 mV. EIS measurements were evaluated by utilizing the generalized distribution of relaxation times (gDRT) analysis. For temperature-dependent ionic conductivity measurements, the temperature was controlled with a climate chamber (80–25 °C). For each temperature step, the impedance spectrum is recorded after an equilibration interval of 1.5 h. All of the other electrochemical experiments were performed at 70 °C. Linear sweep voltammograms were recorded at a scan rate of 0.1 mV s^{-1} between OCV and 6 V. The lithium transference number was determined in accordance with the Bruce and Vincent method. The measurement sequence consisted of an initial EIS measurement, a chronoamperometry (CA) interval of 3 h using a polarization potential of 10 mV, and a second EIS measurement immediately after the CA. LPS experiments were conducted at a current density of 0.1 mA cm^{-2} with a half-cycle duration of 1 h. With respect to the cathodes used in this work, 0.1 mA cm^{-2} is equivalent to 0.2C. During LPS experiments, the cycling was stopped intermittently (every 10 half cycles) to perform EIS measurements using the setting described above. Galvanostatic overcharging experiments were conducted using a DC equivalent to a current rate of 0.1C (~50 nA cm–2) starting from the OCV. During cutoff increase cell cycling experiments, battery cells were charged and discharged at a C-rate of 0.2C. The discharge cutoff potential was 2.6 V during the entire measurement. The charge cutoff potential was increased from 3.8 to 5 V in 0.1 V increments. For each cutoff potential, three charge/discharge cycles were recorded. The cycling performance was evaluated by GCPL at a C-rate of 0.2C between 2.6 and 3.8 V for 50 cycles.

III.6 Associated Content

III.6.1 Supporting Information

The Supporting Information is available free of charge at https://pubs.acs.org/doi/10.1021/acsapm.4c00161.

Materials, instrumentation, syntheses, ^{1}H NMR spectra, polymer and electrolyte composition, SEC elugrams, thermal analysis, SEM images, rheology measurements, lithium transference number determination, and LPS experiments (PDF)

III.7 Author Information

III.7.1 Corresponding Author

Mukundan Thelakkat – Applied Functional Polymers, University of Bayreuth, 95447 Bayreuth, Germany; Bavarian Polymer Institute (BPI) and Bavarian Center for Battery Technology (BayBatt), University of Bayreuth, 95447 Bayreuth, Germany; orcid.org/0000-0001-8675-1398; Email: Mukundan.thelakkat@uni-bayreuth.de

III.7.2 Authors

Jannik Petry – Applied Functional Polymers, University of Bayreuth, 95447 Bayreuth, Germany; orcid.org/00000002-1945-3320

Harimohan Erabhoina – Applied Functional Polymers, University of Bayreuth, 95447 Bayreuth, Germany

Markus Dietel – Applied Functional Polymers, University of Bayreuth, 95447 Bayreuth, Germany

Complete contact information is available at: https://pubs.acs.org/10.1021/acsapm.4c00161

III.7.3 Author Contributions

JP: Conceptualization, writing-original draft, synthesis, investigation, methodology, and visualization. HE: Investigation and methodology. MD: Investigation. MT: Conceptualization, funding acquisition, project administration, writing- reviewing and editing, and supervision. The manuscript was written through contributions of all authors. All authors have given approval to the final version of the manuscript.

III.7.4 Funding

Jannik Petry is supported by the Deutsche Bundesstiftung Umwelt (grant no. 20021/714–242). E.H. was financially supported by the Bavarian Center for Battery Technology (BayBATT) at the University of Bayreuth. The authors also thank Bavarian Ministry of State for Research and Arts under the SolTech project.

III.7.5 Notes

The authors declare no competing financial interest.

III.8 Acknowledgments

The authors thank Reiner Giesa, Macromolecular Chemistry I, University of Bayreuth, for rheology measurements. We acknowledge the Bavarian Polymer Institute (University of Bayreuth) for providing access to the Keylab Electron and Optical Microscopy for electron microscopy facilities and Labeesh Kumar for SEM measurements.

III.9 References

(1) Monroe, C.; Newman, J. Dendrite Growth in Lithium/Polymer Systems : A Propagation Model for Liquid Electrolytes under Galvanostatic Conditions. *J. Electrochem. Soc.* **2003**, *150* (10), A1377. https://doi.org/10.1149/1.1606686.

(2) Xu, W.; Wang, J.; Ding, F.; Chen, X.; Nasybulin, E.; Zhang, Y.; Zhang, J.-G. Lithium Metal Anodes for Rechargeable Batteries. *Energy Environ. Sci.* **2014**, *7* (2), 513–537. https://doi.org/10.1039/C3EE40795K.

(3) Schaefer, J. L.; Lu, Y.; Moganty, S. S.; Agarwal, P.; Jayaprakash, N.; Archer, L. A. Electrolytes for High-Energy Lithium Batteries. *Appl Nanosci* **2012**, *2* (2), 91–109. https://doi.org/10.1007/s13204-011-0044-x.

(4) Gorecki, W.; Jeannin, M.; Belorizky, E.; Roux, C.; Armand, M. Physical Properties of Solid Polymer Electrolyte PEO(LiTFSI) Complexes. *J. Phys.: Condens. Matter* **1995**, *7* (34), 6823. https://doi.org/10.1088/0953-8984/7/34/007.

(5) Robitaille, C. D.; Fauteux, D. Phase Diagrams and Conductivity Characterization of Some PEO - LiX Electrolytes. *J. Electrochem. Soc.* **1986**, *133* (2), 315. https://doi.org/10.1149/1.2108569.

(6) Wright, P. V. Electrical Conductivity in Ionic Complexes of Poly(Ethylene Oxide). *British Polymer Journal* **1975**, *7* (5), 319–327. https://doi.org/10.1002/pi.4980070505.

(7) Niitani, T.; Amaike, M.; Nakano, H.; Dokko, K.; Kanamura, K. Star-Shaped Polymer Electrolyte with Microphase Separation Structure for All-Solid-State Lithium Batteries. *J. Electrochem. Soc.* **2009**, *156* (7), A577. https://doi.org/10.1149/1.3129245.

(8) Yang, X.; Sun, X.; Shao, J.; Liu, Y.; Wang, X. Ionic Conductivity of Multiarm Star Polymer/$LiClO_4$ Electrolytes. *Journal of Polymer Science Part B: Polymer Physics* **2004**, *42* (22), 4195–4198. https://doi.org/10.1002/polb.20280.

(9) Lee, S.-I.; Schömer, M.; Peng, H.; Page, K. A.; Wilms, D.; Frey, H.; Soles, C. L.; Yoon, D. Y. Correlations between Ion Conductivity and Polymer Dynamics in Hyperbranched Poly(Ethylene Oxide) Electrolytes for Lithium-Ion Batteries. *Chem. Mater.* **2011**, *23* (11), 2685–2688. https://doi.org/10.1021/cm103696g.

(10) Panday, A.; Mullin, S.; Gomez, E. D.; Wanakule, N.; Chen, V. L.; Hexemer, A.; Pople, J.; Balsara, N. P. Effect of Molecular Weight and Salt Concentration on Conductivity of Block Copolymer Electrolytes. *Macromolecules* **2009**, *42* (13), 4632–4637. https://doi.org/10.1021/ma900451e.

(11) Bannister, D. J.; Davies, G. R.; Ward, I. M.; McIntyre, J. E. Ionic Conductivities of Poly(Methoxy Polyethylene Glycol Monomethacrylate) Complexes with $LiSO_3CH_3$. *Polymer* **1984**, *25* (11), 1600–1602. https://doi.org/10.1016/0032-3861(84)90152-6.

(12) Xia, D. W.; Soltz, D.; Smid, J. Conductivities of Solid Polymer Electrolyte Complexes of Alkali Salts with Polymers of Methoxypolyethyleneglycol Methacrylates. *Solid State Ionics* **1984**, *14* (3), 221–224. https://doi.org/10.1016/0167-2738(84)90102-4.

(13) Barai, P.; Higa, K.; Srinivasan, V. Lithium Dendrite Growth Mechanisms in Polymer Electrolytes and Prevention Strategies. *Phys. Chem. Chem. Phys.* **2017**, *19* (31), 20493–20505. https://doi.org/10.1039/C7CP03304D.

(14) Prabakaran, P.; Manimuthu, R. P.; Gurusamy, S.; Sebasthiyan, E. Plasticized Polymer Electrolyte Membranes Based on PEO/PVdF-HFP for Use as an Effective Electrolyte in Lithium-Ion Batteries. *Chin J Polym Sci* **2017**, *35* (3), 407–421. https://doi.org/10.1007/s10118-017-1906-9.

(15) B, J.; Km, A.; M, M.; V.s, P.; S., J. Development of a Novel Type of Solid Polymer Electrolyte for Solid State Lithium Battery Applications Based on Lithium Enriched Poly (Ethylene Oxide) (PEO)/Poly (Vinyl Pyrrolidone) (PVP) Blend Polymer. *Electrochimica Acta* **2017**, *235*, 210–222. https://doi.org/10.1016/j.electacta.2017.03.118.

(16) Erabhoina, H.; Rosenbach, D.; Mohanraj, J.; Thelakkat, M. Solid Polymer Nanocomposite Electrolytes with Improved Interface Properties towards Lithium Metal Battery Application at Room Temperature. *Electrochimica Acta* **2021**, *387*, 138455. https://doi.org/10.1016/j.electacta.2021.138455.

(17) Judez, X.; Piszcz, M.; Coya, E.; Li, C.; Aldalur, I.; Oteo, U.; Zhang, Y.; Zhang, W.; Rodriguez-Martinez, L. M.; Zhang, H.; Armand, M. Stable Cycling of Lithium Metal Electrode in Nanocomposite Solid Polymer Electrolytes with Lithium Bis (Fluorosulfonyl)Imide. *Solid State Ionics* **2018**, *318*, 95–101. https://doi.org/10.1016/j.ssi.2017.07.021.

(18) Zhao, Y.; Wu, C.; Peng, G.; Chen, X.; Yao, X.; Bai, Y.; Wu, F.; Chen, S.; Xu, X. A New Solid Polymer Electrolyte Incorporating $Li_{10}GeP_2S_{12}$ into a Polyethylene Oxide Matrix for All-Solid-State Lithium Batteries. *Journal of Power Sources* **2016**, *301*, 47–53. https://doi.org/10.1016/j.jpowsour.2015.09.111.

(19) Li, Z.; Huang, H.-M.; Zhu, J.-K.; Wu, J.-F.; Yang, H.; Wei, L.; Guo, X. Ionic Conduction in Composite Polymer Electrolytes: Case of PEO:Ga-LLZO Composites. *ACS Appl. Mater. Interfaces* **2019**, *11* (1), 784–791. https://doi.org/10.1021/acsami.8b17279.

(20) Fu, C.; Venturi, V.; Kim, J.; Ahmad, Z.; Ells, A. W.; Viswanathan, V.; Helms, B. A. Universal Chemomechanical Design Rules for Solid-Ion Conductors to Prevent Dendrite Formation in Lithium Metal Batteries. *Nat. Mater.* **2020**, *19* (7), 758–766. https://doi.org/10.1038/s41563-020-0655-2.

(21) Glynos, E.; Papoutsakis, L.; Pan, W.; Giannelis, E. P.; Nega, A. D.; Mygiakis, E.; Sakellariou, G.; Anastasiadis, S. H. Nanostructured Polymer Particles as Additives for High Conductivity, High Modulus Solid Polymer Electrolytes. *Macromolecules* **2017**, *50* (12), 4699–4706. https://doi.org/10.1021/acs.macromol.7b00789.

(22) Li, W.; Sun, C.; Jin, J.; Li, Y.; Chen, C.; Wen, Z. Realization of the Li + Domain Diffusion Effect via Constructing Molecular Brushes on the LLZTO Surface and Its Application in All-Solid-State Lithium Batteries. *Journal of Materials Chemistry A* **2019**, *7* (48), 27304–27312. https://doi.org/10.1039/C9TA10400C.

(23) Lago, N.; Garcia-Calvo, O.; Lopez del Amo, J. M.; Rojo, T.; Armand, M. All-Solid-State Lithium-Ion Batteries with Grafted Ceramic Nanoparticles Dispersed in Solid Polymer Electrolytes. *ChemSusChem* **2015**, *8* (18), 3039–3043. https://doi.org/10.1002/cssc.201500783.
(24) Xiong, H.-M.; Wang, Z.-D.; Xie, D.-P.; Cheng, L.; Xia, Y.-Y. Stable Polymer Electrolytes Based on Polyether -Grafted ZnO Nanoparticles for All-Solid-State Lithium Batteries. *Journal of Materials Chemistry* **2006**, *16* (14), 1345–1349. https://doi.org/10.1039/B514346B.
(25) Bates, C. M.; Chang, A. B.; Momčilović, N.; Jones, S. C.; Grubbs, R. H. ABA Triblock Brush Polymers: Synthesis, Self-Assembly, Conductivity, and Rheological Properties. *Macromolecules* **2015**, *48* (14), 4967–4973. https://doi.org/10.1021/acs.macromol.5b00880.
(26) Bouchet, R.; Phan, T. N. T.; Beaudoin, E.; Devaux, D.; Davidson, P.; Bertin, D.; Denoyel, R. Charge Transport in Nanostructured PS–PEO–PS Triblock Copolymer Electrolytes. *Macromolecules* **2014**, *47* (8), 2659–2665. https://doi.org/10.1021/ma500420w.
(27) Glynos, E.; Pantazidis, C.; Sakellariou, G. Designing All-Polymer Nanostructured Solid Electrolytes: Advances and Prospects. *ACS Omega* **2020**, *5* (6), 2531–2540. https://doi.org/10.1021/acsomega.9b04098.
(28) Singh, M.; Odusanya, O.; Wilmes, G. M.; Eitouni, H. B.; Gomez, E. D.; Patel, A. J.; Chen, V. L.; Park, M. J.; Fragouli, P.; Iatrou, H.; Hadjichristidis, N.; Cookson, D.; Balsara, N. P. Effect of Molecular Weight on the Mechanical and Electrical Properties of Block Copolymer Electrolytes. *Macromolecules* **2007**, *40* (13), 4578–4585. https://doi.org/10.1021/ma0629541.
(29) Butzelaar, A. J.; Röring, P.; Mach, T. P.; Hoffmann, M.; Jeschull, F.; Wilhelm, M.; Winter, M.; Brunklaus, G.; Théato, P. Styrene-Based Poly(Ethylene Oxide) Side-Chain Block Copolymers as Solid Polymer Electrolytes for High-Voltage Lithium-Metal Batteries. *ACS Appl. Mater. Interfaces* **2021**, *13* (33), 39257–39270. https://doi.org/10.1021/acsami.1c08841.
(30) Kim, D.-W.; Park, J.-K.; Gong, M.-S.; Song, H.-Y. Effect of Grafting Degree and Side PEO Chain Length on the Ionic Conductivities of NBR-g-PEO Based Polymer Electrolytes. *Polymer Engineering & Science* **1994**, *34* (17), 1305–1313. https://doi.org/10.1002/pen.760341702.
(31) Aldalur, I.; Martinez-Ibañez, M.; Piszcz, M.; Rodriguez-Martinez, L. M.; Zhang, H.; Armand, M. Lowering the Operational Temperature of All-Solid-State Lithium Polymer Cell with Highly Conductive and Interfacially Robust Solid Polymer Electrolytes. *Journal of Power Sources* **2018**, *383*, 144–149. https://doi.org/10.1016/j.jpowsour.2018.02.066.
(32) An, S. Y.; Wu, X.; Zhao, Y.; Liu, T.; Yin, R.; Ahn, J. H.; Walker, L. M.; Whitacre, J. F.; Matyjaszewski, K. Highly Conductive Polyoxanorbornene-Based Polymer Electrolyte for Lithium-Metal Batteries. *Advanced Science* **2023**, *10* (27), 2302932. https://doi.org/10.1002/advs.202302932.
(33) Rosenbach, D.; Mödl, N.; Hahn, M.; Petry, J.; Danzer, M. A.; Thelakkat, M. Synthesis and Comparative Studies of Solvent-Free Brush Polymer Electrolytes for Lithium Batteries. *ACS Applied Energy Materials* **2019**, *2* (5), 3373–3388. https://doi.org/10.1021/acsaem.9b00211.
(34) Hayano, S.; Nakama, Y. Iso- and Syndio-Selective ROMP of Norbornene and Tetracyclododecene: Effects of Tacticity Control on the Hydrogenated Ring-Opened Poly(Cycloolefin)s. *Macromolecules* **2014**, *47* (22), 7797–7811. https://doi.org/10.1021/ma502020u.
(35) Walsh, D. J.; Wade, M. A.; Rogers, S. A.; Guironnet, D. Challenges of Size-Exclusion Chromatography for the Analysis of Bottlebrush Polymers. *Macromolecules* **2020**, *53* (19), 8610–8620. https://doi.org/10.1021/acs.macromol.0c01357.
(36) Wang, Y.; Li, R.; Bian, Y.; Zhang, X.; Zhu, X. The Synthesis and Oligomerization of a Monofunctional Bottlebrush-Shaped Polymer Terminated with an Azide Group. *Polym. Chem.* **2019**, *10* (38), 5168–5171. https://doi.org/10.1039/C9PY00985J.
(37) Radzinski, S. C.; Foster, J. C.; Matson, J. B. Preparation of Bottlebrush Polymers via a One-Pot Ring-Opening Polymerization (ROP) and Ring-Opening Metathesis Polymerization (ROMP) Grafting-Through Strategy. *Macromolecular Rapid Communications* **2016**, *37* (7), 616–621. https://doi.org/10.1002/marc.201500672.
(38) Monroe, C.; Newman, J. The Impact of Elastic Deformation on Deposition Kinetics at Lithium/Polymer Interfaces. *J. Electrochem. Soc.* **2005**, *152* (2), A396. https://doi.org/10.1149/1.1850854.
(39) Khurana, R.; Schaefer, J. L.; Archer, L. A.; Coates, G. W. Suppression of Lithium Dendrite Growth Using Cross-Linked Polyethylene/Poly(Ethylene Oxide) Electrolytes: A New Approach for Practical Lithium-Metal Polymer Batteries. *J. Am. Chem. Soc.* **2014**, *136* (20), 7395–7402. https://doi.org/10.1021/ja502133j.
(40) Harry, K. J.; Higa, K.; Srinivasan, V.; Balsara, N. P. Influence of Electrolyte Modulus on the Local Current Density at a Dendrite Tip on a Lithium Metal Electrode. *J. Electrochem. Soc.* **2016**, *163* (10), A2216. https://doi.org/10.1149/2.0191610jes.
(41) Matsen, M. W. Effect of Architecture on the Phase Behavior of AB-Type Block Copolymer Melts. *Macromolecules* **2012**, *45* (4), 2161–2165. https://doi.org/10.1021/ma2027825.
(42) Gai, Y.; Song, D.-P.; Yavitt, B. M.; Watkins, J. J. Polystyrene- Block -Poly(Ethylene Oxide) Bottlebrush Block Copolymer Morphology Transitions: Influence of Side Chain Length and Volume Fraction. *Macromolecules* **2017**, *50* (4), 1503–1511. https://doi.org/10.1021/acs.macromol.6b01415.
(43) Diederichsen, K. M.; Buss, H. G.; McCloskey, B. D. The Compensation Effect in the Vogel–Tammann–Fulcher (VTF) Equation for Polymer-Based Electrolytes. *Macromolecules* **2017**, *50* (10), 3831–3840. https://doi.org/10.1021/acs.macromol.7b00423.

(44) Devaux, D.; Glé, D.; Phan, T. N. T.; Gigmes, D.; Giroud, E.; Deschamps, M.; Denoyel, R.; Bouchet, R. Optimization of Block Copolymer Electrolytes for Lithium Metal Batteries. *Chemistry of Materials* **2015**, *27* (13), 4682–4692. https://doi.org/10.1021/acs.chemmater.5b01273.
(45) Evans, J.; Vincent, C. A.; Bruce, P. G. Electrochemical Measurement of Transference Numbers in Polymer Electrolytes. *Polymer* **1987**, *28* (13), 2324–2328. https://doi.org/10.1016/0032-3861(87)90394-6.
(46) Hernández, G.; Johansson, I. L.; Mathew, A.; Sångeland, C.; Brandell, D.; Mindemark, J. Going Beyond Sweep Voltammetry: Alternative Approaches in Search of the Elusive Electrochemical Stability of Polymer Electrolytes. *J. Electrochem. Soc.* **2021**, *168* (10), 100523. https://doi.org/10.1149/1945-7111/ac2d8b.
(47) Homann, G.; Stolz, L.; Nair, J.; Laskovic, I. C.; Winter, M.; Kasnatscheew, J. Poly(Ethylene Oxide)-Based Electrolyte for Solid-State-Lithium-Batteries with High Voltage Positive Electrodes: Evaluating the Role of Electrolyte Oxidation in Rapid Cell Failure. *Sci Rep* **2020**, *10* (1), 4390. https://doi.org/10.1038/s41598-020-61373-9.
(48) Danzer, M. A. Generalized Distribution of Relaxation Times Analysis for the Characterization of Impedance Spectra. *Batteries* **2019**, *5* (3), 53. https://doi.org/10.3390/batteries5030053.
(49) Hahn, M.; Rosenbach, D.; Krimalowski, A.; Nazarenus, T.; Moos, R.; Thelakkat, M.; Danzer, M. A. Investigating Solid Polymer and Ceramic Electrolytes for Lithium-Ion Batteries by Means of an Extended Distribution of Relaxation Times Analysis. *Electrochimica Acta* **2020**, *344*, 136060. https://doi.org/10.1016/j.electacta.2020.136060.
(50) Eun Park, S.; Shin, K.; Hyuk Yang, J.; Keun Park, B.; Yeun Kim, S.; Kim, H.-S.; Park, M.-S.; Jae Kim, K. Track-Etched Polyimide Separator Decorated with Polyvinylpyrrolidone for Self-Assembling a Robust Protective Layer on Lithium-Metal Anode. *Chemical Engineering Journal* **2022**, *445*, 136801. https://doi.org/10.1016/j.cej.2022.136801.
(51) Zhong, S.; Yuan, B.; Guang, Z.; Chen, D.; Li, Q.; Dong, L.; Ji, Y.; Dong, Y.; Han, J.; He, W. Recent Progress in Thin Separators for Upgraded Lithium Ion Batteries. *Energy Storage Materials* **2021**, *41*, 805–841. https://doi.org/10.1016/j.ensm.2021.07.028.
(52) Wu, J.; Yuan, L.; Zhang, W.; Li, Z.; Xie, X.; Huang, Y. Reducing the Thickness of Solid-State Electrolyte Membranes for High-Energy Lithium Batteries. *Energy Environ. Sci.* **2021**, *14* (1), 12–36. https://doi.org/10.1039/D0EE02241A.
(53) Homann, G.; Stolz, L.; Winter, M.; Kasnatscheew, J. Elimination of "Voltage Noise" of Poly (Ethylene Oxide)-Based Solid Electrolytes in High-Voltage Lithium Batteries: Linear versus Network Polymers. *iScience* **2020**, *23* (6), 101225. https://doi.org/10.1016/j.isci.2020.101225.

III.10 Supporting Information

III.10.1 Materials

Chemicals were used as received, instead otherwise noted. Benzene (99.7 %), ethyl vinyl ether (0.1 % KOH as stabilizer, 99 %), 3rd generation *Grubbs* catalyst, 2-norbornene (99 %), lithium bis(trifluoromethane)sulfonimide (LiTFSI), poly(ethylene glycol) monomethyl ether (PEGME, M_n 2000 g/mol) were purchased from Sigma Aldrich. $PEGME_{2k}$ was dried at 70 °C under high vacuum overnight. Methylene chloride (99.8 %, extra dry, over molecular sieve, AcroSeal™), N-methyl pyrrolidone (99.5 %, extra dry, AcroSeal™) was bought from fisher scientific. Diethyl ether (99.9 %), methanol (99.9 %) and tetrahydrofuran (99.9 %) were retrieved from VWR chemicals. *N,N'*-Dicyclohexyl carbodiimide (DCC), 4-(dimethylamino)pyridine (DMAP) were purchased from Fluka Chemicals. Deuterated solvents ($CDCl_3$, DMSO-d_6, and C_6D_6) were purchased from Deutero. The dialysis membrane (Spectra/Por® 6, pre-wetter RC tubing, MWCO 15 kDa) was purchased from Carl Roth. Button-cell type CR2032 coin cells, the active material (carbon-coated $LiFePO_4$, D10 < 1 µm, D50 3.5±1.0 µm, D90 < 15 µm, carbon content: 1.45 ± 0.2 %), Super P carbon (carbon black, CB), conductive graphite (CG) and C-coated Al current collector were procured from MTI Corporation and used as such during the preparation of cathode. ipPORE™ track-etched hydrophilic polyimide (PI) membranes (pore size: 0.20 µm, pore density: $6.00 \cdot 10^8$ cm^{-2}, thickness: 7 µm) were purchased from it4ip (Belgium). Lithium metal ribbon (purity 99.9 %, thickness 380 µm, width 23 mm) was retrieved from Sigma Aldrich, lithium electrodes were punched from the ribbon using a 14 mm diameter punching die inside the glovebox. P25 (TiO_2 nanoparticles, 21 nm primary particle size) was procured from Degussa. *N*-Hexane was distilled at the University of Bayreuth.

III.10.2 Instrumentation

III.10.2.1 ^{1}H NMR spectroscopy

A Bruker Avance AC250 spectrometer at a working frequency of 300 MHz was used to record ^{1}H NMR spectra. Chemical shifts were calibrated to 7.28 ppm for chloroform-d_1 and 7.16 ppm for benzene-d_6. Chemical shifts are reported as ppm, coupling constants in Hz, and multiplicity are indicated as: s (singlet), d (doubled), t (triplet), m (multiplet).

III.10.2.1 Size exclusion chromatography

SEC was measured utilizing a Waters 515 HPLC pump and THF with 0.25 wt % tetrabutylammonium bromide (TBAB) as eluent at a flow rate of 0.5 mL min^{-1}. 100 µL of polymer solution (1–2 mg mL^{-1}) are injected by a 707 Waters autosampler into a column setup comprising a guard column (Agilent PLgel Guard MIXED-C, 5cm × 0.75 cm, particle size 5 µm) and two separation columns (Agilent PLgel MIXED-C, 30 cm × 0.75 cm, particle size 5 µm). Polymer size distributions were monitored by a Waters 414 refractive index detector. Polystyrene (PS) standard was used for calibration and 1,2-dichlorobenzene was used as an internal reference.

III.10.2.1 Thermogravimetric analysis

TGA thermograms were recorded on a Mettler Toledo TGA/DSC 3. Samples (ca. 10 - 20 mg) were placed in aluminum oxide ceramic crucibles (70 µL) and heated from 30 to 700 °C at a heating rate of 10 K min^{-1} under nitrogen atmosphere.

III.10.2.1 Differential scanning calorimetry

DSC thermograms were obtained using a Mettler Toledo DSC 3. The samples were sealed within aluminum crucibles. The temperature program comprised two cycles of cooling down to –80 °C and subsequent heating up to 150 °C or 200 °C at a cooling/heating rate of 10 K min^{-1}. For the third cycle, a cooling/heating rate of 40 K min^{-1} was chosen. Glass transition temperatures (T_g) are derived as inflection points of the transition temperature and melting points (T_m) are obtained as the peak maximum of the melting peak in the second heating curve.

III.10.2.1 Scanning electron microscopy (SEM)

The surface morphology was analyzed using a Zeiss LEO 1530 scanning electron microscope.

III.10.2.1 Electrochemical measurements

Electrochemical measurements were conducted using a VMP300 potentiostat (BioLogic) equipped with EIS boards. The impedance spectra in this work were reconstructed using the generalized distribution of relaxation times (gDRT) using the software ec–idea provided by the Department of Electrical Energy Systems at the University of Bayreuth. Fitting parameters: Number of time constants: 159, 3-fold number of measured frequencies, extended upper time constant limit by 1 decade, extended lower time constant limit by 1 decade, regularization parameter: 0.1.

III.10.2.1 Polyimide (PI7) Membrane Infiltration

The polymer(s) and the lithium salt are dissolved in small amounts of dry acetonitrile to yield a viscous SPE solution The porous membranes are punched to size and pre-heated on a hot plate at 100 °C. The SPE solution is applied onto the top surface to soak the membranes. The solvent is let to evaporate for approximately 5 minutes before the membrane is transferred onto the pre-cut cathode disc with the covered membrane side facing towards the cathode. The now top surface is subsequently also covered by SPE solution. The SPE-membrane-SPE-cathode stack is then dried in high vacuum at 80 °C for at least 15 hours to ensure that all of the solvent is removed. The stacks are then transferred to a glovebox for cell assembly.

III.10.3 Syntheses

III.10.3.1 Synthesis of Nb-PEGME

Prior to use 52 g (26 mmol, 1 eq.) poly(ethylene glycol monomethyl ether, M_n 2000 g/mol) (PEGME) was dried in a Schlenk flask at 70 °C under high vacuum for 20 h. After cooling down to room temperature 12.88 g (62.4 mmol, 2.4 eq.) dicyclohexylcarbodiimide (DCC) and 7.18 g (52.0 mmol, 2 eq.) 5-norbornene-2-carboxylic acid (Nb-COOH) were added in an argon counter flow. 400 mL of dry methylene chloride (c_{total} = 0.36 M) was added using a transfer cannula. After cooling the solution to 0 °C for 30 min 4-(dimethylamino)pyridine (DMAP) was added in an argon counter flow. The solution was stirred for 24 h at room temperature. White precipitates were removed using a por.4-frit and washed with methylene chloride. The filtrate was concentrated and precipitated in eightfold excess of diethyl ether three times. The product was dried by freeze drying from benzene to yield a white powder.

Yield: 53 g (96 %)
^{1}H-NMR (300 MHz, $CHCl_3$-*d1*): δ (ppm) = 6.18 (dd, 0.66H, $H_{a,endo}$), 6.11 (m, 0.58H, $H_{a,exo}$,$H_{b,exo}$), 5.93 (dd, 0.65H, $H_{b,endo}$), 4.27 – 4.09 (m, 2H, H_k), 3.90-3.38 (m, 189H, H_m), 3.37 (s, 3H, H_n), 3.21 (s, 0.68H, $H_{c,endo}$), 3.04 (s, 0.27H, $H_{c,exo}$), 2.97 (d, 0.67H, $H_{e,endo}$), 2.90 (s, 1H, H_d), 2.29 – 2.22 (m, 0.3H, $H_{e,exo}$), 2.09 – 1.67 (m, 1H, H_f).1.55 –1.49 (d, 0.33H, $H_{h,exo}$), 1.47 – 1.30 (m, 2H, H_g, H_i), 1.29 – 1.24 (d, 0.7H, $H_{h,endo}$)
GPC: M_n: 22800 g mol^{-1}
M_w: 24400 g mol^{-1}
$Đ$: 1.10
eluent: THF+0.25 wt% TBAB, PS calibration
DSC: T_m: 52 °C, ΔH_m: 142.3 J g^{-1}
TGA: $T_{d5\%}$: 360 °C

III.7.3.2 Synthesis of Poly(Nb)$_{90}$ 1

A 500 mL Schlenk flask equipped with a magnetic stirring bar and a septum was baked out at 650 °C under high vacuum. After cooling down to room temperature 0.530 g (5.63 mmol, 90 eq.) norbornene are added under argon counterflow and dissolved in 191 mL anhydrous DCM. The monomer solution was degassed by three *freeze/pump/thaw* cycles. The 3rd generation Grubbs catalyst (55.3 mg, 0.06 mmol, 1 eq.) was weighted in an argon-filled glovebox and dissolved in 0.7 mL anhydrous DCM. The catalyst solution was added by syringe under vigorous stirring. After 1 h the polymerization was terminated by the addition of vinyl ethyl ether.

The reaction solution was concentrated under reduced pressure and precipitated in eightfold excess of diethyl ether three times. The solvent was removed under reduced pressure and the polymers were dried by freeze drying from benzene to yield grey solids.

Yield: 0.49 g (91.5 %)
^{1}H-NMR (300 MHz, $CHCl_3$-d1): δ (ppm) = 5.35 (s, 0.78H, $H_{a\text{-}trans}$), 5.22 (s, 1.2H, $H_{a\text{-}cis}$), 2.96 – 2.66 (m, 1.2H, $H_{b\text{-}cis}$), 2.58 – 2.30 (m, 0.77H, $H_{b\text{-}trans}$), 1.98 – 1.65 (m, 3H, H_c, H_e), 1.48 – 1.21 (m, 2H, H_f), 1.14 – 0.77 (dd, 1H, H_d)
GPC: M_n: 18200 g mol^{-1}
M_w: 20400 g mol^{-1}

M_p: 20300 g mol^{-1}
$Đ$: 1.12
eluent: THF+0.25 wt% TBAB, PS calibration
DSC: T_g: 55 °C
TGA: $T_{d5\%}$: 363 °C

III.10.3.3 Synthesis of Poly(Nb)$_{40}$-graft-PEGME 2.

A 100 mL Schlenk flask equipped with a magnetic stirring bar and a septum was baked out at 650 °C under high vacuum. After cooling down to room temperature 9.975 g (4.71 mmol, 40 eq.) Nb-PEGME was added under argon counterflow and dissolved in 94.1 mL anhydrous methylene chloride. The monomer solution was degassed by three *freeze/pump/thaw* cycles. The 3rd generation Grubbs catalyst (104.0 mg, 0.12 mmol, 1 eq.) was weighted in an argon-filled glovebox and dissolved in 1.5 mL of anhydrous methylene chloride. The catalyst solution was added by syringe under vigorous stirring. After 1.5 h the polymerization was terminated by the addition of 3 mL vinyl ethyl ether.

The reaction solution was concentrated under reduced pressure and precipitated in eightfold excess of diethyl ether three times. The grey product was dissolved in MeOH and dialyzed for three days. The dialysis fluid is exchanged daily. The solvent was removed under reduced pressure and the polymer was dried by freeze drying from benzene to yield a white powder.

Yield: 9.6 g (96 %)
GPC: M_n: 63300 g mol^{-1}
M_w: 71600 g mol^{-1}
M_p: 74600 g mol^{-1}
$Đ$: 1.13
eluent: THF+0.25 wt% TBAB, PS calibration
DSC: T_m: 63 °C, ΔH_m: 134.8 J g^{-1}
TGA: $T_{d5\%}$: 376 °C

III.10.3.4 Synthesis of Poly(Nb)$_{40}$-graft-PEGME-block-(Nb)$_{68}$ 3

The block copolymerization of poly(ethylene glycol) monomethyl ether-5-norbornene-2-carboxylate and norbornene was performed under argon atmosphere in dried Schlenk tubes equipped with a magnetic stirring bars and a septum. 4.525 g (2.13 mmol, 40 eq.) Nb-PEGME **1** was dissolved in 42.7 mL of anhydrous methylene chloride ($c_{Nb\text{-}PEGME}$ = 0.05 mol L^{-1}). In a second Schlenk flask 0.452 g (4.8 mmol, 90eq.) norbornene was dissolved in 19.2 mL of anhydrous methylene chloride (c_{Nb} = 0.25 mol L^{-1}). Both monomer solutions were degassed by three *freeze/pump/thaw* cycles. The 3rd generation Grubbs catalyst was weighted (47.2 mg, 0.05 mmol, 1 eq.) in an argon-filled glovebox and dissolved in 0.7 mL anhydrous methylene chloride. The Nb-PEGME solution was cooled to 15 °C. The polymerization was initiated by the addition of the catalyst solution. After 1 h the temperature was reduced to 0 °C. After the temperature was reached a small aliquot was withdrawn from the reaction solution and quenched with vinyl ethyl ether. Afterwards the norbornene solution was added by syringe. After 30 minutes the reaction was terminated by the addition of 3 mL vinyl ethyl ether.

The polymer were purified by precipitation in excess of diethyl ether three times. Afterwards the polymer were dialyzed in THF for three days. The dialysis medium was exchanged daily. The polymers were dried by freeze-drying from benzene to yield a white/grey powder.

Yield: 4.7 g (94 %)

^{1}H-NMR (300 MHz, $CHCl_3$-*d*1): δ (ppm) = 5.83 – 5.05 (br, 2H, H_a), 5.35 (s, 2H, $H_{a'\text{-trans}}$), 5.22 (s, 2H, $H_{a'\text{-cis}}$), 4.62 – 3.96 (m, 2H, H_c), 3.86 – 3.37 (m, 189H, H_d), 3.36 (s, 3H, H_e), 3.25 – 0.69 (br, 7H, H_b), 2.99 – 2.65 (br, 1H, $H_{f\text{-cis}}$), 2.53 – 2.41 (br, 1H, $H_{f\text{-trans}}$), 2.19 – 1.71 (m, 2H, H_i, H_h), 1.60 – 1.39 (m, 2H, H_g)

GPC values in brackets correspond to the first polymer segment, before the addition of the second monomer. Analysis is performed on the small aliquot described in the synthetic procedure.

GPC:

M_n: (66200) 76300 g mol^{-1}

M_w: (74800) 89900 g mol^{-1}

M_p: (78100) 88900 g mol^{-1}

$Đ$: (1.13) 1.18

(eluent: THF+0.25 wt% TBAB, PS calibration)

DSC: T_m: 50°C, ΔH_m: 108.8 J g^{-1}

TGA: $T_{d5\%}$: 389 °C

III.10.4 ^{1}H NMR Spectroscopy and Size Exclusion Chromatography

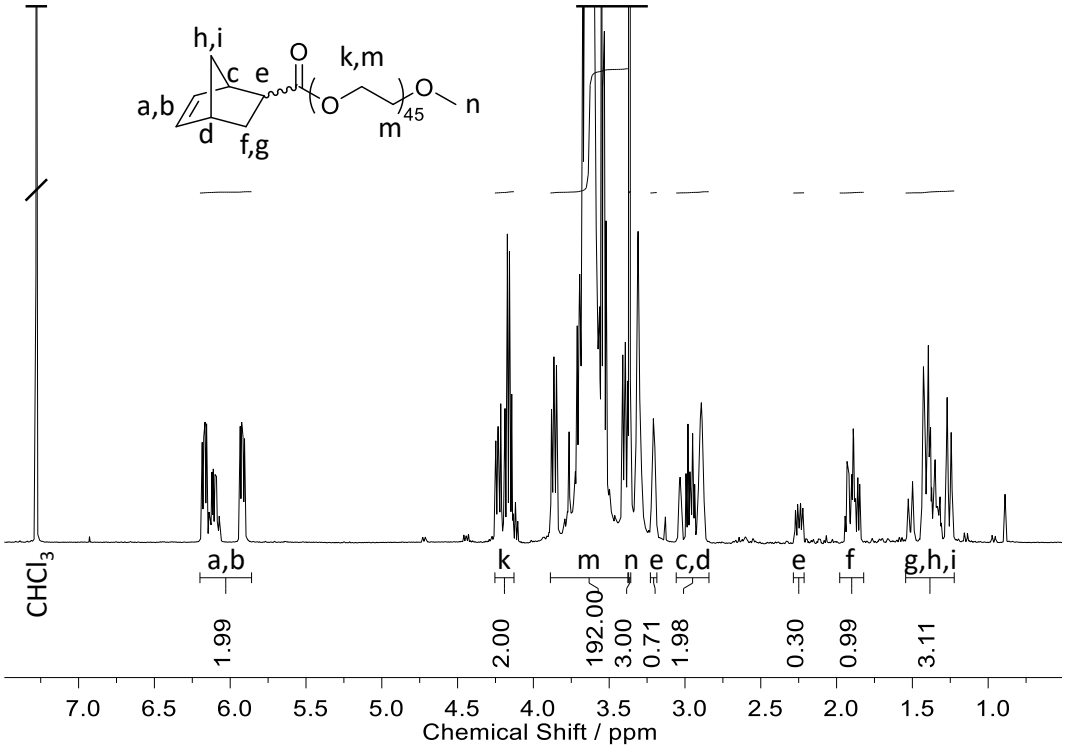


Figure S.III.1. ^{1}H NMR (300 MHz, $CDCl_3$) spectrum of poly(ethylene glycol) monomethyl ether-5-norbornene-2-carboxylate Nb-PEGME.

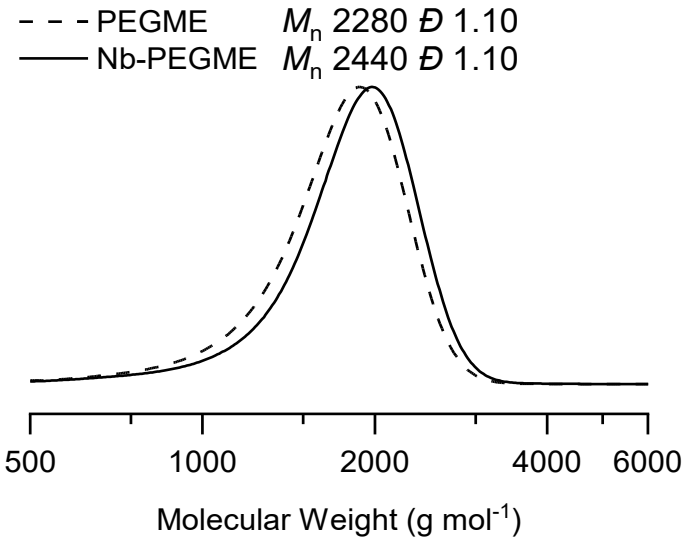


Figure S.III.2. SEC curves (THF+0.25 wt% TBAB, PS calibration, RI detector) of commercially available PEGME and the corresponding macromonomer Nb-PEGME.

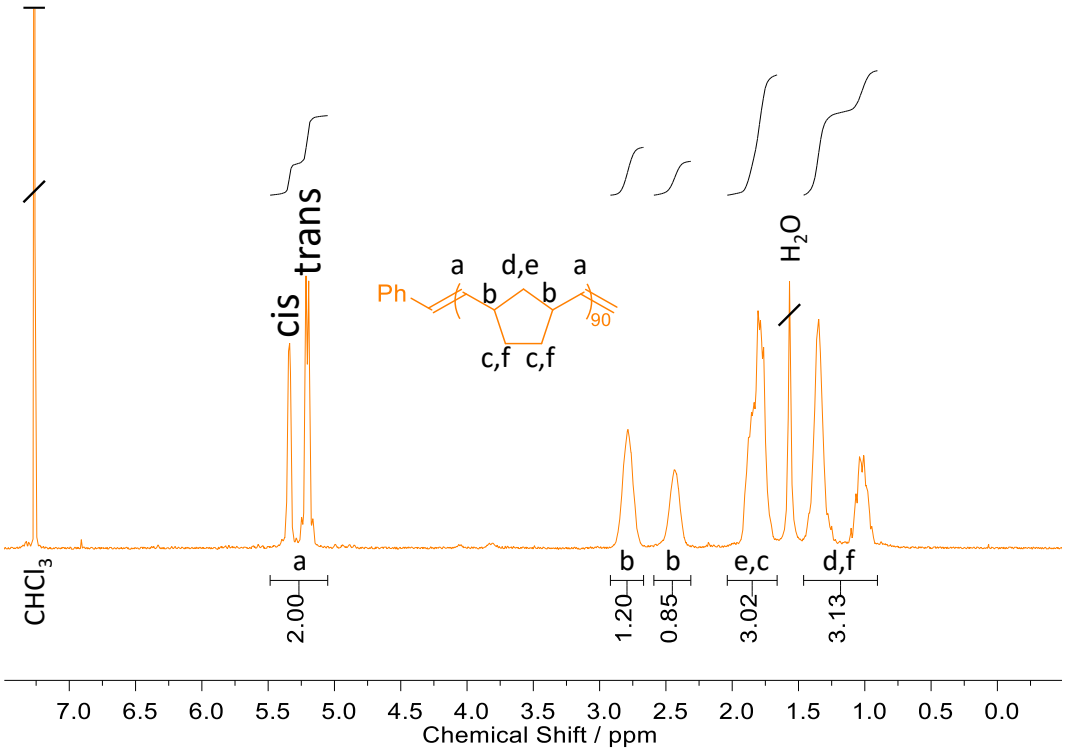


Figure S.III.3. ^{1}H NMR (300 MHz, $CDCl_3$) spectrum of polynorbornene poly(Nb)$_{90}$ (**1**).

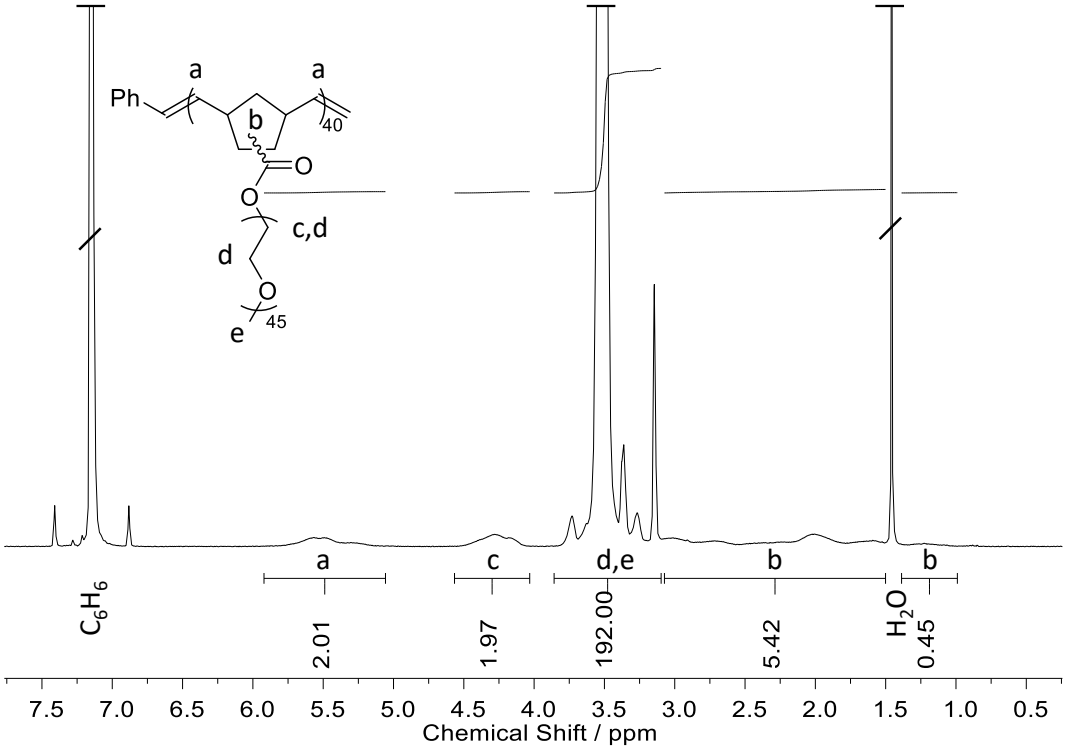


Figure S.III.4. ^{1}H NMR (300 MHz, $CDCl_3$) spectrum of polynorbornene-graft-(poly(ethylene glycol) monomethyl ether) poly(Nb)$_{40}$-graft-PEGME (**2**).

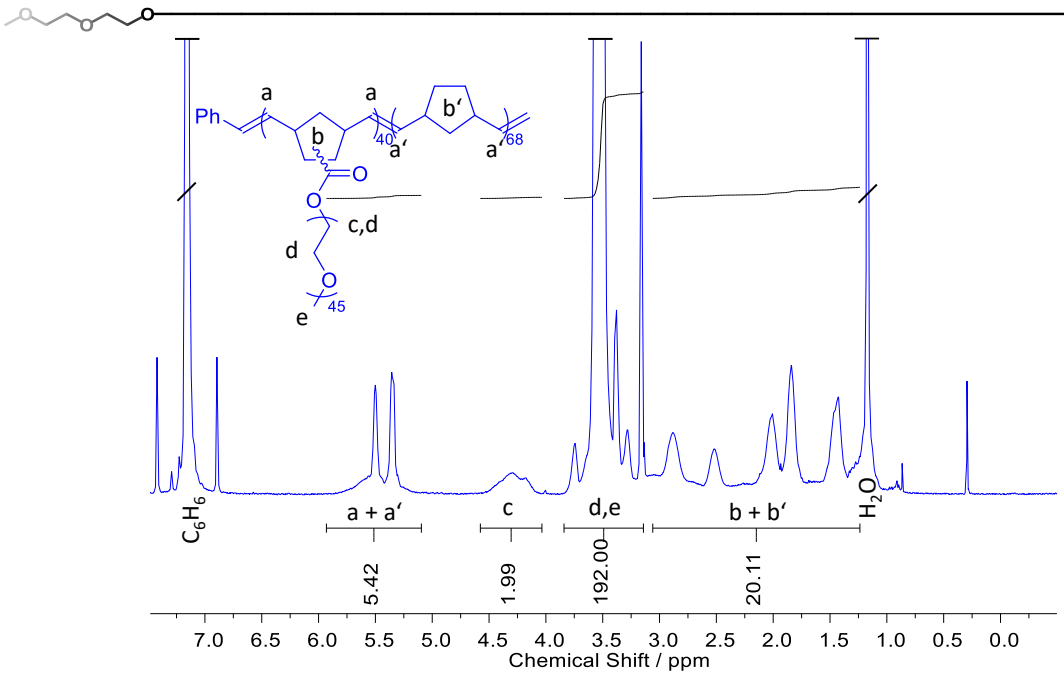


Figure S.III.5. ^{1}H NMR (300 MHz, $CDCl_3$) spectrum of polynorbornene-graft-(poly(ethylene glycol) monomethyl ether)-block-norbornene poly(Nb)$_{40}$-graft-PEGME-block-poly(Nb)$_{68}$ (**3**)

III.10.5 Polymer Composition

The polymer composition of the synthesized bottlebrush block copolymer (BB-BCP, **3**) was evaluated by ^{1}H NMR spectroscopy.

The relative Nb-PEGME/Nb composition ([Nb-PEGME]/[Nb]) was calculated under the assumption, that the peaks corresponding to the PEGME side chains are not affected during the polymerization of the poly(Nb) segment. For the poly(Nb)-*graft*-PEGME the PEGME signal is normalized to 192 protons corresponding to an average molecular weight of 2089 g/mol (= 47 repeating units). Accordingly, the number of double bond protons of Nb-PEGME equals 2 ($\sum_{DB,Nb\text{-}PEGME}$ = a). The normalization of the PEGME peaks is also used for the BB-BCP (**Figure S.III.5**). Both Nb moieties of the poly(Nb)-*graft*-PEGME and poly(Nb) segment in the block copolymer exhibit similar chemical shifts resulting in overlapping peaks. Correspondingly, the broad peaks between 5.9 ppm and 5.3 ppm can be attributed to the sum of double bond protons ($\sum_{DB,total}$: a+a') of Nb-PEGME (a) and Nb (a'). The double bond proton integral of the Nb segment is thus $\Sigma_{DB,Nb}=\Sigma_{DB,total}-\Sigma_{DB,Nb\text{-}PEGME}$. With respect to the degree of polymerization of the first segment ($DP_{Nb\text{-}PEGME}$ = 40) the relative DP_{Nb} can be determined.

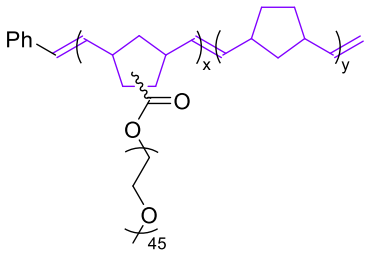
Table S.III.1. Calculation of BB-BCP polymer composition based on ^{1}H NMR spectra of BB-BCP.

	$\Sigma_{DB,tot}$	$\Sigma_{DB,Nb\text{-}PEGME}$	$\Sigma_{DB,Nb}=\Sigma_{DB,tot}-\Sigma_{DB,Nb\text{-}PEGME}$	[Nb-PEGME]/[Nb]	$DP^{a}_{Nb\text{-}PEGME}$/DP_{Nb}
BB-BCP	5.42	2	3.42	1/1.71	40/68

[a] DP of Nb-PEGME is determined by [Nb-PEGME]/[G3]

III.10.6 Calculation of Norbornene Content

The total weight fraction of norbornene in the synthesized polymers was determined based on the segment length (x and y) and the molecular weights of the macromonomer ($M_{Nb\text{-}PEGME}$) and norbornene (M_{Nb}). The phenyl end group established during the initiation using G3 is neglected for the calculation. The total weight of norbornene in the synthesized polymers corresponds to the total degree of polymerization of norbornene (x+y) multiplied by the molecular weight of norbornene. The total weight of norbornene was divided by the calculated total molecular weight of the block copolymer which is accessible by multiplication of the degree of polymerization of both polymer segments (x, y) with the molecular weight of the repeating unit, respectively.



$$wt\%\ (Nb) = \frac{(x+y)\cdot M(Nb)}{x\cdot M(Nb-PEGME)+y\cdot M(Nb)}\cdot 100\ \%$$

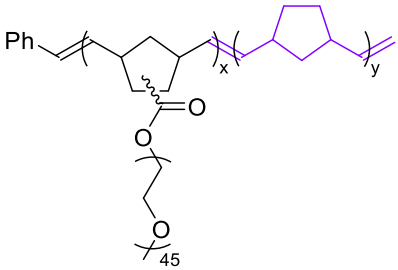
For poly(**Nb**)$_{90}$ **1**: x = 0, y = 90 wt% (Nb) = 100

poly(**Nb**)$_{40}$-*graft*-PEGME **2**: x = 40, y =0 wt% (Nb) = 4

poly(**Nb**)$_{40}$-*graft*-PEGME-*block*-(**Nb**)$_{68}$ **3**: x= 40, y = 68 wt% (Nb) = 11

The weight and volume fraction of the second polymer segment (poly(Nb)$_{68}$) in BB-BCP **3** was determined as follows. The weight fraction was determined based on the degree of polymerization and molecular weight of the Nb (M(Nb)) repeating unit with respect to the total molecular weight of the polymer.

For the volume fraction the bulk densities of polynorbornene (ρ(PNb) = 0.98) and poly(ethylene glycol) (ρ(PEG) = 1.08) were considered. As the bottlebrush polymer architecture can influence the effective polymer density, especially close to the central polymer backbone, the calculated values might not represent the effective volume proportions.



$$wt\%\ (poly(Nb)_{68}) = \frac{(y)\cdot M(Nb)}{x\cdot M(Nb-PEGME)+y\cdot M(Nb)}\cdot 100\ \%$$

$$vol\%\ (poly(Nb)_{68}) = \frac{(y)\cdot M(Nb)\cdot \rho(PNb)}{x\cdot M(Nb-PEGME)\cdot \rho(PEG)+y\cdot M(Nb)\cdot \rho(Nb)}\cdot 100\ \%$$

For poly(Nb)$_{40}$-*graft*-PEGME-*block*-(**Nb**)$_{68}$ **3**: x= 40, y = 68 wt% (poly(**Nb**)$_{68}$) = 7

vol% (poly(**Nb**)$_{68}$) = 8

III.10.7 Thermal Characterization

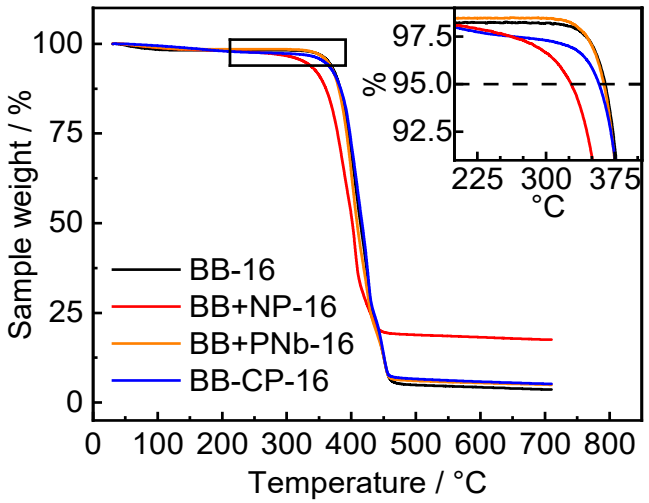


Figure S.III.6. Thermogravimetry measurements of the bottlebrush, bottlebrush nanocomposite, bottlebrush blend and bottlebrush block copolymer electrolytes. The two respective homopolymers (**1**+**2**) were blended at the same ratio as observed in the block copolymer BBCP **3**.

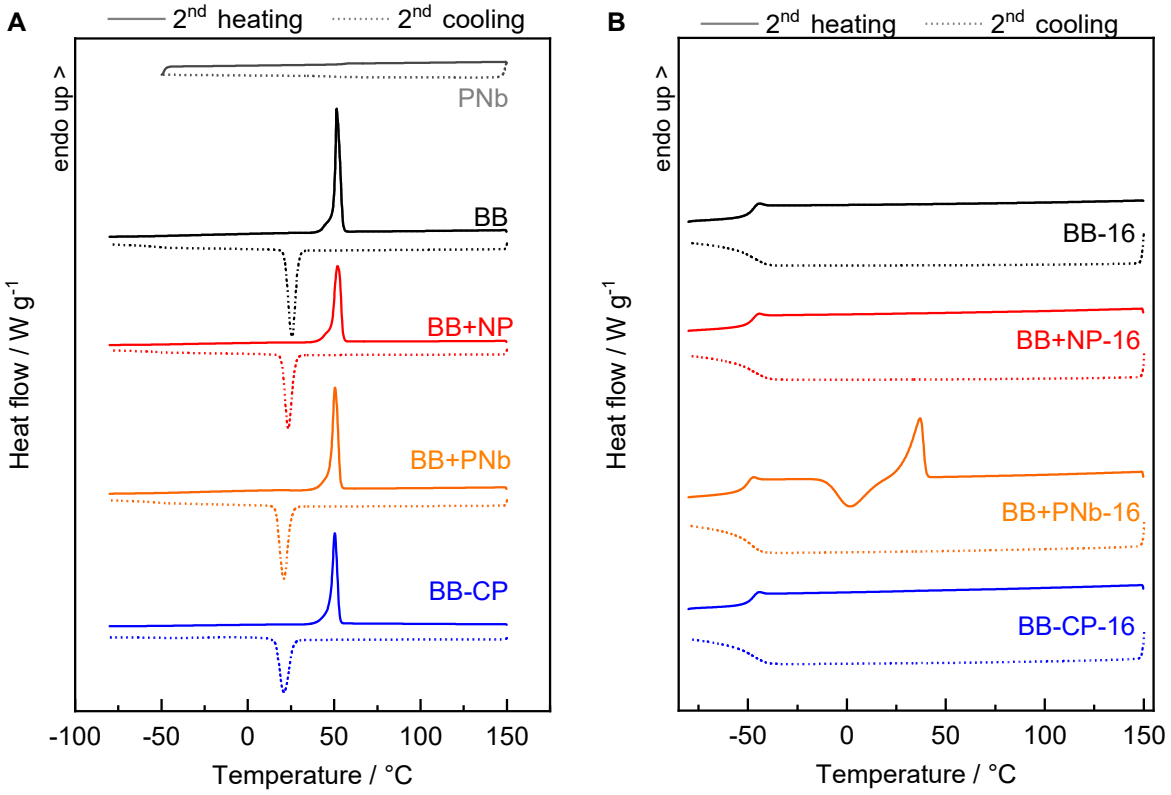


Figure S.III.7. Differential Scanning Calorimetry of (**A**) synthesized polymers (BB, BB-BCP) and mixtures (BB+NP, BB+PNb) and (**B**) the respective electrolyte system at an O/Li ratio of 16 using LiTFSI as Li-salt. Transition enthalpies and temperatures are given in the manuscript.

III.10.8 Electrolyte Composition – Salt Concentration

The bottlebrush polymer (BB **2**) was mixed with LiTFSI at three different molar concentration between the polyethylene glycol oxygen atom and the lithium (O/Li). The conductivity and mechanical properties of the polymer matrix are dependent on the LiTFSI concentration. For linear PEO, the highest ionic conductivity can be observed at around O/Li 12.[1,2] Whereas the use of lower salt concentrations of O/Li 20 is also prominent to retain a higher degree of mechanical stability.[3,4]

In our case, we selected the O/Li ratios of 12, 16, and 20 and selected O/Li 16 for any further characterization beyond the ionic conductivity.

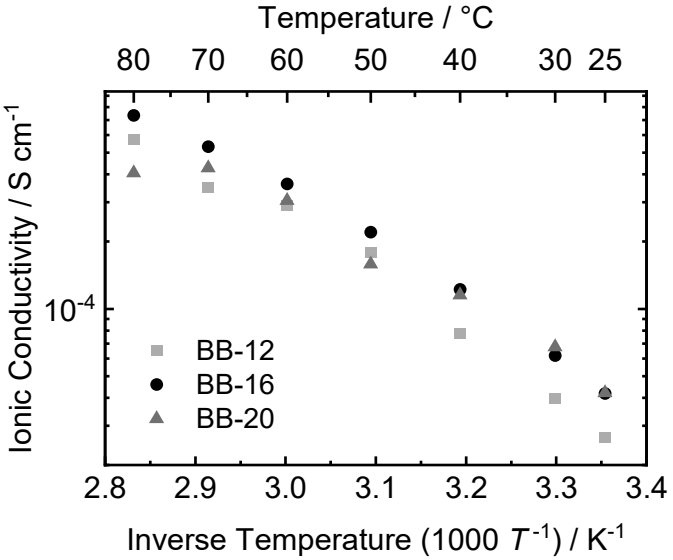


Figure S.III.8. Variation of LiTFSI salt concentration in PNb-g-PEGME (BB). The salt concentration of O/Li 16 was selected for further characterization.

Table S.III.2. Overview of electrolyte composition for BB-16, BB+PNb-16, BB+NP-16, and BB-BCP-16.

Electrolyte	BB-16	BB+PNb-16	BB+NP-16	BB-CP-16
O/Li	16	16	16	16
poly(Nb)$_{90}$ **1**		5.2 wt%		
poly(Nb)$_{40}$-*graft*-PEGME **2**	72.4 wt%	68.7 wt%	65.2 wt%	
poly(Nb)$_{40}$-*graft*-PEGME-*block*-(Nb)$_{68}$ **3**				73.9 wt%
LiTFSI	27.6 wt%	26.1 wt%	24.8 wt%	26.1 wt%
TiO_2 (P25)			10 wt%	

III.10.9 Ionic Conductivity

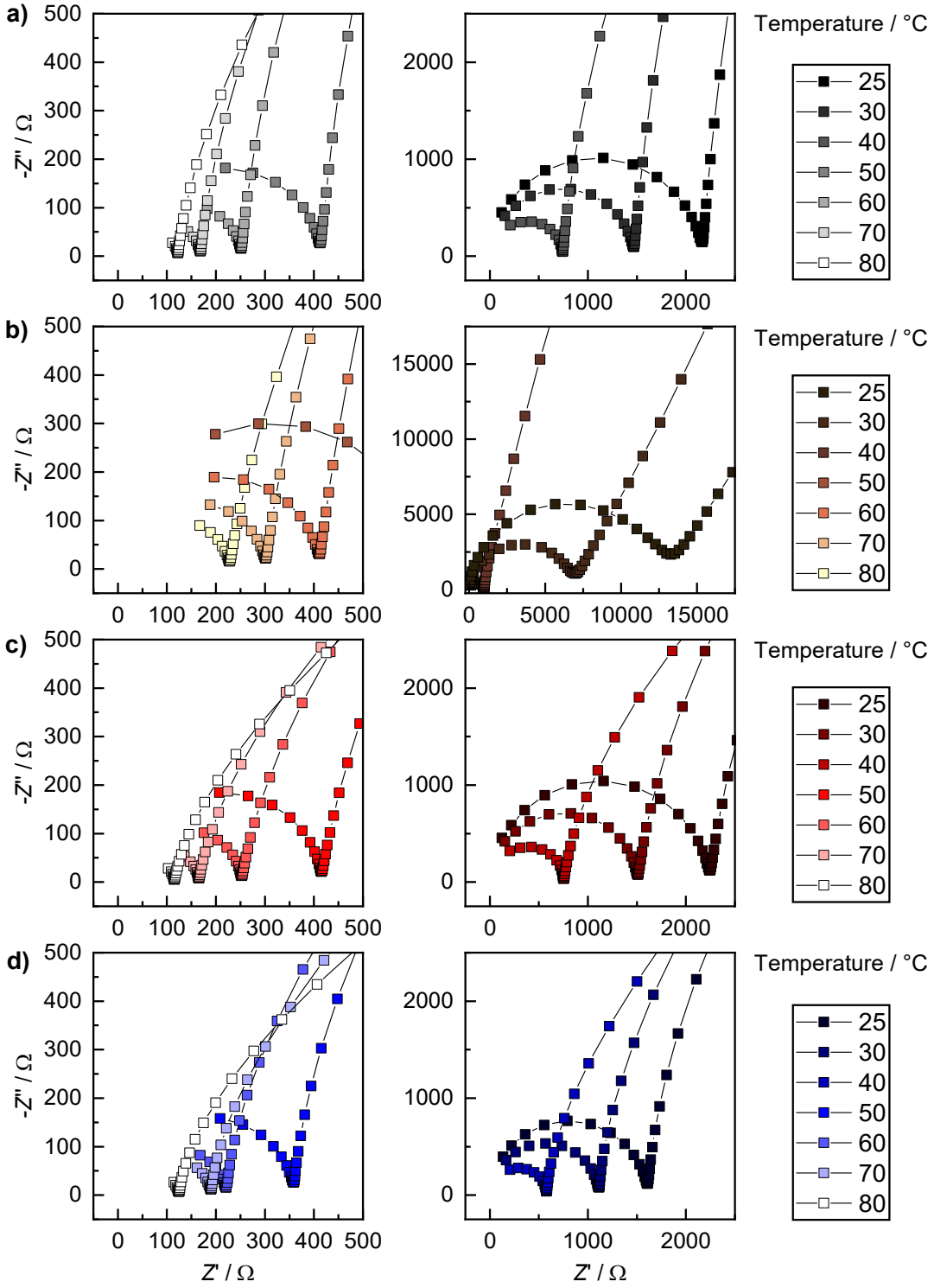


Figure S.III.9. Nyquist plots of temperature-dependent EIS measurements for all electrolytes at a O/Li ratio of 16 in StSt/SPE/StSt cells (electrolyte geometry: diameter 4 mm, thickness 136 µm). (a) BB-16, (b) BB+PNb-16, (c) BB+NP-16, and (d) BB-BCP-16.

III.10.10 Lithium Transfer Number

The lithium transfer number was evaluated in accordance to the Bruce and Vincent method. The calculation was performed using the following equation: $t_+ = \frac{I_{ss}*(\Delta V - I_0*R_{0,Li})}{I_0*(\Delta V - I_{ss}*R_{ss,Li})}$

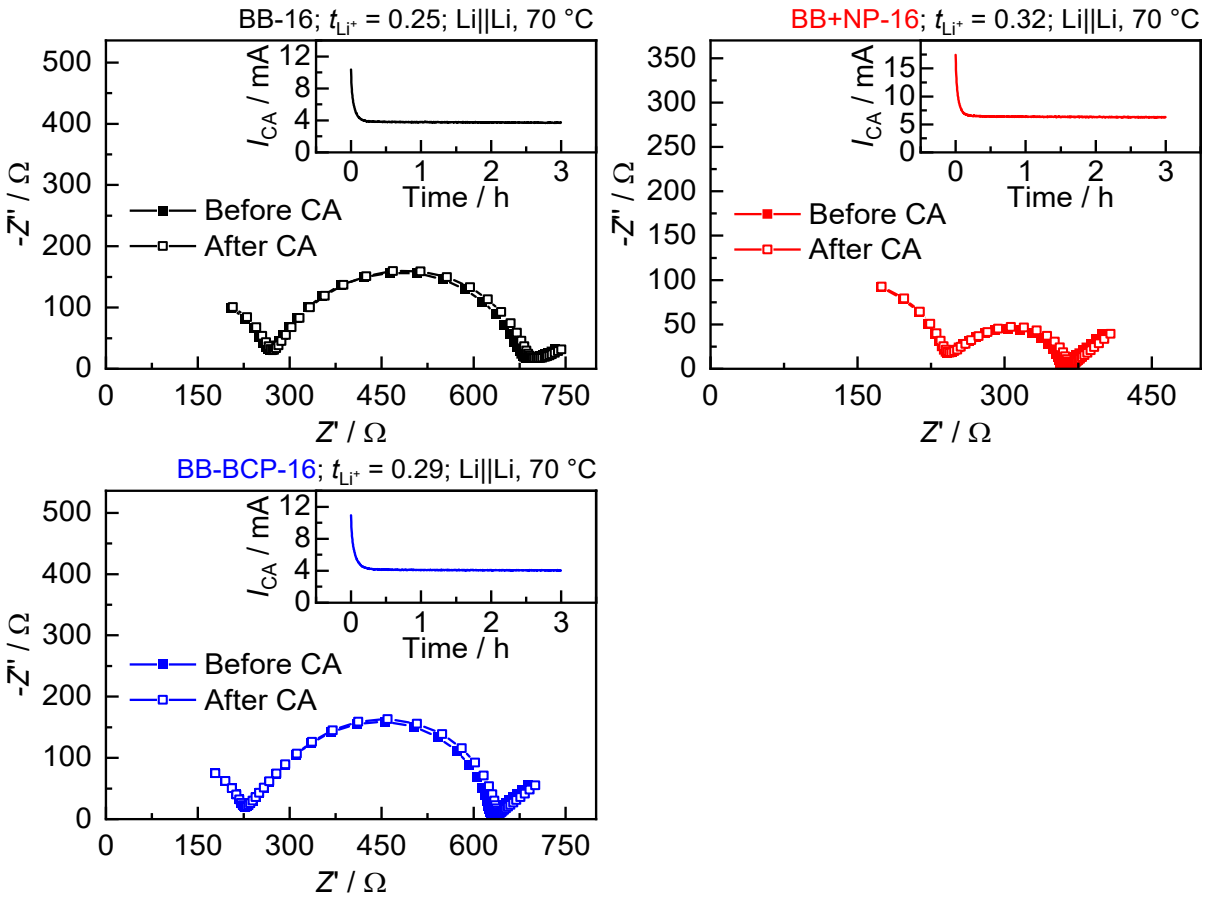


Figure S.III.10. Chronoamperometry and EIS measurements for the lithium transference number determination according to Bruce and Vincent.

Table S.III.3. Initial and steady state values for the interface resistance and current.

SPE	I_o	I_{SS}	ΔV	$R_{o,Li}$	$R_{SS,Li}$	t_{Li^+}
	A	A	V	Ω	Ω	1
BB-16	1.04E-05	3.69E-06	0.01	375.34	383.96	0.25 (0.24±0.01)
BB+NP-16	1.74E-05	6.28E-06	0.01	99.96	104.90	0.32 (0.30±0.02)
BB-BCP-16	1.07E-05	4.34E-06	0.01	369.31	379.92	0.29 (0.28±0.02)

III.10.11 Lithium Plating and Stripping

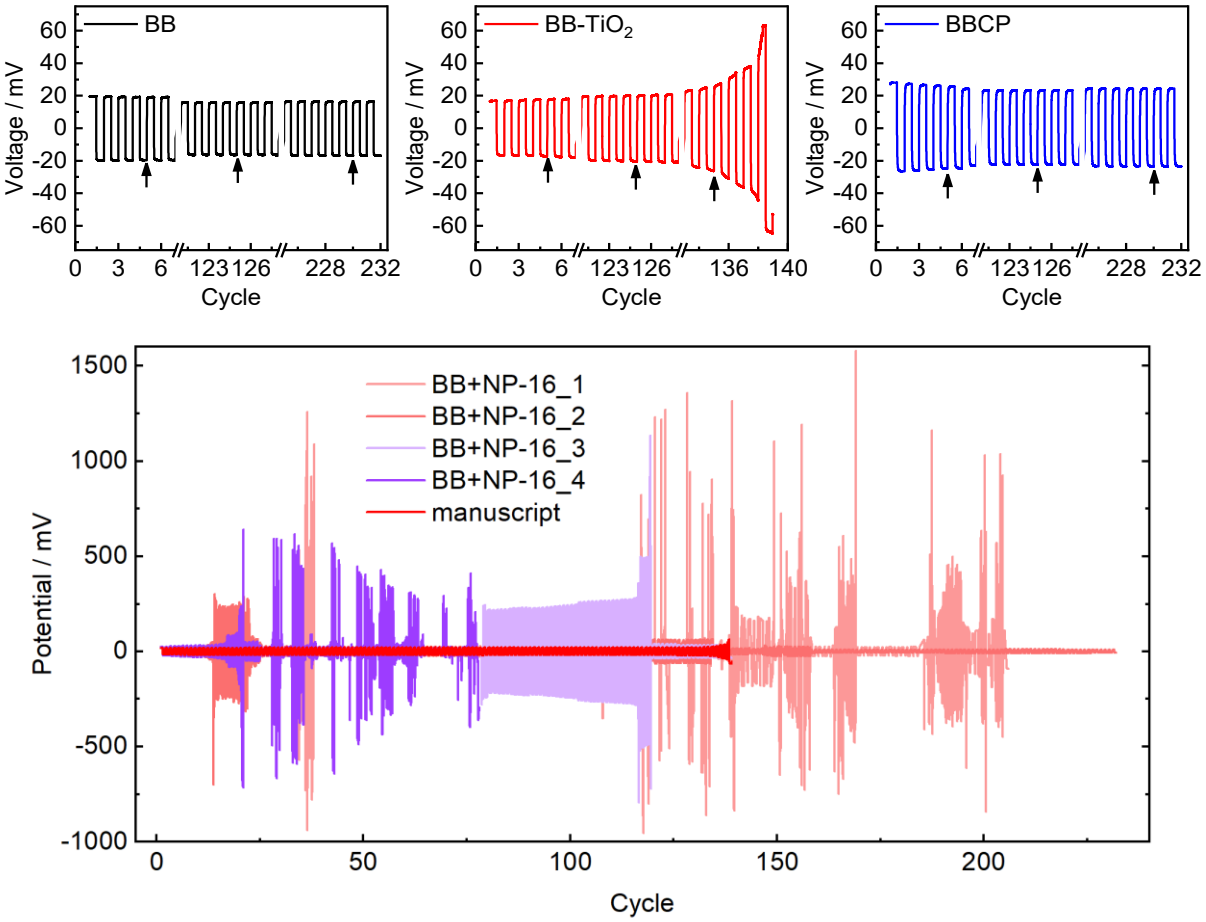


Figure S.III.11. (top) Exemplary excerpts of lithium and plating cycles for (left) the bottlebrush polymer BB-16, (middle) the solid polymer nanocomposite electrolyte BB+NP-16, and (right) bottlebrush block copolymer BB-BCP-16. Cycling was performed in Li/electrolyte/Li symmetrical cells at a current density of 0.1 mA cm^{-1}. (bottom) Lithium plating and stripping data for four additional cells to the data presented in the main text. The overpotential for cells -1 to -4 show significant fluctuations and very high overpotentials of up to 1.5 V.

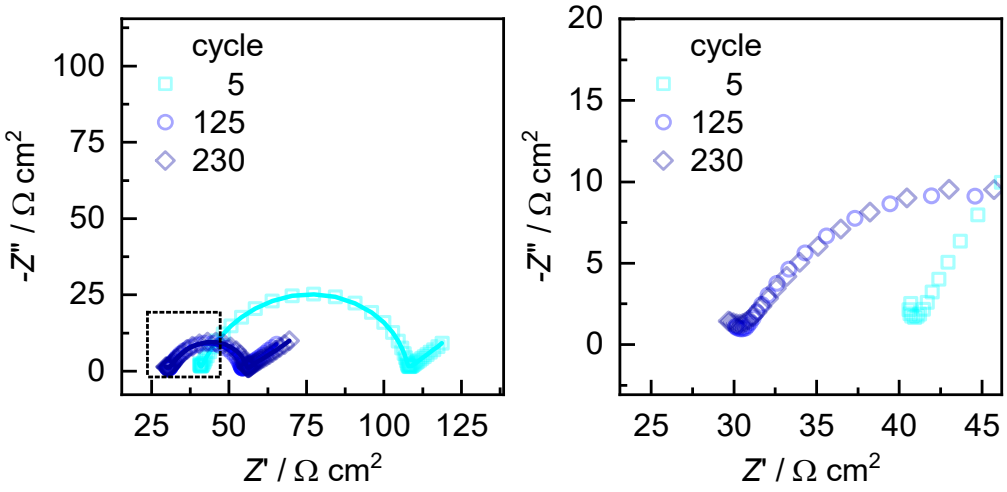


Figure S.III.12. Nyquist plots of EIS measurements performed during LPS experiments in Li/SPE/Li cells for BB-BCP-16 (electrolyte geometry: diameter 16 mm, thickness 7 µm).

III.10.12 SEM Images of Polyimide Membrane (pristine and filled)

For battery measurements a porous track-etched polyimide membrane (0,2µm pore size, 28 % porosity, 7 µm thickness) was used. with indicated membrane thickness, which is in good agreement with the manufacturers information. The pores are clearly visible in the pristine membrane. The membrane was filled following the procedure stated in the SI to yield a membrane-electrolyte-composite. At low magnification the coverage of the pores can be observed. Upon further magnification, the polymer in the pores is gradually removed from the pores by the electron beam during imaging. This can be clearly observed in the surface image of the filled PI7 membrane (middle). The red box highlights an area after exposure at high magnification. The boxed area was exposed at higher magnification before zooming out at the same spot to take that image. Comparing the cross-sectional images the impregnation with polymer electrolyte is apparent.

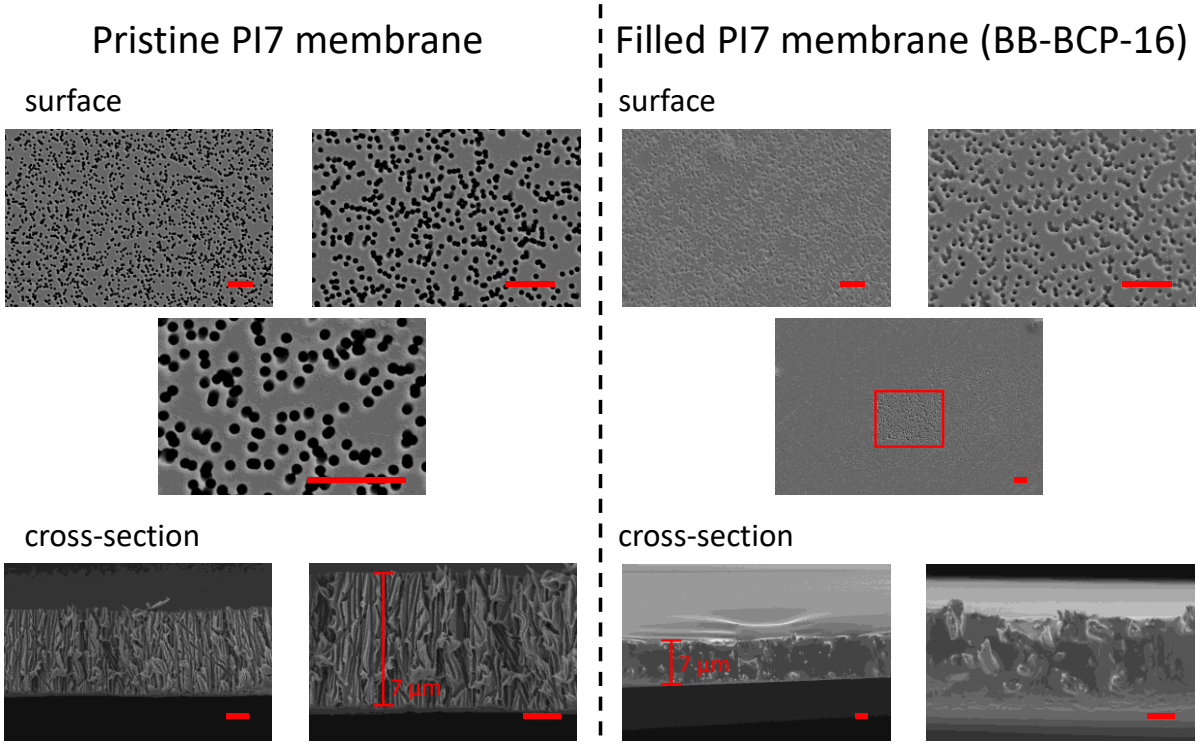


Figure S.III.13. SEM images of the (left) pristine and (right) electrolyte filled polyimide membrane (PI7) at different magnifications. The scale bar is equivalent to 2 µm in all of the images.

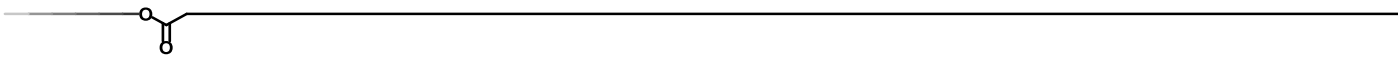
III.10.12 References

(1) Panday, A.; Mullin, S.; Gomez, E. D.; Wanakule, N.; Chen, V. L.; Hexemer, A.; Pople, J.; Balsara, N. P. Effect of Molecular Weight and Salt Concentration on Conductivity of Block Copolymer Electrolytes. *Macromolecules* **2009**, *42* (13), 4632–4637. https://doi.org/10.1021/ma900451e.

(2) Zhao, Q.; Chen, P.; Li, S.; Liu, X.; A. Archer, L. Solid-State Polymer Electrolytes Stabilized by Task-Specific Salt Additives. *Journal of Materials Chemistry A* **2019**, *7* (13), 7823–7830. https://doi.org/10.1039/C8TA12008K.

(3) Judez, X.; Zhang, H.; Li, C.; González-Marcos, J. A.; Zhou, Z.; Armand, M.; Rodriguez-Martinez, L. M. Lithium Bis(Fluorosulfonyl)Imide/Poly(Ethylene Oxide) Polymer Electrolyte for All Solid-State Li–S Cell. *J. Phys. Chem. Lett.* **2017**, *8* (9), 1956–1960. https://doi.org/10.1021/acs.jpclett.7b00593.

(4) Judez, X.; Piszcz, M.; Coya, E.; Li, C.; Aldalur, I.; Oteo, U.; Zhang, Y.; Zhang, W.; Rodriguez-Martinez, L. M.; Zhang, H.; Armand, M. Stable Cycling of Lithium Metal Electrode in Nanocomposite Solid Polymer Electrolytes with Lithium Bis (Fluorosulfonyl)Imide. *Solid State Ionics* **2018**, *318*, 95–101. https://doi.org/10.1016/j.ssi.2017.07.021.



IV Semi-Interpenetrating Network Electrolytes Utilizing Ester-Functionalized Low T_g Polysiloxanes in Lithium-Metal Batteries

Jannik Petry[a], Markus Dietel[a] and Mukundan Thelakkat*[abc].

[a] Applied Functional Polymers, University of Bayreuth, Universitätsstraße 30, 95447 Bayreuth, Germany
[b] Bavarian Polymer Institute (BPI), University of Bayreuth, Universitätsstraße 30, 95447 Bayreuth, Germany
[c] Bavarian Center for Battery Technology (BayBatt), University of Bayreuth, Universitätsstraße 30, 95447 Bayreuth, Germany

* Corresponding Author
E-mail: mukundan.thelakkat@uni-bayreuth.de

Reproduced with permission from Advanced Energy Materials, 2025, 15, 2403531
Copyright 2024 The Author(s), Wiley-VCH GmbH

IV.1 Abstract

Solid polymer electrolytes (SPE) obtained from polyesters are viable alternatives to polyethylene oxide-based materials, especially for room-temperature applications. In SPEs, the ion conduction is dependent on the polymer segmental mobility and is thus facilitated by low glass transition temperature (T_g). Here we synthesized an ester-functionalized polysiloxane-based polymer electrolyte with an exceptionally low T_g of -76 °C, resulting in a high ionic conductivity of 2.6×10^{-5} S cm^{-1} at room temperature and a lithium transference number of 0.72. However, the low T_g and consequently low mechanical stability require reinforcement to promote the formation of stable lithium-electrolyte interfaces in lithium plating stripping experiments and stable battery cycling in lithium-metal batteries (LMBs). For this, the SPE was incorporated into a network structure to yield a semi-interpenetrating network electrolyte (SPE20-SIPN) which results in significantly improved storage modulus by three orders of magnitude and maintained ionic conductivity upon crosslinking. The SPE20-SIPN exhibits stable cycling for up to 50 cycles with fluctuation (voltage noise) in some of the cells. A combination of crosslinking and nanoparticle addition (SPE20-N10-SIPN) overcomes the voltage noise and results in high coulombic efficiencies and high capacity retention above 80 % for 200 cycles in solvent-free, all-solid-state LMBs at 30°C.

IV.2 Introduction

Batteries are driving electronic devices in a multitude of applications and different ranges of current and potential requirements. Especially for mobile applications, in electric vehicles, or portable power stations, the energy density of the battery is a deciding aspect for its integration. Current state-of-the-art lithium-ion batteries (LIBs) are reaching their theoretical energy density limit, requiring new concepts for further improvements.[1] In Lithium-metal batteries, elemental lithium (Li^0) substitutes typical graphite anodes and thereby promises a significantly improved specific capacity by up to 10 times. However, the Li-metal anodes also require new electrolyte systems, as the liquid systems employed in LIBs are not compatible with the lithium anodes and tend to form uneven and dendritic lithium growth during battery operation.[2–5] Solid polymer electrolytes (SPEs), describing dry (i.e. non-swollen, solvent-free) mixtures of polymer matrixes and lithium-salts, are one potential candidate to be applied in LMBs. In the field of SPEs, poly(ethylene oxide) (PEO) has dominated the research focus with different polymer architectures, copolymers, and additives tested to overcome some inherent challenges linked to its application as SPE.[6,7] Namely, the high degree of crystallization limits the ionic conductivity at temperatures below its melting point (T_m) of around 65 °C. In addition, the electrochemical stability of only up to 4.6 V also limits the applicability of PEO in combination with high-voltage cathode systems. Furthermore, the strong coordination free electron pairs of the ether-oxygen to lithium cations restricts the cation mobility, resulting in low lithium transference numbers (LTN, t_{Li^+}) between 0.1 – 0.3.[8,9] The low LTN can manifest in pronounced ion concentration gradients during cycling.[8,10,11]

Alternatives to polyether-based electrolytes are commonly summarized as beyond-PEO materials which include e.g. polyesters and polycarbonates. In polyester-based materials like poly(ε-caprolactone) (PCL) the coordination of lithium cation is mostly through carbonyl-oxygen (C=O) atoms.[12,13] The C=O---Li^+ interaction is significantly weaker, resulting in considerably improved t_{Li^+} to values above 0.5.[9,14,15] Polyesters also persist a higher oxidative stability of up to 4.8 V revising the library of applicable cathode materials. However, similarly to PEO, PCL is semi-crystalline and therefore suffers from low ionic conductivity below its melting T_m of around 56 °C.[12] In general, different synthetic approaches for polyesters have been applied to improve both the overall ionic conductivity as well as at room temperature.[16–20] Recently, we demonstrated the successful use of poly(meth-)acrylate-based SPEs with different diester side chains. The amorphous materials showed high ionic conductivities even at lower temperatures. Similar to commonly observed trends, the series of diester polymers also showed a distinct scaling of the ionic conductivity with the glass transition temperature of the different polymer electrolytes: higher ionic conductivities being accessible with low T_g electrolyte systems.[12,13,21]

Herein we present a pathway to further decrease the glass transition temperature of ester-functionalized polymer electrolytes for improved ionic conductivity properties. The polysiloxanes backbone shows some of the lowest accessible glass transition temperatures due to the high backbone flexibility. In polysiloxanes, depending on their substitution pattern of the polymer backbone, many different functionalities and therefore properties can be tailored by the selection of side chain motifs.[22–24]

However, the very low T_g polysiloxane electrolytes come with the challenge of maintaining mechanical stability of the electrolyte. A certain mechanical integrity and softness of the

electrolytes is essential to establish a stable lithium-electrolyte interface and to prevent an uncontrolled and/or dendritic lithium deposition upon cycling.[17] Cross-linking is a common strategy to enhance the mechanical properties of an electrolyte. Here we want to distinguish between systems where a) a polymer electrolyte contains reactive functional groups, which form a network structure on its own or with an additional crosslinker (elastomers/duroplasts) and b) the polymer electrolyte (without reactive groups) is entrapped in an external network structure (semi-interpenetrating networks, SIPNs). In both cases, the crosslinked structure can increase the Young's modulus or the mechanical properties of the polymer electrolyte in general. For the former approach, reported works used bifunctionalized oligoethylene glycols (OEG) as crosslinkers.[25–27] One of the most widely studied crosslinked systems involving polysiloxane consists of a oligoethylene glycol- functionalized poly(siloxane-g-ethylene oxide). Here. short OEG telechelics were used as crosslinker, but detailed interface impedance or plating/stripping and battery cycling data is not available for this system.[26,28,29] In the field of SIPNs different combinations of polyether-based electrolytes and networks have been demonstrated.[30–33] The SIPN strategy does not demand the functionalization of the polymer electrolyte with reactive groups and any polymer electrolyte can be incorporated into a variety of in-situ formed network structures.

To realize a full polyester-based SIPN, we synthesized a new polysiloxane carrying pendent diester side chains. Further, we used a polyester-based telechelic diacrylate instead of OEG telechelics as crosslinker. As both constituents only feature ester moieties, high LTNs can be expected. First, we studied the electrolyte characteristics of the polysiloxane-based SPE. Then the SPE is combined with the crosslinker which can be cured in situ inside the test cells to obtain SPE-SIPN electrolytes, providing both high ionic conductivity, high LTN and improved mechanical stability. We investigated the influence of the network formation on the ion transport, mechanical properties, as well as the stability and reversibility of the lithium-electrolyte interface. Both the mechanical and interfacial stability could be significantly improved in the SPE20-SIPN, while maintaining high ionic conductivity. Furthermore, the charge/discharge and cycling performance was studied using Li|electrolyte|lithium iron phosphate (LFP) test cells demonstrating good discharge capacities at 30 °C its high retention after 200 cycles.

IV.3. Results and Discussion

IV.3.1 Material Synthesis

Two different polymers have been synthesized for this work: a polysiloxane with pendent diester side chains (poly(methyl-[butyl-4-{methyl adipate}])siloxane, PM(BMA)S and a polycaprolactone diacrylate telechelic (poly(caprolactone)diacrylate, PCLDA) as crosslinker. The syntheses, monomers/intermediates and polymers are illustrated in **Figure IV.1**a. Due to a variety of possible functional olefins, tailored functional polysiloxanes are accessible from poly(methyl hydro)siloxane (PMHS). The PM(BMA)S was synthesized utilizing the Karstedt's catalyst in a hydrosilylation reaction between commercially available PMHS and synthesized but-3-en-methyl adipate (BM3A) to be used as side chain. The hydrosilylation reaction involves an Pt-catalyzed olefin addition to the PMHS backbone. For synthetic details of BM3A refer to the SI. The PM(BMA)S and PCLDA are later combined to form the SIPN structure by radical polymerization (**Figure IV.1**b). The reactions were monitored using ^{1}H NMR spectroscopy (**Figure IV.1**c). For PM(BMA)S the quantitative side chain addition can be observed by the diminished proton signal of PM*H*S at 4.7 ppm.

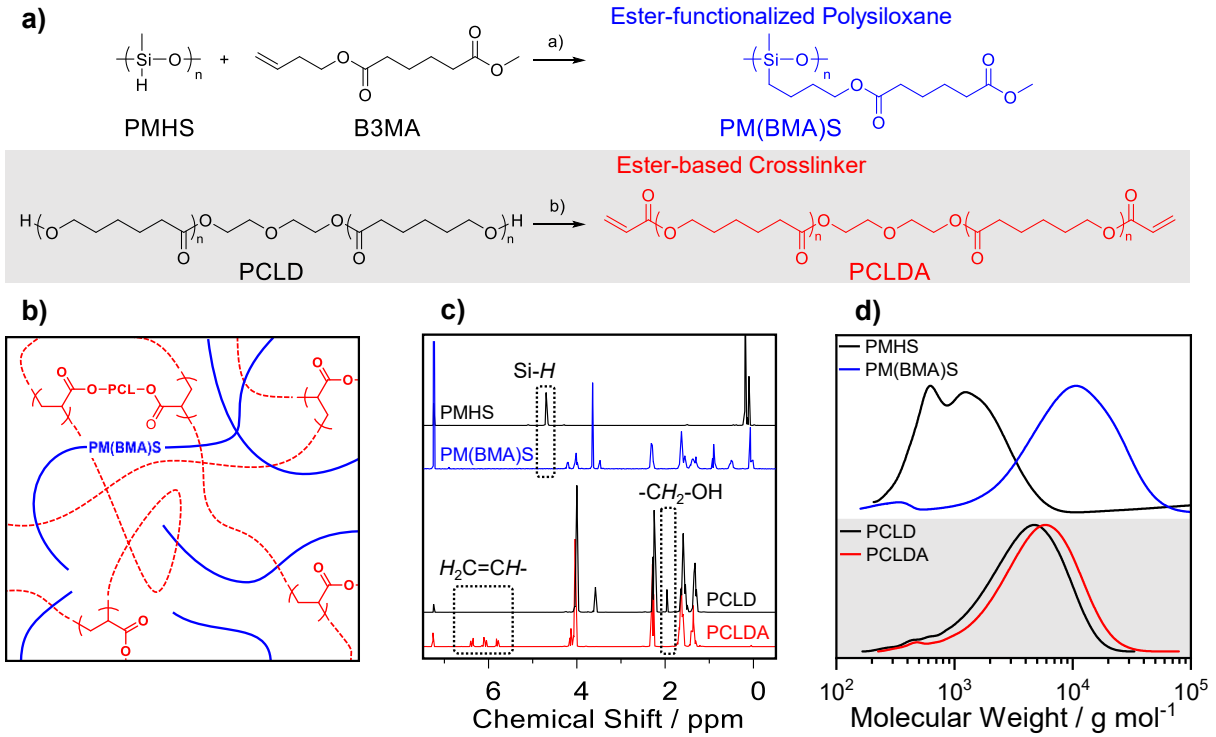


Figure IV.1. (a) Reaction scheme for the synthesis of (top) the siloxane-based polymer electrolyte PM(BMA)S and (bottom) the polycaprolactone-based network former PCLDA. (b) Schematic illustration of the SIPN structure obtained from PM(BMA)S and PCLDA. (c) 1H NMR spectra of the products and the respective precursors. (d) Molecular weight distributions determined by size-exclusion chromatography (THF+0.25wt% TBAB, PS calibration).

The low-molecular weight PCLDA crosslinker was synthesized by an esterification reaction of commercially available polycaprolactone diol (PCLD, M_n 3300 g mol^{-1}) with acryloyl chloride. Here, the introduction of the polymerizable acrylate moieties can be traced by the appearance of H_2C=C*H*-R double bond proton signals (6.5 – 5.5 ppm) and the shifted proton signal for the PCL-CH_2-OH (shifted from 3.6 to 4.1 ppm) due to the esterification reaction. Detailed peak assignment can be found in the supporting information (**Figure S.IV.1-3**). The addition of B3MA and the

acrylate moiety can be further observed in SEC measurements (**Figure IV.1**d). As the BMA side chain constitutes a large proportion of the PM(BMA)S the shift of molecular weight is more pronounced than for PCLDA as only the end groups of PCLD are functionalized. The commercial PMHS shows a bimodal molecular weight distribution, which cannot be observed in the synthesized PM(BMA)S.

Thermal characterization was conducted by thermogravimetric analysis (TGA) and differential scanning calorimetry (DSC) (**Figure S.IV.4-6**). Both PM(BMA)S and PCLDA show significantly higher thermal stability than the respective precursor materials and with that sufficient thermal stability for battery applications. The incorporation of diester side chains in PM(BMA)S resulted in a drastic increase of the glass transition temperature (T_g) to -76 °C compared to -138 °C for PMHS. With that, PM(BMA)S still undercuts the T_g of commonly used linear poly(ethylene oxide) (PEO) $T_{g,PEO}$ = -50 °C and linear poly(ε-caprolactone) (PCL) $T_{g,PCL}$ = -65 °C.[34,35] Furthermore, PM(BMA)S is amorphous and exhibits no further thermal transitions. Contrarily, both PCLD and PCLDA show distinct melt and crystallization transitions typical for linear poly(caprolactone)s. An overview of molecular weights, polymer dispersity, and thermal properties is given in **Table IV.1**.

Table IV.1. Overview of the molecular weights and thermal properties of the synthesized polymers and their respective precursors.

Polymer	M_n[a)]	$Đ$[b)]	$T_{d,5\%}$ [°C]	T_g[c)] [°C]	T_{cry}[c)] [°C]	T_m[c)] [°C]	ΔH_m[c)] [J g^{-1}]
PMHS	900	1.6	212	-138 [d)]	-	-	-
PM(BMA)S	7400	1.8	351	-76	-	-	-
PCLD	2400	2.0	258	-	35	48	83.4
PCLDA	3300	2.0	303	-	26	44	77.6

[a)] determined SEC, eluent: THF + 0.25 wt% TBAB, PS calibration; [b)] based on SEC results: M_w/M_n; [c)] determined from the second heating or cooling curve (10 K min^{-1}); [d)] value taken from literature.[36]

IV.3.2 Ionic Conductivity and Characteristics

The synthesized PM(BMA)S is converted to a solid polymer electrolyte (SPE10-50, XX=LiTFSI wt%) by the addition of LiTFSI (**Table S.IV.1**). The ionic conductivity of the obtained SPEs was characterized by electrochemical impedance spectroscopy (EIS) at various temperatures and salt concentrations between 10 and 50 wt% in symmetrical stainless-steel cells (StSt|electrolyte|StSt). Individual EIS measurements were evaluated by the general distribution of relaxation times (gDRT) giving access to bulk resistance and thus the ionic conductivity of the polymer electrolytes. Details of the DRT method and analysis are published by us in earlier works.[12,13,37] In DRT, electrochemical processes are transduced from the frequency into the time domain. Thereby, processes can be individually observed and clearly distinguished by their relaxation time constant (τ). The ionic conductivity was calculated by **Equation IV.1** based on the determined bulk resistance (R_b) and with the electrolyte geometry (L thickness of the electrolyte, A area of the electrolyte).

$$\sigma = \frac{L}{R_b \cdot A} \tag{IV.1}$$

The corresponding Arrhenius plots of the determined conductivities are depicted in **Figure IV.2**a. The corresponding impedance spectra are shown in **Figure S.IV.7**.

The polymer electrolytes do not show strict Arrhenius behavior (i.e. a linear temperature dependence) but a curved temperature dependence described by the Vogel-Tammann-Fulcher-(VTF)-model. In addition to an Arrhenius-type temperature dependence, the VTF-model accounts for the dependence of the ionic conductivity on the segmental mobility commonly observed in polymer electrolytes. This correlation results in the typical curved dependencies. The determined conductivity data was evaluated and fitted using the VTF model (**Equation IV.2**, **Figure S.IV.8**). The VTF fit parameters are given in the supporting information **Table S.IV.2**.

$$\sigma = A \cdot exp\left(-\frac{B}{R(T - T_0)}\right) \tag{IV.2}$$

The prefactor A is mostly associated with the salt/charge carrier concentration in the electrolyte, while the VTF pseudo-activation energy (B) includes the segmental mobility. The ionic conductivity is not only dependent on the temperature of the measurement but also on the so-called Vogel temperature (T_o). As an estimation for polymer electrolytes, this T_o is often defined as $T_o = T_g - 50$ °C.[38] Hence, the observed electrolyte glass transition temperature (T_g) influences the ionic transport properties, even if the observed temperature range is considerably higher than the T_g. From the VTF fits, the dependence of the ionic conductivity on the charge carrier concentration and the activation energy can be deduced. The activation energy increases steadily with increasing salt concentration from SPE10 to SPE50 (**Table S.IV.2**). Despite the electrolyte with 10 wt% LiTFSI (SPE10) exhibiting the lowest activation energy, the overall ionic conductivity is limited by the low concentration of charge carriers. Only after the addition of 20 – 30 wt% LiTFSI the charge carrier concentration is sufficient to ensure high ionic conductivities. At higher salt concentrations the ionic conductivity is then limited by the increasing activation energy (**Table S.IV.2**). The highest room temperature ionic conductivity of 2.6×10^{-5} S cm^{-1} was observed at a salt concentration of 20 wt% (**Table IV.2**).

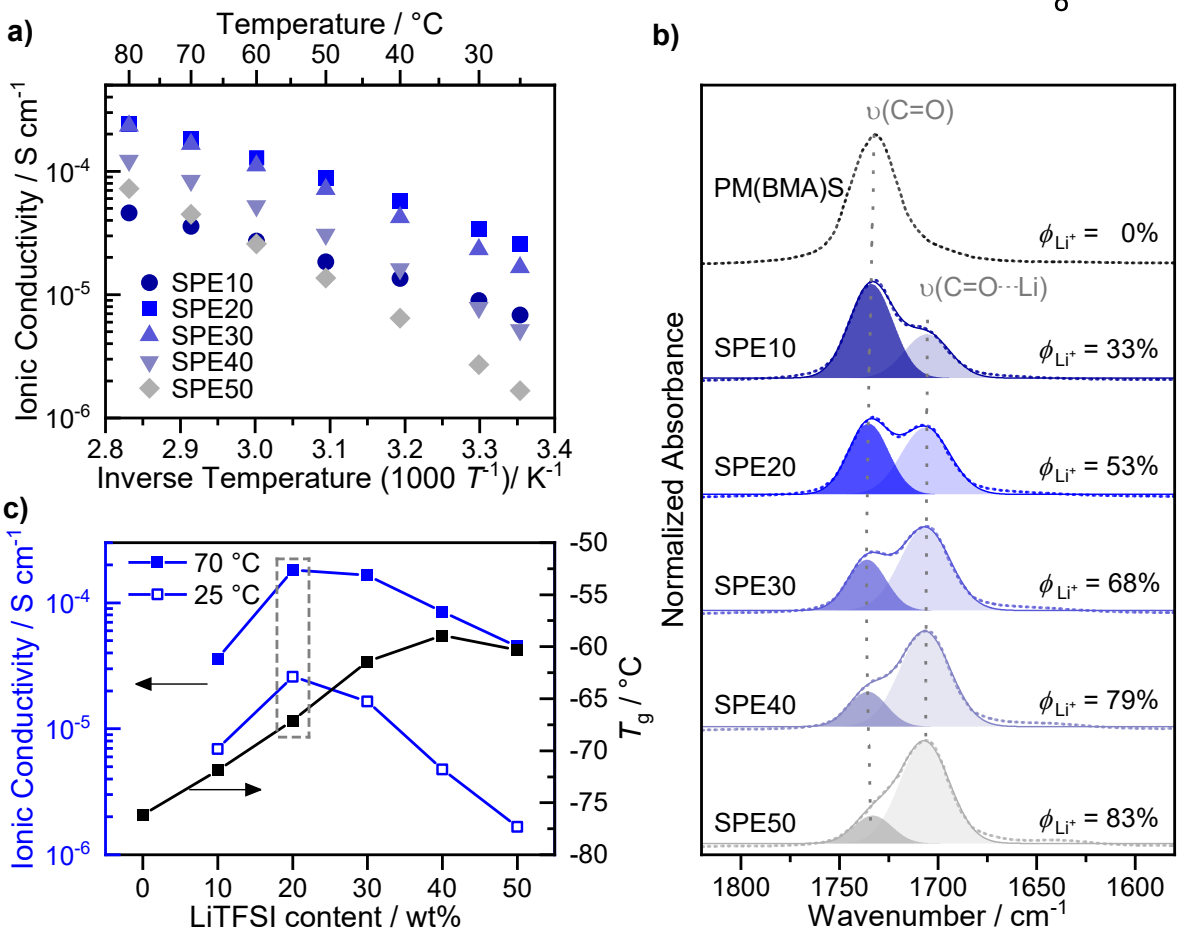


Figure IV.2. (a) Arrhenius plots of the temperature-dependent ionic conductivity measurements of SPEs with different LiTFSI salt concentrations between 10 and 50 wt%. (b) (dotted lines) recorded FT-IR spectra, (solid lines) cumulative fit, (dark shared area) fit for ν(C=O)-peak at 1730 cm^{-1} and (light shaded area) fir for ν(C=O---Li)-peak at 1705 cm^{-1}. Each spectrum is normalized to the cumulative peak area. The fraction of coordinated carbonyl groups (ϕ_{Li^+}) is calculated as the ratio of $A_{\nu(C=O\cdots Li)}/(A_{\nu(C=O)}+A_{\nu(C=O\cdots Li)})$. (c) LiTFSI salt concentration variation between 10 and 50 wt%. (blue) Ionic conductivity at (squares) 70 °C, (hollow squares) 25 °C. (black) The glass transition temperature of the pristine polymer and the solid polymer electrolytes. Solid lines in (c) are a guide to the eye.

In addition, the glass transition temperature (T_g) was determined by differential scanning calorimetry to correlate the T_g to the ionic conductivity (**Figure S.IV.9**). Often, an optimum of the ionic conductivity is observed at salt concentrations establishing a sufficient concentration of charge carriers while retaining a low glass transition temperature for the electrolyte. With increasing salt concentration, the T_g was increased from -76 °C (for 0 wt% salt) to a plateau at around – 60 °C for SPE30-SPE50. In the case non-crosslinked SPE based on PM(BMA)S the best trade-off and the highest ionic conductivity could be observed for SPE20 at a salt concentration of 20 wt% (corresponding to a ratio of carbonyl groups to lithium ions of C=O/Li = 8.4) (**Figure IV.2**b).

Besides the overall ionic conductivity, the lithium transference number (t_{Li^+}) was determined to understand the contribution of the Li-ion conductivity of the total ionic conductivity. The evaluation was performed in accordance with the Bruce and Vincent method consisting of two electrochemical impedance spectra and an intermediate polarization period.[39] Based on the changes in the Li-electrolyte interface resistance before and after the polarization period as well as the current response during the chronoamperometric polarization, a lithium transference

number can be calculated (data and evaluation can be found in **Figure S.IV.10** and **Table S.IV.3**). For the SPE20 the LTN was determined as 0.72±0.04, which is slightly higher than for linear polycaprolactone (PCL).[40] A high transference number above 0.5 is desirable, as the effective Li-ion conductivity constitutes a higher proportion of the overall ionic conductivity. Furthermore, possible polarization gradients due to an over-polarization of the counter anions (i.e. $TFSI^-$) can be reduced. Such gradients can impede effective charge transport and transfer reactions limiting the electrolyte performance.[11,41] The high LTN observed for ester-based electrolytes are in contrast to ether-based (e.g. PEO-based) electrolytes, where the strong Li-ion complexation by the free electron pairs of the ether oxygen atoms result in low transference numbers around 0.1-0.3.[9]

Furthermore, the Li^+-carbonyl oxygen coordination was investigated by FT-IR spectroscopy for SPE10 to SPE50 (**Figure IV.2**c). The carbonyl stretching vibration region between 1600 and 1800 cm^{-1} is an indicator of the coordination environment between the carbonyl moieties and lithium ions. The PM(BMA)S without any Li-salt only exhibits one peak at 1734 cm^{-1} corresponding to the stretching vibration of the free carbonyl groups (ν(C=O)). Upon the addition of salt, a secondary peak arises at around 1705 cm^{-1} which can be attributed to the stretching vibration of carbonyl groups taking part in lithium coordination (ν(C=O---Li)).[12] The IR signals were deconvoluted by nonlinear double-peak Gaussian fitting of the two peaks (**Table S.IV.4**). The ratio of the resulting area (A) of the individual fits $A_{\nu(C=O)}$ and $A_{\nu(C=O\text{---}Li)}$ are used to determine the fraction of carbonyl groups involved in Li^+ coordination (ϕ_{Li^+}). As observed in our previous studies the maximum ionic conductivity was observed for a ϕ_{Li^+} of around 50 % indicating that an equal amount of complexing and free carbonyl groups are indicative for efficient ion transport.[12,13]

Table IV.2. Overview of the glass transition temperature, achieved ionic conductivities and fraction of coordinating carbonyl groups for the electrolytes SPE10-50.

Electrolyte	LiTFSI wt%	CO/Li	T_g °C	σ@25°C S cm^{-1}	σ@70°C S cm^{-1}	ϕ_{Li^+} %
SPE10	10	18.9	-71.9	6.8×10^{-6}	3.6×10^{-5}	33
SPE20	20	8.4	-67.1	2.6×10^{-5}	1.8×10^{-4}	53
SPE30	30	4.9	-61.5	1.7×10^{-5}	1.7×10^{-4}	68
SPE40	40	3.1	-58.9	5.2×10^{-6}	8.4×10^{-5}	79
SPE50	50	2.1	-60.3	1.7×10^{-6}	4.5×10^{-5}	83

IV.3.4 Semi-interpenetrating Network – Ionic Conductivity and Rheology

So far we demonstrated, that the low glass transition temperature of the polysiloxane-based diester electrolyte translates well to high ionic conductivity, while the contributing ester-moieties result in high LTN. However, the pursuit of low-T_g, flexible and soft polymer electrolytes faces problems with interfacial instabilities, as the consequence of low mechanical structural integrity and mechanical stability. Amongst other approaches, the use of network-forming polymers has been shown to improve mechanical stability as well as cyclability.[42] Therefore, we employed the synthesized PCLDA crosslinker to establish a coherent framework to improve the mechanical stability of the electrolyte system. Exemplary optical images of SPE20 and SPE20-SIPN are depicted in **Figure S.IV.11**.

For further investigation, we utilize the crosslinker PCLDA in combination with the PM(BMA)S. The SPE20-SIPN is obtained by homogenously mixing PM(BMA)S, PCLDA, LiTFSI, and a radical initiator (azobisisobutyronitrile, AIBN) in solution. For the sake of comparability, the ester moieties of the PCLDA were taken into account for the calculation of the salt concentration The total LiTFSI content was maintained at 20 wt%, resulting in a comparable C=O/Li ratio of 8.9 (**Table S.IV.5**). During cell preparation, the electrolytes were thoroughly dried and thermally crosslinked to yield semi-interpenetrating network structures (SPE20-SIPN). The effect of the network formation was evaluated by comparative ionic conductivity and rheological measurements (**Figure IV.3**).

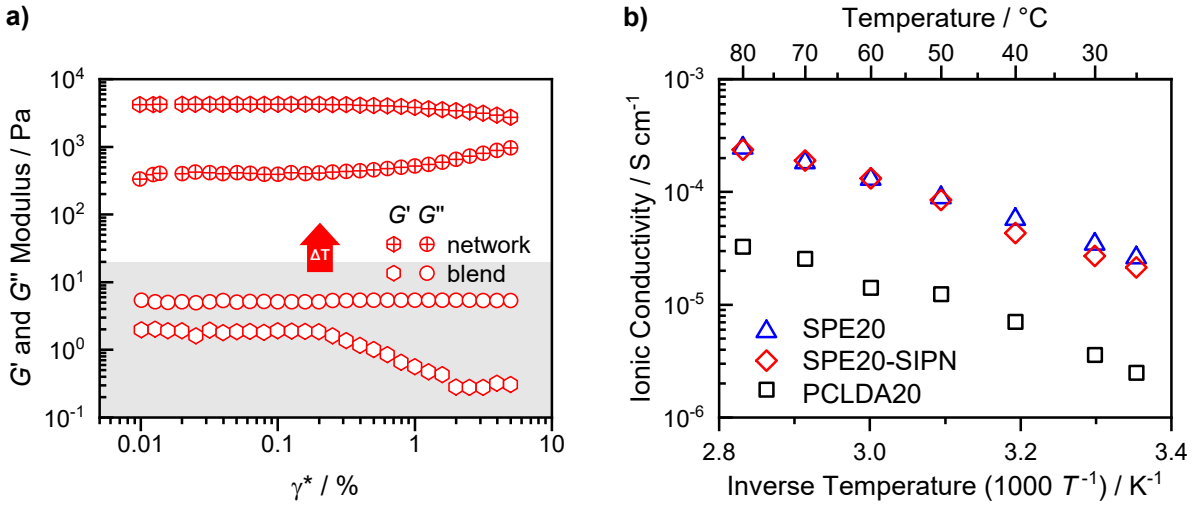


Figure IV.3. (a) Rheological strain sweep measurement at 1 Hz and 60 °C of (hollow symbols) the pristine blend of PM(BMA)S and PCLDA before crosslinking and (hashed symbols) the obtained network after thermal crosslinking. (b) Temperature-dependent ionic conductivity of the SPE20 (PM(BMA)S + 20 wt% LiTFSI), the crosslinked electrolyte (SPE20-SIPN), and the crosslinker electrolyte PCLDA20 (PCLDA + 20 wt% LiTFSI) without the incorporation of the polysiloxane-based polymer.

The ionic conductivity of both the SPE20 and SPE20-SIPN were similar at temperatures above 40 °C. At lower temperatures, the network shows a marginally reduced ionic conductivity, most likely due to the restriction of polymer segmental mobility in the network structure. Based only on the polymeric constituents of SPE20-SIPN, the polymer matrix consists of ca. 55 wt% PM(BMA)S and 45 wt% PCLDA, respectively. Even though the network constitutes almost half of the ion-conducting matrix, the effective ionic conductivity is very similar to SPE20. Furthermore, the PCLDA and 20 wt% of LiTFSI were used as network electrolyte without any PM(BMA)S. The network (PCLDA20) itself showed significantly reduced ionic conductivities over the whole temperature range and an ionic conductivity of 2.7×10^{-6} S cm^{-1} at 25 °C. The observed conductivities are in the same range as observed by Jalbert et al., who used the crosslinker as a 3D network electrolyte, as the crosslinker in combination with a Li-salt. The network showed a high Youngs's modulus of 5.5×10^{6} Pa, however, the observed room temperature conductivity was 3.6×10^{-6} S cm^{-1} at a salt concentration of 40 wt%.[43]

A comparison of a fully cross-linked polyester PLCDA20 with the SPE20-SIPN clearly indicates that a certain amount of segmental mobility is to be guaranteed in crosslinked electrolytes to achieve high ionic conductivities, especially at room temperature.

The effect of the network formation on the mechanical properties was evaluated by rheological measurements. Therefore, a non-crosslinked blend of PM(BMA)S and PCLDA and the corresponding cured and crosslinked semi-interpenetrating network were evaluated (**Figure IV.3**a, blend and network). The pure PM(BMA)S was not investigated individually, as we wanted to evaluate the direct influence of the network formation by comparing the blend (before crosslinking) and network (after crosslinking). It should also be noted that we did not use any Li-salt during the rheology measurements, due to the hygroscopic nature under ambient conditions of measurements. The storage (*G'*) and loss (*G''*) moduli were recorded during strain-sweep measurement (**Figure IV.3**a) and frequency sweep measurements (**Figure S.IV.12**). Deviations from the linear viscoelastic regime (e.g. horizontal plateau) above an applied strain of 0.2 % indicate the loss of structural integrity and non-reversible deformation of the polymer structure. The polymer blend shows predominantly viscous behavior with *G'*<*G''*. Upon SIPN formation the change to a predominantly elastic behavior (*G'*>*G''*) demonstrates the significant influence of the structure-giving PCLDA network. The storage modulus (at 0.1 % strain) could be increased by more than three orders of magnitude from 2 Pa for the blend to 4250 pa for the network. In frequency-sweep measurements, the cured network system showed steady *G'* and *G''* with *G'* > *G''* across the frequency range, typical for crosslinked polymer systems. The non-cured mixture however exhibited different plateaus and transitions between viscous and elastic behavior, most likely related to the combination of two vastly different polymer structural domains.

In combination, the results from the ionic conductivity and rheological measurements underline the importance of adequate network design offering both mechanical stability while retaining a high ionic conductivity. Further studies on the applicability in context with lithium-metal batteries will be discussed in the following sections.

IV.3.5 Electrochemical Stability Window and Lithium Compatibility

The electrochemical stability window (ESW) of the SPE20 was evaluated by linear sweep voltammetry in Li|SPE|StSt test cells (**Figure IV.4**a). The degradation potential $V_{d,LSV}$ was determined geometrically at the transition from the faradaic to the non-faradaic regime ($V_{d,geo}$) and as the potential where a threshold current density of 0.1 mA cm^{-2} ($V_{d,th}$) is reached.[44] Both methods result in similar decomposition values of 5.28 V and 5.34 V for $V_{d,geo}$ and $V_{d,th}$, respectively. However, in LSV experiments the electrochemical stability is often overestimated as influences of the cathode electrolyte interface (CEI) are neglected.[45,46] Thus, we conducted additional galvanostatic overcharging (GO) experiments in Li|SPE20|LFP cells mimicking the operational conditions of later battery cells. After three equilibration cycles, the battery was charged without a cut-off potential at 0.1C. The GO charging profile exhibits the LFP-typical plateau at 3.5 V with a distinct increase of the potential after completed charging. At 4.8 V a second plateau substantiates, marking the limit of oxidative stability ($V_{d,GO}$) under operational conditions (**Figure IV.4**b). The differences between $V_{d,LSV}$ and $V_{d,GO}$ demonstrate the importance of the evaluation of the electrochemical stability under operational conditions. The ESW of 4.8 V (vs. Li/Li$^+$) could benefit the application of high-voltage cathode systems. However, we exclusively used LFP-based cathodes in this work.

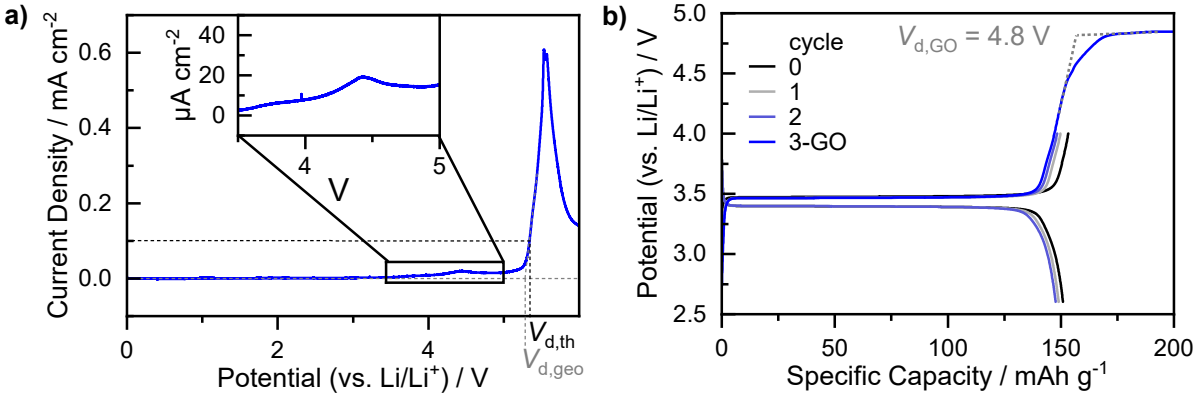


Figure IV.4. (a) Linear sweep voltammetry of SPE20 using Li|SPE|StSt cells from 0 V to 6 V at a sweep rate of 0.1 V s^{-1} at 70 °C. (b) Galvanostatic overcharging in Li|SPE20|LFP cells at 70 °C at 0.1 C. Before charging without a cut-off potential, three cycles between 2.6 and 4.0 V are performed.

To elaborate on the compatibility between lithium-metal electrodes and the synthesized PM(BMA)S as well as the obtained semi-interpenetrating network, we conducted lithium plating/stripping experiments in Li|electrolyte|Li symmetrical cells (**Figure IV.5**a). To attain a more in-depth understanding of the interfacial processes and changes we employed intermittent EIS measurements. The EIS measurements were evaluated by the generalized distribution of relaxation times-(gDRT)-analysis.[13,37,47–49]

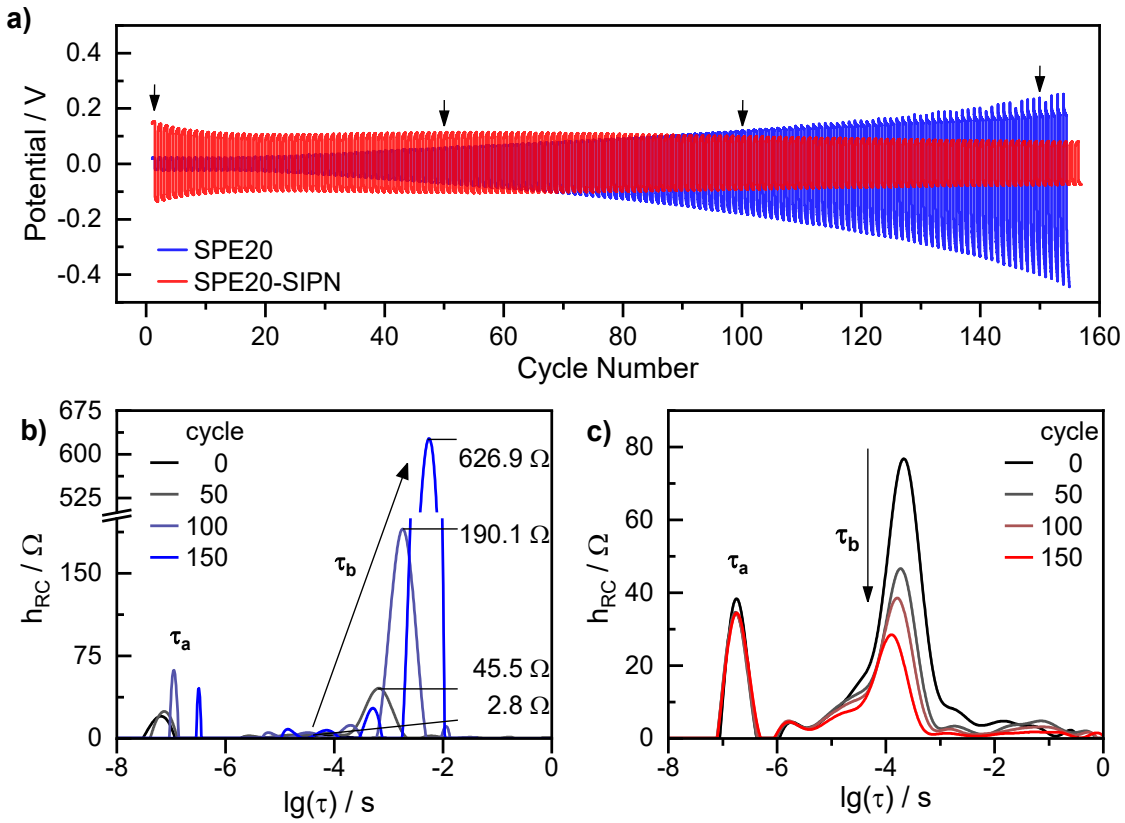


Figure IV.5. (a) Lithium plating/stripping cycling data using Li|electrolyte|Li symmetrical cells (electrolyte thickness 136 µm, diameter 4 mm) at 70 °C using a half cycle time of 1h and a current density of 0.1 mA cm^{-1}. Cycling data for (blue) SPE20 and (red) SPE20-SIPN. Arrows indicate the cycles analyzed by EIS and gDRT. (b,c) gDRT analysis for the 0th, 50th, 100th, and 150th cycle. The results are represented by the absolute distribution function h(τ). Peaks τ_a and τ_b can be attributed to the ionic conductivity and the charge transfer processes, respectively.

As a consequence of the charge transfer processes, interfacial resistances, and the electrolyte conductivity an overpotential is induced during plating/stripping experiments.[50] For the SPE20 the overpotential is very low initially (20 mV), but steadily increases asymmetrically to 250 and 450 mV for the different half cycles, respectively. The gDRT analysis shows two main contributions (**Figure IV.5**b+c). The ionic conductivity of the bulk electrolyte and the charge transfer resistance across the lithium electrolyte interface can be observed at shorter and longer relaxation times and are denoted as τ_a and τ_b, respectively. With prolonged cycling, the contributing processes for SPE20 (**Figure IV.5**b) exhibit slower relaxation times as well as increased polarization (i.e. process resistances) with increasing cycle numbers. Especially the interface resistance contribution (τ_b) increases from 2.8 to 626.9 Ω during plating/stripping for 150 cycles. This indicates that the SPE20 can form intimate contact with the Li-metal anodes, enabling a very efficient charge transfer. However, due to its very soft nature, the deposition and depletion of lithium might occur in an inhomogeneous manner, most likely leading to the formation of mossy or dead lithium agglomerates on the lithium electrode surface, manifesting in increasing overpotentials.

Contrarily, the overpotential for the crosslinked SPE20-SIPN shows a stable overpotential evolution after a short equilibration phase in the first cycles. Throughout the performed cycling experiment up to 150 cycles, the overpotential decreases from 140 to 80 mV. On the other hand, SPE20-SIPN electrolyte exhibits significantly higher initial interfacial resistances of 80 Ω (**Figure IV.5**c). However, during cycling the interface resistance is decreasing to 30 Ω, underlining the effective stabilization of the lithium electrolyte interface.

IV.3.6 Battery Application and Cycling Performance

Finally, the cyclability and applicability of the polymer electrolytes were investigated using Li|electrolyte|LFP cells (**Figure IV.6**). The composition of electrolytes is summarized in **Table S.IV.5**. As the electrolyte SPE20 showed significantly increasing charge-transfer resistances in lithium plating and stripping experiments (**Figure IV.5**a,b), we did not consider the electrolyte for battery cycling experiments. For the cell fabrication, we have optimized a procedure for low T_g systems using thin polyimide (PI) membrane support.[12,13,51] Thin membranes are of high advantage, as they enable defined and small electrode distances for higher energy densities.[52–54] For this, we soaked a porous polyimide membrane with the electrolyte solution and applied those to the LFP-based cathodes (**Figure S.IV.13,14**). The cell preparation details are given in the SI (**Scheme S1**). A comparative evaluation of the effect of the incorporation of polyimide membrane on the ionic conductivity is provided in **Figure S.IV.15**.

At first, we investigated the SPE20-SIPN electrolyte at 30 °C and 0.1C (**Figure IV.6a**). The cycling performance and electrochemical impedance across different cells is presented in **Figure S.IV.16** and **Table S.IV.6**. It was possible to attain stable charge and discharge profiles for SPE20-SIPN. However, out of four measured cells, two cells showed overcharging or unstable voltage profiles in some of the cycles, where the cut-off potential is not reached but a continuous charging process can be observed (**Table S.IV.6**). This behavior is also referred to as *voltage noise* and is ascribed to an unstable lithium-electrolyte interface, resulting in the formation of semi-reversible soft shorts during the charging process.[42] In literature, it was reported that for thin electrolyte layers, such fluctuations can be observed especially for soft electrolytes.[46] However, a variation in electrolyte thickness was not performed in this study.

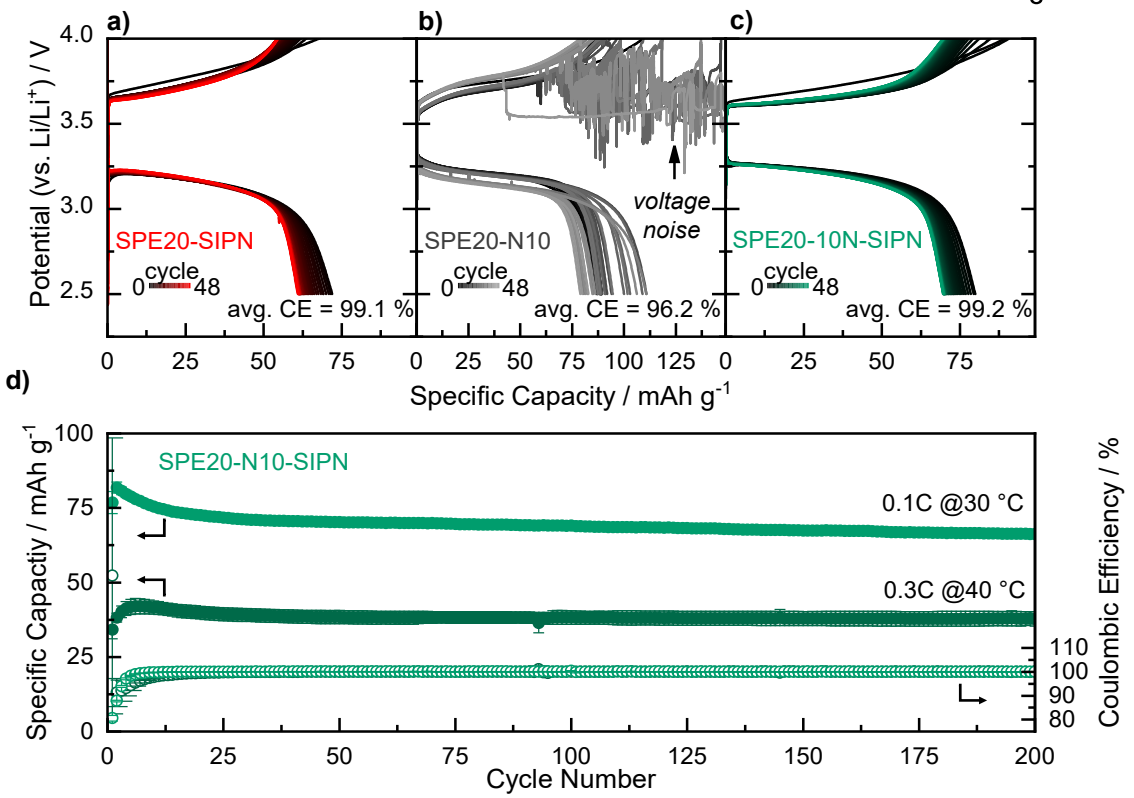


Figure IV.6. Battery cycling data in Li|SPE20-SIPN/SPE20-N10/SPE20-N10-SIPN|LFP test cells at a given temperature and C-rate. For all cells, an electrolyte-infiltrated PI7 membrane is used. Data for (red) SPE20-SIPN (SPE20+crosslinking), (gray) SPE20-N10 (SPE20+10 wt% TiO_2) and (green) SPE20-N10-SIPN (SPE20+10 wt% TiO_2+crosslinking). Charge and discharge profiles for the three systems, for cycles 0 to 50. Cells were cycled between (a) 2.5-4.2 V, (b)-(c) 2.5 – 4 V. (d) Cycling performance (2.5 - 4.2 V) over 200 charge and discharge cycles of SPE20-N10-SIPN at (green) 0.1C and 30 °C and (dark green) 0.3C and 40 °C. Cycling data in (d) displays an average and corresponding error of three cells.

Another alternative approach to improve the battery cycling characteristics of soft electrolytes is the addition of small amounts of nanoparticles to the electrolyte.[12,48,55,56] Therefore, we wanted to examine if the addition of nanoparticles can improve the crosslinking strategy to avoid the voltage noise phenomena, even in very thin, soft electrolytes. This can be easily tested by adding 10 wt% of TiO_2 to SPE20-SIPN before crosslinking. A comparative evaluation of the effect of the nanoparticle addition and crosslinking on the ionic conductivity is shown in **Figure S.IV.17**. The crosslinked nanocomposite electrolyte (SPE20-N10-SIPN) shows extremely stable battery cycling, where none of the cycles exhibited voltage noise phenomena. An optical image of the cured electrolyte is displayed in **Figure S.IV.11**.

For SPE20-N10-SIPN, the discharge capacity stabilized after the first few cycles with average Coulombic efficiencies of 99.1 % for the first 50 cycles. The improved efficiency and stable charging and discharging behavior exemplify the significant influence of the network incorporation together with nanoparticle addition and the importance of adequate lithium-electrolyte interface stability. Further, we performed long-term cycling experiments using the SPE20-N10-SIPN electrolyte at different C-rates of 0.1 and 0.3C. Battery cycling at 70 °C (0.1C) exhibits an initial specific capacity of 152.2±3.1 mAh g^{-1} (**Figure S.IV.18**). Since we aim to develop electrolyte systems working at room temperature, we focused on long-term cycling at reduced temperatures (30 °C and 40 °C) Prior to cycling experiments, no additional pre-cycling was

performed. The discharge capacity and Coulombic efficiency for both cycling conditions are depicted in **Figure IV.5**d. Both cycling conditions show an equilibration phase of around 25 cycles after which a stable discharge capacity can be observed. At 0.1C a maximum discharge capacity of 81.8±1.9 mAh g^{-1} was available in the second cycle which decreased to 66.2±1.1 mAh g^{-1} after 200 cycles, representing a capacity retention of 81 %. If the equilibration phase (till 25 cycles) is considered as cell conditioning, the capacity retention is above 90 %. As expected for increased C-rates accessible discharge capacity was lower at 0.3C and 40 °C. Even though the achieved specific capacity is low, the capacity retention was high in the range of 90 %.

On the other hand, a nanocomposite electrolyte without crosslinking (SPE20-N10) showed extreme fluctuations, overcharging, and reduction of the Coulombic efficiency in battery cycling (**Figure IV.6**b, **Table S.IV.6**). These results of battery cycling indicate that a combination of reinforcing strategies is required to enable very thin and soft electrolyte materials. Probably, the strategies adopted such as crosslinking, or nanoparticle addition depend on the nature of the electrolyte as well as the electrodes used in the cell setup.

In summary, a combination of crosslinking and addition of nanoparticles enabled stable battery cycling for 200 cycles under different cycling conditions. However, further improvement with regard to increasing the specific capacity at low temperatures and high C-rates is required.

IV.4. Conclusion

We synthesized and studied a SIPN electrolyte system for lithium-metal batteries. The system consists of only ester-based solid polymer electrolytes and crosslinkers. For the SPE we synthesized a low T_g polysiloxane with pendent diester sidechains and used a polyester telechelic for crosslinking. This SPE has a high lithium transfer number in the range of 0.7. The non-crosslinked SPE20 exhibited the highest ionic conductivity of 2.6×10^{-5} S cm^{-1} at 25 °C but showed low mechanical stability and therefore unstable cycling behavior in lithium plating and stripping experiments.

On the other hand, the crosslinked electrolyte system (SPE20-SIPN) maintains the high ionic conductivity while also having significantly improved mechanical properties. The semi-interpenetrating network structure (PM(BMA)S-SIPN) showed a predominantly elastic behavior ($G'>G''$) and induced significantly improved mechanical stability (from 2 Pa to 4250 Pa) compared to the non-crosslinked blend, demonstrating the effect of the network-establishment. Consequently, stable lithium electrolyte interfaces, low charge transfer resistances, and stable overpotentials could be achieved in lithium plating and stripping experiments. As a result of this, SPE20-SIPN is suitable for battery cycling in combination with lithium-metal anodes and LFP-base composite cathodes. For its application at room temperature addition of nanoparticles enabled long-term stable cycling with high Coulombic efficiency. Thus, a combination of low T_g electrolyte, crosslinking, and nanoparticle addition strategy (SPE20-N10-SIPN) offers benefits for low-temperature battery applications, especially in thin devices.

IV.5. Experimental Section

IV.5.1 Electrolyte Formulation

The polysiloxane-based electrolytes (SPEXX, XX=LiTFSI wt%) were prepared by combining the PM(BMA)S polymer and LiTFSI in acetonitrile at different weight proportions (10-50 wt% LiTFSI). The solution was allowed to stir overnight. Afterward, the solvent is removed under reduced pressure at 80 °C overnight. The SPE-SIPN was prepared by dissolving PM(BMA)S, PCLDA, LiTFSI, and AIBN in acetonitrile. The solution was stirred overnight. Drying was conducted only at RT over two days in high vacuum. Dried electrolytes are used for IC, LSV, LPS, LTN experiments. For SPE20-N10 (SPE20+10wt% TiO_2 nanoparticles) and SPE20-N10-SIPN (SPE20-SIPN+10wt% TiO_2 nanoparticles) the nanoparticles are dispersed in acetonitrile using a ultrasonication for 30 minutes. Afterward, the remaining constituents are added and processed under the same conditions. Electrolytes used in battery cells (Li|electrolyte|cathode) are not dried but used as solution during cell preparation. The exact composition of the electrolytes is given in Tables **S.IV.1** and **S.IV.5**.

IV.5.2 Annealing procedure

For test cells (IC, LSV, LPS, LTN) dried electrolytes are used during cell preparation. After sealing the cells inside an Ar-filled glovebox the cells are transferred to an oven at 100 °C overnight for annealing. For all cells using SPE20-SIPN or SPNE20-N10-SIPN the annealing step at 100 °C leads to the in-situ formation of the crosslinked system inside the cell. For all battery (Li-SPE-cathode) cells, cathode-supported electrolytes are employed (see section IV.4.4). Crosslinking is also achieved during the drying/curing step at 100 °C overnight under high vacuum. The experimental procedure for crosslinking during rheology measurements is explained in the supporting information.

IV.5.3 Cathode Formulation

The cathodes were prepared by dispersing the cathode constituents in a combination of acetonitrile and N-methyl pyrrolidone (1:2 vol). 2.1 mL of solvent mixture was used per 1 g of active material. The cathode composition was active material: carbonaceous additives(super P carbon and graphitic carbon): PVDF binder: SPE20 electrolyte = 70:10:15:5. The cathode mixture is homogenized by ball milling for 1.5 h (9 cycles of 10 min milling and 10 min resting phase). The cathode slurry is coated onto carbon-coated aluminum current collectors by doctor blade technique with a gap height of 380 µm. The cathode laminates are left to passively dry overnight. Afterward, the cathodes are transferred to a vacuum oven for further drying at 80 °C under high vacuum overnight. The cathode laminate is densified at 60 °C by applying stepwise increasing pressure of 1, 2, 3, and 4 tons for 2 minutes at each pressure. The cathodes were punched into discs with a diameter of 14 mm (area 1.54 cm^2). The active material mass loading was around 3.2 mg cm^{-2} (0.54 mAh cm^{-2}).

IV.5.4 Cell fabrication

All electrochemical measurements were conducted using CR2032-type coin cells. For the determination of the ionic conductivity (IC), stainless steel (StSt) blocking electrodes were used (StSt|electrolyte|StSt). For linear sweep voltammetry (LSV) measurements StSt working electrode (WE) and lithium as reference and counter electrode (RE and CE) was used (StSt|electrolyte|Li). The lithium transference number (LTN) determination and lithium plating and stripping (LPS) was conducted using symmetrical lithium cells (Li|electrolyte|Li). For IC, LSV, LTN, and LSV measurements a Kapton® spacer (thickness 130 µm, diameter 16 mm) with a hole of defined diameter (4 mm) was used. The cavity is filled with electrolyte during coin cell assembly. For battery test cells consisting of lithium metal and the prepared cathodes (Li|electrolyte|LFP) a track-etched polyimide separator (porosity 28 %) with a thickness of 7/25 µm (PI7/PI25) is used. The separator is preheated and a thin coating of an electrolyte solution is applied. After two minutes the semi-coated separator is placed on a cathode disc with the electrolyte coating facing the electrode. Subsequently, the uncoated separator is also coated with the electrolyte solution. The assembly of the cathode and electrolyte-infiltrated separator is dried at 100 °C under high vacuum and then transferred to a glovebox. There lithium-metal anodes (diameter 14 mm) are applied.

IV.5.5 Electrochemical measurements

Electrochemical impedance spectroscopy (EIS) was conducted in a frequency range of 3 MHz – 0.1 Hz with a sinusoidal excitation potential of 20 mV. A climate chamber was used for temperature-dependent EIS measurements. IC cells were annealed at 70 °C for 12 h. Afterwards, the individual measurements were taken at 60, 80, 70, 60, 50, 40, 30, and 25 °C after an equilibration period of 1.5 h for each temperature step. All other electrochemical test cells were annealed at the temperature of the subsequent measurement: LTN, LSV, LPS, GO at 70 °C for 12 h at OCV; battery cycling at 30 °C or 40 °C for 5 hours at OCV. Linear sweep voltammetry was conducted between 0–6 V at a scan rate of 0.1 mV s^{-1}. Lithium transference number determinations were performed following the Bruce and Vincent method consisting of an initial EIS measurement, a chronoamperometric polarization (potential 10 mV, duration 3h), and a second EIS measurement immediately after the polarization interval. Lithium plating and stripping (LPS) experiments were performed using a current density of 0.1 mA cm^{-2} with a half-cycle duration of 1 h. Every 5 full cycles the LPS was stopped to perform an EIS measurement. Before galvanostatic overcharging, three battery cycles at 0.1 C (2.6 – 4.0 V) were performed. Afterward, the cell is charged without a cut-off at 0.1 C. Further battery cycling was conducted between 2.5 and 4.2 V using different C-rates and temperatures (0.1C at 30 °C, 0.3C at 40 °C).

IV.6. Supporting Information

Supporting Information is available from the Wiley Online Library or from the author.

IV.7. Acknowledgements

This work was supported by the Bavarian Ministry of State for Research and Arts under the SolTech project. J.P. was supported with a fellowship by the Deutsche Bundesstiftung Umwelt (grant no. 20021/714-242). The authors thank Reiner Giesa for rheology measurements. The authors acknowledge the Bavarian Polymer Institute (University of Bayreuth) for providing access to the Keylab Electron and Optical Microscopy for electron microscopy facilities and Martina Heider for conducting SEM measurements.

Open access funding enabled and organized by Projekt DEAL.

IV.8. Conflict of Interest

The authors declare no conflict of interest.

Author Contributions J.P. conceptualized the idea for the study; wrote the original draft; performed synthesis; designed the methodology; performed investigation; and visualized the idea for the study. M.D. performed the synthesis; designed the methodology; and performed the investigation. M.T. performed the funding acquisition, project administration, and supervision; and wrote, reviewed, and edited the manuscript. The manuscript was written through the contributions of all authors. All authors have given approval to the final version of the manuscript.

IV.9. Data Availability Statement

The data that support the findings of this study are available from the corresponding author upon reasonable request.

IV.10. Keywords

crosslinking, mechanical stability, nanocomposites, polyester, solid polymer electrolytes

IV.11. References

(1) Xu, W.; Wang, J.; Ding, F.; Chen, X.; Nasybulin, E.; Zhang, Y.; Zhang, J.-G. Lithium Metal Anodes for Rechargeable Batteries. *Energy Environ. Sci.* **2014**, *7* (2), 513–537. https://doi.org/10.1039/C3EE40795K.

(2) Bieker, G.; Winter, M.; Bieker, P. Electrochemical in Situ Investigations of SEI and Dendrite Formation on the Lithium Metal Anode. *Phys. Chem. Chem. Phys.* **2015**, *17* (14), 8670–8679. https://doi.org/10.1039/C4CP05865H.

(3) Harry, K. J.; Higa, K.; Srinivasan, V.; Balsara, N. P. Influence of Electrolyte Modulus on the Local Current Density at a Dendrite Tip on a Lithium Metal Electrode. *J. Electrochem. Soc.* **2016**, *163* (10), A2216. https://doi.org/10.1149/2.0191610jes.

(4) Barai, P.; Higa, K.; Srinivasan, V. Lithium Dendrite Growth Mechanisms in Polymer Electrolytes and Prevention Strategies. *Phys. Chem. Chem. Phys.* **2017**, *19* (31), 20493–20505. https://doi.org/10.1039/C7CP03304D.

(5) Stolz, L.; Winter, M.; Kasnatscheew, J. Perspective on the Mechanism of Mass Transport-Induced (Tip-Growing) Li Dendrite Formation by Comparing Conventional Liquid Organic Solvent with Solid Polymer-Based Electrolytes: Original Scientific Paper. *Journal of Electrochemical Science and Engineering* **2023**, *13* (5), 715–724. https://doi.org/10.5599/jese.1724.

(6) Zhang, D.; Li, L.; Wu, X.; Wang, J.; Li, Q.; Pan, K.; He, J. Research Progress and Application of PEO-Based Solid State Polymer Composite Electrolytes. *Front. Energy Res.* **2021**, *9*. https://doi.org/10.3389/fenrg.2021.726738.

(7) Wang, H.; Sheng, L.; Yasin, G.; Wang, L.; Xu, H.; He, X. Reviewing the Current Status and Development of Polymer Electrolytes for Solid-State Lithium Batteries. *Energy Storage Materials* **2020**, *33*, 188–215. https://doi.org/10.1016/j.ensm.2020.08.014.

(8) Yu, X.; Hoffman, Z. J.; Lee, J.; Fang, C.; Gido, L. A.; Patel, V.; Eitouni, H. B.; Wang, R.; Balsara, N. P. A Practical Polymer Electrolyte for Lithium and Sodium Batteries: Poly(Pentyl Malonate). *ACS Energy Lett.* **2022**, *7* (11), 3791–3797. https://doi.org/10.1021/acsenergylett.2c02128.

(9) Rosenwinkel, M. P.; Andersson, R.; Mindemark, J.; Schönhoff, M. Coordination Effects in Polymer Electrolytes: Fast Li+ Transport by Weak Ion Binding. *J. Phys. Chem. C* **2020**, *124* (43), 23588–23596. https://doi.org/10.1021/acs.jpcc.0c08369.

(10) Diederichsen, K. M.; McShane, E. J.; McCloskey, B. D. Promising Routes to a High Li+ Transference Number Electrolyte for Lithium Ion Batteries. *ACS Energy Lett.* **2017**, *2* (11), 2563–2575. https://doi.org/10.1021/acsenergylett.7b00792.

(11) Stolz, L.; Homann, G.; Winter, M.; Kasnatscheew, J. The Sand Equation and Its Enormous Practical Relevance for Solid-State Lithium Metal Batteries. *Materials Today* **2021**, *44*, 9–14. https://doi.org/10.1016/j.mattod.2020.11.025.

(12) Rosenbach, D.; Krimalowski, A.; Erabhoina, H.; Thelakkat, M. Solid Polymer Electrolytes from Polyesters with Diester Sidechains for Lithium Metal Batteries. *Journal of Materials Chemistry A* **2022**, *10* (16), 8932–8947. https://doi.org/10.1039/D2TA00800A.

(13) Krimalowski, A.; Rosenbach, D.; Erabhoina, H.; Thelakkat, M. Versatile Solid Polymer Electrolytes from Clickable Poly(Glycidyl Propargyl Ether) for Lithium Metal Batteries. *Journal of Energy Storage* **2023**, *65*, 107348. https://doi.org/10.1016/j.est.2023.107348.

(14) Eriksson, T.; Mace, A.; Mindemark, J.; Brandell, D. The Role of Coordination Strength in Solid Polymer Electrolytes: Compositional Dependence of Transference Numbers in the Poly(ε-Caprolactone)–Poly(Trimethylene Carbonate) System. *Phys. Chem. Chem. Phys.* **2021**, *23* (45), 25550–25557. https://doi.org/10.1039/D1CP03929F.

(15) Andersson, R.; Hernández, G.; Mindemark, J. Quantifying the Ion Coordination Strength in Polymer Electrolytes. *Physical Chemistry Chemical Physics* **2022**, *24* (26), 16343–16352. https://doi.org/10.1039/D2CP01904C.

(16) Imholt, L.; Dörr, T. S.; Zhang, P.; Ibing, L.; Cekic-Laskovic, I.; Winter, M.; Brunklaus, G. Grafted Polyrotaxanes as Highly Conductive Electrolytes for Lithium Metal Batteries. *Journal of Power Sources* **2019**, *409*, 148–158. https://doi.org/10.1016/j.jpowsour.2018.08.077.

(17) Chen, Y.-H.; Hsieh, Y.-C.; Liu, K. L.; Wichmann, L.; Thienenkamp, J. H.; Choudhary, A.; Bedrov, D.; Winter, M.; Brunklaus, G. Green Polymer Electrolytes Based on Polycaprolactones for Solid-State High-Voltage Lithium Metal Batteries. *Macromolecular Rapid Communications* **2022**, *43* (20), 2200335. https://doi.org/10.1002/marc.202200335.

(18) Eriksson, T.; Mindemark, J.; Yue, M.; Brandell, D. Effects of Nanoparticle Addition to Poly(ε-Caprolactone) Electrolytes: Crystallinity, Conductivity and Ambient Temperature Battery Cycling. *Electrochimica Acta* **2019**, *300*, 489–496. https://doi.org/10.1016/j.electacta.2019.01.117.

(19) Pei, D.; Li, Y.; Huang, S.; Liu, M.; Hong, J.; Hou, S.; Jin, H.; Cao, G. Polycaprolactone-Poly(Vinylidene Fluoride) Blended Composite Polymer Electrolyte with Enhanced High Power Performance and Interfacial Stability for All-Solid-State Li Metal Batteries. *Chemical Engineering Journal* **2023**, *461*, 141899. https://doi.org/10.1016/j.cej.2023.141899.

(20) Chen, Y.-H.; Lennartz, P.; Liu, K. L.; Hsieh, Y.-C.; Scharf, F.; Guerdelli, R.; Buchheit, A.; Grünebaum, M.; Kempe, F.; Winter, M.; Brunklaus, G. Towards All-Solid-State Polymer Batteries: Going Beyond PEO with Hybrid Concepts. *Advanced Functional Materials n/a* (n/a), 2300501. https://doi.org/10.1002/adfm.202300501.

(21) Butzelaar, A. J.; Liu, K. L.; Röring, P.; Brunklaus, G.; Winter, M.; Theato, P. A Systematic Study of Vinyl Ether-Based Poly(Ethylene Oxide) Side-Chain Polymer Electrolytes. *ACS Appl. Polym. Mater.* **2021**, *3* (3), 1573–1582. https://doi.org/10.1021/acsapm.0c01398.

(22) Mukbaniani, O.; Titvinidze, G.; Dundua, A.; Doroshenko, M.; Tatrishvili, T. Synthesis of Polysiloxanes with Pendant Methoxy-Substituted Aromatic Fragments. *Journal of Applied Polymer Science* **2008**, *107* (4), 2567–2571. https://doi.org/10.1002/app.27133.
(23) Suguro, M.; Mori, A.; Iwasa, S.; Nakahara, K.; Nakano, K. Syntheses and Electrochemical Properties of TEMPO Radical Substituted Silicones: Active Material for Organic Radical Batteries. *Macromolecular Chemistry and Physics* **2009**, *210* (17), 1402–1407. https://doi.org/10.1002/macp.200900251.
(24) He, D.; Gui, X.; Dong, Y.; Lin, S.; Tu, Y.; Hu, J.; Li, S.; Zhao, J. An Efficient Catalytic and Solvent-Free Method for the Synthesis of Mono-Organofunctionalized Polymethylhydrosiloxane Derivatives. *Polymers for Advanced Technologies* **2023**, *34* (6), 1979–1989. https://doi.org/10.1002/pat.6025.
(25) Grewal, M. S.; Tanaka, M.; Kawakami, H. Free-Standing Polydimethylsiloxane-Based Cross-Linked Network Solid Polymer Electrolytes for Future Lithium Ion Battery Applications. *Electrochimica Acta* **2019**, *307*, 148–156. https://doi.org/10.1016/j.electacta.2019.03.172.
(26) Zhang, Z. C.; Jin, J. J.; Bautista, F.; Lyons, L. J.; Shariatzadeh, N.; Sherlock, D.; Amine, K.; West, R. Ion Conductive Characteristics of Cross-Linked Network Polysiloxane-Based Solid Polymer Electrolytes. *Solid State Ionics* **2004**, *170* (3), 233–238. https://doi.org/10.1016/j.ssi.2004.04.007.
(27) Fu, C.; Iacob, M.; Sheima, Y.; Battaglia, C.; Duchêne, L.; Seidl, L.; Opris, D. M.; Remhof, A. A Highly Elastic Polysiloxane-Based Polymer Electrolyte for All-Solid-State Lithium Metal Batteries. *J. Mater. Chem. A* **2021**, *9* (19), 11794–11801. https://doi.org/10.1039/D1TA02689E.
(28) Fish, D.; Khan, I. M.; Wu, E.; Smid, J. Polymer Electrolyte Complexes of $LiClO_4$ and Comb Polymers of Siloxane with Oligo-Oxyethylene Side Chains. *British Polymer Journal* **1988**, *20* (3), 281–288. https://doi.org/10.1002/pi.4980200320.
(29) Oh, B.; Vissers, D.; Zhang, Z.; West, R.; Tsukamoto, H.; Amine, K. New Interpenetrating Network Type Poly(Siloxane-g-Ethylene Oxide) Polymer Electrolyte for Lithium Battery. *Journal of Power Sources* **2003**, *119–121*, 442–447. https://doi.org/10.1016/S0378-7753(03)00187-3.
(30) Min, K. H.; Kim, D. B.; Kang, Y. K.; Suh, D. H. Ionic Conductivity and Morphology of Semi-Interpenetrating-Type Polymer Electrolyte Entrapping Poly(Siloxane-g-Allyl Cyanide). *Journal of Applied Polymer Science* **2008**, *107* (3), 1609–1615. https://doi.org/10.1002/app.27276.
(31) Zeng, X.-X.; Yin, Y.-X.; Li, N.-W.; Du, W.-C.; Guo, Y.-G.; Wan, L.-J. Reshaping Lithium Plating/Stripping Behavior via Bifunctional Polymer Electrolyte for Room-Temperature Solid Li Metal Batteries. *J. Am. Chem. Soc.* **2016**, *138* (49), 15825–15828. https://doi.org/10.1021/jacs.6b10088.
(32) Chen, P.; Liu, X.; Wang, S.; Zeng, Q.; Wang, Z.; Li, Z.; Zhang, L. Confining Hyperbranched Star Poly(Ethylene Oxide)-Based Polymer into a 3D Interpenetrating Network for a High-Performance All-Solid-State Polymer Electrolyte. *ACS Appl. Mater. Interfaces* **2019**, *11* (46), 43146–43155. https://doi.org/10.1021/acsami.9b14346.
(33) Khurana, R.; Schaefer, J. L.; Archer, L. A.; Coates, G. W. Suppression of Lithium Dendrite Growth Using Cross-Linked Polyethylene/Poly(Ethylene Oxide) Electrolytes: A New Approach for Practical Lithium-Metal Polymer Batteries. *J. Am. Chem. Soc.* **2014**, *136* (20), 7395–7402. https://doi.org/10.1021/ja502133j.
(34) Fonseca, C. P.; Rosa, D. S.; Gaboardi, F.; Neves, S. Development of a Biodegradable Polymer Electrolyte for Rechargeable Batteries. *Journal of Power Sources* **2006**, *155* (2), 381–384. https://doi.org/10.1016/j.jpowsour.2005.05.004.
(35) Mindemark, J.; Sun, B.; Törmä, E.; Brandell, D. High-Performance Solid Polymer Electrolytes for Lithium Batteries Operational at Ambient Temperature. *Journal of Power Sources* **2015**, *298*, 166–170. https://doi.org/10.1016/j.jpowsour.2015.08.035.
(36) Zalewski, K.; Chyłek, Z.; Trzciński, W. A. A Review of Polysiloxanes in Terms of Their Application in Explosives. *Polymers* **2021**, *13* (7), 1080. https://doi.org/10.3390/polym13071080.
(37) Hahn, M.; Rosenbach, D.; Krimalowski, A.; Nazarenus, T.; Moos, R.; Thelakkat, M.; Danzer, M. A. Investigating Solid Polymer and Ceramic Electrolytes for Lithium-Ion Batteries by Means of an Extended Distribution of Relaxation Times Analysis. *Electrochimica Acta* **2020**, *344*, 136060. https://doi.org/10.1016/j.electacta.2020.136060.
(38) Diederichsen, K. M.; Buss, H. G.; McCloskey, B. D. The Compensation Effect in the Vogel–Tammann–Fulcher (VTF) Equation for Polymer-Based Electrolytes. *Macromolecules* **2017**, *50* (10), 3831–3840. https://doi.org/10.1021/acs.macromol.7b00423.
(39) Evans, J.; Vincent, C. A.; Bruce, P. G. Electrochemical Measurement of Transference Numbers in Polymer Electrolytes. *Polymer* **1987**, *28* (13), 2324–2328. https://doi.org/10.1016/0032-3861(87)90394-6.
(40) Eriksson, T.; Gudla, H.; Manabe, Y.; Yoneda, T.; Friesen, D.; Zhang, C.; Inokuma, Y.; Brandell, D.; Mindemark, J. Carbonyl-Containing Solid Polymer Electrolyte Host Materials: Conduction and Coordination in Polyketone, Polyester, and Polycarbonate Systems. *Macromolecules* **2022**, *55* (24), 10940–10949. https://doi.org/10.1021/acs.macromol.2c01683.
(41) Krachkovskiy, S. A.; Bazak, J. D.; Werhun, P.; Balcom, B. J.; Halalay, I. C.; Goward, G. R. Visualization of Steady-State Ionic Concentration Profiles Formed in Electrolytes during Li-Ion Battery Operation and Determination of Mass-Transport Properties by in Situ Magnetic Resonance Imaging. *J. Am. Chem. Soc.* **2016**, *138* (25), 7992–7999. https://doi.org/10.1021/jacs.6b04226.
(42) Homann, G.; Stolz, L.; Winter, M.; Kasnatscheew, J. Elimination of "Voltage Noise" of Poly (Ethylene Oxide)-Based Solid Electrolytes in High-Voltage Lithium Batteries: Linear versus Network Polymers. *iScience* **2020**, *23* (6), 101225. https://doi.org/10.1016/j.isci.2020.101225.

(43) Jalbert, P.-M.; Commarieu, B.; Daigle, J.-C.; Claverie, J. P.; Zaghib, K. A 3D Network Based on Poly(ε-Caprolactone) Macromonomers as Polymer Electrolyte for Solid State Lithium Metal Batteries. *J. Electrochem. Soc.* **2020**, *167* (8), 080527. https://doi.org/10.1149/1945-7111/ab8de0.
(44) Aldalur, I.; Martinez–Ibañez, M.; Piszcz, M.; Zhang, H.; Armand, M. Self–Standing Highly Conductive Solid Electrolytes Based on Block Copolymers for Rechargeable All–Solid–State Lithium–Metal Batteries. *Batteries & Supercaps* **2018**, *1* (4), 149–159. https://doi.org/10.1002/batt.201800048.
(45) Hernández, G.; Johansson, I. L.; Mathew, A.; Sångeland, C.; Brandell, D.; Mindemark, J. Going Beyond Sweep Voltammetry: Alternative Approaches in Search of the Elusive Electrochemical Stability of Polymer Electrolytes. *J. Electrochem. Soc.* **2021**, *168* (10), 100523. https://doi.org/10.1149/1945-7111/ac2d8b.
(46) Homann, G.; Stolz, L.; Nair, J.; Laskovic, I. C.; Winter, M.; Kasnatscheew, J. Poly(Ethylene Oxide)-Based Electrolyte for Solid-State-Lithium-Batteries with High Voltage Positive Electrodes: Evaluating the Role of Electrolyte Oxidation in Rapid Cell Failure. *Sci Rep* **2020**, *10* (1), 4390. https://doi.org/10.1038/s41598-020-61373-9.
(47) Hahn, M.; Schindler, S.; Triebs, L.-C.; Danzer, M. A. Optimized Process Parameters for a Reproducible Distribution of Relaxation Times Analysis of Electrochemical Systems. *Batteries* **2019**, *5* (2), 43. https://doi.org/10.3390/batteries5020043.
(48) Erabhoina, H.; Rosenbach, D.; Mohanraj, J.; Thelakkat, M. Solid Polymer Nanocomposite Electrolytes with Improved Interface Properties towards Lithium Metal Battery Application at Room Temperature. *Electrochimica Acta* **2021**, *387*, 138455. https://doi.org/10.1016/j.electacta.2021.138455.
(49) Plank, C.; Rüther, T.; Jahn, L.; Schamel, M.; Schmidt, J. P.; Ciucci, F.; Danzer, M. A. A Review on the Distribution of Relaxation Times Analysis: A Powerful Tool for Process Identification of Electrochemical Systems. *Journal of Power Sources* **2023**, 233845. https://doi.org/10.1016/j.jpowsour.2023.233845.
(50) Chen, K.-H.; Wood, K. N.; Kazyak, E.; LePage, W. S.; Davis, A. L.; Sanchez, A. J.; Dasgupta, N. P. Dead Lithium: Mass Transport Effects on Voltage, Capacity, and Failure of Lithium Metal Anodes. *J. Mater. Chem. A* **2017**, *5* (23), 11671–11681. https://doi.org/10.1039/C7TA00371D.
(51) Petry, J.; Erabhoina, H.; Dietel, M.; Thelakkat, M. Comparative Study of the Mechanical Reinforcement by Blending, Filling, and Block Copolymerization in Bottlebrush Polymer Electrolytes. *ACS Appl. Polym. Mater.* **2024**, *6* (9), 5109–5120. https://doi.org/10.1021/acsapm.4c00161.
(52) Zhong, S.; Yuan, B.; Guang, Z.; Chen, D.; Li, Q.; Dong, L.; Ji, Y.; Dong, Y.; Han, J.; He, W. Recent Progress in Thin Separators for Upgraded Lithium Ion Batteries. *Energy Storage Materials* **2021**, *41*, 805–841. https://doi.org/10.1016/j.ensm.2021.07.028.
(53) Wang, Z.; Shen, L.; Deng, S.; Cui, P.; Yao, X. 10 Mm-Thick High-Strength Solid Polymer Electrolytes with Excellent Interface Compatibility for Flexible All-Solid-State Lithium-Metal Batteries. *Advanced Materials* **2021**, *33* (25), 2100353. https://doi.org/10.1002/adma.202100353.
(54) Wu, J.; Yuan, L.; Zhang, W.; Li, Z.; Xie, X.; Huang, Y. Reducing the Thickness of Solid-State Electrolyte Membranes for High-Energy Lithium Batteries. *Energy Environ. Sci.* **2021**, *14* (1), 12–36. https://doi.org/10.1039/D0EE02241A.
(55) Judez, X.; Piszcz, M.; Coya, E.; Li, C.; Aldalur, I.; Oteo, U.; Zhang, Y.; Zhang, W.; Rodriguez-Martinez, L. M.; Zhang, H.; Armand, M. Stable Cycling of Lithium Metal Electrode in Nanocomposite Solid Polymer Electrolytes with Lithium Bis (Fluorosulfonyl)Imide. *Solid State Ionics* **2018**, *318*, 95–101. https://doi.org/10.1016/j.ssi.2017.07.021.
(56) Fu, C.; Venturi, V.; Kim, J.; Ahmad, Z.; Ells, A. W.; Viswanathan, V.; Helms, B. A. Universal Chemomechanical Design Rules for Solid-Ion Conductors to Prevent Dendrite Formation in Lithium Metal Batteries. *Nat. Mater.* **2020**, *19* (7), 758–766. https://doi.org/10.1038/s41563-020-0655-2.

IV.12. Supporting Information

IV.12.1 Materials

Instead otherwise noted, chemicals were used as received. Acetonitrile (99.9 %), diethyl ether (99.5 %), methanol (99.9 %), methylene chloride (99.5 %), tetrahydrofuran (99.8 %), sodium bicarbonate (99.8 %) were purchased from Fisher Scientific. Activated charcoal, ammonium chloride (99.5 %), and magnesium sulfate (99 %) were retrieved from Grüssing. THF was dried over CaH_2 and distilled. CaH_2 (97 %), Celite S, lithium bis(trifluoromethanesulfonyl)imide (99 %), polycaprolactone diol (average M_n 2000 g mol^{-1}), polymethylhydrosiloxane (M_n 1700-3200) and Karsteadt's catalyst (2 wt% in xylene) were bought from Sigma Aldrich. Triethyl amine (96 %), methyl adipoyl chloride (96 %) were purchased from abcr. Pyridine (99.5 %), toluene (99.85 %), and N-methyl-2-pyrrolidone were bought from Acros Organics. Acryloyl chloride (96 %) was purchased from Merck Millipore and was recondensed before use. But-3-en-1-ol (98 %) was bought from TCI. Silica 60 was retrieved from Macherey-Nagel for chromatography. Solvents for chromatography were distilled in-house. Coin cell parts were bought from MTI corporation. Deuterated chloroform was purchased from Deutero. CR2032 coin cells, the active material (carbon-coated $LiFePO_4$, D10 < 1 µm, D50 3.5±1.0 µm, D90 < 15 µm, carbon content: 1.45 ± 0.2 %), Super P carbon (carbon black, CB), conductive graphite (CG) and C-coated Al current collector were procured from MTI Corporation and used as such during the preparation of cathode. ipPORE™ track-etched hydrophilic polyimide (PI) membranes (pore size: 0.20 µm, pore density: $6.00 \cdot 10^8$ cm^{-2}, thickness: 7 µm) were purchased from it4ip (Belgium). Lithium metal ribbon (purity 99.9 %, thickness 380 µm, width 23 mm) was retrieved from Sigma Aldrich, lithium electrodes were punched from the ribbon using a 14 mm diameter punching die inside the glovebox. P25 (TiO_2 nanoparticles, 21 nm primary particle size) was procured from Degussa.

IV.12.2 Methods and Instrumentation

IV.12.2.1 ^{1}H nuclear magnetic resonance (NMR) spectroscopy

A Bruker Avance AC250 spectrometer at a working frequency of 300 MHz was used to record ^{1}H NMR spectra. Chemical shifts were calibrated to 7.28 ppm for chloroform-d1. Chemical shifts are reported as ppm, coupling constants in Hz, and multiplicity are indicated as: s (singlet), d (doubled), t (triplet), m (multiplet).

IV.12.2.2 Size exclusion chromatography

SEC was measured utilizing a Waters 515 HPLC pump and THF with 0.25 wt % tetrabutylammonium bromide (TBAB) as eluent at a flow rate of 0.5 mL min–1. 100 µL of polymer solution (1–2 mg mL^{-1}) are injected by a 707 Waters autosampler into a column setup comprising a guard column (Agilent PLgel Guard MIXED-C, 5cm × 0.75 cm, particle size 5 µm) and two separation columns (Agilent PLgel MIXED-C, 30 cm × 0.75 cm, particle size 5 µm). Polymer size distributions were monitored by a Waters 414 refractive index detector. Polystyrene (PS) standard was used for calibration and 1,2-dichlorobenzene was used as an internal reference.

IV.12.2.3 Thermogravimetric analysis

TGA thermograms were recorded on a Mettler Toledo TGA/DSC 3. Samples (ca. 10 - 20 mg) were placed in aluminum oxide ceramic crucibles (70 µL) and heated from 30 to 700 °C at a heating rate of 10 K min^{-1} under nitrogen atmosphere.

IV.12.2.4 Differential scanning calorimetry

DSC thermograms were obtained using a Mettler Toledo DSC 3. The samples were sealed within aluminum crucibles. The temperature program comprised two cycles of cooling down to –80 °C and subsequent heating up to 150 °C or 200 °C at a cooling/heating rate of 10 K min^{-1}. For the third cycle, a cooling/heating rate of 40 K min^{-1} was chosen. Glass transition temperatures (T_g) are derived as inflection points of the transition temperature and melting points (T_m) are obtained as the peak maximum of the melting peak in the second heating curve. For PMHS and PM(BMA)S a Netzsch 204F1 Phoenix system was used between -120 and-50 °C at a heating rate of 10K min^{-1}.

IV.12.2.5 Scanning electron microscopy (SEM)

SEM analysis was conducted using a Zeiss Ultra plus equipped with a field emission gun. Samples were sputtered with platinum with a thickness of 2.8 nm.

IV.12.2.6 Electrochemical measurements

Electrochemical measurements were conducted using a VMP300 potentiostat (BioLogic) equipped with EIS boards.

IV.12.3 Syntheses

IV.12.3.1 Synthesis of but-3-en-1-yl-methyl adipate (BM3A)

In a round bottom flask but-3-en-1-ol (6.73 g, 0.09 mol, 1 eq.) and pyridine (15.51 g, 0.20 mol, 2.1 eq.) were dissolved in 13.5 mL of methylene chloride. The mixture is stirred over CaH_2 for 30 minutes and subsequently filtered into a flame-dried, argon-filled three-necked Schlenk flask equipped with a dripping funnel. The mixture is cooled down to 0°C. Methyl adipoyl chloride (19.17 g, 0.11 mol, 1.15 eq.) is dissolved in 80 mL of methylene chloride and filled into the dripping funnel. The solution of methyl adipoyl chloride is added dropwise into the Schlenk flask. After complete addition, the ice bath is removed and the reaction mixture is allowed to stir overnight.

For purification, the reaction mixture was diluted with n-hexane to precipitate the formed pyridinium chloride. The precipitates are removed by filtration and the solution is concentrated under reduced pressure. The obtained product is dissolved in diethyl ether and washed with saturated NH_4Cl and subsequently twice with deionized water. The aqueous phases were extracted with diethyl ether. The combined organic phase was dried over $MgSO_4$. The solvent is removed and the product is isolated by column chromatography (hexane:ethyl acetate; 7:3). The solvent is removed under reduced pressure to yield a colorless liquid.

Yield: 15.56 g (77.8 %)
^{1}H NMR (300 MHz, $CDCl_3$): 5.80 (ddt, J = 17.0, 10.2, 6.7 Hz, 1H, -C*H*=CH_2), 5.19 – 5.04 (m, 2H, -CH=C*H*$_2$), 4.14 (t, J = 6.7 Hz, 2H, -CH=C*H*$_2$), 3.69 (s, 3H, -OCH_3-), 2.50 – 2.24 (m, 6H, -CH_2-), 1.76 – 1.58 (m, 4H, -CH_2-)

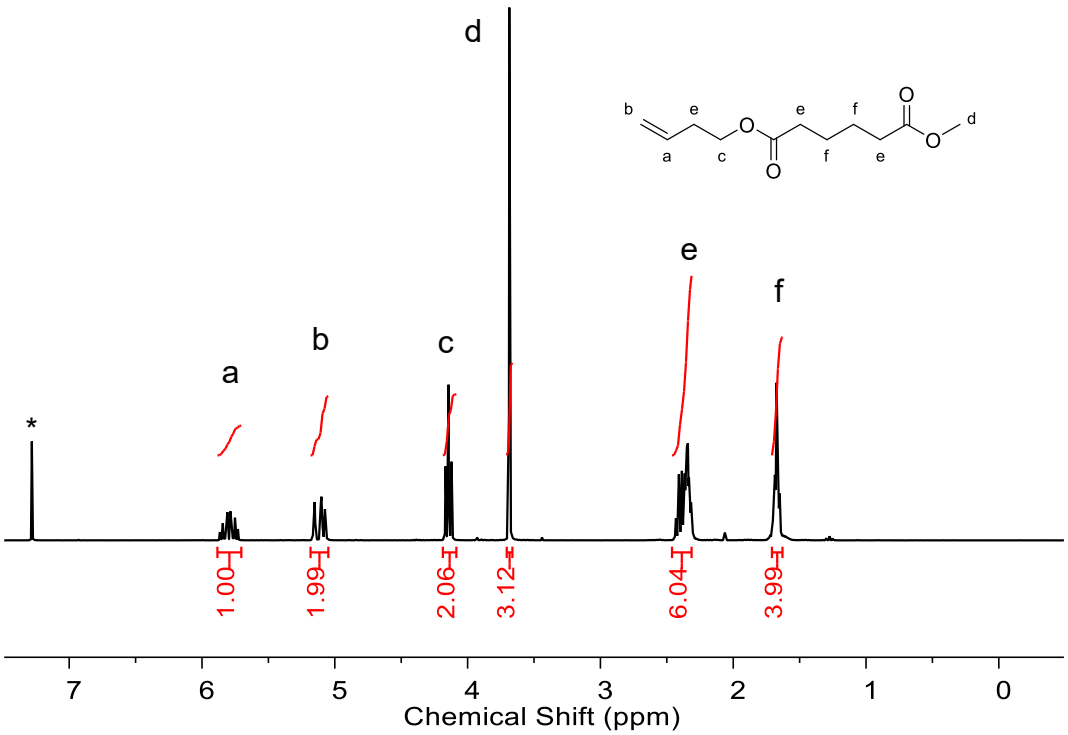


Figure S.IV.1. ^{1}H NMR ($CDCl_3$, 400 MHz) spectra of the synthesized but-3-en-1-yl-methyl adipate to be used in the hydrosilylation reaction. Asterisks indicate residual solvent peaks ($CHCl_3$ 7.26 ppm).

IV.12.3.2 Synthesis of poly(methyl-[butyl-4-{methyl adipate}])siloxane (PM(BMA)S)

In a flame-dried 250 mL Schlenk flask polymethylhydrosiloxane (2.9 g, 48.2 mmol with respect to the repeating unit of PMHS, 1eq.) and BM3A (12.4 g, 0.057 mmol, 1.2 eq.) were dissolved in 72 mL of dry toluene. The Karsteadt's catalyst (0.0015 g, 7.3 mmol with respect to the platinum centers, 0.087 mL) was added by syringe. The reaction was allowed to stir overnight. To deactivate and bind the catalyst, activated charcoal was added to the solution. After stirring for 30 minutes, the mixture is filtered over Celite S. The obtained filtrate was concentrated under reduced pressure, redissolved in a small amount of methylene chloride, and precipitated into cold n-hexane 5 times. It is worth mentioning that during the precipitation, the polymer rather forms a second liquid phase, instead of crushing out as a solid. After the final precipitation step, the polymer is dried at 60 °C under vacuum overnight. To yield a colorless/pale yellow viscous liquid.

Yield: 9.50 g (71.8 %)
^{1}H NMR (300 MHz, $CDCl_3$): δ 4.03 (t, J = 6.8 Hz, 2H, -COOCH_2-), 3.66 (s, 3H, -OCH_3), 2.32 (td, J = 7.2, 7.2 Hz, 4H, -CH_2COO-), 1.75 – 1.51 (m, 8H, -CH_2-), 1.46 – 1.24 (m, 1H, -CH_2-), 0.64 – 0.43 (m, 2H, Si-CH_2-), 0.07 (m, 3.5H, Si-CH_3).

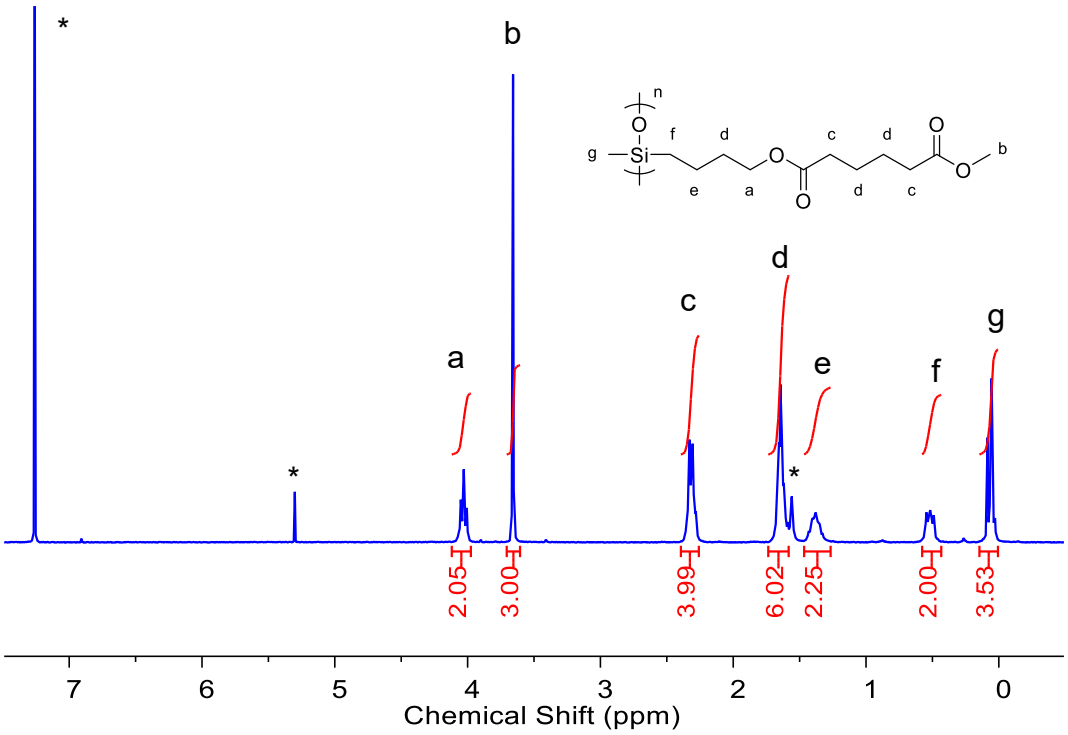


Figure S.IV.2. ^{1}H NMR ($CDCl_3$, 400 MHz) spectra of the synthesized but-3-en-1-yl-methyl adipate to be used in the hydrosilylation reaction. Asterisks indicate residual solvent peaks ($CHCl_3$ 7.26 ppm; DCM 5.30 ppm; H_2O 1.56 ppm).

IV.12.3.3 Synthesis of poly(ε-caprolactone)diacrylate (PCLDA)

In a flame-dried 250 mL Schlenk flask polycaprolactone diol (8.00 g, 0.004 mol, 1 eq.) is dried under high vacuum over night. THF and triethyl amine are individually dried over CaH_2 overnight. THF (65 mL) is added via a transfer cannula. Triethylamine (0.89 g, 1.23 mL, 2.2 eq.) is added via syringe. The reaction mixture was cooled down to 0 °C after which acryloyl chloride (0.91 g, 0.82 mL, 0.01 mol, 2.5 eq.) was added dropwise. The reaction is allowed to stir overnight. For purification, the solvent was removed using a rotary evaporator with a heating bath set to 30 °C. The crude product is dissolved in methylene chloride and washed twice with a saturated $NaHCO_3$ solution and twice with deionized water. The aqueous phases are extracted with a small amount of DCM. The combined organic phases are dried over Na_2SO_4. The solvent is removed under reduced pressure. The product is redissolved in benzene and subsequently freeze-dried to yield a white solid.

Yield: 7.01 g (87.5 %)
^{1}H NMR (300 MHz, $CDCl_3$): δ 6.45 – 6.30 (dd, J = 17.3, 1.7 Hz, 2H, -CH=CH_2), 6.09 (dd, J = 17.3, 10.4 Hz, 2H, -CH=CH$_2$), 5.86 – 5.74 (dd, J = 17.3, 1.7 Hz, 2H, -CH=CH_2), 4.13 (t, J = 6.7 Hz, 4H, -COOCH_2-), 4.04 (t, J = 6.7 Hz, 31H, -COOCH_2-), 2.29 (td, J = 7.5, 2.5 Hz, 32H, -CH_2-COO-), 1.63 (m, 69H, -CH_2-), 1.49 – 1.26 (m, 33H, -CH_2-).

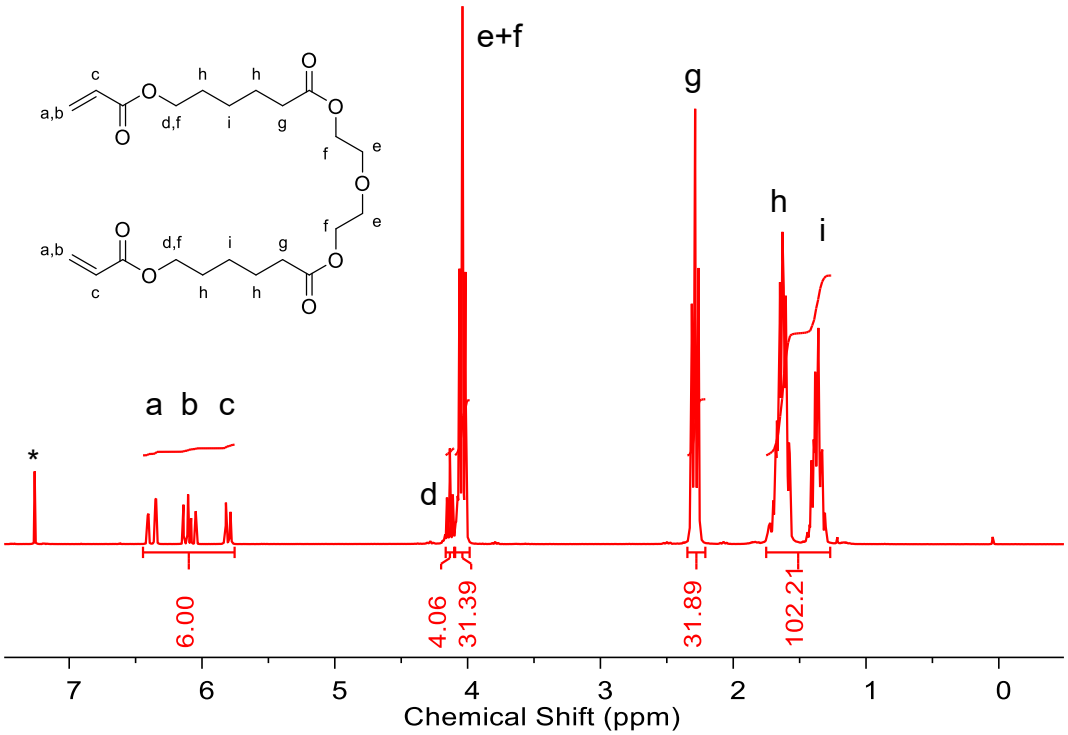


Figure S.IV.3. ^{1}H NMR ($CDCl_3$, 400 MHz) spectrum of the synthesized network former poly(ε-caprolactone)diacrylate (PCLDA). Asterisks indicate residual solvent peaks ($CHCl_3$ 7.26 ppm).

IV.12.4 Thermal Characterization – Thermal Stability

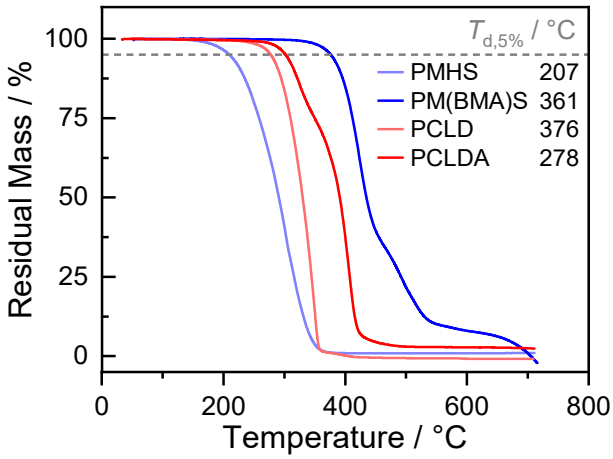


Figure S.IV.4. Thermogravimetric analysis of the (light blue) polymethylhydrosiloxane PMHS, (blue) poly(methyl-[butyl-4-{methyl adipate}])siloxane PM(BMA)S, (light red) polycaprolactonediol PCLD, and (red) polycaprolactonebisacrylate PCLDA.

IV.12.5 Thermal Characterization – Thermal Transitions

DSC measurements were conducted using a Mettler Toledo DSC 3 with an external cryostat. Below temperatures of -50 °C the a cooling rate of -10 K/min is not maintained resulting in perceived increases of the heat flow (cf. **Figure S.IV.5+6**). Therefore, glass transition temperatures were only evaluated from the heating curves. For low temperature measurements, a different setup was used, but cooling rates were also restricted. Therefore, only heating curves are reported here in **Figure S.IV.6**.

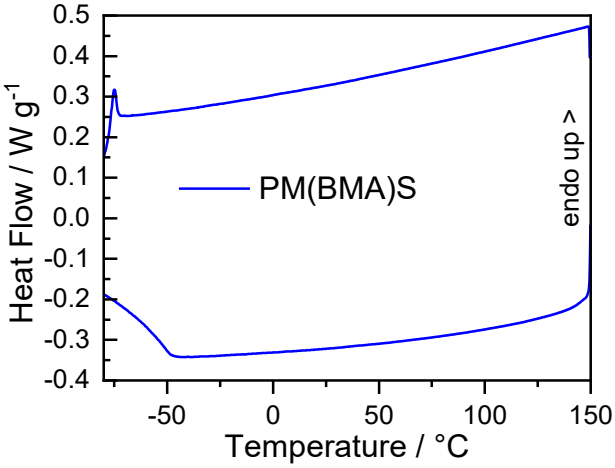


Figure S.IV.5. Differential scanning calorimetry (second heating and cooling curve, 10 K min^{-1}, -70 °C – 150 °C) of the pristine poly(methyl-[butyl-4-{methyl adipate}])siloxane PM(BMA)S showing no glass transition or melting/crystallization in the observed temperature window.

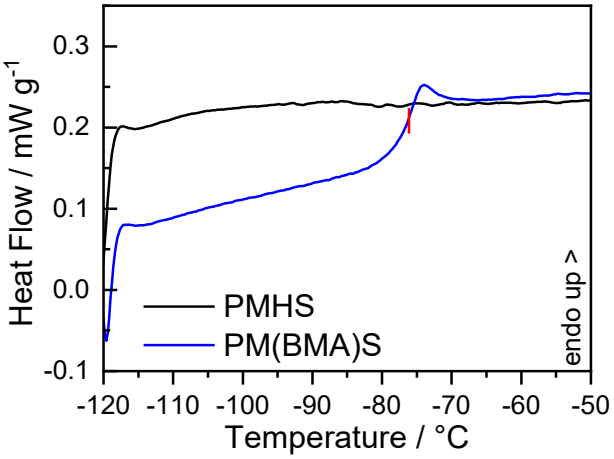


Figure S.IV.6. Differential scanning calorimetry (second heating curve, 10 K min^{-1}, -120 °C – 50 °C) of the polymethylhydrosiloxane PMHS and poly(methyl-[butyl-4-{methyl adipate}])siloxane PM(BMA)S. Only the heating curve is shown, due to cooling rate limitations. The glass transition of PM(BMA)S is marked by the red indicator at -76 °C. PMHS shows no thermal transitions in the observed temperature range.

IV.12.6 Electrolyte Composition

Table S.IV.1. Electrolyte composition and further data for the electrolytes used for temperature-dependent ionic conductivity measurements, LTN determinations, and FT-IR analysis.

Electrolyte	PM(BMA)S	LiTFSI	LiTFSI	C=O/Li	T_g
	mg	mg	wt%		°C
SPE10	129.9	14.5	10	18.9	-71.9
SPE20	128.4	32.4	20	8.4	-67.1
SPE30	103.2	44.3	30	4.9	-61.5
SPE40	84.6	56.6	40	3.1	-58.9
SPE50	77.9	77.9	50	2.1	-60.3

IV.12.7 Nyquist Plots of the temperature-dependent ionic conductivity for SPE10-SPE50

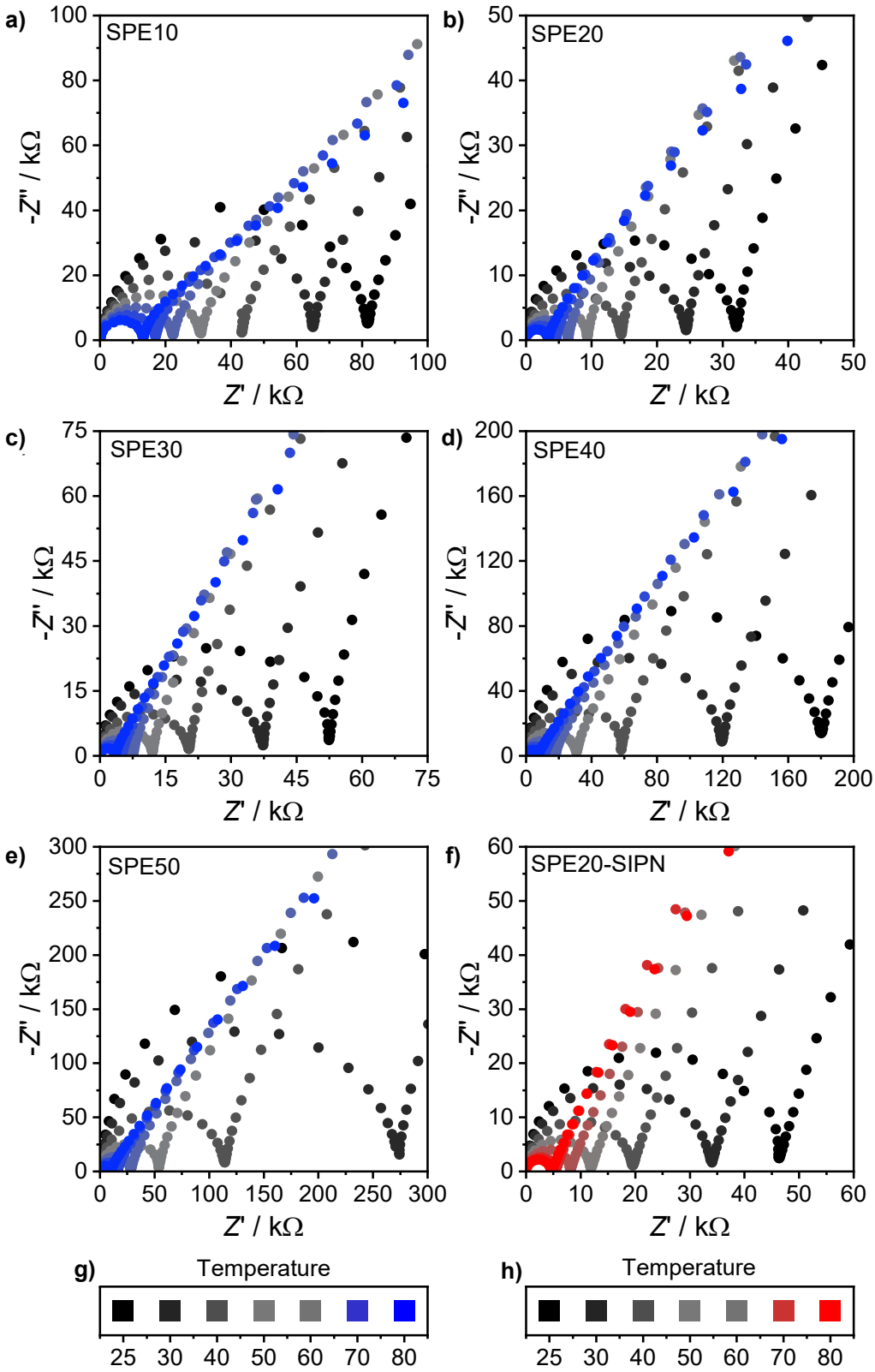


Figure S.IV.7. Nyquist plots of the temperature-dependent ionic conductivity measurements of (a-e) the solid polymer electrolyte with different salt concentrations as stated and (f) of the semi-interpenetrating network electrolyte at a salt concentration of 20 wt%. (g+h) represent the color codes for the different measurement conditions from 80 to 25 °C.

IV.12.8 Ionic Conductivity - Impedance Spectroscopy and VTF Evaluation

The temperature-dependent ionic conductivity was fitted using **Equation S.IV.1**. The equation was linearized to yield **Equation S.IV.2**. The data for the temperature-dependent ionic conductivity for SPE10-SPE50 was plotted as ln(σ) vs. $1/(T\text{-}T_0)$ as depicted in **Figure S.IV.8**. Linear fit parameters are summarized in **Table S.IV.2**. The pseudo-activation energy (B) was extracted from the slope. The activation energy is steadily increasing for increasing salt concentrations.

$$\sigma = A \cdot exp\left(-\frac{B}{R(T-T_0)}\right) \quad \text{(Eq. S.IV.1)}$$

$$ln(\sigma) = -\frac{B}{R} * \frac{1}{(T-T_0)} + ln(A) \quad \text{(Eq. S.IV.2)}$$

With A: pre-exponential factor, B: VTF-pseudo-activation energy, R: ideal gas constant.

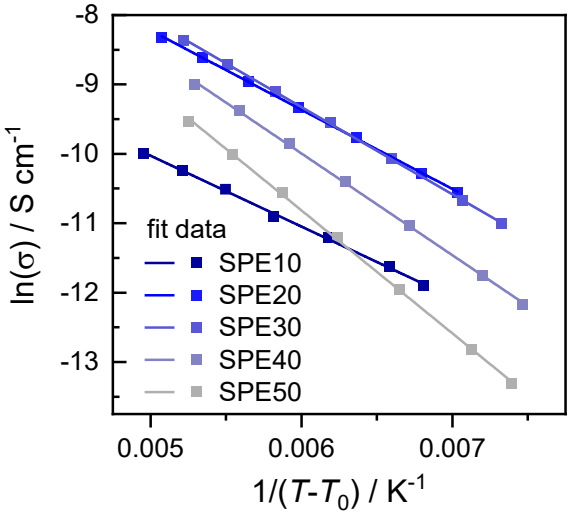


Figure S.IV.8. Linearized temperature-dependent ionic conductivity plots and linear fits.

Table S.IV.2. VTF fitting parameters of SPEs at different salt concentrations between 10 and 50 wt%.

Electrolyte	ln(*A*) S cm^{-1}	Slope K	R^2	*B* kJ mol^{-1}
SPE10	-4.92 ± 0.09	-1021.43 ± 14.62	0.999	8.49 ± 0.12
SPE20	-2.51 ± 0.04	-1142.71 ± 6.34	0.999	9.50 ± 0.05
SPE30	-1.77 ± 0.05	-1259.37 ± 7.64	0.999	10.47 ± 0.06
SPE40	-1.20 ± 0.10	-1466.23 ± 15.76	0.999	12.19 ± 0.13
SPE50	-0.18 ± 0.10	-1772.19 ± 15.15	0.999	14.73 ± 0.13

IV.12.9 Thermal Properties of the Electrolytes

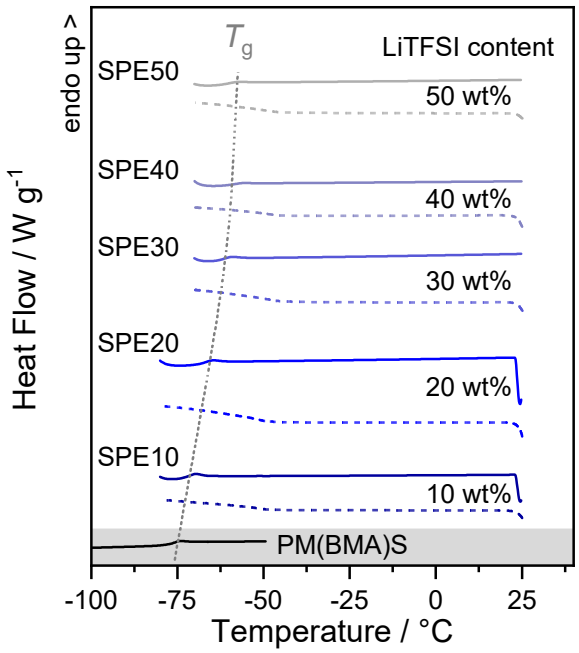


Figure S.IV.9. Differential scanning calorimetry of the pristine poly(methyl-[butyl-4-{methyl adipate}])siloxane PM(BMA)S and the corresponding electrolyte with LiTFSI contents between 10 and 50 wt%. The glass transitions shifts to higher temperature with increasing salt concentration.

IV.12.10 Lithium Transference Number

The lithium transfer number was evaluated in accordance with the Bruce and Vincent method. The calculation was performed using the following equation: $t_+ = \frac{I_{ss}*(\Delta V - I_0*R_{0,Li})}{I_0*(\Delta V - I_{ss}*R_{ss,Li})}$

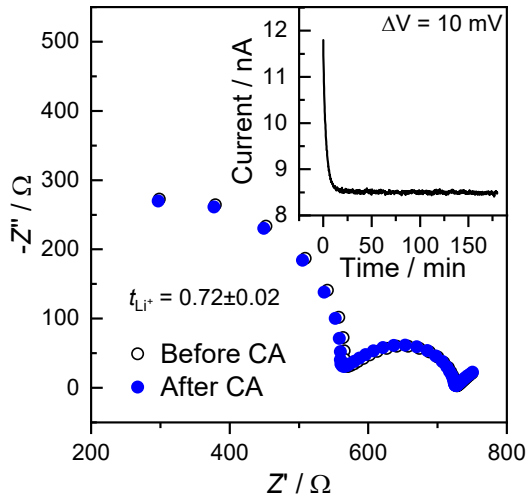


Figure S.IV.10. EIS and (inset) CA for the determination of the lithium transference number following the Bruce and Vincent method. Exemplary data is shown for SPE20-LTN1. The experiment is conducted at 70 °C.

Table S.IV.3. Determined values for the LTN calculation for two cells.

Polymer	ΔV	I_o	I_{ss}	$R_{Li,o}$	$R_{Li,ss}$	LTN
	V	A	A	Ω	Ω	
SPE20-LTN1	0.01	1.18E-05	8.47E-06	138.10	141.93	0.68
SPE20-LTN2	0.01	7.33E-06	5.82E-06	300.98	313.46	0.76

IV.12.11 Attenuated total reflectance Fourier transform infrared spectroscopy (FT-IT).

IR spectra were recorded using a PerkinElmer Spectrum 100 FT-IR spectrometer. IR data was recorded in total reflectance mode in the form of transmission information. The data was normalized to 0 to 1. The deconvolution process of the free and coordinating carbonyl moiety was performed by Gaussian nonlinear fitting by a Levenberg Marquardt iteration algorithm with 4 parameters for each peak. For the pristine polymer without any salt, only a single-peak fitting was performed. Fitting was performed using the following equation (Equation S.IV.3):

$$y = y_0 + \frac{A}{w \cdot \sqrt{\frac{\pi}{4 \cdot ln2}}} \cdot exp^{\left(-4 \cdot ln2 \frac{(x-x_c)^2}{w^2}\right)} \qquad \text{(Eq. S.IV.3)}$$

With y_0 as y-axis offset, A as the area of the distribution function, w as the variance, and x_c as the center of the peak position

Table S.IV.4. Double/single Gaussian FTIR-analysis of the coordinating and non-coordinating carbonyl moiety of PM(BMA)S at different salt concentrations.

Polymer	Peak 1 (C=O)				Peak 2 (C=O---Li)				ϕ_{Li^+}
	y_0	x_c	A	w	y_0	x_c	A	w	%
PM(BMA)S	0.961 ±0.002	1731.956 ±0.105	-29.247 ±0.246	29.961 ±0.263	-	-	-	-	0
SPE10	0.966 ±0.001	1733.792 ±0.187	-22.015 ±0.365	26.073 ±0.318	0.966 ±0.001	1705.412 ±0.418	-10.767 ±0.368	27.334 ±0.730	33
SPE20	0.964 ±0.001	1735.116 ±0.211	-15.618 ±0.335	24.118 ±0.371	0.964 ±0.001	1706.250 ±0.262	-17.800 ±0.348	29.062 ±0.501	53
SPE30	0.966 ±0.001	1735.888 ±0.292	-8.942 ±0.288	22.797 ±0.542	0.966 ±0.001	1706.442 ±0.221	-19.286 ±0.308	30.004 ±0.458	68
SPE40	0.968 ±0.001	1735.455 ±0.494	-5.176 ±0.292	22.502 ±0.906	0.968 ±0.001	1706.487 ±0.231	-18.904 ±0.312	30.115 ±0.471	79
SPE50	0.973 ±0.001	1732.982 ±0.830	-3.579 ±0.358	22.788 ±1.317	0.973 ±0.001	1706.686 ±0.303	-16.976 ±0.373	29.578 ±0.529	83

IV.12.12 Optical Images of the SPE20, SPE20-SIPN, and SPE20-N10-SIPN

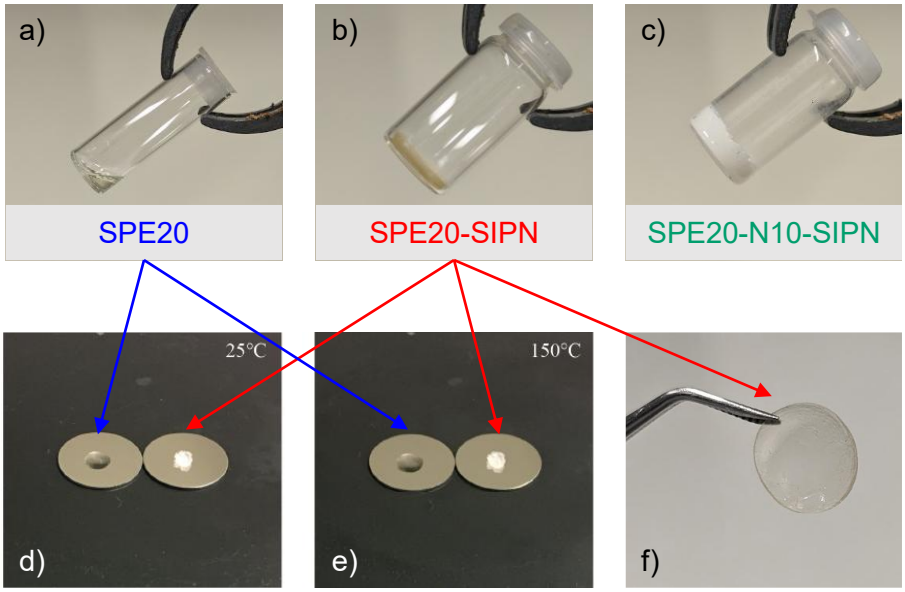


Figure S.IV.11. Optical images of (a-c) different electrolytes, SIPN systems have been cured before taking the picture at 100 °C in high vacuum overnight. (d-e) Electrolytes at different temperatures. SPE20 is a tacky low-viscosity material at room temperature while SPE20-SIPN retains its shape up to 150 °C. (f) Self-standing film obtained from SPE20-SIPN after curing.

IV.12.13 Electrolyte Composition

Table S.IV.5. Electrolyte composition and further data of electrolyte systems.

Electrolyte[a]	m (PM(BMA)S) mg	m (LiTFSI) mg	m (PCLDA) mg	m (AIBN) mg	m (TiO_2) mg
SPE20	128.4	14.5	-	-	-
SPE20-SIPN	179.4	81.6	146.8	8.3	-
PCLDA20		38.1	152.5	3.9	-
SPE20-N10	115.9	28.9	-	-	16.1
SPE20-N10-SIPN	505.4	229.7	413.5	23.4	130.2

[a] All the electrolytes contain around 20 wt% LiTFSI

IV.12.14 Rheology – Frequency Sweep Measurement

The mixture of PM(BMA)S, PCLDA, and AIBN was prepared in accordance to the composition of SPE20-SIPN. However, LiTFSI was not added due to its highly hygroscopic nature under ambient conditions. The mixture was applied to the rheometer and heated to 60 °C for the experiment. Afterwards, the mixture was annealed on the rheometer (without oscillatory excitation) at 100 °C for 3 hours. Subsequently the temperature was reduced back to 60 °C to repeat the initial experiment for the cured system.

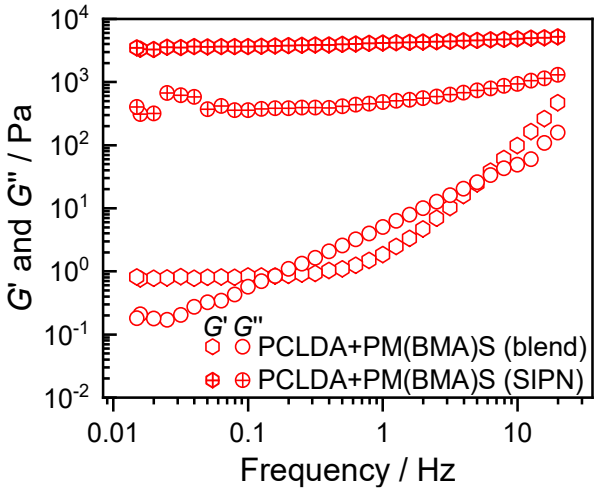
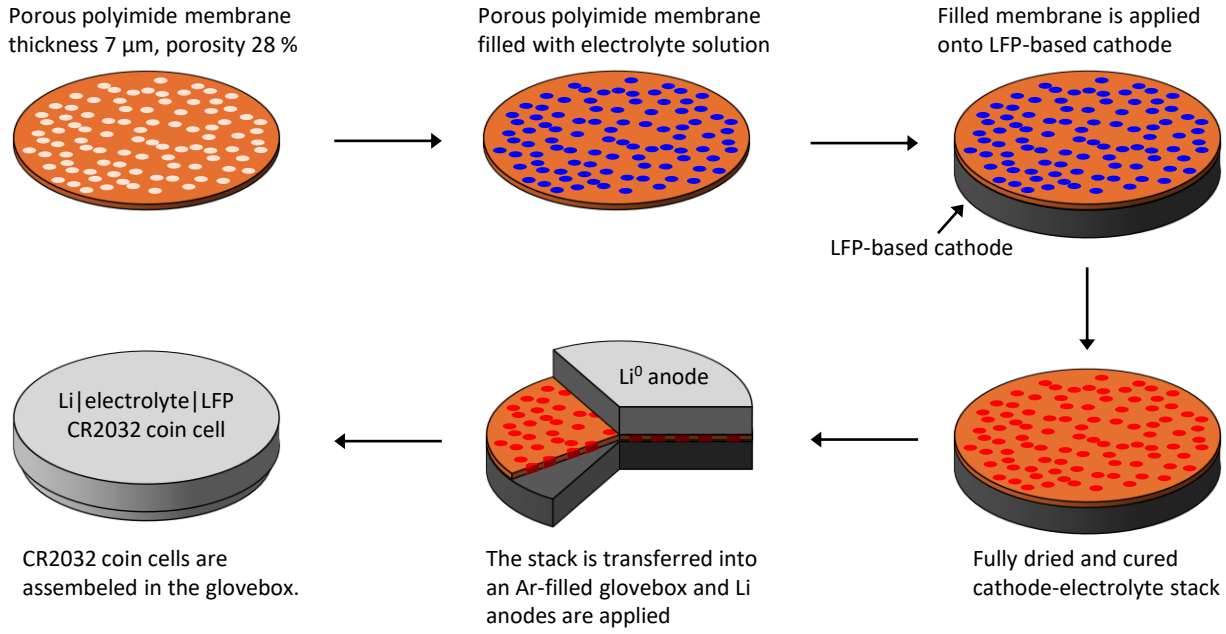


Figure S.IV.12. Frequency sweep measurements of the (hollow symbols) pristine blend of PCLDA and PM(BMA)S before crosslinking and (crossed symbols) the SIPN network structure after curing. The measurement was performed at 60 °C and 0.5 % strain.

IV.12.15 Battery Cell Preparation



Scheme S.IV.1. Illustration of the cell preparation procedure. The membrane is soaked with an electrolyte solution, placed on top of a pre-cut (14 mm diameter) cathode. The stack is cured and dried at 100 °C under high vacuum. In the case of SPE20-N10, there is no crosslinking reaction during drying. The stack is transferred to an Ar-filled glovebox for cell assembly.

IV.12.16 SEM Images of Polyimide Membrane

SPE-20-N10-SIPN-impregnated SEM samples were prepared by soaking the membrane from both sides. The membrane was dried and cured at 100 °C in high vacuum for 15 h. The membranes were held up using clamps to ensure homogenous drying from both sides. For the cross-sectional images, the membrane was cooled in liquid nitrogen and broken along the investigated edge. **Figure S.IV.13** shows the top-view images of the pristine and impregnated membrane. Well-dispersed nanoparticles can be observed across the electrolyte surface. **Figure S.IV.14** depicts cross-sectional images. In the cross-section, the brighter region in the middle of the stack corresponds to the polyimide membrane with a thickness of around 6 µm to 7µm. Nanoparticles can be identified throughout the entire electrolyte-membrane assembly.

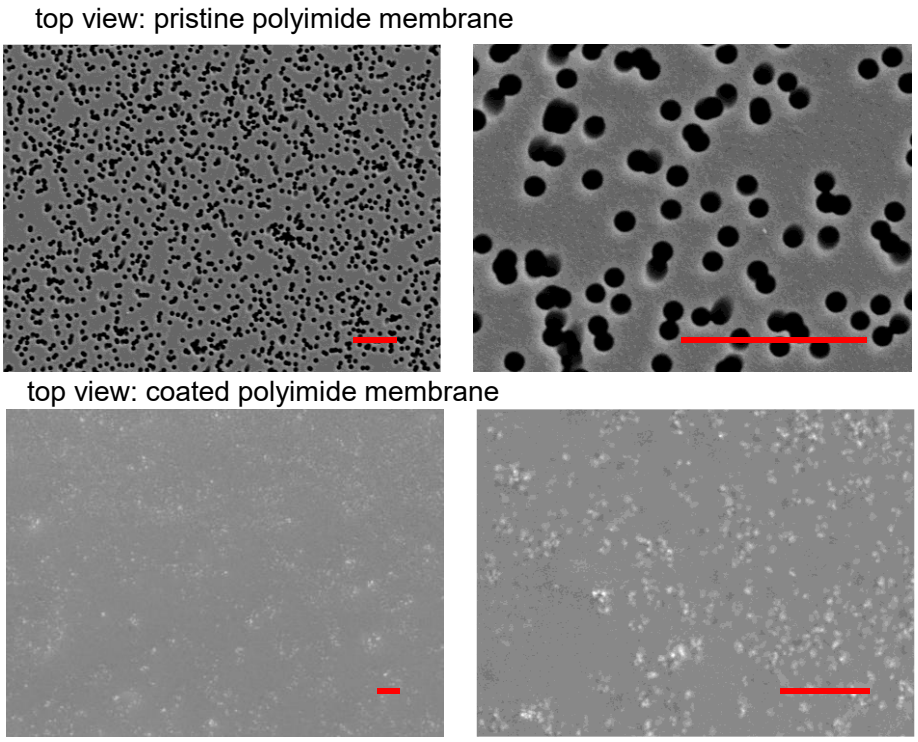


Figure S.IV.13. SEM images of the pristine polyimide membrane and the membrane impregnated with SPE20-N10-SIPN at different magnifications. The scale bar represents 2 µm for all images.

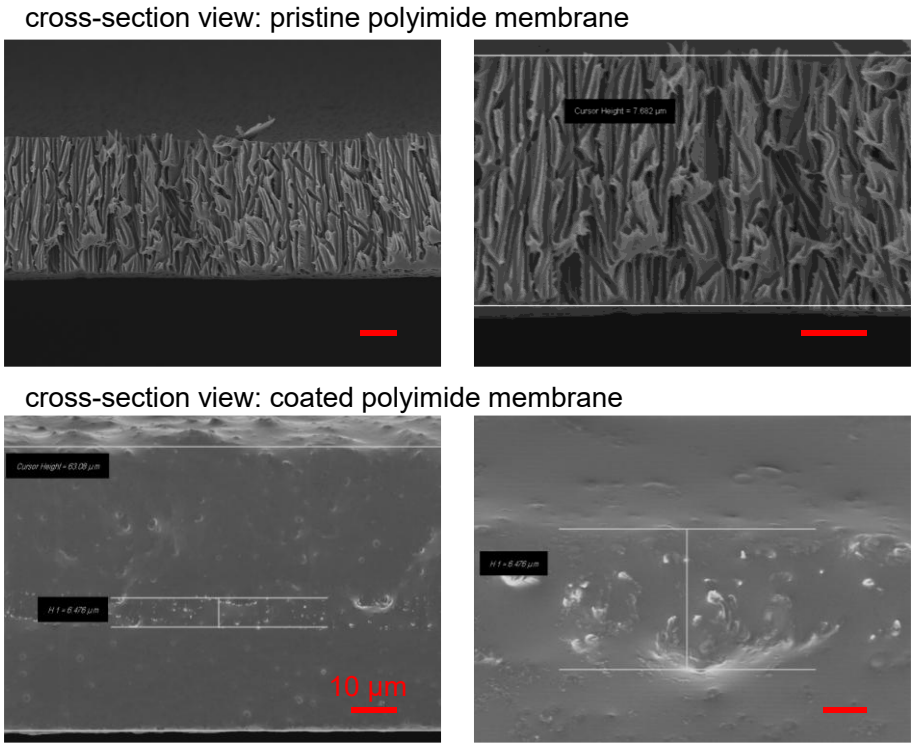


Figure S.IV.14. Cross-sectional SEM images of the pristine polyimide membrane and the membrane impregnated with SPE20-N10-SIPN at different magnifications. The scale bar represents 2 µm for all images instead indicated otherwise. The membrane channels are filled and cannot be identified after impregnation.

IV.12.17 Influence of the Polyimide Membrane on the Ionic Conductivity of SPE20-based Electrolytes

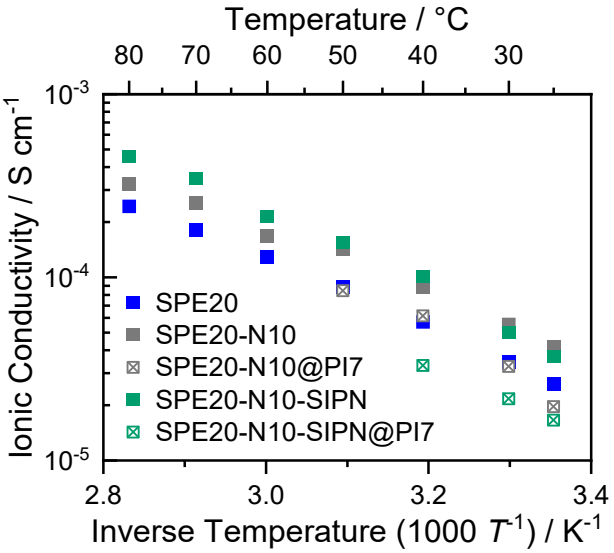


Figure S.IV.15. Comparison of the temperature-dependent ionic conductivity of (blue) SPE20 and the influence of (gray solid symbols) nanoparticle addition (SPE20-N10). (gray/green crossed symbols) SPE20-N10 and SPE20-N10-SIPN electrolytes are incorporated into a thin polyimide membrane (PI7). Determining the electrolyte thickness is more challenging for the thin electrolyte than for the non-PI7 measurements. The bulk resistance of non-PI7 systems was determined using a 500 µm thick Teflon® spacer to minimize the influence of the electrolyte thickness.

IV.12.18 Comparison of Cycling Curves and Nyquist Plots for the electrolytes SPE20 vs. SPE20-N10 vs SPNE20-N10-SIPN

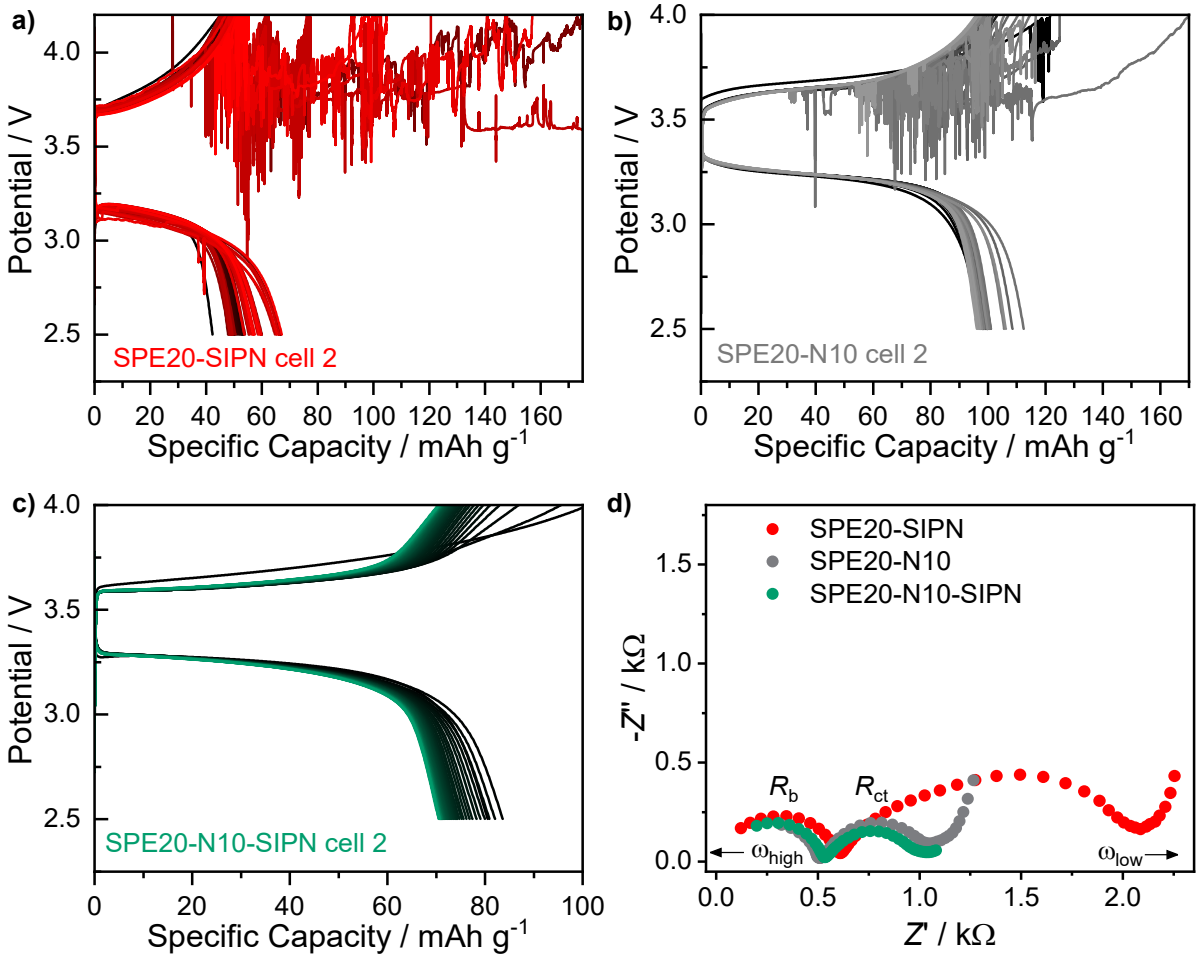


Figure S.IV.16. (a-c) Charge and discharge profiles for SPE20-SIPN, SPE20-N10 and SPE20-N10-SIPN. Presented are all cycles from 0 to 50. (d) Nyquist plots of the cell impedance for the different electrolytes. In all cells, the polyimide membrane ensures similar device geometry, i.e. electrolyte thickness for the materials. The bulk resistance (R_b) is very similar for the different electrolytes. The charge transfer resistance (R_{ct}) is significantly higher for SPE20-SIPN, with no nanoparticles. Together with the cycling performance in (c) for SPE20-N10-SIPN this clearly demonstrates the importance of both the mechanical stabilization by the SIPN and the improved charge transfer characteristics due to the nanoparticle addition.

Table S.IV.6. Statistics of cycles showing overcharging in for different electrolytes and individual cells.

Electrolyte	Cell	Number of overcharging cycles within 50 battery cycles	Coulombic Efficiency [%]
SPE20-SIPN	cell1	none	99.1
	cell2	8	95.4
	cell3	8	99.3
	cell4	none	98.7
SPE20-N10	cell1	15	97.8
	cell2	11	94.9
SPE20-N10-SIPN	cell1	none	99.2
	cell2	none	99.2

IV.12.19 Influence of Crosslinking of SPE20-based Electrolytes

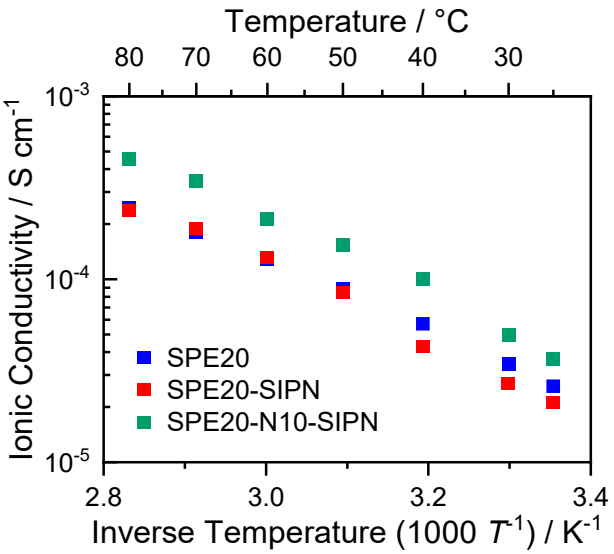


Figure S.IV.17. Comparison of different electrolyte systems based on SPE20. Data for (blue) the non-crosslinked SPE20, (red) crosslinked electrolyte SPE20-SIPN, and (green) the electrolyte SPE20-N10-SIPN after crosslinking and nanoparticles addition.

IV.12.20 Cycling Performance of SPE20-N10-SIPN at 70 °C

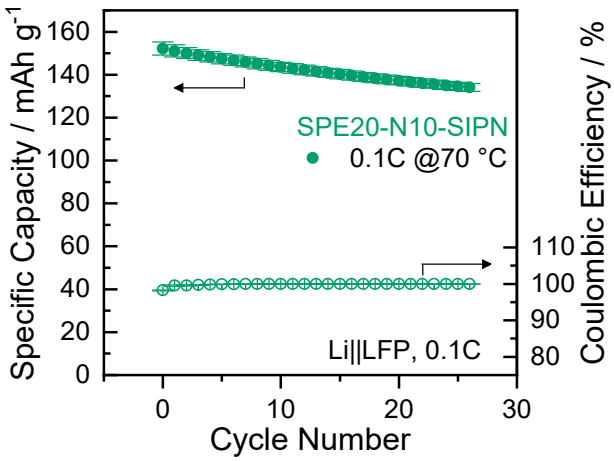


Figure S.IV.18. Cycling performance of SPE20-N10-SIPN at 70 °C and 0.1C in Li|SPE20-N10-SIPN|LFP cells.

4 List of Publications

Part of this thesis

Easily accessible linear and hyperbranched polyesters as solid polymer electrolytes

Jannik Petry[1], Krishna Dan[1], Atish Nag[1], Mukundan Thelakkat and Suhrit Ghosh*

Eur. Polym. J. **2024**, 210, 112965

([1] contributed equally to this work)

DOI: 10.1016/j.eurpolymj.2024.112965

Comparative Study of the Mechanical Reinforcement by Blending, Filling, and Block Copolymerization in Bottlebrush Polymer Electrolytes

Jannik Petry, Harimohan Erabhoina, Markus Dietel, and Mukundan Thelakkat*

ACS Appl. Polym. Mater. **2024**, 6, 5109–5120

DOI: 10.1016/j.eurpolymj.2024.112965

Semi-Interpenetrating Network Electrolytes Utilizing Ester-Functionalized Low T_g Polysiloxanes in Lithium-Metal Batteries

Jannik Petry, Markus Dietel, and Mukundan Thelakkat*

Adv. Energy Mater. **2024**, 15, 2403531

DOI: 10.1002/aenm.202403531

Additional Publication

Synthesis and Comparative Studies of Solvent-Free Brush Polymer Electrolytes for Lithium Batteries

Dominic Rosenbach, Nicolas Mödl, Markus Hahn, Jannik Petry, Michael A. Danzer, and Mukundan Thelakkat*

ACS Appl. Energy Mater, **2019**, 2, 5, 3373-3388

DOI: 10.1021/acsaem.9b00211

5 Appendix

5.1 Additional General Information on Battery Materials

Table A5.1. Overview of the theoretical specific capacity and operating potential for different anode and cathode active materials.

Name	Composition	Structure (Mechanism)	Spec. Capacity mAh g^{-1}	Potential V (vs. Li/Li^+)	Ref.
Anode Active Materials					
Graphite	LiC_6	Layered (intercalation)	372	0.01	[1]
LTO	$Li_4Ti_5O_{12}$	Spinel (intercalation)	175	1.5	[2]
Lithium	Li^0	Bulk (conversion)	3861	0	[3]
Silicon	$Li_{22}Si_5$	Bulk (alloying)	4199	0.3-0.6	[4]
Cathode Active Materials					
LTS	$LiTiS_2$	Layered (intercalation)	225	2.2	[5]
LCO	$LiCoO_2$	Layered (intercalation)	274	3.8	[6]
NMC811	$LiNi_{0.8}Mn_{0.1}Co_{0.1}O_2$	Layered (intercalation)	276	3.6	[7]
NMC111	$LiNi_{1/3}Mn_{1/3}Co_{1/3}O_2$	Layered (intercalation)	278	3.6	[7]
NCA	$LiNi_{0.8}Co_{0.15}Al_{0.05}O_2$	Layered (intercalation)	279	3.7	[8]
NMO	$LiNi_{0.5}Mn_{1.5}O_4$	Spinel (intercalation)	147	4.7	[9]
LFP	$LiFePO_4$	Olivine (intercalation)	170	3.4	[10]
Sulfur	S_8	Bulk (conversion)	1675	2.1	[11]
Oxygen	O_2	Bulk (conversion)	3153	2.9	[12]

Table A2. Overview of electrochemical properties of exemplary electrolyte systems.

Composition	Material Class	σ (25°C) S cm^{-1}	t_{Li^+}	ESW V (vs. Li/Li^+)	Ref.
Liquid Electrolytes					
$LiPF_6$ in EC/DMC	carbonate	1×10^{-2}	0.4	1.3 – 4.6	[13]
LiFSI in DOL/DME	ether	2×10^{-2}	0.5	n/a - 3.7	[14]
$LiClO_4$ in EC/PC in PAN	gel	2×10^{-3}	0.5	1 - 4.6	[13]
Solid Polymer Electrolytes					
LiTFSI in PEO	polyether	8×10^{-6}	0.19	4.25	[15]
LiTFSI in PCL	polyester	4×10^{-6}	0.7	5.2	[16]
Solid State Electrolytes					
LLZO	oxide	1×10^{-3}	1	9.0	[17]
LGPS	sulfide	1.2×10^{-3}	1	5.0 <	[18]

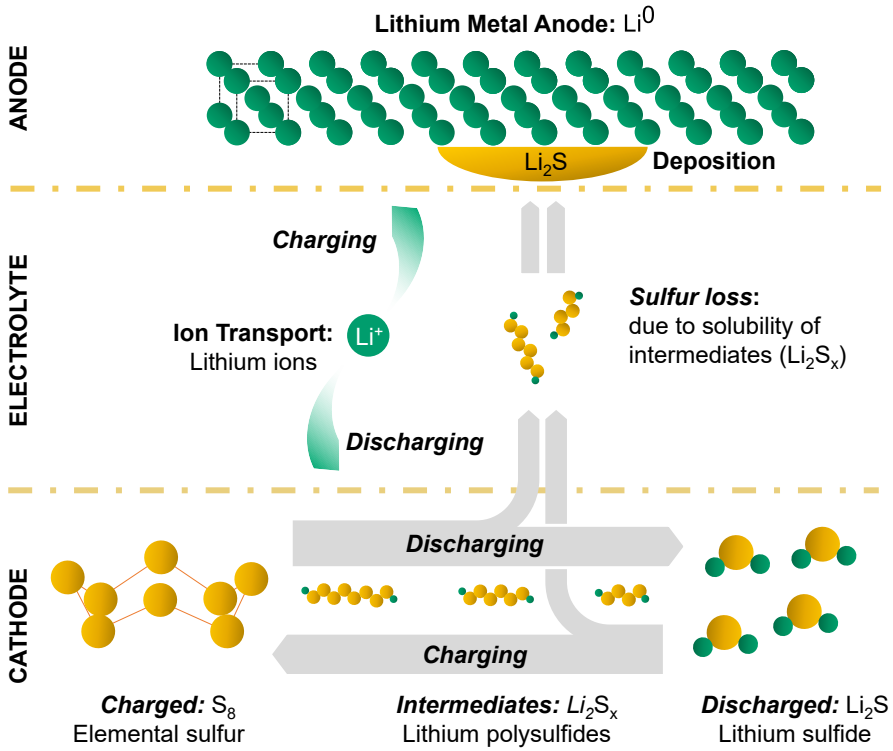
5.2 Polymer-Sulfur Composite Cathodes

Alongside the core study on solid polymer electrolytes, a separate line of work is devoted to sulfur-based cathode systems. In this context, synthesized polymer materials are combined with elemental sulfur to prepare composite cathode materials. Although strategic polymer design principles and the monomer-to-battery cell approach are also applied in this context, the specific concept follows distinct research questions that do not align with the main focus of the chapters presented in the main part of this dissertation. The following introduces the main aspects of the theoretical background and presents condensed experimental results not part of published work.

5.2.1 Theoretical Background

5.2.1.1 Shuttle Effect in Lithium-Sulfur Batteries

During discharge operation, the elemental sulfur in the cathode is lithiated to form the discharge product lithium disulfide (Li_2S). S_8 and Li_2S are insoluble in the electrolyte. However, the intermediate lithium polysulfides (Li_2S_x) can dissolve into the electrolyte and diffuse to the anode side. There, they are reduced to form Li_2S deposits on the anode. This process parasitically consumes sulfur and successively reduces the battery capacity.



Scheme A1.1. Schematic illustration of the fundamental processes in lithium-sulfur batteries. During the gradual conversion of sulfur (S_8 rings) to the final discharge product, lithium sulfide (Li_2S) intermediate polysulfides form. These intermediates can dissolve into and be transported by the electrolyte in the direction of the anode. At the anode surface, polysulfides can be reduced parasitically to Li_2S, forming an insulating deposit. This polysulfide shuttle process diminishes the battery capacity gradually.

5.2.1.2 Sulfur Confinement at the Cathode

Various approaches are applied to minimize the shuttle effect. Porous materials are used to physically confine sulfur within the cathode composite. Carbon-based materials are commonly used, but they lack sufficient interaction strength to mitigate sulfur dissolution entirely. Redox catalysts based on metal sulfides, oxides, or nitrides are employed to prevent the dissolution by enhancing the rate of conversion reactions and thereby limiting sulfur loss kinetically. Alternatively, sulfur-repelling interlayers can be introduced on the cathode surface or as functional separators in the electrolyte layer. Covalent anchoring of sulfur to stationary host materials is investigated and offers potential synergistic effects based on the chemistry of the host material.

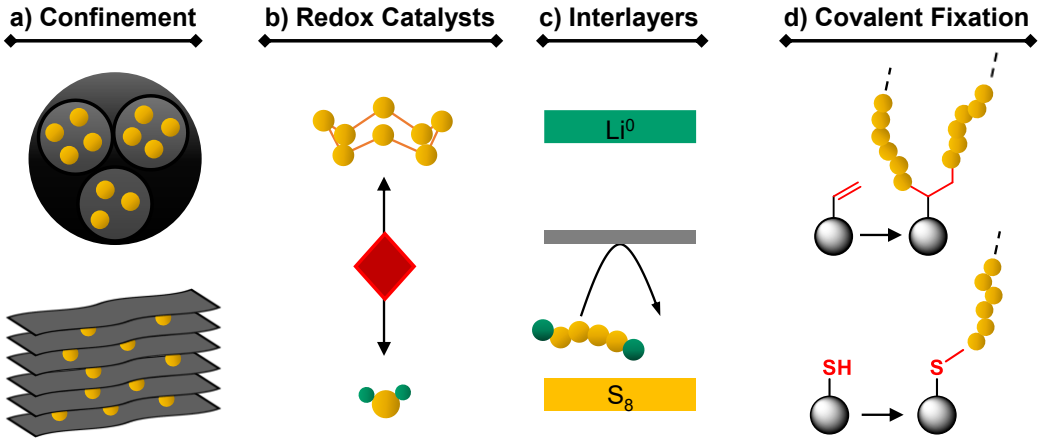
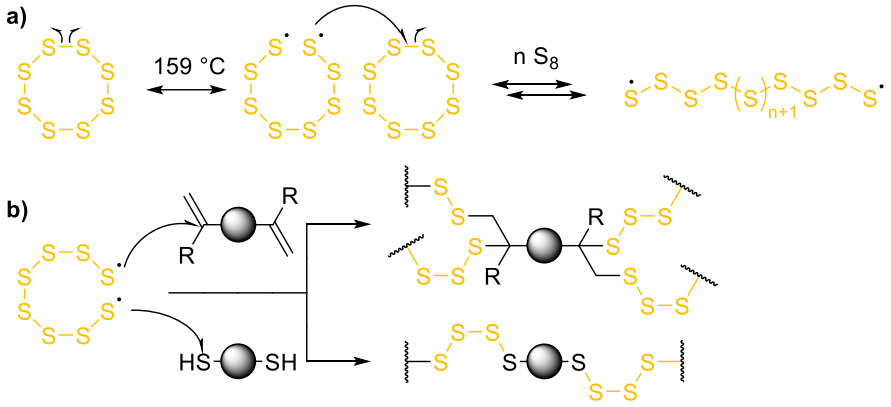


Figure A1.1. Schematic illustration of four common approaches to mitigate the dissolution of lithium polysulfides by (a) physical confinement in porous host materials, (b) addition of redox catalysts to enhance redox kinetics between the charge and discharge products, (c) the use of lithium polysulfide repelling or retaining interlayers, and (d) the covalent fixation sulfur at exemplary functional groups (double bonds or thiols). Illustrations adapted and modified from reference.[19–22]

5.2.1.3 Inverse Vulcanization of Sulfur

Historically, sulfur has found application in the vulcanization of rubbery or elastomeric materials. The process of crosslinking polymers by vulcanization in combination with sulfur was pioneered by Goodyear in 1839 and patented in 1844.[23] Thereby, small amounts of sulfur are used to establish covalent intermolecular connections. The sulfur content varies in the range of 1.8 – 2.5 %, and the common sulfur chain length is 1 – 4 sulfur atoms.[24,25] Elemental sulfur can polymerize to form homopolymers above its floor temperature (T_F) of 159 °C. Homolytic cleavage of eight-membered sulfur rings (S_8) results in radical species inducing a ring-opening polymerization (ROP) reaction (**Scheme A1.1**a). Sulfur homopolymers are thermodynamically unstable and tend to depolymerize at temperatures below T_F to form S_8 rings. The polymeric form of sulfur can be stabilized in sulfur copolymers obtained by inverse vulcanization (**Scheme A1.1**b).[26]

Small amounts of functional organic molecules are used as a comonomer for an excess of elemental sulfur, inverting the proportionality between sulfur and organic constituents compared to classical vulcanization. Possible functional groups include C=C double bonds and thiols, which can be incorporated into various molecular structures. Different experimental procedures have been investigated for the inverse vulcanization reaction. Most protocols require temperatures above the T_F of 159 °C.

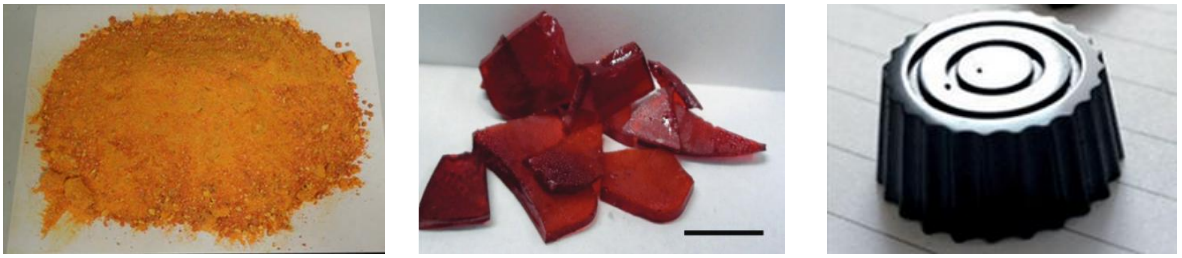


Scheme A1.1. (top) Auto polymerization of sulfur at temperatures above 159 °C. Homolytic cleavage of sulfur bonds generates radical species, which can include the homopolymerization of sulfur. (bottom) The radical species can be used to obtain copolymers in combination with vinyl- or thiol-based comonomers.

Alternative approaches are reported to use lower temperatures, utilizing the auto-initiation of the organic constituent to initiate the copolymerization with sulfur.[27] In other studies, accelerator additives are used, similar to classical vulcanization reactions, to facilitate low-temperature inverse vulcanization.[28,29] **Table A1.1** gives an overview of applied protocols for the inverse vulcanization reaction. Depending on the reaction conditions and the specific combination of sulfur and comonomer the resulting materials can exhibit different properties. The sulfur copolymers can show material properties ranging from highly crosslinked vitrified materials to moldable rubbery elastomers.[30,31]

Table A1.1. Overview of experimental procedures for the inverse vulcanization reaction.

Sulfur content (wt%)	Comonomer	Experimental conditions	Ref
50-90	1,3-DIB	Mixing at 185 °C for a few min, curing at 200 °C for 30 min.	[26]
90	1,3-DIB	Mixing and curing at 130 °C for 2 h under stirring.	[27]
90	1,4-DVB	Mixing at 185 °C, after vitrification, curing at 120 °C for 3 h.	[32]
50	MMA	Additive: Et_2N-CSSNa, curing at 95 °C for 108 h.	[29]
80	PANI-SH	Mixing at 150 °C for 1 h, curing at 170 for 8 h.	[33]
80-95	Allyl-P3HT	Allyl-P3HT added as a solution in *o*DCB at 170 °C, curing for 1 h.	[34]
66	Vinyl-COF	Mixing at 155 °C for 15 h, curing at 200 °C for 10 h.	[35]



10 wt % 1,3-DIB [27] 30 wt % 1,3-DIB [26] 50 wt % DCPD [36]

Figure A1.2. Optical images of sulfur-copolymers at different comonomer concentrations.

5.2.2 Synthesis – Kumada Catalyst Transfer Polymerization

Conjugated polymers are commonly synthesized via metal-catalyzed cross-coupling reactions. Suitable monomer combinations include dibrominated aromatic compounds together with distannylated (Stille), diborylated (Suzuki), or diprotonated (DARP) aromatic compounds. These AA/BB coupling reactions offer limited control over molecular weight, dispersity, and the regioregularity of the polymers. When the same reactions are conducted with asymmetric AB-functionalized monomers, some control over polymer end groups and regioregularity is gained, although high control over molecular weight distribution remains elusive.

Polythiophenes are a class of conjugated polymers exhibiting high charge carrier mobility and versatile modification for different fields of application, including transistors, solar cells, and light-emitting diodes (LEDs).[37] Poly-(3-alkyl-thiophene-2,5-diyl) (P3AT) are most commonly used, due to their good processability and various synthetic protocols with precise control over the polymer microstructure. Mechanistically, the polymers are prepared by individual step-growth-like monomer additions. However, for the polymerization of thiophenes, the development of chain-transfer polymerizations (CTP) allowed a transition from a step-growth to a chain-growth polymerization mechanism for Stille, Suzuki, and Kumada CTP (**Figure A1.3**).[38–40] This work focused on the controlled synthesis of polythiophene derivatives using Kumada catalyst transfer polymerization (KCTP), which will be described in the following.

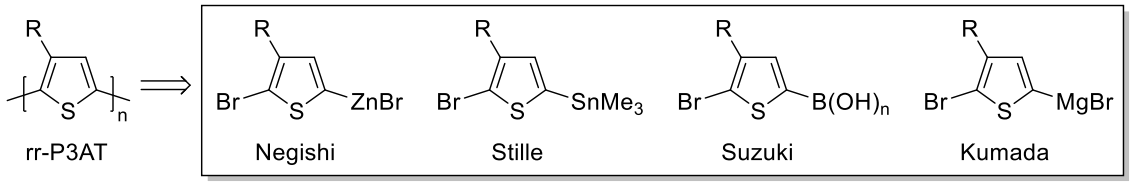
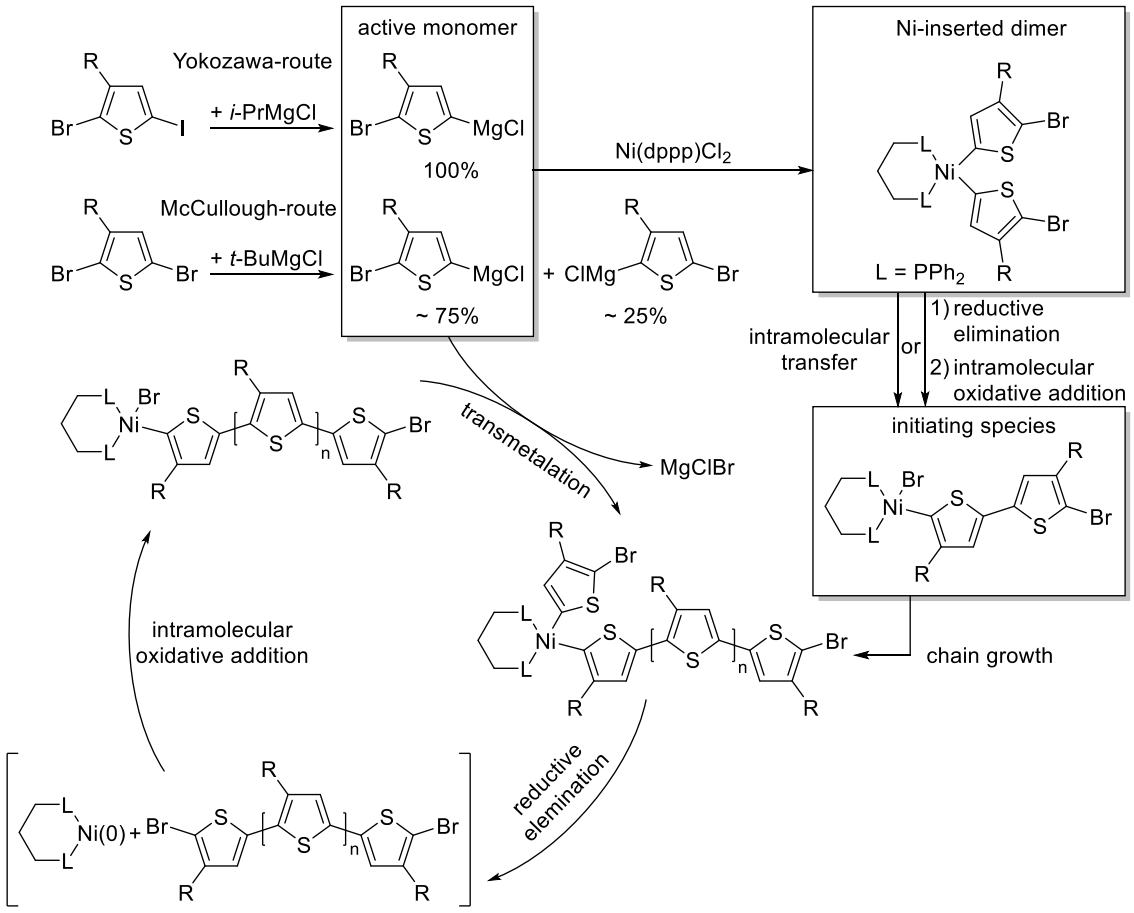


Figure A1.3. Possible monomers for different synthetic routes to regioregular poly(3-alkyl-thiophene-2,5-diyl) (rr-P3AT) based on metal-catalyzed cross-coupling reactions.[38,39,41–44]

The active monomer for a KCTP is a 2-bromo-3-alkyl-5-(bromo-/chloro-magnesio)-thiophene (**Scheme A1.2**). The active monomer is accessible by two different routes, which were described in independent studies in 2004 by Yokozawa and McCollough, respectively.[39,45] A Grignard metathesis (GRIM) of 2,5-halogenated thiophenes results in the formation of the active monomer. For 2,5-dibrominated thiophene, the side chain in the 3-position results in the formation of two GRIM reaction products (Grignard reaction at the 2- or 5-position). Due to steric hindrance for the Grignard product in the 2-position, this species is not incorporated into the polymer chain. In the case of the Yokozawa route, the more reactive iodo-5-position is quantitatively converted to the active monomer species. The polymerization is initiated by the addition of the Nickel-based precatalyst (dichloro(1,3-bis-(diphenylphosphino)-propane)nickel, Ni(dppp)Cl_2). In the initiating step, a transmetallation forms a Ni-inserted dimer with two thiophenes attached at the sterically less hindered 5-position, resulting in a tail-tail coupling in the symmetrical dimer. The subsequent step consists of the reductive elimination of the Ni-catalyst, leading to the formation of a thiophene-thiophene bond and a Ni(0) species. The catalyst stays loosely attached to the π-electron system of the thiophene and migrates to the chain end, often referred to as *ring-walking*. At the chain end, the catalyst is reinserted via an oxidative addition step, yielding a new active Ni(I)Br species available for a subsequent catalytic cycle. Chain growth proceeds following the same three steps of transmetallation, reductive elimination, and final intramolecular oxidative addition. The polymerization is quenched by the addition of a terminating agent to remove the catalyst from the chain end and to introduce defined end groups. Possible quenching agents include, e.g., hydrochloric acid, allyl-magnesium bromide, or ethinyl-magnesium bromide to establish Br/H, Br/-$CHCH_2$, or Br/-CCH end groups.[34,46,47]



Scheme A1.2. Illustration of the Grignard metathesis reaction (GRIM) and the mechanism of the following Kumada catalyst transfer polymerization (KCTP). The GRIM reaction can form the active monomer by two different routes (Yokozawa-route: *i*-PrMgCl; McCullough-route: *t*-BuMgCl). Two equivalents of the active monomer and Ni(dppp)Cl_2 form the initiating species for the polymerization reaction. Chain propagation starts with a transmetalation of the initiating species and the active monomer. Adapted from reference.[48,49]

Various functional groups can be introduced at the 3-position to introduce advanced functionality. Poly(3-(ω-bromohexyl)thiophene) (P3BrHT, **Figure A1.4**a) can be prepared by KCTP and represents a versatile platform for post-polymerization functionalization. Thereby, the polymer side chain can be ω-functionalized with different chemical functional groups **Figure A1.4**b.

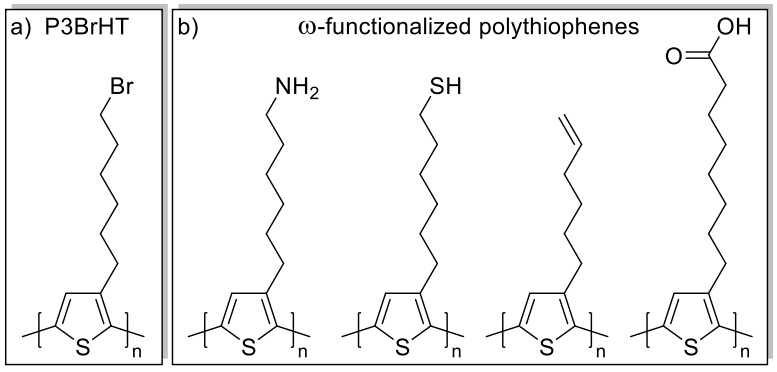


Figure A1.4. (a) P3BrHT as precursor polymer for post-polymerization functionalization (b) with amino-, thiol-, double-bond, or carboxylic acid-functional groups.[50,51]

5.2.3 Research Concept

The main focus of this study is to mitigate the sulfur shuttle effect in lithium-sulfur batteries by covalent fixing of sulfur to polymer-based host materials. To reduce the polysulfide dissolution, sulfur is connected to anchor groups of the host material by inverse vulcanization. During the inverse vulcanization reaction, sulfur is copolymerized with functional groups (e.g., carbon-carbon double bonds) to yield composite materials. Polythiophene-derived materials with pendant double-bond moieties in the side chain are used as organic hosts. The double-bond functionalized polymers are prepared by Kumada-Catalyst Transfer Polymerization (KCTP) and subsequent polymer-analogous functionalization. The anchor group density along the polymer is systematically varied to modulate the polysulfide binding strength and degree of crosslinking. The polythiophene-sulfur copolymers are evaluated as cathode active material in lithium-sulfur batteries. The materials are evaluated based on accessible discharge capacities and capacity retention.

5.2.4 Results and Discussion

5.2.4.1 Monomer Synthesis

Two monomers were used for the preparation of a series of different polythiophene-based homo- and copolymers. 2,5-Dibromo-3-(6-bromohexyl)thiophene was synthesized starting from 3-bromothiophene **1** and 1,6-dibromohexane to yield 3-(6-bromohexyl)thiophene **2**. In a subsequent step, the thiophene core is brominated in 2- and 5-position to yield the monomer **3**. 2,5-dibromo-3-hexylthiophene was commercially available.

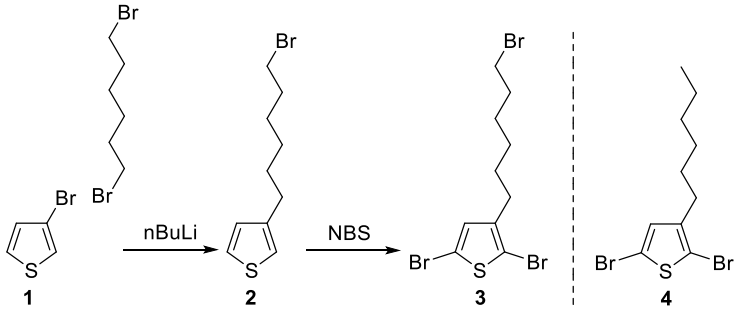


Figure A1.5. Chemical structures of di-bromo-monomers (3) 2,5-dibromo-3-(6-bromohexyl)thiophene (3BrHT) and (4) 2,5-dibromo-3-(6-bromohexyl)thiophene (3HT, commercially available). 3BrHT was synthesized starting from 3-bromothiophene (1). In the first step, the bromo-hexyl side chain is attached by a lithium-halogen exchange reaction, followed by nucleophilic substitution. In the second step, the thiophene ring is brominated in the 2- and 5-position using NBS.

The monomer synthesis can be monitored by ^{1}H NMR spectroscopy (**Figure A1.6**). Compared to 1,6-dibromohexane, the methylene unit adjacent to the thiophene core is upfield shifted from 3.45 ppm to 2.55 ppm. The central methylene units of the hexyl chain also perceive different chemical environments derived from the bromine and thiophene neighbors. Therefore, the corresponding two distinct multiplets split into four signals for the individual methylene units. After the bromination of the thiophene core, only a singlet of the isolated aromatic proton remains.

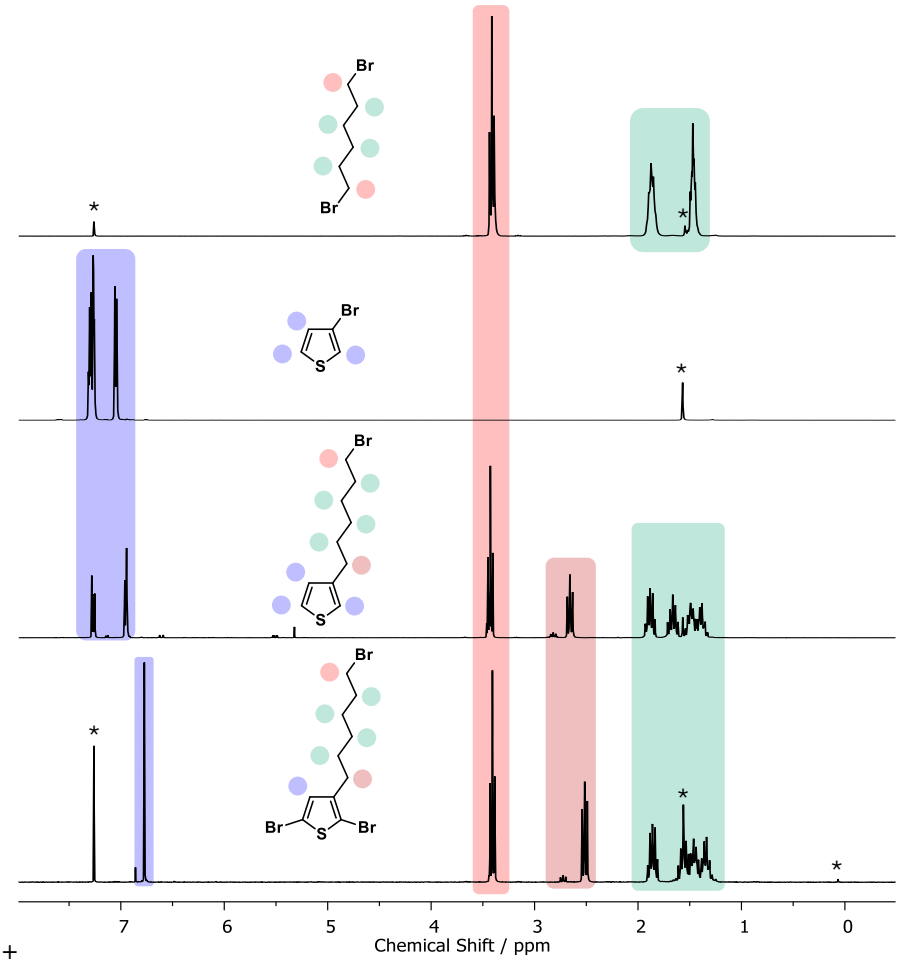


Figure A1.6. ^{1}H NMR spectra of the starting compounds (1,6-dibromohexane and 3-bromothiophene), intermediate products (3-(6-bromohexyl)thiophene) and the final product (2,5-dibromo-3-(6-bromohexyl)thiophene).

5.2.4.2 Polymer Synthesis

The polymers are prepared following the McCoullough route described in **Scheme A1.1**. For the preparation of P3BrHt, the active monomer was generated by a Grignard metathesis reaction (GRIM). Afterwards, the Ni(dppp)Cl_2 catalyst is added to the reaction to initiate and propagate the polymerization. The polymerization was monitored by ^{1}H NMR spectroscopy (**Figure A1.7**). The established polythiophene backbone results in downfield shifts of the aromatic proton and the first methylene unit adjacent to the thiophene core. All peaks show distinct peak broadening.

Similarly, copolymers can be prepared by combining different active monomer species. Depending on the synthetic protocol, gradient or block copolymers can be obtained. Due to the living character of the KCTP, a second monomer can be sequentially added to the reaction mixture to proceed with the polymerization after completion of the first polymer segment. Alternatively, gradient copolymers are commonly obtained when both active monomer species are combined before initiation. The individual monomer reactivities induce a concentration gradient of the individual monomers along the polymer backbone. Here, the active monomer species of 2,5-3-(6-bromohexyl)thiophene and 2,5-hexylthiophene are combined to yield gradient copolymers.

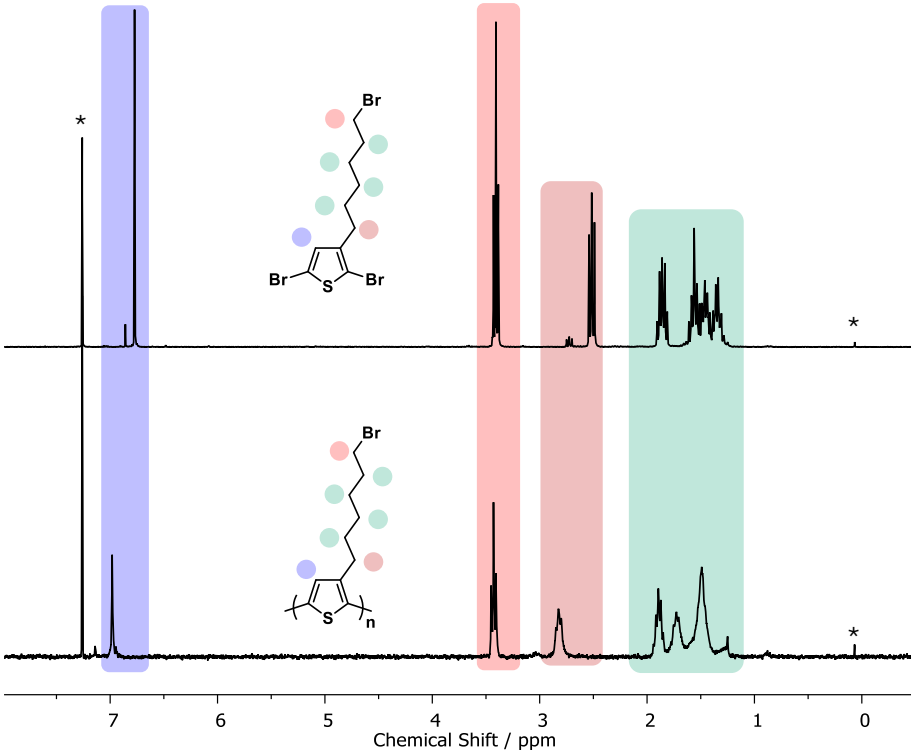


Figure A1.7. ^{1}H NMR spectra of the monomer (2,5-dibromo-3-(6-bromohexyl)thiophene) and the corresponding isolated polymer (poly(3-(6-bromohexyl)thiophene).

5.2.4.3 Polymer-analogous Functionalization

The ω-bromo functional group of the poly(3-(6-bromohexyl)thiophene establishes a platform for further functionalization reactions. In this work, a C=C double bond is established in a two-step process (**Figure A1.8**). At first, the ω-bromo functional group is converted to a ω-iodo functional group in a Finkelstein reaction to introduce a better leaving group for the subsequent elimination reaction toward the double bond.

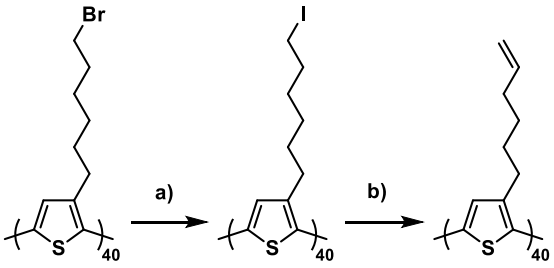


Figure A1.8. Polymer analogous reactions from ω-bromo- to ω-iodo and ω-double-bond-functionalized polythiophenes. Reaction conditions: a) potassium iodide (30 eq.), tetra-n-butylammonium-bromide (0.65 eq.), toluene:water (2:1 v:v), reflux, 1 day; b) KO^{t}Bu (3 eq.), THF, 0 °C, overnight.

The chemical conversion can be monitored by ^{1}H NMR spectroscopy (**Figure A1.9**). The methylene unit adjacent to the ω-bromo functional groups exhibits a chemical shift of around 3.5 ppm. After the Finkelstein reaction, the methylene unit shows an upfield shift to 3.25 ppm. After the elimination reaction, three new peaks arise corresponding to the double bond protons (-C*H*-CH_2) in the region of 5 – 6 ppm and the methylene unit adjacent to the double bond (-CH_2-CH-

CH_2) at 2.15 ppm. More distant methylene units and the aromatic thiophene ring proton are not affected by the chemical conversions in the ω-position.

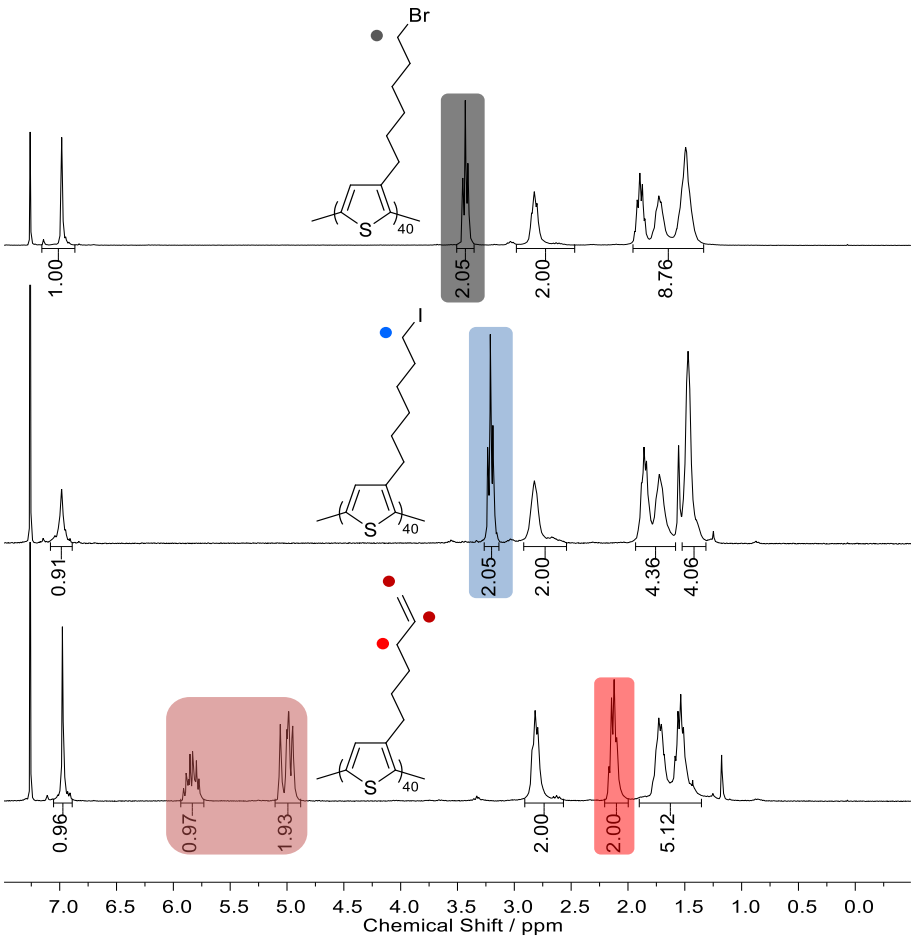


Figure A1.9 ^{1}H NMR spectra of the different stages of the polymer-analogous conversion of the synthesized polymer (poly(3-(6-bromohexyl)thiophene) to poly(3-(6-iodohexyl)thiophene and the double-bond functionalized poly(3-(hex-5-en-1-yl)thiophene. The conversion of the hexane-ω-group can be observed due to the peak shifts from (gray) bromo- to (blue) iodo-, and finally (red) double-bond functionalization. Residual water contents show overlapping peaks at 1.56 ppm, leading to increased peak areas for the aliphatic methylene units.

5.2.4.4 Variation of the Anchor Group Density

Following the general procedure of double-bond functionalization, a variety of gradient copolymers have been prepared. The combination of different molar ratios of 2,5-dibromo-3-hexylthiophene and 2,5-dibromo-3-(6-bromohexyl)thiophene enabled a variation of the double-bond anchor group density. In **Figure A1.10**, the corresponding ^{1}H NMR spectra of the resulting double-bond functionalized polymers are presented. For reference, a P3HT homopolymer (**Figure A1.10**, top) was synthesized, showing no ω-group suitable for covalent anchoring of sulfur. In addition to the P3HeT homopolymer illustrated above, two copolymers with ω-functionalization degrees of 35 mol% and 60 mol% were synthesized.

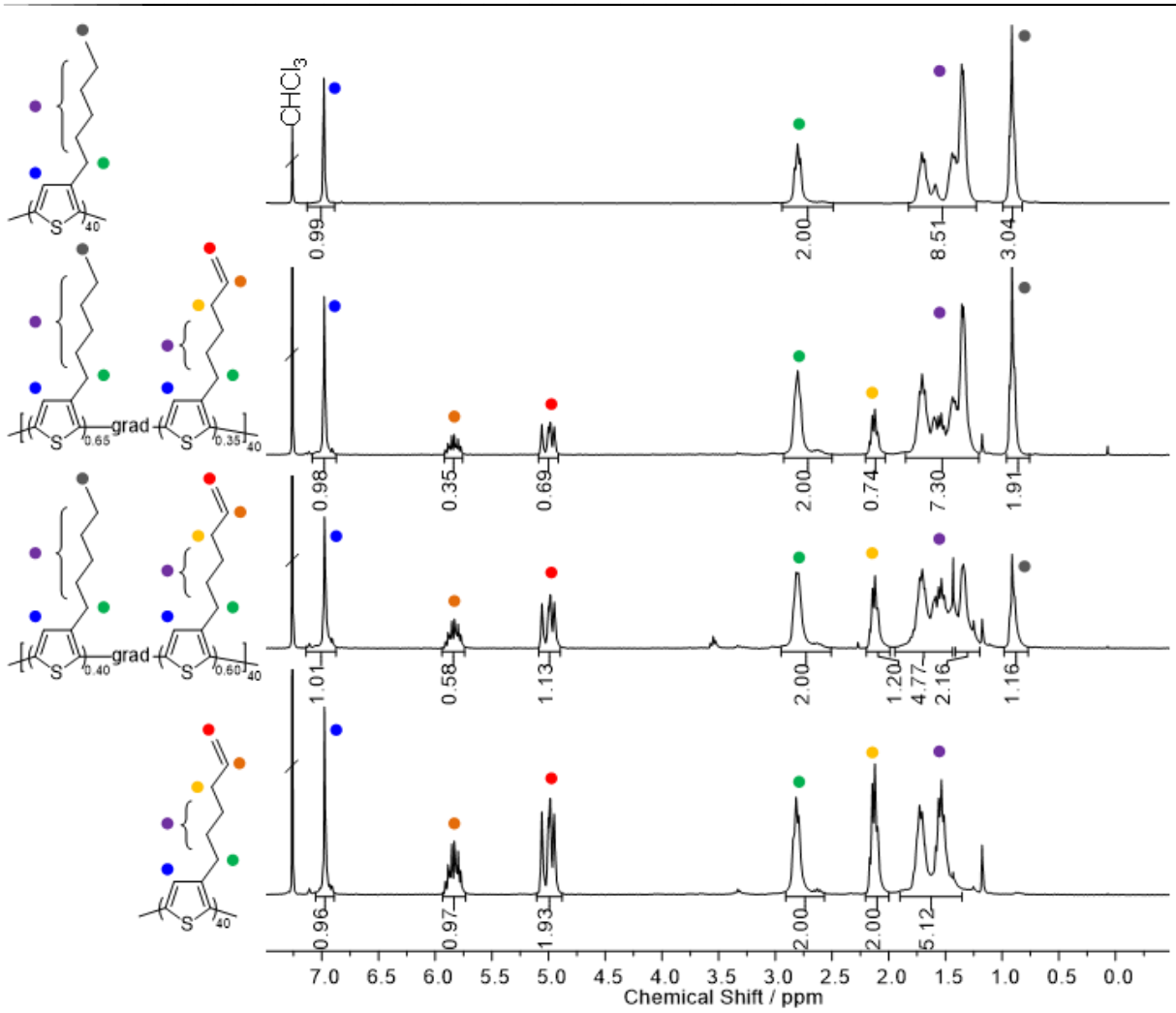


Figure A1.10. ^{1}H NMR spectra of different homo- and copolymers with different double-bond contents in the final polymer. (top) The P3HT homopolymer with only hexane side chains shows a broad peak at around 0.95 ppm corresponding to the (gray) ω-groups (-CH_3) and no additional peaks in the region between 5 – 6 ppm. (bottom) The P3HeT with 100 % double-bond functionalization exhibits two peaks corresponding to the (red, orange) double-bond protons and no peak at 0.95 ppm. The copolymers show contributions of -CH_3 and -$CH{=}CH_2$ ω-groups in accordance with their chemical composition.

P3HeT (100 mol% double-bond functionalization) and P3HT-grad-P3HeT (35 mol% double-bond functionalization) were used in inverse vulcanization reactions with elemental sulfur to yield polymer-co-S_x cathode active materials. The resulting materials are red in color, brittle, highly crosslinked, and insoluble. For the preparation of the composite cathodes, the polythiophene-sulfur copolymers were first ground using a ball mill. Afterwards, additional components (conductive carbon additives, binder, and solvent) were added to the cathode active material to form a cathode slurry. The slurry is homogenized by additional ball milling cycles and subsequently coated onto carbon-coated aluminum current collectors for later use in battery cell fabrication.

5.2.4.5 Battery Cycling Experiments

For battery cycling experiments, lithium-sulfur batteries were fabricated. As anode material, metallic lithium was used. For the electrolyte, a porous Cellgard separator was soaked with an organic liquid electrolyte based on LiTFSI dissolved in a 1:1 (v:v) ratio of 1,3-dioxalone and dimethyl ether. The liquid electrolyte is selected over an SPE-based electrolyte because sulfur

dissolution is much more pronounced in liquid systems. Therefore, the effects of the covalent anchoring of sulfur can be directly observed. **Figure A1.11** shows charge and discharge profiles using P3HeT-co-S_x and elemental sulfur (S_8), respectively. The S_8-based system shows higher accessible charge and discharge capacities. The maximum specific discharge capacity during the first cycle was 910 mAh g^{-1}. However, the capacity is decreasing rapidly, especially during the first cycles. After 10 cycles, the specific capacity was only 800 mAh $g^{-1,}$ and around 600 mAh g^{-1} after 150 cycles. On the other hand, the polythiophene-sulfur-copolymer showed a significantly lower specific capacity of 630 mAh g^{-1}, 610 mAh g^{-1}, and 520 mAh g^{-1} after the same number of cycles.

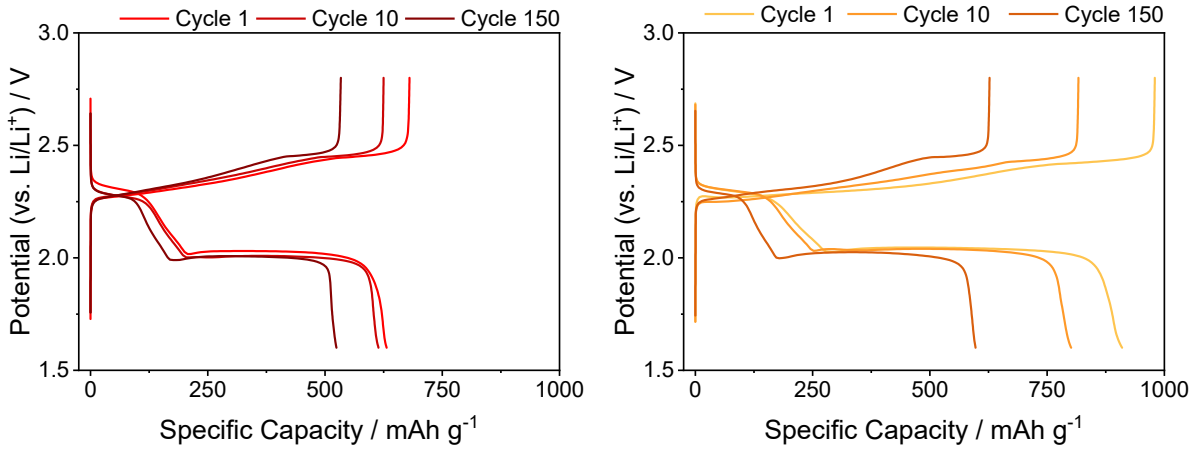


Figure A1.11. Charge and discharge profiles (25 °C, 0.5 C) of lithium-sulfur batteries in a Li|DOL:DME (1:1 v/v)-LiTFSI|S cell configuration. The cathode active material is based on either (left) polythiophene-sulfur copolymer (P3HeT-co-S_x) or (right) elemental sulfur (S_8). The sulfur content of the cathode composite is 48 wt% for both systems.

Despite the overall lower capacities for P3HeT-co-S_x, the system showed good cyclability for up to 450 cycles. Further, the rate of capacity decline was more gradual over the entire cycling experiment. As observed for the reference system and (P3HT-grad-P3HeT)-co-S_x, a decrease in specific capacity is observed during the first formation cycles and subsequently slows down during prolonged cycling. For P3HeT, the high anchor group density could effectively decelerate the dissolution of sulfur.

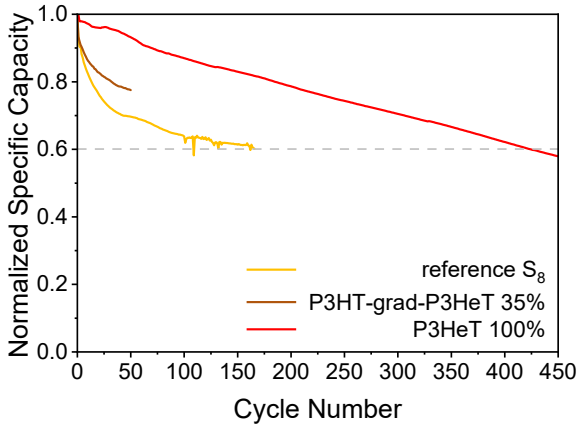


Figure A1.12. Normalized specific capacity for three cathode systems based on (yellow) elemental sulfur, a polythiophene-copolymer with 35 % double-bond functionalization, and (red) a polythiophene with 100 % double-bond functionalization. Batteries using the cathode systems based on P3HT-grad-P3HeT showed cycling instabilities and overcharging after 50 cycles.

5.3 References – Appendix

(1) Yoshino, A.; Sanechika, K.; Nakajima, T. Secondary Battery. US4668595A, May 26, 1987. https://patents.google.com/patent/US4668595A/en (accessed 2025-06-15).

(2) Nemeth, T.; Schröer, P.; Kuipers, M.; Sauer, D. U. Lithium Titanate Oxide Battery Cells for High-Power Automotive Applications – Electro-Thermal Properties, Aging Behavior and Cost Considerations. *Journal of Energy Storage* **2020**, *31*, 101656. https://doi.org/10.1016/j.est.2020.101656.

(3) Besenhard, J. O.; Eichinger, G. High Energy Density Lithium Cells: Part I. Electrolytes and Anodes. *Journal of Electroanalytical Chemistry and Interfacial Electrochemistry* **1976**, *68* (1), 1–18. https://doi.org/10.1016/S0022-0728(76)80298-7.

(4) Ma, D.; Cao, Z.; Hu, A. Si-Based Anode Materials for Li-Ion Batteries: A Mini Review. *Nano-Micro Lett.* **2014**, *6* (4), 347–358. https://doi.org/10.1007/s40820-014-0008-2.

(5) Whittingham, M. S. Chemistry of Intercalation Compounds: Metal Guests in Chalcogenide Hosts. *Progress in Solid State Chemistry* **1978**, *12* (1), 41–99. https://doi.org/10.1016/0079-6786(78)90003-1.

(6) Mizushima, K.; Jones, P. C.; Wiseman, P. J.; Goodenough, J. B. LixCoO2 (o<x<-1): A New Cathode Material for Batteries of High Energy Density. *Materials Research Bulletin* **1980**, *15* (6), 783–789. https://doi.org/10.1016/0025-5408(80)90012-4.

(7) Xia, Y.; Zheng, J.; Wang, C.; Gu, M. Designing Principle for Ni-Rich Cathode Materials with High Energy Density for Practical Applications. *Nano Energy* **2018**, *49*, 434–452. https://doi.org/10.1016/j.nanoen.2018.04.062.

(8) Majumder, S. B.; Nieto, S.; Katiyar, R. S. Synthesis and Electrochemical Properties of LiNio.8o(Coo.2o–xAlx)O2 (X=o.o and o.o5) Cathodes for Li Ion Rechargeable Batteries. *Journal of Power Sources* **2006**, *154* (1), 262–267. https://doi.org/10.1016/j.jpowsour.2005.03.186.

(9) Ohzuku, T.; Takeda, S.; Iwanaga, M. Solid-State Redox Potentials for Li[Me1/2Mn3/2]O4 (Me: 3d-Transition Metal) Having Spinel-Framework Structures: A Series of 5 Volt Materials for Advanced Lithium-Ion Batteries. *Journal of Power Sources* **1999**, *81–82*, 90–94. https://doi.org/10.1016/S0378-7753(99)00246-3.

(10) Whittingham, M. S. History, Evolution, and Future Status of Energy Storage. *Proceedings of the IEEE* **2012**, *100* (Special Centennial Issue), 1518–1534. https://doi.org/10.1109/JPROC.2012.2190170.

(11) Yamin, H.; Peled, E. Electrochemistry of a Nonaqueous Lithium/Sulfur Cell. *Journal of Power Sources* **1983**, *9* (3), 281–287. https://doi.org/10.1016/0378-7753(83)87029-3.

(12) *The Lithium Air Battery: Fundamentals*; Imanishi, N., Luntz, A. C., Bruce, P., Eds.; Springer New York: New York, NY, 2014. https://doi.org/10.1007/978-1-4899-8062-5.

(13) Jr, D. T. H.; Balsara, N. P. Polymer Electrolytes. *Annual Review of Materials Research* **2013**, *43* (Volume 43, 2013), 503–525. https://doi.org/10.1146/annurev-matsci-071312-121705.

(14) Cheng, P.; Zhang, H.; Ma, Q.; Feng, W.; Yu, H.; Huang, X.; Armand, M.; Zhou, Z. Highly Salt-Concentrated Electrolyte Comprising Lithium Bis(Fluorosulfonyl)Imide and 1,3-Dioxolane-Based Ether Solvents for 4-V-Class Rechargeable Lithium Metal Cell. *Electrochimica Acta* **2020**, *363*, 137198. https://doi.org/10.1016/j.electacta.2020.137198.

(15) Erabhoina, H.; Rosenbach, D.; Mohanraj, J.; Thelakkat, M. Solid Polymer Nanocomposite Electrolytes with Improved Interface Properties towards Lithium Metal Battery Application at Room Temperature. *Electrochimica Acta* **2021**, *387*, 138455. https://doi.org/10.1016/j.electacta.2021.138455.

(16) Rosenbach, D.; Krimalowski, A.; Erabhoina, H.; Thelakkat, M. Solid Polymer Electrolytes from Polyesters with Diester Sidechains for Lithium Metal Batteries. *Journal of Materials Chemistry A* **2022**, *10* (16), 8932–8947. https://doi.org/10.1039/D2TA00800A.

(17) Liu, Q.; Geng, Z.; Han, C.; Fu, Y.; Li, S.; He, Y.; Kang, F.; Li, B. Challenges and Perspectives of Garnet Solid Electrolytes for All Solid-State Lithium Batteries. *Journal of Power Sources* **2018**, *389*, 120–134. https://doi.org/10.1016/j.jpowsour.2018.04.019.

(18) Kamaya, N.; Homma, K.; Yamakawa, Y.; Hirayama, M.; Kanno, R.; Yonemura, M.; Kamiyama, T.; Kato, Y.; Hama, S.; Kawamoto, K.; Mitsui, A. A Lithium Superionic Conductor. *Nature Mater* **2011**, *10* (9), 682–686. https://doi.org/10.1038/nmat3066.

(19) Su, Y.-S.; Manthiram, A. A Facile in Situ Sulfur Deposition Route to Obtain Carbon-Wrapped Sulfur Composite Cathodes for Lithium–Sulfur Batteries. *Electrochimica Acta* **2012**, *77*, 272–278. https://doi.org/10.1016/j.electacta.2012.06.002.

(20) Jayaprakash, N.; Shen, J.; Moganty, S. S.; Corona, A.; Archer, L. A. Porous Hollow Carbon@sulfur Composites for High-Power Lithium-Sulfur Batteries. *Angewandte Chemie International Edition in English* **2011**, 50 (26), 5904–5908. https://doi.org/10.1002/anie.201100637.

(21) Su, Y.-S.; Fu, Y.; Manthiram, A. Self-Weaving Sulfur-Carbon Composite Cathodes for High Rate Lithium-Sulfur Batteries. *Physical chemistry chemical physics : PCCP* **2012**, *14* (42), 14495–14499. https://doi.org/10.1039/c2cp42796f.

(22) Fang, R.; Xu, J.; Wang, D.-W. Covalent Fixing of Sulfur in Metal–Sulfur Batteries. *Energy & Environmental Science* **2020**, *13* (2), 432–471. https://doi.org/10.1039/c9ee03408k.

(23) Charles Goodyear. Improvement in India-Rubber Fabrics. 3633, 1844.

(24) Biederbick, K. *Kunststoffe: kurz und bündig*, unveränd. Nachdr. d. 4., neubearb. u. erw. Aufl. 1977.; Kamprath-Reihe Kurz und bündig Technik; Vogel: Würzburg, 1983.

(25) Akiba, M.; Hashim, A. S. Vulcanization and Crosslinking in Elastomers. *Progress in Polymer Science* **1997**, *22* (3), 475–521. https://doi.org/10.1016/S0079-6700(96)00015-9.
(26) Chung, W. J.; Griebel, J. J.; Kim, E. T.; Yoon, H.; Simmonds, A. G.; Ji, H. J.; Dirlam, P. T.; Glass, R. S.; Wie, J. J.; Nguyen, N. A.; Guralnick, B. W.; Park, J.; Somogyi, A.; Theato, P.; Mackay, M. E.; Sung, Y.-E.; Char, K.; Pyun, J. The Use of Elemental Sulfur as an Alternative Feedstock for Polymeric Materials. *Nature chemistry* **2013**, *5* (6), 518–524. https://doi.org/10.1038/nchem.1624.
(27) Griebel, J. J.; Li, G.; Glass, R. S.; Char, K.; Pyun, J. Kilogram Scale Inverse Vulcanization of Elemental Sulfur to Prepare High Capacity Polymer Electrodes for Li-S Batteries. *Journal of Polymer Science Part A: Polymer Chemistry* **2015**, *53* (2), 173–177. https://doi.org/10.1002/pola.27314.
(28) Halls, D. J. The Properties of Dithiocarbamates A Review. *Mikrochim Acta* **1969**, *57* (1), 62–77. https://doi.org/10.1007/BF01216666.
(29) Zhang, B.; Gao, H.; Yan, P.; Petcher, S.; Hasell, T. Inverse Vulcanization below the Melting Point of Sulfur. *Materials Chemistry Frontiers* **2020**, *4* (2), 669–675. https://doi.org/10.1039/C9QM00606K.
(30) Orme, K.; Fistrovich, A. H.; Jenkins, C. L. Tailoring Polysulfide Properties through Variations of Inverse Vulcanization. *Macromolecules* **2020**, *53* (21), 9353–9361. https://doi.org/10.1021/acs.macromol.0c01932.
(31) Yan, P.; Zhao, W.; Tonkin, S. J.; Chalker, J. M.; Schiller, T. L.; Hasell, T. Stretchable and Durable Inverse Vulcanized Polymers with Chemical and Thermal Recycling. *Chem. Mater.* **2022**, *34* (3), 1167–1178. https://doi.org/10.1021/acs.chemmater.1c03662.
(32) Gomez, I.; Mecerreyes, D.; Blazquez, J. A.; Leonet, O.; Ben Youcef, H.; Li, C.; Gómez-Cámer, J. L.; Bondarchuk, O.; Rodriguez-Martinez, L. Inverse Vulcanization of Sulfur with Divinylbenzene: Stable and Easy Processable Cathode Material for Lithium-Sulfur Batteries. *Journal of Power Sources* **2016**, *329*, 72–78. https://doi.org/10.1016/j.jpowsour.2016.08.046.
(33) Zeng, S.; Li, L.; Xie, L.; Zhao, D.; Wang, N.; Chen, S. Conducting Polymers Crosslinked with Sulfur as Cathode Materials for High-Rate, Ultralong-Life Lithium-Sulfur Batteries. *ChemSusChem* **2017**, *10* (17), 3378–3386. https://doi.org/10.1002/cssc.201700913.
(34) Oschmann, B.; Park, J.; Kim, C.; Char, K.; Sung, Y.-E.; Zentel, R. Copolymerization of Polythiophene and Sulfur To Improve the Electrochemical Performance in Lithium–Sulfur Batteries. *Chemistry of Materials* **2015**, *27* (20), 7011–7017. https://doi.org/10.1021/acs.chemmater.5b02317.
(35) Chen, J.-M.; Duan, H.; Kong, Y.; Tian, B.; Ning, G.-H.; Li, D. Improving Lithium–Sulfur Batteries' Performance via Inverse Vulcanization of Vinylene-Linked Covalent Organic Frameworks. *Energy Fuels* **2022**, *36* (11), 5998–6004. https://doi.org/10.1021/acs.energyfuels.2c01035.
(36) Parker, D. J.; Jones, H. A.; Petcher, S.; Cervini, L.; Griffin, J. M.; Akhtar, R.; Hasell, T. Low Cost and Renewable Sulfur-Polymers by Inverse Vulcanisation, and Their Potential for Mercury Capture. *J. Mater. Chem. A* **2017**, *5* (23), 11682–11692. https://doi.org/10.1039/C6TA09862B.
(37) Amna, B.; Siddiqi, H. M.; Hassan, A.; Ozturk, T. Recent Developments in the Synthesis of Regioregular Thiophene-Based Conjugated Polymers for Electronic and Optoelectronic Applications Using Nickel and Palladium-Based Catalytic Systems. *RSC Adv 10* (8), 4322–4396. https://doi.org/10.1039/c9ra09712k.
(38) Qiu, Y.; Mohin, J.; Tsai, C.-H.; Tristram-Nagle, S.; Gil, R. R.; Kowalewski, T.; Noonan, K. J. T. Stille Catalyst-Transfer Polycondensation Using Pd-PEPPSI-IPr for High-Molecular-Weight Regioregular Poly(3-Hexylthiophene). *Macromolecular Rapid Communications* **2015**, *36* (9), 840–844. https://doi.org/10.1002/marc.201500030.
(39) Yokoyama, A.; Miyakoshi, R.; Yokozawa, T. Chain-Growth Polymerization for Poly(3-Hexylthiophene) with a Defined Molecular Weight and a Low Polydispersity. *Macromolecules* **2004**, *37* (4), 1169–1171. https://doi.org/10.1021/ma0353960.
(40) Yokozawa, T.; Suzuki, R.; Nojima, M.; Ohta, Y.; Yokoyama, A. Precision Synthesis of Poly(3-Hexylthiophene) from Catalyst-Transfer Suzuki–Miyaura Coupling Polymerization. *Macromolecular Rapid Communications* **2011**, *32* (11), 801–806. https://doi.org/10.1002/marc.201100037.
(41) King, A. O.; Okukado, N.; Negishi, E. Highly General Stereo-, Regio-, and Chemo-Selective Synthesis of Terminal and Internal Conjugated Enynes by the Pd-Catalysed Reaction of Alkynylzinc Reagents with Alkenyl Halides. *J. Chem. Soc., Chem. Commun.* **1977**, No. 19, 683–684. https://doi.org/10.1039/C39770000683.
(42) Chen, T. A.; Rieke, R. D. The First Regioregular Head-to-Tail Poly(3-Hexylthiophene-2,5-Diyl) and a Regiorandom Isopolymer: Nickel versus Palladium Catalysis of 2(5)-Bromo-5(2)-(Bromozincio)-3-Hexylthiophene Polymerization. *J. Am. Chem. Soc.* **1992**, *114* (25), 10087–10088. https://doi.org/10.1021/ja00051a066.
(43) Carrillo, J. A.; Ingleson, M. J.; Turner, M. L. Thienyl MIDA Boronate Esters as Highly Effective Monomers for Suzuki–Miyaura Polymerization Reactions. *Macromolecules* **2015**, *48* (4), 979–986. https://doi.org/10.1021/ma502542g.
(44) McCullough, R. D.; Lowe, R. D.; Jayaraman, M.; Anderson, D. L. Design, Synthesis, and Control of Conducting Polymer Architectures: Structurally Homogeneous Poly(3-Alkylthiophenes). *J. Org. Chem.* **1993**, *58* (4), 904–912. https://doi.org/10.1021/jo00056a024.
(45) Sheina, E. E.; Liu, J.; Iovu, M. C.; Laird, D. W.; McCullough, R. D. Chain Growth Mechanism for Regioregular Nickel-Initiated Cross-Coupling Polymerizations. *Macromolecules* **2004**, *37* (10), 3526–3528. https://doi.org/10.1021/ma0357063.
(46) Jeffries-El, M.; Sauvé, G.; McCullough, R. D. Facile Synthesis of End-Functionalized Regioregular Poly(3-Alkylthiophene)s via Modified Grignard Metathesis Reaction. *Macromolecules* **2005**, *38* (25), 10346–10352. https://doi.org/10.1021/ma051096q.

(47) Reichstein, P. M.; Gödrich, S.; Papastavrou, G.; Thelakkat, M. Influence of Composition of Amphiphilic Double-Crystalline P3HT-b-PEG Block Copolymers on Structure Formation in Aqueous Solution. *Macromolecules* **2016**, *49* (15), 5484–5493. https://doi.org/10.1021/acs.macromol.6b01305.
(48) Lohwasser, R. H.; Thelakkat, M. Toward Perfect Control of End Groups and Polydispersity in Poly(3-Hexylthiophene) via Catalyst Transfer Polymerization. *Macromolecules* **2011**, *44* (9), 3388–3397. https://doi.org/10.1021/ma200119s.
(49) Verswyvel, M.; Monnaie, F.; Koeckelberghs, G. AB Block Copoly(3-Alkylthiophenes): Synthesis and Chiroptical Behavior. *Macromolecules* **2011**, *44* (24), 9489–9498. https://doi.org/10.1021/ma2021503.
(50) Zhai, L.; Pilston, R. L.; Zaiger, K. L.; Stokes, K. K.; McCullough, R. D. A Simple Method to Generate Side-Chain Derivatives of Regioregular Polythiophene via the GRIM Metathesis and Post-Polymerization Functionalization. *Macromolecules* **2003**, *36* (1), 61–64. https://doi.org/10.1021/ma0255884.
(51) Miyanishi, S.; Tajima, K.; Hashimoto, K. Morphological Stabilization of Polymer Photovoltaic Cells by Using Cross-Linkable Poly(3-(5-Hexenyl)Thiophene). *Macromolecules* **2009**, *42* (5), 1610–1618. https://doi.org/10.1021/ma802839a.

Danksagung

few can foresee whither their road will lead them, till they come to its end – J.R.R Tolkien

Am Ende dieses Weges stehe ich nun – dankbar für all die Weggefährtinnen und Weggefährten, denen ich unterwegs begegnet bin, die mich in unterschiedlichen Abschnitten begleitet haben und mich auf individuelle Art und Weise unterstützt haben und so maßgeblich zum Entstehen dieser Arbeit beigetragen haben.

An erster Stelle möchte ich mich bei meinem Doktorvater **Prof. Dr. Mukundan Thelakkat** für sein Vertrauen und seine Unterstützung in mich und meine Ideen bedanken. Seit deiner Ringvorlesung während meines Bachelors war ich fasziniert von deiner Art der Forschung und bin froh, dass ich meinen Weg gemeinsam mit dir bis zur Promotion beschreiten durfte. Du warst stets mit offenem Ohr, aber auch Herz für mich und meine wissenschaftliche Arbeit da, und hast mich in vielen Diskussionen, mit fundierten Ideen und durch kritisches Fragen auf dem Weg gehalten.

Der gesamten Makromolekularen Chemie 1 danke ich für das angenehme Arbeitsklima und die Unterstützung über die letzten zehn Jahre, welche ich bei Praktika und Abschlussarbeiten genießen konnte. Ein großer Dank geht an **Dr. Christian Neuber** und **Dr. Reiner Giesa**, sowie an die Technikerinnen **Martina Fried**, **Jutta Failner**, **Sandra Opel** und **Rika Schneider** für ihre vielfältige technische, methodische und chemische Unterstützung. Ich danke **Philip Schmode**, **Florian Meichsner**, **Julian Hungenberg** und **Sebastian Städter** für ihren Einsatz und Kampf mit der GPC und der Messung meiner Proben. Auch danke ich **Alexander Kern**, der bei allen infrastrukturellen Problemen eine Lösung parat hatte. Ein besonderer Dank gilt außerdem **Petra Weiss** und **Christina Frank**, die stets den Überblick über administrative und bürokratische Hürden hatten und mir bei deren Überwindung geholfen haben.

Ein großer Dank gilt der gesamten AFUPO Gruppe für den familiären Umgang während der Arbeit und den zahlreichen Aktivitäten abseits des Labors. Meinen Mitstreitern der Batterieforschung gilt dabei ein großer Dank für die gegenseitige Unterstützung, lange konstruktive Diskussionsrunden, Hilfe bei Problemen und das Teilen von Erfahrungswerten, insbesondere danke ich **Dr. Dominic Rosenbach** und **Dr. Alexander Krimalowski** aber auch **Dr. Harimohan Erabhoina und Dr. Hubertus Burchart-Tofaute**. Darüber hinaus war meine Zeit in der AFUPO-Exklave B6 geprägt von einem konstruktiven Syntheseaustausch, helfenden Händen, guten Ideen, hervorragenden Kaffeespezialitäten und einem Hauch Anarchie, danke **Dr. Gert Krauss**, **Dr. Pankaj Dharpure**, **Dr. Labeesh Kumar** und **Dr. Mahima Goel**. Mein besonderer Dank gilt zudem **Dr. Andreas Erhardt** und **Julian Hungenberg**, den beiden zuletzt verbliebenen Wegbegleitern, für euren kollegialen und freundschaftlichen Zusammenhalt, der mich durch diese letzte Etappe getragen hat.

Ich möchte mich außerdem bei meinen Praktikanten, HiWis und Masteranden bedanken: **Tamino Rössler**, **Bastian Treiber**, **Leo Gerschmann**, **Markus Dietel**, **Marcel Sticher** und **Gabriele Caputo** für ihre tatkräftige Unterstützung bei der Synthese, eure Mühen mit meinen Synthesevorschriften und dafür, dass euch fehlgeschlagenen Synthesen nicht entmutigt haben. Besonders bei **Markus Dietel**, der in vielen Projekten dieser Arbeit mitgewirkt hat. Ich hoffe, ich konnte euch im Gegenzug etwas für euren eigenen Weg mitgeben.

Meine Zeit in Bayreuth wurde von vielen großartigen Menschen bereichert und ist durch diese zu einem unvergesslichen Abschnitt meines Lebens geworden. Mit euch (in alphabetischer Reihenfolge) **Alexander G.**, **Alexander Ke.**, **Alexander Kr.**, **Andreas**, **Dennis**, **Dominic**, **Felix**, **Florian, Gert**, **Jonas**, **Julian**, **Marina**, **Simon**, **Teresa** und **Timon** war die Zeit geprägt von gemeinsamen Momenten bei Bouldersessions, Weinproben, Buddakuang, Zwiwwelhaxe und Spieleabenden, aber auch motivierenden Gesprächen und kritischen Diskussionen. Danke für die Zeit mit euch.

Außerdem möchte ich mich bei meinen Kooperationspartnern **Prof. Dr. Suhrit Ghosh**, **Krishna Dan**, und **Atish Nag** der Indian Association for the Cultivation of Science in Kolkata für die Zusammenarbeit und die gemeinsame Veröffentlichung bedanken.

Für die Förderung meines Promotionsvorhabens danke ich der Deutschen Bundesstiftung Umwelt (DBU), die mich mit umfassender finanzieller und ideeller Förderung unterstützte, und auf Seminaren und Tagungen stets mit vielfältigen und inspirierenden Themen und Menschen in Kontakt brachte. Insbesondere bei meiner Betreuerin **Dr. Katrin Anneser** bedanke ich mich für die persönliche und stets interessierte Betreuung.

Der größte Dank geht an die wichtigsten Menschen in meinem Leben. **Meine Familie**. Allen voran danke ich meinen Eltern, **Kerstin** und **Edelbert**. Ihr habt mir erst ermöglicht diesen Weg anzutreten und ohne euch wäre ich nicht derjenige, der ich heute bin. Auch wenn es für euch reine Selbstverständlichkeit ist, danke ich euch dennoch von Herzen für euren bedingungslosen Rückhalt, eure Unterstützung und dafür, dass ihr über die gesamte Zeit und den langen Weg immer an meiner Seite standet. Außerdem danke ich meinem Bruder **Julian** als gleichgesinnten Wegbegleiter. Danke für unsere brüderliche Freundschaft, deine interessierte und begeisterungsfähige Art, sowie deine inspirierenden Fragen und Impulse. Danke auch an **Frank**, **Doreen** und meine gesamte **Schwiegerfamilie**, dass ihr immer mit mir mitgefiebert habt.

Mein allerherzlichster Dank gilt meiner Frau **Sandra**. Seit nunmehr fast zehn Jahren gehen wir gemeinsam unseren Weg, du motivierst mich, erdest mich und bereicherst mein Leben. Auch wenn dieser Abschnitt nun zu Ende geht, blicke ich mit Freude jedem weiteren Tag entgegen, den wir von hier an zusammen weitergehen. Ich freue mich auf alles, was die Zukunft für uns bereithält, auf wunderbare gemeinsame Momente und die Gewissheit, dich immer an meiner Seite zu haben. *Danke für alles*!

Eidesstattliche Versicherungen und Erklärung

(§ 9 Satz 2 Nr. 3 PromO BayNAT)
Hiermit versichere ich eidesstattlich, dass ich die Arbeit selbstständig verfasst und keine anderen als die von mir angegebenen Quellen und Hilfsmittel benutzt habe
(vgl. Art. 97 Abs. 1 Satz 8 BayHIG).

(§ 9 Satz 2 Nr. 3 PromO BayNAT)
Hiermit erkläre ich, dass ich die Dissertation nicht bereits zur Erlangung eines akademischen Grades eingereicht habe und dass ich nicht bereits diese oder eine gleichartige Doktorprüfung endgültig nicht bestanden habe.

(§ 9 Satz 2 Nr. 4 PromO BayNAT)
Hiermit erkläre ich, dass ich Hilfe von gewerblichen Promotionsberatern bzw. –vermittlern oder ähnlichen Dienstleistern weder bisher in Anspruch genommen habe noch künftig in Anspruch nehmen werde.

(§ 9 Satz 2 Nr. 7 PromO BayNAT)
Hiermit erkläre ich mein Einverständnis, dass die elektronische Fassung meiner Dissertation unter Wahrnehmung meiner Urheberrechte und des Datenschutzes einer gesonderten Überprüfung unterzogen werden kann.

(§ 9 Satz 2 Nr. 8 PromO BayNAT)
Hiermit erkläre ich mein Einverständnis, dass bei Verdacht wissenschaftlichen Fehlverhaltens Ermittlungen durch universitätsinterne Organe der wissenschaftlichen Selbstkontrolle stattfinden können.

Ort, Datum, Unterschrift